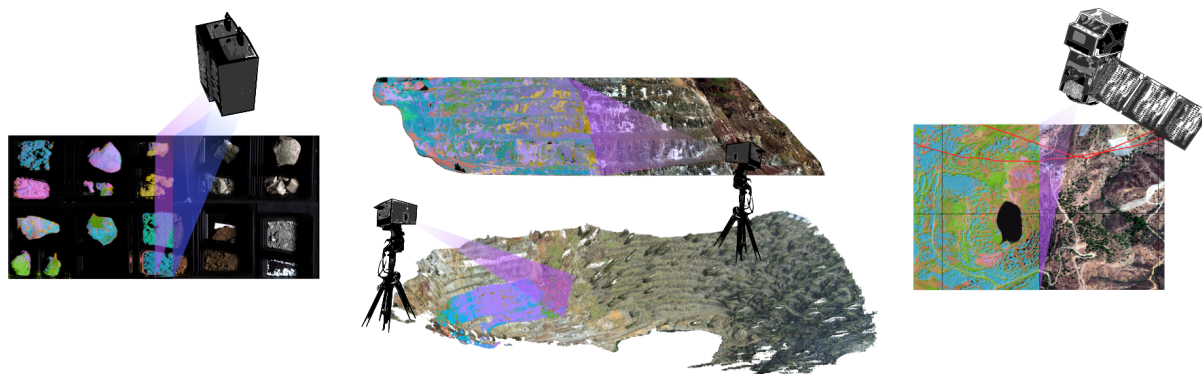


Hybrid imaging spectroscopy approaches for open pit mining

-

Applications for virtual mine face geology



Friederike Magdalena Koerting

Dissertation for the degree

"Doctor rerum naturalium"

(Dr. rer. nat.)

in Geosciences

Submitted at the Faculty of Science
of the University of Potsdam

Carried out at the German Research Centre of
Geosciences GFZ Potsdam

Disputed 04th of March, 2021, Potsdam



This work is licensed under a Creative Commons License:
Attribution 4.0 International.
This does not apply to quoted content from other authors.
To view a copy of this license visit
<https://creativecommons.org/licenses/by/4.0>

Friederike Koerting

*Hybrid imaging spectroscopy approaches for open pit mining
- Applications for virtual mine face geology*
Doctoral Thesis

Supervisors:

apl. Prof. Dr. Uwe Altenberger
apl. Prof. Dr. Helmut Echter

Referees:

apl. Prof. Dr. Uwe Altenberger – University of Potsdam, Germany
Prof. Dr. Konstantinos Nikolakopoulos – University of Patras, Greece
Dr. Christian Rogass – Helmholtz Centre for Environmental Research UFZ, Leipzig, Germany
Submitted 28th of October 2020, Berlin

Published online on the
Publication Server of the University of Potsdam:
<https://doi.org/10.25932/publishup-49909>
<https://nbn-resolving.org/urn:nbn:de:kobv:517-opus4-499091>

Declaration of Independence

I hereby declare that this PhD thesis is the product of my own independent work. All content and ideas drawn directly or indirectly from external sources are indicated as such. The thesis has not been submitted to any other examining body and has not been published.

Berlin,

Acknowledgements

My sincere gratitude goes to a number of people who have contributed advice, provided support for this project and encouraged and supported me to keep going. First of all, I want to thank my supervisors apl. Prof. Dr. Uwe Altenberger and apl. Prof. Dr. Helmut Echlert for their support during this work and the opportunity to do this project. I want to thank my colleagues at the German Research Centre for Geosciences (GFZ), Dr. Christian Rogaß, Dr. Christian Mielke, Nicole Köllner, Friederike Klos, Constantin Hildebrand, Helge Dämpfling, Agnieszka Kuras and Marcel Horning for inspiring and fruitful discussions. My thank also goes to my office mates Magda and Freddy without whom and our shared break dog-walks and associated venting I might have thrown in the towel early on. It was a pleasure, to work in such a social and productive working group. I also remember fondly our numerous field works starting as early as in 2012 for me, successful measurement campaigns together all over Europe in a variety of projects and shared social events and conferences.

I would like to thank Chris Hadjigeorgiou, Ioulia Georgiadou and their colleagues from the Geological Survey Department of the Republic of Cyprus (GSD) for their kind help, advise and for accompanying me on the field work in March 2018 in the Republic of Cyprus. Without their help I would not have been able to locate the proper, inactive mine site and access them. I've learned a lot due to their support and am grateful for the time they invested in me during the field work. Same goes for the companies from Brazil that provided me with the samples from active mine site in the Minas Gerais district and my colleague Bertram Heinze from InnovBrazil who so kindly provided the contact & the samples and with whom I visited one of the mine sites in October 2019. Thank you for your kind encouragement and support over the last years. My thank goes to Christina Günter for her support with the XRF analysis at the University of Potsdam, to Pia Brinkmann and her assistance with the LIBS measurements earlier on in the Ph.D. project and to Nicolai Klitscher for the preparation of the samples prior to the BVM analysis. Trond Løke, Julio Hernandez and Ivar Baarstad from Norsk Elektro Optikk A/S are sincerely thanked for the introduction to the HySpex scanner handling and technical support over the years – in numerous projects not only this one - and who made it possible for me to handle the scanners with ease for my PhD work in the field and in the lab. My thanks goes to the ESA Third Party Mission Program for providing me with commercial WorldView-3 data under the TMP project 61058.

I would like to thank the Helmholtz Centre Potsdam GFZ German Research Centre for Geosciences for providing the infrastructure and personnel support to conduct my research. My gratitude also goes to the German Federal Ministry of Education and Research and the r4 subsidy program for innovative technologies for resource efficiency, which supported the "REEMAP" scientific project. Furthermore,

this work would not have been possible without additional funding provided by the EU-ERAMIN-2 joint project “LiGHTS” in which part of my non-PhD related research took place and which funding allowed me to work on my own project in my additional time. Some additional words of thanks go again to my mentor Dr. Christian Rogaß who introduced me to the world of Remote Sensing back when I was a B.Sc. student in 2012 and with whom I had the privilege to work with until 2018 before his career changed path away from the GFZ. Your opinions have always inspired me and I am grateful to have worked with you as a colleague, scientific mentor and friend.

The work of this thesis benefited a lot from open-source software. I am thankful for the developers of for example QGIS3 and Python packages such as *scikit-learn*, *pandas*, *NumPy*, *matplotlib* and the HypPy, Spy and PySp toolboxes.

I am writing this thesis during the time of the Covid-19 global pandemic and a wave of necessary changes demanded by the Black Lives Matter movement. I acknowledge my privileges in being a white, able-bodied woman in the scientific community, which held fewer barriers in academia for me. I was able to work from home and not be affected financially due to Covid-19 so I am thankful for the people in the health system and in jobs of systemic importance who contribute towards supporting society and stopping this crisis.

Special words of gratitude go to my friends who have always been a major support when things became more than just a bit discouraging. The last few years have been filled with a lot of ups and downs and I could never have done it without you. Clara, Marie, Sabrina, Greg, Robert, Matthias, Desi, Adrian, Nico, Eike, Caro, Gregor, Nani, Tobi, Gosia, Emna, Lisa, Carsten, Björn, Tim and Linda—either of you helped so much with this project, all the dead ends, unnecessary turn of events and even cliffhangers. I am forever grateful for your support, all the coffee dates, take out evenings, boxing matches, Yoga exercises and in these times of Covid-19 our numerous Skype calls for virtual face time. Thank you for all of our shared time over the years.

Finally, I would like to thank my family to whom I owe a great deal. Great appreciation and enormous thanks goes to my mum and dad and my sisters Elisabeth and Clara, who have been a constant source of support and encouragement. I am especially grateful for your unshakeable confidence in me, even when I decided to found a start-up company during my PhD time and on top of that take care of a shelter dog, which resulted in a lot more work, more love and even more occasions where I needed to talk things out, clear my head or even ask for dog-sitting when I was out and about for my field work. I assume it’s going to be quieter as soon as this PhD has run its course ;)

Abstract

This work develops hybrid methods of imaging spectroscopy for open pit mining and examines their feasibility compared with state-of-the-art. The material distribution within a mine face differs in the small scale and within daily assigned extraction segments. These changes can be relevant to subsequent processing steps but are not always visually identifiable prior to the extraction. Misclassifications that cause false allocations of extracted material need to be minimized in order to reduce energy-intensive material re-handling. The use of imaging spectroscopy aspires to the allocation of relevant deposit-specific materials before extraction, and allows for efficient material handling after extraction. The aim of this work is the parameterization of imaging spectroscopy for pit mining applications and the development and evaluation of a workflow for a mine face, ground-based, spectral characterization. In this work, an application-based sensor adaptation is proposed. The sensor complexity is reduced by down-sampling the spectral resolution of the system based on the samples' spectral characteristics. This was achieved by the evaluation of existing hyperspectral outcrop analysis approaches based on laboratory sample scans from the iron quadrangle in Minas Gerais, Brazil and by the development of a spectral mine face monitoring workflow which was tested for both an operating and an inactive open pit copper mine in the Republic of Cyprus.

The workflow presented here is applied to three regional data sets: 1) Iron ore samples from Brazil, (laboratory); 2) Samples and hyperspectral mine face imagery from the copper-gold-pyrite mine Apliki, Republic of Cyprus (laboratory and mine face data); and 3) Samples and hyperspectral mine face imagery from the copper-gold-pyrite deposit Three Hills, Republic of Cyprus (laboratory and mine face data). The hyperspectral laboratory dataset of fifteen Brazilian iron ore samples was used to evaluate different analysis methods and different sensor models. Nineteen commonly used methods to analyze and map hyperspectral data were compared regarding the methods' resulting data products and the accuracy of the mapping and the analysis computation time. Four of the evaluated methods were determined for subsequent analyses to determine the best-performing algorithms: The spectral angle mapper (SAM), a support vector machine algorithm (SVM), the binary feature fitting algorithm (BFF) and the EnMap geological mapper (EnGeoMap). Next, commercially available imaging spectroscopy sensors were evaluated for their usability in open pit mining conditions. Step-wise downsampling of the data - the reduction of the number of bands with an increase of each band's bandwidth - was performed to investigate the possible simplification and ruggedization of a sensor without a quality fall-off of the mapping results. The impact of the atmosphere visible in the spectrum between 1300–2010nm was reduced by excluding the spectral range from the data for mapping. This tested the feasibility of the method under realistic open pit data conditions. Thirteen datasets based on the different, downsampled sensors were analyzed with the four predetermined methods. The optimum

sensor for spectral mine face material distinction was determined as a VNIR-SWIR sensor with 40nm bandwidths in the VNIR and 15nm bandwidths in the SWIR spectral range and excluding the atmospherically impacted bands. The Apliki mine sample dataset was used for the application of the found optimal analyses and sensors. Thirty-six samples were analyzed geochemically and mineralogically. The sample spectra were compiled to two spectral libraries, both distinguishing between seven different geochemical-spectral clusters. The reflectance dataset was downsampled to five different sensors. The five different datasets were mapped with the SAM, BFF and SVM method achieving mapping accuracies of 85-72%, 85-76% and 57-46% respectively. One mine face scan of Apliki was used for the application of the developed workflow. The mapping results were validated against the geochemistry and mineralogy of thirty-six documented field sampling points and a zonation map of the mine face which is based on sixty-six samples and field mapping. The mine face was analyzed with SAM and BFF. The analysis maps were visualized on top of a Structure-from-Motion derived 3D model of the open pit. The mapped geological units and zones correlate well with the expected zonation of the mine face. The third set of hyperspectral imagery from Three Hills was available for applying the fully-developed workflow. Geochemical sample analyses and laboratory spectral data of fifteen different samples from the Three Hills mine, Republic of Cyprus, were used to analyse a downsampled mine face scan of the open pit. Here, areas of low, medium and high ore content were identified.

The developed workflow is successfully applied to the open pit mines Apliki and Three Hills and the spectral maps reflect the prevailing geological conditions. This work leads through the acquisition, preparation and processing of imaging spectroscopy data, the optimum choice of analysis methodology, and the utilization of simplified, robust sensors that meet the requirements of open pit mining conditions. It accentuates the importance of a site-specific and deposit-specific spectral library for the mine face analysis and underlines the need for geological and spectral analysis experts to successfully implement imaging spectroscopy in the field of open pit mining.

Zusammenfassung

In dieser Dissertation wird die Machbarkeit und Anwendung moderner und eines eigen entwickelten Hybridverfahrens in der bildgebenden Spektroskopie für den Tagebau untersucht.

Die Materialverteilung innerhalb einer Abbaufont unterscheidet sich oft innerhalb eines kleinen Maßstabs und variiert zudem innerhalb täglich zugeordneter Abbausegmente. Diese Veränderungen können für nachfolgende Verarbeitungsschritte relevant sein, sind aber vor dem Abbau nicht immer visuell erkennbar. Falsche Klassifizierungen des Materials führen zu Fehlverteilungen des abgebauten Materials, die minimiert werden müssen, um den energie-intensiven Materialtransport zu reduzieren. Mit Hilfe der bildgebenden Spektroskopie wird angestrebt, relevante Lagerstätten-spezifische Materialien vor der Extraktion korrekt zuzuordnen und ein effizientes Materialhandling nach der Extraktion zu ermöglichen. Ziel dieser Arbeit ist die Parametrisierung der bildgebenden Spektroskopie für den Bergbau und die Entwicklung und Evaluierung eines Workflows zur spektralen Charakterisierung von offenem Bergbau mittels bodengebundener Sensorik. Dies wurde durch die Evaluierung bestehender Ansätze zur hyperspektralen Aufschlussanalyse erreicht, die auf Grundlage von Laborscans von Proben aus dem Eisernen Vierecks in Minas Gerais, Brasilien, durchgeführt wurde. Eine spektralen Abbaufontanalyse wurde mithilfe von Daten eines aktiven und eines inaktiven Kupfer-Tagebaus in der Republik Zypern entwickelt.

Der in dieser Arbeit vorgestellte Arbeitsablauf wird auf drei regionale Datensätze angewandt: 1) Eisenerzproben aus Brasilien (Labordaten); 2) Proben und hyperspektrale bildgebende Daten der Abbaufont aus dem Kupfer-Gold-Pyrit-Tagebau Apliki, Republik Zypern (Labor- und Abbaufontdaten); und 3) Proben und hyperspektrale bildgebende Daten der Abbaufont aus der Kupfer-Gold-Pyrit-Lagerstätte Three Hills, Republik Zypern (Labor- und Abbaufontdaten). Der hyperspektrale Labordatensatz von fünfzehn brasilianischen Eisenerzproben wurde zur Evaluierung verschiedener Analysemethoden und verschiedener Sensormodelle verwendet. Neunzehn gebräuchliche Methoden zur Analyse und Kartierung hyperspektraler Daten wurden im Hinblick auf ihre resultierenden Datenprodukte, die Genauigkeit der Kartierung und die Berechnungszeit der Analyse verglichen. Vier der evaluierten Methoden wurden für nachfolgende Analysen bestimmt: Der Spectral Angle Mapper (SAM), ein Support Vector Machine Algorithmus (SVM), der Binary Feature Fitting Algorithmus (BFF) und der EnMap Geological Mapper (EnGeoMap). Als nächstes wurden kommerziell erhältliche bildgebende Spektroskopiesensoren auf ihre Verwendbarkeit unter Tagebaubedingungen evaluiert. Ein schrittweises Reduzieren der Datenkomplexität, das sog. "downsampling" (die Verringerung der Anzahl der Bänder und gleichzeitige Erhöhung der Bandbreite jedes Bandes), wurde durchgeführt, um eine Vereinfachung der Sensorkomplexität ohne Qualitätseinbußen der Kartierungsergebnisse zu untersuchen. Der Einfluss der Atmosphäre, die im

Spektrum zwischen 1300-2010nm sichtbar ist, wurde reduziert, indem der Spektralbereich aus den Daten für die Kartierung ausgeschlossen wurde. Dadurch wurde die Durchführbarkeit der Methode unter realistischen Tagebaubedingungen getestet. Dreizehn Datensätze, die auf den verschiedenen Sensoren basierten, wurden mit den vier vorher benannten Methoden analysiert. Der optimale Sensor für die spektrale Unterscheidung von Abbaufrontmaterial wurde als VNIR-SWIR-Sensor mit 40nm Bandbreite im VNIR- und 15nm Bandbreite im SWIR-Spektralbereich bestimmt, der atmosphärisch beeinflusste Spektralbereich wurde ausgeschlossen. Nun wurde der Datensatz von der Mine in Apliki verwendet, um die vorher bestimmten Analysen und Sensoren anzuwenden. Sechszwanzig Proben wurden geochemisch und mineralogisch analysiert. Die Probenspektren wurden zu zwei Spektralbibliotheken zusammengestellt, die beide zwischen sieben verschiedenen geochemisch-spektralen Clustern unterscheiden. Die Reflexionsdaten wurden auf fünf verschiedene Sensoren heruntergerechnet. Diese fünf verschiedenen Datensätze wurden mit der SAM-, BFF- und SVM-Methode kartiert, wobei entsprechende Kartierungsgenauigkeiten von 85-72%, 85-76% bzw. 57-46% erreicht wurden. Ein Scan der Abbaufront von Apliki wurde verwendet, um den entwickelten Arbeitsablauf auf Daten unter realistische Bedingungen anzuwenden. Die Kartierungsergebnisse wurden auf der Grundlage der Feldbeprobung und einer geologischen Zonierungskarte der Abbaufront validiert. Die Abbaufront wurde mit SAM und BFF analysiert und die Analysekarten wurden auf einem von „Structure-from-Motion“ abgeleiteten 3D-Modell des Tagebaus visualisiert. Die kartographierten geologischen Einheiten und Zonen korrelierten gut mit der erwarteten Zonierung der Abbaufront. Ein dritter Datensatz stand für die Anwendung des entwickelten Arbeitsablaufs zur Verfügung. Geochemische Probenanalysen und Laborspektraldaten von fünfzehn verschiedenen Proben aus dem offenen Tagebau Three Hills in der Republik Zypern wurden zur Analyse eines Datensatzes der Abbaufront des Tagebaus verwendet. Dabei wurden Bereiche mit niedrigem, mittlerem und hohem Erzgehalt identifiziert.

Der in der Arbeit entwickelte Arbeitsablauf konnte erfolgreich für die offenen Tagebaue Apliki und Three Hills angewandt werden. Die errechneten Spektralgeologischen Karten stellen die örtliche geologische Situation korrekt dar. Der entwickelte Arbeitsablauf erläutert die Erfassung, Aufbereitung und Verarbeitung von Daten aus der bildgebenden Spektroskopie und beschreibt die Wahl der Analysemethodik sowie die Verwendung robuster Sensoren, die den Anforderungen der Tagebaubedingungen entsprechen. Sie hebt die Bedeutung einer standort- und lagerstättenspezifischen Spektralbibliothek für die Analyse von Abbaufrenten hervor und unterstreicht die nötige Einbindung von Experten im Bereich der Geologie und der Spektralanalyse für eine erfolgreiche Implementierung der bildgebenden Spektroskopie im Kontext des Abbaus von Material in offenen Tagebauten.

Preface

This thesis has been submitted in compliance with the requirements for the Ph.D. degree at the Faculty of Science, University of Potsdam, Germany. The work described in this Ph.D. dissertation was undertaken at the Institute of Geosciences, University of Potsdam and the Helmholtz Centre Potsdam, GFZ German Research Centre for Geosciences in Section 1.4 Remote Sensing and Geoinformatics. The work was carried out from June 2017 to October 2020. Apl. Prof. Dr. Uwe Altenberger was the principal supervisor from the Institute of Geosciences, University of Potsdam. For the German Research Centre, apl. Prof. Dr. Helmut Echtler acted as co-supervisor and Dr. Christian Rogass (Helmholtz Centre for Environmental Research UFZ) acted as co-supervisor and mentor throughout the whole project.

This work was funded in part by the “REEMAP” scientific project, supported by the r4 subsidy program for innovative technologies for resource efficiency and the German Federal Ministry of Education and Research. Furthermore, this work would not have been possible without additional funding provided by the EU-ERAMIN-2 joint project “LiGHTS”, in which part of my non-PhD related research took place. The aim of this project was to evaluate existing approaches of imaging spectroscopy for the mining sector and present a conclusive workflow to utilize imaging spectroscopy for open pit mining. The outcomes of this investigation are presented in this monographic dissertation. Current approaches are reviewed, challenges of the commonly used methods and sensors are highlighted and discussed and recommended procedures are presented. This work guides through a workflow of the application of imaging spectroscopy in the laboratory and for mine faces. The manuscript starts with an introduction into open pit mining conditions as well as imaging remote sensing principles and hyperspectral mine face scanning. The geological background of the utilized materials is presented as well as the datasets. The presented near-field imaging spectroscopy workflow starts with an introduction to the commonly used classification methods and an evaluation of these methods. This is followed by a theoretical investigation of an optimal robust imaging spectroscopy sensor for open pit mining. A workflow to handle laboratory imaging reflectance and radiance data is followed by a detailed description of a workflow for acquiring and analyzing imaging spectroscopy field data in open pits. The presented methods and workflows are applied to three regionally different datasets: 1) Laboratory hyperspectral scans of iron ore samples from the Minas Gerais district, Brazil, 2) Laboratory and mine face hyperspectral scans of surface materials from the copper-gold-pyrite mine Apliki, Nicosia District, Republic of Cyprus, and 3) and Laboratory and mine face hyperspectral scans of samples from the Three Hills deposit in the operating copper-gold-pyrite mine Skouriotissa, Nicosia District, Republic of Cyprus. A section about the discussion of all workflow sections, a conclusion and an outlook complete the manuscript.

Table of contents

Declaration of Independence	v
Acknowledgements.....	vii
Abstract	ix
Zusammenfassung.....	xi
Preface.....	xiii
Table of contents.....	xiv
Table of figures.....	xvii
Abbreviations.....	xxvii
1 Motivation	1
2 Introduction	4
2.1 INTRODUCTION INTO OPEN PIT MINING: CONDITIONS AND REQUIREMENTS.....	4
2.2 IMPORTANT DEFINITIONS.....	7
2.2.1 Spectroscopy	7
2.2.2 Wavelength ranges	9
2.2.3 Terms of spectroscopic systems	10
2.2.4 Outcrop/ Mine face scanning.....	11
2.2.5 Hyperspectral mapping.....	11
2.3 INTRODUCTION TO REMOTE SENSING PRINCIPLES	12
2.3.1 Electromagnetic radiation.....	12
2.3.2 Interaction with the surface.....	15
2.3.3 Spectra of materials	16
2.3.4 Spectral properties of rocks and minerals.....	19
2.3.5 Influencing factors for the spectral response.....	20
2.4 HYPERSPECTRAL MINE FACE SCANNING	21
2.4.1 Research Groups and predominant methodology	21
2.4.2 VNIR and SWIR proximal scanning in mining applications.....	24
3 Materials.....	32
3.1 INVESTIGATED SAMPLES	32
3.2 DATASETS	32
3.3 SAMPLE AREA	34
3.3.1 Minas Gerais, Brazil	34
3.3.2 Republic of Cyprus.....	36
3.4 SAMPLE PREPARATION	49
3.5 DATA ACQUISITION.....	52
3.5.1 Laboratory HSI data acquisition.....	52

3.5.2	<i>Laboratory HSI data processing</i>	54
3.5.3	<i>Geochemical sample analysis for validation</i>	56
3.5.4	<i>Field HSI data acquisition</i>	60
3.5.5	<i>Cyprus field work</i>	60
3.5.6	<i>Apliki HSI field data</i>	61
3.5.7	<i>Three Hills HSI field data</i>	70
4	Near-Field Imaging Spectroscopy Methods	74
4.1	ANALYSIS OF IMAGING SPECTROSCOPY DATA	74
4.2	CORRECTION OF DATA – REFLECTANCE RETRIEVAL	75
4.3	DATA DIMENSIONALITY REDUCTION	77
4.4	EM EXTRACTION AND SPECTRAL LIBRARIES.....	77
4.5	SPECTRAL PROCESSING.....	79
4.5.1	<i>Continuum removal (CR)</i>	81
4.5.2	<i>Spectral processing methods</i>	84
5	Near-field Imaging Spectroscopy results	96
5.1	OVERVIEW OF APPLIED WORKFLOW	96
5.2	I) MAPPING METHOD COMPARISON - RESULTS FOR BRAZILIAN IRON ORE SAMPLES	97
5.2.1	<i>Analyzed data</i>	97
5.2.2	<i>Resulting EM spectral libraries</i>	98
5.2.3	<i>Mapping Results</i>	102
5.2.4	<i>Comparison of the results</i>	117
5.3	II) ROBUST SENSOR MODELING	119
5.3.1	<i>Data dimensionality reduction</i>	122
5.3.2	<i>Downsampling of hyperspectral to superspectral (VNIR-SWIR)</i>	122
5.3.3	<i>Analysis of the superspectral VNIR+SWIR downsampled data</i>	124
5.3.4	<i>Excluding atmospheric features</i>	129
5.3.5	<i>Analysis of the VNIR+SWIR downsampled data (atmospheric band excluded)</i>	130
5.3.6	<i>Downsampling to VNIR-only data</i>	131
5.3.7	<i>Analysis of the VNIR-only downsampled data</i>	132
5.4	III) APLIKI SAMPLE DATA - ANALYSIS OF LABORATORY SCANS	136
5.4.1	<i>Apliki mine sample – reflectance data</i>	136
5.4.2	<i>Apliki mine sample – radiance data</i>	148
5.5	IV) PROPOSED FIELD WORKFLOW RELATED TO APLIKI MINE	151
5.5.1	<i>Ground truth for the Apliki mine</i>	153
5.5.2	<i>Superspectral analysis of downsampled Apliki mine face data</i>	156
5.6	V) THREE HILLS MINE – APPLICATION FOR PROPOSED WORKFLOW FOR LABORATORY & FIELD DATA	161

5.6.1	<i>Three Hills sample laboratory data</i>	161
5.6.2	<i>Analysis of Three Hills mine face</i>	163
6	Discussion	165
6.1	IRON ORE SAMPLE MAPPING RESULTS	165
6.2	ROBUST SENSOR MODELING	171
6.2.1	<i>Spectral downsampling of VNIR & SWIR</i>	171
6.2.2	<i>Reduction of atmospheric impact</i>	173
6.2.3	<i>VNIR-only downsampling</i>	173
6.3	APLIKI LABORATORY SCAN ANALYSIS	176
6.4	MINE FACE MAPPING RESULTS	178
6.4.1	<i>Apliki mine</i>	178
6.4.2	<i>Three Hills mine</i>	184
7	Conclusion	186
8	Outlook	191
8.1	APPLICATION TO WORLD-VIEW 2 SATELLITE DATA	191
8.2	TOPICS OF FUTURE RESEARCH	194
9	References	197
10	Appendix	207
10.1	HYSPEX LABORATORY DATA ACQUISITION SETTINGS.....	207
10.2	BRAZILIAN IRON ORE SAMPLES DETECTION LIMITS AND DESCRIPTIONS	208
10.3	APLIKI MINE SAMPLE DESCRIPTION AND LOCATION OF SAMPLING	209
10.4	GEOCHEMICAL ANALYSIS OF APLIKI MINE SAMPLES.....	214
10.5	XRD DIFFRACTOGRAMS OF APLIKI MINE SAMPLES	217
10.6	THREE HILLS MINE SAMPLE DESCRIPTION AND LOCATION OF SAMPLING	253
10.7	GEOCHEMICAL ANALYSIS OF THREE HILLS MINE SAMPLES	256
10.8	HYSPEX FIELD DATA ACQUISITION SETTINGS FOR APLIKI AND THREE HILLS	257
10.9	3D RECONSTRUCTION PARAMETERS FOR APLIKI AND THREE HILLS	259
10.10	DOWNSAMPLING OF DATA FROM HYPERSPECTRAL TO SUPERSPECTRAL DIMENSIONS.....	261
10.11	SPECTRAL FEATURES IN THE VNIR AND SWIR	266
10.12	GEOCHEMICAL CLUSTERING OF APLIKI SAMPLE DATA	269

Table of figures

<i>Figure 1 Hyperspectral Imaging in Mining - Vision for future adaptations of hyperspectral mapping in the whole life cycle of open-pit mining.</i>	2
<i>Figure 2 Lassonde Curve: Life cycle of a mine, connected risks and the possible implementations of remote sensing.</i>	6
<i>Figure 3 Simplified representation of the information contained in hyperspectral imagery.</i>	8
<i>Figure 4 Schematic visualization of bandwidth and band number differences between hyper-, super- and multispectral sensors.</i>	9
<i>Figure 5 The electromagnetic spectrum and the different types of interactions between EMR and material</i>	9
<i>Figure 6 The simplified HySpex optical system.</i>	11
<i>Figure 7 Solar irradiation and absorption of various atmospheric gases at the top of the atmosphere and at sea level, from Jensen (2010).</i>	17
<i>Figure 8 Method development based on the five available data sets.</i>	32
<i>Figure 9 Locations of Minas Gerais and Quadrilatero Ferrifero.</i>	34
<i>Figure 10 Visit to a major open pit mine in the state of Minas Gerais in October 2019.</i>	35
<i>Figure 11 Left: Schematic cross sections of ore mineralization/ alteration zones Right: Hydrothermal alteration mineral zones. Modified from Lowell and Guilbert (1970).</i>	37
<i>Figure 12 Simplified geological map of the Troodos Ophiolite, Cyprus and a simplified structural cross-section of Troodos based on Martin et al., 2018. Contains modified Copernicus Sentinel-2 data (Sept. and Oct. 2019, RGB (490 nm, 560 nm, 665 nm)).</i>	38
<i>Figure 13 Sulfide cover zonation (Top) and characteristics of an idealized volcanogenic massive sulfide deposit (Bottom). Modified from Lydon (1984) and Galley, Hannington and Jonasson (2007).</i>	39
<i>Figure 14 Map of Cyprus showing the location of the Three Hills deposit in the SE of Skouriotissa and the Apliki deposit ca. 5km SW of the operating Skouriotissa mine, based on Copernicus Sentinel-2 data from 2019.</i>	41
<i>Figure 15 Skouriotissa mine location of the pits Phoenix, Phoukasa and Three Hills and fault zone location based on Adamides (2010b).</i>	42
<i>Figure 16 Hyperspectral scan within Three Hills open pit. View from the SSW wall (left) to the NNE entrance to the pit (right).</i>	43
<i>Figure 17 Sketch of areas with clayish (low Cu grade) and greenish (chloritic, stockwork) appearance, indicating zones of pyrite oxidization and leached zones. Based on visual interpretation.</i>	43
<i>Figure 18 Left: Striated cubes of pyrite on top of quartz crystals in former cavity. Right: Striated, hypogene chalcopyrite mineral cluster. Supergene chalcocite blanket is indicated by black remnants. Photos from field work in March 2018 in Three Hills. The photo size is approximately 5cm x 5cm.</i>	44
<i>Figure 19 Apliki deposit, interpretation from (Antivachis, 2015; Martin et al., 2018).</i>	45
<i>Figure 20 Left: Satin spar gypsum found in Apliki, ca. 7cm x 20cm. Right: Sulfate evaporates, possibly Chalcantinite, found in Apliki.</i>	46
<i>Figure 21 Schematic geological section of the Northern part of Apliki from Antivachis (2015).</i>	47

<i>Figure 22 Schematic cross-section of Apliki massive sulfide ore body and associated stockwork, from Antivachis (2015).</i>	48
<i>Figure 23 Brazilian iron ore samples hyperspectral scan (R: 640nm - band 63, G: 549nm - band 38, B: 458nm - band 13).</i>	50
<i>Figure 24 Apliki mine samples hyperspectral scan compilation (R: 640nm – band 63, G: 549nm – band 38, B: 458nm – band 13).</i>	51
<i>Figure 25 Skouriotissa - Three Hills open pit samples. Collated hyperspectral scan of all 15 samples.</i>	52
<i>Figure 26 The HySpex translation stage setup (Körting, 2019).</i>	54
<i>Figure 27 RGB representation of the hyperspectral sample scans. Left: Brazilian iron ore samples. Right: Apliki mine samples.</i>	55
<i>Figure 28 RGB representation of the hyperspectral sample scan of the Skouriotissa mine samples. Color-coded outline represents the mapping color-scheme for the analysis based on the spectral library created from these samples. Pink: ore, red: low grade ore, yellow: waste.</i>	56
<i>Figure 29 ROIs of sample position. Left: 15 Brazilian iron ore sample ROIs with masked shadow areas, 280 x 280 pixels. Right: 36 Cyprus Apliki surface sample ROIs, 1250 x 1280 pixels.</i>	56
<i>Figure 30 Approximated pixel size with mine face height variations and proximity to sensor variations, relative to the HySpex SWIR-320m-e with a FOV of 28° and 320 pixels per line.</i>	62
<i>Figure 31 Position of HySpex and reflectance targets in the Apliki open pit (outlined in black).</i>	63
<i>Figure 32 A: HySpex and target setup shown in close-up photos. B: Position of the targets along the mine face from left to right: 5%, 20%, 50%, 90% large, 90% small, 95%.</i>	63
<i>Figure 33 Data acquisition at Apliki outcrop - computer setup.</i>	64
<i>Figure 34 Apliki mine face - expected lithology and extraction level numeration.</i>	65
<i>Figure 35 PCA based on SWIR radiance data marking spectrally homogeneous regions with red stars for possible field sampling.</i>	66
<i>Figure 36 Sampling locations identified from SWIR radiance PCA analysis and marked as ROIs in the SWIR grey-scale image.</i>	66
<i>Figure 37 NDVI of the Apliki field reflectance scan, shown in levels of grey.</i>	68
<i>Figure 38 NDVI & shadow masked reflectance field scan. Vegetation and areas of shadow (high SNR) are masked out and shown in black. (RGB composition: R: band 63, G: band 38, B: band 13.)</i>	68
<i>Figure 39 RGB digital outcrop model of the Apliki open-pit area, showing the NNE to SSW walls of the pit. One extraction level is approximately 10m of height.</i>	69
<i>Figure 40 Close-up RGB model of the mine face in the NNE scanned by the hyperspectral system.</i>	69
<i>Figure 41 Top: Skouriotissa Mine overview; Bottom: Close-up of Three Hills deposit with marked sensor and target positions.</i>	71
<i>Figure 42 Data acquisition setup at Skouriotissa - Three Hills mine.</i>	72
<i>Figure 43 RGB representation of the superspectral mine face data of Skouriotissa, Three Hills, Republic of Cyprus. Viewers' direction is approximately towards NNW.</i>	72
<i>Figure 44 The resulting 3D model, textured with the orthophoto mosaic of all available Nikon photos.</i>	73

Figure 45 The resulting 3D model, textured with the RGB hyperspectral scan overlaid on the RGB photo texture.	73
Figure 46 Schematic generic workflow of how HSI is processed and analyzed.	75
Figure 47 Spectral library based on visual spectrum extraction over a 5x5 pixel average.	78
Figure 48 Taxonomic tree describing spectral processing methods as described in (Asadzadeh and de Souza Filho, 2016). Highlighted in red, dashed lines are the methods used for comparison in this work.	80
Figure 49 Continuum Removal for a spectrum from Sample 3 (Right) and Sample 13 (Left) of the Brazilian Iron Ore samples. The continuum free spectrum is shown for both samples based on the ENVI, HypPy and PySp toolbox convex hull algorithms and the Geometric hull retrieval by Mielke et al. (2015).	83
Figure 50 Results for the continuum removal algorithms for USGS spectral library entry "Siderite" in blue. The continuum definition is shown in green, based on the geometric hull by Mielke et al., 2015 (a) and based on the Tetracorder expert system by Clark et al., 2003 (b). The found feature and their depth are shown in red. From Mielke et al. (2015).	93
Figure 51 Processing chain and key elements of the MICA image analysis from Koerting et al. (2015) modified after Kokaly (2011).	94
Figure 52 Simplified illustration of the EnGeoMap processing chain from Körting (2019) modified after Boesche et al. (2016).	95
Figure 53 Methods and hybrid method development performed on the different HSI datasets.	96
Figure 54 Left: Validation PNG file including the shadow mask applied to the data; Right: ENVI classification file for supervised learning-based methods.	98
Figure 55 Spectra of all Brazilian iron ore samples in HySpex resolution (408 bands), each sample represented by a 5x5 pixel average and SAM analysis based on the library.	99
Figure 56 SAM analysis (left) based on the hyperspectral library reduced to geochemical cluster centers (right).	99
Figure 57 Brazilian iron ore SMAACC EMs.	100
Figure 58 Thirty random spectra from the area of sample 03 (HySpex sensor, 408 bands).	100
Figure 59 SAM analysis (left) of the Brazilian iron ore samples with the SMAACC 10 EM spectral library (right).	101
Figure 60 Six spectral EMs from PPI and n-D visualization tool.	101
Figure 61 SAM analysis (left) of the Brazilian iron ore samples and the PPI + n-D 6 EM spectral library (right).	102
Figure 62 Spectra of Brazilian iron ore samples in WorldView-3 resolution (16 bands).	102
Figure 63 RGB (left), iron content based on XRF analysis (center) and ferrous iron index based on WorldView-3 band ratio (right).	103
Figure 64 RGB (left), iron content based on XRF analysis (center) and ferric oxide index based in WorldView-3 band ratio (right).	103
Figure 65 Brazilian iron ore true color image (left) and PCA image (R: PC band 1, G: PC band 2, B: PC band 4) (left).	103
Figure 66 Mimimum wavelength mapping for the large AIOH feature between 2160 - 2220nm. Left: RGB of samples, Center-Left: Al ₂ O ₃ content based on geochemistry, Centre-Right: MWL feature position mapping (color	

<i>stretched from 2160nm-blue to 2220nm-red), Right: MWL feature depth mapping (color stretched from 0-blue to 0.2-red).</i>	104
<i>Figure 67 Minimum wavelength map of AIOH, feature position shown by the color-coding, feature depth by the color-saturation.</i>	104
<i>Figure 68 Minimum wavelength mapping for the broad iron feature between 850 - 1100 nm. Left: RGB of samples, Center-Left: Fe content based on geochemistry, Centre-Right: MWL feature position mapping (color stretched from 850nm-blue to 1050nm-red), Right: MWL feature depth mapping (color stretched from 0-blue to 0.2-red).</i>	105
<i>Figure 69 k-Means clustering for Brazilian iron ore, 15 clusters, defined after 100 iterations.</i>	105
<i>Figure 70 k-Means clustering for Brazilian iron ore, 7 clusters, defined after 100 iterations.</i>	106
<i>Figure 71 SAM classification result (left), incorrectly classified pixels (center) and overall correct vs. incorrect classified pixels (right).</i>	106
<i>Figure 72 Classification result of BFF for the sample derived spectral library. RGB and ground truth are shown at the top, below from left to right: the best-fit classification image, the incorrect classification shown in the incorrect color with the correct ROI overlaid in gray and the correctly (gray) vs. incorrectly (black) classified areas in the image.</i>	107
<i>Figure 73 Spectral Feature Fitting. Greyscale image of the scale for spectral library entry 01 (left) and user-defined classes for sample 01 and 03 (right). Classes were defined from their respective 2D RMS and Scale scatterplots.</i>	107
<i>Figure 74 True color and ground truth image of the Brazilian iron ore samples (upper part) and GML results and accuracy (lower part).</i>	108
<i>Figure 75 MHD results and accuracy for Brazilian iron ore samples.</i>	108
<i>Figure 76 True color image of the Brazilian iron ore samples (left), prediction of respective model (center) and 40% ground truth for testing (right), shown for the SVM, 1D NN, 1D CNN and 3D CNN.</i>	111
<i>Figure 77 "HyperRandomForest" classification results for Brazilian iron ore samples.</i>	112
<i>Figure 78 MTMF classification, MF image of spectral library entry 01 (left) and user defined classes for spectral library entry 01 and 03 from their respective MF and infeasibility 2D scatterplots (right).</i>	113
<i>Figure 79 Left: Labeled true color composite of the Brazilian iron samples, right: ICA RGB composite (band 4 - band 6 - band 7).</i>	113
<i>Figure 80 PRISM MICA group 2 classification of the Brazilian iron ore.</i>	114
<i>Figure 81 MICA group 2 spectral library analysis of the Brazilian iron ore samples with MICA (top left), SAM (top right), EnGeoMap (bottom left) and BFF (bottom right).</i>	115
<i>Figure 82 The dominantly mapped material spectra mapped from the MICA group 2 spectral library. (dark blue: kaolinite, medium blue: kaolinite mixture, light blue: Montmorillonite, pink: alunite + kaolinite, dark red: pyrophyllite, dark red-brown: pyrophyllite + alunite, yellow: Buddingtonite, orange: Muscovite, purple: carbonate Fe-bearing, light brown: vegetation green, brown: vegetation dry)</i>	115
<i>Figure 83 Classification results of EnGeoMap 2.0 and EnGeoMap 2.1 with the sample derived spectral library. RGB and ground truth are shown at the top, below from left to right: the best fit classification image, the</i>	

<i>incorrect classification shown in the incorrect color with the correct ROI overlaid in gray and the correctly (gray) vs. incorrectly (black) classified areas in the image.</i>	116
<i>Figure 84 Schematic successive downsampling and band reduction including the exclusion of wavelength ranges impacted by the atmosphere (between 1300 - 2010nm).</i>	123
<i>Figure 85 Band number vs. accuracy for SAM, SVM, EnGeoMap 2.1 and BFF.</i>	125
<i>Figure 86 Accuracy and computation time with increasing band number.</i>	126
<i>Figure 87 Wavelength position of the two detected kaolinite features with changing band number. Blue: position and linear trend of the position with changing band number for feature 1. Red: position and linear trend of the position with changing band number for feature 2.</i>	127
<i>Figure 88 - Part 2 MWL feature position and depth results and spectral library visualization for downsampled data with bandwidth between 10nm and 20nm.</i>	128
<i>Figure 89 BFF, EnGeoMap 2.1 and SAM accuracies for sensors with systematically downsampled band numbers from 37 to 417, (excluding the results for the 242 bands EnMap sensor).</i>	131
<i>Figure 90 Comparison of the SAM, EnGeoMap 2.1 and BFF accuracies of all tested theoretical sensors.</i>	133
<i>Figure 91 BFF and EnGeoMap 2.1 accuracy vs. computation times for all presented sensors. Time [s] (dotted line) and Accuracy [%] (continuous line) is logarithmically denoted on the y-axis</i>	134
<i>Figure 92 Spectral libraries and mapping results of the BFF analysis for the 15 nm and 40 nm full sensors (left, 414 – 2498nm), the 15 nm, 40 nm, and 40 nm VNIR-15 nm SWIR sensors with the clipped wavelength range influenced by atmospheric absorptions (middle, 414 – 2498nm) and the two VNIR-only sensors with 15 nm and 40 nm bandwidth (right, 414 – 1000nm).</i>	135
<i>Figure 93 Hyperspectral scan of the Apliki samples showing all 36 samples used for geochemical clustering, spectral library extraction and analysis.</i>	137
<i>Figure 94 Bottom-up hierarchic cluster dendrogram for 7 clusters based on the full bulk geochemistry of 36 samples.</i>	138
<i>Figure 95 Geochemical clusters color-coded for the hyperspectral sample scan. 36 samples where clustered into 7 geochemically and spectrally distinct clusters.</i>	138
<i>Figure 96 Bottom-up hierarchic dendrogram with 7 clusters for 36 samples, showing the samples and spectra allocated to each cluster. Cluster 1 – 7 show the geochemically determined clusters. "Spectral cluster 2" compares sample 15a, 15b, 15c, and 7e to show their spectral similarity. Cluster 7 is the geochemically determined cluster from which sample 7e was excluded and re-sorted to the "spectral cluster 2".</i>	140
<i>Figure 97 Sampling point location in decimal latitude and longitude and each sample points color-coding according to its cluster.</i>	141
<i>Figure 98 Spectral library based on geochemical and spectral clustering into 7 clusters with a total of 11 sample spectra and 4 laboratory "background" spectra.</i>	141
<i>Figure 99 Comparison of spectra 1e and 15b showing their spectral shape for the five different sensors. A: 40nm VNIR and 15nm SWIR with and without clipping and interpolating the spectral range influence by atmospheric absorptions (1300–2010nm), B: VNIR-only 40nm sensor, WorldView-3 and HySpex</i>	145

<i>Figure 100 Apliki sample scan classification accuracies for five different sensors and three different classification algorithms (SAM, BFF and SVM).</i>	146
<i>Figure 101 Computations times plotted for each sensor for the Apliki sample dataset.</i>	146
<i>Figure 102 Mapping of 36 Apliki mine sample reflectance data. 1st column: validation image, 2-6th column: classification results for the five different sensors. Left to right: SVM, SAM 11 sample spectra, SAM 36 sample spectra, BFF 11 sample spectra, BFF 36 sample spectra.</i>	147
<i>Figure 103 Complied radiance data set of eleven samples and a 50% white reference panel. Red rectangles mark the area of spectra extraction for the spectral library.</i>	148
<i>Figure 104 Radiance sample spectra for 11 Apliki mine samples.</i>	149
<i>Figure 105 VNIR radiance data analysis with SAM and BFF for HySpex 160band (bottom) and 40nm-bandwidth 15band data (center) compared to a validation image containing color-coded ROIs (top)</i>	150
<i>Figure 106 Hyperspectral mine face acquisition, processing and analysis workflow.</i>	151
<i>Figure 107 Spectral library spectra of 11 Apliki samples, downsampled to 40nm VNIR - 15nm SWIR. The atmospheric range between 1300–2010nm was clipped and interpolated.</i>	152
<i>Figure 108 Field sampling positions marked in imagery. Color-coding of circles (sample points) and spectra of spectral library (laboratory based) is according to the 7 identified geochemical and spectral clusters for the Apliki samples.</i>	153
<i>Figure 109 Apliki HySpex mine face scan RGB (top) and geological interpretation based on Antivachis (2015) (bottom).</i>	154
<i>Figure 110 Combination of hydrothermal alteration zones and schematic geological section for the northern open cut in Apliki mine, Republic of Cyprus. Information derived from maps created by Antivachis (2015).</i>	155
<i>Figure 111 Field sampling position, color-coded according to geochemical and spectral cluster identity.</i>	157
<i>Figure 112 BFF analysis results for three different sensors. From top down: RGB representation of the mine face, analysis result for 40nm VNIR - 15nm SWIR sensor, 40nm VNIR-only sensor and WorldView-3 sensor.</i>	157
<i>Figure 113 SAM analysis result for three different sensors. From top down: RGB representation of the mine face, analysis result for 40nm VNIR - 15nm SWIR sensor, 40nm VNIR-only sensor and WorldView-3 sensor.</i>	158
<i>Figure 114 Analysis results for 40nm VNIR - 15nm SWIR data with atmospheric bands removed. From Top to Bottom: BFF analysis result, SAM analysis result, MWL mapping: wavelength position map for AIOH, feature depth map for AIOH.</i>	159
<i>Figure 115 Binary Feature Fitting analysis of 51 bands-dataset visualized on DOM of the full Apliki open pit.</i>	160
<i>Figure 116 MWL analysis for the AIOH feature wavelength position between 2160 - 2220 nm (Top) and the AIOH feature depth (Bottom) visualized on the DOM of the full Apliki open pit.</i>	160
<i>Figure 117 SAM results visualized on DOM.</i>	161
<i>Figure 118 Three Hills sample laboratory scan. Color-coded outline of the samples is based on the mapping colors for the image-retrieved spectral library. Red, dashed rectangles mark the position of 5x5 pixel average spectra retrieval.</i>	162
<i>Figure 119 Spectral library plot of the Three Hills mine samples.</i>	163

<i>Figure 120 The analysis result of the BFF algorithm for Skouriotissa Three Hills, overlaid on the HySpex RGB representation.</i>	163
<i>Figure 121 Textured 3D model with the BFF analysis result as an overlay over the RGB 3D model.</i>	164
<i>Figure 122 Hard classifier analysis results (accuracy) and computation times.</i>	170
<i>Figure 123 BFF results and spectral library of the 3 dataset with excluded atmospheric wavelength ranges (left) (414–2498nm) and of the two VNIR-only datasets (414 – 1000nm). The spectra of the spectral library are shown stylized to highlight the changes in the overall spectrum.</i>	174
<i>Figure 124 Plot of the data size of the successively downsampled data of the Brazilian iron ore hyperspectral scan.</i>	175
<i>Figure 125 Apliki sample scan classification accuracies for five different sensors and three different classification algorithms (SAM, BFF and SVM).</i>	176
<i>Figure 126 Computations times plotted for each sensor for the Apliki sample dataset.</i>	176
<i>Figure 127 BFF and SAM mapping for 40nm VNIR - 15nm SWIR data of 390 spectral bands, compared to the validation field sampling points.</i>	178
<i>Figure 128 BFF (B) and SAM (C) analysis results for 40nm VNIR - 15nm SWIR data compared to the geological mapping of the open cut (A), based on Antivachis (2015).</i>	180
<i>Figure 129 Spectral Library from 11 Apliki mine samples - full 400 bands, HySpex spectra. Color-coded is based on 7 clusters.</i>	181
<i>Figure 130 Spectral Library from 11 Apliki mine samples - downsampled, 40nm VNIR - 15nm SWIR spectra with interpolated spectral range between 1300 - 2010nm. Color-coding is based on 7 clusters.</i>	181
<i>Figure 131 BFF analysis of Apliki based on 6 clusters, excluding cluster 7 (gypsum).</i>	182
<i>Figure 132 Apliki mine face map based on SVM trained on laboratory data. Note the different color-coding compared to the BFF and SAM maps.</i>	183
<i>Figure 133 Three Hills deposit, fault position and Cu-grade trend.</i>	184
<i>Figure 134 RGB vision based sketch of areas of clayish and chloritic appearance (yellow and pink respectively) and of areas of oxidized pyrite (red outline) and leached zones (white outline).</i>	184
<i>Figure 135 Mapping result of BFF with color-coding based on high, medium and low copper grade.</i>	184
<i>Figure 136 RGB imagery of the WV2 scene from 15th of August 2018. European Space Imaging WorldView-2 data has been provided the European Space Agency ESA within TPM Project ID 61058.</i>	191
<i>Figure 137 Quality map, pixels with high spectral contrast and therefore low possible classification error are represented in light colors. European Space Imaging WorldView-2 data has been provided the European Space Agency ESA within TPM Project ID 61058.</i>	192
<i>Figure 138 BFF analysis of the Apliki WV2 data with site-specific spectral library with 35 samples, color-coded within 6 geochemical clusters. European Space Imaging WorldView-2 data has been provided the European Space Agency ESA within TPM Project ID 61058.</i>	193
<i>Figure 139 X-Ray diffractogram for sample 1b</i>	217

Table of Tables

<i>Table 1 List of not commonly known terms used throughout the work (acronyms).</i>	<i>xxvii</i>
<i>Table 2 Challenges and requirements of the open pit mining industry for hyper- or hyperspectral monitoring.</i>	<i>6</i>
<i>Table 3 Spectrally detectable mineralogy at Highland Valley from Lypaczewski et al. (2020).</i>	<i>27</i>
<i>Table 4 Absorption feature wavelength positions of minerals mapped by Murphy et al. (2015).</i>	<i>28</i>
<i>Table 5 Bulk rock composition of itabirite and its weathering products from Dorr (1964).</i>	<i>36</i>
<i>Table 6 Geochemical composition of samples received from the Minas Gerais district. Reduced to components stated by Dorr (1964). Categorization after Dorr (1964) and from information provided by Mine Site 2.</i>	<i>36</i>
<i>Table 7 Summary of Apliki and Three Hills deposit based on Adamides (2010b, 2010a).</i>	<i>41</i>
<i>Table 8 HySpex VNIR-1600 and SWIR-230m-e sensor parameters from the HySpex User Manual (hyspex.no/products/disc.php, 2019).</i>	<i>53</i>
<i>Table 9 Sample type and corresponding geochemical validation method.</i>	<i>56</i>
<i>Table 10 Geochemistry provided for the samples from the two active mining sites. Values below the detection limit are labeled as “< DL”. The LOI is the loss mass during heating at 1000°C for 60 minutes.</i>	<i>57</i>
<i>Table 11 Apliki mine samples and the corresponding analysis type and BVM code</i>	<i>58</i>
<i>Table 12 Apliki mine sample mineralogy based on XRD. Sample 15a, b and c were additionally analysed semi-quantitatively with the Rietveld-method.</i>	<i>59</i>
<i>Table 13 Three Hills mine sample numbers and the corresponding BVM analysis codes.</i>	<i>60</i>
<i>Table 14 Approximate distance of sensor to mine face and expected, rounded pixel size at-mine-face for the HySpex VNIR-1600 and SWIR-320m-e cameras.</i>	<i>61</i>
<i>Table 15 Latitude and Longitude of the HySpex and the six targets.</i>	<i>62</i>
<i>Table 16 White reference target size in pixel, cm, and approximate pixel size of the reflectance targets at the outcrop.</i>	<i>67</i>
<i>Table 17 Latitude and Longitude of the HySpex and the target position.</i>	<i>70</i>
<i>Table 18 Training based (1D NN, 1D CNN, 3D CNN and SVM) analysis parameters and results.</i>	<i>110</i>
<i>Table 19 Settings for EnGeoMap 2.0 and EnGeoMap 2.1 analysis.</i>	<i>116</i>
<i>Table 20 Comparison of the applied HSI analysis method, input spectral library, number of EMs (EM), overall mapping accuracy [%] and software used to carry out the analysis.</i>	<i>117</i>
<i>Table 21 Influencing factors, implication and solutions for spectral sensor development in active mining operations.</i>	<i>119</i>
<i>Table 22 Downsampling approaches of the Brazilian iron ore samples.</i>	<i>123</i>
<i>Table 23 Accuracy and computation time of SVM, EnGeoMap 2.1 and BFF analysis and accuracies of the SAM analysis for the different theoretical sensors.</i>	<i>124</i>
<i>Table 24 MWL for the kaolinite feature with changing band number. “None” entries represent no possible detection of a feature by MWL. The offset of the detected feature position and the expected feature position is noted. Expected positions: Feature 1: 2205nm, Feature 2: 2156nm.</i>	<i>127</i>

<i>Table 25 Sensors with bands from 417 - 37, including the sensors with clipped wavelength ranges influenced by the atmosphere ($\approx 1300 - 2010$ nm). The accuracies for SAM, EnGeoMap 2.1 and BFF are compared.</i>	130
<i>Table 26 HySpex VNIR - 1600 and SWIR - 230m-e sensor parameters from the HySpex User Manual</i>	132
<i>Table 27 Accuracies of SAM, EnGeoMap 2.1 and BFF of the VNIR only sensors compared to the sensors with the clipped wavelength affected by the atmosphere ($\approx 1300-2010$ nm).</i>	133
<i>Table 28 Spectral libraries after geochemical clustering and visual spectral similarity assessment</i>	139
<i>Table 29 Average geochemistry of the samples in a cluster. Highest value per oxide and element, marked in grey. (Part 1)</i>	142
<i>Table 30 Average geochemistry of the samples in a cluster. Highest value per oxide and element, marked in grey. (Part 2)</i>	142
<i>Table 31 Zonation based on Antivachis (2015), correlated with the predominant geochemical average of each cluster.</i>	143
<i>Table 32 Apliki mine sample clusters, associated sample IDs and cluster mineralogy.</i>	143
<i>Table 33 Sensor specifications for the five datasets classified and compared of the Apliki sample laboratory data, sorted by descending band numbers.</i>	144
<i>Table 34 Sensor characteristics for the downsampled sensors, downsampled from 390 band, pre-processed Apliki field reflectance data.</i>	152
<i>Table 35 Apliki mine sample clusters, dominant geochemistry and mineralogy and linked geological units.</i>	156
<i>Table 36 Three Hills mine samples with associated copper content. Color-coding is based on Cu mass fraction: pink: $> 0.27\%$ Cu; red: $0.27\% < \text{Cu} < 0.1\%$; yellow: $< 0.1\%$ Cu</i>	162
<i>Table 37 Comparison of the mapping results with a validation image (expected mapping, if available).</i>	165
<i>Table 38 Hard classifier analysis computation time and accuracy.</i>	170
<i>Table 39 Classification accuracy mean compared for SAM and BFF and the two different spectral libraries utilized.</i>	177
<i>Table 40 Challenges for superspectral measurement equipment in the context of mine face scanning and possible solutions as a result of this work.</i>	189
<i>Table 41 HySpex settings for laboratory measurements of the Brazilian samples.</i>	207
<i>Table 42 HySpex setting for the laboratory measurements of the unprepared Apliki samples.</i>	207
<i>Table 43 HySpex setting for the laboratory measurements of the unprepared Skouriotissa samples.</i>	208
<i>Table 44 Detection limit for the geochemical results from mine site 1 (sample 3, 4, 7, 8, 11, 12 and 15).</i>	208
<i>Table 45 Detection limit for the geochemical results from mine site 2 (sample 1, 2, 5, 6, 9, 10, 13 and 14).</i>	208
<i>Table 46 Sample descriptions for samples from mine site 1, for sample 3, 4, 7, 8, 11, 12, 15.</i>	208
<i>Table 47 Apliki mine samples, including description, coordinates of sampling in March 2018 and a field photo of the sample (Koerting, Rogass, et al., 2019)</i>	209
<i>Table 48 Sample preparation and description of BVM codes, from Koerting et al. (2019b).</i>	214
<i>Table 49 Main geochemical components for 36 Apliki field samples in [wt.%] with sample location in decimal latitude and longitude.</i>	215

<i>Table 50 Skouriotissa - Three Hills mine samples, including a description, the coordinates of sampling in March 2018 and a lab photo of the sample.</i>	253
<i>Table 51 Main geological components for the Three Hills mine field samples with sampling location.</i>	256
<i>Table 52 HySpex data acquisition parameters for Apliki mine.</i>	257
<i>Table 53 HySpex data acquisition parameters for Three Hills mine.</i>	258
<i>Table 54 3D reconstruction parameters for the Apliki DOMs with Agisoft Professional PhotoScan Software</i>	259
<i>Table 55 3D reconstruction parameters for the Three Hills DOM with Agisoft Professional PhotoScan Software</i>	260
<i>Table 56 Downsampling approaches of the Brazilian iron ore samples.</i>	261
<i>Table 57 Wavelength ranges, wavelength and FWHM characteristics of the different theoretical sensors.</i>	265
<i>Table 58 VNIR and SWIR response of common silicate minerals after Krupnik and Khan (2019). Absorption bands within the range of atmospheric absorptions (1300–1500nm and 1750–2000nm) are not included. Absorption features from additional literature centered on open pit mining where added and are explicitly referenced in the table.</i>	266
<i>Table 59 VNIR and SWIR response of common non-silicate minerals after Krupnik and Khan (2019). Absorption bands in within the range of atmospheric absorptions (1300–1500nm and 1750–2000nm) are not included. Absorption features from additional literature centered on open pit mining where added and are explicitly referenced in the table.</i>	268
<i>Table 60 Adaptation of the element and oxide geochemical values that could not clearly be denoted as they were below or above the detection limit.</i>	269

Abbreviations

Table 1 List of not commonly known terms used throughout the work (acronyms).

Terms	Abbreviation	Description
Abbreviations	VNIR	Visible light and near infrared
	SWIR	Short wave infrared
	TIR	Thermal infrared
	SNR	Signal to noise ratio
	FWHM	Full width at half maximum
	EMR	Electromagnetic radiation
	HSI	Hyperspectral Imagery
	EnMAP	Environmental Mapping and Analysis Program: future earth observation satellite mission (www.enmap.org) ¹
	CCRSS-A	China Commercial Remote Sensing Satellite System: future earth observation satellite mission
	HISUI	Hyperspectral Imager Suite: future earth observation satellite mission
	DOM	Digital Outcrop Model
	LiDAR	Light detection and ranging
	SfM	Structure-from-Motion
Instruments	HySpex VNIR-1600	HySpex pushbroom spectrometer, VNIR camera
	HySpex SWIR-320m-e	HySpex pushbroom spectrometer, SWIR camera
	HySpex ground	HySpex operational software for laboratory and near-field application
	HySpex rad	HySpex calibration software to transform raw DN into radiance data
Spectral analytical terms	EM	Endmember
	CR	Continuum Removal
	SMACC	Sequential Maximum Angle Convex Cone
	PPI	Pixel Purity Index
	PCA	Principle Component Analysis
	MWL	Minimum Wavelength Mapping
	SAM	Spectral Angle Mapper
	BFF	Bi-Triangleside Feature Fitting
	SFF	Spectral Feature Fitting
	PSLR	Prinicipal Least Squares Regression
	GML	Gaussian Maximum Likelihood
	MHD	Mahalanobis Distance Likelihood
	ANN	Artificial Neural Network
	CNN	Convolutional Neural Networks
	SVM	Support Vector Machines
	RF	Random Forest
	MTMF	Mixture Tuned Matched Filtering
	ICA	Independent Component Analysis
	LSU	Linear Spectral Unmixing
	ML	Machine Learning
PRISM - MICA	Processing Routines in IDL for Spectroscopic Measurements - Material identification and characterization algorithm (Kokaly, 2011)	
EnGeoMap	EnMap Geological Mapper (Rogass <i>et al.</i> , 2013)	
Software and System	IDL [®]	Interactive Data Language (L3Harris-Geospatial-Solutions, 2018),IDL [®] 8.7.0

	ENVI®	ENVI® image analysis software (L3Harris-Geospatial-Solutions, 2018),
	Python	3.7.6 packages by conda-forge, IPython 7.13.0
	R Studio	R 3.6.2, RStudio 1.2.5033
	System Linux	Ubuntu 18.04.4, Processor Intel® Core™ i7-8550U CPU 1.80GHz x 8, Graphik Intel® UHD Graphics 620, OS type 64-bit, Memory 31,3GiB
	System Windows	Intel® Core™ i7-2860QM CPU @ 2.50 GHz x 2.50 GHz, Memory 32 GB, 64-bit
	Agisoft	Agisoft Photoscan Professional v.1.2.6.2834
	rad. Data ReSens ⁺	rad. Data Spectral Analytics UG (haftungsbeschränkt) and licenced ReSens ⁺ spectral analysis algorithm
	QGIS	Quantum GIS, QGIS3, version 3.4.12
Python Toolboxes	DeepHyperX	(Audebert, 2020)
	Spy	Spectral Python (spectralpython.net/, 2020)
	PySp	Tools for hyperspectral imaging (Therien, 2020)
	HypPy	Hyperspectral Python (Bakker and Oosthoek, 2020)
	scikit-learn	Scikit-learn: Machine learning in Python (Pedregosa <i>et al.</i> , 2011)
Commercial Institutes	BVM	Bureau Veritas Minerals is an industry leader in the analysis of minerals for the Exploration and Mining industries. BVM is a service company that provides mineral preparation and laboratory testing services.
Research and federal institutes or governmental-funded projects	USGS	United States Geological Survey
	GSD	Geological Survey Department, Ministry of Agriculture, Rural Development and Environment, Republic of Cyprus
	HCM	Hellenic Copper Mines
	UP	University of Potsdam
	GFZ	German Research Centre for Geosciences
	REEMAP	Rare Earth Element MAPping: Research project for the development of a modular multi-sensor processing chain for modern imaging spectrometers to detect REEs

1 Motivation

A rapidly increasing world population drives an ever-increasing global demand for metals and other mining products. This demand is additionally fueled by ever-changing technology trends and the digitization of different sectors. In order to meet this demand in a sustainable manner or even to maintain a competitive edge in times of sharply dropping demand, mining companies implement innovative technologies that help further reduce environmental impact through more selective mining. The UN Sustainable Development Goals incorporate the need for meeting the metal demand in a sustainable manner in their Goal 9: “[To] build resilient infrastructure, promote sustainable industrialization and foster innovation” (sustainabledevelopment.un.org/, 2020). Middle-income countries particularly benefit from entering the basic and fabricated metals industries to support inclusive and sustainable industrialization. Based on estimates from the International Labour Organisation ILO, 30,000,000 people were employed by the mining industry in 2013 (IGF, 2013). It is a sector that has always imposed stress on the environment and the people working in mining and living around mine sites due to its extractive nature and the number of technologies and workforce employed in it (Bowell, 2017). A sustainable approach to mining is not based on the reduction of extraction alone, but on developing technologies to create a safer, highly efficient extraction-, sorting and recycling process. Multispectral and hyperspectral remote sensing techniques already play a role in a number of mining activities. These range from satellite- and aerial surveys prior to mining (Kruse *et al.*, 2011; Kruse, 2012; Mielke *et al.*, 2014; Notesco *et al.*, 2014; Swayze *et al.*, 2014; Salehi, 2018), aerial mapping approaches of open mine pits in order to update deposit models (Jakob, Zimmermann and Gloaguen, 2017; Kirsch *et al.*, 2018) and laboratory based drill core and sample scanning to digitizing data for the process of mine development (<http://www.corescan.com.au/>, 2013; Koerting *et al.*, 2015; Körting, 2019; Kraal and Ayling, 2019). The hyperspectral scanning of mine faces, fresh extraction sites and mine waste piles has been the objective of a number of publications (Kurz *et al.*, 2008; Kruse *et al.*, 2011; Kurz *et al.*, 2012; Buckley, Kurz and Schneider, 2012; Kurz, Buckley and Howell, 2013; Dalm, Buxton and van Ruitenbeek, 2017; Jakob, Zimmermann and Gloaguen, 2017; Kirsch *et al.*, 2018; Lorenz *et al.*, 2018; Salehi *et al.*, 2018). Many of these methods were approached in the name of science or as a proof of concept and have yet to be implemented in the day-to-day activity of the mining industry as seen in a vision for the hyperspectral mining future in Figure 1.

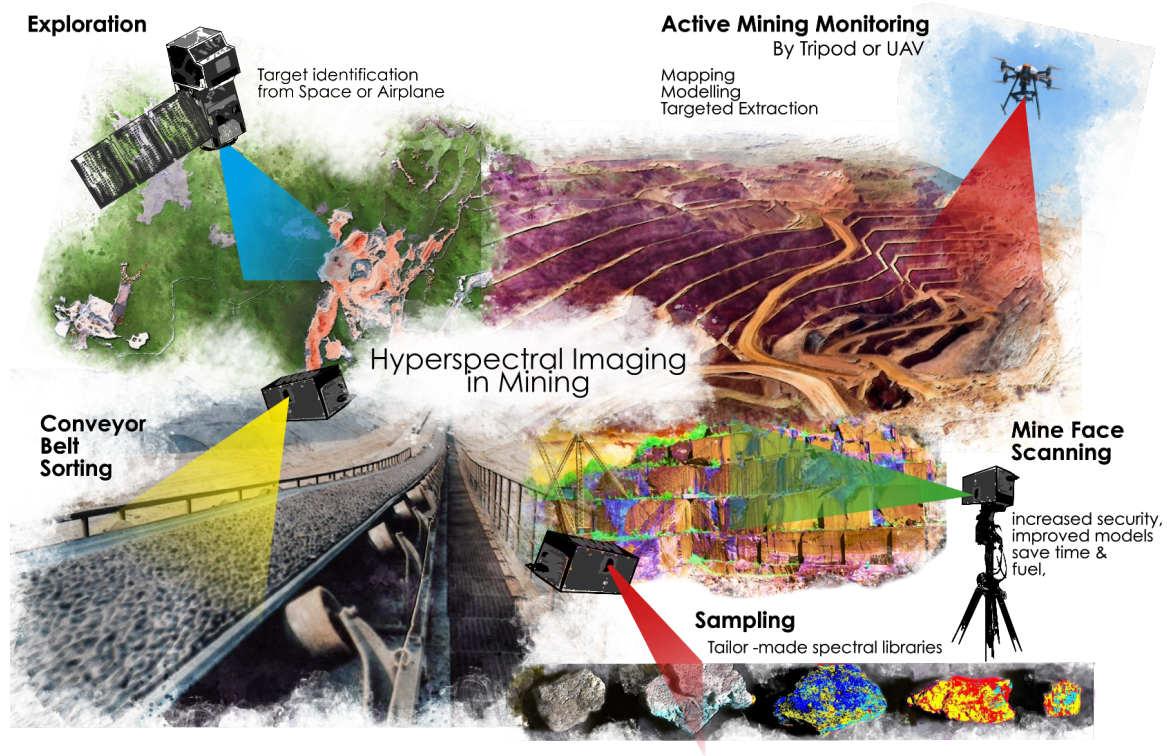


Figure 1 Hyperspectral Imaging in Mining - Vision for future adaptations of hyperspectral mapping in the whole life cycle of open-pit mining. (Image sources: Conveyor belt: <https://www.metso.com/contentassets/78a90df835f44b468a17d28465b8802b/conveyor-solutions-belts.jpg>, open pit: <https://i.ytimg.com/vi/ibzVZc7Qmeg/maxresdefault.jpg>)

In 2003, the International Council on Mining & Metals (ICMM) established 10 principles to respond to key challenges in the mining sector. Principle 4 states the implementation of risk management strategies based on valid data and sound science. Principle 5 builds on the improvement of public health and safety performances and principle 6 seeks continual improvement of the environmental performances of mining (ICMM, 2013). All of these aims can be supported by implementing remote sensing technologies, for example by providing sound virtual outcrop models (e.g. (Buckley *et al.*, 2019; virtualoutcrop.com, 2020). These outcrop models can define the areas of mineralization in a highly efficient manner and refine existing mine development models. This could reduce extraction to the area of highest mineralization and reduce the impact of the subsequent sorting and refinery processes. They can also map fault systems and areas of instability and decrease the direct contact with potentially risk-induced environments. This technology and the use of it requires a new workforce in mining, as well as new training for the geoscientists of the future (Jébrak and Montel, 2017). This is also indicated in the “Ernest & Young Top 10 Business risks facing mining and metals” in which the challenges facing the mining industry are ranked each year (EY, 2018). “Digital Effectiveness” and “Maximizing Portfolio Returns” has been in the top ranks since 2018 and EY repeatedly state the need for digital initiatives and innovation that span the entire value chain and induce a transformation rather than only applying digital solutions to singular issues. Investing a higher amount of the budget

to digital solutions is also one key point to increase the operation's efficiency substantially (EY, 2018). Digitalization throughout the mining value chain has to happen across different disciplines; this includes production and value chain optimization, asset performance management and a workforce transformation (Aveva, 2020). Manish Chawla, Global Managing Director for Energy & Natural Resources at IBM, sees a future cognitive enterprise. These cognitive enterprises will be driven by AI and cognitive technology applications in geological, supply chain, production, equipment, worker safety and enterprise intelligence (Brightmore and Deane, 2020). Examples of the digital mining transformation include applying artificial intelligence to retain the knowledge of a retiring workforce, as is happening e.g. for Australia's largest oil and gas company Woodside by implementing IBM Watson (IBM, 2020). It also means implementing machine learning algorithms to leverage exploration and reduce the cost of high-risk greenfield exploration by using the mining industries biggest asset – multisource data (Goodbody, 2018). The use of AI extends to route optimization for trucks, optimization of smelters and incident analysis for safety optimizations (Brightmore and Deane, 2020). A report on "Digital in Mining – Progress and Opportunity" by Accenture Consulting that is based on another report from the World Economic Forum (WEF) (Callahan and Long, 2017) compares the application level of digital solutions in the mining and mineral sector. According to Callahan and Long, in-mine operations embrace new digital technologies the heaviest in the sector, with 54% of the questioned mining companies applying robotics and automation for the mining operations. Real-time analytics, predictive machine learning analytics and image analytics are being applied at 35%, 38% and 37% of the mines respectively. Exploration, mine development and ore processing are lagging behind in the race for digitalization. The successful implementation of hyper and superspectral monitoring approaches depends on a number of factors, these include the safety of operators and equipment, the scheduling of measurements within a busy mine planning schedule, the limitations of data quality by the incident light and atmospheric conditions (clouds, dust, humidity) and the robustness and simplicity of the spectral equipment.

The objective of this work is:

1. The development of a digital spectral mine face monitoring based on hyperspectral analysis methods for from an operating and an inactive open pit copper mine in Cyprus
2. The evaluation of existing hyperspectral outcrop analysis approaches related to samples from the iron quadrangle in Minas Gerais, Brazil
3. The parameterization of imaging spectroscopy for pit mining applications
4. The development and evaluation of an imaging spectroscopy workflow for a mine face, ground-based characterization of open pit mine

2 Introduction

2.1 Introduction into open pit mining: conditions and requirements

A short overview about the challenges facing the short-term planning in the open-pit mining environment is given here and is based mainly on the review paper by Blom et al. (2019).

Metal ore like iron, copper and gold as well as resources like coal and limestone are commonly extracted using the open-pit mining method. Here, horizontal layers of material are extracted from the top down. The extraction is divided in long-term planning processes (life-of-mine), short-term planning (from a week to about 2 years) and to the day-to-day, shift-to-shift planning. In the long-term planning the mine is divided into a grid of equally sized blocks assigned with their respective ore grade and other attributes like clay or silica content. A geologist selects the blocks that are to be extracted each year. For the short-term plan, the block model of the pre-selected blocks is divided into irregularly shaped blocks – the ore and waste blocks. These areas are blasted and a geologist partitions these blocks by their grade based on prior sampling. This material is referred to as the “broken stock” of the mine. In the day-to-day activities, the planner decides which material from the broken stock is fed to the crusher or processing plant in order to achieve the daily production rate (Blom, Pearce and Stuckey, 2019). As seen in Figure 2 remote sensing can aid multiple processes along the life-of-mine value chain but also already prior to opening the mine in the exploration phase. By including remote sensing in this process, some of the financial risks connected to mining can be evaluated earlier and possibly avoided (e.g. target detection by satellite to avoid over-sampling and over-drilling). Short-term planning handles various uncertainties; these include the geological uncertainty (stability, ore grade), the equipment-based uncertainty (availability, reliability) and the economic uncertainty (commodity price, fuel price) (Blom, Pearce and Stuckey, 2019). It is predictable, that mine face and stockpile scanning and mapping by hyper- or hyperspectral sensors will play an important role in the future in optimizing short-term objectives like: maintaining the grade of ore production within the desired bounds for the extraction period or sorting the material that is sent to the crushers or waste site to minimize re-handling investments made in 2020 into AI companies and remote sensing companies like Plotlogic Pty Ltd solidify my expectations (im-mining.com/2020/04/30/plotlogic-raises-profile-funds-bhp-iron-ore-contract/ and Gleeson, 2020). The need for imaging spectroscopy in mining is well summarized by a quote from the Founder & CEO of Plot Logic Andrew Job, who said: *“The mining industry is years behind other industries in utilising big data and AI: as a result, there is a lack of fast and accurate orebody knowledge that ultimately restricts yield. With our technology we can grade every tonne of ore accurately, before it even leaves the ground – driving efficiency, sustainability, and profitability. Plotlogic [in this case hyperspectral imaging and AI] can optimise the mining process from*

pit-to-port with pinpoint precision." ([im-mining.com/2020/04/30/plotlogic-raises-profile-funds-bhp-iron-ore-contract/](https://www.im-mining.com/2020/04/30/plotlogic-raises-profile-funds-bhp-iron-ore-contract/) and Gleeson, 2020).

Keeping the ore grade at the desired level for each extracted block can be aided by scanning the samples and cores from each assigned build or by scanning the mine face prior to blasting and the broken stock after blasting (Blom, Pearce and Stuckey, 2019). Hyper- and hyperspectral mine face scanning can be utilized as a tool to increase the certainty for mined ore grade. This can assist by maximizing the level of contaminants while remaining below upper limits in order to prolong the life of the mine. It ensures a correct ore-grade based stockpiling and minimizes the re-handling of material by correct deposition at stockpiles, processing plants or waste dumps. Built-in as real-time "vision" monitors into equipment, systems like these can optimize shovel allocation and excavator location and keep machinery movement at an optimum. Blasted mine faces will not only be evaluated in real-time for excavator activities but the mine face mapping will allow a precise modeling of extractive activities for the subsequent mine faces. By reducing misclassifications (in which waste is sent to the processing and ore to the waste dumps), the total operating cost can be minimized.

In terms of energy consumption from mine to comminution, milling and material handling diesel account for the biggest consumers in a mine with 40% and 17% of respectively of total energy consumption (Lessard, De Bakker and McHugh, 2014). Ore sorting technologies operating on the run-of-mine (ROM) stream can reduce the energy consumption by distinguishing the valuable material from the waste material. The ROM stream represents material of a size around 5cm that has been through preliminary, relatively low energy, crushing operations. An example from a molybdenum mine from (Lessard, De Bakker and McHugh, 2014) showed that 90% of the molybdenum was found in 7.4% of the mass of stone. By rejecting rocks below a certain cut-off grade and classifying them as waste, not only the material handling could be minimized but also, the energy consumption per ton of valuable ore could be reduced dramatically. The study by (Lessard, De Bakker and McHugh, 2014) used dual-energy X-ray transmission studies in order to sense the whole rock volume, but the reduction of transported material by sorting for base metals and industrial metals by VNIR, SWIR and TIR can also be applied to this assumption. These sensors identify the outermost few micrometers of the surface and thereby do not represent the whole rock volume. They do however work without the need of an active X-Ray source and decrease the associated risk.

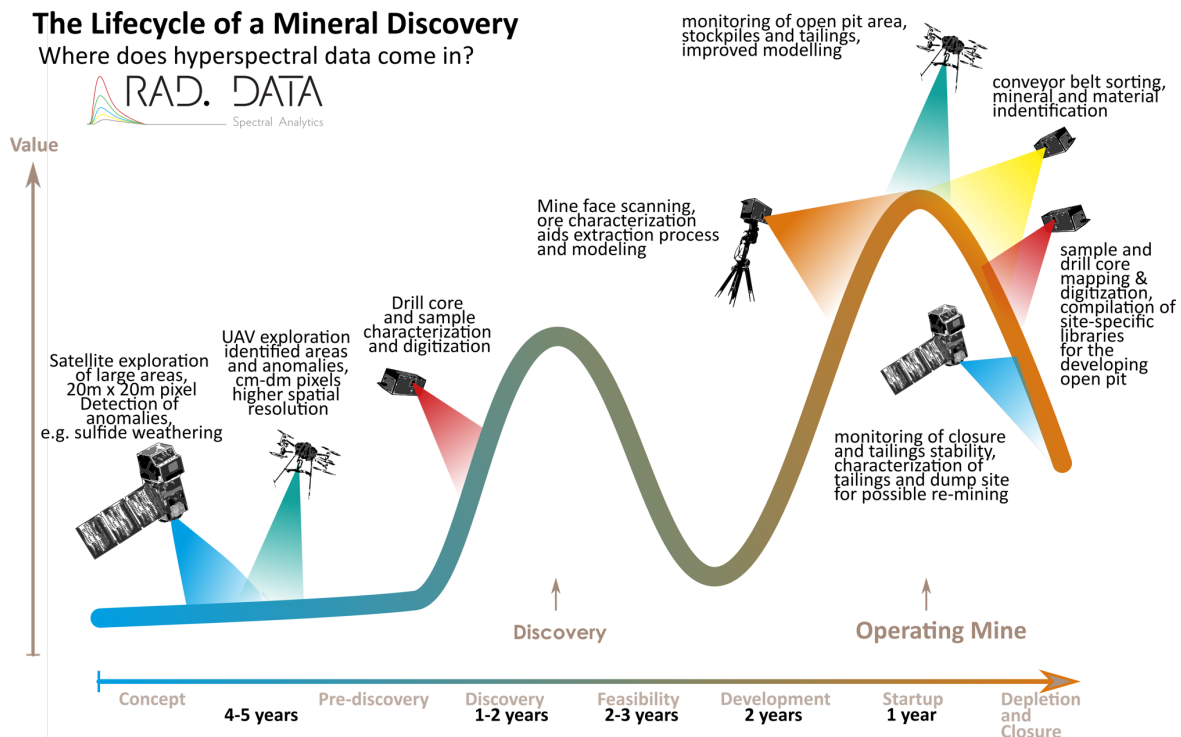


Figure 2 Lassonde Curve: Life cycle of a mine, connected risks and the possible implementations of remote sensing, modified from LePan (2019), created by Friederike Koerting as promotional material for rad.Data Spectral Analytics UG.

In order to implement hyper- and superspectral sensors into the open pit mining environments, a few challenges have to be addressed. A non-extensive list of requirements for hyper- or superspectral open pit monitoring systems are listed in Table 2.

Table 2 Challenges and requirements of the open pit mining industry for hyper- or superspectral monitoring.

#	Challenges	Development of Solution
1	Ruggedness	Protective casing, dust-proof ventilation, GUI adjusted to outdoor conditions & handling with Personal Protective Equipment
2	Speed of Sensor and Analysis	Optimal balance between spectral bands and spatial resolution to keep pace with the dynamics of mining operations; reduction of sensor complexity to decrease acquisition and analysis times; near-real time decision making
3	Spatial Resolution	Resulting grid resolution adjustable or matching with common grids used for geological mapping and modeling in mining operations
4	Site Specific Analysis	Sensor can be calibrated with site-specific spectral reference libraries for use along mine life cycle; adaptable to new or multiple operations; sensors spectral resolution and range adapted to the deposit type
5	Size & Weight	Sensor weight and UAVs that do not require special pilot, Sensors can be safely handled by one person.
6	Power Consumption	Battery and UAV optimization with respect to needed measurement and flight times and needed monitoring frequency
7	Cooling	Efficient and dust-proof cooling system to withstand high temperatures
8	Albedo Correction	Automated pre-processing of data, at-sensor reflectance retrieval and feature retrieval enabling faster, flexible and easy to analyze datasets
9	Humidity & Dust	Spectrally inactive, easy to replace hardware filters against dust and wear on the lens

In order to make advances towards those requirements, this work discusses the simplification of the spectral dimensions of the data (theoretical hardware/ sensor development), the speed of data acquisition, processing and analysis (comparison of methods and application of different spectral regions) and to discuss how the demands for mining environments can be met by hardware or software adaptations in the future.

2.2 Important definitions

As the terminology for remote sensing is used with a variety of slightly different meanings in the community but is rather unknown outside of it, the main terms are described here for the context of this work.

2.2.1 Spectroscopy

Minerals absorb and scatter incident light characteristically and can thus be distinguished from each other. Minerals absorb photons by a variety of processes, which are wavelength dependent (Clark, 1999). **Spectroscopy** describes the study of light as a function of wavelength. **Spectrum** refers to a plot of the intensity of reflection (y) as a function of wavelength (x) (Hunt, 1989). Spectroscopy can be applied to crystalline and amorphous materials alike and is sensitive to the chemical bonds in the material and the crystalline structure and the texture of the surface. Simplified, minerals can be identified by the position and shape of their absorption feature and semi-quantified by the depth of this feature (Figure 3). The differing chemical composition leads to position shifts and shape changes of the spectral features and makes them a complex study object. By identifying these changes and shifts, not only small changes of chemistry in the rock can be defined, but also some proxies for elements and substitution of elements in one mineral (Clark, 1999).

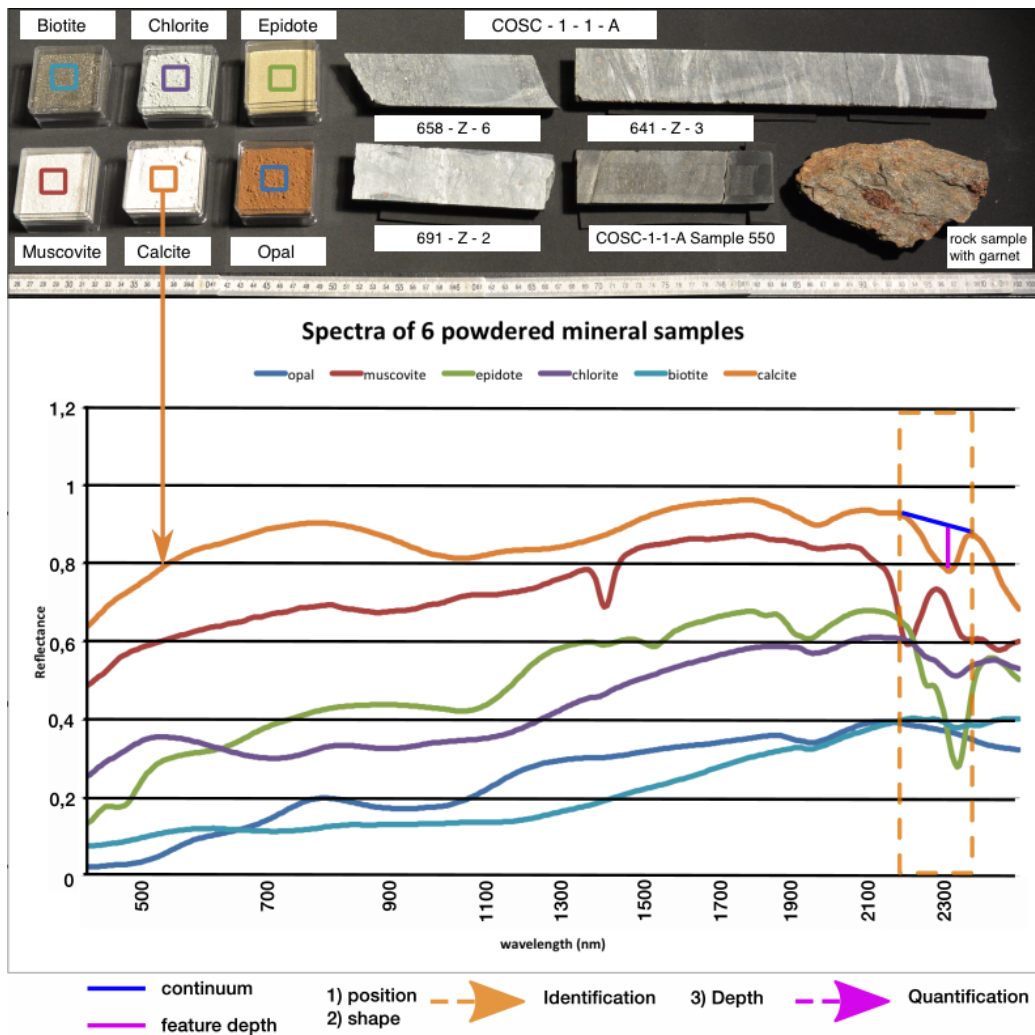


Figure 3 Simplified representation of the information contained in hyperspectral imagery (Körting, 2019).

Multispectral imaging collects the incoming signal in a small number of specific wavelength ranges so called “bands” (typically between 3-15) along the electromagnetic spectrum. **Hyperspectral** imaging collects the incoming light within narrow, consecutive, overlapping wavelength ranges (between 100 and 500+ bands). Due to the narrow, overlapping nature of the bands, narrow spectral absorption features can be resolved. **Superspectral** imagery is a term loosely describing imagery with band numbers between the multi- and hyperspectral resolution (between 15 and 100 bands). Superspectral imagery is able to distinguish broad spectral features (e.g. iron absorptions) but does not resolve narrow features. Figure 4 shows a comparison of bandwidths and numbers of hyper-, super- and multispectral data. For multispectral data, the Sentinel-2 spectral resolution is shown as an example and the hyperspectral data is shown schematically. The superspectral sensor example shows schematically how the band distribution of a VNIR-40nm bandwidth and SWIR-15nm bandwidth sensor would look like that does not collect spectral bands in the wavelength range that is influenced by

atmospheric absorptions (ca. 1300-2010nm). Additionally, the superspectral WorldView-3 satellite band setting is shown as an example for one existing superspectral sensor. The bands are shown without the overlap to distinguish the different width of the individual bands.

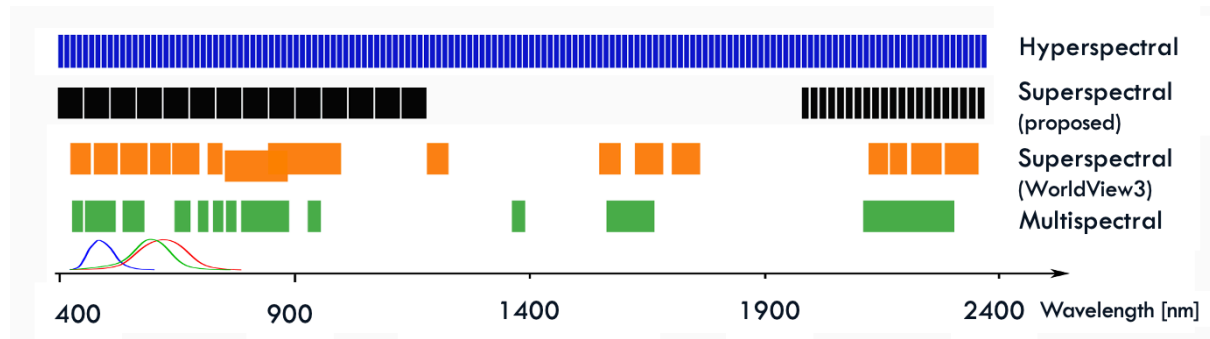


Figure 4 Schematic visualization of bandwidth and band number differences between hyper-, super- and multispectral sensors.

2.2.2 Wavelength ranges

For geological remote sensing, the following wavelength ranges are of importance (Figure 5): the visible light (VIS 0.4 – 0.7 μm) the near-infrared energy (NIR) from 0.7 – 1.0 μm , the middle-infrared region (in remote sensing often referred to as shortwave-infrared SWIR) which spans from 1.0 – 2.5 or 3 μm and the thermal infrared (TIR) with two useful ranges at 3 – 5 μm and 8 –14 μm (Jensen, 2010). In this work, the VNIR (0.4 – 1.0 μm) and the SWIR (1.0 – 2.5 μm) are focused on, as the HySpex system for laboratory and outcrop scans is active in this wavelength range.

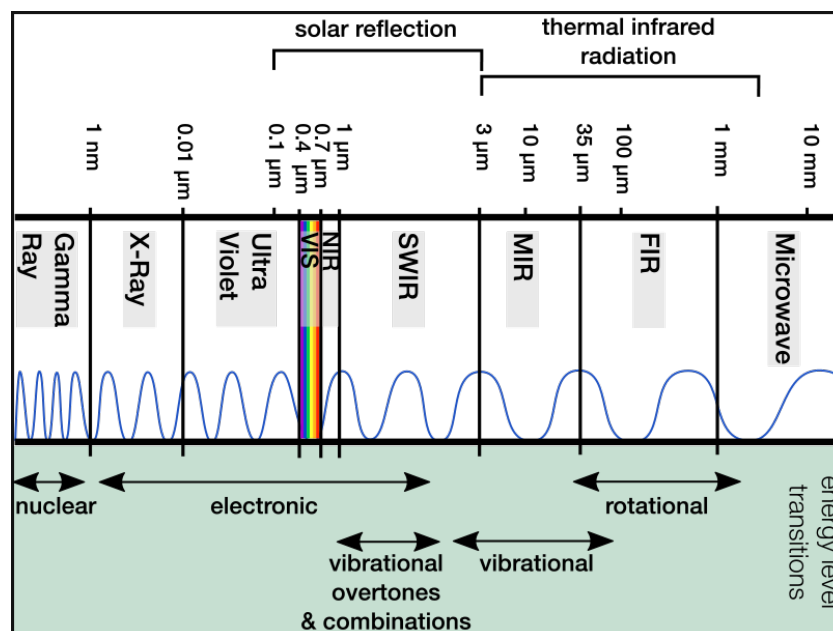


Figure 5 The electromagnetic spectrum and the different types of interactions between EMR and material (Körting, 2019).

2.2.3 Terms of spectroscopic systems

Imaging spectrometers can produce a 3D cube with two spatial dimensions and a third dimension in the spectral range. The **spectral range** describes the region of wavelengths in which the sensor is able to collect quasi-continuously data. Data is being collected in defined spectral “channels” or “bands” of a certain bandwidth and sensitivity. The HySpex VNIR and SWIR system for example collects the spectral information in 408 bands in a spectral range from 414nm to 2498nm. The **spectral bandwidth** is the region of wavelengths of each individual channel in the spectrometer. In an ideal system, each channel collects only the light from a narrow wavelength range and rejects the rest. Only with continuously spaced, narrow bands adjacent to each other and overlapping, narrow absorption features can be detected. The full-width at half maximum (FWHM) spectral response of a spectrometer defines the **width of the bandpass** (Swayze *et al.*, 2003). The distance in wavelengths between the centers of adjacent spectral channels is called **spectral sampling**. The HySpex VNIR sensor collects 160 spectral bands in the range of 414 – 1000nm with a spectral sampling of 3.7nm. The HySpex SWIR collects from 1000 – 2498nm in 256 bands with a sampling of 6.25nm. And finally, the **signal-to-noise ratio (SNR)** is defined as the mean signal level divided by one standard deviation of the signal variety or noise (Swayze *et al.*, 2003). To record details in the spectrum, the SNR has to be high enough to detect the spectral features of interest. The spectral bandwidth and the intensity of light reflected or emitted from the surface influence the SNR (Clark, 1999).

In a **grating imaging spectrometer** - as the HySpex sensors used in this work - the spectral sampling is set by the geometry of the sensor. The dispersion of the grating of the prism, the focal length of the camera and the spacing of the adjacent centers of the detector elements affect the spectral sampling. The bandpass can be affected by the interplay between the sensor geometry, optical deviations and diffraction (Swayze *et al.*, 2003). The maximum information is already obtained by a sampling interval at half the FWHM, as stated in the Nyquist theorem (“critical sampling”). The dominant bandpass in spectrometers is designed to have a Gaussian profile (Clark, 1999), as a Gaussian of varying order optimally approximate the band related spectral sensitivity and allows a quasi-continuous spectrum of spectrally adjacent bands at their FWHM. Figure 6 shows the simplified optical system of the HySpex sensors ((hispex.no/products/disc.php, 2019).

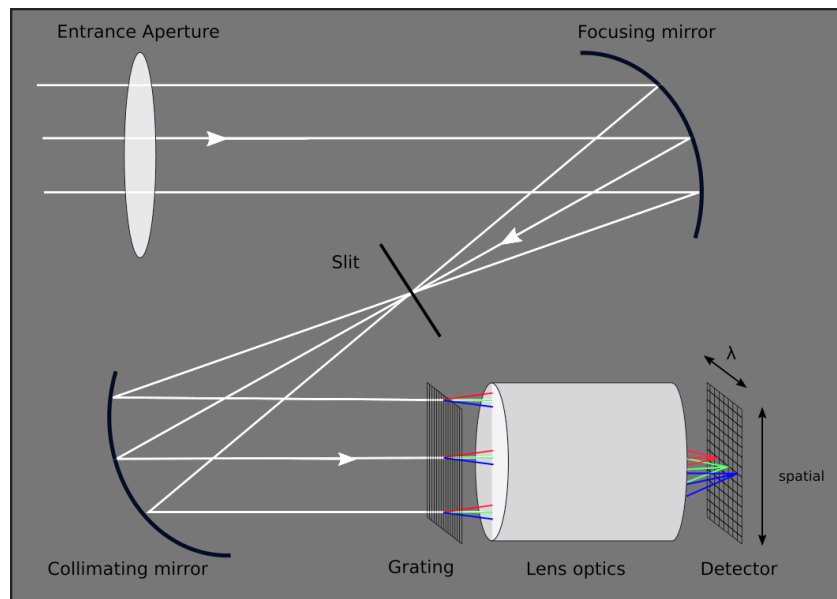


Figure 6 The simplified HySpex optical system after (Körting, 2019) modified from (hyspex.no/products/disc.php, 2019).

2.2.4 Outcrop/ Mine face scanning

The terms “**outcrop**” and “**mine face**” are used interchangeably and describe near-vertical man-made cliff faces in the mining environment produced by extraction of material. Depending on the scale of the mining project, the scales of these vertical cliff faces may vary, in general each horizon of extraction spans around 10-20m of height.

Outcrop scanning refers to the data acquisition of hyperspectral imagery from a distance. As the line scanners of the used sensor are moved line-by-line across the outcrop face by a rotation system, the outcrop is “scanned” hyperspectrally. Hyperspectral data can either be acquired by **point spectrometers** sampling one spectrum per location/ sample or by **hyperspectral imaging spectrometers**. **Hyperspectral imagery (HSI)** is referred to as a data cube with three dimensions (the spatial x- and y- dimensions and the third spectral dimension). Each pixel of the resulting image represents the full spectral information for said location on the outcrop face.

2.2.5 Hyperspectral mapping

Hyperspectral maps are the analysis result of hyperspectral imaging. Each pixel and spectrum of the hyperspectral scan can be analyzed and compared based on its spectral information. The term “**mapping**” is used for the final result of the analysis, usually a color-coded representation of the expected materials within the hyperspectral scan. The most common result is a hard classifier map in which each pixel is labeled and color-coded.

2.3 Introduction to remote sensing principles

In order to use the information from the reflection of any given surface and to extract geological information from it, the way electromagnetic radiation interacts with the surface has to be considered. Hunt (1989) gives a brilliant introduction to the topic in his book chapter “Spectroscopic Properties of Rocks and Minerals” and focuses on the origin of the spectral signatures of rocks and minerals. In the following section a brief introduction to the physical principles of hyperspectral imaging (HSI) remote sensing will be given, in order to facilitate an understanding of the pros and cons of the method, this is based on Clark (1999) and Hunt (1989). The acquisition of information without direct contact to the object is one of the main advantages of remote sensing. HSI remote sensing describes the way of capturing whole image scenes in which each pixel represents a continuous spectrum of light in the given sensor ranges. From the light source to the object of measurement and to the collection in the sensor, the energy recorded by a remote sensing system is changed in many different ways. For passive satellite remote sensing the main energy source is the sun. The incoming energy is scattered, absorbed, transmitted and reflected first by particles in the atmosphere and then by the Earth’s surface and interacts again with the atmosphere on its way to the sensor. In the sensor, the incoming light is dispersed, filtered and interacts with the detectors (Jensen, 2010). The light source, the travel path and the surface interactions define the energy that is collected by the sensor, each will be explained in more detail below.

2.3.1 Electromagnetic radiation

Electromagnetic radiation (EMR) has different sources of creation. Radioactive decay, energy level changes in electrons, electrical charge acceleration or thermal interactions and motion in molecules are mechanisms for EMR creation. The wave nature of EMR was described by James Clerk Maxwell’s *wave model* of EMR in the 1860s, whereas the explanation for the particulate nature of EMR is based on Sir Isaac Newton’s particle model from 1704 which is explained later on (Jensen, 2010). EMR can be characterized by its wavelength λ and its frequency ν , both are related (see Equation 1).

Equation 1 Relationship between wavelength and frequency of EMR

$$c = \lambda\nu$$

c is the speed of light, constant at 299,792,458 m/s (Jensen, 2010).

All objects above absolute zero (0K or -273°C) emit electromagnetic energy. The sun is the main source of energy in remote sensing systems. Simplified, the sun is equivalent of a blackbody with a temperature of 5700K. A blackbody emits energy with perfect efficiency and radiates energy at the maximum possible rate per unit area at each wavelength (Jensen, 2010). Temperature variations are

the only influence on its efficiency as a radiator. *Kirchoff's law* states the energy preservation in such a blackbody, meaning the ratio of absorbed radiation and emitted radiation is equal (Campbell and Randolph, 2011). The *Stefan-Boltzmann law* defines the relationship between the total emitted radiation from a blackbody and its absolute temperature (Equation 2). The higher the temperature of an object, the higher is the amount of radiated energy by the object and the shorter the wavelength of the radiation peak.

Equation 2 Stefan-Boltzmann law describing the total emitted radiation from a blackbody $M(\lambda)$

$$M(\lambda) = \sigma \times T^4$$

σ is the Stefan-Boltzmann constant ($5.6697 \times 10^{-8} \text{Wm}^{-2}\text{K}^{-4}$) and T is the absolute temperature [K] (Jensen, 2010).

The sun produces a continuous spectrum of electromagnetic radiation from very short wavelengths, very high frequency gamma and cosmic waves to very long wavelength, very low frequency radio waves. *Wien's displacement law* defines the wavelength of maximum emission, which is in dependence to the absolute temperature of the object (Equation 3). The sun with a temperature of around 6000K has its dominant wavelength at $0.483\mu\text{m}$ (Jensen, 2010).

Equation 3 Wien's displacement law

$$\lambda_{max} = \frac{k}{t}$$

where k is a constant ($2898\text{K } \mu\text{m K}$) and T is the absolute temperature [K] (Jensen, 2010).

EMR cannot only be described as a wave, but EMR is also transmitted as a stream of indivisible particles traveling in a straight line. Sir Isaac Newton was the first to recognize the dual nature of light and the discrete and continuous behavior of electromagnetic radiation (Campbell and Randolph, 2011). Niels Bohr and Max Planck discovered that EMR is absorbed and emitted in discrete units or packages of energy called "photon" or "quanta". They proposed the "quantum theory" of electromagnetic radiation (Equation 4).

Equation 4 Quantum energy expressed by the frequency of radiation and the Planck constant

$$Q = h\nu$$

where Q is the energy of a quantum [J], h is the Planck constant ($6.626 \times 10^{-34} \text{Js}$) and ν is the frequency of the radiation [Hz].

Spectral sensors collect the number of photons that are emitted or reflected per wavelengths by the material in each measured ground pixel. The type of reflecting surface varies. *Specular reflection* occurs from smooth reflecting surfaces where the reflected energy leaves the surface at an equal angle but opposite to the incident energy. Calm water bodies are near-perfect specular reflectors. If the surface exhibits a large surface height compared to the size of the wavelength of the incident energy (rough surfaces), the energy is reflected in many directions. This is called diffuse reflection. For perfect diffuse reflectors the “Lambertian surfaces” the reflected energy leaving the surface is constant for any angle of reflectance (Jensen, 2010).

The time rate of flow of energy through, off of and onto a surface is called radiant flux (Φ) [W] (Jensen, 2010). The exact monitoring of the incident radiant flux characteristics and its interaction with the surface allow a characterization of the surface itself. The *radiation budget equation* (Equation 5) states that the total amount of radiant flux in specific wavelengths incident to the terrain ($\Phi_{i\lambda}$) is the total amount of the radiant flux reflected from, absorbed by and transmitted through the surface (Jensen, 2010).

Equation 5 Radiation budget equation

$$\Phi_{i\lambda} = \Phi_{reflected\lambda} + \Phi_{absorbed\lambda} + \Phi_{transmitted\lambda}$$

By dividing each variable by the original incident radiant flux ($\Phi_{i\lambda}$), Equation 5 can be rewritten as:

Equation 6 Radiation budget equation (2)

$$reflected_{\lambda} + absorbed_{\lambda} + transmitted_{\lambda} = 1$$

Kirchoff found that in the infrared portions of a spectrum the spectral emissivity (ϵ) equals its spectral absorbance (a_{λ}), often stated as “*good absorbers are good emitters and good reflectors are poor emitters*” (Jensen, 2010)(Equation 6).

Equation 7 Kirchoff's law

$$a_{\lambda} = \epsilon_{\lambda}$$

Spectral sensors collect the number of photons that are emitted or reflected per wavelengths. The photons are collected by the sensor in raw digital numbers (DN) format. The DN values are transformed into radiance values [$W \times sr^{-1} \times m^{-2} \times nm^{-1}$] using manufacturer predefined sensor characteristic radiometric calibration coefficients. Radiance expresses the emitted energy per time unit from a specific direction of an area unit. The collected photons are made up from the total amount of radiance exiting the target study area (L_T) and additional radiance from different paths that are in the field of

view (FOV) of the sensors (*path radiance* L_p) (Jensen, 2010). The total radiance collected at the sensor (L_s) can be described as seen in Equation 8.

Equation 8 Total radiance recorded by the sensor.

$$L_s = L_T + L_p$$

L_p describes all radiance that intercepts the radiance exiting the target study area, either from neighboring areas or from scattering within the reflectance path from target to sensor (e.g. scattering of the reflected energy by dust particles or molecules within the atmosphere before it is collected by the sensor) (Jensen, 2010). The path radiance can have a high impact on the collected radiance at the sensors and distort the true signal of a measured target surface. This holds especially true for proximal remote sensing with a high amount of possible neighboring reflectors from concave surface trends e.g. in open pit mines with concave mine face increments.

The collected data is transformed from radiance to reflectance by calculating the ratio of incident radiance (irradiance) and the backscattered, collected radiance of the surface. It aims to make use only of the material information independent from the source of energy. For near-field spectral data collection (e.g. measuring a mine face within a 100m distance) the influence of L_p is usually seen as negligible.

2.3.2 Interaction with the surface

The main focus of surface reflectance retrieval is to characterize the interaction of the EMR with the surface of interest and the resulting flux of energy. In the application for the field of geology the matter interacting with the incoming radiation are rocks and minerals, depending on the spatial resolution of the measurement and the size of crystallization. Rocks are an assemblage of minerals; The individual mineral grains can be interlocked by growth patterns or cemented together by fine-grained minerals (often silica or calcium carbonate). Most rock surfaces consist of a variety of grain sizes and minerals, all of which influence the interaction with the incoming EMR in a different manner (Clark, 1999; Jensen, 2010). The interaction of the incoming light or radiant flux in a specific wavelength with the matter can reveal important information about the matter itself. If the reflection, absorption or transmittance through a surface dominates in this interaction is dependent on the nature of the surface, the angle of illumination and the wavelength of the EMR (Jensen, 2010).

On the rock or mineral scale, photons of incident light are reflected from the grain surface or pass through the surface and onto another mineral grain (refracted). Those particles are referred to as "scattered". The scattered photons can find their way onto another mineral grain or can be scattered away from the surface where they might be collected and measured by a remote sensing device (Jensen, 2010). A mineral grain can also absorb the photons. Each mineral at a temperature above absolute zero will additionally actively emit electromagnetic energy at certain wavelengths. Generally though, in laboratory experiments enough light is directed at the sample and the amount of photons emitted by the material can be neglected (Clark, 1999). At the outcrop scale, especially for a concave situation of an observer as in the open pit environment, adjacent effects of scattered EMR over multiple surfaces, topography induced illumination differences and diffuse illumination leading to multiple surface-light interactions can play an important role in altering the signal before reaching the detector and challenge the pre-processing and reflectance retrieval of the collected data (Kurz, Buckley and Howell, 2013; Lorenz *et al.*, 2018).

2.3.3 Spectra of materials

The spectra of materials are affected by different factors, inherent to the material as the molecular composition and state of crystallization, and external factors that are caused by surrounding factors as the atmosphere or topographic shadows. Absorption features in satellite remote sensing are highly influenced by the atmospheric particles causing scattering, transmission and absorption. As this work is based in the near field range and on laboratory work, the distance from sensor to object of interest is kept small and an atmospheric correction of the data is not needed (Kurz, Buckley and Howell, 2013; Jakob, Zimmermann and Gloaguen, 2017; Lorenz *et al.*, 2018). The measurements are nevertheless depending on the sun as a light source, therefore the absorption features of the atmosphere play a role in restricting the incoming energy in the wavelength regions of the atmospheric windows where the EMR is transmitted. Most absorptions of EMR in the atmosphere occur due to ozone, oxygen, carbon-dioxide and water (Clark, 1999). Figure 7 from Jensen (2010) shows the absorption of the Sun's incident EMR in the region from 0.1 to 30 μ m by various atmospheric gases and the cumulative result of all atmospheric constituents comparing the solar radiation at the top of the atmosphere and at sea level.

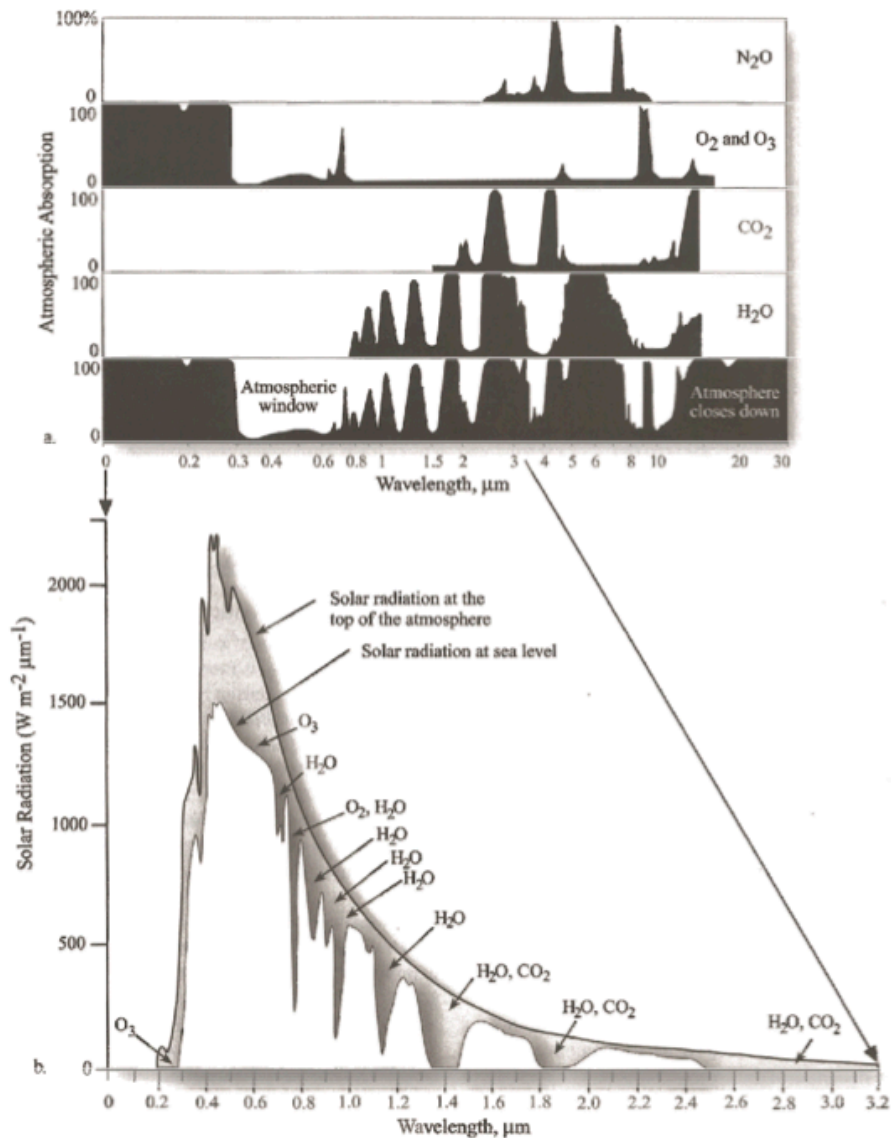


Figure 7 Solar irradiation and absorption of various atmospheric gases at the top of the atmosphere and at sea level, from Jensen (2010).

2.3.3.1 Absorption features and their causes

As mentioned before, different materials show different characteristic spectra due to different reactions to the incoming light on a molecular and atomic level. Absorption bands are created due to the change of energy state when a photon of a specific wavelength is absorbed or emitted. When an isolated atom or ion with a discrete energy state absorbs a photon its energy state changes. The energy emitted due to this process is not equal to the energy of absorption, causing emission at a different wavelength and creating "absorption bands" or "absorption features". Their position, depth and width are due to the different absorption processes taking place, the absorbing ion or molecule and its position in the crystal lattice, the kind of chemical bond and the elements involved. These absorption features the VNIR wavelength region (400 to 1000nm) are caused by electronic and vibrational

processes within the crystal lattice in. Electronic processes require higher energies and therefore cause broad absorption features in the shorter wavelengths of the VNIR. Vibrational processes take place in the infrared regions (SWIR (1000 to 2500nm) and thermal regions (1.2 to 40+ μm)) and cause sharp, small absorption features (Hunt, 1989; Clark, 1999) In the case of minerals, only hyperspectral sensors with a spectral bandwidth resolution of approximately 10nm or less can capture the very fine differences in reflectance at certain wavelength positions (Jensen, 2011).

2.3.3.2 *Electronic processes*

Absorption features related to electronic transition processes can be caused by crystal field effects, charge transfer absorption, conduction band transitions and color centers. The most common electronic process is related to unfilled electron shells of transition elements such as Cu, Ni, Cr, Ti, Co and especially Fe (Hunt, 1989; Jensen, 2010). These transition metal ions have discrete energy states. The absorption of a photon of a certain wavelength results in a jump into a higher energy state, this is called **crystal field effect**. The transition between these new energy levels is determined by the oxidation state of the ion (e.g. Fe^{2+} vs. Fe^{3+}), its coordination number, its position in the crystal lattice and the type of connected ligand (Hunt, 1989; Kurz, 2011). The absorption of a photon of a certain wavelength does not usually cause the emission of the photon of the same wavelength. Variations in the crystal structure in minerals cause a variety of different absorption features (position, depth, width) even when the same ion is involved (Clark, 1999). An exception is the group of rare earth (REE) ions. The electrons lie deep and are shielded from the surrounding crystal field. The absorption features in REEs are diagnostic for the presence of the ion in the mineral and not the mineralogy. On the contrary, iron is a very common substitute element with very active bonding in the crystal lattice in the VNIR and SWIR. Even low iron concentrations cause broad absorption features and often dominate the spectral feature range of a material, not being diagnostic for iron presence in the mineral but rather in the wider mineralogical scale (Kurz, 2011). Absorbed energy can also cause the migration of an electron between neighboring ions or ions and ligands. This process is called **charge transfer absorptions** (Hunt, 1989). This occurs preferably when metal ions with different oxidation states are present in a mineral. Those absorption bands are usually diagnostic of the mineralogy and are stronger developed than those of the crystal field (Clark, 1999). The absorption maxima is found in the ultraviolet range but the edges extend towards the VNIR region (Kurz, 2011). Some minerals have two energy levels in which the electrons reside. The "valence bands" represent lower energy levels with atom-attached electrons. The "conduction band" is a level of higher energy in which the electrons move freely through the lattice. These two zones are separated by the "forbidden gap" or "band gap" a zone of energies which the electrons may not enter (Clark, 1999). The edge of the conduction band to the band gap shows an intense absorption edge in the VNIR (Hunt, 1989). The yellow color of some

minerals, e.g. sulfur is caused by such an absorption edge (Clark, 1999). This electronic process of exciting an electron across the forbidden gap is called **conduction band transition**. The fourth electronic process in minerals is called **color centers**. Those are discrete energy levels of excited electrons bound to lattice defects e.g. impurities. The energy of a photon can move electrons into the defect and causes an absorption (Hunt, 1989; Kurz, 2011).

2.3.3.3 Vibrational processes

The presence of different chemical bonds in a molecule or crystal lattice can cause the system to displace atoms within this lattice. This is causing a vibration similar to the oscillation of weights connected by a spring. The frequency of vibration depends on the strength of the bond in the molecule and the mass of each element in a molecule (Clark, 1999). The vibration is made up from a restricted number of simple motions the so-called **fundamentals** (Hunt, 1989). In general, the fundamentals produce spectral features at wavelengths longer than $2.7\mu\text{m}$. If a fundamental mode is excited with more than 1 quanta of energy it produces vibrations with frequencies of integer multiplications of the fundamental frequencies, called **overtones**. When two or more fundamentals or overtones interact – are added or subtracted - a **combination tone** feature occurs. Features of geologic materials caused by overtones or combinations usually occur in the NIR region of light (Hunt, 1989). Carbonate ions, hydroxyl ions and water in a material for example show overtones and combination tones with very high fundamental frequencies. H_2O has 3 fundamental vibrations, two caused by the symmetric OH stretch and one by the H O H bent ($2.738\mu\text{m}$, $2.553\mu\text{m}$ and $6.270\mu\text{m}$ respectively). H_2O bearing minerals show the overtones of water in their reflectance spectra. The OH stretch overtones occur at about $1.4\mu\text{m}$ and the H O H bend and OH stretch combinations are found near $1.9\mu\text{m}$. The occurrence of an absorption feature at $1.4\mu\text{m}$ but not at $1.9\mu\text{m}$ indicates the existence of hydroxyl (Clark, 1999).

2.3.4 **Spectral properties of rocks and minerals**

The spectrum of a rock is not as well defined as the spectra of its constituents as it is a mixture of overlapping and substituting minerals and elements. The features appear muted and minor constituents, impurities or substitutions often dominate the spectral appearance of a rock, allowing only a qualitative determination of its mineral assemblage but not its quantities within the rock matrix (Hunt, 1989). This is complicated by the fact that some minerals such as quartz and feldspar do not possess absorption features in the VNIR and SWIR region of light, whereas others as iron ions, organic material and hydroxyl ions dominate the spectrum and hide identifiable features of other constituent minerals. Generally, the identification of proxy minerals for a rock unit or area of interest enables the mapping of regions in a sample or outcrop instead of providing a detailed analysis of a petrographic manner. The proxy minerals that need to be matched to the unknown spectra are usually provided by

a number of accessible spectral libraries or can be built based on field samples or in-situ handheld spectroscopy. The spectral signatures of minerals and rocks have been studied widely and are presented in a number of works Clark (1999, 2003a), Hunt (1989), Hunt and Ashley (1979) and Swayze et al. (2003). The currently most distributed libraries of spectra is provided by the USGS as the USGS Spectral Library splib06a and splib07a (Clark *et al.*, 2007; Kokaly *et al.*, 2017). These spectra are usually based on powdered mineral samples, are measured with different spectrometers and are available online. I have contributed to the goal of making spectral libraries publicly available by publishing spectra of materials and their corresponding geochemical analysis (Koellner *et al.*, 2019; Koerting, Herrmann, *et al.*, 2019; Koerting, Rogass, *et al.*, 2019).

2.3.5 Influencing factors for the spectral response

As already summarized in Kurz (2011), this paragraph summarizes his findings and adds to them. Most of the factors influencing and modifying the spectral curve of rocks and minerals affect the overall brightness and contrast and do not shift the absorption features. Some of these properties are visible in the laboratory, such as the effect of porosity (Hapke, 2008) but are negligible in the outcrop scale due to low spatial resolution and a high noise level (Kurz, 2011; Hapke, 2012). The particle size, mineral mixture, view geometry and surface roughness might alter the spectral curve. This is especially true for outcrop imagery due to large mixed pixels (mineral mixes and surface coatings) and a higher surface roughness (Hapke, 1981, 2012; Hapke and Wells, 1981). As stated earlier, the depth of the absorption feature is an indicator for the amount of light absorbed and is therefore a semi-quantitative measure for the abundance of the absorber (Clark, 1999). In non-opaque material, the intensity of absorption increases with grain or particle size, whereas the overall reflectance decreases. This is due to greater internal path travelled by the EMR in larger particles (Clark, 1999, 2003a).

Mixtures of materials (mineral mixtures and grain size mixtures) alter the spectral response. We distinguish four different types of spectral mixtures: linear -, intimate -, molecular mixture and mixing due to coating (Clark, 1999; Kurz *et al.*, 2012). Optically separate materials without multiple scattering between components result in a linear mixture. In this spatial mixture, the mixed spectrum is a linearly weighted sum of the individual components. In this kind of areal mixture, brighter components tend to dominate the spectrum (Clark, 2003a). Intimate mixtures are characterized by multiple scattering between materials with ingrown material borders, as is the case for minerals in a rock. The result is a complex non-linear mixed spectrum. Here, the darker of the two spectral components tends to dominate the spectrum (Clark, 2003a). Molecular mixtures occur at molecular levels, for example when liquids or liquids-solids are mixed. Examples would be interlayered water in clays or on a bigger scale debris- or mudflows. Molecular mixtures result in band shifts in the spectrum. Coating leads to several scattering-transmittance layers for each coat, with different optical

thicknesses and material dependent absorption properties. Coating effects are to be expected in a mining environment due to work related settling dust and fresh reactive surfaces prone for oxidation. If each component in the mix is known and a spatial separation of different materials can be assumed, linear spectral unmixing can determine the fraction of each component present in the pixel as e.g. done by the EnGeoMap algorithm (Mielke *et al.*, 2016).

2.4 Hyperspectral mine face scanning

Hyperspectral geological applications have been developed in big jumps over the past decades in the large field of remote sensing applications, as the development is both based on the innovation of technology and the era of machine learning and algorithm development. The most common platforms for geological hyperspectral applications include multispectral satellite-based and airborne imagery (van der Meer *et al.*, 2012, 2002; Kruse, 2003; Bellian, Beck and Kerans, 2007; Bedini, 2011; Kokaly, King and Hoefen, 2011; Savage, Levy and Jones, 2012; Ngcofe *et al.*, 2013; Mielke *et al.*, 2014; Notesco *et al.*, 2014; Yokoya, Chan and Segl, 2016; Kokaly, Graham, *et al.*, 2016). Laboratory scale hyperspectral geological analyses were conducted to build precise spectral libraries (Clark *et al.*, 2007; Baldridge *et al.*, 2009; Koellner *et al.*, 2019; Koerting, Herrmann, *et al.*, 2019; Koerting, Rogass, *et al.*, 2019; Meerdink *et al.*, 2019) and to characterize hand specimen and drill cores in spatially high resolution imagery (Kruse *et al.*, 2011; Zaini, van der Meer and van der Werff, 2014; Koerting *et al.*, 2015; Hierold, 2016; Körting, 2019; Kraal and Ayling, 2019). In the last decade, the first studies were conducted on hyperspectral outcrop scanning (Kurz *et al.*, 2008, 2012; Kruse *et al.*, 2011; Kurz, 2011; Buckley, Kurz and Schneider, 2012; Boesche, 2015; Kirsch *et al.*, 2018; Lorenz *et al.*, 2018; Salehi *et al.*, 2018) and only a few of them focus purely on the context of mining or aim at robust and cost-efficient technological developments to improve mining efficiency and security. (Krupnik and Khan, 2019) review the close-range, ground-based hyperspectral studies for mining applications thoroughly in their article from 2019, their findings are summarized below and added to. As this work is focused on raw material mapping, only details of studies that deal with mineral exploration, sedimentology and diagenesis are being shared here.

2.4.1 Research Groups and predominant methodology

Several working groups led advances in geological HSI in the past; a few of them are stated below. As a short disclaimer: the author realizes that the list and the respective research is subjective and hardly extensive to all groups focused on this topic and has a bias towards European and Northern American research groups. It is only used to introduce current state-of-the-art approaches. Even though the eight

groups listed below are representative of the geological proximal remote sensing community they are by no means covering the wide range of research activity in that field.

1) The scientific group around Prof. Dr. van der Meer and Dr. van Ruitenbeek, from the **Department of Earth Systems Analysis of the University of Twente**. Van der Meer's group works in several scales from infrared rock mineralogy and microstructure to broad satellite imagery analysis for hydrothermal structure detection. Hyperspectral efforts were focused on non-imaging point-spectrometers and spectral analysis of sample spectra (van der Meer *et al.*, 2012; Dalm *et al.*, 2014; Zaini, van der Meer and van der Werff, 2014; Dalm, Buxton and van Ruitenbeek, 2017; Hecker *et al.*, 2019) but also ventured into SWIR imaging of porphyry copper related samples (Dalm, Buxton and van Ruitenbeek, 2017) where spectral angle mapping (SAM) based on manually selected sample spectra and Minimum Wavelength Mapping (MWL) are used to assess white mica composition, white mica crystallinity and chlorite composition.

2) The division **Exploration Technology at the Helmholtz-Institute Freiberg for Resource Technology** led by Dr. Richard Gloaguen, which focuses on multi-scale activities and UAV based remote sensing. They proposed new correction approaches for reflectance retrieval as well as geometric correction of the data based on LiDAR and RGB-photos for close- and long-range applications (Rosa *et al.*, 2016; Kirsch *et al.*, 2018; Lorenz *et al.*, 2018; Salehi *et al.*, 2018). The mapping approaches include: Deriving spectral libraries of lithological endmembers (EMs) by pixel purity (PPI) EM extraction and visual EM spectral analysis of outcrop image- and from point-spectrometer sampling (Kirsch *et al.*, 2018; Salehi *et al.*, 2018). Laboratory-collected freely available spectral libraries as the USGS Spectral Library (Kokaly *et al.*, 2017) are also used (Kirsch *et al.*, 2018). These spectral libraries are then utilized for SAM. Additionally, minimum and maximum "peak" wavelength mapping of various wavelength ranges is performed with the Hyperspectral Python (HypPy) toolbox (van der Meer *et al.*, 2018; Bakker and Oosthoek, 2020). MWL is performed in order to highlight variations in mineral abundances in the outcrop image. Some studies also include a minimum wavelength depth mapping (Lorenz *et al.*, 2018). Band ratio determination for mica crystallinity index mapping is also part of the analysis. For the LWIR data, a random forest classification is performed based on abundance features retrieved from the lithological EM extraction (Kirsch *et al.*, 2018).

3) The **hyperspectral imaging group** lead by Benoit Rivard at the **University of Alberta** works on HSI techniques for mineral exploration. Even though their focus is on airborne remote sensing, they advanced VNIR-SWIR lithological mapping efforts, REE mineral, crude oil and shale mapping in outcrops and samples via imaging HSI (Rogge *et al.*, 2014; Turner, Rivard and Groat, 2014; Scafutto, de Souza Filho and Rivard, 2016; Entezari *et al.*, 2017; Feng, Rogge and Rivard, 2018). Only recently, large

amounts of samples and drill cores from a Cu porphyry deposit were analyzed with the purpose of applying the found metric for distinction to facilitate ore-sorting in a controlled environment (Lypaczewski *et al.*, 2019, 2020). The proposed spectral alteration score has been developed for SWIR HSI. HSI of this group has been studied with an emphasis on the applicability for northern regions and tropical forests.

4) The Remote Sensing Unit of the Czech Republic Survey around Veronika Kopackova-Strnadova focuses on soil parameter mapping and monitoring mainly from airborne or satellite-based hyperspectral sensors (Kopackova *et al.*, 2012; Notesco *et al.*, 2014; van der Meer *et al.*, 2018).

5) The United States Geological Survey (USGS) Geological and Mineral Mapping around Gregg A. Swayze, Raymond Kokaly and Roger N. Clark (formerly USGS, now the non-profit “Planetary Science Institute”) (Clark, Swayze and Gallagher, 1992; Kokaly, King and Hoefen, 2011; King *et al.*, 2012; Swayze *et al.*, 2014). The USGS was among the first to approach geological hyperspectral mapping and ventured into long-range HSI for tests on outcrops in Alaska (Kokaly, Graham, *et al.*, 2016; Kokaly, Hoefen, *et al.*, 2016). Their approach is based on the Material Identification and Classification Algorithm MICA (Kokaly, King and Hoefen, 2011) and the Tetracorder (Clark, 2003a) as a tool to map the mineral assemblages of VNIR-SWIR airborne, SWIR ground-based and VNIR-SWIR laboratory data.

6) The geological remote sensing efforts at the Rio Tinto Centre for Mine Automation at the University of Sydney, centered around Richard Murphy, who is also affiliated with Plotlogic Pty Ltd, and Sven Schneider who led some of the efforts during his Ph.D. (Schneider *et al.*, 2011). Plotlogic Pty Ltd. is a supplier of AI-based ore characterization technology (im-mining.com/2020/04/30/plotlogic-raises-profile-funds-bhp-iron-ore-contract/ and Gleeson, 2020). The group concentrates on the topic of autonomous mapping of mine face geology in combination with LIDAR based 3D-modeling of open pit surfaces (Murphy, Monteiro and Schneider, 2012; Monteiro *et al.*, 2013; Murphy *et al.*, 2015). Regarding vertical geological mapping, SAM was found superior to Support Vector Machine (SVM) approaches for shadowed surfaces that are common in natural surface geometries (Murphy, Monteiro and Schneider, 2012). Their take on the influence of incident illumination for the classification is worth considering for the irregular surfaces vertical geology mapping has to deal with (Schneider *et al.*, 2011).

7) And then there is the group “GEOMAP”, the working group of the author, under Dr. Christian Mielke, formerly formed by Dr. Christian Rogass from the Helmholtz Centre Potsdam - German Research Centre of Geosciences GFZ Potsdam (GFZ). The group leads the geological, algorithm developments for the German satellite mission EnMap (Guanter *et al.*, 2015). Within the EnMapBox, a geometric hull continuum removal and feature extraction was developed by Rogass and Mielke starting in 2013 (Rogass *et al.*, 2013; Mielke *et al.*, 2015, 2016, 2018). This EnGeoMap algorithm was used for the geological mapping in the GEOMAP group and is showcased for outcrops and laboratory samples e.g.

in the Rare Earth Element Mapping report by Köllner et al. (2019). For REE detection, multi-temporal averaging was applied to reduce noise and Richardson-Lucy de-convolution in order to sharpen the small REE absorption features was utilized (Boesche, 2015). The MICA algorithm (Kokaly, 2011) was successfully applied on drill core characterization and compared to the EnGeoMap results (Hierold, 2016; Körting, 2019). These mapping and characterization approaches are currently developed further in the scientific projects: “Remote Monitoring of Tailings using satellite and drones” (REMON) (Koellner, 2020) and “Lightweight Integrated Ground and Airborne Hyperspectral Topological Solution” (LIGHTS) (lights.univ-lorraine.fr/, 2020). Multispectral and superspectral mapping approaches are currently being developed for the REMON project, including the here presented “Binary Feature Fitting” (BFF) (Köllner *et al.*, 2020; Mielke *et al.*, 2020). The GFZ spin-off “rad. Data Spectral Analytics UG” which the author co-founded, advanced the BFF and EnGeoMap algorithms further to provide turnkey solutions along the whole value chain in the mining and metals industry under the name of “ReSens+” (Hummel and Krupa, 2020). ReSens+ is utilizing the advanced BFF algorithms in combination with other machine learning approaches and expert knowledge. The ReSens+ algorithms were successfully applied to 40+ satellite imagery based projects around the world in 2018, 2019 and 2020 (www.raddata.io, 2020).

2.4.2 VNIR and SWIR proximal scanning in mining applications

HSI in the VNIR and SWIR range has been used prototypically for sulfide ore detection, mainly focusing on iron and copper sulfides. Other research is based around easily detectable carbonate and clay features in the SWIR range. In the following paragraphs selected studies relevant to this work are listed and explained.

Dalm et al. (2014, 2017) tested a set of rock samples being 5-7cm in diameter from a semi-autogenous grinding (SAG) mill at a South American mining operation. The capability of sorting by using VNIR-SWIR point-spectrometers (Dalm *et al.*, 2014) and SWIR-only hyperspectral imaging techniques (Dalm, Buxton and van Ruitenbeek, 2017) was tested. The general results showed the possibility of identifying SWIR-active mineralogy but not Cu-bearing minerals. The SWIR-active mineralogy showed an indirect relation to Cu grade as SWIR-active mineral assemblages represent different hydrothermal alteration zones. By determining white mica NIR crystallinity and relative contents of chlorite, tourmaline and ferrous minerals, sub-economic ore samples could be identified. The sorting of ore vs. waste in porphyry copper systems by NIR sensors can therefore be accomplished. Open questions in this area are the prediction of bulk grade from surface measurements, the tolerability of surface contamination and the influence of water on the spectral characteristics. The samples by (Dalm *et al.*, 2014; Dalm, Buxton and van Ruitenbeek, 2017) also represent solely the output of the SAG mill at a specific time

and might not be representative of the whole deposit. The data acquisition took place under controlled laboratory conditions and is therefore not representative of open pit mining or on-site sorting machinery.

Kirsch et al. (2018) tested a multi-scale HSI approach in the Naundorf Quarry in Saxony, eastern Germany. The site is known for a polymetallic sulfide vein network and quartz bound copper occurrences. The approach included UAV-based VNIR data, ground-based VNIR, SWIR and LWIR data of former mine face scans and handheld VNIR-SWIR point spectroscopy. MWL was applied in order to identify areas with features chosen to indicate Al-OH (2160–2220nm), Fe-OH (2230–2295nm), CO₃/Mg-OH (2300–2360nm) and Fe (415–500nm). MWL mapping was also applied to the VNIR UAV data between 675–800nm to visualize existing lithologies. EM based classification (SAM and random forests (RF)) was performed based on EM derived by PPI. Additionally, a band ratio calculation (2002nm / 1943nm) was performed on the data. Two lithological zones could be identified and the hydrothermal zones could be delineated. The image-derived spectra utilized for reflectance retrieval can be influenced by noise and it was found that the resulting reflectance data exhibits a shift in wavelength position from the image spectra to the reference mineral spectra. Additionally, supergene iron minerals were identified by hyperspectral means but not validated by XRD or thin sections. Kirsch et al. (2018) reasoned that iron spectrally tends to dominate the spectrum even if the abundance of occurrence is very low. It is argued that it therefor might be picked up by HSI but not XRD or in the thin section. As stated earlier however, iron absorptions do not necessarily indicate mineralogical presence but an overall presence of iron as an element substitute in the crystal lattice and are therefore highly influential for the crystal field (Kurz, 2011). Sample bias can also play a role when low alteration parts were sampled instead of areas showing iron alteration crust. This has to be investigated further. Kirsch et al. (2018) applied the open source HypPy toolbox for their data analysis and their own “Mineral Exploration Python Hyperspectral Toolbox” (MEPHySTo) (Jakob, Zimmermann and Gloaguen, 2017) for image pre- and post-processing and data integration.

Lorenz et al. (2018) investigated the Corta Atalaya mine near Mina de Rio Tinto in Spain. The mine started extracting iron and copper sulfides and closed in 1991 after mainly concentrating on the extraction of sulfur. VNIR and SWIR data was collected in the range of 380–2500nm in three scan lines, one from March 2016 and the second and third from October 2016. Radiometric correction is based on deriving a singular atmospheric correction spectrum automatically from the hyperspectral image itself. MWL mapping for the Al-OH feature position and depth (2190–2215nm) was conducted with the HypPy toolbox (Bakker and Oosthoek, 2020) for all three scenes and was validated by spectral field sampling. The resulting maps coincide well with the expected lithologies. The data was not topographically corrected as the pit walls were assumed to be evenly illuminated and the shadowed

areas were excluded from the subsequent analysis. The possible surface alteration changes between image acquisition times (March to October) were not taken into account and neither was the low density of ground sampling.

Kruse et al. (2011) studied the inactive Trinity silver mine in Nevada, USA by means of aerial, ground-based and laboratory HSI. Aerial scans of the area (1m pixel resolution), tripod-based scans of the mine face (4cm pixel resolution) and proximal laboratory scans of the drill-chips were conducted. The analysis is based on dimensionality reduction by minimum noise fraction, PPI EM determination and extraction by n-D scatter plotting and visualization. Mineral EMs were identified by visual inspection and spectral library comparison. Mineral maps were produced by MTMF. Again, the shift of wavelength minimum of the muscovite/ illite spectral feature is used as a proxy for Al content in muscovite and related to high-temperature hydrothermal alteration. Additionally, jarosite is included as an EM and used as a proxy for oxidized pyrite and thus un-mined reduced silver ore. The mapping of 23 core boxes and the mine-face scan showed a clear correlation between the area mapped as jarosite and the centrally exposed sulfide. Kaolinite is additionally mapped and associated with the periphery of the sulfide exposure indicating lateral movement of acidic fluids (Kruse *et al.*, 2011).

The recently published study of Lypaczewski et al. (2020) measures the relative abundance of twelve minerals and estimates white mica grain size with an additional metric. Coarse-grained white mica is associated with copper mineralization in two of four major porphyry Cu systems in the Highland Valley Copper district in British Columbia, Canada. In a third Cu system, tourmaline and epidote occurrence is linked to Cu mineralization. High spatial resolution HSI in the SWIR was achieved for 755 samples and 400m of continuous drill core. Absorption features produced by cation-OH bonds in hydrated minerals are used to identify the mineralogy. The mineralogy is detected by mapping the wavelength position of distinct absorption features for each mineral in combination with excluding absorption features that would interfere with or are not distinct enough for the sought minerals. The diagnostic absorption features utilized for mapping in Lypaczewski et al. (2020) are listed in Table 3.

Table 3 Spectrally detectable mineralogy at Highland Valley from Lypaczewski et al. (2020).

General Group	Mineral	Diagnostic absorptions [nm]	Interference with
Al-bearing	Montmorillonite (Mt)	1467	-
	Kaolinite (Kaol)	2160	Mt, Ms, Tr
	Muscovite (Ms)	2125, 2200 (coarse grained only)	Kaol, Mt, Tr
Ca-bearing	Gypsum (Gyp)		Pump
	Prehnite (Prh)	1477	Chl (2250nm)
	Pumpellyite (Pmp)	1510	-
(Fe,Mg)-bearing	Epidote (Ep)	1540, 2250	Chl(2250nm), Tr
	Amphibole (Am)	2330, 2390	Chl
	Chlorite (Chl)	2000, 2250	Amp, Ep, Tr
	Tourmaline (Tur)	2205, 2245, Slope 1000/1180	Ms, Kaol, Mt, Chl (2250nm)
Spectrally inactive	Sulfides (Sulf.)	Flat spectrum	-
	Quartz (Qz)	Inferred from 1450 H ₂ O absorption	-

Murphy et al. (2012) evaluated classification techniques with a spectral library taken under different illumination conditions. SVM and SAM results are compared. SAM is of importance here, because it is known to be less sensitive towards changes in albedo, illumination and topography. For both approaches, independent spectral libraries were used which were built from samples under different light conditions instead of retrieving spectra from the HSI itself. Spectrally pure core samples (homogeneous areas extending over the field of view of the sensor) were measured under “sunlit” and “shadowed” conditions as well as with an oblique illumination angle. Additionally, “whole” rock sample spectra (not spectrally homogeneous) were taken of the same rock types as the samples above. The classification showed changes between “no shadow” and “shadow” data, possibly induced by an increased slope between VNIR and SWIR in the spectrum caused by the detector jump. This reflectance offset leads to a change of spectral slope, causing a change of class/ rock type with increasing shadow. SVM outperformed SAM in classifying the spectral libraries but was inferior in the natural environment of the outcrop. Constructing a spectral library in the laboratory for shadowed areas proved difficult, as the influence of shadow is always a combination of influences of the adjacent environment and the scattering and absorption at each wavelength by the atmosphere and the surrounding rocks. Changes in illumination and topography have to be accounted for in the choice of spectral library, nevertheless albedo-insensitive techniques like SAM perform well for mine face geology. Schneider et al. (2011) took this approach in 2011 when comparing three mapping techniques: SAM and two machine learning techniques within a probabilistic Gaussian process (GP) framework. They were tested for their effectiveness under different conditions of illumination. The observation angle dependent (OAD) covariance functions (kernel) GP was found superior, as it showed to be insensitive to illumination

variability within and between imagery and can map geological zones utilizing an independent spectral library without a prior knowledge. The spectral library that was used differed from the outcrop conditions in the presence of illumination differences and the amounts of noise. Both SAM and the GP-OAD were found superior due to being based on spectral angle instead of the distance-based method. The GP-OAD modeled the variability within a class of rock of the training data and was therefore superior in mapping the geology for unknown targets (not included in the library).

Murphy et al. (2015) used hyperspectral and LiDAR data to map vertical geological surfaces. Clay was mapped in an open pit environment of an iron-ore mining operation in the Pilbara, Western Australia. Clays are not only useful due to their clear diagnostic absorption feature between 2000–2500nm, they also often act as marker horizons between different geological units and can represent lines of stratigraphical weaknesses. Mapping clay can aid both the geological mapping as well as safety considerations for the extraction of material. Automated Feature Extraction (AFE) can be used to identify the strongest absorption features. AFE identifies and quantifies the deepest absorption feature in each spectrum, its wavelength position & feature depth. The feature depth and width provide information about mineral type and mineral relative abundance respectively. AFE thereby, is comparable or even identical in theory to the MWL approach utilized by e.g. Lorenz et al. (2018) with the HypPy toolbox. The spectral data was co-registered with geometric information provided by LiDAR. A mean distance error of 0.48m for the registration error between the LiDAR and the hyperspectral data was calculated and found to be acceptable at a mine front of around 700m width and at a distance of 120 to 700m away from the camera. In total, seven minerals were identified. The features used for spectral identification are listed in Table 4. The areal estimates for these minerals varied up to a factor of 2, under- and overestimating the area depicted in the 2D mineral map compared to the LiDAR co-registered 2.5D map. This is caused by the difference in distance from the mine face to the sensor. Higher situated areas were underestimated in the 2D mineral map, whereas lower situated areas (closer to the sensor) were overestimated.

Table 4 Absorption feature wavelength positions of minerals mapped by Murphy et al. (2015).

Mineral	Main Absorption feature for identification [nm]
Illite-smectite	main: 2208, weak 2235
Ferruginous (Fe) smectite	2208 and 2233 (Fe and Al in octahedral sites)
Nontronite	2282 - 2288 (Fe-OH)
Kaolinite	2196 & 2202 (Al-OH absorption doublet)
Chlorite	2319 (broad absorption centered around this wavelength)
Talc	2041 – 2380 (several sharp features), strongest at 2306

The advantages found for AFE is the applicability to any data without the use of a spectral library or a prior knowledge. It does however “underuse” the data by neglecting the importance of the overall shape of the spectral curve and the variability within a spectrum apart from one distinct spectral feature. AFE (or likewise the MWL) can only be utilized well for data with a low level of noise and a high spectral resolution in order to identify sharp, narrow features and when the variability for the minimum of the feature is low (only a few nanometers of difference).

Kurz (2011) developed the first workflow to utilize imaging spectroscopy from a ground-based setup to create Virtual Outcrop Models (VOMs). The focus was to analyze the mineralogical, lithological or geochemical variations in near-vertical outcrops and combine HSI data products with 3D LiDAR models. Two case studies with the HySpex SWIR-320m sensor were presented in carbonate systems. The images showed a significant amount of image artifacts, especially intensity gradients along-track. Atmospheric correction is applied by Empirical Line correction based on calibrated white reference panels; image noise was separated and removed by Maximum Noise Fraction transform. Close-range scanning showed to follow a conic-directional reflectance model due to a restricted view of the upper hemisphere. The obtained reflectance imagery was analyzed by band ratios, SAM, SFF and Mixture Tuned Matched Filtering. VOMs were integrated and textured with HSI based on a cylindrical camera model, reaching accuracies of 1 pixel (2.3–7.5cm for images with scanning ranges of 30–100m). Further research is advised in the areas of the:

- 1) Extension of the spectral range from the VNIR to LWIR to map the major rock forming minerals
- 2) Correction of image non-uniformities that are enhanced by close-range measurements (e.g., intensity gradients in along-track direction),
- 3) Development of a more sophisticated reflectance retrieval method that includes solar illumination parameters and the viewing geometry from other systems (e.g., LiDAR),
- 4) Finding automated ways for photogrammetric processing and
- 5) Enhancing the visualization in this case the multi-texturing of the resulting VOMs.

Not all working groups have taken the utilized sensors’ spectral performance and distortion patterns into account or analyzed the results critically based on the performance of the utilized sensors, neither is the aim of this study to characterize the HySpex sensor systems technical performance. The latter is still part of on-going research. For application and implementation in the mining industry, these off-the-shelf solutions need to be bullet proof and easily adaptable.

The tests mentioned above were conducted in areas of inactive or dormant mining related to copper-, iron-, carbonate- and clay mineralization. They show promising results regarding a broad mapping approach of lithological zones. The quality of the reflectance data however is very dependent on the radiometric correction and the pre-processing of the data and relies on different approaches and different assumptions of the different working groups. MWL mapping of spectral features which is indicative of hydrothermal alteration conditions is mostly used for copper ore zone characterization. Even Kruse et al. (2011), utilizing the presented mineral abundance mapping instead of using MWL, concentrate the analysis and classification on the shift of features in the distinct EM spectra. Thereby, in this work, the principles of MWL were taken into account for the hard mineral classification. Similarly, Murphy et al. (2015) utilize AFE to map the wavelength position and depth of certain minerals to find geological unit delimiters. A large part of the methodology needed for industry relevant geological solar optical mapping has been discussed theoretically and as part of feasibility studies in the scope of this PhD thesis and on-going research. In order to being able to map quickly and reproducibly in active mining conditions, robust pre-processing and quick, reliable and reproducible analysis routines have yet to be developed and implemented.

This includes:

- Finding an optimum, illumination insensitive mapping algorithm
- The selection of spectral characteristics (MWL or spectral libraries) for mapping
- The determination of equipment (sensor characteristics, number of bands, complexity of the system, handling, pricing)
- A robust reflectance retrieval routine without the need of targets that have to be placed in inaccessible regions and smart data pre-processing for reproducible results.

This work aims to give an overview about the existing methodology and aims to develop a joint approach of existing methods and new approaches in order to address mine face geological mapping under open pit conditions.

3 Materials

3.1 Investigated samples

Two sample suites and one mine face scan were investigated for the method development in this study. Additionally, one mine face scan and one sample suite were used for the application of the developed workflow. The datasets were utilized as shown in Figure 8.

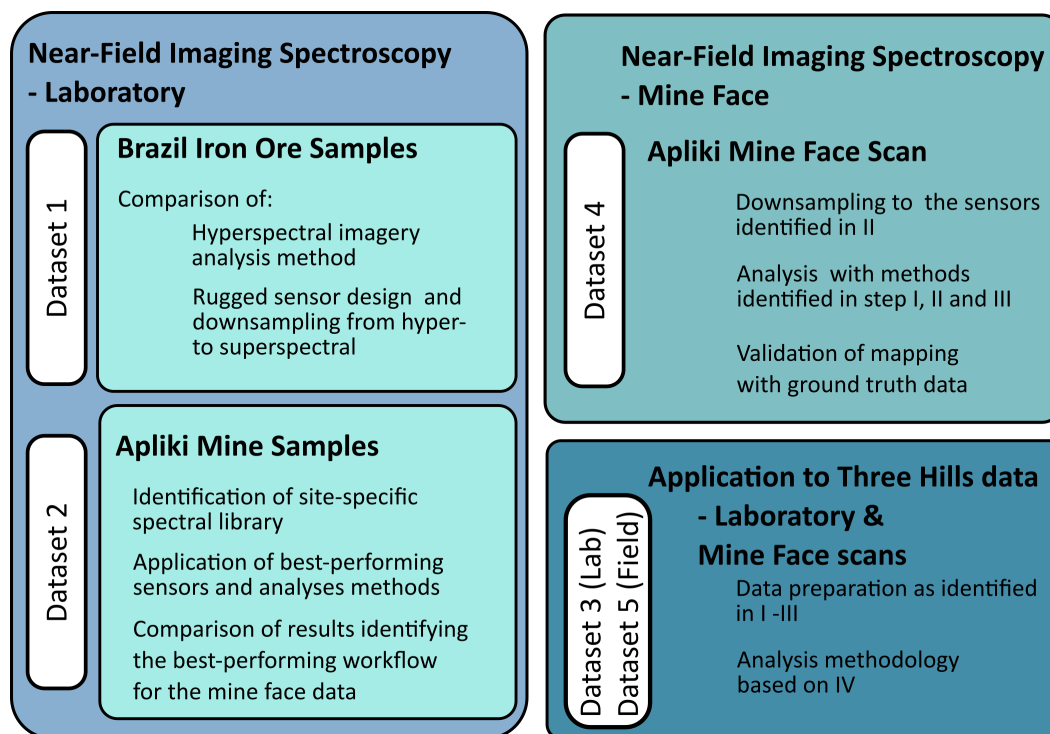


Figure 8 Method development based on the five available data sets.

3.2 Datasets

Five spectral datasets will be discussed in detail in this work.

1. **Dataset 1:** The hyperspectral laboratory scan includes 15 iron ore samples from two mine sites in Brazil. These samples and their respective geochemical analysis were provided by clients from rad. Data Spectral analytics (www.raddata.io, 2020) who do not wish to be disclosed. This hyperspectral scan is used to review the common methods for *hyperspectral data classification* that are explained in Part I (p. 97) and for the *robust sensor modeling* (Part II, p. 119). The most promising methods are then applied to the other datasets with samples from the Apliki and Skouriotissa copper mine, Republic of Cyprus.

2. **Dataset 2:** This dataset includes samples taken in Apliki, Republic of Cyprus. A total of 9 hyperspectral laboratory scans was combined to one big data set, including 44 samples from 14 different sampling locations on the mine face. Only 36 of the 44 samples were analyzed geochemically, the spectral and geochemical data for these were published in 2019 (Koerting, Rogass, *et al.*, 2019). This dataset is used to test the most promising algorithms and sensors found from dataset 1. Dataset 2 mainly utilizes the 36 samples and their reflectance data scan. Additionally, a smaller 11 samples radiance dataset was compiled to test a mapping approach based on radiance data. All of this is utilized in Part III (p. 136).
3. **Dataset 3:** The samples taken in the Skouriotissa Three Hills deposit, Republic of Cyprus were combined into one laboratory data set. A total of 3 hyperspectral scans was combined to one big data set, including 15 samples from 5 different sampling locations on the mine face. Dataset 3 is used to apply the data preparation workflow explained in Part III (spike correction, detector jump correction and downsampling) and to build a site-specific spectral library for the Skouriotissa Three Hills open pit in Part V (p. 161).
4. **Dataset 4:** This hyperspectral field scan of the mine face in Apliki, Republic of Cyprus utilized for Part IV, (p. 151) is used to demonstrate the *field data workflow*, including the data acquisition, -preparation & -pre-processing and the application of the analysis methods developed under laboratory conditions.
5. **Dataset 5:** The hyperspectral field scan of the Three Hills open pit, in the Skouriotissa Mine, Republic of Cyprus is used to apply of the methods developed for the data from laboratory conditions and field conditions for the Apliki datasets 2 & 4. The site specific-library from Dataset 3 is utilized and the analysis is aimed at mapping high-grade ore (<0.27% Cu), ore (0.27%< Cu <0.1%) and waste (<0.1% Cu). This is demonstrated successfully in Part V (p. 161).

The different datasets will be described in detail regarding the sampling location, the geology of the area of origin, the samples characteristics, their geochemistry, the data acquisition and the specifics of the data analysis.

3.3 Sample area

The samples from dataset 1 originate in the state of Minas Gerais, Brazil and are related to iron ore mining. The other datasets (2-5) originated in the Republic of Cyprus in the inactive and active copper mines Apliki and Skouriotissa.

3.3.1 Minas Gerais, Brazil

Two sample suites of iron ore and related material were supplied from the state of Minas Gerais, in the South-East of Brazil, North of Rio de Janeiro (Figure 9). The mining companies supplying the samples from their sites are not to be disclosed in the scope of this work, neither are the exact locations of sampling. It was agreed upon the possibility for the samples and geochemistry to be included in this work.

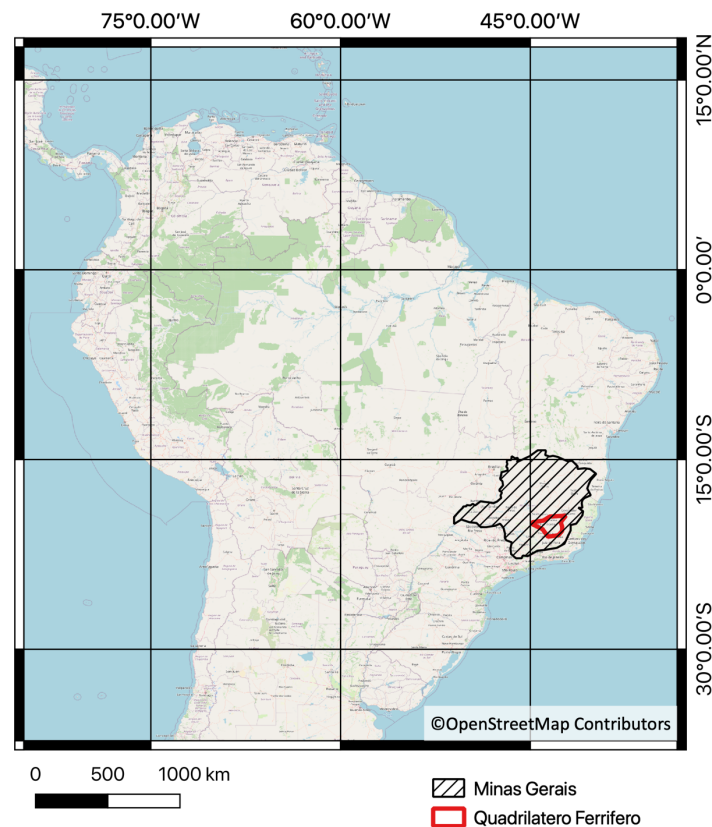


Figure 9 Locations of Minas Gerais and Quadrilátero Ferrífero. Base map source: ©OpenStreetMap Contributors.

Figure 10 shows a photo from a visit from one of the mine sites that provided the samples.



Figure 10 Visit to a major open pit mine in the state of Minas Gerais in October 2019.

The supergene iron ores of Minas Gerais and Quadrilatero Ferrifero are divided into three categories: enriched itabirite, intermediate grade ore and Canga (Dorr, 1964). Itabirite is a “laminated, metamorphosed, oxide-facies iron formation [...] in which the iron is present as hematite, magnetite or martite” (Dorr, 1964) and the original jasper or chert bands have been recrystallized into granular quartz. Dolomite and amphiboles locally substitute for quartz and when substituted, magnetite and its oxidation products are present. Fresh Itabirite is dense, brittle, hard and resistant to mechanical erosion (Dorr, 1964). All supergene iron ores result from the weathering of itabirite, and degrade based on the same geological processes but undergo this weathering under varying degrees of intensity. They are therefore intergradational and clear lines of demarcation are impossible to draw. *Enriched itabirite* is a disaggregated rock residually enriched in iron and leached of quartz and other constituents by supergene fluids. *Intermediate grade ore* is defined as material with an upper limit of iron content of about 65.5% and a lower limit of 57% iron and <7% SiO₂. It derives from strong residual and secondary enrichment of itabirite (Dorr, 1964). Canga forms as consolidated, extensive blanket deposits at or near erosion surfaces. It is resistant to erosion and chemical weathering and composed of varying detrital materials derived from limonite cemented high-grade hematite ore or itabirite. (Dorr, 1964) defines the average composition of itabirite and its weathering products as presented in Table 5 and Table 6.

Table 5 Bulk rock composition of itabirite and its weathering products from Dorr (1964).

Element or Oxide	Unleached Itabirite [wt. %]	Enriched Itabirite [wt. %]	Intermediate grade ore [wt. %]	Canga [wt. %]
Fe	37.9	48.7	63.3	62.2
Fe ₂ O ₃	54.1	69.6	90.4	88.8
SiO ₂	44.7	25.4	2.35	1.7
Al ₂ O ₃	0.5	1.3	2.6	2.8
P	0.05	0.06	0.08	0.1
H ₂ O plus	0.3	Nd	4.6	5.4

Table 6 Geochemical composition of samples received from the Minas Gerais district. Reduced to components stated by Dorr (1964). Categorization after Dorr (1964) and from information provided by Mine Site 2.

ID	Fe [%]	SiO ₂ [%]	Al ₂ O ₃ [%]	P [%]	Categories after Dorr, 1964	Categories based on Mine Site 2	Mine Site No.
1	55,05	16,81	0,61	0,14	Itabirite	Medium value ore	2
2	49,72	18,51	1,05	0,11	Itabirite	Medium value ore	2
3	24,40	21,69	22,14	0,60	Itabirite, high clay contamination	Low value ore	1
4	46,39	30,33	1,41	0,04	Itabirite	Medium value ore	1
5	38,06	41,16	0,43	0,06	Itabirite	Low value ore	2
6	44,47	31,59	1,97	0,10	Itabirite	Medium value ore	2
7	58,22	10,14	3,94	0,09	Enriched Itabirite	High value ore	1
8	35,37	49,02	0,28	0,02	Itabirite	Low value ore	1
9	44,46	32,99	0,53	0,08	Itabirite	Medium value ore	2
10	68,49	0,53	0,45	0,05	Canga	High value ore	2
11	30,58	56,5	<0,05	<0,005	Itabirite	Low value ore	1
12	47,92	13,29	9,26	0,21	Itabirite	Medium value ore	1
13	37,17	41,64	1,29	0,18	Itabirite	Low value ore	2
14	38,23	37,45	1,54	0,05	Itabirite	Low value ore, high Mn contamination	2
15	64,93	1,32	1,48	0,11	Intermediate grade ore	High value ore	1

3.3.2 Republic of Cyprus

3.3.2.1 *Porphyry copper systems and hydrothermal alteration*

Porphyry ore systems consist of large areas of hydrothermally altered rock centered on a porphyry stock intrusion. These may also contain skarn, carbonate-replacement, sediment-hosted and high- and intermediate-sulfidation epithermal base mineralization. They are typically formed as magmatic arcs above active subduction zones and convergent plate margins. Currently, nearly 3 quarters of the world's Cu is supplied by porphyry copper systems, along with half the Mo, one-fifth of the Au, most of the Re and minor amounts of Ag, Pd, Te, Se, Bi, Zn and Pb (Sillitoe, 2010; Okrusch and Matthes, 2014). The alteration and mineralization in porphyry copper systems is zoned outwards from the stocks or dike swarms and occupy many cubic kilometers of rock (Sillitoe, 2010) (Figure 11). Oxidized magma intrudes and is saturated with sulfide and metal rich aqueous fluids. These fluids penetrated the

surrounding rock and due to the involved temperature and pressure this leads to addition, removal and/or redistribution of the pre-existing rock components (Dalm *et al.*, 2014). The intensity of this alteration decreases with increasing distance from the intrusion and forms concentric hydrothermal alteration zones with characteristic mineral assemblages. The zonation is dominated from the bottom up by barren, early sodic-calcic to potentially ore grade potassic, chlorite-sericite, sericitic to argillic and finally the lithocaps of up to 1km thickness if erosion is not interfering. Cooling down of the fluid and intrusion from 700 °C to 300 °C leads to the formation of the chalcopyrite and bornite assemblage (potassic zone), whereas temperatures below 350°C and a low- to moderate salinity liquid are associated with sericite-chlorite and sericitic alteration and associated mineral assemblages (Lowell and Guilbert, 1970; Sillitoe, 2010; Dalm *et al.*, 2014). The main ore zone is related to the boundary of potassic to phyllic hydrothermal alteration, but these spatial relations can be offset by the telescoping within the porphyry system (overprint of older alteration zone by more recent alteration), breccia intrusions and/or diatreme intrusions (Dalm *et al.*, 2014).

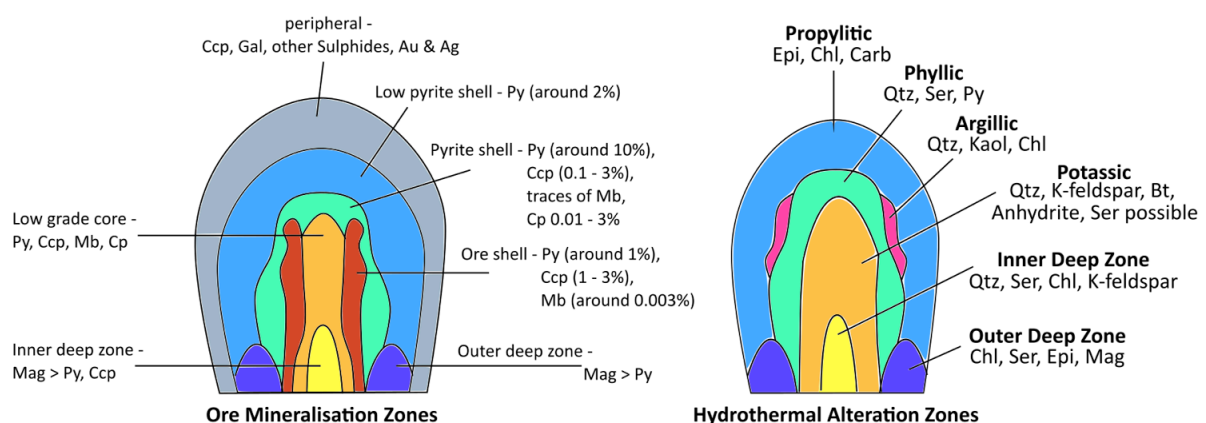


Figure 11 Left: Schematic cross sections of ore mineralization/ alteration zones (Ccp – Chalcopyrite, Au – Gold, Ag – Silver, Py – Pyrite, Cp – Copper, Mb - Molybdenite). Right: Hydrothermal alteration mineral zones. (Chl - Chlorite, Epi - Epidote, Carb - Carbonate, Qtz - Quartz, Ser - Sericite, Py - Pyrite, Kaol - Kaolinite, K-feldspar - Potassium feldspar, Bt – Biotite, Mag – Magnetite). Modified from Lowell and Guilbert (1970). Typical dimensions are given as 1.2 x 2 km horizontally and 3 km vertically (Dalm *et al.*, 2014).

3.3.2.2 Geology of Cyprus copper ore deposits

The Island of Cyprus became synonymous with copper in Late Antiquity. The Latin word “Cuprum” is based on “Aes Cyprium” = Cypriot copper, as Cyprus was one of the main sources of copper in the Old World (Kassianidou, 2013). All to-date mined ore bodies had surface indications stemming from activities of the Antiquity, showing major slag heaps close to the old mining centers (Adamides, 2010b). 4 million tons of copper slag in 40 different locations have been estimated to exist in the proximity of Troodos (Kassianidou, 2013). Cyprus therefore became the ultimate test site for me in order to study hydrothermal alteration and copper ore deposits within Europe.

The Cyprus sulfide deposits belong to the mafic type of volcanogenic massive sulfides (VMS) and are associated with a supra-subduction zone fore-arc setting of the Troodos ophiolite complex around 91 ma ago (Adamides, 2010b, 2010a). The ophiolite comprises a complete sequence from ultramafic rocks at the base overlain by gabbroic rock as sheeted dyke complexes and pillow lavas, topped by pelagic sediments (Adamides, 2010a). Structural studies of Cyprus identified several asymmetrical N-NW-trending graben defined by opposing inward-dipping sheeted dyke complex domains. These domains correlate with major sulfide mineralization. These graben are, from west to east, Solea, Mitsero and the Larnaca Graben (Figure 12) (Adamides, 2010a; Martin *et al.*, 2018). The Solea graben hosts the Apliki and the Skouriotissa deposit.

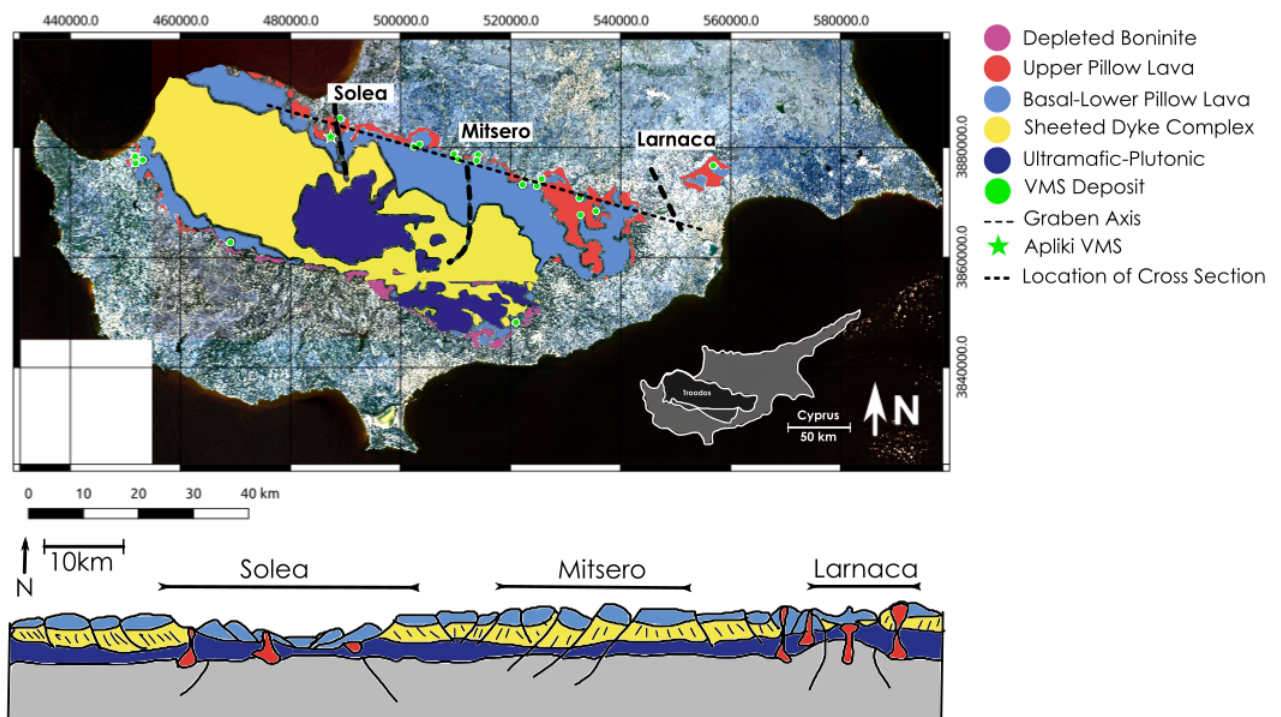


Figure 12 Simplified geological map of the Troodos Ophiolite, Cyprus and a simplified structural cross-section of Troodos based on Martin *et al.*, 2018. Contains modified Copernicus Sentinel-2 data (Sept. and Oct. 2019, RGB (490 nm, 560 nm, 665 nm)).

The classic Cyprus-type VMS deposit is characterized by an exhalative lens underlain by a stockwork zone which represents the channel veins by which the hydrothermal fluid reached the sea floor (Figure 13) (Lydon, 1984; Galley, Hannington and Jonasson, 2007).

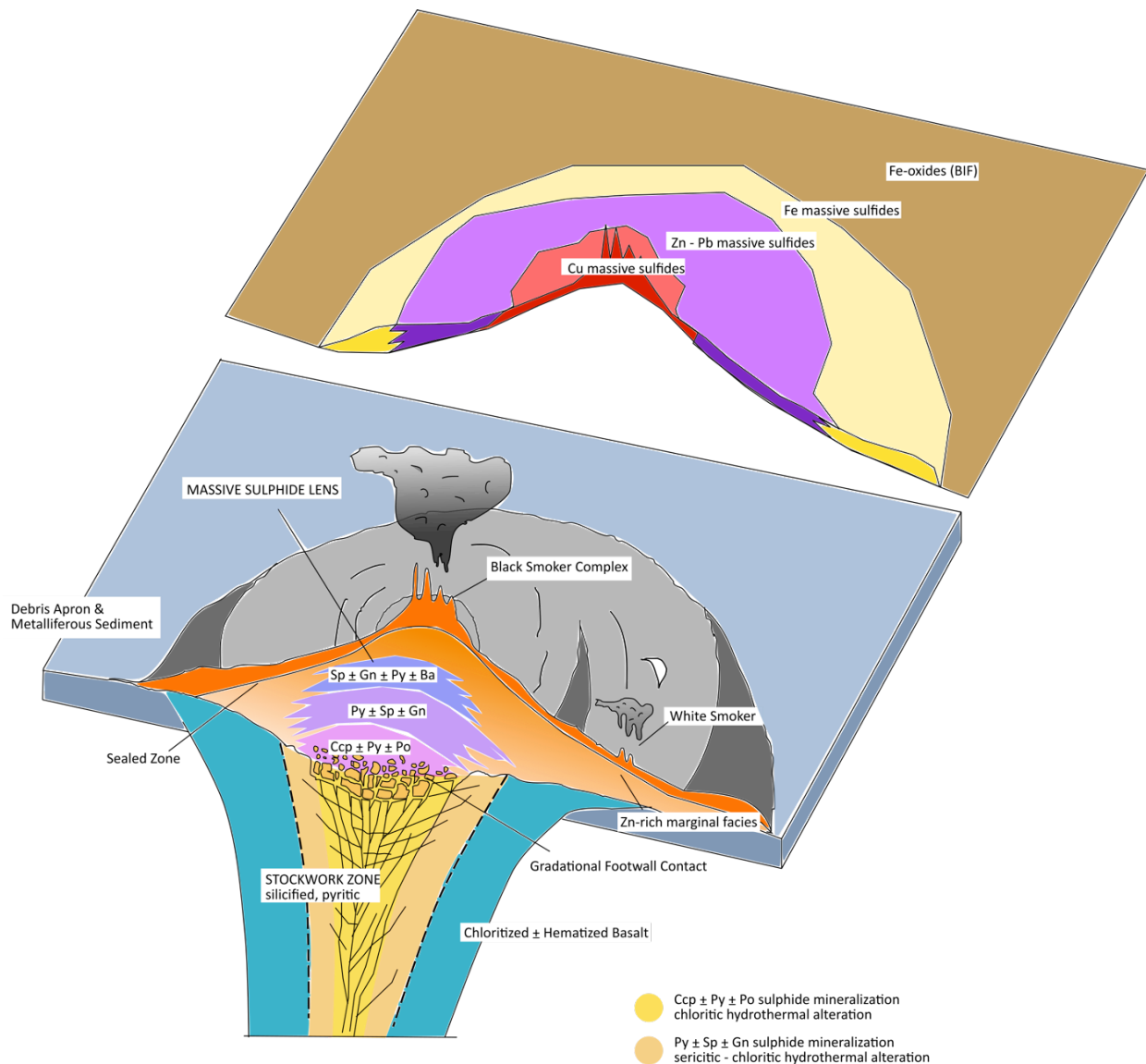


Figure 13 Sulfide cover zonation (Top) and characteristics of an idealized volcanogenic massive sulfide deposit (Bottom). Abbreviations in Figure: Sp - Sphalerite, Gn - Galena, Py - Pyrite, Ba - Barite, Ccp - Chalcopyrite, Po – Pyrrhotite. Modified from Lydon (1984) and Galley, Hannington and Jonasson (2007).

Some deposits show variations and some lack suitable observable structures that allowed access to the sea floor. Where no structural control is obvious as for the Skouriotissa deposit, a more deep-seated heat source is suggested (Adamides, 2010b). The Cyprus-type VMS is a hydrothermal ore deposit, which is formed by the interaction of mafic country rocks under greenschist-facies metamorphic conditions (350 °C) and evolved seawater (2 °C). The cold seawater reacts with volcanic glass by entering trough fractures and fissures in the rock, lowering the pH of the water. As it continues moving downwards, it becomes heated to 350-400 °C in the sheeted dyke complex with a pH of around 2. Here, the seawater and the rock go into exchange and epidotes are formed, they are suggested to be the main source of base and trace metals in the Cyprus-type VMS of Troodos (Martin *et al.*, 2018). Metal-laden from the exchange, hydrothermal fluids follow pathways of normal faults to the seafloor

where they are exhaled. The hot, reduced fluid mixes with the seawater and sulfides are precipitated to form VMS. The VMS mineralogy is dominated by pyrite, chalcopyrite and sphalerite with inclusions of galena and secondary copper-bearing minerals like covellite, digenite and chalcocite. The alteration around the VMS is silica and chlorite dominated and includes disseminated pyrite (Martin *et al.*, 2018). Alteration mineralization is typified by feldspar destruction, quartz-chlorite growth, the removal of alkali elements from the inner parts of the ore zone and their deposition in the periphery of the ore bodies (Adamides, 2010b). K-feldspar and illite are associated with the margins of the deposits and seem related to the leaching of alkalis from the proximal ore zone. Epidote alteration is present at the margins of some hydrothermal systems and levels immediately underlying the stockwork zones. It is commonly associated with hematitic jasper as veins or interpillow glass replacement. Interaction between hydrothermal fluid and seawater through the permeable pillow lavas result in an alteration envelope of marginal chlorite passing inwards into silica and finally into the sulfide mineralization in the central part of the system (Adamides, 2010b). This is coherent with the hydrothermal alteration zones associated with porphyry copper deposits identified by Lowell and Guilbert (1970) and Rowan *et al.* (2006).

The Cyprus deposits can be defined by two classes of deposits, these two classes are based on observations from Adamides (2010b):

1. The deposit exhibits definite signs that hydrothermal fluids reached the sea floor. Exhalative processes deposited massive sulfides in the form of exhalative lenses. Evidence for this process is the presence of sedimentary structures, of sea-floor dwelling organisms and sea floor weathering of the sulfides.
2. The deposit exhibits definite signs of sub-floor deposition of sulfides. It lacks the evidence of hydrothermal fluids reaching the sea floor and shows extensive zones of hydrothermally altered rock which grades inwards into ubiquitously mineralized rock. Agrokippa B, Skouriotissa - Three Hills and the West Apliki deposit show strong evidence for this deposition.

This study will focus on the Skouriotissa group deposits “Three Hills” and “Apliki” (Figure 14), as these were the open pits that I had access to in March 2018 to conduct sampling and a hyperspectral measurement campaign. These deposit’s main characteristics are summarized in Table 7. Geographically, both deposits are situated within the Nicosia district and are located close to the ceasefire line South of the UN-controlled buffer zone.

Copernicus Sentinel-2 data from Sept. & Oct. 2019, RGB (R: 2190 nm, G: 783 nm, B: 665 nm)
 Zoom in to Skouriotissa and Apliki area

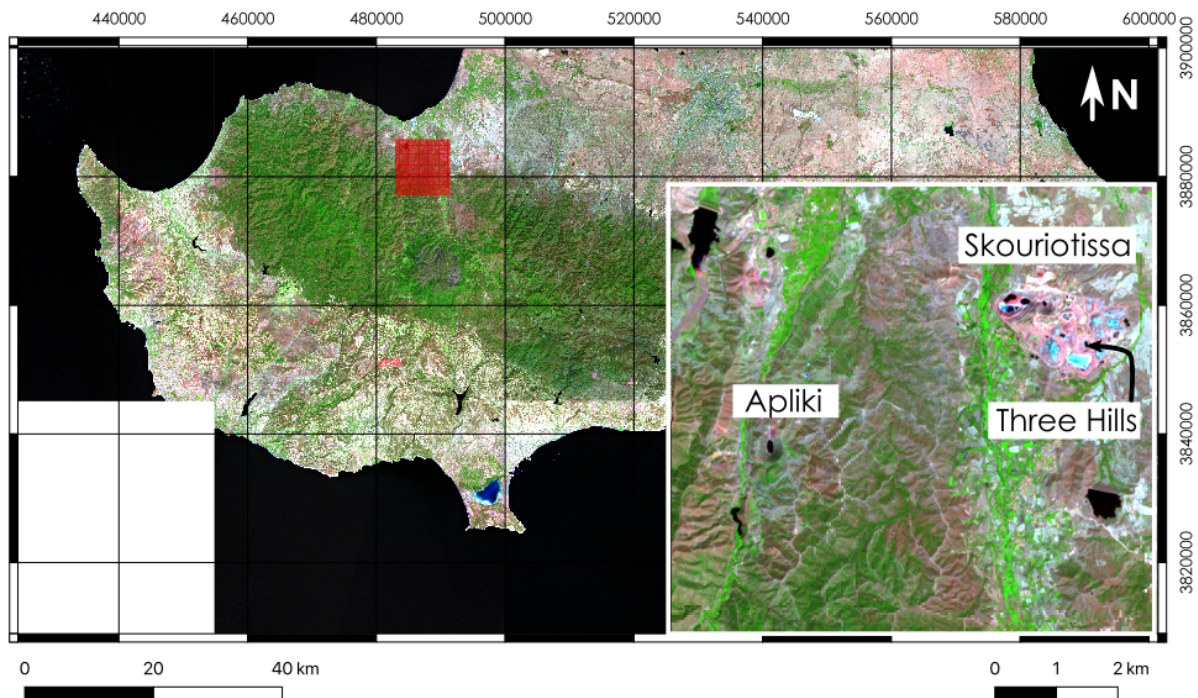


Figure 14 Map of Cyprus showing the location of the Three Hills deposit in the SE of Skouriotissa and the Apliki deposit ca. 5km SW of the operating Skouriotissa mine, based on Copernicus Sentinel-2 data from 2019.

Table 7 Summary of Apliki and Three Hills deposit based on Adamides (2010b, 2010a).

Deposit	Three Hills
<i>History</i>	Detected by drilling in area of alteration and weak oxidation. Explored by adit and cross-cut. Presently mined by Hellenic Copper Mining Ltd. (HCM)
<i>Tonnage and grade</i>	6.2mt, 0.37% Cu
<i>Mineralization type</i>	Vein type deposit composed of pyrite and chalcopyrite, with limited supergene enrichment at the upper levels (chalcocite and covellite)
<i>Structural control</i>	North-northwest-striking structures
<i>Stratigraphic position</i>	Within Upper Pillow Lavas surrounded by chloritic alteration envelope
Deposit	Apliki
<i>History</i>	Detected during gold exploration in 1930s, initially mined underground followed by open cut mining in the 1960s. Operations ceased in 1973 but low-grade resource remains as well as the stockpiled oxidized ore.
<i>Tonnage and grade</i>	1.65mt, 1.8% Cu, 36.0% S
<i>Mineralization type</i>	Massive sulfides with underlying stockwork in chlorite-bearing and silicified lavas
<i>Structural control</i>	Graben structure defined by two North-striking faults
<i>Stratigraphic position</i>	Contact between Lower and Upper Pillow Lavas

3.3.2.3 Three Hills, Republic of Cyprus

The Three Hills deposit, often referred to as K-zone by HCM, was exploited in 2003 for a brief period of time and has not been exploited since (Naden *et al.*, 2006; Adamides, 2010b). The Three Hills open pit is located in the western part of the Skouriotissa open pit mining area. Its surface expression is unimpressive only showing weak iron staining (Adamides, 2010b), the mineralization shows to be highly brecciated, highly silicified stockwork with hypogene mineralization (Naden *et al.*, 2006). Based on maps by Adamides (2010b), the stockwork mineralization is enclosed by an EW-trending fault in the northern part and a NS-trending fault in the eastern part of the deposit (Figure 15). Communication with HCM confirmed the location of the fault in the open pit and the successive enrichment in Cu grades towards the SW and top down within the open pit (sketched out in Figure 16). This can be visually distinguished by cream-colored clay alterations of the siliceous matrix, distinct green colors of the host rock (presence of chlorite) and brown colors related to pyrite oxidation (Naden *et al.*, 2006) (sketched out in Figure 17).



Figure 15 Skouriotissa mine location of the pits Phoenix, Phoukasa and Three Hills and fault zone location based on Adamides (2010b). Source: "Skouriotissa Three Hills Deposit", 35°05'50.72"N, 32°53'48.81"E, GOOGLE EARTH, 3rd of April 2018, retrieved 21st of July 2020 (Google, 2018)

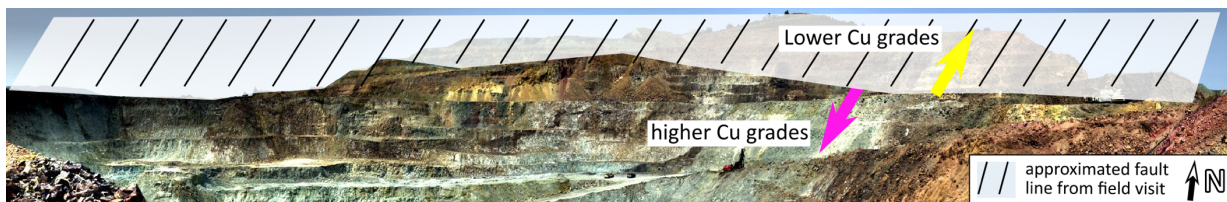


Figure 16 Hyperspectral scan within Three Hills open pit. View from the SSW wall (left) to the NNE entrance to the pit (right). Including line of fault as communicated during the field measurements by HCM and trend in Cu grades within the pit.

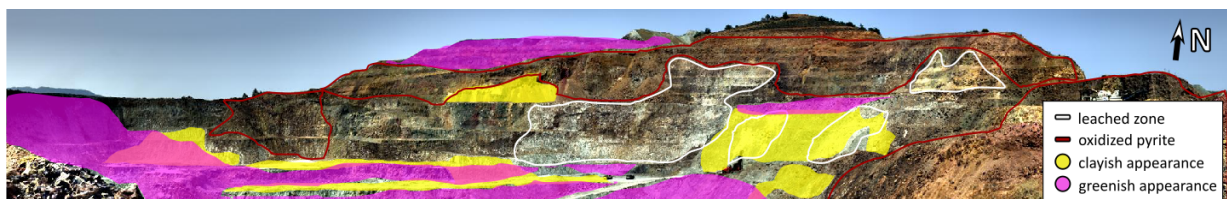


Figure 17 Sketch of areas with clayish (low Cu grade) and greenish (chloritic, stockwork) appearance, indicating zones of pyrite oxidization and leached zones. Based on visual interpretation.

The ore comprises pyrite, chalcopyrite and local sphalerite (hypogene mineralization). In the oxidized zone, common pyrite is replaced by hydroxides of goethite-lepidocrocite (Adamides, 2010b). Pillow lavas define the lithology, interspersed by local non-pillow units; Dykes are absent. The rocks are chloritized in the area around the deposit and an alteration envelope surrounds and partly overlies the deposit (Adamides, 2010b). Pyrite is mainly disseminated with the rock body or occupies the walls of veins and is deposited onto quartz in fractures (Adamides, 2010b). In areas of intense mineralization pockets of massive pyrite formed and replace the total host rock. Pyrite occurs in well-developed striated cubes or pyritohedrals (Figure 18, left). Chalcopyrite is present (Figure 18, right) but often replaced by secondary minerals, as chalcocite and covellite (Adamides, 2010b). Para-genetical pyrite appears to be the earliest sulfide to crystallize from hydrothermal fluids, covering the walls of veins. Chalcopyrite occupies central parts of veins often with sphalerite. Quartz is the sole gangue mineral in all parts of the deposits and fills veins and vesicles. In the chloritized zones it forms thin veinlets of euhedral clear crystals, in the ore zone (mineralized zone) it accompanies sulfides and lines the walls of veins. It's intergrowth with sulfide shows the persisting precipitation throughout the mineralization episode. The hypogene mineralization is dominated by pyrite, marcasite and chalcopyrite, the sequence of supergene mineralization paragenesis was found to be digenite -> chalcocite -> bornite -> covellite (Naden *et al.*, 2006)

Expected ore mineralogy in the open-cut of Three Hills is based on Adamides (2010b) and Naden et al. (2006):

1. pyrite, marcasite, chalcopyrite, local sphalerite (hypogene)
2. digenite, chalcocite, bornite, covellite (supergene)
3. quartz as sole gangue mineral
4. chloritized lava
5. hematite, jarosite, goethite, lepidocrocite as replacement of pyrite in oxidized zones

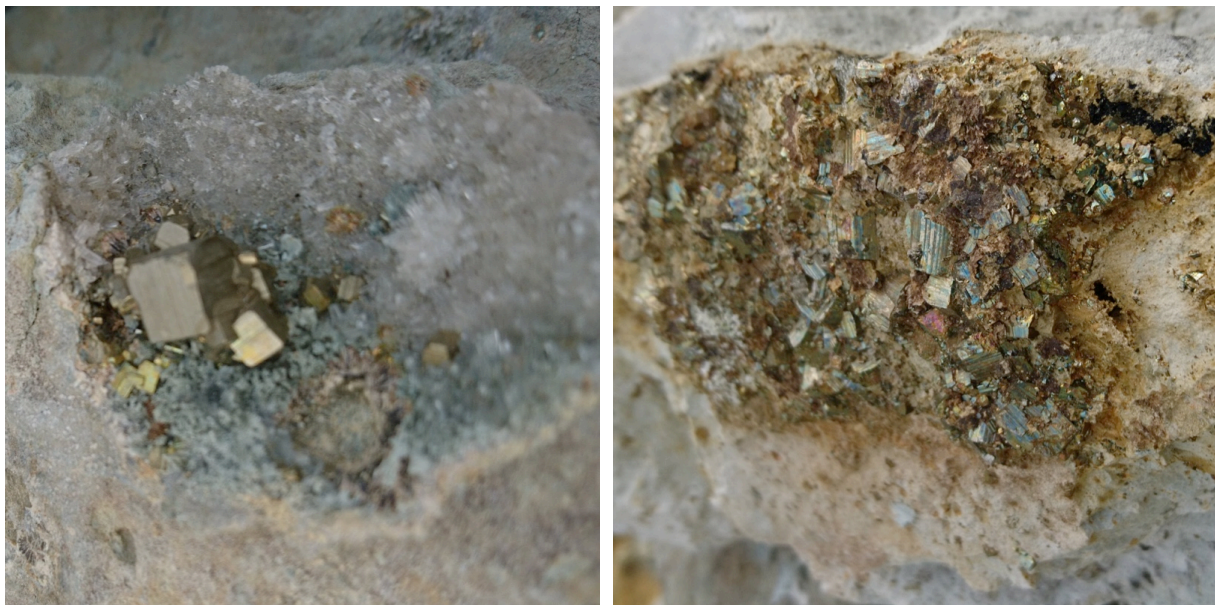


Figure 18 Left: Striated cubes of pyrite on top of quartz crystals in former cavity. Right: Striated, hypogene chalcopyrite mineral cluster. Supergene chalcocite blanket is indicated by black remnants. Photos from field work in March 2018 in Three Hills. The photo size is approximately 5cm x 5cm.

3.3.2.4 *Apliki, Republic of Cyprus*

Apliki is a structurally controlled deposit, situated within the Lower Pillow Lava stratigraphy and confined by two axis parallel (N-S) normal faults. At depth the two faults are inferred to truncate in a major detachment surface (Adamides, 2010b; Martin *et al.*, 2018), see Figure 19. Based on historic data and field observations by Martin et al. (2018), Apliki VMS is interpreted to be a typical Cyprus-type VMS – a massive sulfide lens overlain by a cupriferous stockwork of quartz, jasper and sulfide veins within the basaltic host Lower Pillow Lavas (Antivachis, 2015). Adamides (2010a) reports a grade of 1.6wt.% of copper grade, whereas Antivachis (2015) reports grades between 0.01 to 3.5wt.% Cu. The mineralization does not cross the fault contact of the two faults and suggests a mineralization post fault movement. The fault-bound zone of mineralization is around 100 m wide and consists of silicified, chloritized, brecciated Lower Pillow Lava. Disseminated pyrite occurs but no massive sulfide mineralization.

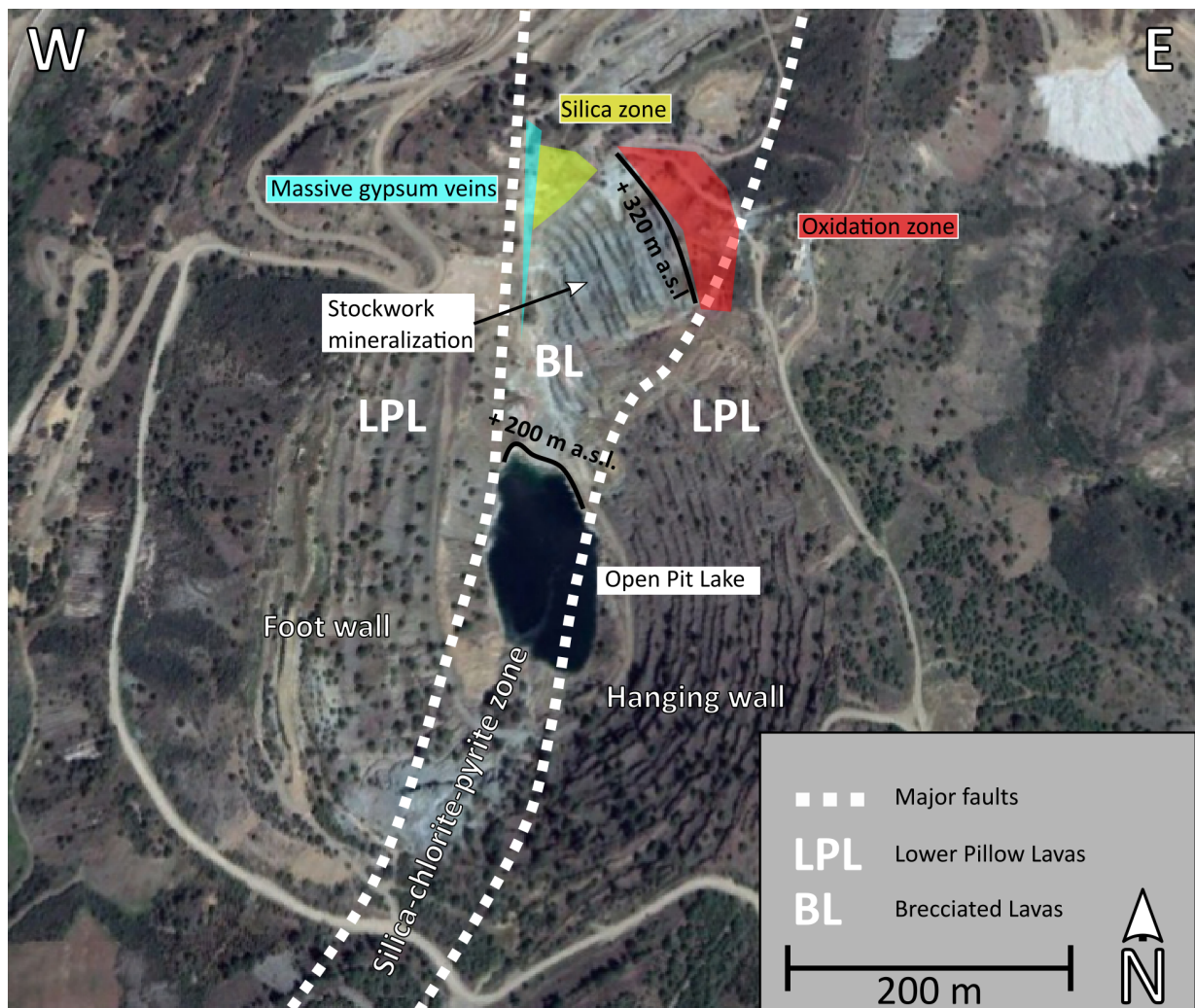


Figure 19 Apliki deposit, interpretation from (Antivachis, 2015; Martin *et al.*, 2018). Source: "Apliki mine", 35°04'28.78"N, 32°50'35.40"E, GOOGLE EARTH, 03.04.2018, retrieved 23.07.2020.

The eastern wall of the cut shows unmineralized Pillow Lavas and is associated with hyaloclastic material in between thick columnar-jointed flows. The lava east of the fault is increasingly chloritized and quartz is accompanied by analcime as vesicle-filling material. In the western site, the fresh, hyaloclastic-rich pillow lavas are exposed. The northern wall represents the contact with the ore zone. The Northern open cut area is approximately 150m in height and 150m width, the pit bottom located at around 200 m a.s.l (Antivachis, 2015). Satin spar gypsum veining occurs at the northern part of the open cut (Figure 20, left) and is associated with leached lava, chloritic breccia and intense shearing (Adamides, 2010b). Sulfate evaporates, possibly chalcantite, covered the surface of the cut terraces in areas of surface water flow (Figure 20, right). As the cupriferous massive sulfide ore has been mined out, Apliki is a typical

example of an oxidation zone overlying a stockwork type sulfide mineralization in chlorite-bearing and silicified lavas (Antivachis, 2015).

The typical stockwork type mineralization shows cavity and vein fillings of pyrite and subordinate chalcopyrite in the southern part of the open pit. The altered lava shows occurrence of widespread jasper. The ore zone continues northwards as low-grade disseminated mineralization. The massive sulfide was originally on top of the stockwork zone and covered by Upper Pillow Lavas and tuffaceous sediments. Prior to mining, maps suggested a cover of shales and limestones (Adamides, 2010b).



Figure 20 Left: Satin spar gypsum found in Apliki, ca. 7cm x 20cm. Right: Sulfate evaporates, possibly Chalcantinite, found in Apliki.

The Apliki VMS outcrop that was scanned in 2018 shows 5 ½ levels of in the Northern part of Apliki VMS, situated in the fault bound zone of chloritized-silicified brecciated Pillow Lava. In the supergene enrichment succession it is directly below the iron cap and in the leached and oxide zone (after Asmus (2013)).

Antivachis (2015) identified five facies within the mineralized zone: 1) a stockwork zone, 2) veins of amorphous silica in the NNW, 3) massive veins of Gypsum in the NNW, 4) the “red zone”, an oxidized vein of mineralization and 5) the oxidation zone at the top. Figure 21 from (Antivachis, 2015) shows a stylized, geological sketch.

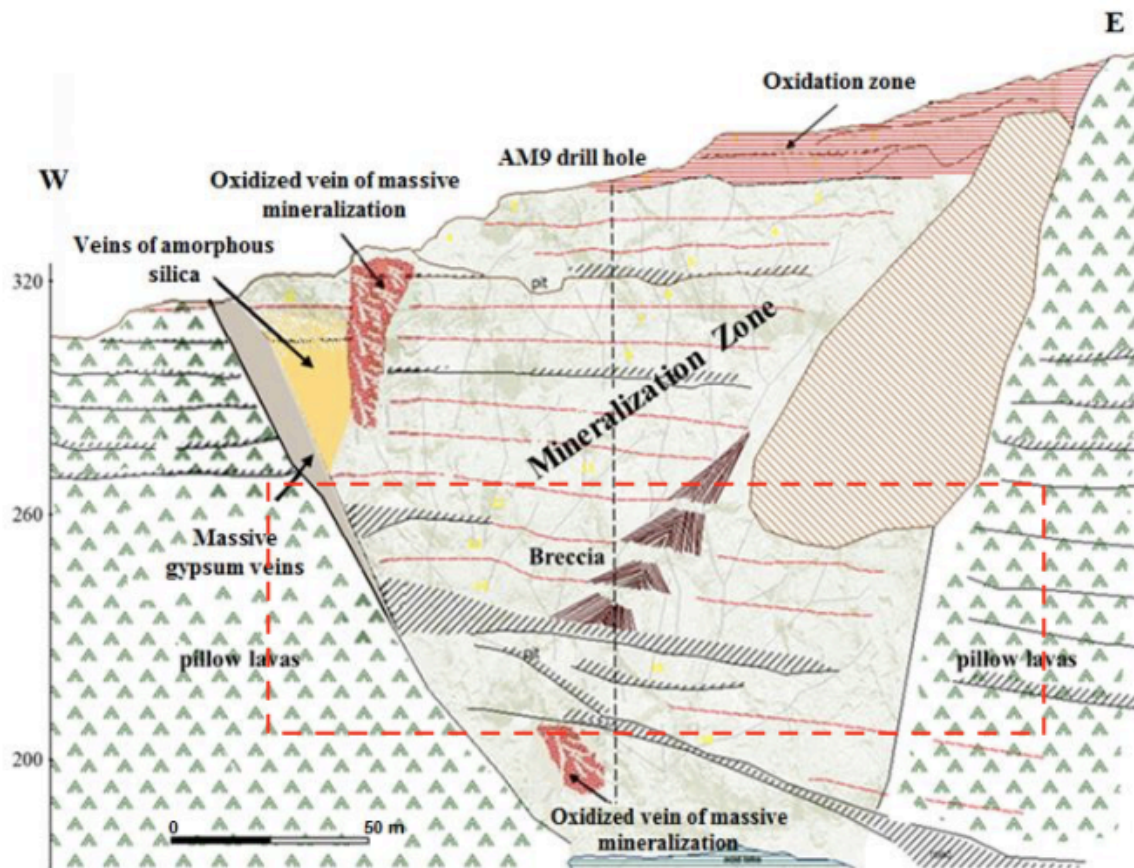


Figure 21 Schematic geological section of the Northern part of Apliki as shown in Antivachis (2015). Red, dashed window represents the dimensions of the hyperspectral mine face scan.

The associated stockwork zone (“mineralization zone” in Figure 21) dominates the area captured by the hyperspectral sensors in 2018. This zone is dominated by a network of quartz and jasper veins within the brecciated pillow lavas (Antivachis, 2015). The brecciation is assumed to be a result of the explosive hydrothermal activity within the W and E delimited fault zone (Antivachis, 2015).

The expected mineralization and hydrothermal alteration zone identification of the stockwork zone is based on the work of Antivachis (2015) who studied 66 samples of the north wall of the open cut. In the stockwork zone chlorite, clay minerals, albite, iron and titanium oxides and quartz are common. Chlorite is the main mineral of the non-metallic minerals formed by hydrothermal alteration of clinopyroxene and volcanic glass and often fills fractures in pyrite. Clay minerals are found in the chloritized ground mass and replace volcanic glass. Magmatic plagioclase was albitized and formed pure albite. Plagioclase and pyroxene are partially replaced by calcite that acts as filling material or within the groundmass. Iron-titanium oxides and ilmenite is replaced by anatase.

The prevailing alteration in the mineralized zone is chloritization, which can spatially be classified into three subzones (see Figure 22):

1) Smectitic: montmorillonite, illite and limited chlorite; 2) Chloritic-smectitic: stronger chlorite content as replacement of pyroxenes; 3) Chloritic: magmatic minerals are absent, chlorite dominates (Antivachis, 2015).

Jasper is widespread in the brecciated lavas that mainly constitute of quartz, goethite and hematite with minor amounts of clays and carbonates and jarosite (Antivachis, 2015). Contained sulfides are pyrite and minor sphalerite and chalcopyrite. Predominant ore minerals are pyrite, marcasite and chalcopyrite, with accessories of bornite, sphalerite, galena and barite. Chalcopyrite often shows inclusions of sphalerite. Chalcopyrite replacement by covellite and chalcocite due to supergene processes is also documented.

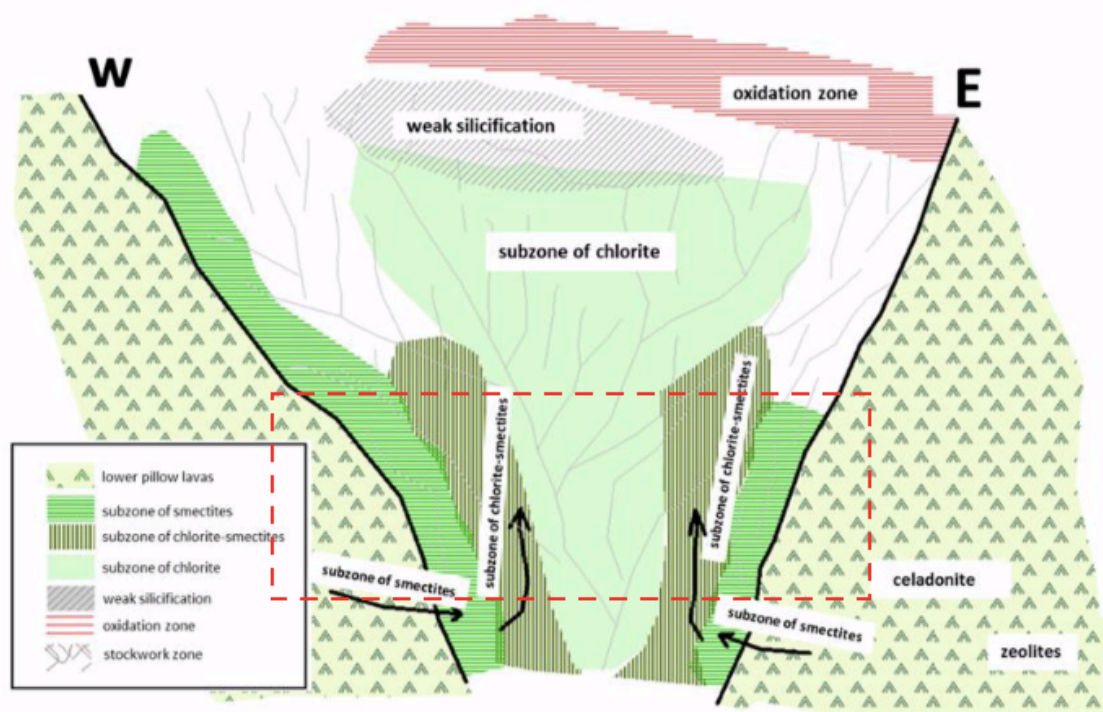


Figure 22 Schematic cross-section of Apliki massive sulfide ore body and associated stockwork, from Antivachis (2015). Red, dashed lines indicate the hyperspectral mine face scan dimensions. The scanned area is dominated by three hydrothermal alteration subzones: smectitic, chloritic-smectitic and chloritic.

The expected surface mineralization for the northern open cut is comprised of quartz, jasper, iron-oxides (goethite, hematite), chlorite-group minerals (clinochlore), smectite-group minerals (montmorillonite, illite), sulfides (pyrite, marcasite, chalcopyrite, accessories of sphalerite, bornite, galena; chalcopyrite is often replaced by covellite and chalcocite); sulfates (barite, gypsum, Chalcantinite, jarosite), analcime, plagioclase (partly replaced by calcite or albitized to albite) and pyroxene.

3.4 Sample preparation

In order to compare laboratory-derived spectral features with field-derived spectra the samples were not changed from their natural state.

Brazilian iron ore samples

Two companies operating open pit copper extraction in Brazil provided two sets of samples with the corresponding geochemical data. The open pits are located within the Iron Quadrangle of Brazil in the central-southern part of the Brazilian state Minas Gerais. The area is known for its large gold, diamond and iron ore deposits. Due to a non-disclosure agreement (NDA) we are not able to disclose the companies' names or the detailed mine site locations in the context of this thesis. They will be called "Mine Site 1" and "Mine site 2" from here on. Mine Site 1 delivered 8 samples with the sample ID 3, 4, 7, 8, 11, 12 and 15. Mine Site 2 delivered 7 samples of the sample ID 1, 2, 5, 6, 9, 10, 13 and 14. The total of 15 samples was left to dry, arranged in approximately 4x4cm squares on a black rubber lining and scanned without any sample preparation (Figure 23).

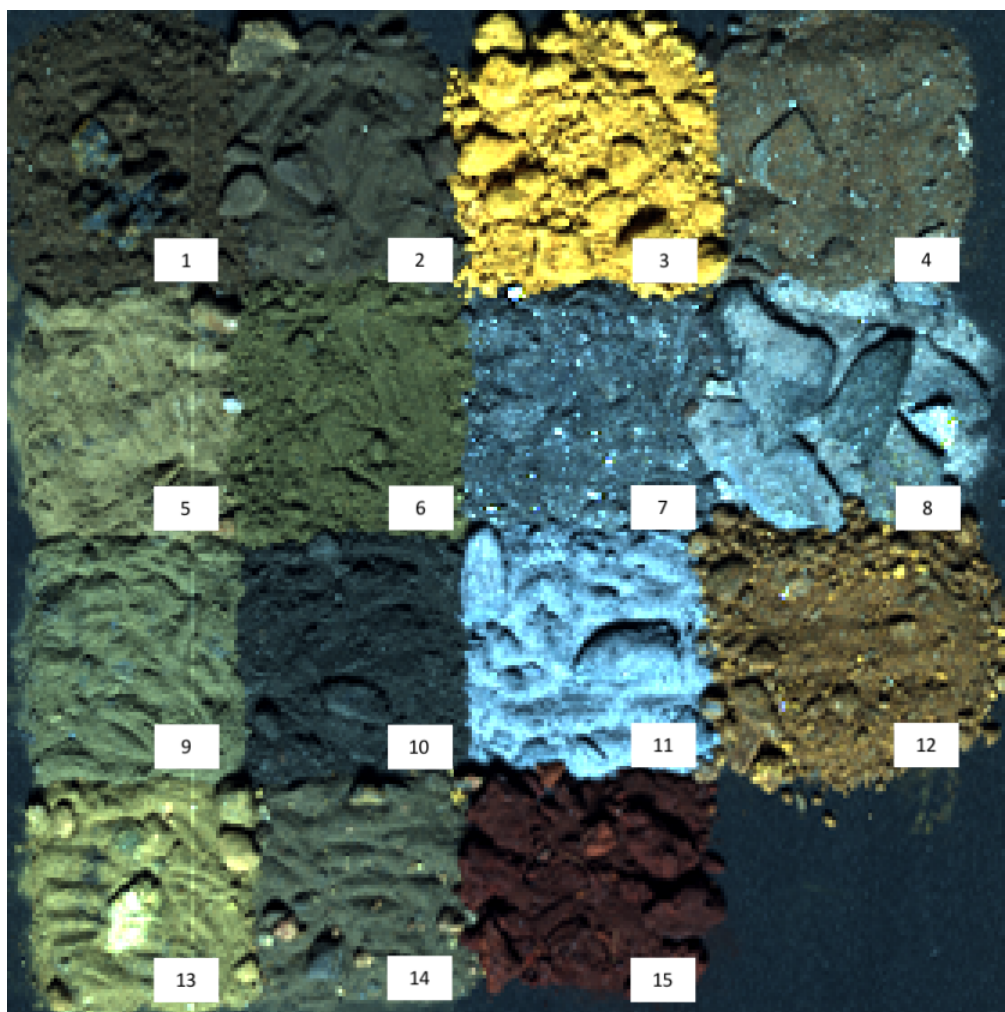


Figure 23 Brazilian iron ore samples hyperspectral scan (R: 640nm - band 63, G: 549nm - band 38, B: 458nm - band 13).

Apliki mine samples

37 samples were taken in March 2018 in the copper-gold-pyrite mine Apliki in the Republic of Cyprus during a measurement campaign of the Geological Survey Department of the Republic of Cyprus (GSD) and the German Research Centre for Geosciences (GFZ). The samples were scanned directly after the field expedition; all of the sampled material is present in the hyperspectral scan. For the scans, the samples were left in their natural state: partly dusty, showing heterogeneity in the small scale e.g., differently colored soil grains from the same sample location, inhomogeneous tarnish across individual samples and in a variety of states (e.g., soil, crystallized evaporitic material, fresh rock surface, tarnished rock, oxidation zones). The resulting laboratory scans represent exactly what we found in the field without changing the crystal lattice (e.g., by grinding the samples) or the small-scale heterogeneity (e.g., by homogenizing and grinding samples) and thereby changing the spectral signal of the material. For scanning, the samples were placed in black, plastic containers. The inside of the containers was sprayed with black spray-paint leaving them with a matt finish to avoid backscattering of plastic features from the box surface onto the samples (Figure 24). For rock samples, the original

surface that was directed at the sensor in field conditions was marked. This surface was directed towards the sensors for laboratory scanning. The bulk rock itself is not represented at the surface of the mine face but the rock's weathered and altered state from external physical and chemical conditions. A total of 9 scans were taken of 36 samples and combined into one big data set (Figure 24). Only the samples that yielded enough sample weight for a geochemical analysis were considered excluding sample 1a from the analysis. For the subsequent geochemical analysis, sub-samples were taken with ranging sampling weights between 20,9g (sample 3b) to 237,5g (sample 10c). In case of rock samples, the original marked surface was separated from the whole rock sample to allow a geochemical analysis of the weathering crust only. A table with the sampling location, a sample description and sample photos can be found in the Appendix (Table 47, p. 209).

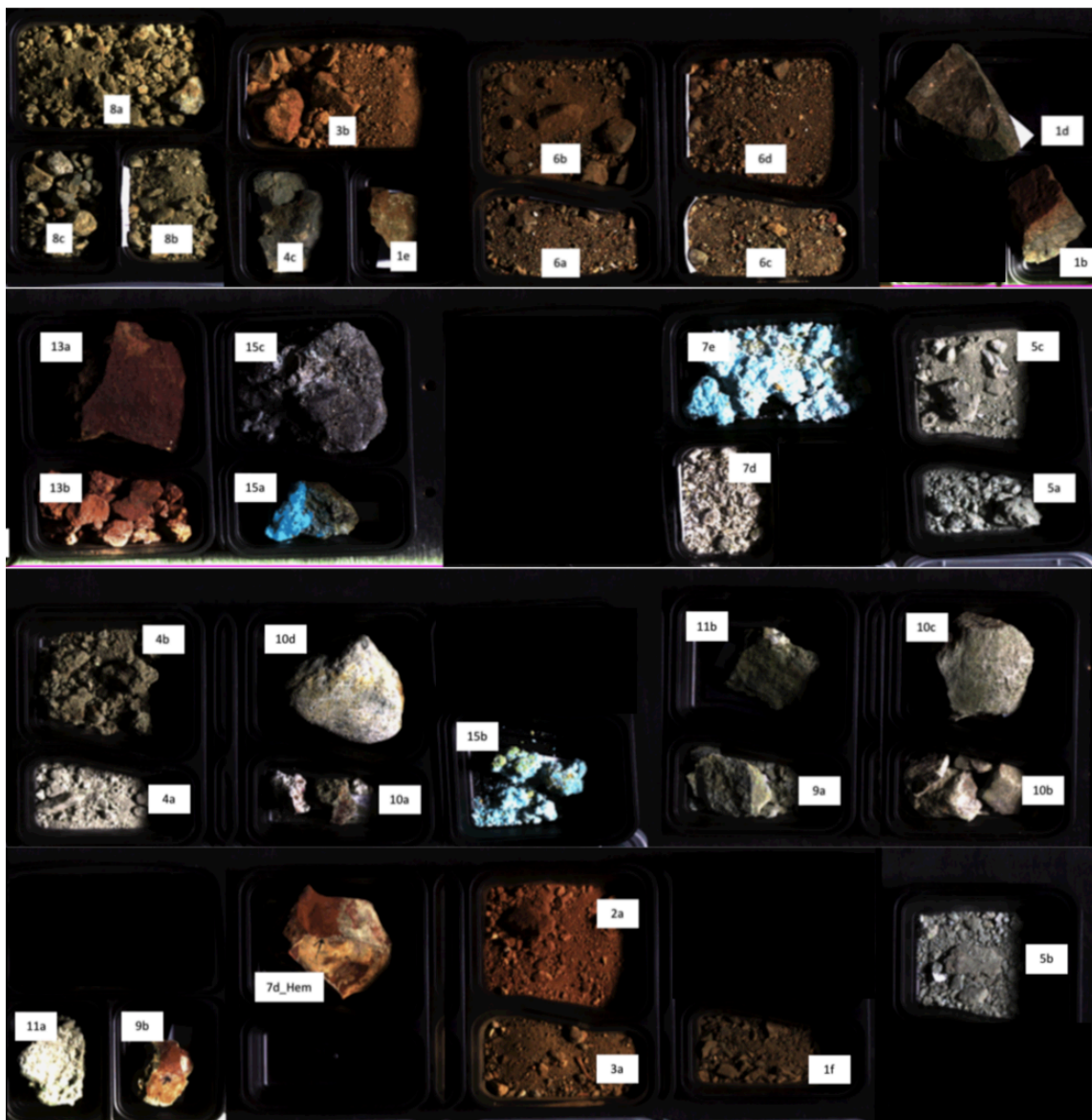


Figure 24 Apliki mine samples hyperspectral scan compilation (R: 640nm – band 63, G: 549nm – band 38, B: 458nm – band 13).

Skouriotissa mine – Three Hills samples

A total of 15 samples have been collected in the Three Hills open pit of Skouriotissa mine in March 2018. The samples have been handled similar to the Apliki mine samples and were scanned with the HySpex system under laboratory conditions before preparing them for geochemical analysis. A total of three hyperspectral scans has been combined into one large dataset containing all samples. The samples were scanned without any sample preparation (Figure 25). For rock samples, the original surface that was directed at the sensor in field conditions was marked. This surface was also directed towards the sensors for laboratory scanning and was later on separated from the bulk rock for geochemical analysis. A table with the sampling location, a sample description and sample photos can be found in the Appendix (Table 50, p. 253).

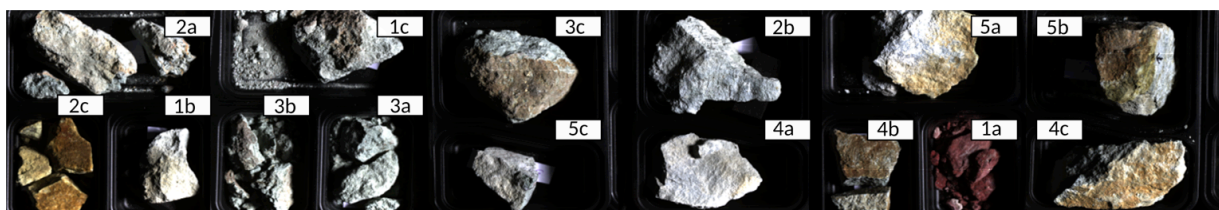


Figure 25 Skouriotissa - Three Hills open pit samples. Collated hyperspectral scan of all 15 samples.

3.5 Data acquisition

3.5.1 Laboratory HSI data acquisition

The **HySpex VNIR-1600** and **SWIR-320m-e** (technical description available at: (hypex.no/products/disc.php, 2019)) are two pushbroom line-scanning cameras that are mounted in parallel. The cameras cover the range of the visible to near infrared (VNIR, 414 – 1000nm) and the shortwave infrared (SWIR, 1000 – 2498nm). They record an array-line of 1600 pixel (VNIR) and 320 pixels (SWIR). Every pixel contains a spectrum with a total spectral sampling number of 408 bands in total. The signal collected from each pixel is decomposed to its spectral components by a grating (see Figure 6, p. 11). The field of view (FOV) captures the spectral dimension (λ) for each pixel of a line of pixels (y-dimension). The pixels per line are fixed for each sensor. This is measured by a two dimensional focal plane array such as a silicon charge coupled device (silicon CCD) detector (VNIR-sensors) or a mercury cadmium telluride (MCT) detector (SWIR-sensors) (Köhler, 2016). The spatial x dimension is acquired by subsequent collection of consecutive lines and a movement perpendicular to the line of pixels spanned by the FOV. Either the sensor or the object of interest can move perpendicular to the FOV, in the laboratory the movement of the samples is accomplished by the

movement of a translation stage, in the field the sensor head rotates the FOV line by line by use of a rotation stage. The sensor parameters are presented in Table 8. Noteworthy for in-pit scanning and robust sensor requirements, is the increase in size and weight from the VNIR to the SWIR sensor and the technical requirement for cooling the SWIR MCT detector to 195 K for data collection with e.g. a nitrogen liquid cooling device (Lin *et al.*, 2009; Köhler, 2016; Spragg, 2017).

Table 8 HySpex VNIR-1600 and SWIR-230m-e sensor parameters from the HySpex User Manual (hyspex.no/products/disc.php, 2019).

<i>Parameter</i>	VNIR-1600	SWIR-320m-e
<i>Spectral Range</i>	400-1000nm	1000-2500nm
<i>Spectral Bands</i>	160	256
<i>Spectral Sampling</i>	3.7nm	6.25nm
<i>Spatial Pixels</i>	1600	320
<i>Field of View (FOV) across track (y-dimension)</i>	17°	13.5°
<i>Pixel FOV across track (y-dimension)</i>	0.18mrad	0.75mrad
<i>Pixel FOV along track (x-dimension)</i>	0.36mrad	0.75mrad
<i>Detector</i>	Si CCD 1600 x 1200	HgCdTe 320 x 256
<i>FPA temperature</i>	N/A	195 K / -78.15°C
<i>Sensor head power consumption</i>	6W	100W
<i>Sensor head weight</i>	4.6kg	7.5kg
<i>Sensor head dimension [cm]</i>	31.5 x 8.4 x 13.8	36.0 x 14.0 x 15.2

The HySpex cameras are provided with two acquisition modes, one for airborne data collection and one for laboratory measurements. In laboratory mode, the cameras are combined with a trigger pulse moving sleight (translation stage) of definable frame period, which depends on the integration time of every array-line acquisition. The configuration of the translation stage framework, the cameras and the light source (45° illumination angle) are fixed, while the translation stage and the samples are moving through the focal plane (Rogass *et al.*, 2017). The reflectance level of a white reference panel, placed in line with the samples, is chosen according to the albedo of the samples. The higher the albedo of the sample, the higher is the diffuse reflectance factor of the matching reference panel. The Brazilian iron ore samples as well as the Apliki and Skouriotissa mine samples required a 50% reflectance white reference panel. Both the geometrical setup and the heat up time of the lamp influence the configuration of the light source. The maximum illumination was obtained with a certain angle of 45° between incident light and the vertical plane. The distance between lamp and HySpex cameras was higher compared to the distance between samples and sensor to ensure diffuse illumination and to avoid thermal influence on the cameras and the samples. The integration time (= measurement time for each image line) was tested to be as high as possible to suppress the impact of signal uncorrelated Gaussian white noise and at the same time as low as needed to avoid detector saturation visible in the pre-view images during image capture. For all measurements the integration time was chosen with

respect to the sample albedo. The used settings for the Brazilian samples are listed in Table 41 (Appendix, p. 207), for the Apliki mine samples in Table 42 (Appendix, p. 207) and for the Skouriotissa mine samples in Table 43 (Appendix, p. 208). The laboratory is equipped with black-painted walls and doors, as well as black curtains to avoid reflected or transmitted light from surfaces other than the sample, an exemplary setup can be seen in Figure 26. The laboratory conditions were kept stable, the air temperature was regulated to $21\pm 0.5^\circ\text{C}$ and the humidity was between 50 - 60% for all measurements. Black cellular rubber is used as a base material for all samples for hyperspectral data acquisition. It reflects less than 5% on average of the incoming radiation (Herrmann, 2019). Detailed descriptions for the GFZ' standard measurements and the process chain can be found in Rogass et al. (2017).

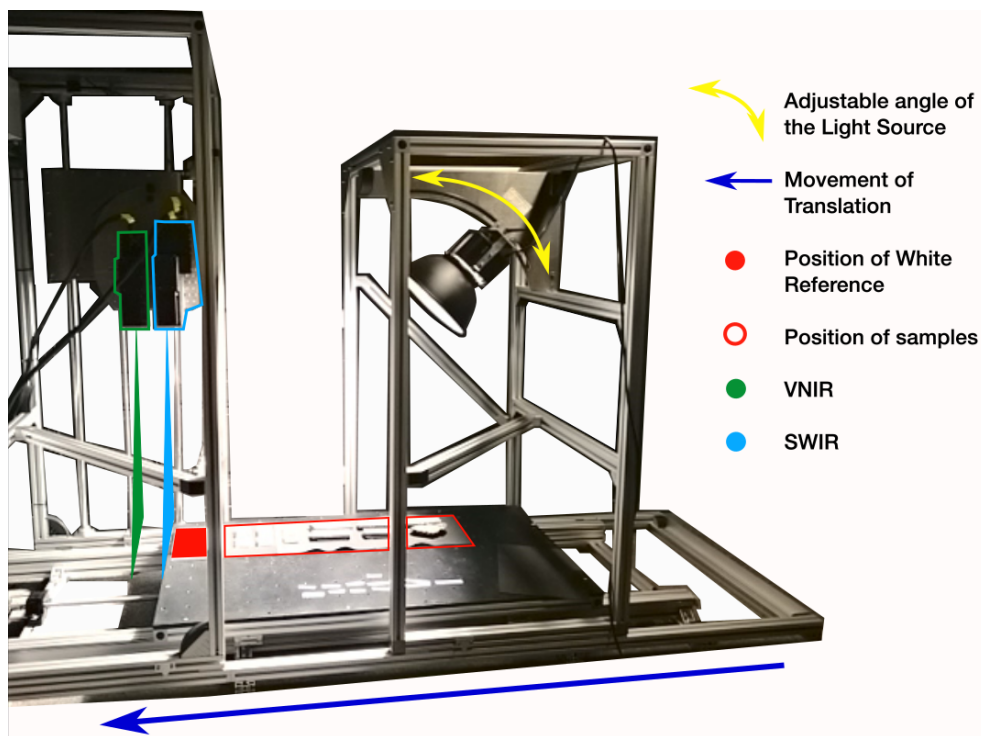


Figure 26 The HySpex translation stage setup (Körting, 2019).

3.5.2 Laboratory HSI data processing

Each measurement run produces one VNIR and one SWIR 3D-data cube. The three dimensions are the two spatial x-, y- and the spectral z-dimension. The 3D image cubes are produced, by sensing a moving sled with a homogeneous reflecting white reference panel and the samples through the focal plane of the two sensors. The software 'HySpex ground' is used to perform the measurements and the software 'HySpex rad' is used to perform the radiometric calibration on the image data (Koerting *et al.*, in prep). The measured image cubes (VNIR and SWIR) are then co-registered, resized and stacked to a

continuous image cube. For the **laboratory scans**, in order to produce a reflectance image, the image pixels that show the white standard were averaged to a one-line reference spectrum. The reflectance was calculated by dividing every image line spectrum by its reference spectrum from the reflecting white reference panel (Rogass *et al.*, 2017). After the reflectance retrieval, the data was digitally cropped to the spatial sample extend, in case of the Brazilian iron ore samples that meant only creating a subset of the sample area. For the Brazilian iron ore samples, a visual check of the 280 x 280 pixels data did not reveal bad bands or the occurrence of a detector jump around 1000nm and therefore only the areas of low SNR (shadows and black rubber) were masked out. For the Apliki mine and the Three Hills mine samples, the single sample containers had to be cropped and combined into one big data frame containing all samples (Apliki: 1250x1280 pixel, Three Hills: 1500 x 250 pixel). The RGB representation of the Brazilian iron ore and the Apliki samples is shown in Figure 27. Figure 28 shows the RGB representation of the Three Hills data. After visual inspection of the data, the pre-processing and correction included an interpolation of bad bands (spikes), a correction of the detector jump around 1000nm and a low SNR/ shadow masking. By masking pixels with reflectance values < 10%, shadowed areas, the black rubber and parts of the pixels of the sample containers were excluded from the data. Some areas of the non-matted sample containers reflected the incoming light back to the sensor and are still present in the data. In order to visually compare the classification results with a ground truth, regions of interest (ROIs) were created encompassing the identifiable samples for both datasets. The ROIs for the iron ore and the Apliki samples are shown in Figure 29.

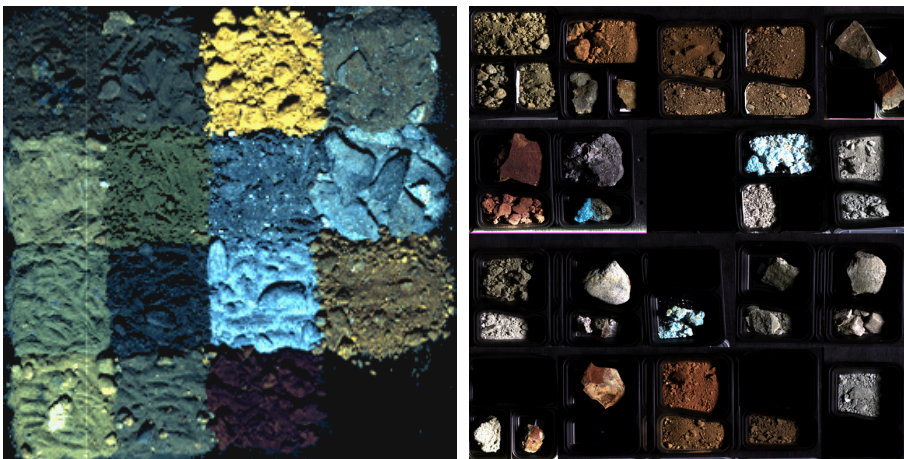


Figure 27 RGB representation of the hyperspectral sample scans. Left: Brazilian iron ore samples. Right: Apliki mine samples.

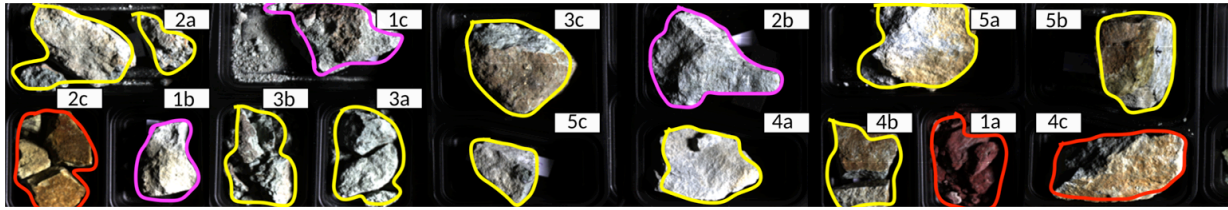


Figure 28 RGB representation of the hyperspectral sample scan of the Skouriotissa mine samples. Color-coded outline represents the mapping color-scheme for the analysis based on the spectral library created from these samples. Pink: ore, red: low grade ore, yellow: waste.

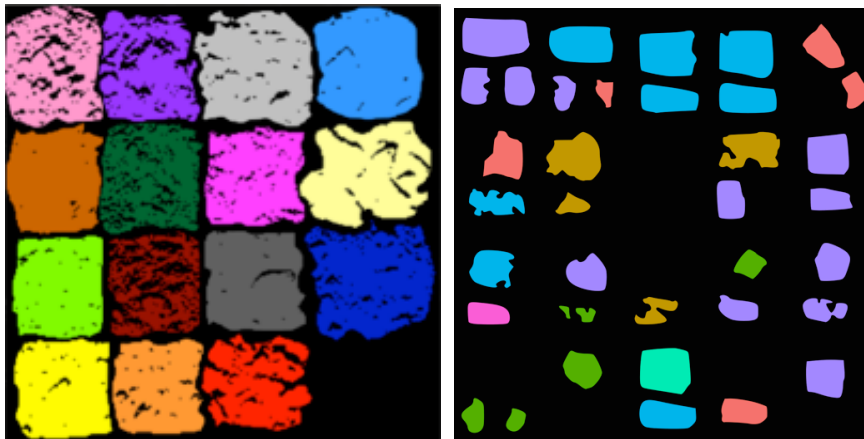


Figure 29 ROIs of sample position. Left: 15 Brazilian iron ore sample ROIs with masked shadow areas, 280 x 280 pixels. Right: 36 Cyprus Apliki surface sample ROIs, 1250 x 1280 pixels.

3.5.3 Geochemical sample analysis for validation

Depending on the sample type, the geochemical validation methods differ. The methods used for each sample type, can be found in Table 9.

Table 9 Sample type and corresponding geochemical validation method.

Sample type	Concentration level determination
Brazilian iron ore samples (Mine site 1)	Samples grinded and pulverized at 150 Tyler mesh (0.105 mm), analysis by fire assay XRF. Provided by company.
Brazilian iron ore samples (Mine site 2)	Sample grinded at 250 Tyler mesh (0.083 mm) and fused with lithium tetraborate. Analysis by XRF (Lithium Tetraborate Fusion Tablet). Provided by company.
Apliki mine samples (Koerting at al., 2019b)	Bureau Veritas Minerals Analysis Lithochemical Whole Rock Fusion, LiBO ₂ /LiB ₄ O ₇ fusion ICP-ES analysis & Carbon and Sulfur Analysis or Ultra Trace Geochemical Aqua Regia digestion, 1:1:1 Aqua Regia digestion (HNO ₃ -HCl acid digestion), Ultratrace ICP-MS analysis
Skouriotissa – Three Hills mine samples	Bureau Veritas Minerals Analysis Lithochemical Whole Rock Fusion, LiBO ₂ /LiB ₄ O ₇ fusion ICP-ES analysis, Carbon and Sulfur Analysis

3.5.3.1 *Brazilian iron ore samples – geochemical analysis*

The samples provided by Mine Site 1 and Mine Site 2 were analyzed differently. Sample 3, 4, 7, 8, 11, 12 and 15 (Mine Site 1) were ground and meshed to below 0.105 mm and analyzed by “fire assay XRF” analysis (as described by the company). Sample 1, 2, 5, 6, 9, 10, 13 and 14 (Mine Site 2) were ground to below 0.083 mm, fused with lithium tetraborate and analyzed by X-ray fluorescence (XRF). The only information regarding the XRF system used is the name “XRF79C” for Mine Site 2, no information about the instrument parameters were supplied. The elements and oxides contents were provided for Fe, SiO₂, Al₂O₃, P, Mn, CaO, MgO, TiO₂, Na₂O, K₂O and loss of ignition (LOI). The Fe content of the 15 samples varies from 24.40-68.49%, the Si content from 0.53-49.02% and Al₂O₃ varies from 0.43-22.14% (Table 10).

In the comparison of Mine Site 1 and 2 and geochemical clustering, the Na₂O and K₂O content was not taken into consideration, as only Mine Site 1 provided those values. The LOI normalized geochemical data as later used for a hierarchical clustering to find geochemical clusters of the samples (geochemically similar samples) for the spectral library EM determination that presented in Section 5.2.2 (p. 99).

Table 10 Geochemistry provided for the samples from the two active mining sites. Values below the detection limit are labeled as “< DL”. The LOI is the loss mass during heating at 1000°C for 60 minutes.

ID	Fe [%]	SiO ₂ [%]	Al ₂ O ₃ [%]	P [%]	Mn [%]	CaO [%]	MgO [%]	TiO ₂ [%]	Na ₂ O [%]	K ₂ O [%]	LOI [%]	Mine Site
1	55.05	16.81	0.61	0.135	0.052	0.018	0.074	0.059	-	-	2.970	2
2	49.72	18.51	1.05	0.110	4.032	0.025	0.049	0.072	-	-	3.120	2
3	24.40	21.69	22.14	0.60	<0.015	0.023	0.12	7.66	< DL	0.33	12.03	1
4	46.39	30.33	1.41	0.037	0.047	0.008	<0.05	0.26	< DL	< DL	1.20	1
5	38.06	41.16	0.43	0.063	0.899	0.011	0.002	0.014	-	-	2.070	2
6	44.47	31.59	1.97	0.104	0.130	0.010	0.051	0.055	-	-	2.580	2
7	58.22	10.14	3.94	0.090	<0.015	0.008	0.14	0.27	< DL	< DL	1.85	1
8	35.37	49.02	0.28	0.017	0.048	0.013	<0.05	0.012	< DL	< DL	0.13	1
9	44.46	32.99	0.53	0.081	0.063	0.009	0.023	0.026	-	-	2.120	2
10	68.49	0.53	0.45	0.050	0.054	0.010	0.013	0.027	-	-	0.870	2
11	30.58	56.5	< DL	< DL	< DL	0.006	< DL	< DL	< DL	< DL	0.07	1
12	47.92	13.29	9.26	0.21	0.015	0.010	0.088	2.87	<0.10	0.13	5.84	1
13	37.17	41.64	1.29	0.184	0.051	0.012	0.025	0.062	-	-	4.220	2
14	38.23	37.45	1.54	0.053	1.505	0.013	0.061	0.309	-	-	2.630	2
15	64.93	1.32	1.48	0.11	< DL	< DL	<0.05	0.32	< DL	< DL	3.74	1

The samples provided from one of the active mine site Nr. 1 were delivered including a threshold value for their geochemical analysis (Appendix, Table 44, p. 208) and a sample description (Appendix, Table 46, p. 208). For mine site 2, only the analysis thresholds were provided (Appendix, Table 45, p. 208).

3.5.3.2 *Apliki mine sample - geochemical analysis*

BVM

The Apliki mine samples were analyzed by the Bureau Veritas Minerals laboratories (BVM). The analysis was split in groups based on three analysis types: “aquatic”, “rock” and “soil”. The sample and their analysis type and BVM analysis codes can be found in the Table 11, an explanation of the BVM analysis codes is provided in the Appendix Table 48 (p. 214). One sample was analyzed with the aquatic analysis type, the rock analysis type included twenty-five samples and soil analysis type included eleven samples. A spectral library of the samples and their geochemistry was published in 2019 (Koerting, Rogass, et al., 2019). The main geochemical analysis results of the Apliki mine samples can be found in in the Appendix (Table 49, p. 215).

Table 11 Apliki mine samples and the corresponding analysis type and BVM code, from Koerting et al. (2019b).

Analysis type	Samples with prefix “AP/1-A”-	BVM code
Aquatic	1a	SHP01, CRU80, PULHP, AQ250
Rock	1b, 1d, 1e, 4c, 5a, 5b, 5c, 7d, 7d-Hem, 7e, 8a, 8b, 8c, 9a, 9b, 10a, 10b, 10c, 10d, 11a, 11b, 13a, 15a, 15b, 15c	SHP01, PRP70-250, LF302-EXT, TC000
Soil	1f, 2a, 3a, 3b, 4a, 4b, 6a, 6b, 6c, 6d, 13b	SHP01, PRP70-250, DISP2, LF302-EXT, TC000

X-Ray dffractometry

For the samples powders, X-Ray diffractometry (XRD) was performed to obtain qualitative sample mineralogy results. XRD data was collected on a PANalytical Empyrean powder X-ray diffractometer in a Bragg–Brentano geometry. It was equipped with a PIXcel1D detector using Cu K_α radiation ($\lambda = 1.5419 \text{ \AA}$) operating at 40 kV and 40 mA. θ/θ scans were run in a 2θ range of 4-70° with step size of 0.0131° and a sample rotation time of 1s. It was equipped with a programmable divergence and anti-scatter slit and a large Ni-beta filter. The detector was set to continuous mode with an active length of 3.0061°. Sample 15a, b and c were additionally analysed semi-quantitatively with the Rietveld-method. The XRD detected mineralogy for each sample is presented in Table 12. The diffractograms can be found in the Appendix (Section 10.5, pp. 217 - 252).

Table 12 Apliki mine sample mineralogy based on XRD. Sample 15a, b and c were additionally analysed semi-quantitatively with the Rietveld-method.

Sample	Mineralogy based on XRD (in no particular order)
1b	Andesine (anorthic), Quartz, Magnetite, Montmorillonite
1d	Anorthite, Magnetite, Diopside, Quartz, Montmorillonite
1e	Magnetite, Quartz, Montmorillonite, Diopside, Anorthite
1f	Magnetite, Anorthite, Quartz, Montmorillonite, Pyrite
2a	Goethite, Quartz, Clinocllore, Jarosite-Natrojarosite, Andesine, Gypsum
3a	Andesine (anorthic), Quartz, Gypsum, Clinocllore, Jarosite, Montmorillonite
3b	Quartz, Andesine, Clinocllore, Gypsum, Jarosite, Montmorillonite
4a	Gypsum, Quartz, Clinocllore, Rozenite (Iron sulfate hydrate)
4b	Quartz, Clinocllore, Andesine, Gypsum, Montmorillonite
4c	Quartz, Clinocllore
5a	Clinocllore, Gypsum, Quartz
5b	Gypsum, Quartz, Clinocllore
5c	Quartz, Gypsum, Clinocllore, Goethite, Hexahydrite
6a	Quartz, Pyrite, Analcime, Goethite, Montmorillonite, Clinocllore, Anorthite
6b	Anorthite, Quartz, Magnetite, Diopside, Montmorillonite, Gypsum, Goethite
6c	Quartz, Clinocllore, Analcime, Gypsum, Calcite, Jarosite, Pyrite, Montmorillonite
6d	Quartz, Pyrite, Anorthite, Analcime, Clinocllore, Montmorillonite
7d	Quartz, Hexahydrite (Mg sulfate), Clinocllore, Gypsum, Pyrite
7d-Hem	Pyrite, Hematite, Quartz, Gypsum, Clinocllore
7e	Rozenite, Goethite, Quartz, Apjohnite, Ferrohexasahydrite (Fe sulfate hydrate)
8a	Quartz, Clinocllore, Pyrite, Ajoite (minor copper ore)
8b	Quartz, Clinocllore, Pyrite, Ajoite
8c	Quartz, Ajoite, Clinocllore, Pyrite
9a	Quartz, Clinocllore (Mn), Clinocllore
9b	Quartz, Clinocllore, Pyrite, Hematite
10a	Clinocllore, Hematite, Quartz
10b	Quartz, Clinocllore
10c	Quartz, Clinocllore
10d	Quartz, Clinocllore, Pyrite
11a	Quartz, Clinocllore, Gypsum, Bassanite (Ca sulfate)
11b	Quartz, Clinocllore, Sphalerite
13a	Andesine, Quartz, Magnetite, Montmorillonite-Chlorite, Diopside
13b	Clinocllore, Quartz, Montmorillonite
15a	Quartz (82.6%), Pyrite (7.5%), Chalcopyrite (0.8%), Pentahydrate (cuprian) (9.1%) Cu sulfate)
15b	Quartz (86.1%), Pyrite (4.5%), Pentahydrate (cuprian) (7.1%), Covellite (2.4%)
15c	Covellite (18.9%), Quartz (39.9%), Chalcanthite (21.8%), Pyrite (20.0%)

3.5.3.3 *Skouriotissa Three Hills samples – geochemical analysis*

The Skouriotissa mine samples were analyzed in the Bureau Veritas Minerals laboratories (BVM). The samples and their analysis type and BVM analysis codes can be found in Table 13, an explanation of the BVM codes is provided in Table 48 in the Appendix (p. 214). All 15 samples were analyzed with the BVM “rock” analysis. The main components of geochemical analysis results of the Skouriotissa samples are listed in Table 51 in the Appendix (p. 256).

Table 13 Three Hills mine sample numbers and the corresponding BVM analysis codes.

Analysis type	Samples with prefix “Sko1_B_”-	BVM code
Rock	1a, 1b, 1c, 2a, 2b, 2c, 3a, 3b, 3c, 4a, 4b, 4c, 5a, 5b, 5c	SHP01, PRP70-250, TC000

3.5.4 *Field HSI data acquisition*

In the following paragraphs the Apliki and Three Hills mine field data acquisition workflow is explained in detail. It describes the data acquisition, sampling, reflectance retrieval, data pre-processing and 3D model reconstruction.

3.5.5 *Cyprus field work*

In the following chapter, the HSI data acquisition and processing in the field in the Apliki mine is explained. The correct field setup and sampling for validation is crucial and should be considered in depth before any analysis takes place (3D reconstruction, BFF, SAM or MWL). All the work in the Republic of Cyprus was conducted under the Permit to conduct a Geological Survey, Ref. No. 02.13.005.002.005.022 from the 19th of March 2018, granted by the Geological Survey Department Cyprus, Ministry of Agriculture, Rural Development and Environment (GSD) and the Director Dr. Costas Constantinou. The permit terminated in 18th of September 2018. An agreement for a Memorandum of Understanding and Framework (MoU) for cooperation in the area of geo-science between the GSD and the Helmholtz Centre Potsdam (GFZ) German Research Centre for Geosciences was reached in March 2019 including the objective of “hyperspectral mapping of secondary minerals in the field of existing drill cores e.g. in abandoned mines or for the purpose of environmental monitoring”. This work is linked to both, the field sampling permit from March 2018 and the MoU agreement reached in March 2019.

3.5.6 Apliki HSI field data

In order to scan the Apliki mine face, the open pit mine was accessed with supervision by the GSD from the SSW. As the Apliki mine is in close proximity to the UN buffer zone, the movement was limited to the SSE, the Northern-most accessible point was the NNE accessible levels of the mine face. The HySpex sensor was placed approximately parallel to the outcrop face at a distance of 100 m SEE to the mine face. The HySpex placement and distance was based on the accessibility and the safety for both the operator and the sensor. The placement of the sensors influences the height of the mine face that can be captured and the pixel sizes at mine face levels. The pixel size has to be small enough to capture deposit relevant changes. Furthermore, it has to capture the white reflectance targets with sizes of 20 cm x 20 cm for the reflectance retrieval. For the HySpex system, the approximate pixel size captured at the mine face level for different sensor – mine face distances are presented in Table 14.

Table 14 Approximate distance of sensor to mine face and expected, rounded pixel size at-mine-face for the HySpex VNIR-1600 and SWIR-320m-e cameras.

	VNIR-1600		SWIR-320m-e	
<i>FOV (with FOV expander)</i>	34°		28°	
<i>Pixels per line</i>	1600		320	
Distance	Expected pixel size	Captured mine face height	Expected pixel size	Captured mine face height
<i>200m</i>	3.8cm	122m	15.6cm	100m
<i>150m</i>	2.8cm	91m	11.7cm	75m
<i>100m</i>	1.9cm	61m	7.8cm	50m
<i>10m</i>	0.2cm	6.1m	0.8cm	5m

As the mine face is not level with the sensors view, the uppermost levels will be more distant, whereas the lower levels will be closer to the sensor, resulting in different pixel sizes. This is due to the man-made topography of the levels in the mine and also the upward sensing geometry of the sensor. The expected pixel size in the lowermost, closest levels will be < 2.4cm and in the higher, most distant levels > 24cm. The mine face area represented by each pixel does not only vary line by line but also within the pixels of one line (mine face height). Figure 30 schematically shows the changes in pixel size not only with outcrop height but also with proximity of the sensor to the mine face.

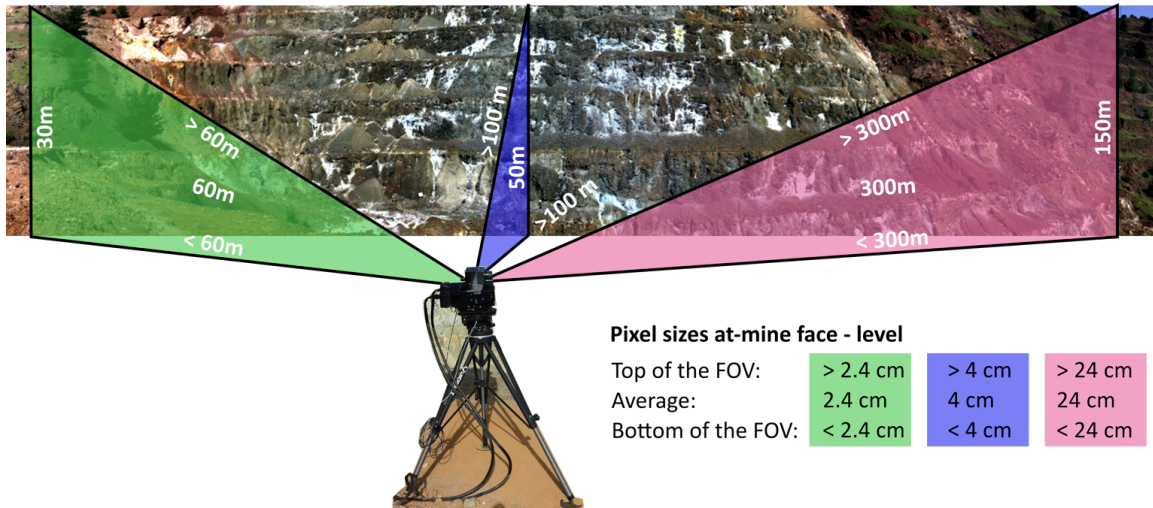


Figure 30 Approximated pixel size with mine face height variations and proximity to sensor variations, relative to the HySpex SWIR-320m-e with a FOV of 28° and 320 pixels per line.

Six white reflectance panels or “targets” were placed at the accessible part of the mine face. The reference panels are 5%, 20%, 50%, 90% and 95% calibrated reflectance standards and approximate an optimal Lambertian reflectance surface. Five smaller targets are placed with increasing reflectance standard from left to right along the outcrop face. A large 90% target (80 cm x 80cm) is placed at the center of the face, in-between the smaller 50% and 90% targets (20 cm x 20cm). The normal surface of each panel is oriented parallel to the mine face and the reflective surface is facing the sensors at 150 m distance. The GPS positions of the sensor and the targets are listed in Table 15 and are based on the internal GPS system of the NIKON 1 AW1 camera. A sketch of the position of the HySpex within the open pit is shown in Figure 31 and the position and placement of the targets along the mine face is shown in Figure 32.

Table 15 Latitude and Longitude of the HySpex and the six targets.

	Latitude	Longitude
<i>HySpex</i>	35° 4' 35,49" N	32° 50' 33,66" E
<i>5% target</i>	35° 4' 37,39" N	32° 50' 35,73" E
<i>20% target</i>	35° 4' 37,28" N	32° 50' 35,78" E
<i>50% target</i>	35° 4' 36,91" N	32° 50' 35,86" E
<i>90% target</i>	35° 4' 36,72" N	32° 50' 36,14" E
<i>95% target</i>	35° 4' 36,39" N	32° 50' 36,21" E
<i>Big target, 90%</i>	35° 4' 36,89" N	32° 50' 35,95" E

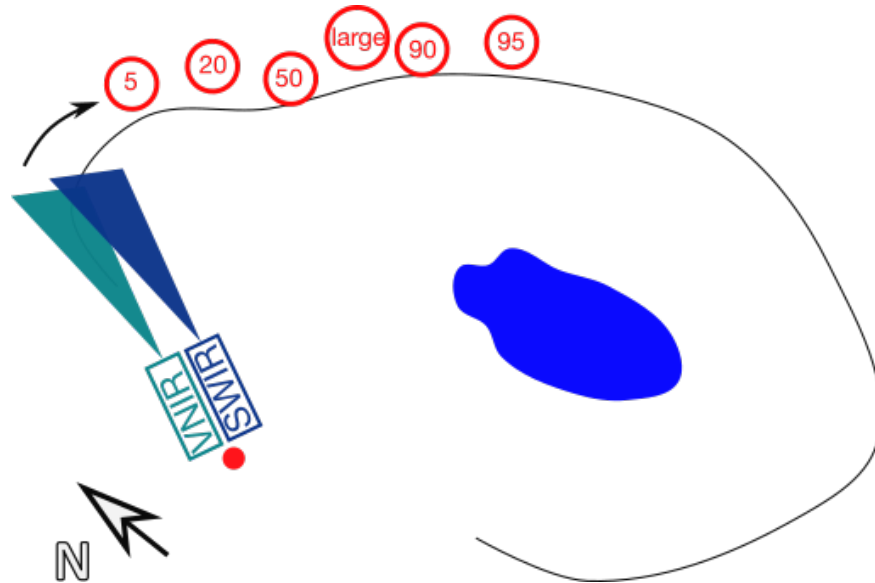


Figure 31 Position of HySpex and reflectance targets in the Apliki open pit (outlined in black).

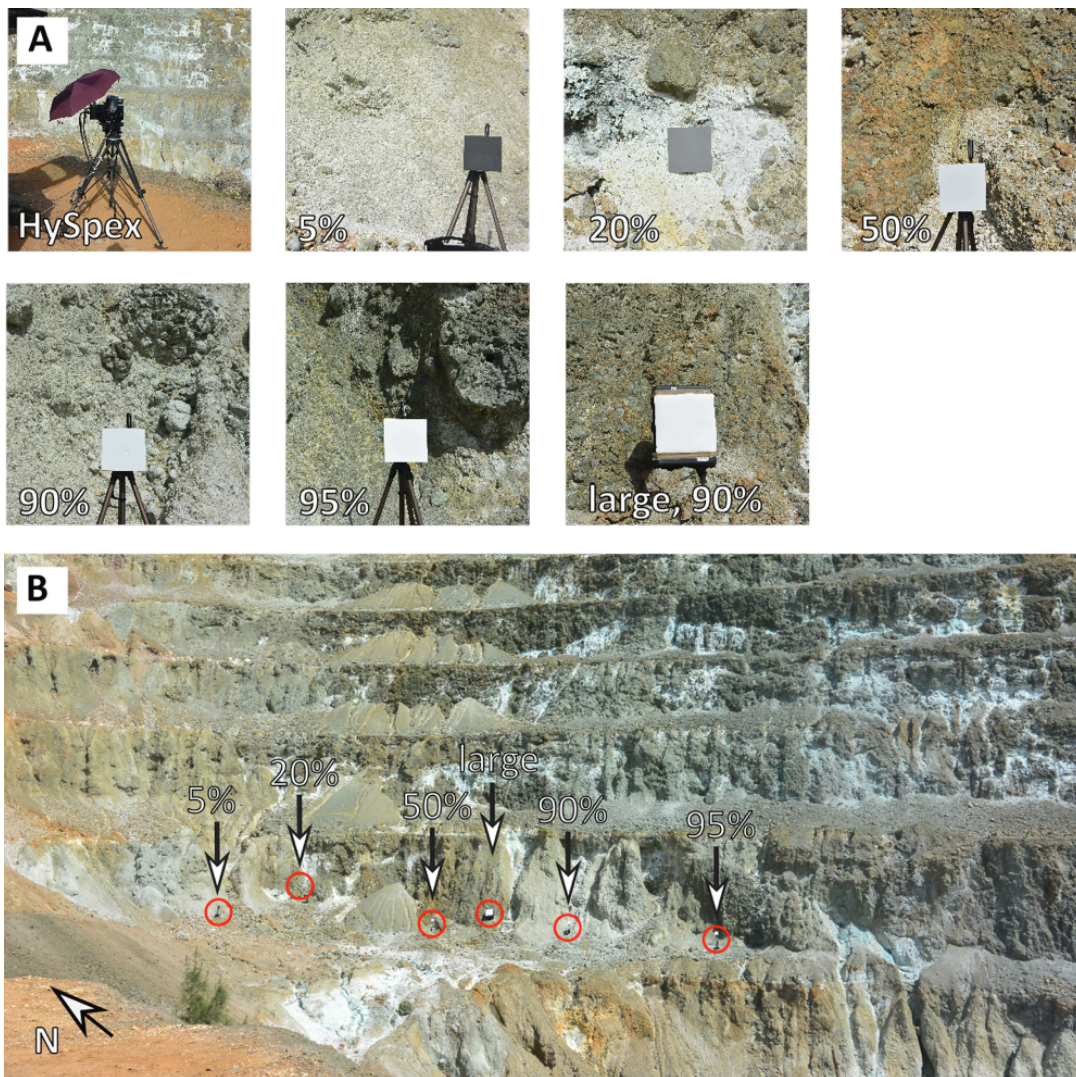


Figure 32 A: HySpex and target setup shown in close-up photos. B: Position of the targets along the mine face from left to right: 5%, 20%, 50%, 90% large, 90% small, 95%.

The HySpex sensor head was at an approximate height of 1.50 m. The sensors were protected from the sun by a customary umbrella. The HySpex computer was placed in the nearby car trunk to protect it from the sun and dust (Figure 33), the system was powered by a generator (Honda EU 10 i inverter) that was positioned at a distance, downwind of the HySpex. An image series of eleven HySpex VNIR and SWIR images was recorded, beginning at 13:46 UTC+3 under the conditions of a solar azimuth angle of approximately 200° and a sun elevation angle of approximately 52° with occasional cirrus clouds covering a maximum of 20% of the visible sky. The data acquisition parameters can be found in the Appendix (Table 52, p. 257).

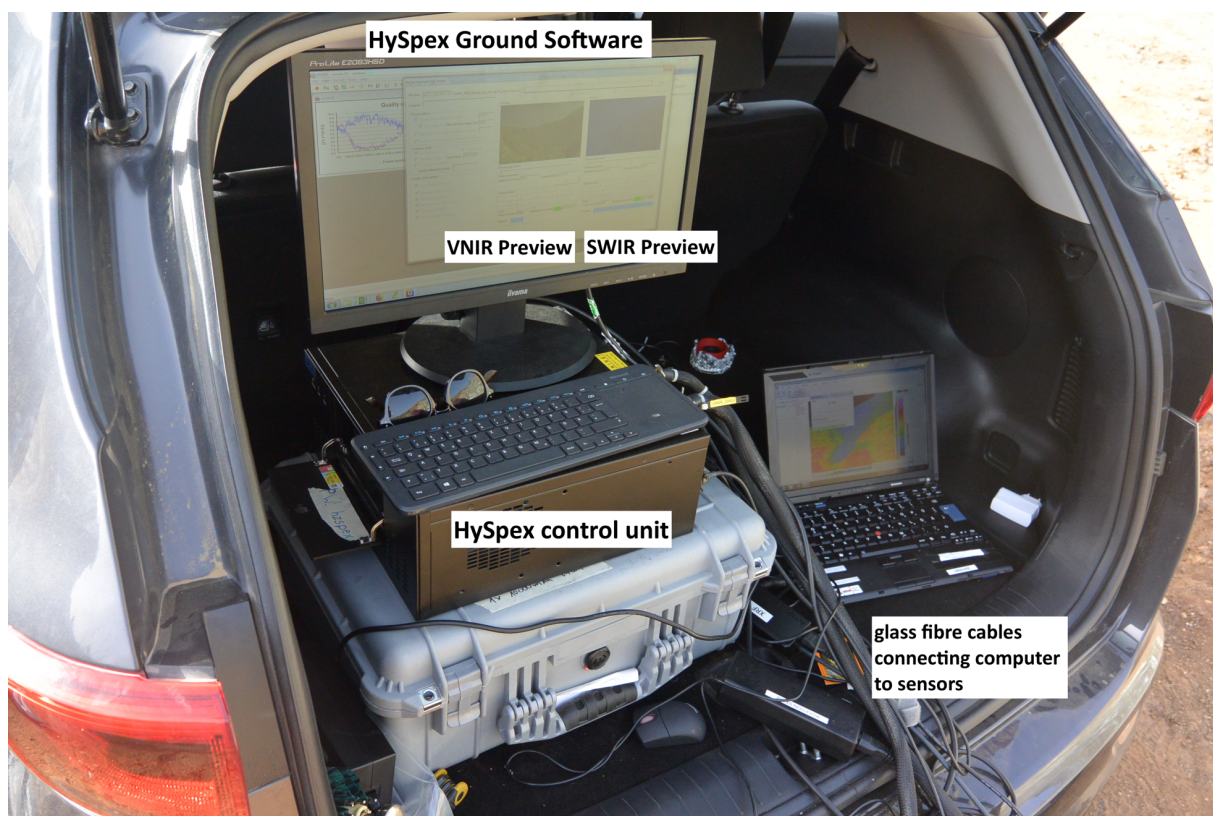


Figure 33 Data acquisition at Apliki outcrop - computer setup.

3.5.6.1 *Apliki field sampling*

Figure 34 shows the expected lithology of the outcrop. Ten levels have been counted in total, each face of an approximate height of 10m. The high level of weathering, that has been taking place since the 1970s, results in downhill weathering of secondary mineralogy from the gossans cap at the top of the mine face. The levels are dominated by landslides - triangular cones of debris displaced from the levels on top - and by water carved troughs, wide at the top of an individual level face, narrowing down

towards the bottom of the level face. These troughs seem to have formed from surface runoff.

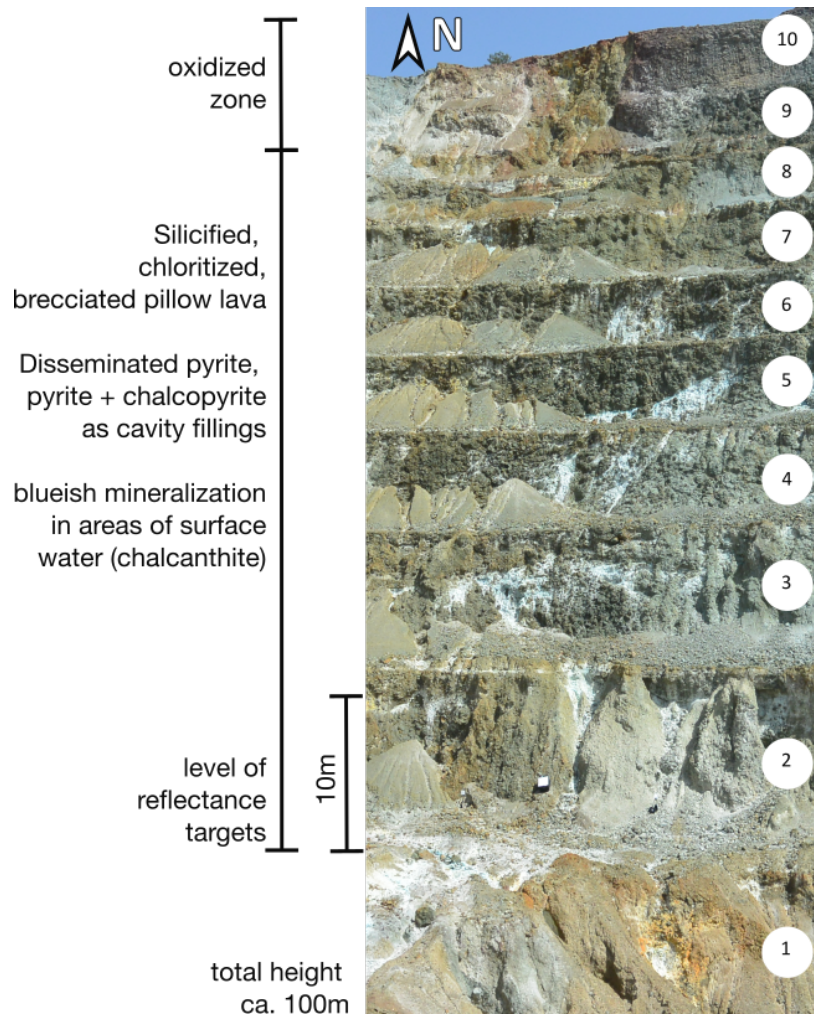


Figure 34 Apliki mine face - expected lithology and extraction level numeration.

These trough surfaces are covered in white-blue mineralization. Only the two lower most levels were accessible and of those, only level 2 was within the spatial range of the HySpex sensors. Sampling therefore concentrated on level 2. In order to identify spectrally homogenous regions for sampling, a PCA was calculated from the SWIR radiance data. The PCA method that was used is explained in general terms on page 84 and for the Brazil dataset on page 103. Instead of the reflectance data as for the Brazil dataset, here the radiance SWIR data was used to calculate the PCA and find spectrally homogeneous areas in the field. The RGB visualization of PCA band 3-5-6 is shown in Figure 35. Field sampling was conducted in the areas indicated by red stars in the PCA. Thirty-seven samples were collected on-site from fourteen different sampling areas (see Figure 36). Area 1 and 2 were located on the level of the HySpex sensor, area 3-11 and 14-15 were located on level 2 of the mine face. Area 12

was inaccessible for field sampling. The landslide marked as area 13 was sampled from the bottom of the open pit (level 1) where it was safely accessible.

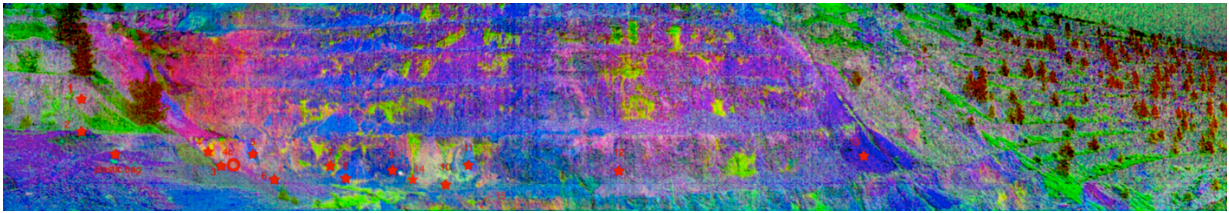


Figure 35 PCA based on SWIR radiance data marking spectrally homogeneous regions with red stars for possible field sampling.

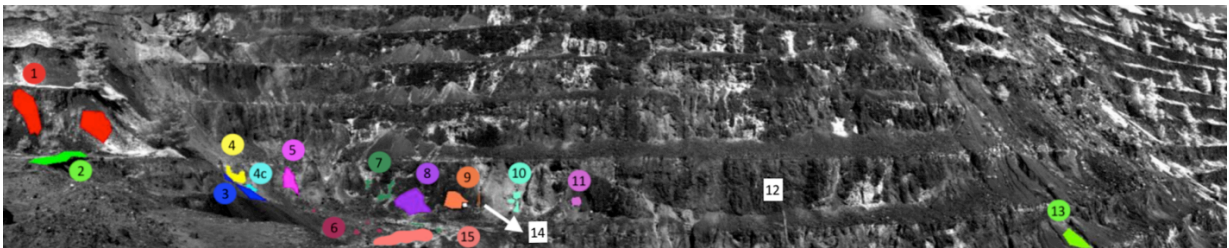


Figure 36 Sampling locations identified from SWIR radiance PCA analysis and marked as ROIs in the SWIR grey-scale image. Sample area 1-11, 13 and 15 were included in the spectral characterization of the mine face (marked in their ROI color), area 12 & 14 were excluded (labeled in white).

Several samples have been collected from each sample area and were analyzed spectrally and geochemically as described in the laboratory section of this work (and in Koerting, Rogass, *et al.*, 2019). For the spectral library based on geochemical clustering of the samples (Subsection 5.4.1.1, p.136), only twelve sample areas were considered. Area 12 and 14 were excluded from the spectral characterization of the mine face and are marked by white rectangles in Figure 36 above.

3.5.6.2 *Apliki field data reflectance retrieval*

The raw Digital Number (DN) sensor output data is radiometrically scaled to radiance ($W \cdot sr^{-1} \cdot m^{-2} \cdot nm^{-1}$) using manufacturer predefined sensor characteristic radiometric calibration coefficients. The mean radiance spectrum of each reflectance target is calculated and normalized according to their relative reflectance level. The incident direct and diffuse irradiance is modelled polynomially for every spatial position (pixel) and for all bands of the reflectance panels present in the HSI. The reflectance targets are marked by ROIs in the ENVI software for this purpose. Table 16 lists the reflectance targets utilized for the Apliki mine face with the number of detectable pixels for each target. The irradiance model calculated for each target is applied to every HSI pixel to retrieve the reflectance value for each band. If an averaging over more than one HSI measurement is applied, a weighted average of all data cubes is calculated according to their spectral homogeneity. Consequently, for Apliki eleven data cubes

were averaged and combined into one reflectance dataset that was further processed and downsampled. Table 16 also states the variable area depicted by a pixel inferred from the known size of the different reflectance panels. As discussed above, the area depicted by each pixel varies due to the rotational manner of the measurement and the various distances from surface to sensor (along-track and within the captures line of pixels). For the white reference targets, this variation of area depicted by one pixel flank varied from 7.0 – 11.4 cm. For every image the spectral homogeneity of the calibrated reflectance standards was determined using the standard deviation of all pixel spectra at the reflectance standard locations (Boesche et al. 2015). The resulting data cube was then used for the analysis of the surface mineralogy.

Table 16 White reference target size in pixel, cm, and approximate pixel size of the reflectance targets at the outcrop.

Target	Number of pixels found in SWIR per target lateral length	Size of target	Lateral pixel size at white reflectance target position [cm]
5%	2.5	20 cm x 20cm	8
20%	2	20 cm x 20cm	10
50%	2	20 cm x 20cm	10
90%	3	20 cm x 20cm	7
95%	2.5	20 cm x 20cm	8
90%	7	80 cm x 80 cm	11.4

3.5.6.3 *Apliki field data pre-processing*

The reflectance was retrieved from an image series average of eleven scans in total, acquired around noon (13:46 CEST) of an evenly lit mine face. Each scan was subject to slightly different illumination conditions due to the movement of clouds. Averaging the scenes results in an approximately evenly illuminated outcrop. The VNIR-SWIR scan has a size of 3013 x 320 pixel, including parts of the open pit in the Southeast. The scan was clipped to the extent of the mine face to 1600 x 320 pixel. The reflectance retrieval by Christian Rogaß (Boesche et al., 2015, explained above) includes a smoothing with a Gaussian filter with a sigma of 2. The smoothed data was clipped to the wavelength range of 414 – 2390 nm, excluding the last 18 bands due to prevalent noise. The atmospheric bands, visible as broad spikes in the data, were clipped around bands 209 – 239 and bands 284- 327 and a shadow and Normalized Difference Vegetation Index (NDVI) masking was performed based on the Indexdatabase (indexdatabase.de/, 2020). The resulting vegetation mask is shown in Figure 37 and the shadow and NDVI-masked imagery is shown as an RGB in Figure 38.

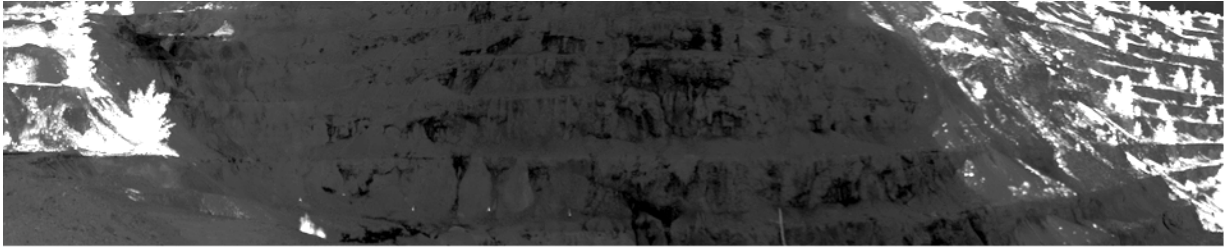


Figure 37 NDVI of the Apliki field reflectance scan, shown in levels of grey. NDVI values ≥ 0.1 are depicted in light shades.



Figure 38 NDVI & shadow masked reflectance field scan. Vegetation and areas of shadow (high SNR) are masked out and shown in black. (RGB composition: R: band 63, G: band 38, B: band 13.)

3.5.6.4 Apliki mine 3D reconstruction

The digital outcrop model was reconstructed on a Lenovo Thinkpad, Windows 10 64-bit, Intel® Core™ i7-2860QM CPU @ 2.50 GHz x 2.50 GHz and 32 GB Memory. The processing times of the 3D reconstruction are based on this hardware. The 3D modeling was performed in Agisoft Photoscan Professional v.1.2.6.2834. Neither the method of Structure-from-Motion (SfM) reconstruction nor the models' accuracies are of particular interest in this work, the "digital outcrop models" are purely created for visualization purposes in the context of location within the open pit. To reconstruct a 3D model of the outcrop – often called a "digital outcrop model" (DOM) - 117 photos taken by a NIKON 1 AW1, lens 11.0 – 27.5 mm, f/ 3.5 – 5.6 (4608 x 3072 pixels) and 1 HySpex RGB scan (1600 x 320 pixels) were utilized for SfM reconstruction. SfM allows us to align overlapping photos to form geometric 3D meshes (Caravaca *et al.*, 2019). Similar points across the photo set, so-called matching tie points are detected and linked to create a sparse point cloud. Each tie-point is projected into 3D space, the position of each point is being calculated from the apparent displacement across several photos (Caravaca *et al.*, 2019). Points detected not correlating to the outcrop itself are removed before calculating a dense point cloud. A network of vertices delimitating triangular polygons is calculated by linking the points of the dense point cloud, thereby creating a 3D mesh (Caravaca *et al.*, 2019). The vertices are color-coded according to the RGB colors of the original source photo. The visualization of the single RGB representation of the HySpex scan is included in the SfM reconstruction to match tie points and construct a 3D model. To visualize the RGB HySpex scan within the 3D model or to visualize the resulting maps of the same spatial dimensions, the HySpex imagery (or map) is used as a single texture for the mesh, and visualized on top of the RGB photo-based DOM. This results in a

photorealistic representation of the digital outcrop model that is able to visualize the mapping results on the 3D texture. Two RGB DOMs for Apliki were reconstructed, the first one showing a wider view of the open pit and a second one showing a close-up of the mine face in the NNE of the open pit. The parameters for the two digital outcrop model reconstructions are listed in Table 54 in the Appendix (p. 259). The dense point clouds of both DOMs are shown in Figure 39 and Figure 40.

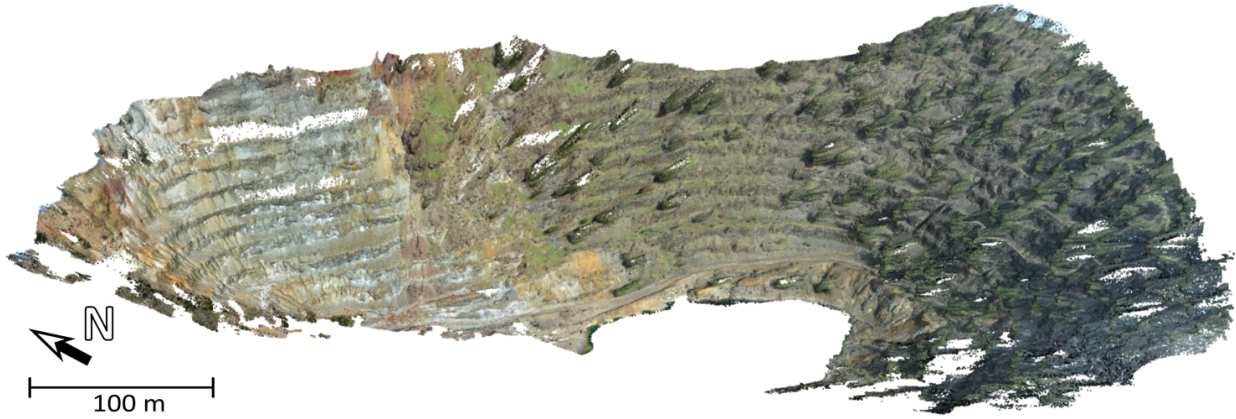


Figure 39 RGB digital outcrop model of the Apliki open-pit area, showing the NNE to SSW walls of the pit. One extraction level is approximately 10m of height.

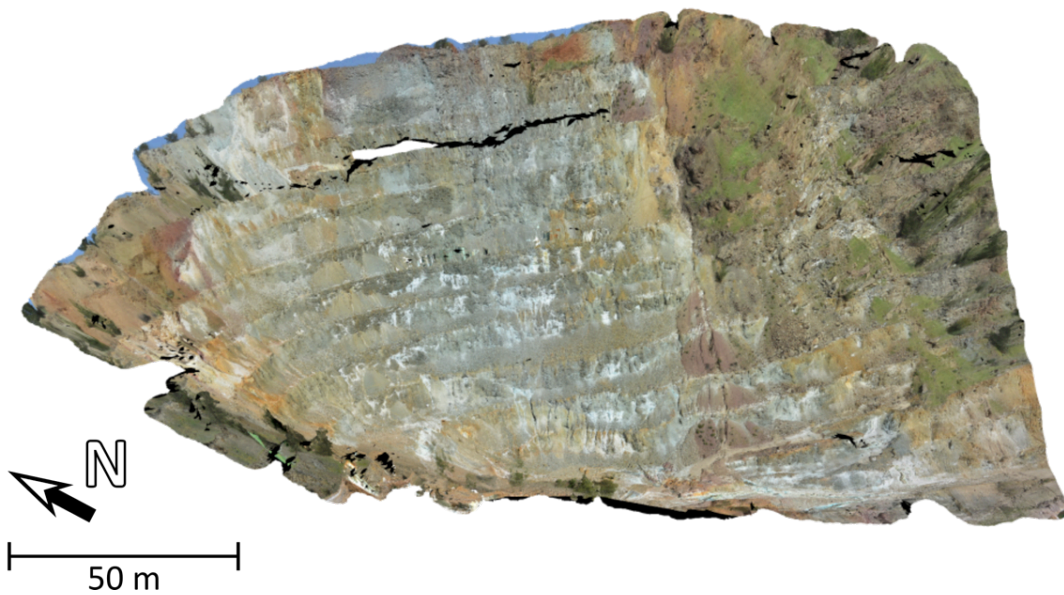


Figure 40 Close-up RGB model of the mine face in the NNE scanned by the hyperspectral system. One terrace is approximately 10m of height.

3.5.7 Three Hills HSI field data

The Three Hills open pit was entered from the Northeast and the HySpex sensors and equipment were placed approximately parallel to the upper outcrop faces at a distance from 100m to 200m from the convex faces on the Eastern flank of the open cut. One white reflectance panel was placed at the accessible part of the mine face NW of the HySpex sensor. The 80cm x 80cm reference panel is calibrated as a 90% reflectance standard. The normal surface of the panel is oriented parallel to the mine face in the North and the reflective surface is facing the sensors from a 100m distance. Only one large WR panel could be placed on an accessible, safe part of the mine that is also visible within the collected image area due to its larger size. It can thus be identified correctly within the VNIR and SWIR scan for the needed reflectance retrieval. The difference to the placement and number of reflectance panels compared to Apliki here, is the accessibility to place the panels within Three Hills, the visibility of the panels within the image and the larger distance from sensor to mine front. The GPS positions of the sensor and the white reflectance panel are listed in Table 17. The position and placement of the sensors and the reflectance target in the open pit is shown in Figure 41 based on Google Earth imagery from April 2018 (Google, 2018). The line of surface sampling is marked, as well as the rotational scanning direction from S to NNW.

Table 17 Latitude and Longitude of the HySpex and the target position.

Position of:	Latitude	Longitude
<i>HySpex</i>	35° 05' 23.58'' N	32° 54' 01.34'' E
<i>Big target, 90%</i>	35° 05' 25.23'' N	32° 54' 00.27'' E

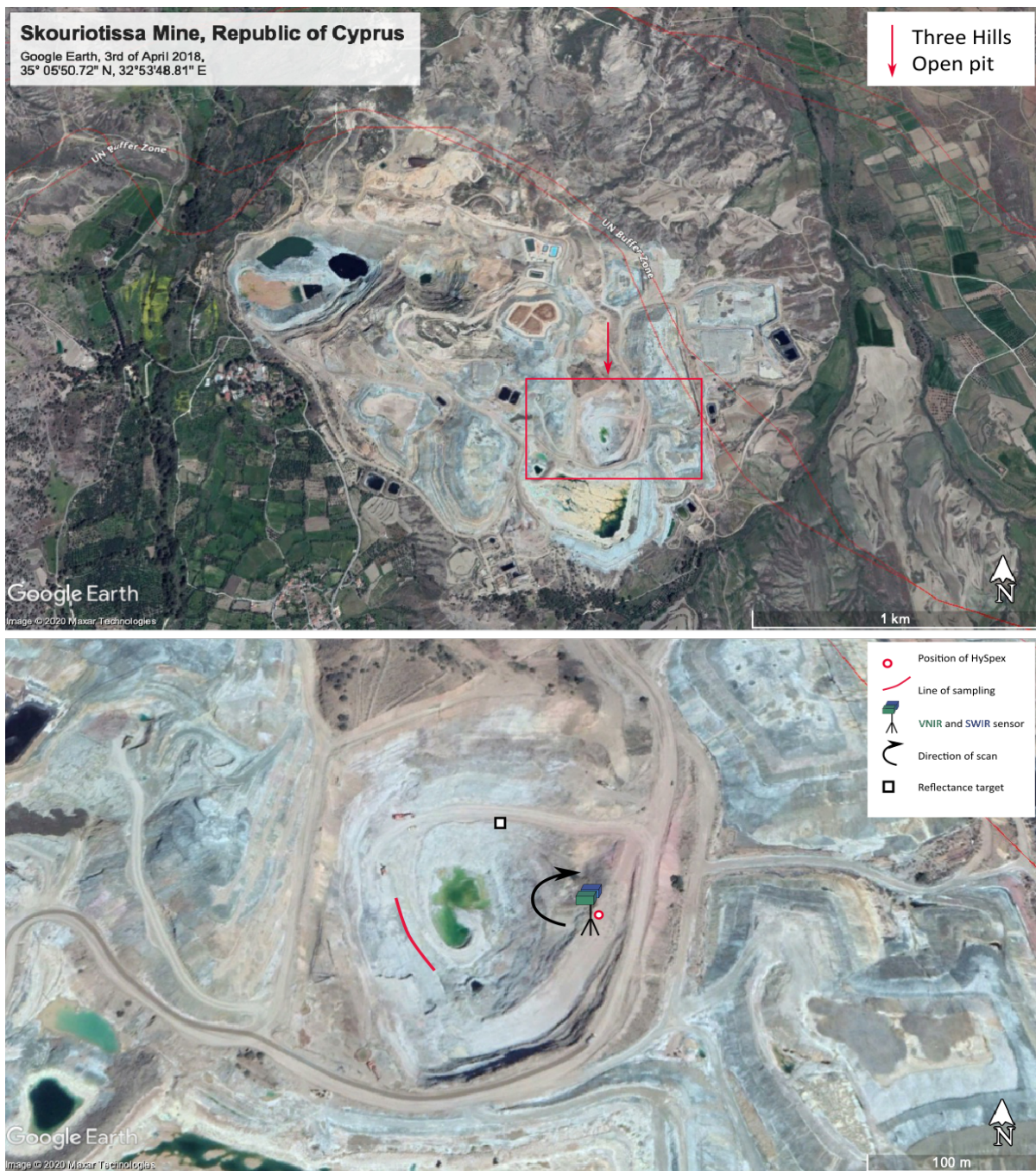


Figure 41 Top: Skouriotissa Mine overview; Bottom: Close-up of Three Hills deposit with marked sensor and target positions. Source: "Skouriotissa Three Hills Deposit", 35°05'50.72"N, 32°53'48.81"E, GOOGLE EARTH, 3rd of April 2018, retrieved 21st of July 2020 (Google, 2018).

The HySpex sensor head was at an approximate height of 1.50m. Figure 42 shows the field setup with the placement of the sensors and equipment across from the open pit. One VNIR and SWIR image was recorded with an averaging of 4 frames, the detailed data acquisition parameters can be found in the Appendix (Table 53, p. 258).



Figure 42 Data acquisition setup at Skouriotissa - Three Hills mine.

3.5.7.1 *Three Hills Field Data Pre-Processing*

The hyperspectral reflectance data derived from the field pre-processing routine from Boesche et al. (2015) and was cleaned up as explained for the Apliki field data including a shadow (<10% reflectance) masking. The field data was downsampled to the optimal sensor “40nm VNIR – 15nm SWIR, without atmospheric bands” (clipped and interpolated between the atmospherically influenced bands between 1300–2010nm). The resulting dataset spans the spectral range of 414–2390nm within 54 spectral bands of 40nm (VNIR) and 15 nm (SWIR) bandwidths, the RGB representation of the mine face scan is shown in Figure 43.



Figure 43 RGB representation of the superspectral mine face data of Skouriotissa, Three Hills, Republic of Cyprus. Viewers' direction is approximately towards NNW.

3.5.7.2 *Three Hills Mine 3D reconstruction*

To reconstruct a digital outcrop model (DOM), 184 photos taken by a NIKON 1 AW1, lens 11.0 – 27.5 mm, f/ 3.5 – 5.6 (4608 x 3072 pixels) and 1 HySpex RGB scan (2500 x 320 pixels) were utilized for Structure-from-Motion (SfM) reconstruction. By including one HySpex RGB scan, the texturization of the DOM with the classification maps can be achieved. One DOM for Skouriotissa Three Hills was reconstructed, showing the open pit from the HySpex view position from approximately SE of the open pit. The dense point cloud model is shown in Figure 44, textured with the orthophoto mosaic of the available Nikon photos and in Figure 45, textured with the RGB hyperspectral scan overlaid on the RGB photo texture. The parameters for the DOM reconstructions are listed in Table 55 in the Appendix (p. 260). The DOM is created for visualization purposes only and neither its accuracy nor the methodology of SfM is under inspection in this work.



Figure 44 The resulting 3D model, textured with the orthophoto mosaic of all available Nikon photos.

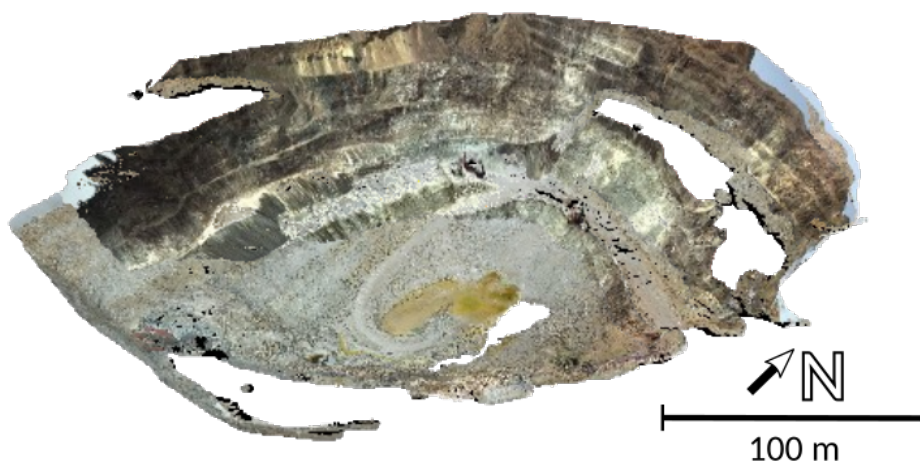


Figure 45 The resulting 3D model, textured with the RGB hyperspectral scan overlaid on the RGB photo texture.

4 Near-Field Imaging Spectroscopy Methods

4.1 Analysis of imaging spectroscopy data

The analysis of any hyperspectral imagery is generally aggravated by the high variability of the material spectra due to subtle changes in chemical and molecular characteristics. By using corrected reflectance data instead of radiance data, the influence of the illumination source and changes is considered as negligible and the changes in the spectrum is considered as purely material dependent. The correction to reflectance is crucial yet handled differently by the different research groups; it is discussed in the following section. When the data is reflectance-corrected, the spectral, material-dependent features can be analyzed and distinguished. Some of the standard knowledge- and data-driven analysis approaches are explained in the following introductory chapter and will be applied to the Brazilian Iron Ore sample data in the subsequent chapter. Figure 46 schematically demonstrates how hyperspectral data is handled, corrected, processed and analyzed. All of the examples mentioned in the figure are explained in detail in this section and the following subsections.

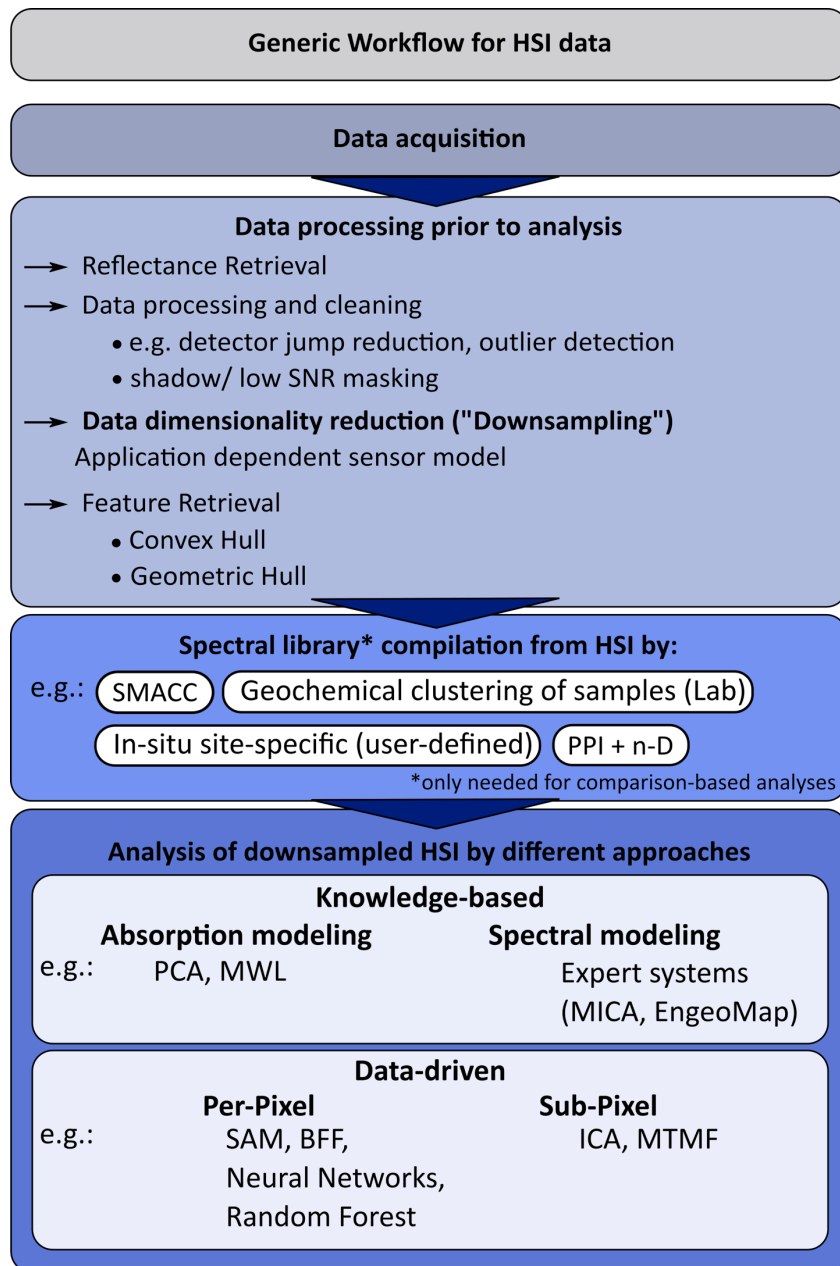


Figure 46 Schematic generic workflow of how HSI is processed and analyzed. Explanation of the examples given in the figure are found here: data dimensionality reduction (pp. 76-77), continuum removal (pp. 81-83), SMACC (pp. 78-79), geochemical clustering (p. 78), in-situ site-specific (p. 77) and PPI + n-D (p. 79). The following methods are found here: PCA (pp. 84-85), MWL (pp. 85-86), MICA (p. 93), EnGeoMap (pp. 94-95), SAM (p. 86), BFF (pp. 86-87), Neural Networks (pp. 89-90), Random Forest (pp. 90-91), ICA (p. 92) and MTMF (p. 91).

4.2 Correction of data – Reflectance Retrieval

In order to acquire close-range data fit for mineral mapping, the collected radiance data has to be corrected and transferred to reflectance values. The radiometric correction is done by a couple of means. An atmospheric correction known for satellite data is not needed as the image acquisition either occurs at low altitudes (UAV) or from a distance of a couple of 10s to 100s of meters (ground-based measurements). The atmospheric influence is therefore negligible, as it will be minimized

through empirical lining. The at-surface reflectance retrieval is usually performed by empirical line calibration. Empirical line methods use a single or a couple of spectrally homogeneous reference panels in the scene, whereas a dark current measurement is used to update the radiometric calibration coefficients (Boesche *et al.*, 2015; Rogass *et al.*, 2017). Another approach is to divide each pixel spectrum by an atmospheric correction spectrum derived from the scene by locating the pixel with the maximum absorption depth of water vapor (at 1126nm) (Rosa *et al.*, 2016; Lorenz *et al.*, 2018). This approach does not account for potential, multiple reflections that deepens the water vapor absorption and occurs in concave environments like open pits. Hence, it would overestimate the impact of the atmosphere on the measured signal. The geometrical fusion of VNIR and SWIR data cubes into a common Integrating the data into a 3D model requires the identification and matching of control points. Those can be picked manually (Kurz, Buckley and Howell, 2013) or automatically by scale invariant feature transform (SIFT) (Nieto, Monteiro and Viejo, 2010; Monteiro *et al.*, 2013). To retrieve a surface model, RGB imagery from a handheld camera and 3D reconstruction by Structure-from-Motion and Multi-View Stereo (SfM and MVS) are facilitated to create rapid 3D models from different image acquisition angles and positions (Kuras, 2017; Köllner *et al.*, 2019). The SfM technique utilizes SIFT as well and can be considered as the state-of-the-art approach for photogrammetric analyses and the computation of digital surface models. This was also deployed for the long-range by Salehi *et al.* (2018) and for the close-range by Kirsch *et al.* (2018). Micro-topography can influence the captured signal, especially for UAV imagery and unpredictable platform shifts (Jakob, Zimmermann and Gloaguen, 2017). Surface geometry is a prominent factor for geological applications. The change of illumination angles can distort the spectral appearance distinctly (Kirsch *et al.*, 2018). In order to correct the data, the research group around Richard Gloaguen attempt a topographic correction for UAV and long-range imagery in rough terrains (Kirsch *et al.*, 2018; Lorenz *et al.*, 2018; Salehi *et al.*, 2018). My experience shows that a topographic correction can be avoided for open-pit imagery by choosing optimal scanning conditions: evenly illuminated mine-faces, close-range sensor position (between 10-200m) and in case of changes in convex and concave mine face behavior to partition the mine face into smaller increments. Shadowed areas are not used for the analysis and cropped out. Lorenz *et al.* (2018) took similar consideration into account when scanning an open pit area at Corta Atalaya, Minas de Rio Tinto, Spain from a distance of 400-1100m and forfeited the topographic correction here as well.

4.3 Data dimensionality reduction

Before an EM extraction or spectral processing methods the spectral dimensionality of the data can be reduced. A reduction of spectral data complexity can be performed based on a de-correlation of the data by maximizing its variance, e.g. with a principal component analysis (PCA). Rodarmel and Shan (2002) for example, showed on HYDICE and AVIRIS data that including only the first 10% of PCA bands still achieves a correct classification rate of about 70% and reducing the PCA bands to the first 50% reaches up to 90% correct classification results.

The data dimensionality can also be reduced based on user defined constraints. The user can choose to exclude bands and wavelength ranges that are not of interest (e.g. exclude complete wavelength ranges due to influencing atmospheric features), clip the data to a shorter wavelength range or to increase the bandwidth of different bands and thereby reducing the band number that is needed to cover the spectral range of interest. A decrease of band number can decrease the noise in the data and the data size and increase the computation time for succeeding processing steps, e.g. the data analysis. Section 5.3 (pp. 122 - 128) shows a successive downsampling of the Brazilian iron ore dataset and how the subsequent analysis results and computation times change with decreasing data dimensionality.

4.4 EM extraction and spectral libraries

In order to settle for an approach to find the right spectral libraries for EM based classification approaches, four different spectral EM libraries were compared.

Visual EM selection based on known sample homogeneity

In case of laboratory-based scans of known sample of homogeneous geochemical parameters, spectral EMs of each sample were extracted in a 5x5 pixel average window. Some of the samples show inhomogeneous regions (different grain sizes, colors of grains compared to the sample average, different materials), here the 5x5 pixel average window was deliberately chosen to incorporate the visual variance in the material, as the geochemical analysis provided was based on bulk material analysis. In order to correlate geochemical and spectral material properties, the spectrum characteristic for each sample has incorporate small-scale mixed materials in the overall sample-scale homogeneous context. The spectral library based one spectrum for each sample can be seen in Figure 47.

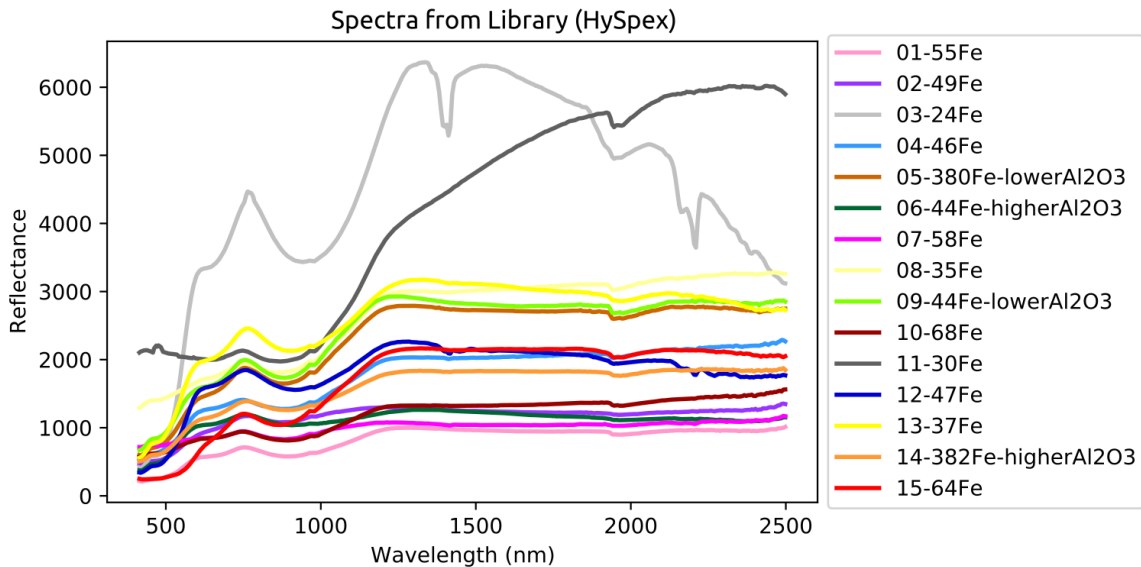


Figure 47 Spectral library based on visual spectrum extraction over a 5x5 pixel average.

Spectral library reduction based on geochemical clusters

Field sampling tends to be biased based on the experience of the sampling person, the time frame in which sampling can take place, the visual understanding and typically prone to oversampling distinct looking lithologies (colorful) and undersampling host rock lithologies that tend to look very similar to each other. Therefore, the samples taken might not represent the actual number of EMs in the sampled area. Geochemical analysis of the samples can additionally reveal that geochemically very similar lithologies have been sample multiple times and thereby several samples represent the same EM. In order to reduce the number of spectral library entries to the number of geochemically distinct EMs, the geochemical results of the samples were clustered hierarchically based on their element and oxide mass fractions. The result of this reduction is based on the geochemical analysis of each sample group (Iron ore samples: p. 57, Apliki mine samples: p. 58,). The geochemical analysis, results and the individual clustering and subsequent EM choice is explained in more detail in the respective sample sections (Iron ore samples: p. 98, Apliki mine samples: p.136, Skouriotissa Three Hills samples: p.162)

Sequential Maximum Angle Convex Cone (SMACC)

The **Sequential Maximum Angle Convex Cone (SMACC)** algorithm initiates with the brightest EM and sequentially and iteratively selects as next EM the spectrally most extreme compared to the current EM set. It is based on the assumption of a linear mixing of EMs and a convex cone that spans the spectral variety as vectors. EMs are identified if they exhibit the largest angle towards the existing

cone. SMACC terminates when the number of permitted EMs is reached or the selected pixel EMs present the greatest spectral angles (Sykas, 2020).

Pixel Purity Index (PPI)

The **Pixel Purity Index (PPI)** is a supervised EM extraction algorithm. It starts with a noise-whitening and dimensionality reduction by MNF transform and then creates a large number of randomly oriented test vectors anchored at the origin of the MNF-transformed coordinate space. The spectral points are projected onto the vector and minimum and maximum projected values are flagged as extreme. After multiple projections the algorithm tallies the number of times a pixel is flagged “extreme” and the pixels above a threshold are defined as EMs. This can also be achieved randomly (R-PPI) (Sykas, 2020).

4.5 Spectral Processing

The spectral analysis or spectral mapping refers to extracting qualitative and/ or quantitative information from remotely sensed data based on albedo or wavelength-dependent properties of materials (Mustard and Sunshine, 1999). Included here are most of the techniques proposed for detection, classification, discrimination, identification, characterization and quantification of materials. These methods can be categorized e.g. by their date of emergence (conventional vs. advanced), their presumed randomness, the data type they are applied to (multi- or hyperspectral), the way the pixels are treated (hard, per-pixel and soft, sub-pixel classifiers), the need for training data. A review of the spectral processing methods for geological remote sensing given by Asadzadeh and de Souza Filho (2016) aims to categorize the well-known methods into knowledge-based and data-driven approaches and this categorization is followed here. Their spectral processing methods review is shown in a taxonomic tree (Figure 48) which in conjunction with categorization and taxonomic tree is taken up for the here-discussed methods. Aside the categorization approach by Asadzadeh and de Souza Filho (2016), this introduction to spectral processing methods is also based on the reviews by Audebert et al. (2019) on deep learning for geological hyperspectral classification and Rajan Girija and Mayappan (2019) on the mapping mineralogical and lithological units. Continuum removal and absorption feature detection prior to the analysis is inherent to many of the presented methods.

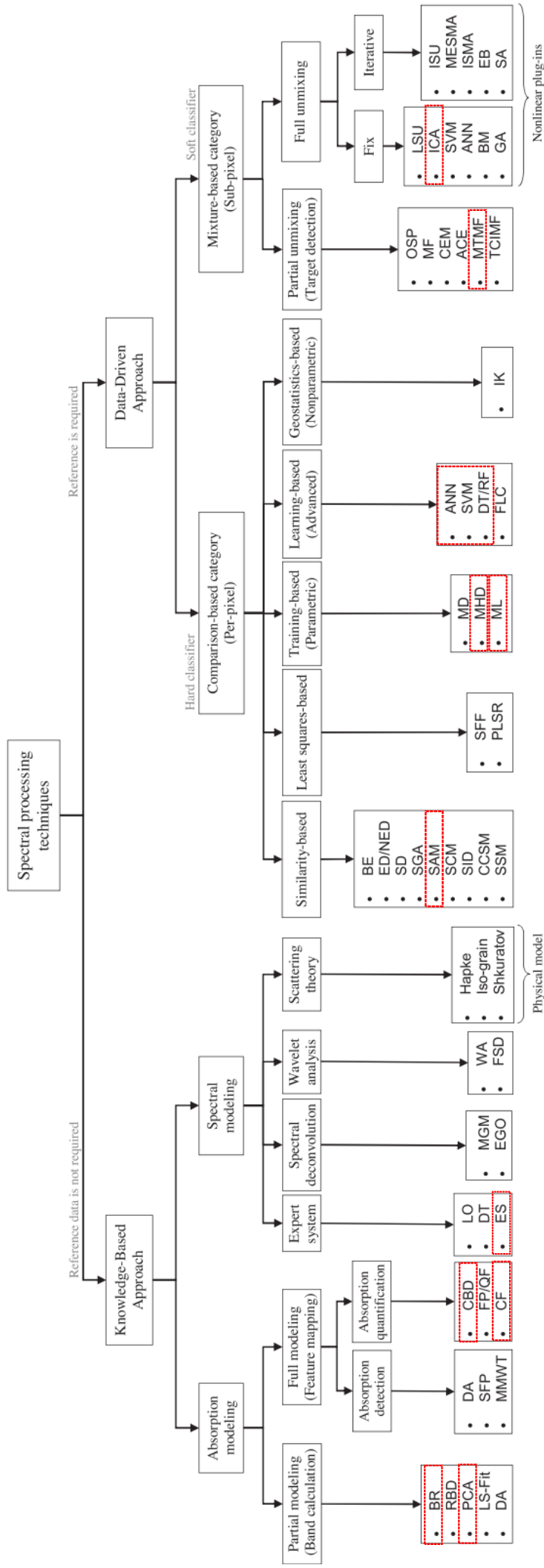


Figure 48 Taxonomic tree describing spectral processing methods as described in Asadzadeh and de Souza Filho (2016). Highlighted in red, dashed lines are the methods used for comparison in this work.

The acronyms used in the tree are: BR: band ratio, RBD: relative absorption band- depth, PCA: principal component analysis, LS-fit: least-square fitting, DA: derivative analysis, SFP: spectral fingerprints, MMWT: maximum modulus wavelet transform, CBD: continuum band-depth, FP: fitted polynomial, QF: quadratic fitting, CF: curve fitting, LO: logical operator, DT: decision tree, ES: expert systems, MGM: modified Gaussian optimization, WA: wavelet analysis, FSD: Fourier self-deconvolution, Hapke: Hapke (bidirectional) scattering theory, Iso-grain: Iso-grain scattering theory, Shkuratov: Shkuratov scattering theory, BE: binary encoding, ED: Euclidean distance, NED: normalized Euclidean distance, SD: spectral distance, SGA: spectral gradient angle, SAM: spectral angle mapper, SCM: spectral correlation mapper, SID: spectral information divergence, CCSM: cross-correlogram spectral match, SSM: spectral similarity mapper, SFF: spectral feature fitting, PLSR: partial least square regression, MD: minimum distance, MHD: Mahalanobis distance ML: maximum likelihood, ANN: artificial neural network, SVM: support vector machines, DT: decision tree, RF: random forests, FLC: fuzzy logic classifier, OSP: orthogonal subspace projection, MF: matched filtering, CEM: constrained energy minimization, ACE: adaptive coherence estimator, MTMF: mixture tuned matched filtering, TCIMF: target-constrained interference-minimized filter, LSU: linear spectral unmixing, ICA: independent component analysis, SVM: support vector machines, ANN: artificial neural network, BM: Bayesian model, GA: genetic algorithm, ISU: iterative spectral unmixing, MESMA: multiple EM spectral mixture analysis, ISMA: iterative spectral mixture analysis, EB: EM bundles, SA: simulated annealing. Figure from (Asadzadeh and de Souza Filho, 2016).

4.5.1 Continuum removal (CR)

The continuum is the background absorption of the material on which finer absorption bands of interest are superimposed. It is thought to be the signal of non-selective multiple scattering due to matrix effects, Fresnel reflectance and spectrally inactive materials (Asadzadeh and de Souza Filho, 2016). The continuum is also influenced by physical (e.g., particle size, texture, surface roughness) and chemical properties and illumination conditions. Most commonly, a convex hull is fitted over the top of the spectrum, linking all reflectance maxima with straight lines and bridging all absorption features. When the original spectrum is divided or subtracted by this continuum, the continuum-removed spectrum highlights the absorption features (Asadzadeh and de Souza Filho, 2016). Four different continuum removals are compared, three of them based on the creation of a convex hull and the last one on a novel approach of a geometric hull.

4.5.1.1 Convex Hull

In the ENVI software (harrisgeospatial.com/docs/using_envi_Home.html, 2020), the standard CR is performed by creating a convex hull over the top of the spectrum by straight-line segments of a Delaunay triangulation and by interpolation between maxima. The spectrum is then divided by the continuum for each pixel, the resulting image is equal to 1 in regions where the actual spectrum and the continuum curve match and below 1 for regions where absorption features occur. The CR of the HypPy hyperspectral python toolbox by Wim Bakker (Bakker, 2018; Bakker and Oosthoek, 2020) offers the CR by creating a convex hull as in ENVI, based on a modified Quickhull approach, followed by either subtraction or division of the continuum curve. Only in case of true reflectance data (scaled from 0 to 1) subtraction is actually an option. A division of the convex hull without cut off wavelengths was utilized to perform the CR here. The open source PySptools hyperspectral python toolbox by Cristian Therien (Therien, 2020) also uses a convex hull removal based on (Clark and Roush, 1984) and removes the convex-hull of the signal by hull quotient.

Mielke et al. (2015) proposed a new approach for a convex hull calculation and continuum removal, the so-called “geometric hull”. The novel approach was tested against state-of-the-art approaches like convex hull, scale-space filtering and alpha shapes and the CR and feature extraction was tested on a the USGS digital spectral library (Clark *et al.*, 2007). The geometric hull is defined by convolving the input spectrum twice with a 2% and 10% boxcar filter each. For each filter a pair of Gaussian distributions is estimated and the largest standard deviation of the difference between the Gaussians is taken as an indicator to find the correct length of the boxcar filter. This ensures the correct identification of absorption features. The smoothed spectra are divided and show the absorption minima of potential features. These minima are taken as nodes to construct a lower hull by linear

interpolation between them. This lower hull is subtracted from the input spectrum to set the preliminary minima to zero. In each non-zero segment, the maximum is found and listed as potential nodes for the upper continuum hull, which is constructed by linear interpolation between these maximum nodes. The points of the upper hull are now subtracted from the input spectrum to check for interference between the two-point sets (re-crossing points). This process is iterated through new emerging maximum nodes until the final geometric hull can be constructed from the final maximum node list. Either subtraction or division of the input spectrum and the continuum hull accomplishes the CR. As for the HypPy CR, division is advised for non-true reflectance data. Mielke et al. (2015) compares the feature extraction quality from the different continuum definition techniques to the expert defined absorption features in the USGS Material Identification and Characterization Algorithm MICA (508 features for 213 spectra) of the USGS spectral library (Clark *et al.*, 2007; Kokaly, 2011).

4.5.1.2 Geometric Hull

Mielke et al. (2015) compares the following features: the position of the absorption maximum, the area of the absorption feature, the overlap between the defined feature shoulder regions, the maximum absorption depth, the albedo difference (height of continuum over absorption maximum) and the slope of the continuum line over the feature and the computational time. The geometric hull algorithm performs best for 5 of the 7 categories. It is outperformed in the computational time by the convex hull algorithm only but performs least of all for the median depth difference of the found absorption features. Here too, the convex hull approach performs best of all. The low performance of the depth characterization of the feature is based on the shape of large absorption features. They often exhibit small convex sections that cause the geometric hull approach to split one large feature into two smaller features. Other than the convex hull approach, the geometric hull is instead able to detect absorption features in an overall concave trend in the spectrum. Especially for the large iron absorptions in the VNIR the geometric hull underperforms and should be used with caution as a preprocessing step. It is advisable to use the ordinary convex hull approach in this case.

4.5.1.3 Continuum Removal in this work

The here used routines rely on a convex hull removal for feature extraction. For laboratory conditions this means, detecting all spectral features, even those of mineral bound water around 1440nm and 1900nm, which makes sense if only laboratory conditions are expected. If classification algorithms tested for the laboratory are supposed to be transferrable to field conditions this will provide trouble. Concave trends in the spectrum are treated as features by the convex hull and the features around 1400nm and 1900nm are taken into account even though field conditions do not allow for utilizing this wavelength range due to strong water band influence (Mielke *et al.*, 2015). When utilizing the convex

hull in field conditions, the wavelength range of the atmospheric water bands has to be masked completely. Otherwise, the geometric hull retrieval for field conditions is advisable, even though it tends to split the large iron feature around 900nm into two smaller features and thereby does not allow for feature depth and width analyses here. A comparison of all above-described continuum removal methods is shown in Figure 49 for two different spectra from the Brazilian Iron Ore dataset. The continuum removal based on convex hull is shown for the ENVI software (green spectrum), the HypPy toolbox (blue) and the PySp toolbox (red). Additionally, the geometric hull continuum retrieved spectrum is shown in yellow.

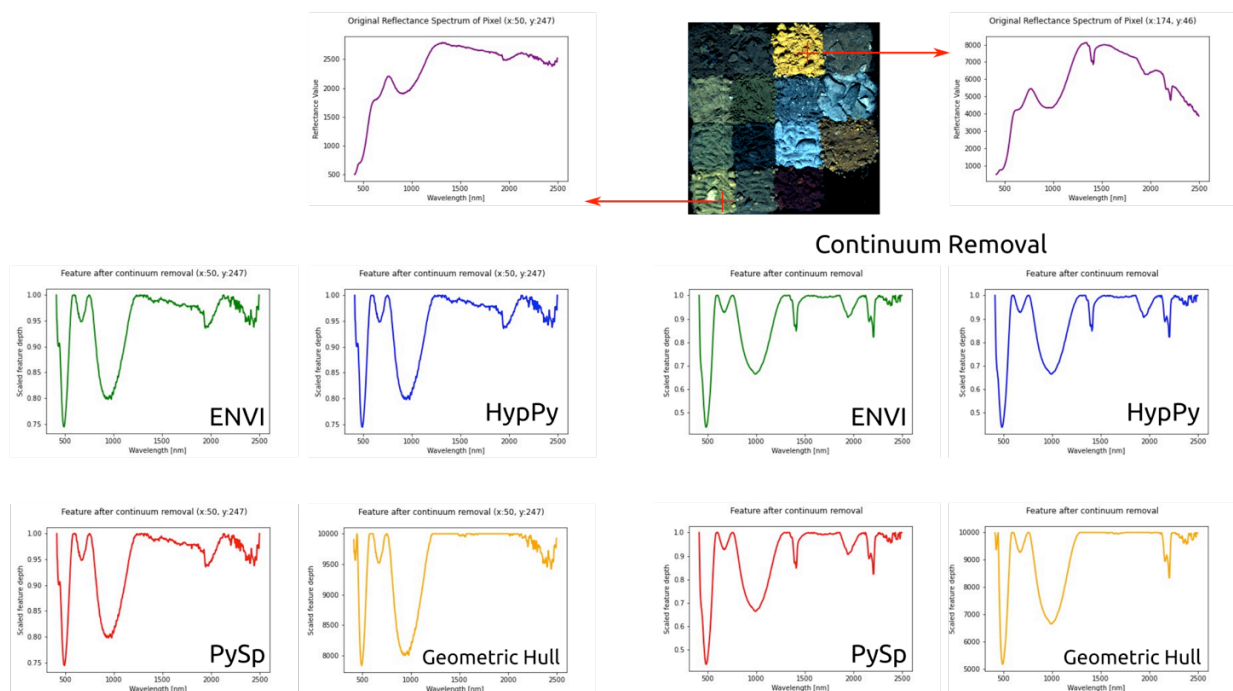


Figure 49 Continuum Removal for two spectra of the Brazil dataset. Showing the spectrum of sample 3 (Right) and sample 13 (Left) of the Brazilian Iron Ore samples. Both samples are marked by red arrows in the RGB image of the Brazil sample set. The regular spectrum is shown on the top (in purple) and the continuum removed spectrum is shown below. For both samples, the continuum was removed by the methods accessible via the ENVI- (green), HypPy- (blue) and PySp toolbox (red). ENVI, HypPy and PySp rely on the convex hull algorithm. The Geometric hull retrieval by Mielke et al. (2015) is also shown (yellow) and noted as “Geometric Hull”. The axes of the small graphs depict the wavelength (400 – 2500nm, x-axis) and the scaled feature depth (0-1 for convex hull, 0-10,000 for Geometric Hull, y-axis).

4.5.1.4 Absorption feature detection

A common method is to identify the local spectral minima in the continuum-removed spectrum. This can be done manually or automatically. (Mielke *et al.*, 2015) proposed a method for a new continuum removal and subsequent automatic feature retrieval. Finding and identifying the absorption features of a spectrum are often preliminary to subsequent analysis methods. Absorption modeling is achieved

by *partial modeling* techniques that focus on band calculations or by *full modeling* that map the whole feature.

4.5.2 Spectral processing methods

4.5.2.1 *I: Knowledge-based approach*

The knowledge-based approach relies on the knowledge of the expected spectral behavior of a desired target. It is based on distinct characteristics of absorption features (position, depth, asymmetry, width) (Asadzadeh and de Souza Filho, 2016). Three basic components describe a spectrum: 1) a continuum, 2) absorption bands and 3) residuals or noise. Asadzadeh et al. (2016) argue, that all knowledge-based approaches aim to estimate the quality or quantity of one or more of these components interactively or automatically. This is done in manner that concentrates either on “absorption modeling” or on a “spectral modeling”, including only parts of the spectrum or the full spectrum to the analysis respectively.

4.5.2.2 *Absorption modeling – Band ratio, PCA and feature modeling*

Band calculation is the most common image processing method and provides a shape or grade of an absorption feature by using band math operations. As it only uses parts of the spectrum, it belongs to the “**partial modeling**” type of the available spectral analyses. **Band ratio** can use the difference in reflectance between an absorption feature band and one of its shoulders – in order to use published and proven band ratios for my hyperspectral test image of iron ore related samples, the data was resampled to the super-spectral resolution of World-View-3 (16 bands) to show an example of band ratios from the Index DataBase (Henrich *et al.*, 2012; indexdatabase.de/, 2020) for ferrous iron (Fe^{2+}) in comparison with the geochemical data delivered with the samples.

Principal component analysis (PCA) uses spectral gradients in a more statistical manner. Images in the VNIR and SWIR range usually do not show sharp features such as the common Raman spectroscopy with its distinct absorption peaks. Due to the presence of rather wide absorption features, most features at different wavelength are highly correlated (Eisele, 2014). Due to that, dimensionality reductions can be performed.

The PCA is based on the mathematical principal of eigenvalue decomposition (Rodarmel and Shan, 2002). In the PCA, the highly dimensional data is reduced to few latent variables. This is achieved by transforming the X variable (the set of spectra) into an equivalent set X' by a linear transformation using an Eigenvalue decomposition. After that, all the new “spectra” or principal components are linearly independent. The PCA minimizes the covariance between the different rows of X', it processes

the spectral data only. The PCA bands are sorted by descending Eigenvalues representing their descending contrast/ variance and it aims to maximize the variance of the data as the data will be decorrelated. The first band shows the highest variance and the last band the lowest possible variance. The first few bands often contain the majority of the information whereas the last bands include a lot of the noise. Using PCA data for subsequent classification allows for a decrease of number of bands whilst also decreasing the noise and thus speeding up the processing time. PCA has been confined mostly to multispectral imagery as it relies on empirically chosen input bands and it is difficult to relate the PCs to specific image features or geological components. Nevertheless, PCA has drawbacks; a relevant one is the inability to reproduce the results.

Feature mapping or full modeling

Feature mapping aims to characterize an absorption feature by attributes like its wavelength position, depth, width or symmetry. Continuum-removed data and absorption feature detection have to typically take place before feature mapping methods can be used.

Spectral feature characteristics (wavelength position, shape and asymmetry) correlate to the mineralogical content of the material. The wavelength position corresponds to the geochemical composition whereas the depth of the feature is related to the abundance of the compound.

Minimum Wavelength Mapping (MWL): Wavelength position and feature depth mapping is often used to map specific mineral assemblages. It is using the **minimum wavelength position and feature depth** to calculate ratios of specific absorption features. Wavelength position maps were first present in context of mapping the Martian surface (Van Ruitenbeek *et al.*, 2014). Here, the position was calculated over the wavelength ranges of 1350–1500nm, 1700–2100nm and 2100–2400nm. Especially for hydrothermal deposits, the mapping of white mica composition, white mica crystallinity and chlorite composition has become a tool to determine mica formation and phyllic or argillic type hydrothermal alteration. For white mica composition the minimum of the feature between 2185nm and 2225nm is mapped (Dalm *et al.*, 2014; Corescan, 2016; Dalm, Buxton and van Ruitenbeek, 2017; Lorenz *et al.*, 2018). The minimum wavelength position for features in the SWIR range of approximately 2190nm to 2390nm is also used to map the likelihood of occurrence of clay, jarosite and carbonate (Krupnik and Khan, 2019). The **minimum wavelength (MWL)** of a spectral feature can act as a proxy of material geochemistry and for certain wavelength ranges it provides information of element substitutions within a mineral between the different EMs.

The wavelength minimum position and depth can be detected by using the HypPy toolbox (Bakker and Oosthoek, 2020). Here, the absorption wavelength at the maximum depth of the absorption feature is

located in a-priori defined wavelength range after continuum removal took place. The depth of the found diagnostic feature can also be calculated in HypPy and is correlated with the abundance. This **continuum band-depth (CBD)** method has a few drawbacks (e.g. depth is proportional to particle size and amount of opaque material, intimate mixing can lead to nonlinear behavior, absorption bands can overlap) but is still the most accepted spectroscopic method for semi-quantification (Asadzadeh and de Souza Filho, 2016).

4.5.2.3 *II: Data-driven approach*

The data-driven approach is based only on the hyperspectral data itself and possibly additional reference data. This reference data is called “training data” or EM sets. These can be derived directly from the image, can be imported in form of generic spectral libraries, such as by (Kokaly *et al.*, 2017; Meerdink *et al.*, 2019) or from ground based in-situ measurements of known areas (Shippert, 2003). Data-driven approaches can be further subdivided into “per pixel” and “sub-pixel” categories (Asadzadeh and de Souza Filho, 2016). The use of spectral libraries and EM extraction methods for this work is explained in Section 4.4 (p. 77).

Per-pixel/ hard classifiers – similarity metric and least-squares estimations

The per-pixel category is also called “hard classifier” as it compares each image pixel with the reference data and assigns one label to the pixel, based on a similarity metric, image statistics or least-square estimations. The most commonly used whole pixel analysis methods for hyperspectral data provided by ENVI are the Spectral Angle Mapper “SAM” (Yuhas, Goetz and Boardman, 1992) and the Spectral Feature Fitting “SFF”. Another least-squares approach, additional to the SFF, is the principle least-squares regression (PLSR). Also part of the classifiers are the training based approaches (Gaussian maximum likelihood and Mahalanobis distance classification) and learning based approaches (support vector machines, random forest classifications and artificial neural networks).

The Spectral Angle Mapper (SAM) is a **similarity-based approach** and was developed by J.W. Boardman as part of the Spectral Image Processing System “SIPS” (Kruse *et al.*, 1992, 1993, 2008; Yuhas, Goetz and Boardman, 1992). SAM, as part of this tool, plots a scatter plot of the pixel values of the bands of a spectral image. In this plot, the pixel spectra vs. the target spectra as points, SAM computes the angle between the vectors going through each of these points. A smaller angle between pixel spectrum and reference spectrum shows a higher similarity. The spectral angle is relatively insensitive to changes in pixel illumination, as the vector direction stays the same only the magnitude is changed by illumination differences (Schneider *et al.*, 2011). The core algorithm of SAM is basically a correlator.

The Binary Feature Fitting or Bi-Triangleside Feature Fitting (BFF) algorithm was developed in 2020 and will be published in more detail (Mielke *et al.*, 2020, in prep.). It aims to bridge the gap between expert system mapping in the hyperspectral domain and multispectral mapping approaches. The BFF algorithm constructs characteristic features from non-continuous spectral data. The overall shape of the spectrum is preserved and characteristic features and spatial relationships between neighboring points are taken into account. The triangulation between three consecutive measurement points establishes feature parameters for the identified triangle. With increasing wavelength, for each new spectral measurement point and the last two points a triangle is established and parameterized. This allows the BFF algorithm to handle the spectral measurements according to their shape parameters instead of pure point data. The spectral reference library is resampled to the image characteristics (spectral resolution) for a subsequent correlation of the shape parameters of the unknown (imagery) with the known (library) spectra. Here, the correlation values are presented in a matrix, denominating the best, second-best, third-best etc. spectral correlation/fit for each pixel. For the library spectra that pass a user-defined threshold after the correlation a bound value least squares (bvls) unmixing the pixel feature data is calculated. The best, second-best, third-best, etc. spectral unmixing results are again presented within a data cube. Hard-classifier maps can be produced depicting only e.g., the best spectral fit or the best spectral unmixing results. Quality maps support the results and are compiled by summarizing the reflectance data and the triangle areas for each data point. The resulting panchromatic images represent the changing albedo within an image. High reflectance/ albedo is represented by bright pixels in the panchromatic image. For the sum of the triangles, pixel without significant features will not yield a high sum of their triangle areas and are represented in dark colors. Multiplying the yields can combine both measures. The resulting grey-scale image identifies areas with low spectral contrast and thereby high possible material identification errors. The strength of this method is the depiction of second- and third-best results as well as the best-fit results. This holds especially true for satellite imagery in which the area depicted within one pixel is prone to represent a mixed spectral signal. The same is however applicable for any natural surface, each is likely to be represented by the mineral assemblages rather than spectrally pure minerals. In order to observe spatial and spectral changes within a geological surface not only the dominant mineral or material is of importance but the change of minerals within the assemblage due to different conditions whilst the surface formation but also processes active post-formation. Another advantage is the theoretical indifference towards changes in illumination as the shape of the spectrum that is depicted by the triangles is only dependent on the relationship of the triangles towards each other to extract useful features.

Spectral Feature Fitting (SFF) belongs to the **least squares-based group** based on Asadzadeh and de Souza Filho (2016) categorization. It examines specific absorption features in the spectrum and compares depth and shape of those features for the test spectrum (y , pixel) and the reference spectrum (x). It uses **linear least square regression** to find the fit between x and y . It can incorporate single or multiple features that can be set individually by the user, for example as part of the SFF tool in the ENVI image analysis software (Clark, Swayze and Gallagher, 1992; Clark, 1995; Shippert, 2003). As the SFF uses the continuum removal procedure and the user knowledge of the features for the regression, it can be categorized as a hybrid method of the knowledge- and data-driven approach. The SFF is presented in a more sophisticated version as the Tetracorder later on (Clark, 2003) and an automated version of the SFF is presented with the EnGeoMap 2.0 (Mielke *et al.*, 2016).

The **Principal Least Squares Regression (PLSR)** inherits features from the PCA analysis and multiple regression and finds a linear regression model to concentrate information from the spectrum in a few optimized variables (Asadzadeh and de Souza Filho, 2016). In other words, it ignores the redundant information in the data whilst simultaneously highlighting the significant spectral information for the variable of interest. It is based on two matrices – the spectral bands (X -variable, independent variables, the spectra) and the y -variable or the Response-Variable. As for the PCA, the PLSR reduces the data to a few latent components, which are sorted with descending variances. In contrast to the PCA though, the PLSR maximizes the co-variance between X and y (Eisele, 2014). PLSR takes into account not only the spectra (X') but also the response values. PLSR is mostly used to relate spectra-inherent information to non-spectral variables. PLSR was considered for this work but the number of samples for which geochemical analyses were present was not sufficient for a PLSR analysis.

The **k-Means unsupervised clustering** iteratively generates clusters. The k-Means algorithm tries to separate samples into k groups of equal variance by minimizing the within-cluster sum-of-squares or inertia (Pedregosa *et al.*, 2011). Inertia is a measurement of the internal coherence of a cluster that offers several drawbacks. It assumes convex and isotropic clusters, which is the case for spatially coherent samples in the laboratory but not for field conditions. Elongated, irregular shaped areas cannot be differentiated well. Inertia is not normalized, in very high dimensional spaces the Euclidean distances tend to become inflated, to alleviate the problem a dimensionality reduction (e.g. PCA) can be used on the data before clustering (Pedregosa *et al.*, 2011). The desired number of clusters to generate (k) has to be provided. The algorithm begins with an initial set of cluster centers before each pixel is assigned to the nearest cluster center, the cluster centers is then recomputed as the centroid

of all pixels assigned to a cluster, this is done iteratively until the specified maximum number of iterations is achieved (spectralpython.net/, 2020).

Training-based classifiers aim to cluster the imagery by comparing the test spectrum with the training classes. This comparison is done by statistical criteria. Here the **Gaussian maximum likelihood (GML) classifier and the Mahalanobis distance (MHD) classifier** were tested on our HSI dataset. The GML uses the mean and covariance matrices of the clusters to calculate a probability distance whereas the MHD is direction sensitive but assumes equal covariance for all classes. Both of these were tested, using the Spectral Python Toolbox (spectralpython.net/, 2020).

Learning-based approaches showed considerable advantages over training-based methods. **Artificial neural networks** are able to learn the relationship between a set of example patterns, to generalize those, combine the results and then apply them to new input patterns (Asadzadeh and de Souza Filho, 2016). ANN attempt to model the biological nervous system to recognize patterns. The basic architecture is made up of a network of primitive functions able to receive multiple weighted inputs. These inputs are evaluated for their ability to discriminate classes. In the training phase, the class weights are adjusted if the separation of inputs and predefined classes results in an error. This proceeds until the iterations reach a decay threshold of yielded error (Cracknell and Reading, 2014). A review on Convolutional Neural Networks (CNN) and geological HSI applications is provided by (Audebert, Le Saux and Lefevre, 2019) along with the Python toolbox DeepHyperX (Audebert, Le Saux and Lefevre, 2019; Audebert, 2020) to perform deep learning experiments.

Choosing the right approach based on the data should consider the following criteria (Audebert, Le Saux and Lefevre, 2019):

- Is the data spatially correlated? This might be the case for large over flights of man-made structures or expected large-scale geological structure and would also be the case for small-scale (laboratory) based sample scan data. In the case of outcrop data, surface alteration and disturbance does not exhibit a high spatial correlation and the material distribution at the surface is based on mechanical, physical chemical processes that tend to happen simultaneously. Each process might happen in a spatial context (oxidation of iron at the surfaces of high water run off) but influence each other and thereby do not exhibit clear spatial correlation.
- What is the number of training samples? A higher number of training samples is required for bigger models with more parameters to optimize. Raczko and Zagajewski (2017) produced acceptable results with solely 76 training pixels per class but other studies recommend at least

400 pixels per class (Kavzoglu and Mather, 2003). Most supervised classifiers are sensitive to the data used for training, in order to avoid bias due to odd sample numbers, the different classes to be represented by roughly the same number of pixels (Raczko and Zagajewski, 2017).

- What is the size of the convolutional kernel? Large 3D kernels tend to be slower and most implementations are optimized for 2D kernels.
- What type of activation function should be used? Non-saturating activation functions help to build deeper networks and compute faster than sigmoidal or other activation function alternatives.
- What choice of input data is used? An optimal band number has to be chosen to represent the variety in the training data. In order for the ANN to work relatively fast and produce robust results the number of input bands can be reduced via dimensionality reduction (Raczko and Zagajewski, 2017).

DeepHyperX uses well-defined train/test splits where samples are extracted from significantly disjointed parts of the image, this is necessary as in hyperspectral data the neighboring pixels are highly correlated which would make a randomly sampled training set very close to a randomly sampled test set (Audebert, Le Saux and Lefevre, 2019). Comparing the different approaches, the 1D base line NN (4 fully connected layers with dropout) from DeepHyperX, the 1D CNN by Hu et al. (2015) and the 3D CNN from Li et al. (2017) yield the best results depending on the HSI dataset.

A common non-parametric approach is the use of **support vector machines (SVM)**. It is based on constructing a hyperplane within an n-dimensional feature space by utilizing the training samples. The margin between the hyperplane and the closest training samples, known as support vectors, is iteratively optimized by a structural risk minimization (Asadzadeh and de Souza Filho, 2016). The maximum margin M (distance) between the support vectors is the indicator to find the optimal decision boundary. In order to work with non-linearly separable classes, the input variables are transformed using a kernel function. An appropriate kernel function and sigma (kernel width) is required to optimize performance (Cracknell and Reading, 2014). For mapping, the linear SVM from the scikit-learn library (Pedregosa *et al.*, 2011) integrated in the DeepHyperX (Audebert, 2020) toolbox was used.

Another non-parametric technique is the decision tree (DT), and a variant of it **the random forest (RF)** (Breiman, 2001). RF is a logic-based learner, and has shown to be superior to ANN and SVM (Cracknell and Reading, 2014). RF randomly subsets a predefined number of variables to split each decision tree

and thus grows multiple trees. Training data for each tree is generated by bagging - by sampling with replacement a number of samples equal to the number of samples in the source data (Cracknell and Reading, 2014). To compare child node class heterogeneity to the parent node the Gini index is used, and determines the best split threshold of input values for the given classes. Cracknell and Reading (2014) found RF performed well in aspects like stability, ease of use, processing time and prediction accuracy, on top of that RF showed to be relatively insensitive to variations in parameter values and are thereby not likely to over fit. The study also highlights the need of 10-25% of training data, but no additional accuracy of classification above 25% of training samples from the total number of samples, which would come at higher computational cost.

Sub-pixel/ soft classifiers – partial and full unmixing

The sub-pixel or soft classifier category allows multiple labels per pixel and finds mixed pixel contents by partial or full unmixing (Asadzadeh and de Souza Filho, 2016). When the aim is to isolate specific spectral features from the background instead of deciphering the whole spectrum and finding all possible EMs, the detection of spectral signals can be reduced to match the known target. This is categorized as partial unmixing. **Mixture tuned matched filtering (MTMF)** is a common target detection algorithm. It is an enhancement of the **matched filtering (MF)** that maximizes the response of the target signature and minimizes the response of the background by a likelihood ratio. MTMF includes an infeasibility image for each target signature. The dominant material in the pixel is determined by using a high MF and a low infeasibility score (Asadzadeh and de Souza Filho, 2016). These scores are calculated for each EM in the spectral library.

Full unmixing aims at decomposing the pixel spectrum linearly or non-linearly into deterministic EM spectra and to estimate their abundances. Linear spectral unmixing takes place when the incoming light only interacts with one material of the checkerboard type macroscopic mixture surface. Multiple scattering between the incident light and the mixed materials in the scene results in nonlinear mixing. Spectral unmixing consists of three steps:

- 1) Finding the number and type of EMs that represent the entire scene variation,
- 2) Finding the best EM subset that accounts for the spectral variation within each pixel and
- 3) Estimating the abundance of each EM in the pixel

The type and number of EMs has a profound effect on the unmixing result and thereby is an active topic of research (Asadzadeh and de Souza Filho, 2016). A way to avoid data based EM extraction is a supervised in-situ sample and spectra collection which is viable in outcrop scanning and proximal scanning approaches and harder to suffice for in satellite and airborne HSI (Rivard *et al.*, 2009).

When the EMs are identified **linear spectral unmixing (LSU)** can take place. **Independent component analysis (ICA)** is only one example of this type of unmixing. ICA is a tool for blind source separation. The IC transformation is based on the assumption of non-Gaussian independent sources. Higher-order statistics are used to highlight features without prior information in the mixing for non-Gaussian hyperspectral data (harrisgeospatial.com/docs/using_envi_Home.html, 2020).

4.5.2.4 *Hybrid models – Tetracorder, MICA and EnGeoMap*

In general terms, the knowledge-based approach is simple, straightforward, easily attributable to mineralogical needs and transferable in different scales but comes with the disadvantages that it does not account for spectral mixing of absorption features. The data-driven approach is more mature and robust but also more complicated, needs more computational power, a high variety, labeled reference data set to initially train the algorithm and is thereby more time consuming (Asadzadeh and de Souza Filho, 2016). This result calls for a hybrid form of models to 1) incorporate spectroscopy knowledge and mixing models and to 2) include geological knowledge with mixture theory. Sophisticated versions of this are **USGS Tetracorder**, its modified version the **material identification and characterization algorithm (MICA)** and the **EnGeoMap Algorithm** with a new convex hull approach (Clark, 2003a; Kokaly, 2011; Rogass *et al.*, 2013; Mielke *et al.*, 2015, 2016). Figure 50 compares the continuum hull and thereby the feature definition of the USGS expert system (lower figure) and the geometric hull (top figure) for the USGS library spectrum “siderite”. Mielke *et al.* (2015) shows that compared to expert feature definition, the proposed geometric hull technique outperformed the state-of-the-art-modified scale-space filtering, the scale-space alpha hull technique and a pure python standard convex hull algorithm, in that order. Without prior knowledge to the expected features, the geometric hull is closest to the expert defined spectral features. It does not however include SNR ratios to isolate characteristic absorption bands. As seen in Figure 50, the geometric hull includes several features that the USGS did not define. A disadvantage of the algorithm is the definition of a local maximum inside the broad iron absorption feature (around 1100nm) and thereby dividing it into two separate smaller features.

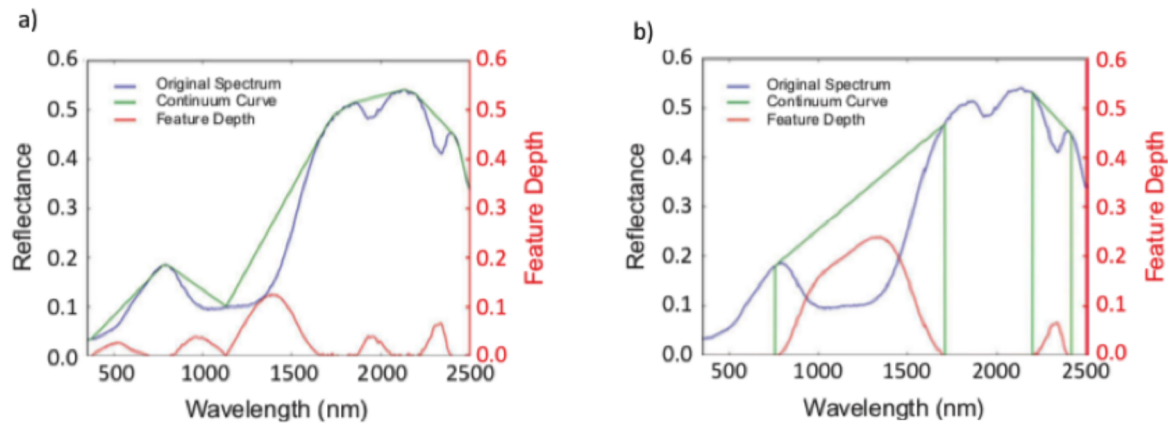


Figure 50 Results for the continuum removal algorithms for USGS spectral library entry "Siderite" in blue. The continuum definition is shown in green, based on the geometric hull by Mielke et al., 2015 (a) and based on the Tetracorder expert system by Clark et al., 2003 (b). The found feature and their depth are shown in red. From Mielke et al. (2015).

MICA is a part of the "Processing Routines in IDL for Spectroscopic Measurements (PRISM)" (Kokaly, 2011) and based on the USGS Tetracorder. The following explanation is based on Clark (2003) and Kokaly (2011). Figure 51 shows the basics of the MICA analysis from Koerting *et al.* (2015). The Tetracorder and MICA are based on expert system rules, implemented in a decision tree structure where multiple algorithms are applied for the material analysis. Applying additional expert rules and algorithms to the initial result can refine this analysis. The goodness of fit (R^2) and the band depth (D) are calculated for the continuum-removed image and the library spectra. The best fitting library spectrum is attached to the pixel after the results of an intelligent expert system decision making framework (Asadzadeh and de Souza Filho, 2016). The Tetracorder is verified by a combination of human verification of spectral analyses, field checking of results and laboratory analysis of collected samples. The analysis focuses on diagnostic absorption features in the spectrally "active" regions of a continuum removed spectrum only. This focus is based on the occurrence of nonlinear mixtures in nature like coatings, intimate mixtures or solutions that are not well distinguishable with simple matching algorithms alone. In order to rule out false identification of materials similar in the diagnostic wavelength regions, complementary spectral areas are taken into consideration. Additionally, to the defined and weighed diagnostic features for each material, spectral library entries also have defined (absolute and relative) "not-features" and the analysis allows a "no answer". In summary, the Tetracorder matches an unknown material with a known reference spectrum by comparing how well the diagnostic features match, the reflectance level, the continuum slope and the presence or absence of key ancillary spectral features. If a match is below a certain threshold, a no detection is assigned as the material sought is not present or the Signal-to-Noise ratio is too low to allow detection (Clark, 2003a).

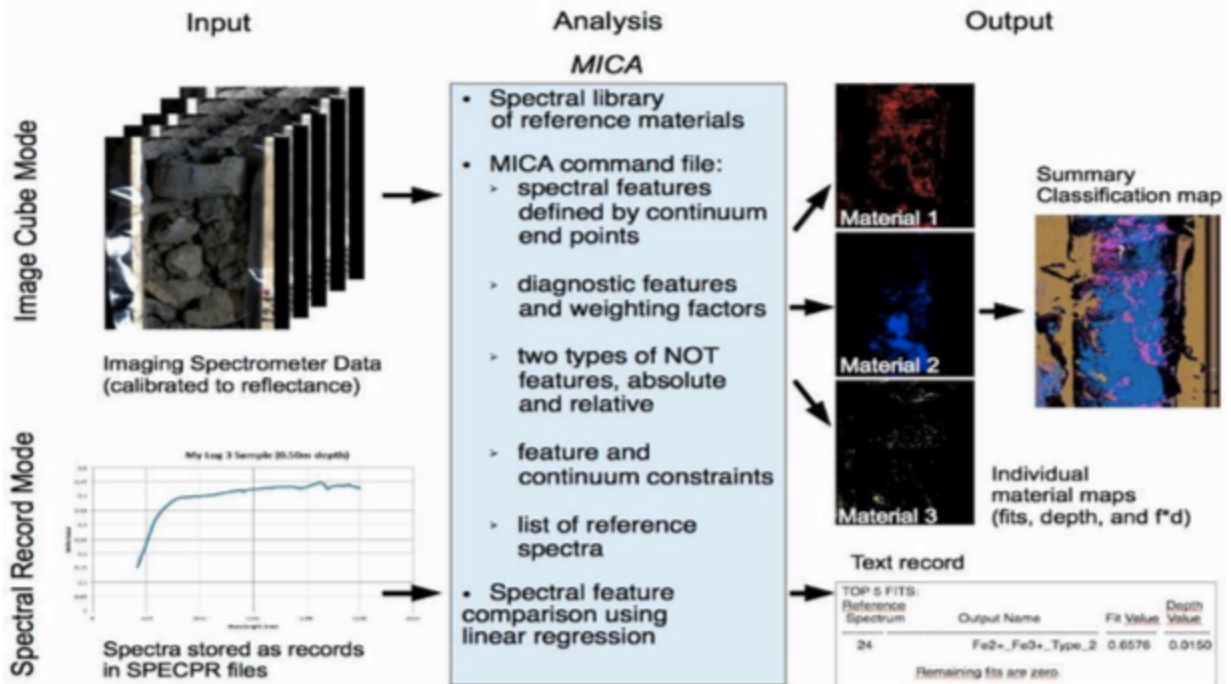


Figure 51 Processing chain and key elements of the MICA image analysis from Koerting et al. (2015) modified after Kokaly (2011). The spectrum shown schematically in the lower left plot reflectance between 0-100% on the y-axis and the wavelength between 450 - 2500nm on x-axis.

The EnGeoMap 2.0 algorithm from Mielke et al. (2016, 2018) is an automated material characterization system. It is based on the EnGeoMap 1.0, the Tetracorder and the MICA algorithm (Clark, 2003b; Kokaly, 2011; Rogass *et al.*, 2013). The EnGeoMap 1.0 algorithm is included in the EnMapBox (van der Linden *et al.*, 2015), now implemented in the QGIS module and available as freeware. It contains two sub-programs, the EnGeoMap-Base for basic mineral mapping and the EnGeoMap REE for rare earth mapping (Boesche, Mielke and Rogass, 2016). The base algorithm can map Al-OH, Ca-O and Fe-O containing minerals. User specific libraries can be imported and assigned to a user-defined color-coding. The difference compared to the Tetracorder and the MICA is the automated continuum removal and subsequent feature extraction. The “geometric hull” (Mielke *et al.*, 2015) retrieves absorption features according to the SNR without expert input, the features are weighed according to their shape and a linear spectral unmixing is performed. The results of the analysis are best-fit maps – based on the spectral shape matching and highest abundance maps based on the unmixing showing the material with the highest dominance in the spectrum. Additionally, spectro-spatial gradients are delivered in a data cube, assigning each pixel with all mapped spectra and their ranking. Figure 52 shows the processing chain of EnGeoMap Base, from Körting (2019).

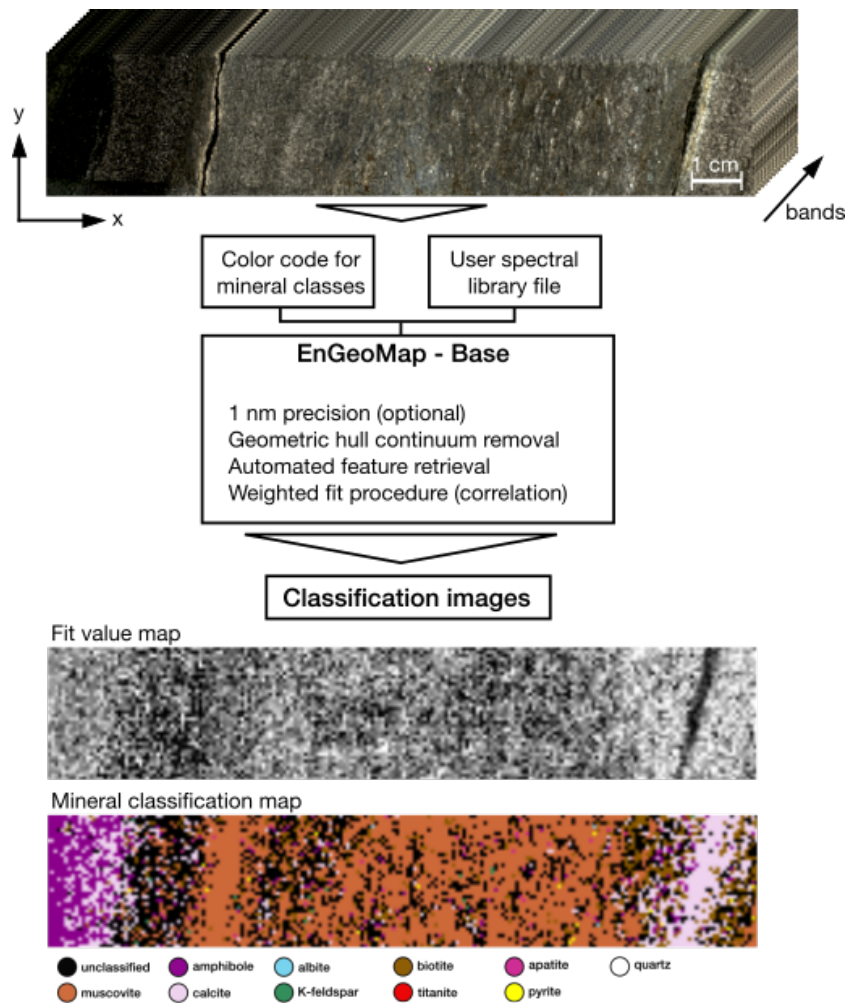


Figure 52 Simplified illustration of the EnGeoMap processing chain from Körting (2019) modified after Boesche et al. (2016).

Geological applications usually show predictable types of target minerals and mineral assemblages. This knowledge should be included in the process chain to allow for unmixing in a geological context. In order to account for this fact, for the samples of the Republic of Cyprus have been compiled into a spectral library to be used for the subsequent analysis of the hyperspectral outcrop scan (Koerting, Rogass, *et al.*, 2019). EnGeoMap offers a standard spectral library, but allows the user to use site-specific spectral libraries and color-coding of the classification results. EnGeoMap 2.1 from 2019 now includes the features derived by the lower geometric hull, additionally to the upper geometric hull (Mielke *et al.*, 2019).

5 Near-field Imaging Spectroscopy results

5.1 Overview of applied workflow

The workflow presented here is based on four successive steps of data preparation and analysis that were tested on three different imaging spectroscopy datasets. This workflow was then applied to a fourth and fifth dataset. The datasets have been described in the “Materials” chapter on pp. 32 – 74. Figure 53 shows the five different successively applied workflow parts that are explained from Section I – V. The identified best-performing approaches will be described in detail in the upcoming workflow parts I – III. The best-performing approaches and their successive implementation for the mine face data analysis is visualized in a conclusive workflow scheme for the HSI mine face data on Figure 106 p. 151.

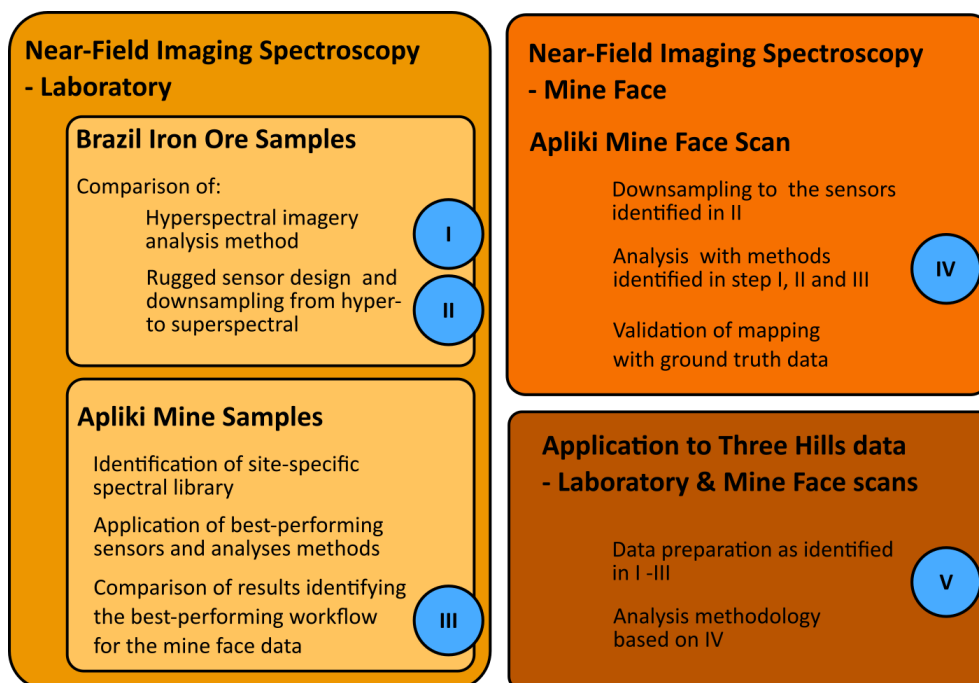


Figure 53 Methods and hybrid method development performed on the different HSI datasets utilized in this work.

Workflow Part I & II) are applied to the hyperspectral laboratory imagery of the Brazilian Iron Ore Samples. Part I) compares different, common methods used to classify spectral imagery and the mapping results. Part II) deals with the need for a rugged, spectral, imaging sensor that can be deployed in the challenging open pit mining environment. Here, different rugged, theoretical sensors are tested to identify the ones best suited for open pit mining. Part III) explains the identification of a site-specific spectral library tailored to the Apliki deposit. The Apliki laboratory sample data is then analyzed according to the methods and the theoretical sensors identified in I) & II). Part IV) applies the data pre-processing and downsampling methods explained in “Methods” and Part II) to the mine face

data. The mine face is then analyzed with the methods identified in Part I) and with the spectral library compiled in Part III) Part I) to IV) represent a workflow for dealing with imaging spectroscopy laboratory and mine face data in a mining context. The aim is to produce sufficient results for decision makers under field conditions. Part V) All the methods explained above are then applied to another open pit mining location: the Skouriotissa – Three Hills deposit and the sample laboratory and mine face derived data from this location.

5.2 I) Mapping method comparison - Results for Brazilian iron ore samples

The different mapping methods were used to analyze the Brazilian Iron ore sample reflectance dataset (Dataset 1) including 15 samples. The analysis results will be compared in this chapter.

The analyses were performed on a Ubuntu 18.04.4 system, Processor: Intel® Core TM i7-8550U CPU @ 1.80 GHz x 8, OS type 64-bit, Memory 32GB. The following Python toolboxes (Python version: 3.7.6.) were utilized: the DeepHyperX toolbox (Audebert, 2020), the Spectral Python SPy toolbox (spectralpython.net/, 2020), the Pysptools toolbox (Therien, 2020), the HypPy toolbox (Bakker and Oosthoek, 2020) and the scikit-learn: Machine Learning in Python tools (Pedregosa *et al.*, 2011). The image analysis software ENVI classic was utilized ENVI® Classic, version 5.5, IDL version 8.7.0 (L3Harris-Geospatial-Solutions, 2018) and geochemical clustering was performed in R (R Studio version 1.2.5033, R version 3.6.2). For the PRISM MICA analysis the following software was utilized: ENVI® Classic 5.3.1, IDL 8.5.1, PRISM processing routines in IDL downloaded in September 2014 for ENVI 5.0 “[usgsprism_v1ae_envi50.sav](https://pubs.usgs.gov/of/2011/1155/)” (pubs.usgs.gov/of/2011/1155/ and Kokaly, 2014). In the following sections only the shorthand for the software and toolboxes will be used.

5.2.1 Analyzed data

The file used for testing different analysis and classification methods is the HySpex scan with masked areas of low SNR/shadow. The file is the output from Rogass *et al.* (2017) translational reflectance retrieval and is otherwise unchanged. For validation purposes of the classification results, a ground truth file was created. Regions of interest (ROIs) for each sample region were created in ENVI® and exported, both as an classification file as well as a PNG file. Only the inner area of each sample was used to create a ROI, as mixing with the adjacent samples is possible around the sample edges. Note that this will lead to a constant overestimation of the different sample areas by the classification methods. As this is the case for every tested method, the results stay comparable. The PNG file was used for the visual comparison of classification results. The color-coding of the samples corresponds to the color-coding chosen for the classification results of EnGeoMap for the spectral library used for

classification. Here, the shadow areas were masked out (Figure 54). The classification file was used for supervised classification, machine learning and deep learning approaches, the shadowed areas of low SNR that were removed in the original file could not be masked out and the color coding is different to the PNG validation file.

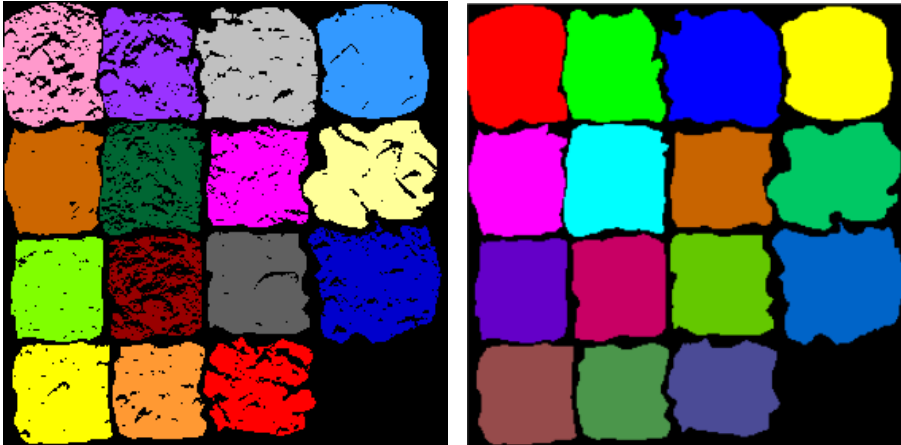


Figure 54 Left: Validation PNG file including the shadow mask applied to the data; Right: ENVI classification file for supervised learning-based methods.

5.2.2 Resulting EM spectral libraries

Four different means to create spectral EM libraries are presented and discussed in the following section. The four resulting spectral libraries are compared and the full spectral library compiled from user-defined spectral EMs is utilized further on for the analyses requiring a spectral library.

Visual user-defined spectral EM library

A spectral library was extracted containing one spectrum for each sample from a 5x5 pixel average window. This spectral library was used further for the methods requiring a user-provided spectral library (e.g. EnGeoMap, SAM). It shows to be the best distinction tool to differentiate between all the 15 samples or sample groups, Figure 55 shows a SAM analysis with the user-defined library and the library itself.

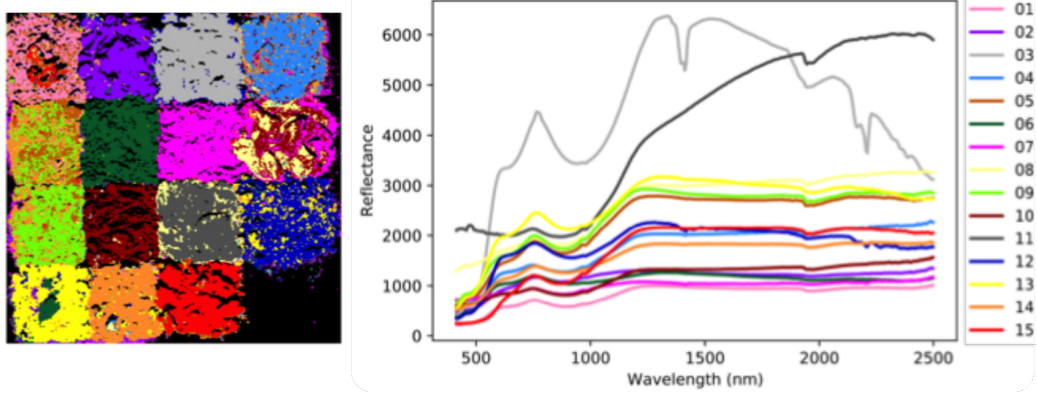


Figure 55 Spectra of all Brazilian iron ore samples in HySpex resolution (408 bands), each sample represented by a 5x5 pixel average and SAM analysis based on the library.

Reduced spectral EMs library by geochemical clustering

In order to identify small clusters of few sample points, agglomerative bottom up clustering of the sample geochemical data was performed in R (R Studio version 1.2.5033, R version 3.6.2). The ward.D2 method was utilized to minimize the total within-cluster variance (Murtagh and Legendre, 2011). The scree plot of the clustering showed an optimal cluster number between 4 and 5. The spectral library was reduced accordingly, choosing one spectrum for each cluster (Figure 56, right). Compared to the full 15 sample spectral library, especially the number of visually similar looking spectra with low spectral contrast is now reduced. A SAM analysis was performed to control how the new cluster center based spectral library translated into the hyperspectral images, the analysis result is shown in (Figure 56, left)., following the color-coding of the spectral library.

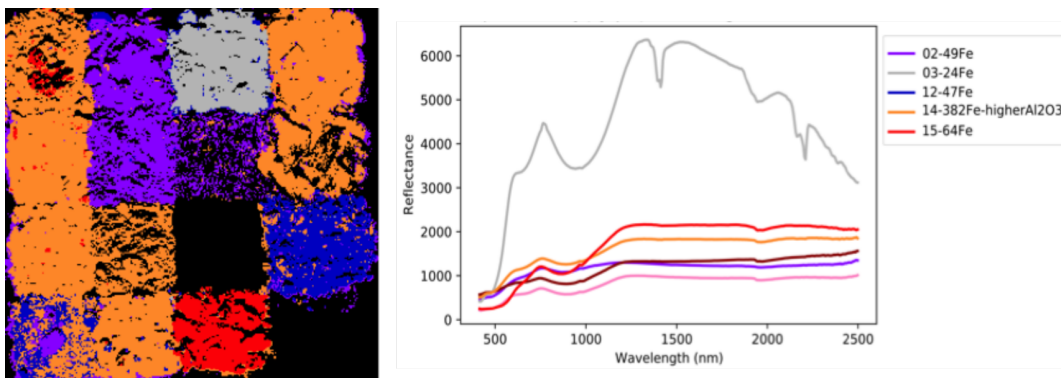


Figure 56 SAM analysis (left) based on the hyperspectral library reduced to geochemical cluster centers (right).

SMACC EM library

The ENVI SMACC tool was used to find EMs (EMs) from the 408 band HySpex data the resulting EMs can be found in Figure 57.

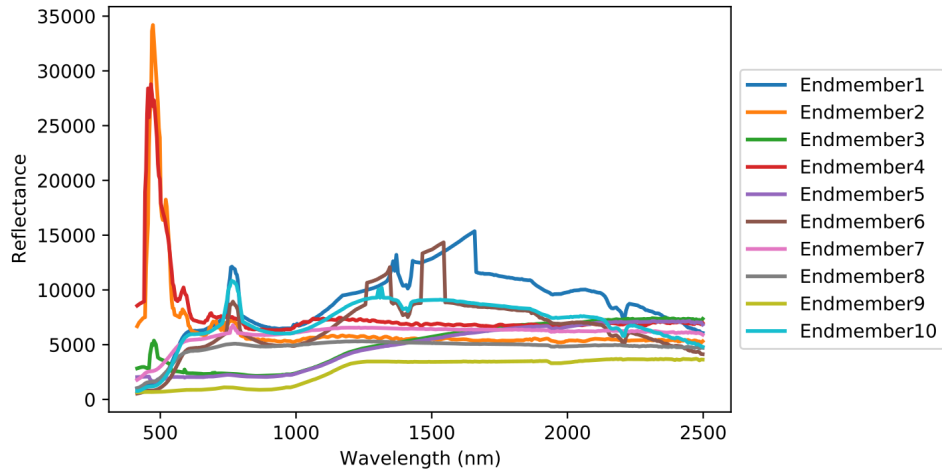


Figure 57 Brazilian iron ore SMACC EMs.

The most extreme spectra were detected for EMs (EM), resulting in the detection of outlier spectra strongly influenced by noise or saturation (EM1, EM2, EM4 and EM6). Figure 58 shows a plot of 30 randomly selected spectra from sample 03, where EM1, EM6 and EM10 are located.

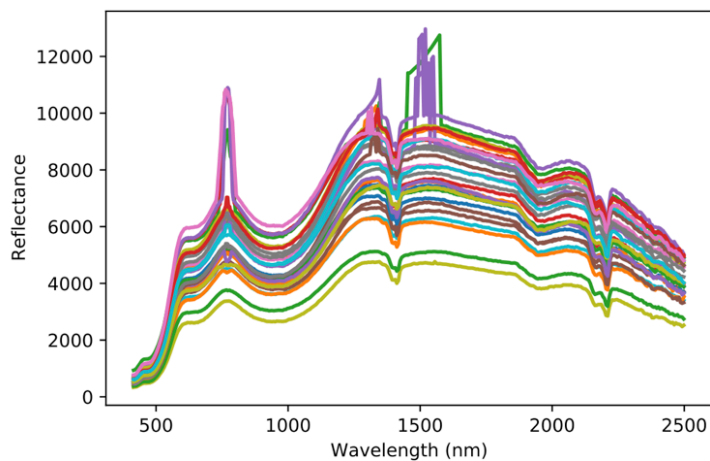


Figure 58 Thirty random spectra from the area of sample 03 (HySpex sensor, 408 bands).

Figure 58 shows that some of the randomly selected spectra from sample 03 exhibit the same outliers as EM1, EM6 and EM10. The spectrum of sample 03 of the visually selected 15 EM spectral library (Figure 59) is similar to the above shown spectra but due to choosing a 5x5 pixel average and a central point for the spectral sampling, no oversaturated pixels were included.

A SAM analysis for the reflectance imagery with the SMACC EMs spectral library shows how unfit the SMACC EM are to represent all relevant samples in this case (Figure 59, left).

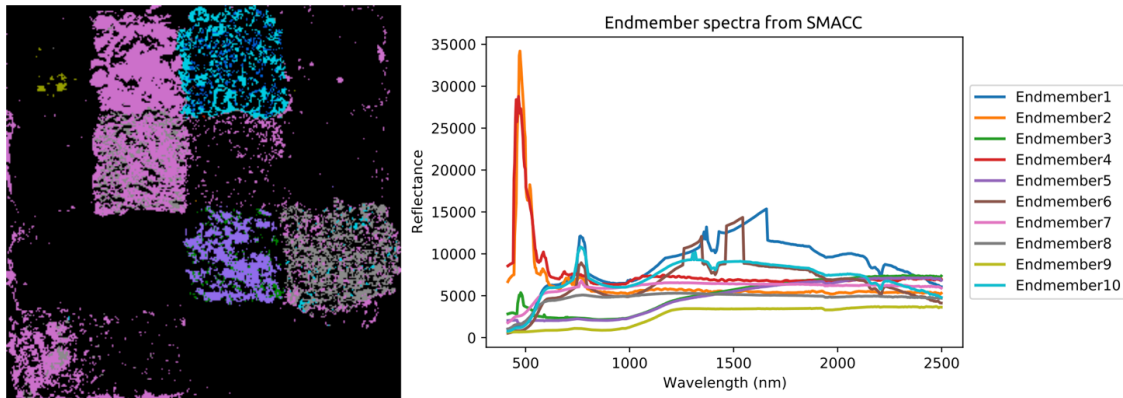


Figure 59 SAM analysis (left) of the Brazilian iron ore samples with the SMACC 10 EM spectral library (right).

PPI and n-D EM library

To use the Pixel Purity Index (PPI) and n-D visualization in ENVI resulted in 6 user-detected EMs (Figure 60).

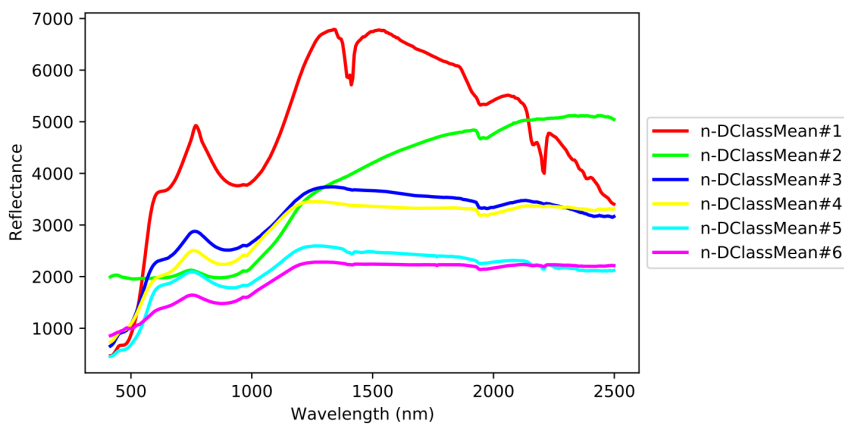


Figure 60 Six spectral EMs from PPI and n-D visualization tool.

Again, a SAM analysis for the reflectance imagery with the PPI + n-D EM spectral library shows the quality of representation of the samples by the found EMs (Figure 61).

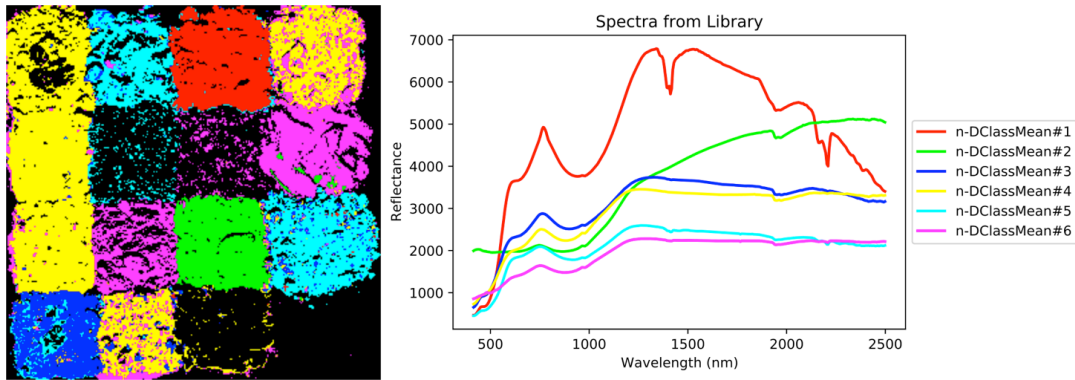


Figure 61 SAM analysis (left) of the Brazilian iron ore samples and the PPI + n-D 6 EM spectral library (right).

5.2.3 Mapping Results

The tests of **knowledge-based approaches** include band ratios, PCA analysis and feature modeling approaches. Of the last, the MWL and Continuum Band Depth are considered separately.

5.2.3.1 Band ratios

In order to work with defined and published band ratios, the data was resampled to WorldView-3 sensor characteristics of 16 bands. To give a visual impression, the spectral library in WorldView-3 characteristics is shown in Figure 62. The exact band setting and position of WorldView-3 is shown in figure 4 (p. 9) and is noted in the appendix in table 57 (p. 266).

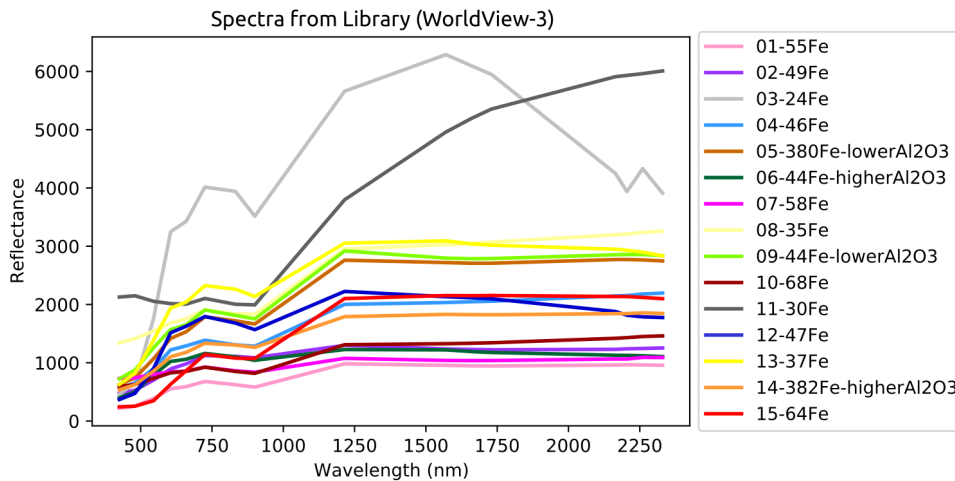


Figure 62 Spectra of Brazilian iron ore samples in WorldView-3 resolution (16 bands).

To give an example of the method and use an established band ratio, a ferrous iron (Fe^{2+}) and ferric oxide (Fe^{3+}) index from the Index Database (Henrich *et al.*, 2012; indexdatabase.de/, 2020) was chosen. The ferrous iron index for WorldView-3 data can be calculated from (SWIR 5/ Near_IR1) + (Green/ Red) (indexdatabase.de/, 2020), the resulting grey-scale image is shown in Figure 63 (right). Figure 63 also

shows an RGB of the samples (left) and the geochemically derived iron content (center). The ferric oxide index for WorldView-3 data can be calculated from (SWIR 3/ Near_IR1) (indexdatabase.de/, 2020), the resulting grey-scale image can be found in Figure 64 (right).

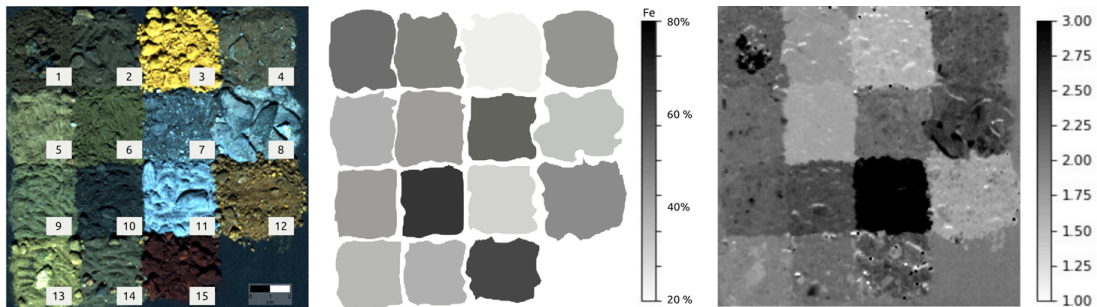


Figure 63 RGB (left), iron content based on XRF analysis (center) and ferrous iron index based on WorldView-3 band ratio (right).

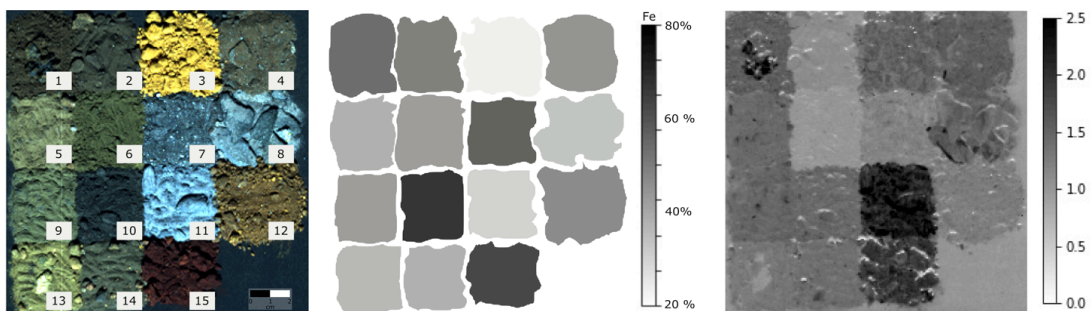


Figure 64 RGB (left), iron content based on XRF analysis (center) and ferric oxide index based in WorldView-3 band ratio (right).

5.2.3.2 PCA

The ENVI® Principal Component Analysis (PCA) Tool was used to calculate PC bands from the reflectance data. Some of the first, theoretically most relevant, PC bands were chosen for the RGB color composite (Figure 65).

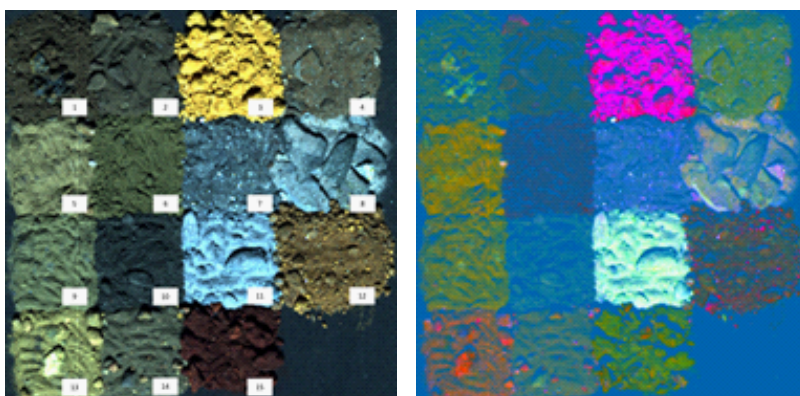


Figure 65 Brazilian iron ore true color image (left) and PCA image (R: PC band 1, G: PC band 2, B: PC band 4) (right).

5.2.3.3 Feature Modeling

The **Minimum Wavelength (MWL) Mapping** of the HypPy toolbox (Bakker and Oosthoek, 2020) was performed on the reflectance data). As an example, the user-defined wavelength range for AIOH feature detection were used as defined in (Kirsch *et al.*, 2018), the broad iron feature wavelength range was defined from the data itself. The AIOH feature was mapped between 2160-2220nm and the broad Fe feature was mapped between 850-1100nm. Figure 66 shows the feature position (center right) and feature depth (right) for the larger of the two AIOH features compared to the AIOH geochemical mapping (center left) based on the sample geochemistry. The MWL map for AIOH is presented in Figure 67 and is color-coded based on the feature position (color) and depth (saturation). Figure 68 shows the feature position (center right) and depth (right) of the iron feature compared to the iron content of the samples (center left).

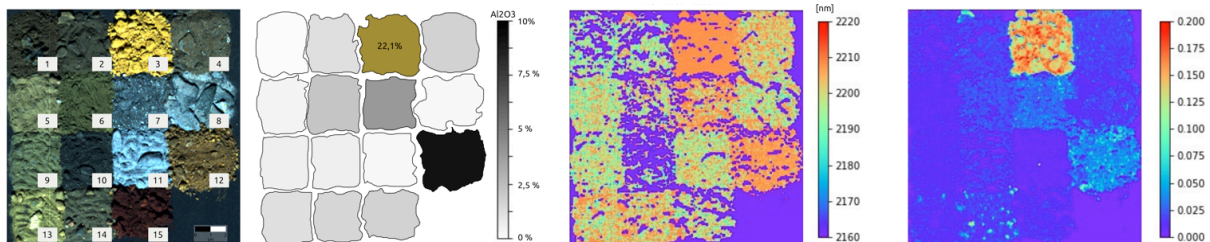


Figure 66 Minimum wavelength mapping for the large AIOH feature between 2160 - 2220nm. Left: RGB of samples, Center-Left: Al_2O_3 content based on geochemistry, Centre-Right: MWL feature position mapping (color stretched from 2160nm-blue to 2220nm-red), Right: MWL feature depth mapping (color stretched from 0-blue to 0.2-red).

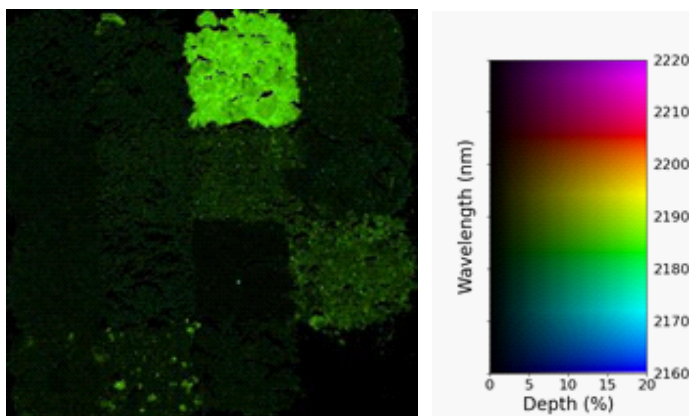


Figure 67 Minimum wavelength map of AIOH, feature position shown by the color-coding, feature depth by the color-saturation.

Mapping Results

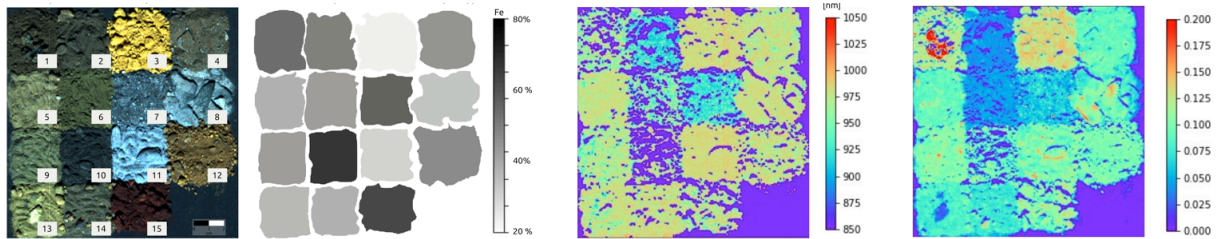


Figure 68 Minimum wavelength mapping for the broad iron feature between 850 - 1100 nm. Left: RGB of samples, Center-Left: Fe content based on geochemistry, Centre-Right: MWL feature position mapping (color stretched from 850nm-blue to 1050nm-red), Right: MWL feature depth mapping (color stretched from 0-blue to 0.2-red).

The data-driven mapping approaches as explained in Section 4.5.2.3 are separated into hard/ per-pixel classifiers and soft/ sub-pixel classifiers. Hard classifiers shown here include k-means clustering, SAM and SFF. Training-based hard-classification is represented by Gaussian Maximum Likelihood (GML) and Mahalanobis Distance (MHD) classifiers, learning-based classification is compared by showing Artificial neural network approaches (ANN), support vector machine learning (SVM) and random forest (RF). For the soft/ sub-pixel classifier, Mixture Tuned Matched Filtering (MTMF) and the Independent Component Analysis (ICA) are shown exemplarily.

5.2.3.4 *k-Means*

The k-means clustering was performed in the SPy toolbox (spectralpython.net/, 2020). k-means clustering took place for 15 (Figure 69) and 7 cluster centers (Figure 70).

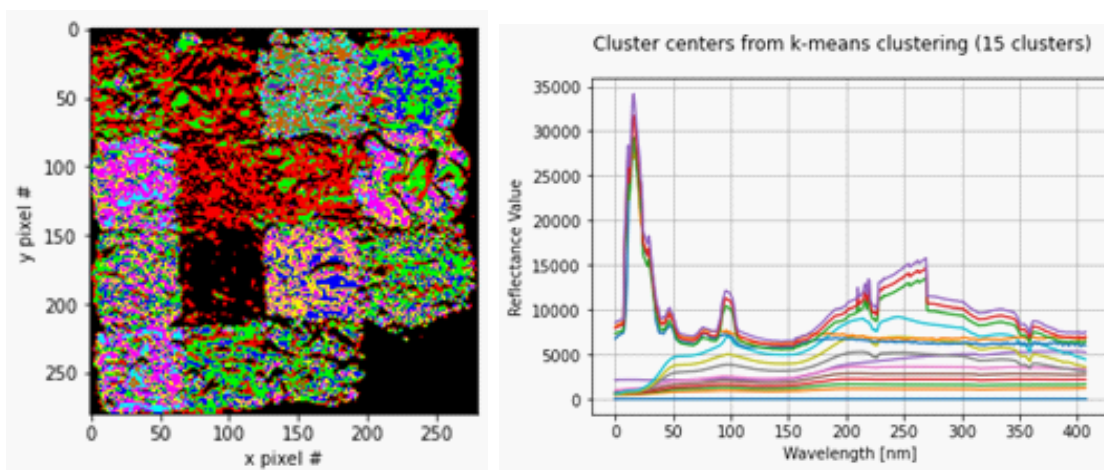


Figure 69 k-Means clustering for Brazilian iron ore, 15 clusters, defined after 100 iterations.

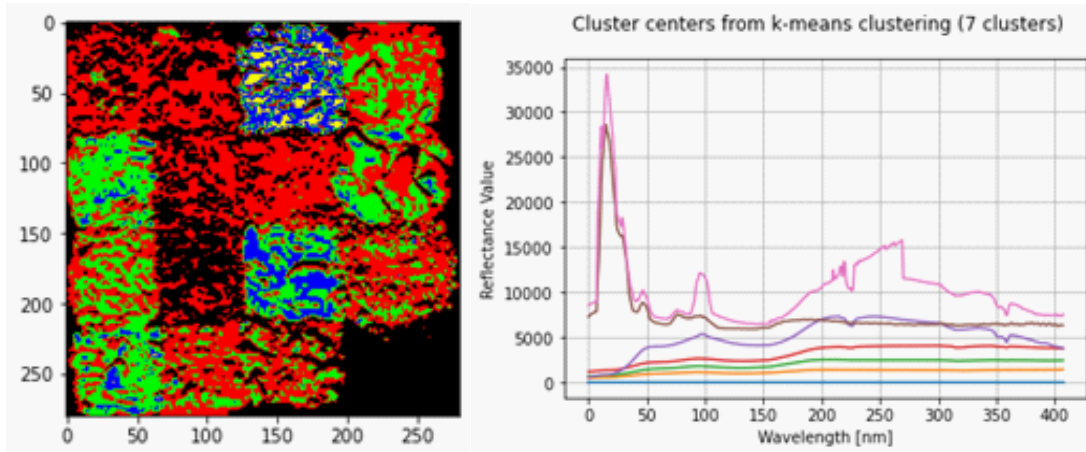


Figure 70 k-Means clustering for Brazilian iron ore, 7 clusters, defined after 100 iterations.

5.2.3.5 SAM

The reflectance data and the 15-EM user-defined spectral library were used for the SAM analysis. The resulting classification image was compared to the ground truth, 51703 of 78400 pixels were classified correctly, resulting in an accuracy of 0,659. The classification image is shown in Figure 71.

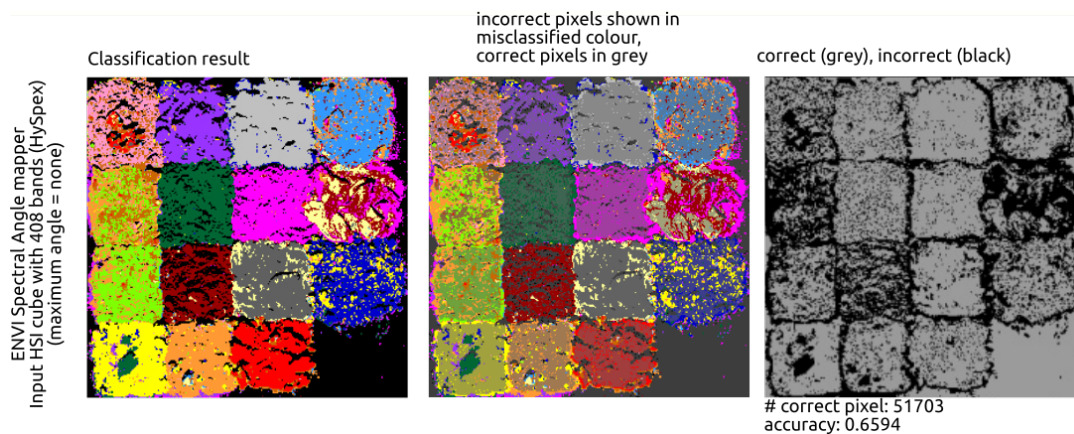


Figure 71 SAM classification result (left), incorrectly classified pixels (center) and overall correct vs. incorrect classified pixels (right).

5.2.3.6 Binary Feature Fitting

The binary feature fitting needs a super- to multispectral input data file for the triangulation. The 408 band HySpex data were downsampled to 42 band data with a constant FWHM of 50nm for each band to test the BFF mapping. The 15 user-defined EM spectral library was downsampled to the same spectral resolution. The third input is the CSV file containing the color palette in RGB. The classification has an overall accuracy of 0,743. The results can be found in Figure 72.

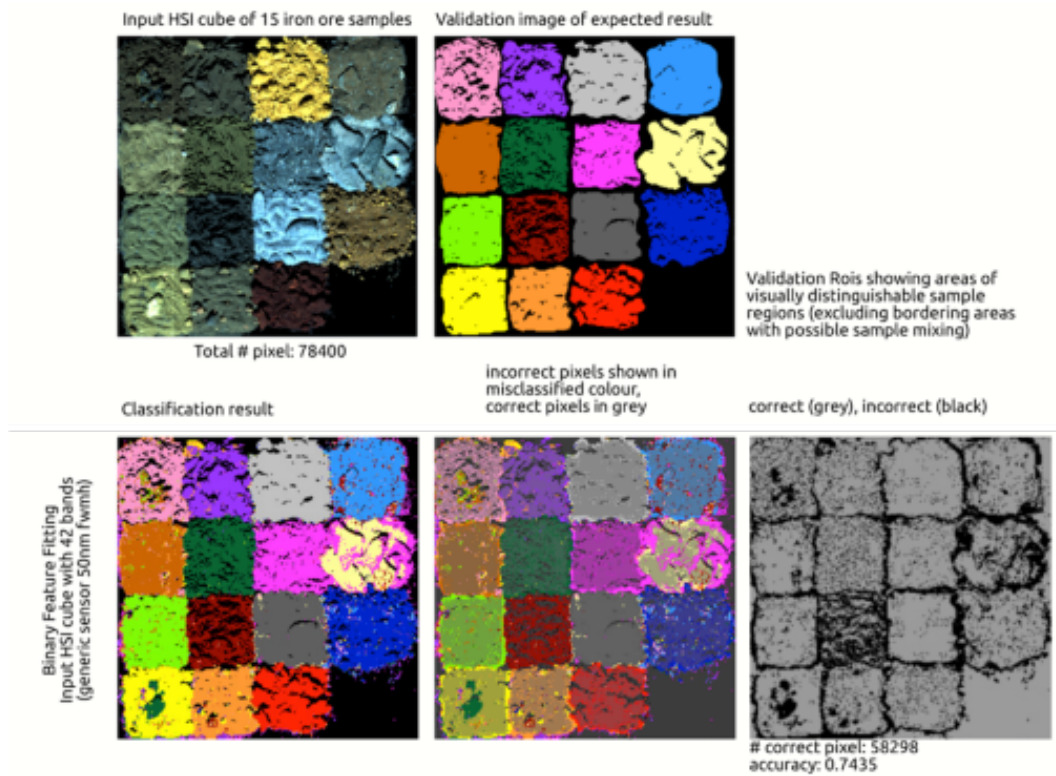


Figure 72 Classification result of BFF for the sample derived spectral library. RGB and ground truth are shown at the top, below from left to right: the best-fit classification image, the incorrect classification shown in the incorrect color with the correct ROI overlaid in gray and the correctly (gray) vs. incorrectly (black) classified areas in the image.

5.2.3.7 SFF

The reflectance data and the 15 EM spectral library data were used for the analysis in ENVI®. Classes had to be defined for each spectral library input RMS + Scale pair. Figure 73 shows the scale image of input spectrum 01 (left) and the user defined classes for sample 01 and 03 (right).

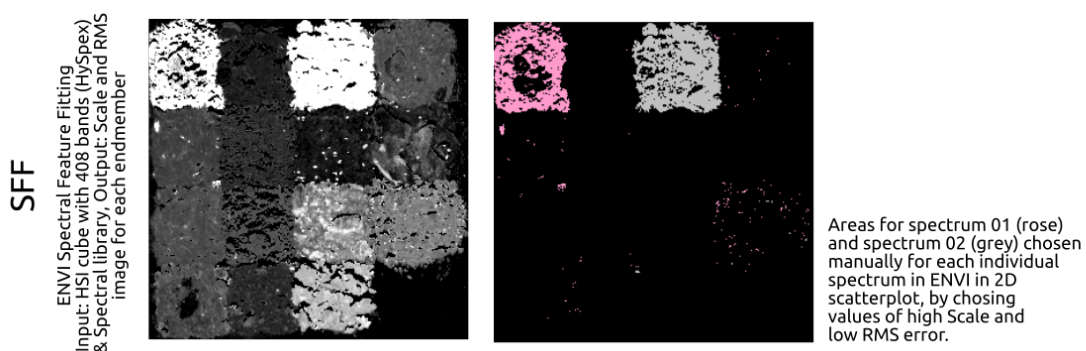


Figure 73 Spectral Feature Fitting. Greyscale image of the scale for spectral library entry 01 (left) and user-defined classes for sample 01 and 03 (right). Classes were defined from their respective 2D RMS and Scale scatterplots.

5.2.3.8 GML

The Gaussian Maximum Likelihood (GML) classification was performed in the Spy toolbox (spectralpython.net/, 2020). GML was performed on the reflectance data with the input of a class file as ground truth. The resulting classification has an accuracy of 0.646 and is shown in Figure 74.

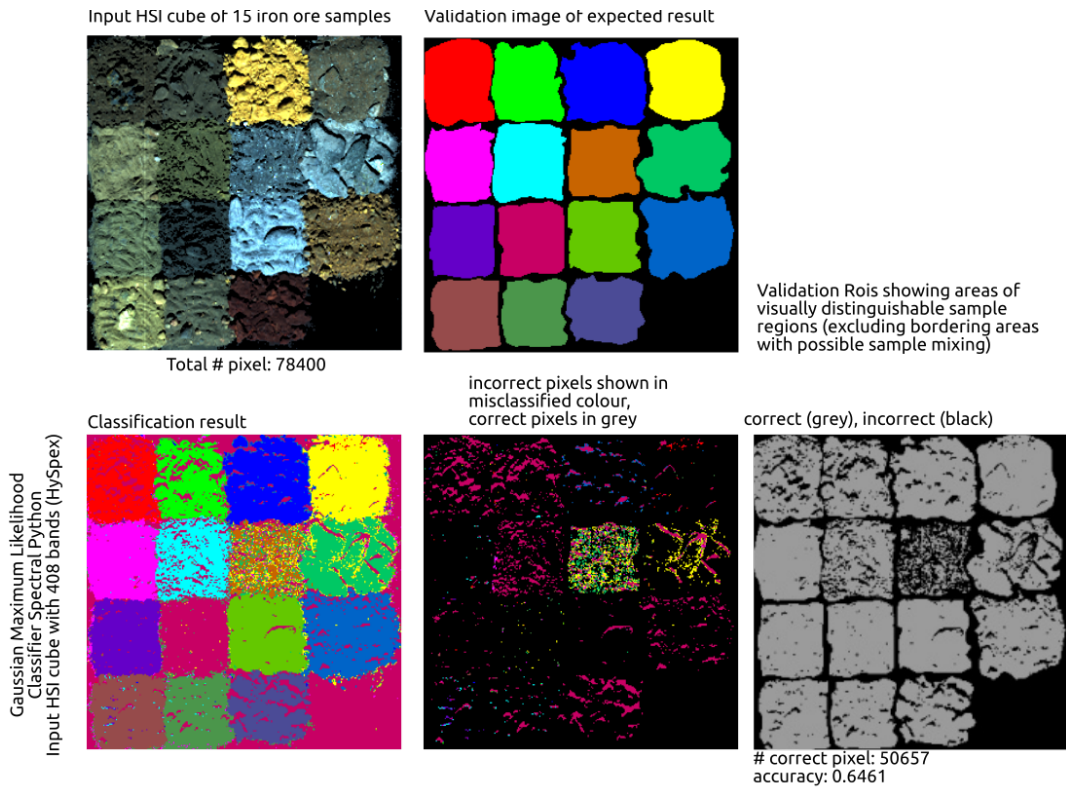


Figure 74 True color and ground truth image of the Brazilian iron ore samples (upper part) and GML results and accuracy (lower part).

5.2.3.9 MHD

The Mahalanobis Distance classifier was performed in the Spy toolbox (spectralpython.net/, 2020) with the same input image and ground truth as for the GML. The resulting classification shows an accuracy of 0.648 as shown in Figure 75.

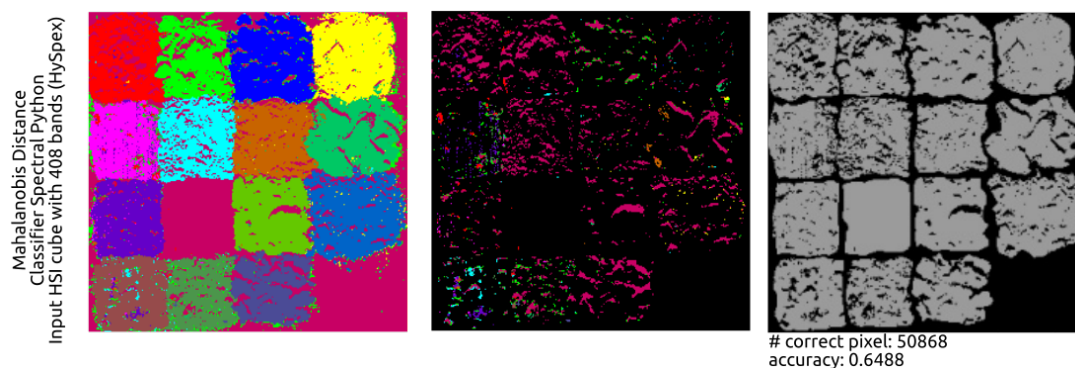


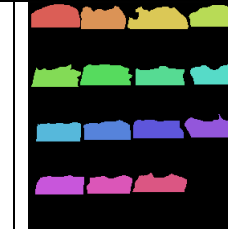
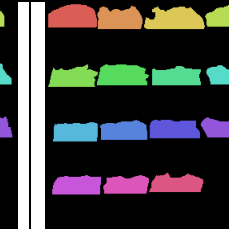


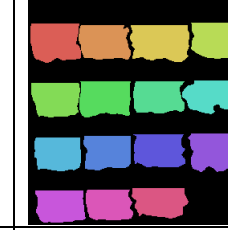
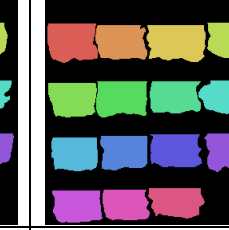


Figure 75 MHD results and accuracy for Brazilian iron ore samples.

5.2.3.10 Learning-based data-driven (SVM, ANN, CNN)

The **learning-based data-driven approach** is represented by the use of a support vector machine (SVM) from the DeepHyperX toolbox (Audebert, 2020) using the scikit-learn SVM (Pedregosa *et al.*, 2011). The artificial neural networks (ANN) are represented by testing a 1D baseline neural network (NN) (Audebert, Le Saux and Lefevre, 2019), a 1D convolutional neural network (CNN) (Hu *et al.*, 2015) and a 3D CNN (Li, Zhang and Shen, 2017). To compare the different NNs, the number of epochs was set to 100 and the number of batches to 100 (not for the SVM). The number of epochs was based on testing with the dataset and evaluating the number of epochs related to a sufficient training loss and validation accuracy within a time limit of 6000s (100min) as an acceptable training time for the end-user. The time limit is based on quick, on-site training of the NNs and achieving classification results within typical 8h-shifts. A training set of 60% was selected for all learning-based approaches, also based on trial and suggested defaults from the DeepHyperX toolbox. Training samples were collected disjoint within the image. The reflectance data as used as input data with the classification ground truth file. Parameters of the models are listed below (Table 18), the classification images for the 1D NN, 1D CNN, 3D CNN and SVM are shown in Figure 76.

Table 18 Training based (1D NN, 1D CNN, 3D CNN and SVM) analysis parameters and results.

Model	1D Baseline NN	1D CNN	3D CNN	SVM
Based on	(Audebert, Le Saux and Lefevre, 2019)	(Hu <i>et al.</i> , 2015)	(Li, Zhang and Shen, 2017)	(Pedregosa <i>et al.</i> , 2011; Audebert, 2020)
Epochs	100	100	100	100
Training sample	0.6	0.6	0.6	0.6
Selected samples	20858	20858	20858	20858
Sampling mode	Disjoint	Disjoint	Disjoint	Disjoint
Patch Size	1	1	5	-
Learning Rate (LR)	0.0001	0.01	0.01	-
Batch size	100	100	100	-
Computation time (real) [s]	5432.5	347.6	5318.4	659.5
Accuracy [%]	89.8	75.2	93.9	84.5
Kappa	89.1	73.4	93.4	83.4
Training ground truth				
Test ground truth				
Comment	Long training time	Fastest but worst accuracy	Best accuracy, long training time	Fast and medium accuracy

I) Mapping method comparison - Results for Brazilian iron ore samples

Mapping Results

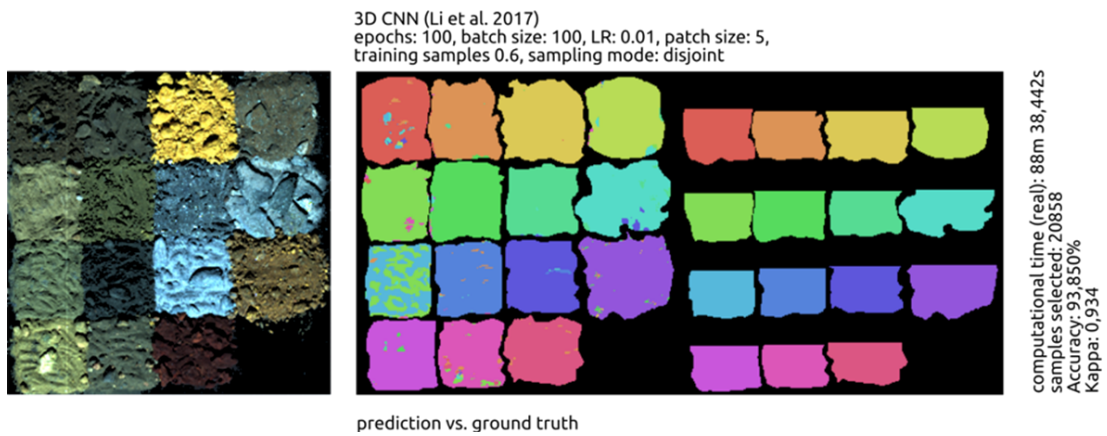
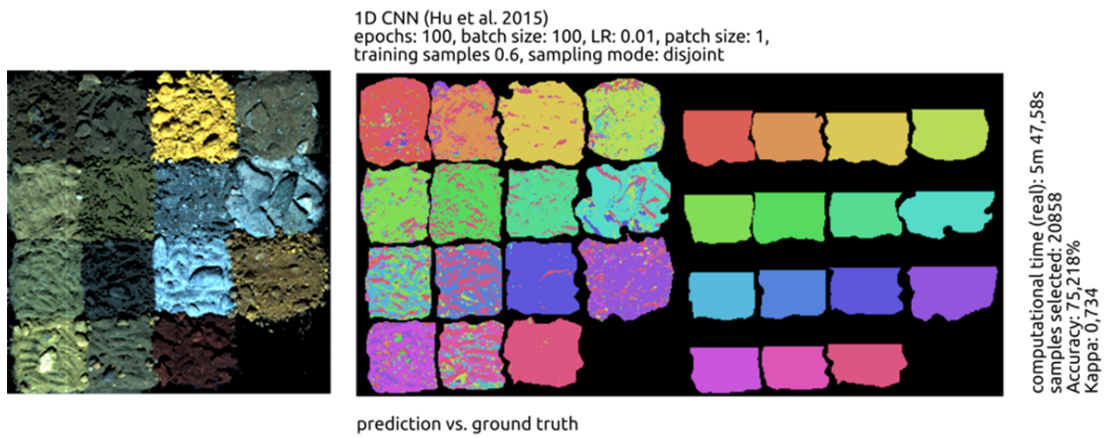
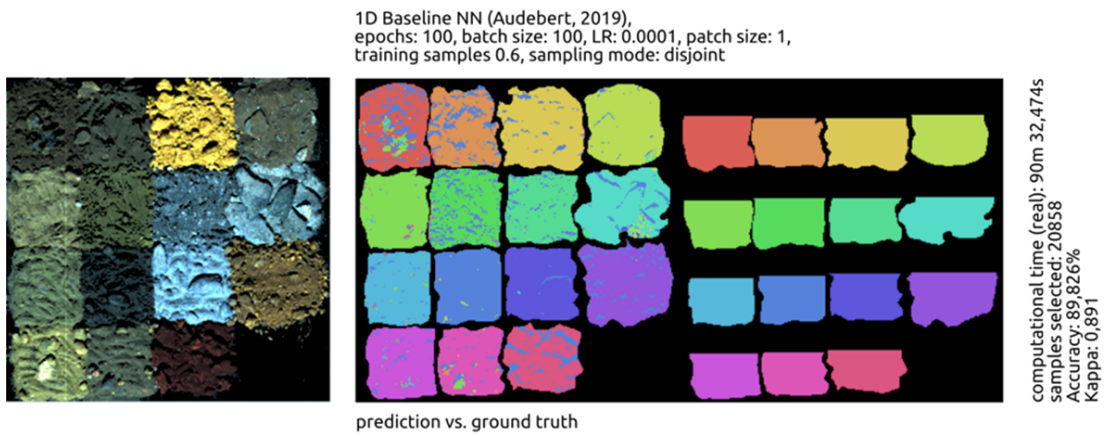
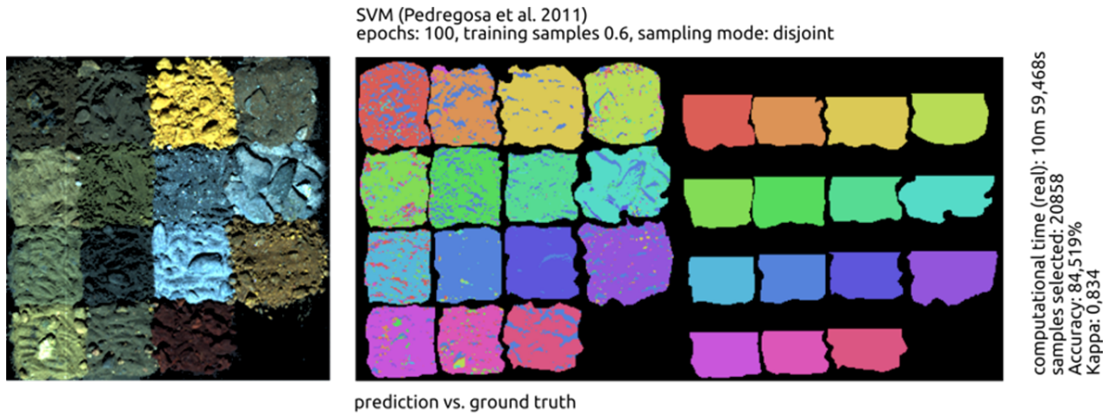


Figure 76 True color image of the Brazilian iron ore samples (left), prediction of respective model (center) and 40% ground truth for testing (right), shown for the SVM, 1D NN, 1D CNN and 3D CNN (from top to bottom).

5.2.3.11 *Random Forest*

The Pysptools “HyperRandomForest Classifier” (Therien, 2020) was trained with the parameters: `n_estimators = 100`, `max_depth = 30`. The data was split into 60% training and 40% test-data and the classifier was fit with an accuracy score of 0.80. Comparing the classification image with the ground truth image, the overall classification accuracy is 0.87 (Figure 77).

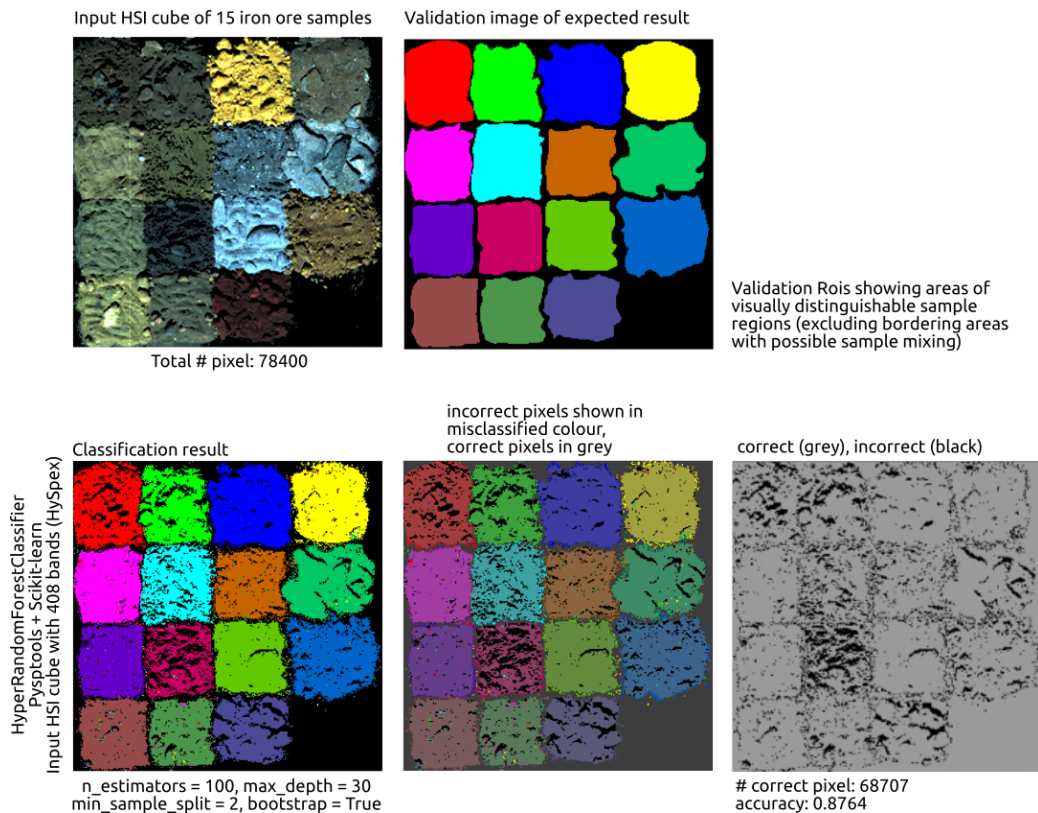


Figure 77 “HyperRandomForest” classification results for Brazilian iron ore samples.

Soft classifiers presented here include the MTMF and the ICA analysis.

5.2.3.12 *MTMF*

The results of the MTMF are 15 MF bands and 15 infeasibility bands, one pair for each EM. An example of a MF band for sample 01 is shown in Figure 78 (left) and of the user-defined classes for sample 01 and 03 are shown in Figure 78 (right).

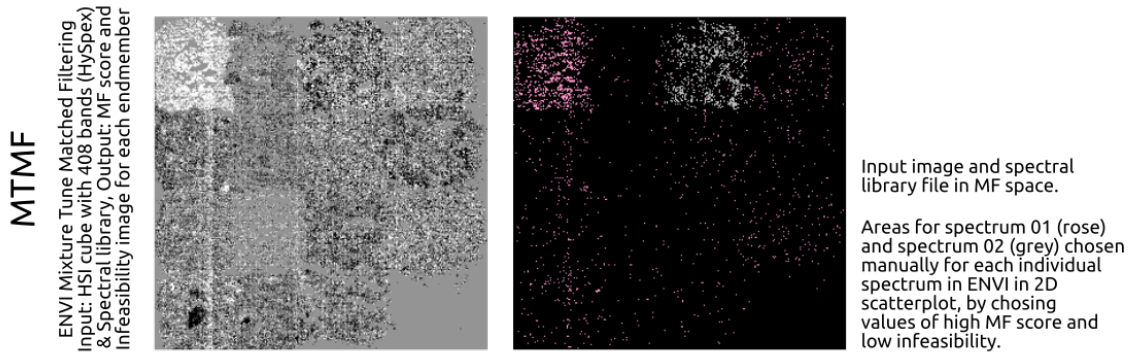


Figure 78 MTMF classification, MF image of spectral library entry 01 (left) and user defined classes for spectral library entry 01 and 03 from their respective MF and infeasibility 2D scatterplots (right).

5.2.3.13 ICA

The independent component analysis was performed in the ENVI® using the reflectance data. The result of ICA are 408 de-correlated IC bands that are sorted by spatial coherence. An RGB color composite of the first, most coherent IC bands (R: band 4, B: band 6, G: band 7), is shown in Figure 79.

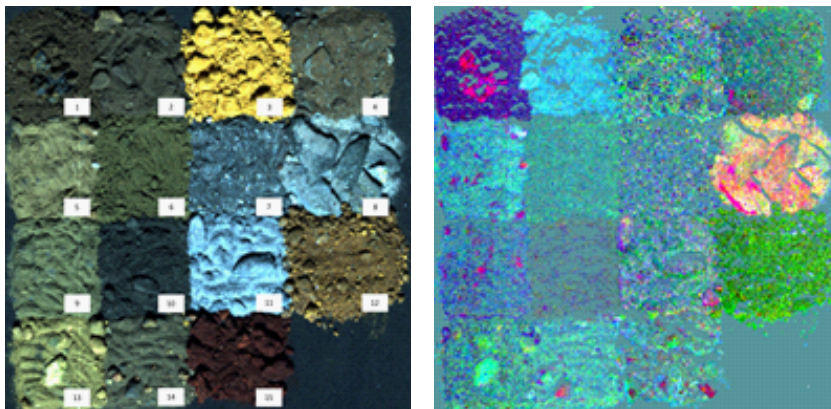


Figure 79 Left: Labeled true color composite of the Brazilian iron samples. Right: ICA RGB composite (band 4 - band 6 - band 7).

5.2.3.14 Hybrid methods

For the hybrid methods, the MICA algorithm and the EnGeoMap 2.0 and EnGeoMap 2.1 were deployed. EnGeoMap 2.0 and 2.1 are based on the 15 EM user-defined spectral library. The MICA classification is based on the USGS splib06a (Clark *et al.*, 2007) and the therein defined diagnostic spectral features and ranges. In order to compare the MICA results, an EnGeoMap BFF and SAM classification was performed on the data utilizing the MICA spectral library and the USGS color-coding scheme.

MICA

MICA is based on splib06 (Clark *et al.*, 2007), a SPECPR file containing the spectral library information and a MICA command file (Kokaly, 2011). The aim is to compare a system with integrated expert

knowledge (MICA) with automated approaches (EnGeoMap and BFF); therefore, a MICA default library and color-coding was used for classification instead of providing a user-defined library. This makes the MICA classification harder to compare to the classifications above as the utilized spectral libraries differ. Therefore, EnGeoMap, BFF and SAM classifications were performed with the MICA default spectral library. The MICA default libraries are split up in “group1” containing iron bearing minerals and “group 2” containing clay-group minerals. To compare the classification results, the “group 2” spectral library and color-coding scheme from the USGS was used, concentrating on the clay features in the SWIR. The default MICA command file for the mapping is based on a spectral library in Hymap spectral resolution. Based on this, the HySpex data was downsampled to 124 band Hymap data resolution. The MICA classification result is shown in Figure 80.

MICA command group 2 classification

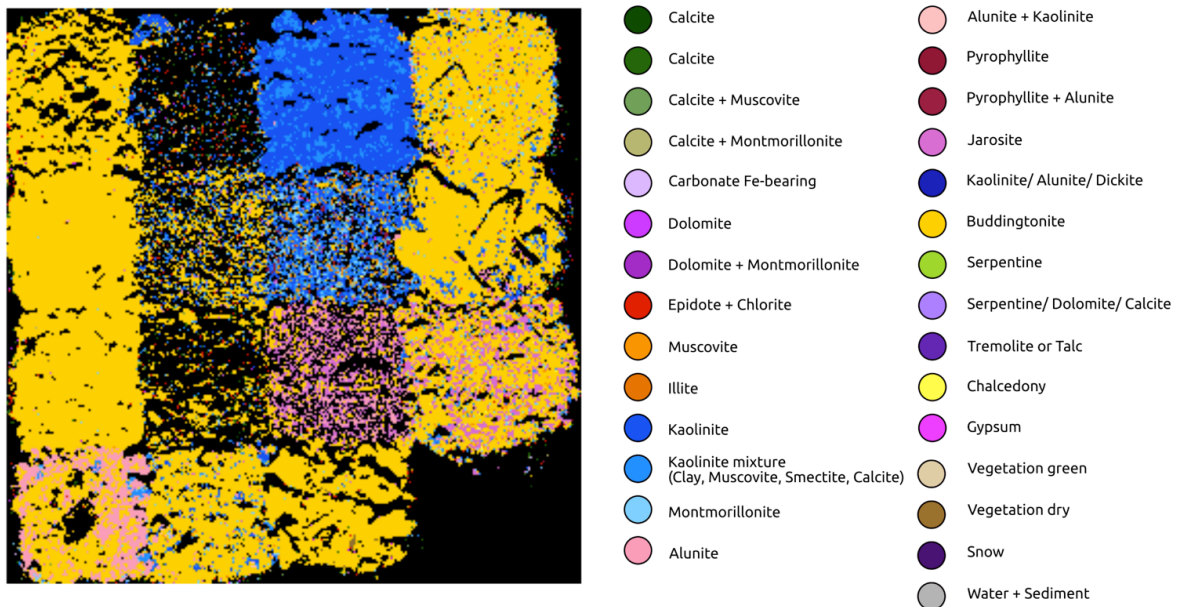


Figure 80 PRISM MICA group 2 classification of the Brazilian iron ore.

To recreate the classification with the other hybrid models and have a comparison between them, the splib06b group 2 was used as a separate spectral library for the EnGeoMap, SAM and BFF algorithm. The results of SAM, EnGeoMap and BFF is shown in Figure 81. The dominantly mapped material spectra are shown in Figure 82.

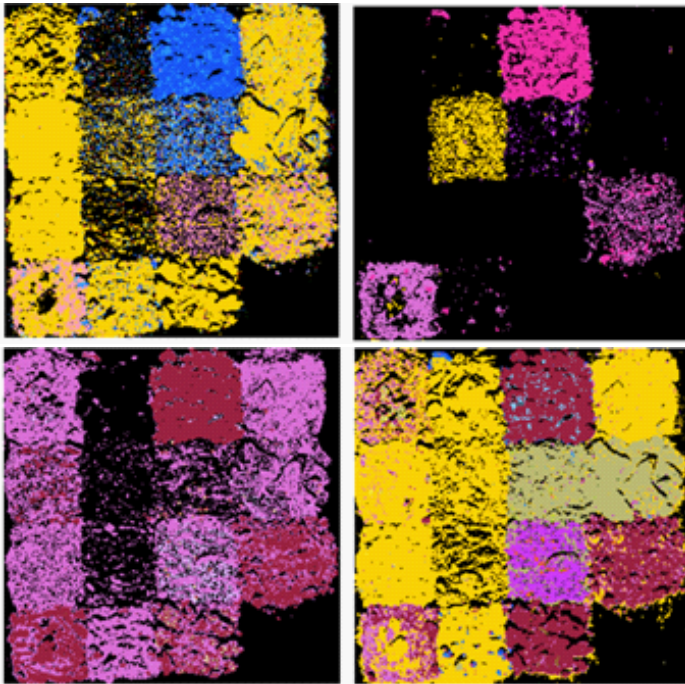


Figure 81 MICA group 2 spectral library analysis of the Brazilian iron ore samples with MICA (top left), SAM (top right), EnGeoMap (bottom left) and BFF (bottom right).

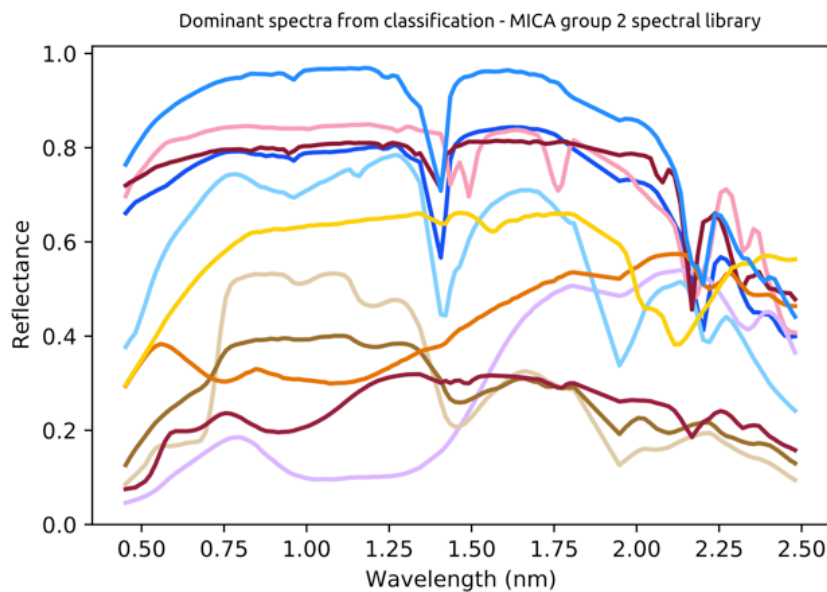


Figure 82 The dominantly mapped material spectra mapped from the MICA group 2 spectral library. (dark blue: kaolinite, medium blue: kaolinite mixture, light blue: Montmorillonite, pink: alunite + kaolinite, dark red: pyrophyllite, dark red-brown: pyrophyllite + alunite, yellow: Buddingtonite, orange: Muscovite, purple: carbonate Fe-bearing, light brown: vegetation green, brown: vegetation dry)

EnGeoMap

EnGeoMap 2.0 (feature retrieval by an upper geometric hull) and EnGeoMap 2.1 (feature retrieval by a lower and an upper geometric hull) were used for the classification. Both classifications were run with the same user-defined settings (Table 19).

Table 19 Settings for EnGeoMap 2.0 and EnGeoMap 2.1 analysis.

Parameter	Setting
<i>Input files</i>	- Masked reflectance data (HySpex 408 bands), - Spectral library file with 15 EM spectra (5x5 pixel average), - Color palette for each EM spectra - Geometric options file including the unmixing thresholds and the sensor SNR model
<i>No. of components for unmixing</i>	15
<i>Unmixing threshold</i>	0.0
<i>SNR estimation</i>	From EnMap sensor

The accuracy of the resulting classification for EnGeoMap 2.0 is 0,419 for EnGeoMap 2.1 is 0,533, the resulting maps can be found in Figure 83.

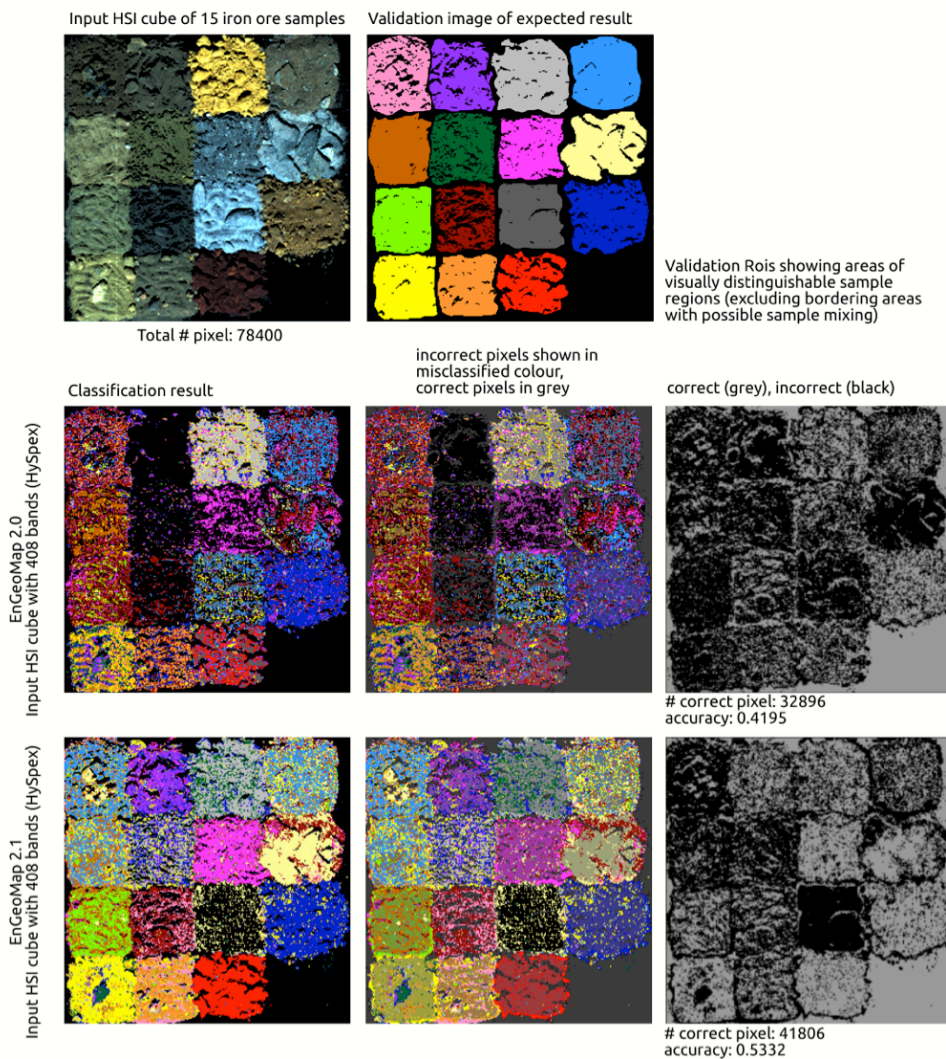


Figure 83 Classification results of EnGeoMap 2.0 and EnGeoMap 2.1 with the sample derived spectral library. RGB and ground truth are shown at the top, below from left to right: the best fit classification image, the incorrect classification shown in the incorrect color with the correct ROI overlaid in gray and the correctly (gray) vs. incorrectly (black) classified areas in the image.

5.2.4 Comparison of the results

The results of the analysis are compared in detail in Chapter 6 “Discussion”, starting at page 165.

The analyses resulting in a hard classifier map (assigning each pixel with the material that is most likely present) are compared quantitatively based on their computation time and accuracy of mapping. The analysis methods resulting in single material likelihood maps are compared qualitatively (Table 37, p. 165 in Section 6.1 “Iron ore sample mapping results”, starting at p.165). Table 20 summarizes the compared methods, input for classification or analysis, number of user specified EMs (EM), the overall accuracy of the data in the case of hard classifier maps and the software used for the analysis. Python 3.7 and ENVI® Classic 5.5 (on IDL 8.7.3) was utilized for the analysis, unless stated otherwise. The input data was the 408 bands HySpex reflectance data for all methods but the band ratio analysis (16 bands, WV-3) and the Binary Feature Fitting (42 bands). The spectral library utilized was compiled from the 408 band data unless stated otherwise in Table 20.

Table 20 Comparison of the applied HSI analysis method, input spectral library (speclib), number of EMs (EM), overall mapping accuracy [%] and software used to carry out the analysis.

Method	Input spectral library	Number of EM	Overall accuracy [%]	Software/ Toolbox
HYBRID				
<i>EnGeoMap 2.0</i>	5x5 AVG speclib	15 EM spectra	0.419	Python 3.6
<i>EnGeoMap 2.1</i>	5x5 AVG speclib	15 EM spectra	0.533	Python 3.6
<i>PRISM MICA</i>	USGS Group 2 for AIOH speclib, 124 bands (HyMap)	61 EM spectra	None	ENVI® 5.3.1, IDL 8.5.1, “usgsprism_v1 ae_envi50.sav”, from 2014
KNOWLEDGE-DRIVEN				
<i>Absorption modeling</i>				
<i>PCA</i>	None	None	None	ENVI®
<i>Band ratios</i>	None	None	None	SPy
<i>Feature modeling</i>		Wavelength range		
<i>Minimum Wavelength Mapping (MWL)</i>	None	2160 - 2220nm	None	HypPy
<i>MWL</i>	None	850 - 1100nm	None	HypPy
DATA-DRIVEN				
<i>Hard classifier</i>				
		Cluster number		
<i>k-means</i>	None	15	None	SPy
	None	7	None	SPy
<i>SAM (ENVI)</i>	5x5 AVG speclib	15 EM spectra	0.659	ENVI®
<i>Binary Feature Fitting</i>	5x5 AVG speclib, 42 bands	15 EM spectra	0.744	Python 3.6
<i>SFF</i>	5x5 AVG speclib	15 EM spectra	None	ENVI®

Method	Input spectral library	Number of EM	Overall accuracy [%]	Software/ Toolbox
<i>Training based</i>				
<i>Gaussian maximum likelihood</i>	Ground truth: class file	15 EM ROIs	0.646	Spy
<i>Mahalanobis Distance</i>	Ground truth: class file	15 EM ROIs	0.649	SPy
<i>Learning based</i>				
<i>SVM:</i>				
<i>SVM (Pedregosa et al., 2011)</i>	None	15 EM ROIs	0.845	DeepHyperX,
<i>ANN:</i>				
<i>1D Baseline NN (Audebert et al, 2019)</i>	None	15 EM ROIs	0.898	DeepHyperX,
<i>1D CNN (Hu et al., 2015)</i>	None	15 EM ROIs	0.752	DeepHyperX,
<i>3D CNN (Li et al., 2017)</i>	None	15 EM ROIs	0.939	DeepHyperX
<i>Random Forest:</i>				
<i>RandomForestClassifier (Pedregosa et al., 2011)</i>	None	15 EM ROIs	0.805	Pysp + scikit-learn
<i>Soft-classifier</i>				
<i>MTMF</i>	5x5 AVG speclib, MNF stats, 408 MNF bands	15 EM spectra	None	ENVI®
<i>ICA</i>	None	None	None	ENVI®

Going forward, four different analysis methods were chosen for the development of a sensor that is robust and can easily be integrated into the mining environment. For the following chapters, the best performing analyses are chosen based on the highest accuracy but also the computation time and repeatability, this decision is discussed in depth in Section 6.1 (pp 165 - 171). The obvious best accuracy reached by the 3D CNN was not considered due to presumptions of overfitting of the NN.

The analysis methods used to test the different theoretical sensors in the following chapter are:

- SAM as the algorithm with the lowest computation time, as time is a key factor in the active extraction process in the mining sector.
- SVM, as the best performing learning-based classifier below 1000s computation time. Keeping in mind that once trained on a specific deposit, the computation time will decrease rapidly.
- BFF, as the best performing comparison-based data-driven method below 1000s.
- EnGeoMap 2.1 despite its lower accuracy, as it is another hybrid data- and knowledge-driven analysis algorithm.

5.3 II) Robust Sensor Modeling

Mining equipment in an open pit mining environment is not only dependent on precise analytics but also on rugged hardware, fast measurements and results (high turnover rate) and soft- and hardware that can be handled by non-engineers and non-computer scientists. In the context of build definition for extraction planning, millimeter-precise spatial result and ppm- precise geochemical distinctions inferred from spectral fingerprints are of secondary importance to a decimeter-scale bulk rock determination of ore, contaminants and waste material.

In order to make spectral analytics available to the mining sector and allow a frequent monitoring, the sensors have to be present in every mining operation. This implies systems of a moderate price range and handling by a variety of non-experts on different work shifts. For UAV based operations the weight of the system is additionally of importance. Most mining operations take place in a tropical environment. The major producers of iron ore (in metric tons) in 2019 were Brazil and Australia (<https://www.statista.com/statistics/267380/iron-ore-mine-production-by-country/>, last visited 12.06.2020), the biggest copper ore producer (in metric tons) in 2019 was Chile (<https://www.statista.com/statistics/264626/copper-production-by-country/>, last visited 12.06.2020). These countries show harsh conditions not only in major changes of surface temperature and near zenith sun angles but in the case of Brazil also due to massive rainfall events. In these cases, the ideal time and sun angle to take measurements in the open pit will decrease to a small window each day, which can additionally be influenced by precipitation. Table 21 summarizes the possible influences on spectral mining equipment, the implications of each influencing factor and a possible theoretical solution.

Table 21 Influencing factors, implication and solutions for spectral sensor development in active mining operations.

<i>Influencing factor</i>	Implication	Possible solution
<i>Rugged Equipment</i>	The sensor needs to be rugged to be handled in uneven terrain and by a work force wearing personal protective equipment (PPE).	Protective casing that does not hinder the ventilation of the sensor. PPE like helmets and glasses can hinder the visibility of the surface interface during measurement, protective gloves need adjustment for the sensor and GUI handling. The GUI and hardware need to be adjusted to these conditions.
<i>Fast measurement</i>	A high turnover rate and short available time frames for measurements ask for a minimal measurement time. This also reduces the in-pit time and thus the risk for the	A smaller number of bands, possibly full frame instead of line scanner and a lower pixel number reduce the measurement time. This needs to be adjusted within the needed spatial and spectral resolution required for the task.

Influencing factor	Implication	Possible solution
	workforce.	
<i>Fast Analysis (real-time)</i>	High turnover rates ask for quick decisions in order to save money and keep succeeding processes in time.	In-sensor reflectance retrieval by at sensor irradiance measurements or quicker reflectance retrieval routines are needed. If VNIR and SWIR is used, the data has to be accessible in the same spatial resolution and grid. Reduced spectral and spatial dimensions optimize analytical computation times.
<i>Determination between ore, main contaminants and waste</i>	A variability of ore grade and contaminants can influence the transport and processing that succeeds the extraction. Broad material categorization before extraction can economize fuel use for transport as well as energy use for crushing (Blom, Pearce and Stuckey, 2019).	Site-specific determination of contaminants that influence the processing; Site-specific spectral libraries able to sort for ore, main contaminants and waste; Sensor with band positions ideal to detect the materials of interest.
<i>Pricing</i>	Lower hardware prices will enable decision makers to purchase systems for each mine site and implement in series.	A smaller band number and smaller spectral range enables lower hardware prices; SWIR detectors and optics are more expensive than VNIR systems.
<i>Size & Weight</i>	Lower hardware weight will enable UAV monitoring; heavy UAVs need specific licenses and pose a higher risk to the work force.	Smaller band numbers will decrease the size and weight of the sensor. VNIR sensors are already small and light and could be used solely for UAV monitoring.
<i>Power consumption</i>	Lower power consumption will enable longer measurements, reducing both strain on batteries or diesel-generator based energy sources. Lower power consumption of the sensor also directly influences the UAV flight time that is based on battery duration.	The HySpex VNIR-1024 system only consumes 6W (https://www.hyspex.com/hyspex-products/hyspex-classic/hyspex-vnir-1024/ , last visited 03.09.2020) in contrast to the 30W of the HySpex SWIR-384 system (https://www.hyspex.com/hyspex-products/hyspex-classic/hyspex-swir-384/ , last visited 03.09.2020). Using VNIR solely could be a solution.
<i>High temperatures</i>	Hot climate conditions take a toll on electric systems. Commercial products for average wear on Earth are not tailored to the extreme conditions of open pit mining. The cone-shaped topography of the pit and near-zenith sun angles in regions of the global south lead to above average conditions in the pit. Similarly, high flight lines of the UAV	VNIR systems work well in hot conditions and the silicon CCD detector does not need to be cooled by liquid nitrogen as the SWIR MCT detector does (Lin <i>et al.</i> , 2009; Spragg, 2017). This makes their utilization more reliable in variable temperature conditions. Murphy <i>et al.</i> (2015) reported in-pit temperatures of >55 °C. Their SWIR system was utilized by additionally enclosing it in an insulated box and passing cold, desiccated air over it.

Influencing factor	Implication	Possible solution
	present below average temperatures for the sensors.	
<i>Sun angles of regions in the global South</i>	Sun angles increase towards the equator; regions close to the equator have higher overall sun angles throughout the year.	High sun angle can be an advantage when field scanning takes place in the deepest points of an open pit. Sun angle variation changes the illumination of walls in the periphery of the pit or different terrace levels. With a lower sun angle variance and shorter time ranges for sunrise and sunset, measurements have a limited time frame for optimum illumination. The end-user screens (e.g., of a GUI) need to well visible even in very reflective, sunny conditions.
<i>Variable incident light and illumination conditions</i>	Mine face scans in active open pit mining have to be acquired on flexible schedules. Acquisition times have to be coordinated with workforce availability, upkeeping safety measures and mine planning schedules. Taking measurements at ideal illumination conditions is secondary to the majority of mine planning parameters.	Classification algorithms must yield consistent results under changing illumination conditions (including shade and shadow and changing data acquisition times). Murphy et al. (2015) found that e.g., SAM is relatively insensitive to changing illumination and performs well also in variably shaded regions. Gaussian process observation angle dependent machine learning (GP-OAD) (Schneider <i>et al.</i> , 2011) was also proposed for the variable illumination. The BFF algorithm showed promising results for measurements with changing incident illumination.
<i>Precipitation</i>	Strong, regular precipitation events change the spectral signal surface of the material by adding non-mineral-bound water-based features.	Not only do precipitation events require different fast, reliable measurements in precipitation free periods, but they also require sensors that are either insensitive to water content regarding the spectral signal or sensors that suppress the water features in the collected spectral signal.
<i>Dust</i>	Machinery activity, deposit mineralogy and climate highly influence the amount of dust present in the air column between the mine face and the sensor.	Sensors need to be deployed during times of lower activity. Mine face scanning could be possible during night times with strong artificial illumination. Measurements have to be coordinate with other ongoing activities. Sensors need protective casing and spectrally inactive safety filters in front of the optical lenses. Murphy et al. (2015) used cooled, desiccated air to keep the lens and optics dust free. They did not find a way to account for the wind-blown dust in the air column between sensor and outcrop.

5.3.1 Data dimensionality reduction

In order to find the ideal compromise between mapping accuracy, sensor complexity, varying impact of atmosphere and illumination and computation time, the Brazilian iron ore data was downsampled to different, successively decreasing band numbers. The downsampled data either includes the full spectral range from approximately 400–2500nm, or additionally excludes the spectral area influenced highly by water related features (between 1300–2010nm) and was downsampled up to the point of only using the VNIR data range (400–1000nm).

As the new, tested sensors are only compared theoretically and downsampled from HySpex data, the minimum and maximum wavelength range of the VNIR and SWIR is dependent on the HySpex characteristics. The downsampling is tested based on the assumption, that with decreasing band numbers the data acquisition time and the computation times for processing and analysis likewise decreases. The same is assumed for the sensor size and cost, both will decrease with decreasing complexity (band number or exclusion of SWIR spectral range).

5.3.2 Downsampling of hyperspectral to superspectral (VNIR-SWIR)

Table 22 shows the entirety of the different downsampling approaches. The corresponding spectral library images, showing the decrease of spectral detail within the absorption features in the progressively downsampled data are shown in Table 56 in the Appendix, (p. 261). The downsampling approaches include sampling down the full wavelength range of the VNIR and SWIR to equal 1nm, 5nm, 10nm, 15nm, 20nm, 25nm, 30nm, 40nm, 50nm, 75nm, 100nm bandwidths and to the WorldView-3 (WV3) sensor characteristics with 16 bands (FWHM varies between 30 and 125 nm) and the EnMap sensor characteristics of 242 bands (FWHM varies between 5.7 and 14.4 nm). WorldView-3 and EnMap are satellite based sensors, that are operating and in design, respectively (Guanter *et al.*, 2015; euspaceimaging.com/about/satellites/worldview-3/, 2018). SAM and SVM analyses were used to compare the quality of the mapping for each of the sensors listed in Table 23. The MWL analysis of the AIOH feature between 2160 and 2220 was also performed to determine to which point of the downsampling analyzing the minimum wavelength position and depth could be performed. EnGeoMap 2.1 and BFF analysis was only performed on the downsampled data with bandwidths of 5nm, 10nm, 15nm, 20nm, 25nm, 30nm, 40nm and 50nm. The best performing sensors were then used in the second scenario in which the wavelength range influenced by atmospheric features was clipped out (1300–2010nm). In the last scenario, not only the range predominated by atmospheric water was clipped out, but the data with the best performing band width was analyzed and compared only taking the VNIR spectral range into account. A schematic overview of the downsampling from a field

Downsampling of hyperspectral to superspectral (VNIR-SWIR)

spectrum, a smoothing of the spectrum, downsampling to 15nm and 40nm bandwidth and the exclusion of the wavelength ranges impacted by the atmosphere is shown Figure 84.

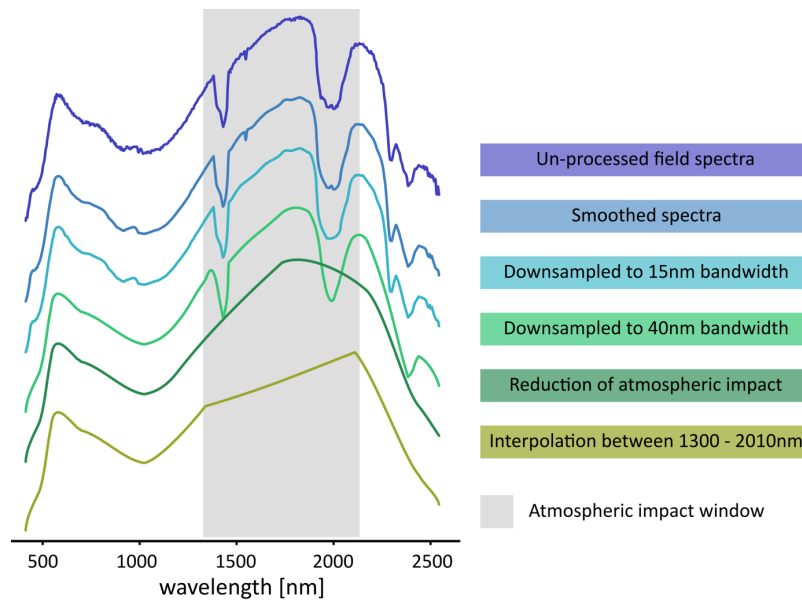


Figure 84 Schematic successive downsampling and band reduction including the exclusion of wavelength ranges impacted by the atmosphere (between 1300 - 2010nm).

Table 22 Downsampling approaches of the Brazilian iron ore samples.

Sensor / band width [nm]	Wavelength range [nm]	Number of bands	Analysis method for testing
1	414-2497	2084	SAM, SVM, MWL
5	414-2494	417	SAM, SVM, MWL, EnGeoMap 2.1, BFF
EnMAP	423-2493	242	SAM, SVM, MWL
10	414-2494	209	SAM, SVM, MWL, EnGeoMap 2.1 2.1, BFF
15	414-2484	139	SAM, SVM, MWL, EnGeoMap 2.1 2.1, BFF
20	414-2494	105	SAM, SVM, MWL, EnGeoMap 2.1 2.1, BFF
15, 1314 – 2004nm clipped	414-2484	94	SAM, EnGeoMap 2.1 2.1, BFF
25	414-2489	84	SAM, SVM, MWL, EnGeoMap 2.1, BFF
30	414-2484	70	SAM, EnGeoMap 2.1 2.1, BFF
40nm VNIR, 15nm SWIR, 1314 – 2004 nm clipped	414-2484	57	SAM, EnGeoMap 2.12.1, BFF
40	414-2494	53	SAM, SVM, MWL, EnGeoMap 2.1 2.1, BFF
50	414-2464	42	SAM, SVM, MWL, EnGeoMap 2.1 2.1, BFF
15nm VNIR only	414-1014	41	SAM, BFF, (EnGeoMap 2.1 unsuccessful)
40nm, 1334 – 2004nm clipped	414-2494	37	SAM, EnGeoMap 2.1 2.1, BFF
75	414-2439	28	SAM, SVM, MWL, EnGeoMap 2.1 2.1, BFF
100	414-2414	21	SAM, SVM, MWL, EnGeoMap 2.1 2.1, BFF
WorldView-3	425-2330	16	SAM, SVM, MWL, EnGeoMap 2.1 2.1, BFF
40nm VNIR only	414-1014	16	SAM, BFF, (EnGeoMap 2.1 unsuccessful)

Table 56 (Appendix, p. 261) presents the wavelength and FWHM characteristic of the successively downsampled data. Table 57 (Appendix, p. 265) list the different systematically downsampled sensors with their respective wavelength range, band numbers and the applied analysis methods.

5.3.3 Analysis of the superspectral VNIR+SWIR downsampled data

5.3.3.1 Hard-pixel classification based on spectral reference library

The downsampled data was analyzed using SVM, SAM, EnGeoMap 2.1 and BFF.

Table 23 lists the accuracies for SVM, SAM, EnGeoMap 2.1 and BFF. The computation times for SVM, EnGeoMap 2.1 and BFF were collected. The SAM analysis collectively took below 5s per scan and was not collected. EnGeoMap 2.1 and BFF were only utilized for the sensors with FWHM bandwidth between 5 and 50 nm.

Table 23 Accuracy and computation time of SVM, EnGeoMap 2.1 and BFF analysis and accuracies of the SAM analysis for the different theoretical sensors.

Sensor/ band width (nm)	no. of bands	SAM accuracy [%]	SVM time [s]	SVM accuracy (kappa) [%]	EnGeo Map accuracy	EnGeo Map time [s]	BFF accuracy [%]	BFF time [s]
1	2084	65.2	3361.8	82.4	-	-	-	-
5	417	65.2	775.1	82.4	48.7	765.8	60.5	2722.5
EnMAP	242	64.5	397.8	83.5	-	-	-	-
10	209	65.2	362.7	82.4	48.8	690.7	67.2	1425.4
15	139	65.1	254.9	82.4	48.9	654.1	70.3	1009.4
20	105	65.3	203.2	82.4	49.0	632.8	71.1	799.6
25	84	65.2	169.5	82.4	48.5	623.6	71.4	691.8
30	70	65.2	150.1	82.4	48.2	625.3	71.5	595.3
40	53	65.3	107.6	82.4	49.3	614.8	71.6	500.5
50	42	65.1	90.6	82.4	44.6	618.6	71.7	450.7
75	28	64.9	71.5	82.2	-	-	-	-
100	21	64.9	66.7	82.2	-	-	-	-
World View3	16	63.9	52.5	83.2	-	-	-	-

The accuracy of the different analysis methods for the different band numbers of the sensors can be seen in Figure 85.

Analysis of the superspectral VNIR+SWIR downsampled data

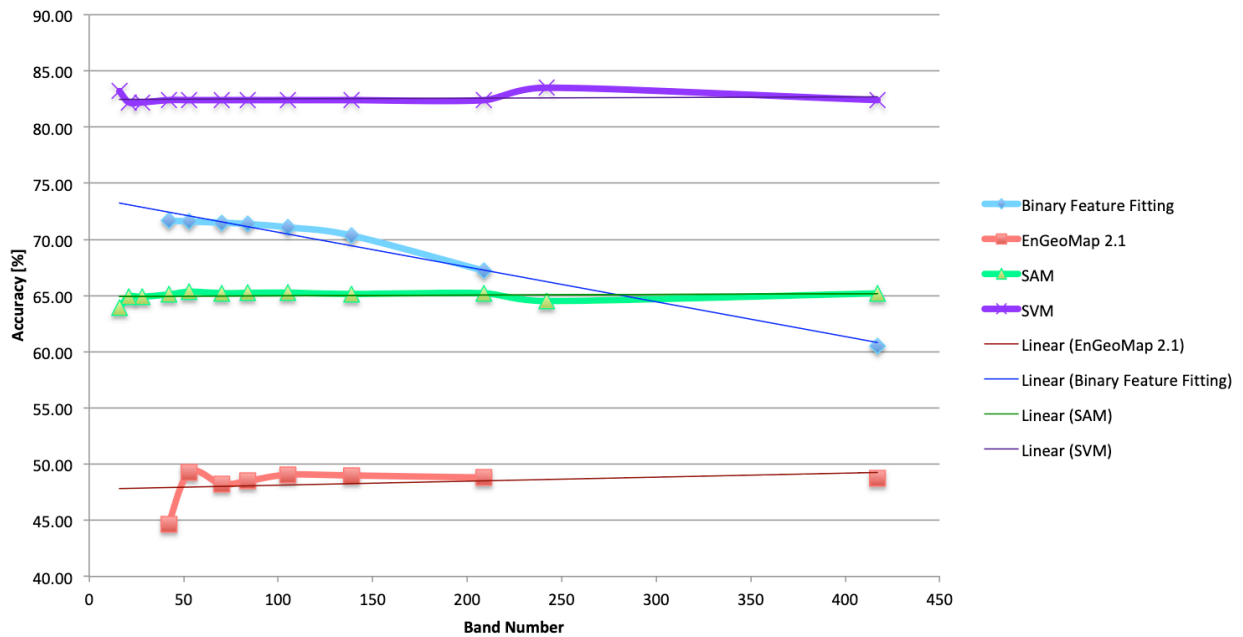


Figure 85 Band number vs. accuracy for SAM, SVM, EnGeoMap 2.1 and BFF.

The mapping accuracies of SVM and SAM are at an approximately constant level with increasing band numbers (from 16 to 2084 bands), around 83% and 65% respectively. SVM training time decreases from 3361.8s (1nm bandwidth) to 52.5s of training time for the WorldView-3 setting (16 bands) but the mapping accuracy (κ) increases from 82.4% to 83.2% respectively.

The BFF mapping results shows a slight increase in accuracies with decreasing band. The computation time for BFF decreases from 2722.5s and 60.5% of accuracy for 5nm bandwidth data to 450.7s and 71.7% of accuracy for 50nm bandwidths. EnGeoMap 2.1 peaks around 53 bands with an accuracy of 49% and stays consistent with increasing band numbers constantly at around 48%.

Figure 86 shows the correlation of computation time and increasing band number. The accuracy of the resulting map does not increase with band number and computation time for SAM, SVM and EnGeoMap 2.1. The BFF mapping accuracy decreases with increasing band number and computation time. A more detailed discussion of these results can be found in Section 6.2 (p. 172 -174).

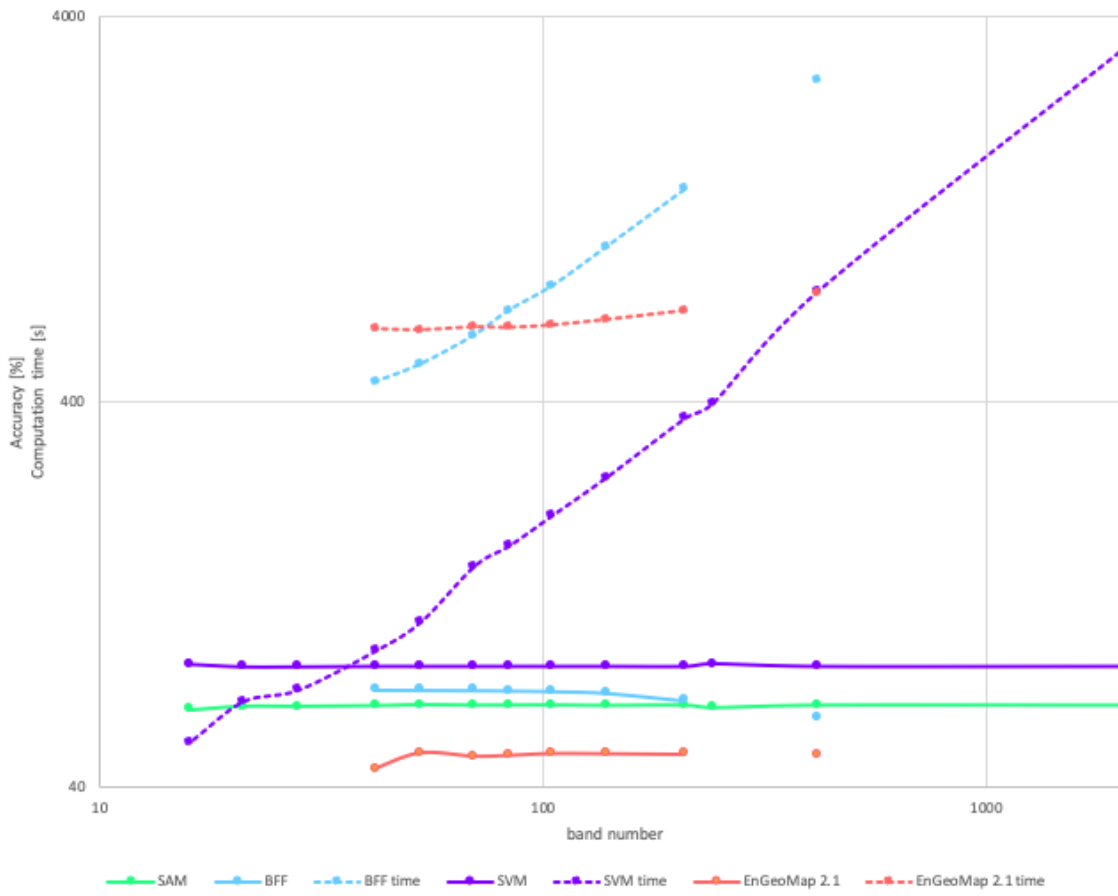


Figure 86 Accuracy and computation time with increasing band number. Note the logarithmic scale for both the band number and the accuracy [%] and computation time [s] sharing the y-axis.

To keep computation times reasonably low for all analysis methods, the downsampling to 53 equal bands with 40nm bandwidth each was determined as one of the optimal downsampling approaches for mining applications. Here the BFF computation time is reasonably low. With increasing band numbers, the BFF computation time outpaces that of the EnGeoMap 2.1.

5.3.3.2 *Hard-pixel classification based on MWL*

In order to compare how well the narrow, distinct features in the SWIR can be mapped, the MWL of the kaolinite feature was calculated with the HypPy Toolbox (Bakker and Oosthoek, 2020). The wavelength range between 2100–2230nm was analyzed to detect two spectral absorption features.

The literature on the wavelength position and range of AIOH spectral feature differs: Lypaczewski et al. (2020) suggest the range of 2195–2215nm for MWL mapping, (Lorenz *et al.*, 2018) uses the range of 2190–2215nm and Kirsch et al. (2018) uses an even broader range of 2160–2220nm. The target features for the Kaolinite feature for comparison were derived from Lypaczewski et al. (2020). Based on (Lypaczewski *et al.*, 2020) the kaolinite AIOH double feature has minimum wavelength positions for *feature 1* at 2205nm and for *feature 2* at 2156nm. Both features can be mapped distinctly until a

Analysis of the superspectral VNIR+SWIR downsampled data

bandwidth of 15nm. The feature positions for each sensor and the difference in regard to the target features (Lypaczewski *et al.*, 2020) are presented in Table 24. Figure 87 shows the change of minimum wavelength for both features with changing band numbers. Here, downsampling to 15nm wide bands in the SWIR showed to be the maximum amount of downsampling that still allowed the detection of two distinct absorption features for Kaolinite. Figure 88 then shows the wavelength position and feature depth mapping by MWL for the sensors with decreasing band numbers from 2084 to 105 bands (1nm to 20nm FWHM).

Table 24 MWL for the kaolinite feature with changing band number. "None" entries represent no possible detection of a feature by MWL. The offset of the detected feature position and the expected feature position is noted. Expected positions: Feature 1: 2205nm, Feature 2: 2156nm.

MWL 2100 – 2230nm	Sensor / band width (nm)	Band nr.	Feature 1 position	Feature 2 position	Feature 1 off target	Feature 2 off target
	1	2084	2206.63	2162.64	1.63	6.64
	5	417	2206.48	2163.19	0.48	7.19
	EnMAP	242	2206.21	2163.22	0.21	7.22
	10	209	2204.17	2164.43	1.83	8.43
	15	139	2201.12	2168.59	4.88	12.59
	20	105	None			
	25	84	2203.00	2175.81	3.00	19.81
	30	70	2201,68	None	4.32	
	40	53	None	2174.00	-	18.00
	50	42	None	2164.00	-	8.00
	75 and higher	28 and lower	None			

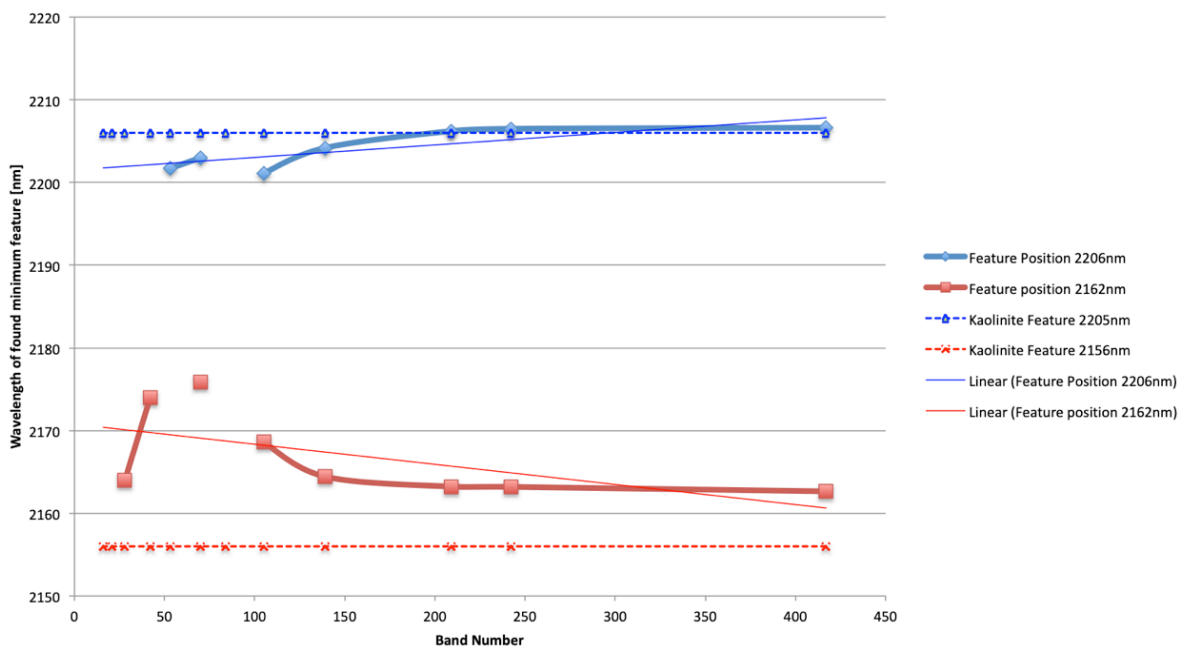


Figure 87 Wavelength position of the two detected kaolinite features with changing band number. Blue: position and linear trend of the position with changing band number for feature 1. Red: position and linear trend of the position with changing band number for feature 2

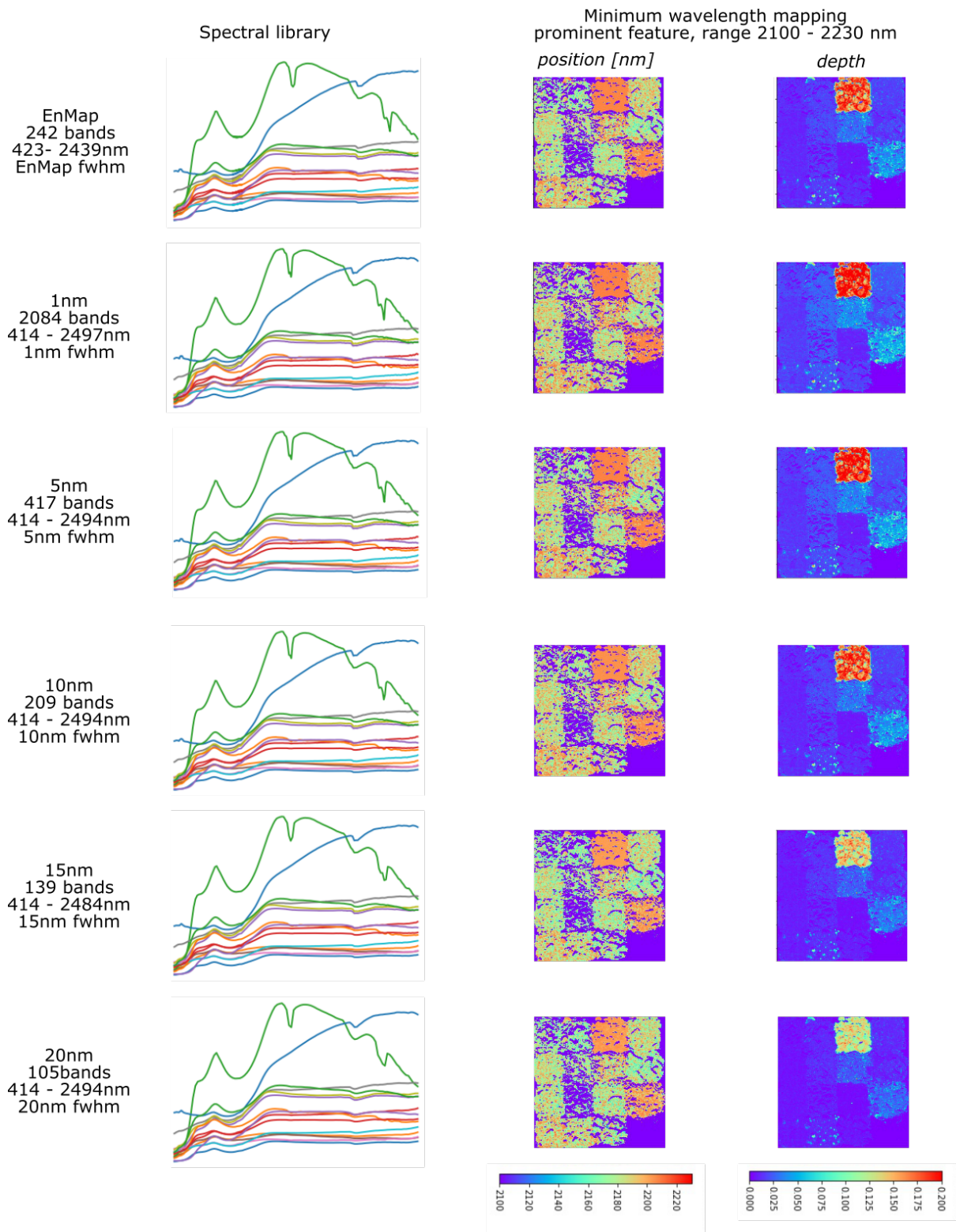


Figure 88 - MWL feature position and depth results and spectral library visualization for downsampled data with bandwidth between 10nm and 20nm. The spectra are shown schematically, the x-axis plots the wavelength [nm] from ca. 400 - 2500, and the y-axis plots the reflectance from 0-100%. The detected feature wavelength minimum position is stretched between 2100nm (blue) and 2220nm (red), and the feature depth stretches between 0 (blue) and 0.2 (red).

5.3.4 Excluding atmospheric features

Both, the mapping of materials and the mapping of wavelength positions of known features was shown successfully for ore-waste-discrimination in laboratory and even conveyor belt settings (Dalm *et al.*, 2014; Dalm, Buxton and van Ruitenbeek, 2017; Lypaczewski *et al.*, 2020). The conditions here were controlled and the samples have assumingly been stored for a sufficient time frame to not be influenced by surface water. It is assumed that the spectral features present in the spectral range of $\approx 1400\text{nm}$ and $\approx 1900\text{nm}$ are caused solely by mineral bound water. The features in the spectral range dominated by atmospheric absorptions include the slope between 1450–1850nm produced by ferrous iron and the absorption depth between 1900/ 2200nm to characterize crystallinity of white mica (Dalm *et al.*, 2014; Dalm, Buxton and van Ruitenbeek, 2017). Lypaczewski *et al.* (2020) uses absorption feature between the total wavelength range of $\approx 1450\text{--}2390\text{nm}$ to detect and classify mineralogy. In a laboratory or conveyor belt setting these predictors work well as the physical distance between the sensor and the sample are small and the air column in between is a negligible factor.

Mine face scanning on the other hand poses the challenge of up to 100m of air column between sensor and sample. Additionally, the influence of run-off and surface water on the rock will affect the material spectrum. The complexity of material distribution and water-run-off patterns increases from within one mine face to within multiple mine faces. The water surface content for one material does not only change spatially but also temporally (e.g., in the case of periodic precipitation events) and creates a high spectral variability of that same material.

So, in order to be able to avoid this influence on hyper- and hyperspectral mapping and still achieve sufficient results, the spectral range influenced by atmospheric absorptions ($\approx 1300\text{--}2010\text{nm}$) was clipped out completely for the 15nm and 40nm bandwidth data. Three different datasets were created and utilized for this purpose; these are:

- 1)** The dataset with 40nm wide band in a range of 414-2494nm was used and the wavelength range between 1314-2014nm was clipped, creating a dataset with 37 bands.
- 2)** The 15nm bandwidth dataset from 414-2484nm was utilized in order to detect smaller absorption features in the SWIR. Here, the wavelength range spanning from 1314-2004nm was clipped and a dataset of 94 bands in total was created.
- 3)** A dataset combining both sensors from 1) & 2) with 40nm wide bands from 414-1314nm and 15nm wide bands from 2004-2484nm. The range from 1314-004nm is excluded thereby creating a sensor with 57 bands.

5.3.5 Analysis of the VNIR+SWIR downsampled data (atmospheric band excluded)

The three sensors listed above were analyzed by SAM, EnGeoMap 2.1 and BFF. The BFF algorithm and SAM take the whole spectral shape into account for mapping, whereas EnGeoMap 2.1 automatically isolates distinct spectral features for characterization and comparison.

Again, all downsampled sensors with bandwidth from 5nm to 50nm are listed with their bandwidths and number of bands and their corresponding mapping accuracies (Table 25). Listing all sensors analyzed by SAM, EnGeoMap 2.1 and BFF is supposed to give a comparison of the analysis results (accuracies) of the full spectral range vs. the new sensors with a spectral range excluding the atmospheric bands.

Table 25 Sensors with bands from 417 - 37, including the sensors with clipped wavelength ranges influenced by the atmosphere ($\approx 1300 - 2010$ nm). The accuracies for SAM, EnGeoMap 2.1 and BFF are compared.

Bandwidth [nm]	Number of bands	Water band range excluded	SAM accuracy [%]	EnGeoMap 2.1 accuracy [%]	BFF accuracy [%]
5	417	No	65.19	48.71	60.52
10	209	No	65.21	48.79	67.20
15	139	No	65.15	48.99	70.34
20	105	No	65.26	49.05	71.08
15nm without atmosphere	94	1314 – 2004 nm	65.09	48.97	69.29
25	84	No	65.24	48.50	71.37
30	70	No	65.22	48.23	71.49
40nm VNIR, 15nm SWIR without atmosphere	57	1314 – 2004 nm	64.84	48.31	71.05
40	53	No	65.34	49.29	71.60
50	42	No	65.34	44.61	71.68
40nm without atmosphere	37	1314 - 2014 nm	65.41	48.28	71.15

Figure 89 shows the accuracy reached by all aforementioned sensors in Table 22 (p. 123). The sensors without atmospheric wavelength affects are the sensors with the band number 37, 57 and 94. It shows that excluding the atmospheric affected wavelength does not affect the SAM results and only slightly affects the results for the 94 bands data for the BFF analysis, resulting in 69.29% of overall accuracy, compared to 70.34% of accuracy for the full VNIR+SWIR range.

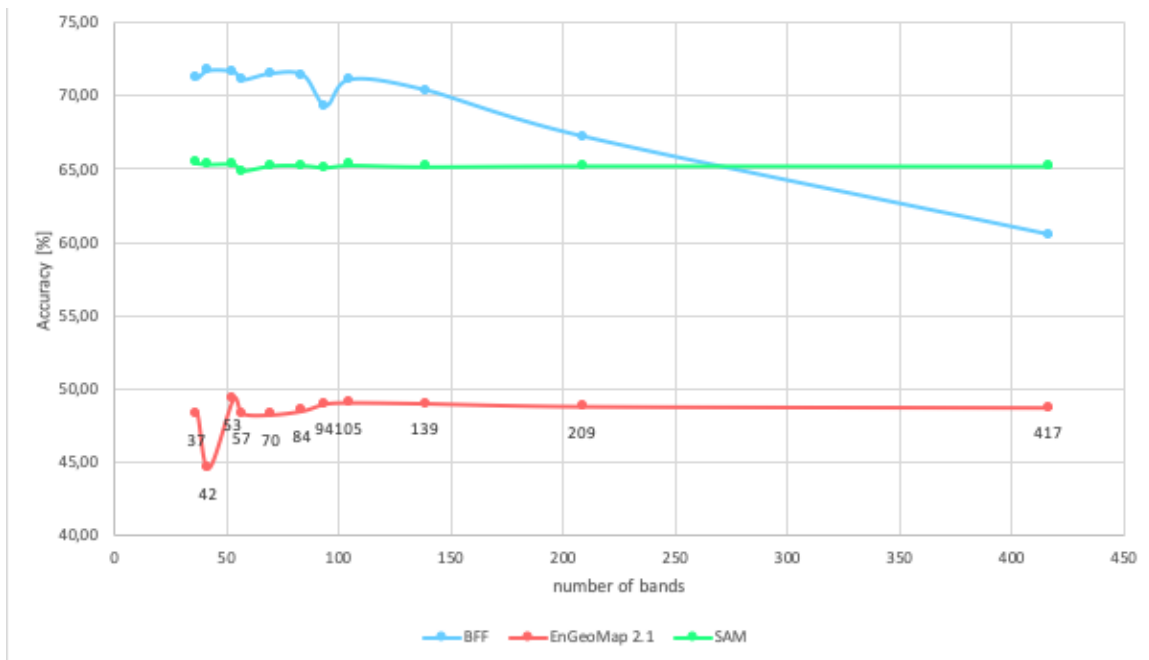


Figure 89 BFF, EnGeoMap 2.1 and SAM accuracies for sensors with systematically downsampled band numbers from 37 to 417, (excluding the results for the 242 bands EnMap sensor).

5.3.6 Downsampling to VNIR-only data

The results of the mapping accuracy for the sensors excluding the entire atmospherically affected wavelength range (between 1300 – 2010 nm) are promising enough to go a step further and exclude the whole SWIR range.

5.3.6.1 Reasons to exclude the SWIR sensor

As an example, the VNIR-1600 and SWIR-320m-e sensor characteristics of the HySpex are compared. Be aware, that with time both the price and size of the digital electronics will decrease further and the spatial resolution (number of pixels) will increase as generally observed for digital electronics by Moore's law. The SWIR-320m-e sensor is also more susceptible to temperature changes as it depends on a cooling with liquid nitrogen (Spragg, 2017) to stabilize the MCT detector performance to enable a high sensitivity and a high speed response. The HySpex SWIR-320m-e operates at FPA temperatures of 195K which is accomplished by 4 stage TE cooling (Lin *et al.*, 2009; boselec.com/wp-content/uploads/Linear/Vigo/VigoLiterature/BEC-Vigo-IR-Detector-Catalog-03-08-19.pdf, 2020). That increases the power consumption of the SWIR-320m-e to a factor higher than that of the VNIR-1600 (hyspex.no/products/disc.php, 2019). These key parameters are again summarized in Table 26. In short, the VNIR-1600-only setup allows for a lighter and smaller sensor with a lower power-consumption, higher tolerance towards temperature changes and a higher spatial resolution.

Table 26 HySpex VNIR - 1600 and SWIR - 230m-e sensor parameters from the HySpex User Manual (hyspex.no/products/disc.php, 2019; Körting, 2019).

Parameter	VNIR-1600	SWIR-320m-e
<i>Spectral Range</i>	400-1000nm	1000-2500nm
<i>Spatial Pixels</i>	1600	320
<i>Field of View (FOV) across track (y-dimension) for objectives (30 cm, 1 m lens)</i>	17°	14°
<i>FOV of FOV expander objective (> 10 m)</i>	34°	28°
<i>Detector</i>	Si CCD 1600 x 1200	HgCdTe 320 x 256
<i>FPA temperature</i>	N/A	195 K / -78.15°C
<i>Sensor head power consumption</i>	6 W	100W
<i>Sensor head weight</i>	4.6 kg	7.5 kg
<i>Sensor head dimension [cm]</i>	31.5 x 8.4 x 13.8	36.0 x 14.0 x 15.2

5.3.6.2 *Distinct spectral features in the VNIR and SWIR*

Excluding the SWIR range excludes the SWIR-only active minerals. To compare the importance of the SWIR response for different minerals, Table 58 and Table 59 in the Appendix (Section 10.11, p. 266) list the most common silicate and non-silicate minerals relevant to hydrothermal deposits with their VNIR and SWIR responses (Krupnik and Khan, 2019). Table 58 (p. 266) Table 59 (p. 268) in the Appendix underline the importance of SWIR features for the majority of the listed minerals. From this list, only iron rich minerals can be detected based on their diagnostic absorption features by VNIR-only data. A detection of materials rich in e.g., carbonates or phyllosilicates based on characteristic absorption features is only possible by including the SWIR. This infers, that to distinguish and map different materials in the VNIR-only data, only data-driven mapping approaches e.g., training-based methods like SVM can be utilized. Here, the whole deposit has to be characterized and “learned” in order to map and detect the materials of interest.

5.3.7 *Analysis of the VNIR-only downsampled data*

Table 27 shows the sensor characteristics of the VNIR-only sensors with bandwidth of 15 nm and 40 nm compared to the sensors with clipped atmospheric absorption feature wavelength ranges and compares their SAM, BFF and EnGeoMap 2.1 analyses results. The automated EnGeoMap algorithm was not able to perform the analysis and to create hard classifier maps. BFF dropped to approximately 68% of accuracy for both VNIR-only sensors, whereas SAM increased compared to the VNIR-SWIR system to approximately 68% of accuracy for both VNIR-only sensors. The SAM, BFF and EnGeoMap 2.1 mapping results are plotted in Figure 90 including the VNIR only sensors marked in bold.

Table 27 Accuracies of SAM, EnGeoMap 2.1 and BFF of the VNIR only sensors compared to the sensors with the clipped wavelength affected by the atmosphere ($\approx 1300\text{--}2010\text{ nm}$).

Bandwidth nm	Number of bands	SAM accuracy [%]	EnGeoMap 2.1 accuracy [%]	EnGeoMap 2.1 time [s]	BFF accuracy [%]	BFF time [s]
15nm w/o water band (1314 - 2004 cut), 94 bands	94	65.09	48.97	Unknown	69.29	717.14
40nm VNIR, 15nm SWIR w/o water band (1314 - 2004 cut), 57 bands,	57	64.84	48.31	682.40	71.05	493.94
15 nm VNIR	41	68.09	No results	No results	68.16	281.19
40nm w/o water band (1334 - 2014 clipped)	37	65.41	48.28	654.78	71.15	400.65
40nm VNIR only	16	67.67	No results	No results	67.71	424.9

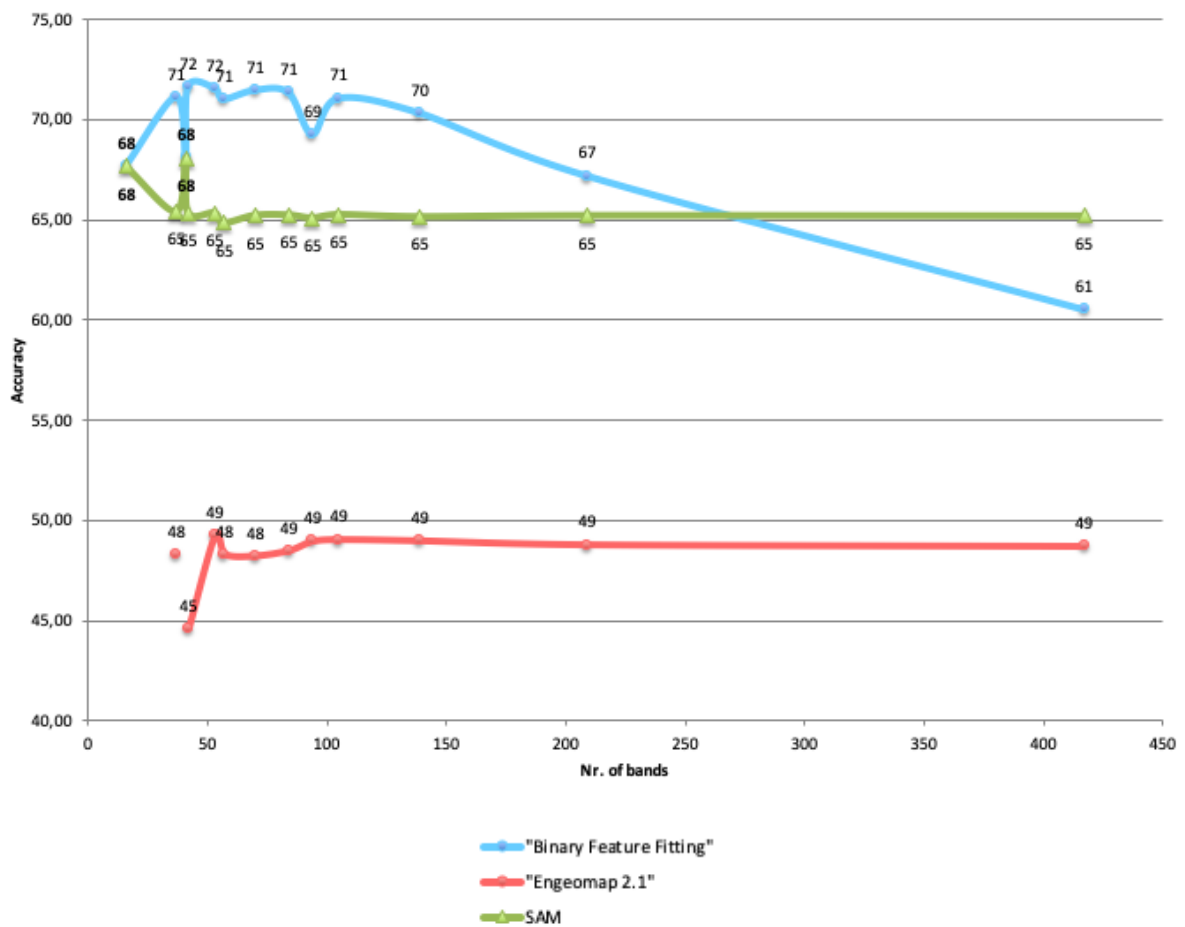


Figure 90 Comparison of the SAM, EnGeoMap 2.1 and BFF accuracies of all tested theoretical sensors.

Figure 91 visualizes the accuracy vs. the computation time for the analysis of *all* presented sensors with EnGeoMap 2.1 and BFF. Note, that EnGeoMap 2.1 was not able to analyze all of the datasets. The BFF analysis shows a constant increase in mapping accuracy and decreasing computation time with decreasing band numbers. The EnGeoMap 2.1 mapping accuracy and computation time appear nearly constant with decreasing band number up to 37. Below 37 bands, EnGeoMap 2.1 is not able to perform a mapping.

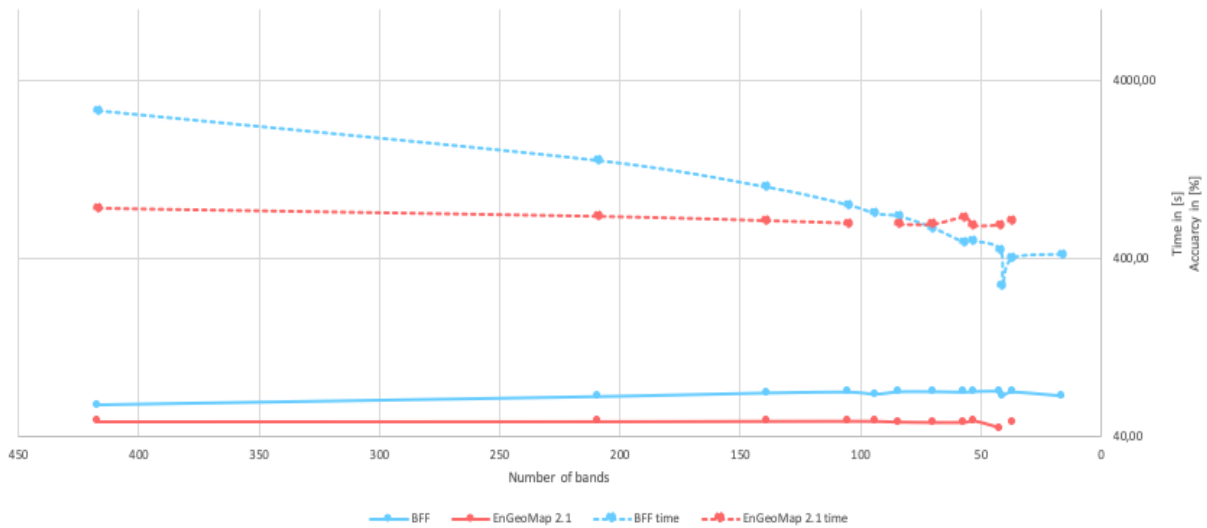


Figure 91 BFF and EnGeoMap 2.1 accuracy vs. computation times for all presented sensors. Time [s] (dotted line) and Accuracy [%] (continuous line) is logarithmically denoted on the y-axis

The resulting maps and corresponding spectral libraries of the mapping for the VNIR-only and atmospheric absorption-free sensors are shown in Figure 92.

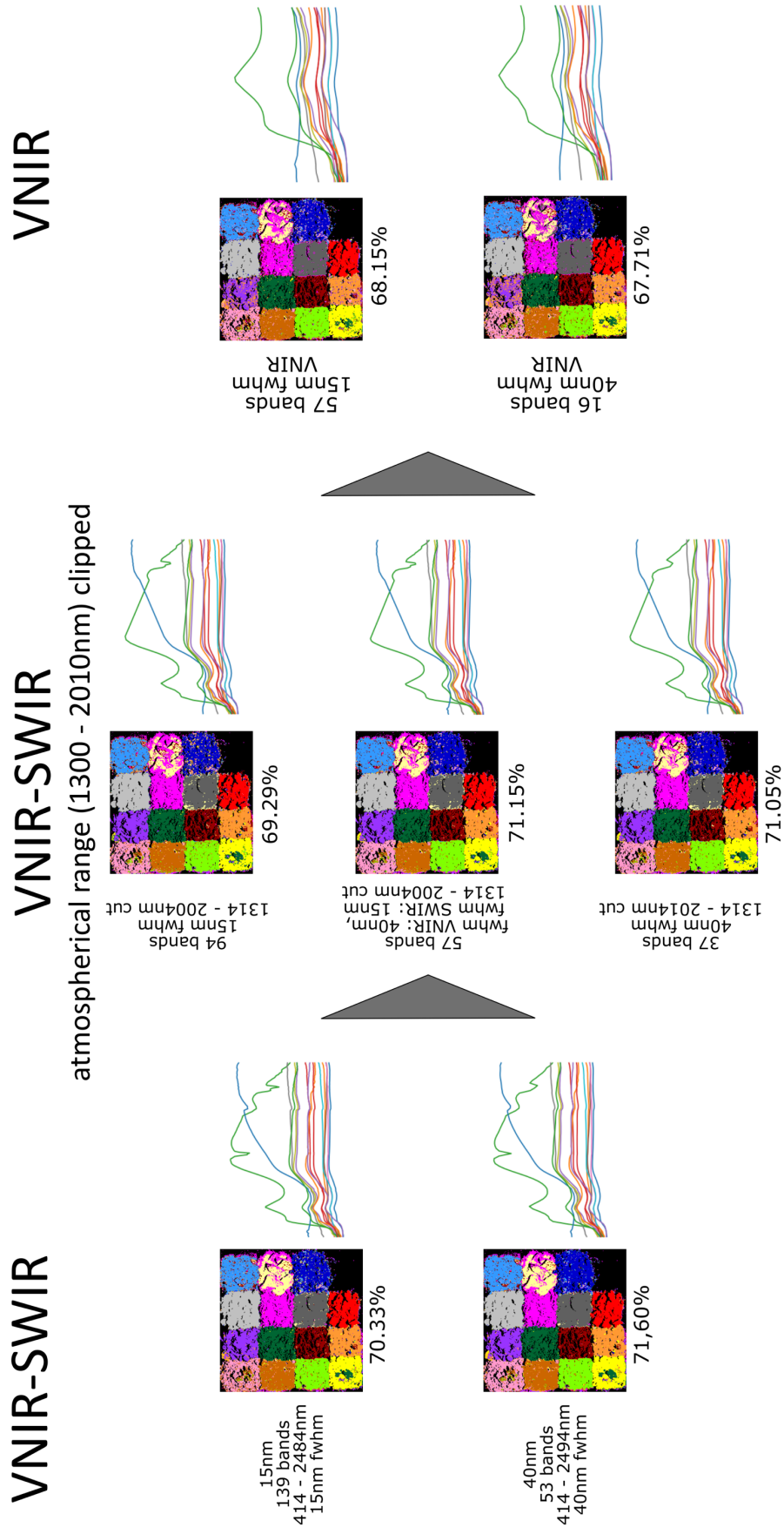


Figure 92 Spectral libraries and mapping results of the BFF analysis for the 15 nm and 40 nm full sensors (left, 414 – 2498nm), the 15 nm, 40 nm and 40 nm VNIR-15 nm SWIR sensors with the clipped wavelength range influenced by atmospheric absorptions (middle, 414 – 2498nm) and the two VNIR-only sensors with 15 nm and 40 nm bandwidth (right, 414 – 1000nm).

A detailed discussion of the presented results for the different robust sensors is presented in the “Discussion” Chapter (pp. 165 - 187).

Going forward, a total of five sensors were modeled for the subsequent analyses:

- 1) the “VNIR-only” sensor with a bandwidth of 40nm,
- 2) the “40nm VNIR – 15nm SWIR, without atmospheric bands” sensor (clipped and interpolated between the atmospherically influenced bands between 1300 – 2010 nm),
- 3) a modified “40nm VNIR – 15nm SWIR” sensor that includes the atmospheric bands in a bandwidth of 40nm. This sensor is able to represent the overall albedo and shape of the spectrum without being able to depict distinct, narrow bands between 1300 – 2010 nm.
- 4) The 400nm HySpex data to compare the mapping results to a validation and
- 5) data based on the WorldView-3 sensor model, in order to compare the results that would be achieved with a well-known satellite-based sensor.

5.4 III) Apliki Sample Data - Analysis of Laboratory Scans

The workflow parts I – II from Section 5.2 and 5.3, (pp. 97 - 136) is applied to the sample scan of the Apliki mine samples in Section V). The method is adjusted for the sample set and applied on the Apliki mine face scan. Mapping is tested for the laboratory reflectance dataset containing 36 samples and a laboratory radiance VNIR-only dataset containing a subset of eleven samples from full Apliki sample suite.

5.4.1 *Apliki mine sample – reflectance data*

The VNIR-SWIR reflectance data of the Apliki mine sample scans is analyzed first. In the following paragraphs, the samples are geochemically and spectrally clustered, a spectral library is compiled. The imaging spectroscopy data is downsampled, pre-processed and analyzed.

5.4.1.1 Geochemical clustering of sample data

Agglomerative bottom-up clustering (Murtagh and Legendre, 2011) of the sample geochemical data was performed in R Studio to identify clusters within the geochemical data of 36 samples and reduce the input spectra for the spectral library. The 36 samples are shown in Figure 93.

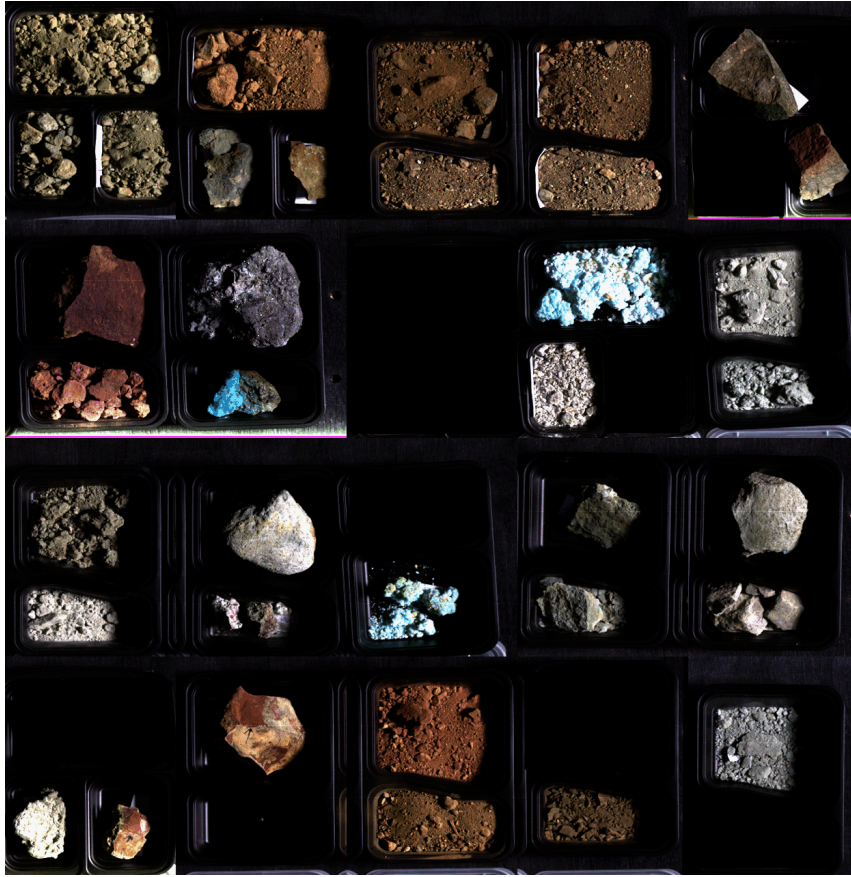


Figure 93 Hyperspectral scan of the Apliki samples showing all 36 samples used for geochemical clustering, spectral library extraction and analysis.

To compare the data, some geochemical results needed to be adjusted in order to be comparable. This applies to element or oxide content yielding below or above the detection limit. The geochemical values were adapted as seen in Table 60 in the Appendix (p. 269).

The ward.D2 method was utilized to minimize the total within-cluster variance. An optimal minimal cluster number of 7 clusters was determined to describe the geochemical variance of the data. The clusters are outlined in red in Figure 94. The full geochemistry of 36 samples was used for the clustering approach. Euclidian distance and the ward.D2 clustering method were applied to cluster 36 samples with a total of 21 different element and oxide concentrations for each sample.

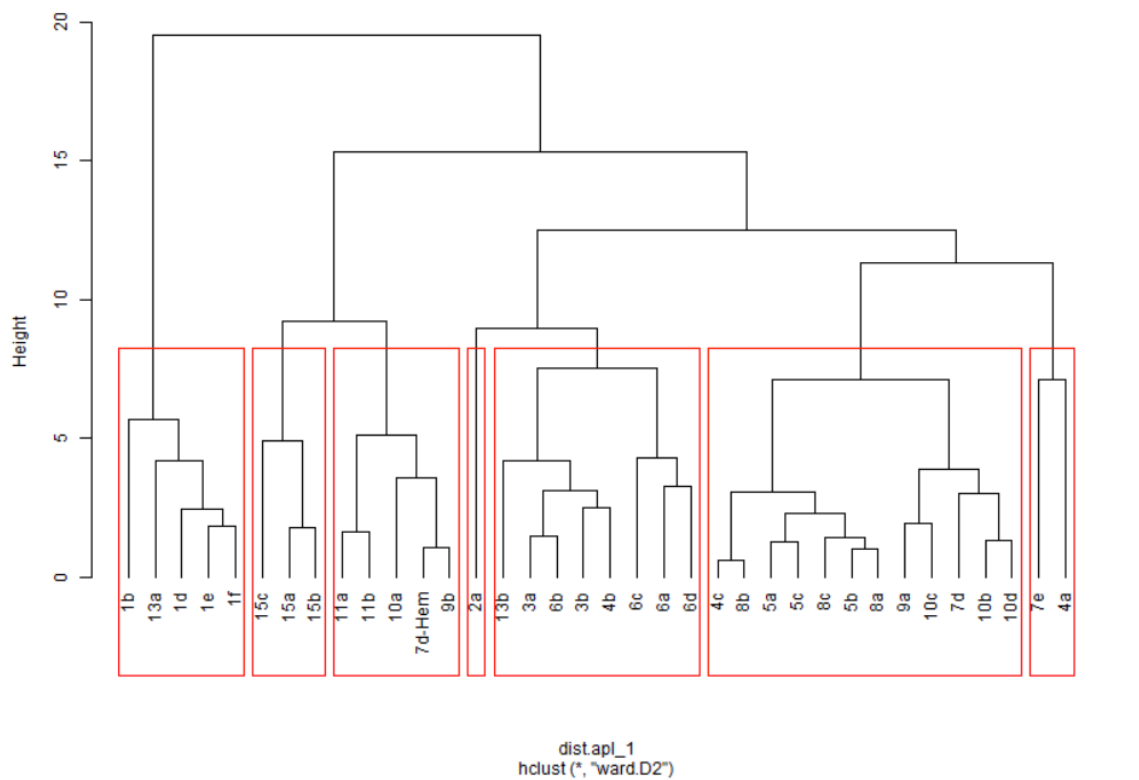


Figure 94 Bottom-up hierarchic cluster dendrogram for 7 clusters based on the full bulk geochemistry of 36 samples.

Figure 95 shows the hyperspectral sample scan color-coded for the determined geochemical clusters.

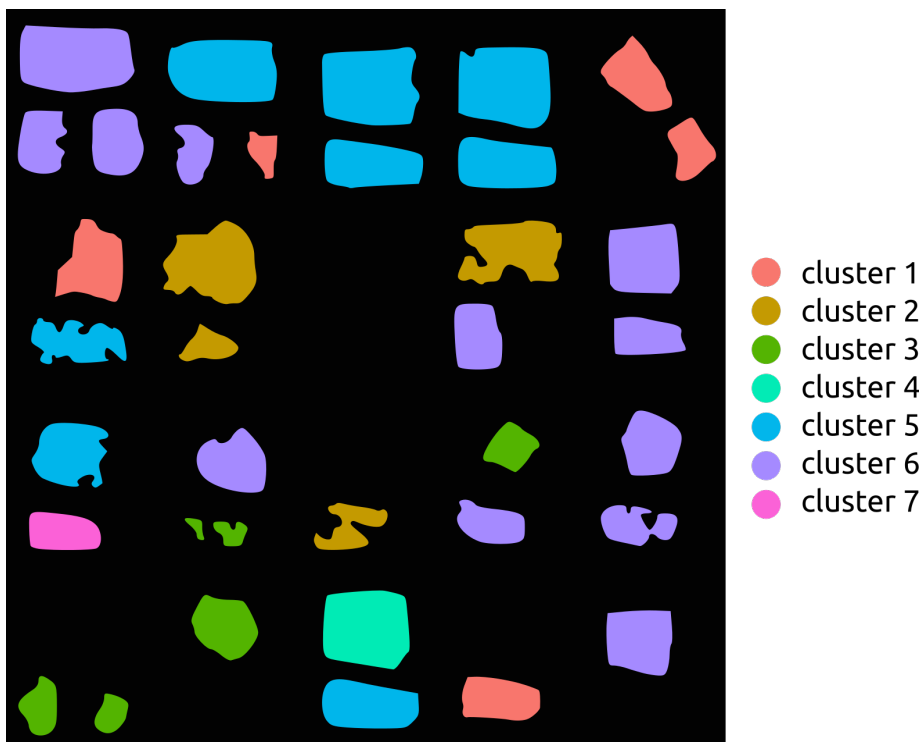


Figure 95 Geochemical clusters color-coded for the hyperspectral sample scan. 36 samples were clustered into 7 geochemically and spectrally distinct clusters.

5.4.1.2 *EM selection*

The sample spectra were compared and manually checked for each of the seven clusters. The spectra of the samples allocated within one *geochemical cluster* show enough spectral similarities to be also accepted as *spectral clusters*. The only exception from that is sample 7e. 7e was sorted into cluster 7 geochemically but its spectral expression is closer to the spectra found in cluster 2, it was therefore sorted to cluster 2 for the spectral library. This new cluster is now called “Spectral Cluster 2”. This re-clustering results in spectral cluster 2 including sample 15a, 15b, 15c and 7e and cluster 7 to be reduced to containing solely sample 4a. The other clusters remain unchanged. For the different spectral clusters see Figure 96.

The following spectral libraries were compiled:

- A spectral library was compiled containing all 36 spectra, one for each sample. Each spectrum in the subsequent classification is color-coded according to their cluster identity (Figure 96)
- A reduced spectral library was compiled containing representative spectra for each cluster. One to three spectra were determined visually and chosen for each cluster resulting in a spectral library of 11 sample spectra within 7 clusters (Figure 98)

The samples and their affiliation within each of the two spectral libraries and their cluster-identity and-color is listed in Table 28.

Table 28 Spectral libraries after geochemical clustering and visual spectral similarity assessment

Full spectral library (36 sample spectra)	Reduced spectral library (11 sample spectra)	Cluster + color-code
1b, 1d, 1e, 1f, 13a	1e, 1f, 13a	1
15c, 15a, 15b, 7e	15c, 15b	2
11a, 11b, 10a, 7d_hem, 9b	10a	3
2a	2a	4
13b, 3a, 3b, 4b, 6b, 6c, 6a, 6d	4b	5
4c, 8b, 5a, 5c, 5b, 8a, 8c, 9a, 10c, 10b, 10d, 7d	9a, 10d	6
4a	4a	7

All geochemical clusters are shown in Figure 96, including the associated sample spectra. The “spectral cluster 2” is shown in addition to highlight the spectral similarity between the samples 15a and 15b with sample 7e (formerly sorted into geochemical cluster 7)

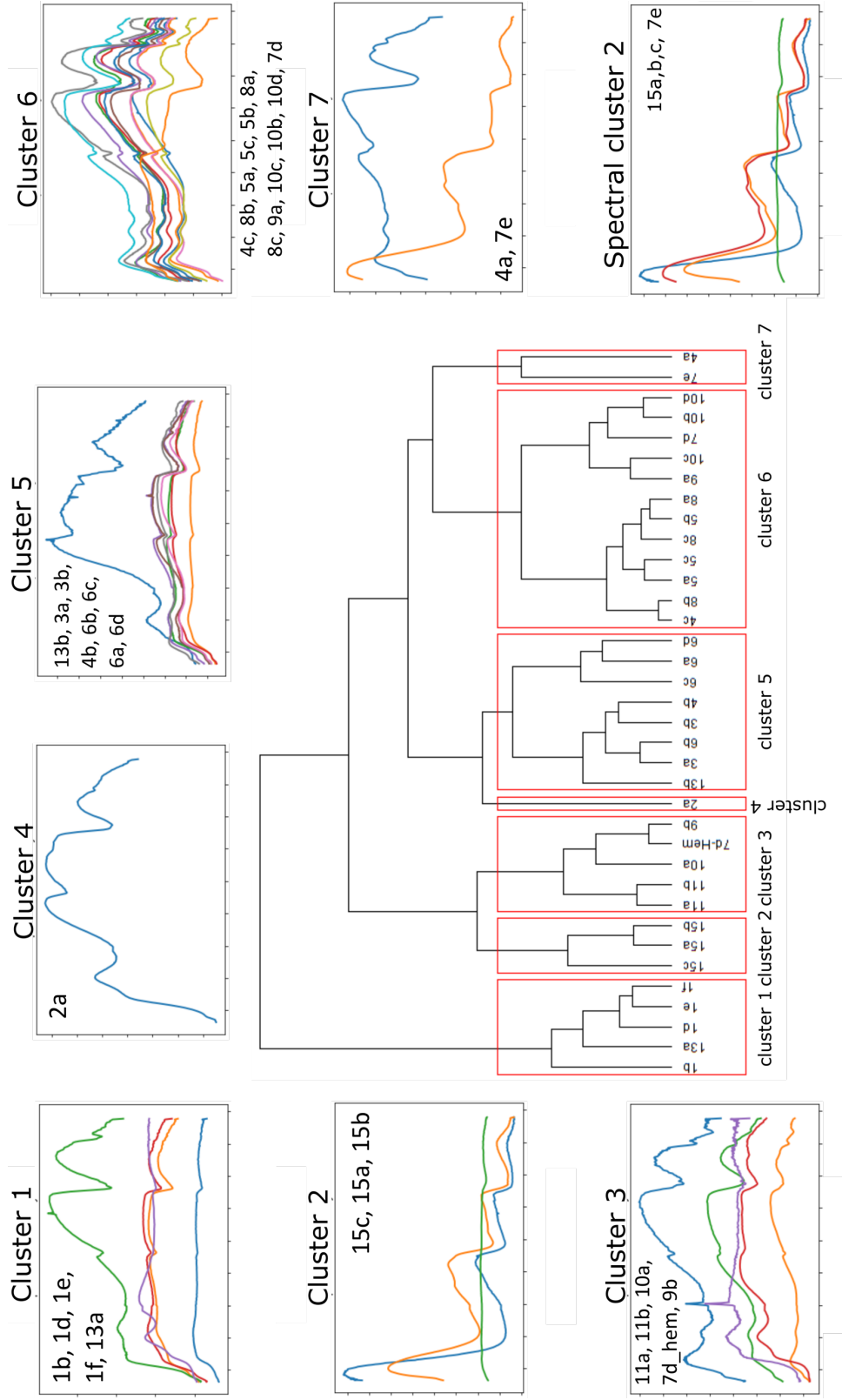


Figure 96 Bottom-up hierarchical dendrogram with 7 clusters for 36 samples, showing the samples and spectra allocated to each cluster. Cluster 1 – 7 show the geochemically determined clusters. “Spectral cluster 2” compares sample 15a, 15b, 15c, and 7e to show their spectral similarity. Cluster 7 is the geochemically determined cluster from which sample 7e was excluded and re-sorted to the “spectral cluster 2”. The spectra in each cluster are shown schematically, the spectral plot shows the wavelength on the x-axis (400-2500nm) and the reflectance on the y-axis.

The location of each sampling point within the outcrop spatial scale and its cluster-identity are shown in Figure 97.

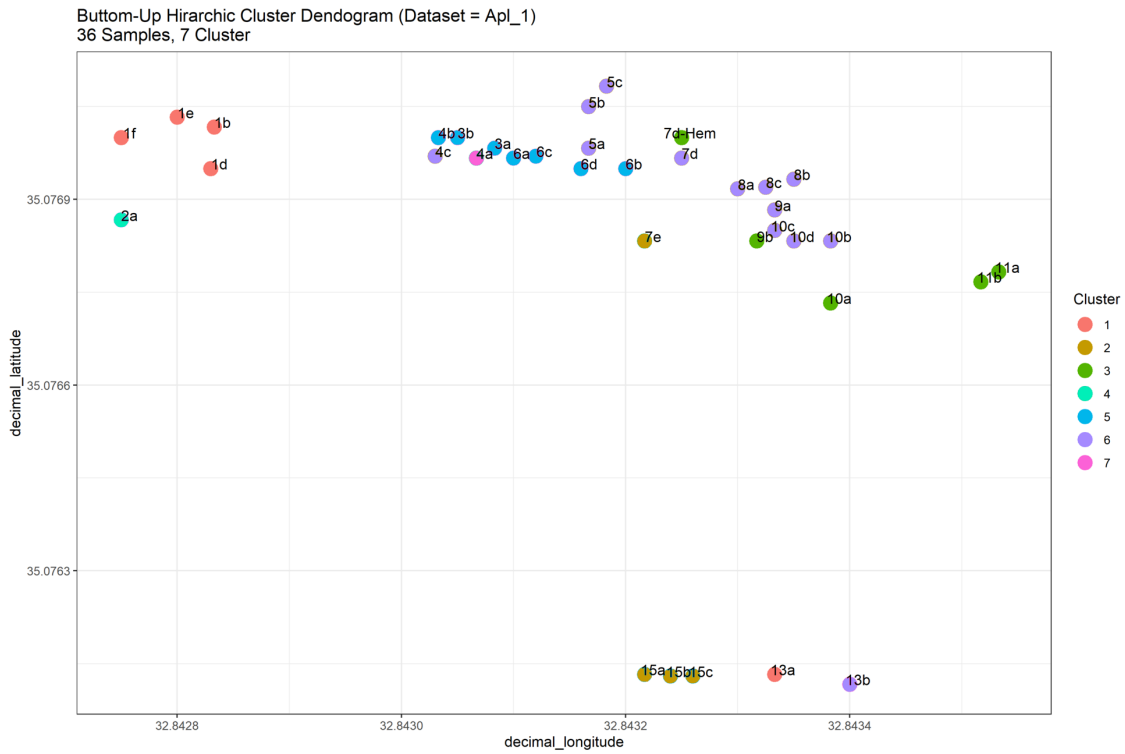


Figure 97 Sampling point location in decimal latitude and longitude and each sample points color-coding according to its cluster.

The reduced spectral library of 11 spectra within 7 clusters is shown in Figure 98.

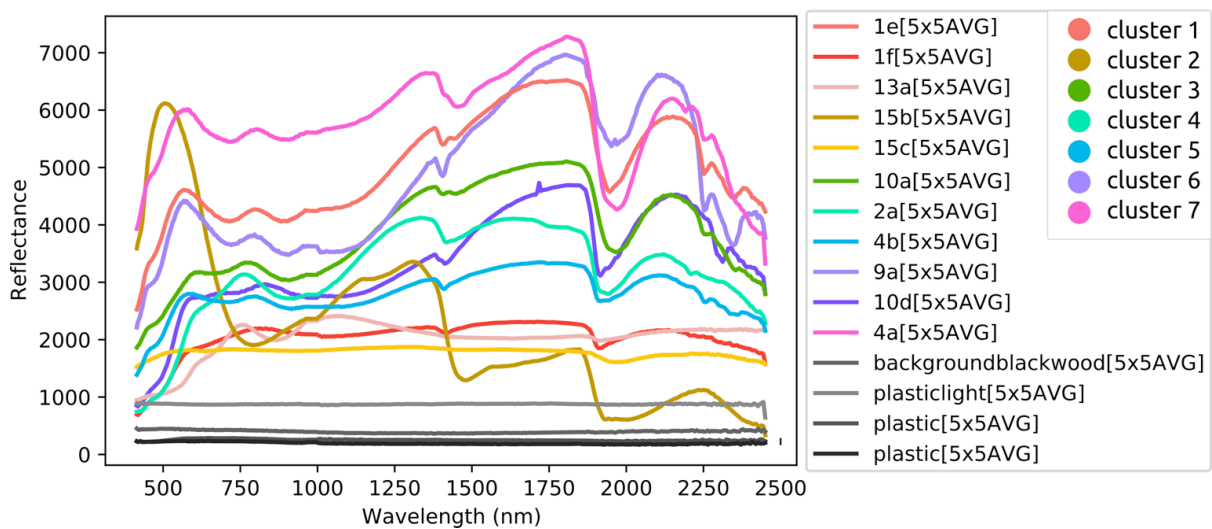


Figure 98 Spectral library based on geochemical and spectral clustering into 7 clusters with a total of 11 sample spectra and 4 laboratory "background" spectra.

The 6 geochemical clusters and the 7th spectral cluster can be validated through their geochemical and mineralogical composition. In the following paragraphs, the geochemical and spectral clusters are validated by their average geochemistry, mineralogy and by linking the 7 cluster to the different geological units and zones in the Apliki mine face described by Antivachis (2015). The XRD results are compared for each sample in one cluster and the dominant cluster mineralogy is defined. This average cluster geochemistry and dominant mineralogy is linked to the associated zones. To compare the geochemistry of each cluster, the geochemistry of the samples within a cluster were averaged. The geochemical average of the main components of each cluster is listed in Table 29 and Table 30.

Table 29 Average geochemistry of the samples in a cluster. Highest value per oxide and element, marked in grey. (Part 1)

Cluster	SiO ₂	Al ₂ O ₃	Fe ₂ O ₃	MgO	CaO	Na ₂ O	K ₂ O	TiO ₂	P ₂ O ₅
	%	%	%	%	%	%	%	%	%
Limit	0.01	0.01	0.04	0.01	0.01	0.01	0.01	0.01	0.01
1	49.14	16.34	12.07	4.84	6.36	2.94	0.73	1.06	0.10
2	44.78	2.31	13.00	3.28	0.08	0.08	0.01	0.12	0.00
3	81.10	3.89	6.61	3.23	0.49	0.05	0.00	0.08	0.04
4	40.72	8.00	31.22	2.67	0.75	0.31	0.67	0.38	0.20
5	40.79	11.58	15.68	4.54	2.14	0.70	0.69	0.50	0.04
6	44.25	12.91	12.62	11.33	0.57	0.06	0.01	0.30	0.00
7	33.97	10.29	10.62	9.96	8.00	0.22	0.02	0.24	0.01

Table 30 Average geochemistry of the samples in a cluster. Highest value per oxide and element, marked in grey. (Part 2)

Cluster	MnO	Cr ₂ O ₃	Cu	Zn	TOT/C	TOT/S
	%	%	%	%	%	%
Limit	0.01	0.002	0.0005	0.0005	0.02	0.02
1	0.14	0.00	0.07	0.01	0.15	0.07
2	0.10	0.01	1.00	0.06	0.02	16.48
3	0.03	0.01	0.10	0.05	0.01	1.28
4	0.24	0.02	0.17	0.05	0.04	2.98
5	0.12	0.02	0.19	0.06	0.05	2.45
6	0.11	0.02	0.08	0.03	0.01	1.16
7	0.35	0.01	0.04	0.36	0.12	6.56

Table 31 lists the dominant cluster geochemistry per cluster and links it to the associated geological units identified in Antivachis (2015). The mineralogical compositions of the samples in a cluster are listed in Table 32 and based on XRD measurements of the samples.

Table 31 Zonation based on Antivachis (2015), correlated with the predominant geochemical average of each cluster.

Cluster	Average cluster geochemistry relative to other clusters	Associated zones and geological units based on (Antivachis, 2015)
1	Highest TiO ₂ , Al ₂ O ₃ , Na ₂ O and K ₂ O content, high TOT/C content	Apliki pillow lavas (main magmatic minerals: iron- and titanium oxides, plagioclase, pyroxenes) and rarely olivine.
2	Highest Cu and TOT/S content	Disseminated sulfide ore, Cu-Fe sulfides and sulfates
3	Highest SiO ₂ content	Quartz veining, areas of silicification
4	Highest Fe ₂ O ₃ and P ₂ O ₅ content	Jasper veining/ amorphous silica, veins of massive mineralization (goethite, jarosite and natrojarosite as predominant minerals, Fe-Ti, Pb, Cu, and Zn oxides as accessories)
5	Medium content of all oxides and elements compared to other clusters, relatively high K ₂ O, Fe ₂ O ₃ , Al ₂ O ₃ and MgO contents	Clay minerals identified in Pillow Lavas and smectitic alteration zone dominated by montmorillonite and illite (both can not easily be distinguished as per Antivachis (2015))
6	Highest MgO content, relatively high Fe ₂ O ₃ content, low K ₂ O	Chloritic stockwork zone
7	Highest CaO, MnO and Zn content, relatively high MgO and TOT/S, medium MgO and Fe ₂ O ₃ , lowest SiO ₂	Gypsum mineralization indicated by high CaO and TOT/S and weathering products from overlying oxidized zone

Table 32 Apliki mine sample clusters, associated sample IDs and cluster mineralogy.

Cluster	Samples	Cluster Mineralogy
01	1b, 1d, 1e, 1f, 13a	Quartz, Plagioclase Feldspar (Andesine, Anorthite), Pyroxene (Diopside), Smectite-group: Montmorillonite, Fe-Oxide: Magnetite, Sulfide: (Pyrite (Fe, one sample only)); <i>Dominated by: Plagioclase and Montmorillonite.</i>
02	15c, 15a, 15b, 7e	Quartz, Fe-Oxide: Goethite, Sulfides (Cu, Fe, CuFe): Covellite, Pyrite, Chalcopryrite, Sulfates (Cu, Fe, Mn-Al, Mg): Chalcantite, Ferroxhydrite, Apjohnite, Rozenite, Pentahydrate (cuprian); <i>Dominated by: Quartz, Sulfates and Sulfides, Fe-Hydrate (7e)</i>
03	11a, 11b, 10a, 7d_hem, 9b	Quartz; Fe-Oxide: Goethite; Sulfides (Cu): Pyrite; Sulfates (Cu, Zn-Fe): Gypsum, Bassanite, Sphalerite; Chlorite group: Clinochlore; <i>Dominated by: Quartz (+ Chlorite-group (sample 11a, 11b))</i>
04	2a	Fe-Oxide: Goethite; Sulfate (K-Fe): Jarosite-Natrojarosite; Quartz; Plagioclase Feldspar (Andesine); Chlorite Group: Clinochlore; <i>Dominated by: Sulfates</i>
05	13b, 3a, 3b, 4b, 6b, 6c, 6a, 6d	Quartz; Plagioclase (Andesine, Anorthite); Analcime; Pyroxene (Diopside); Smectite-group: Montmorillonite; Fe-Oxide: Goethite, Magnetite; Sulfate (K-Fe, Ca): Jarosite, Gypsum; Chlorite-group: Clinochlore; Sulfide (Fe): Pyrite; <i>Dominated by: Clays, Smectite-chlorite group</i>
06	4c, 5a, 5b, 5c, 8a, 8b, 8c, 9a, 10b, 10c, 10d, 7d	Chlorite-group: Clinochlore; Smectite-group: Montmorillonite; Sulfate (Ca, Mg): Gypsum, Hexahydrite; Quartz; Sulfide: Pyrite; Fe-Oxide: Goethite; Ajoite (minor copper ore, silicate hydroxide); <i>Dominated by: Chlorite-group</i>
07	4a	Sulfate (Ca, Fe): Gypsum, Rozenite; Quartz, Chlorite-group: Clinochlore; <i>Dominated by: Gypsum</i>

The mineral assemblages found for each sample in a cluster correlated well within a cluster and can be seen as a cluster-coherent mineral assemblage. The diffractograms of each sample can be found in the Appendix (Section 10.5, p. 217).

The average geochemistry, the cluster-coherent mineralogy and the possible linkage to the geological units and zones described in Antivachis (2015), confirm the 7 geochemically and spectrally defined clusters. These spectral clusters are utilized further for the spectral library-based mapping. For mapping, each spectrum is color-coded according to its cluster-identity.

5.4.1.3 Data preparation

The reflectance data derived from the pre-processing routines by Rogass et al. (2017) was corrected as described in Section 4.2 (p. 75) A total of five sensors were modeled for the subsequent analysis. The data was downsampled to two sensors identified as being well suited for open pit mining applications: the “VNIR-only” sensor with a bandwidth of 40nm and the “40nm VNIR – 15nm SWIR, without atmospheric bands” sensor (clipped and interpolated between the atmospherically influenced bands between 1300–2010nm). A third sensor was included, as modified “40nm VNIR – 15nm SWIR” sensor that includes the atmospheric bands in a bandwidth of 40nm. This sensor is able to represent the overall albedo and shape of the spectrum without being able to depict distinct, narrow bands between 1300–2010nm. As a fourth sensor, the full 400nm HySpex data was used for a comparison for mapping. WorldView-3 is included as a fifth sensor model, in order to compare with a well-known satellite-based sensor. The data specifications are listed in Table 33. Figure 99 shows the spectrum of sample 1e and 15b for each of the sensors used for the different classification approaches.

Table 33 Sensor specifications for the five datasets classified and compared of the Apliki sample laboratory data, sorted by descending band numbers.

Sensor	Wavelength range [nm]	Band number	FWHM VNIR [nm]	FWHM SWIR [nm]
<i>HySpex</i>	414–2450	400	3.6	6.0
<i>40nm VNIR - 15nm SWIR</i>	414–2439	70	40.0	40.0 (974-2004nm) 15.0 (2004-2439nm)
<i>40nm VNIR – 15nm SWIR, atmospheric bands clipped</i>	414–2439 clipped and interpolated 1334–2004 nm	54	40.0	15.0
<i>40nm VNIR-only</i>	414–1014	16	40.0	-
<i>WorldView-3</i>	425–2330	16	40.0–125.0nm	30.0–70.0nm

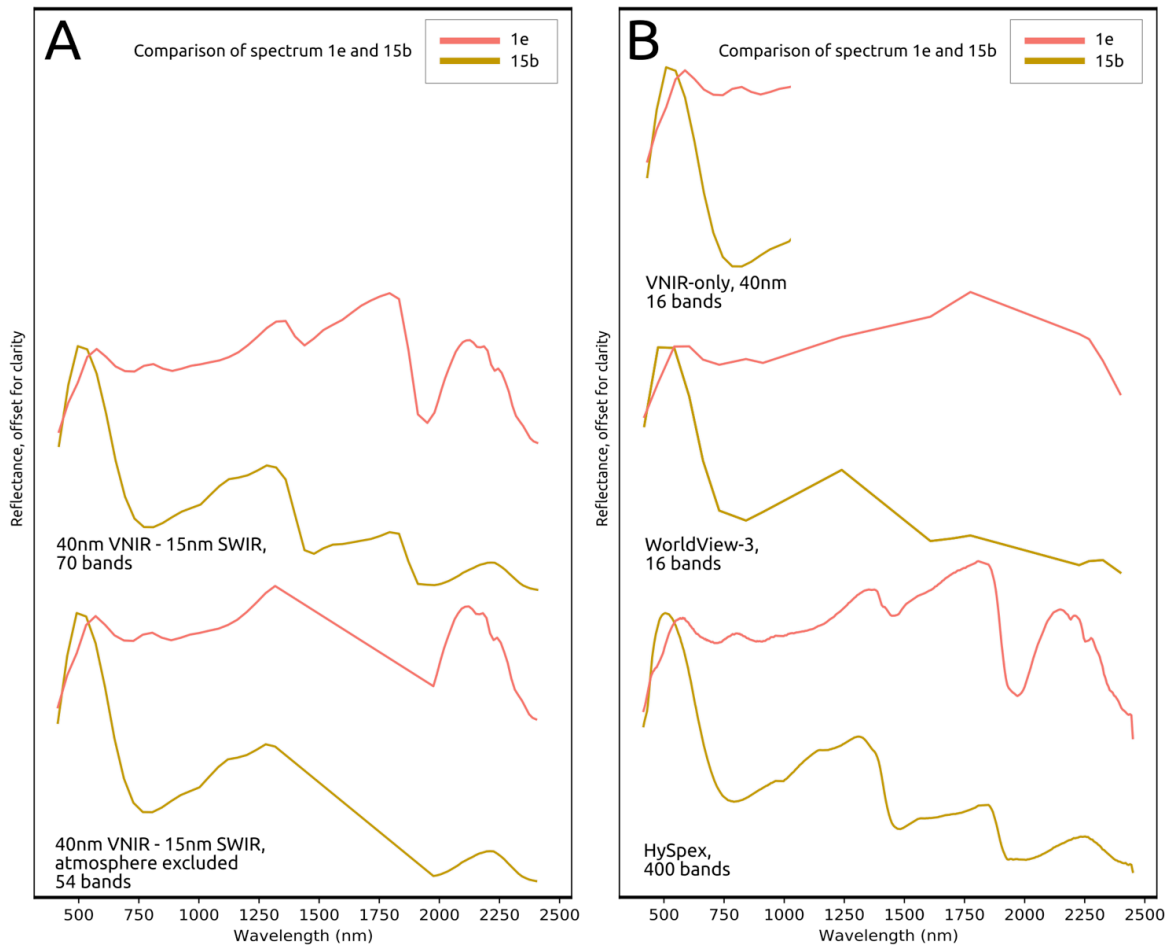


Figure 99 Comparison of spectra 1e and 15b showing their spectral shape for the five different sensors. A: 40nm VNIR and 15nm SWIR with and without clipping and interpolating the spectral range influence by atmospheric absorptions (1300–2010nm), B: VNIR-only 40nm sensor, WorldView-3 and HySpex

5.4.1.4 Analysis and classification

The spectral scan was analyzed with SAM, BFF and the standard SVM from the DeepHyperX toolbox (Audebert, 2020). For SAM and BFF, the data was analyzed with the 36 samples spectra- and the 11 samples spectra- spectral library each. The resulting mapping accuracies are plotted in Figure 100. The SAM, BFF and SVM analysis parameters are described in Sub-Section 5.2.3.10 (p. 109).

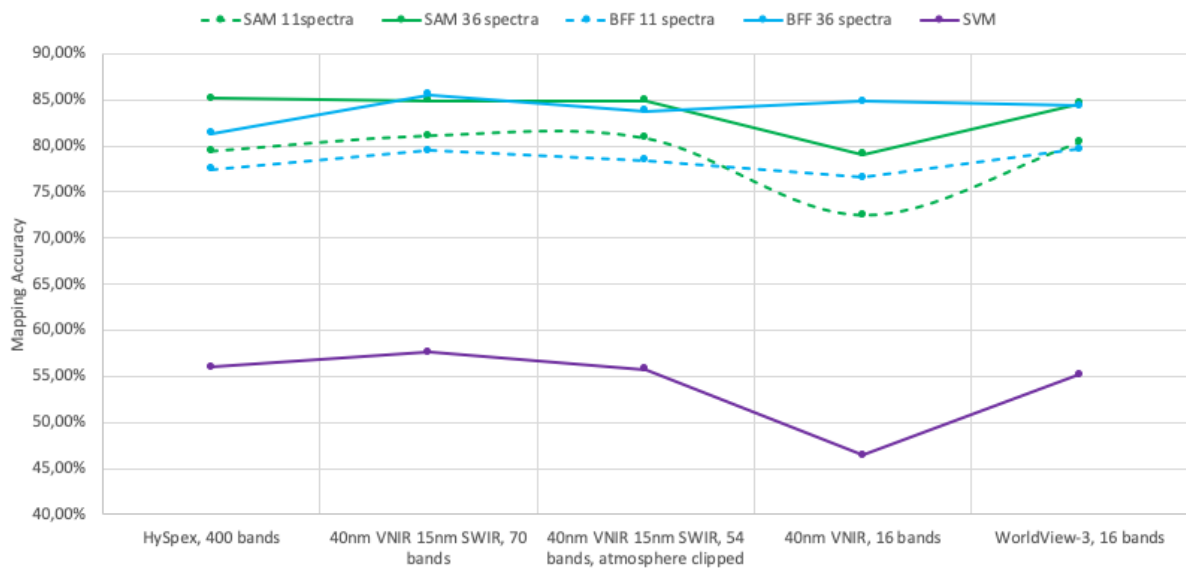


Figure 100 Apliki sample scan classification accuracies for five different sensors and three different classification algorithms (SAM, BFF and SVM).

Figure 101 present the computation times for each sensor, note the logarithmic scale of the y-axis.

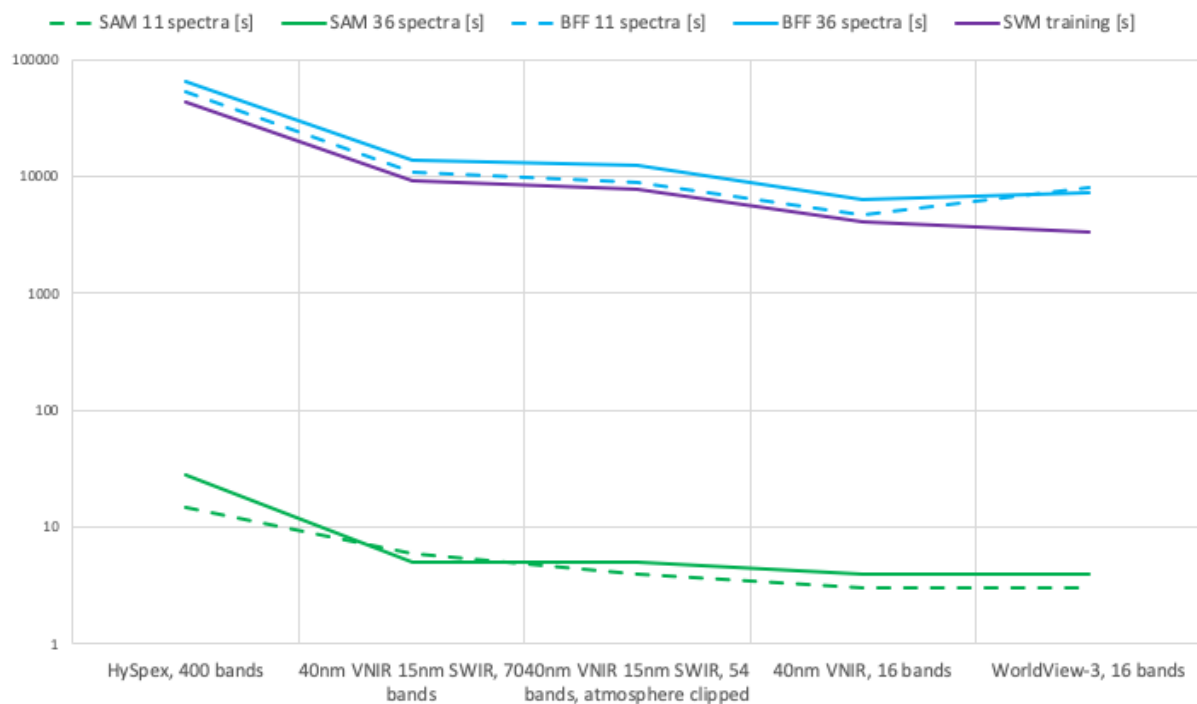


Figure 101 Computations times plotted for each sensor for the Apliki sample dataset.

The mapping results are shown in Figure 102 with the mapping accuracies. The maps are compared to the color-coded validation.

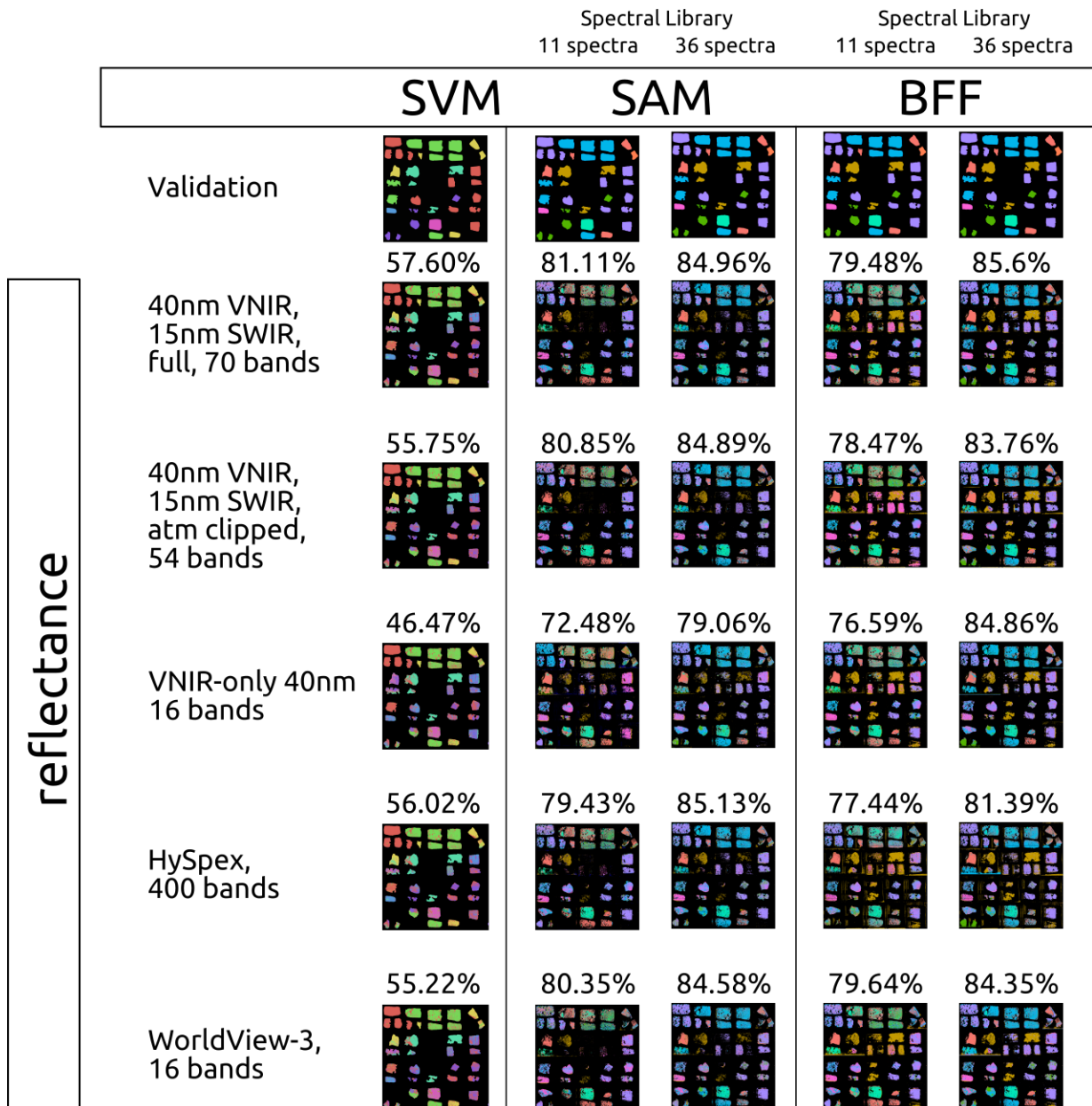


Figure 102 Mapping of 36 Apliki mine sample reflectance data. 1st column: validation image, 2-6th column: classification results for the five different sensors. Left to right: SVM, SAM 11 sample spectra, SAM 36 sample spectra, BFF 11 sample spectra, BFF 36 sample spectra.

Comparing the mean classification accuracies depicted in Figure 102 for the two different libraries, the underperformance of the results from the reduced spectral library (11 samples) becomes apparent. Based on this comparison, the library with the 36 sample spectra was utilized for the following mine face scan analysis. A detailed discussion of the results presented here can be found in Chapter 6, p. 165.

5.4.2 Apliki mine sample – radiance data

5.4.2.1 Data preparation

To test the comparability of the radiance signal of the 11 samples identified for the reduced spectral library, a VNIR radiance data set was compiled for these samples. A data set of the dimensions 1200x1290 pixel was created in the wavelength range of the VNIR from 414–993nm. The original radiance VNIR HySpex data has a spatial resolution of 160 bands with bandwidths of 3.6nm. This original radiance data was downsampled to 15 bands, 40nm bandwidths data. SAM and BFF were utilized for mapping. The RGB of the VNIR radiance dataset and the location of spectra extraction for the spectral library are shown in Figure 103. Eleven spectra were extracted from a 15 x 15 pixel average, one spectrum for each sample, and four background spectra (of the WR panel, the plastic and white paper showing underneath samples). All spectra are shown in Figure 104. The color-coding of the spectra and results is the same as for the 7 clusters identified in Sub-Section 5.4.1, p. 136.

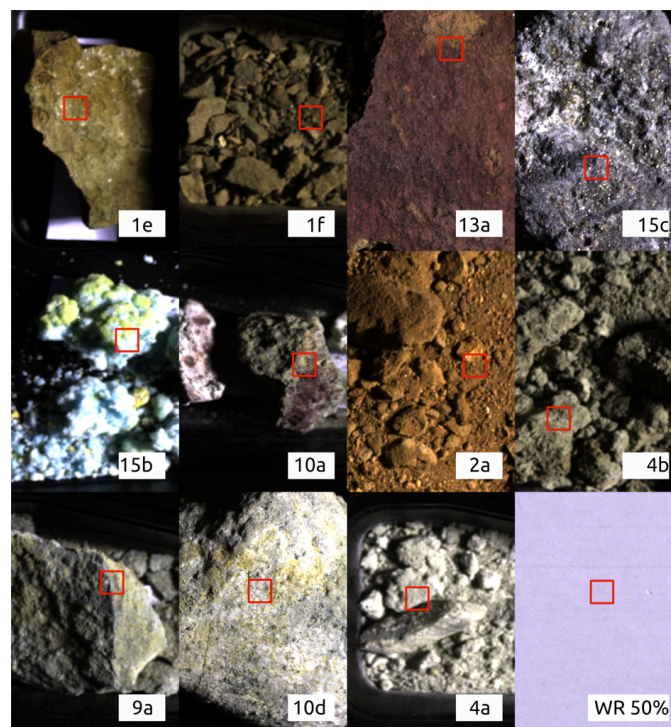


Figure 103 Compiled radiance data set of eleven samples and a 50% white reference panel. Red rectangles mark the area of spectra extraction for the spectral library.

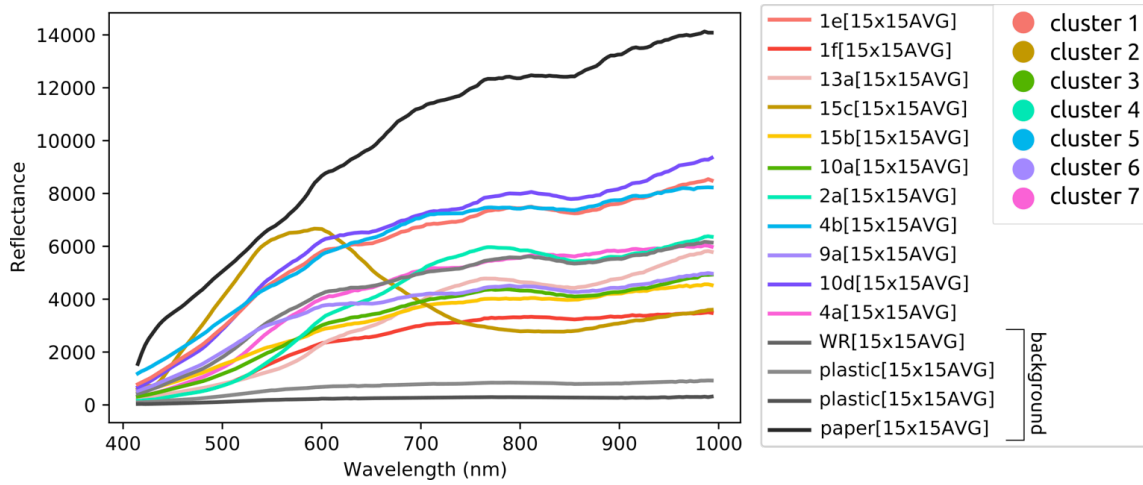


Figure 104 Radiance sample spectra for 11 Apliki mine samples.

5.4.2.2 Analysis and classification

SAM and BFF were performed for the 160 bands “HySpex-VNIR rad” and the 15 bands “40nm-VNIR rad” data. The classification maps and accuracies are shown in Figure 105. The mapping accuracies differ between classes and show an overall higher accuracy for the 40nm downsampled data (SAM: 62%, BFF: 68%) compared to the original HySpex data (SAM: 60%, BFF: 32%).

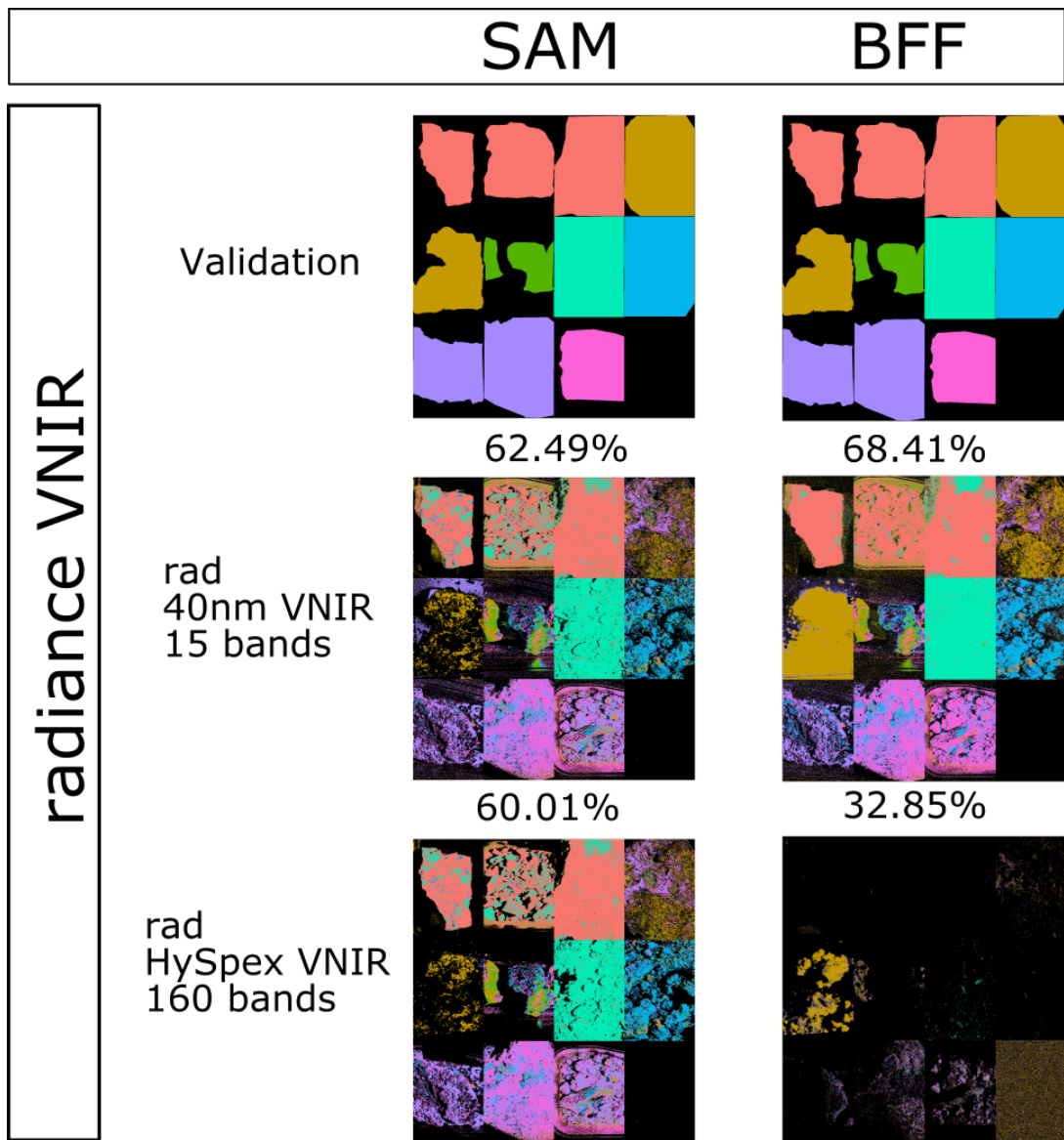


Figure 105 VNIR radiance data analysis with SAM and BFF for HySpex 160band (bottom) and 40nm-bandwith 15band data (center) compared to a validation image containing color-coded ROIs (top).

5.5 IV) Proposed field workflow related to Apliki mine

For the field data, the methods applied in Section I – III) are utilized for the Apliki mine face scan data. In the Materials Chapter, Sub-Section 3.5.4, pp. 60 - 70 the HSI field data acquisition, processing and the field sampling was described in detail. A workflow scheme from data acquisition to the mapping results of the mine face data is presented Figure 106.

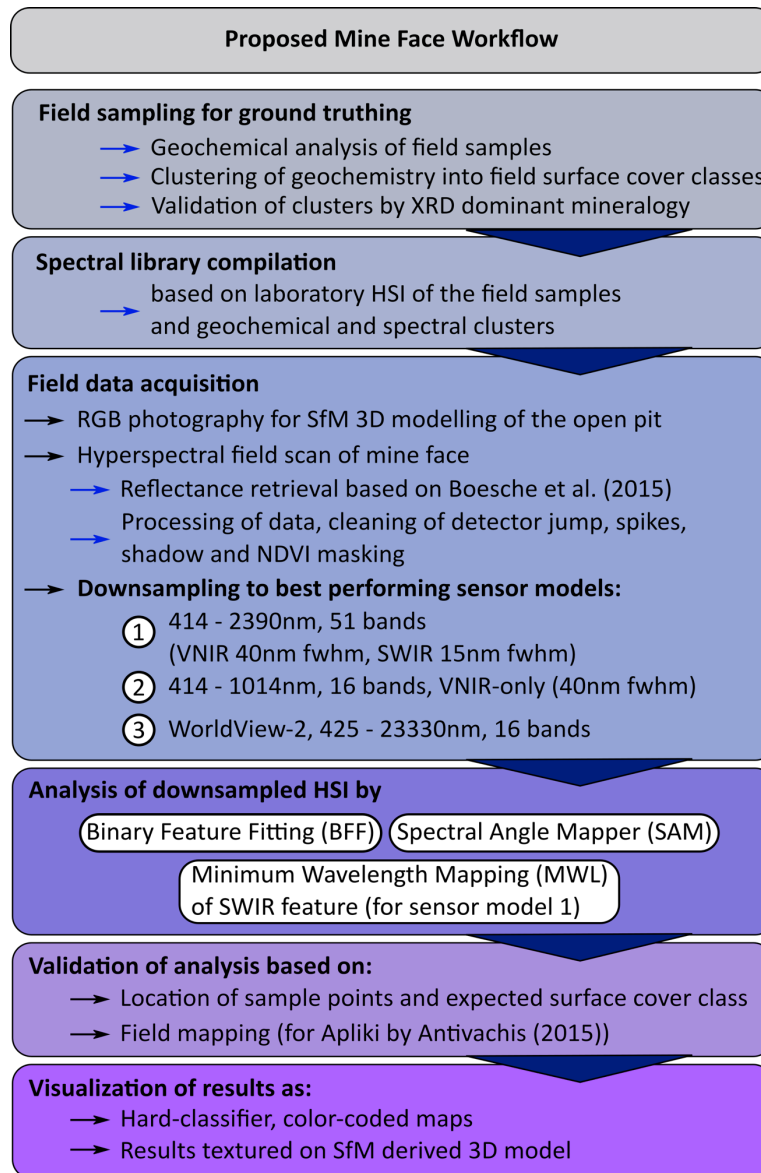


Figure 106 Hyperspectral mine face acquisition, processing and analysis workflow.

The field sampling, data acquisition and pre-processing were explained in detail in Chapter 3 (p. 32). The spectral library compilation and geochemical clustering is described as a result of the laboratory data analysis (Section 5.4, pp. 136).

The reflectance HSI was downsampled to the specifications listed in Table 34. Three sensors were utilized for the subsequent analysis: 1) the 40nm VNIR-15nm SWIR, atmospheric band excluded data, 2) the 40nm VNIR-only data and 3) the WorldView-3 sensor characteristic data.

Table 34 Sensor characteristics for the downsampled sensors, downsampled from 390 band, pre-processed Apliki field reflectance data.

Sensor	Wavelength range [nm]	Band number	FWHM [nm]	VNIR	FWHM SWIR [nm]
40nm VNIR – 15nm SWIR (atmospheric bands clipped)	414-2390; (Interpolated between 1334 – 2004nm)	51	40		15
40nm VNIR-only	414-1014	16	40		-
WorldView-3	425-2330	16	50, 60, 70, 40, 60, 40, 125, 80, 30, 40, 40, 40, 40, 40, 50, 70		

The differences in the overall shape of the spectrum for these three sensors have been visualized in Table 56 when systematically downsampling the Brazilian iron ore samples (Appendix, p. 261). Nevertheless, the spectral library for the “40nm VNIR-15nm SWIR, atmospheric band excluded data” for 11 spectra is shown in Figure 107 to give an insight into the type and shape of spectra that the subsequent mapping and analysis is based on.

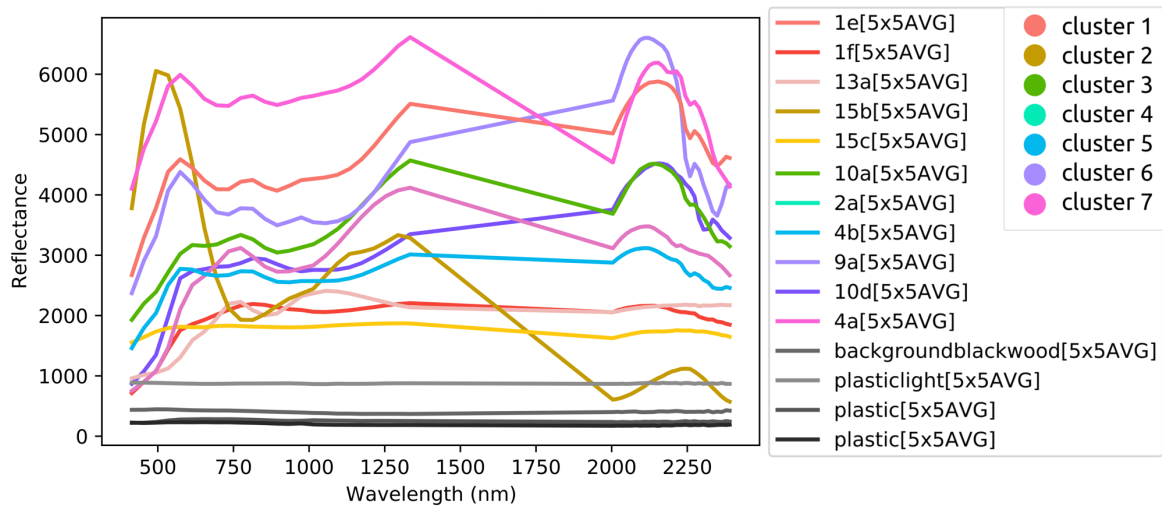


Figure 107 Spectral library spectra of 11 Apliki samples, downsampled to 40nm VNIR - 15nm SWIR. The atmospheric range between 1300–2010nm was clipped and interpolated.

5.5.1 Ground truth for the Apliki mine

In order to validate the HSI maps, the mapping results are compared with two sources of validation for the spatial data: 1) the known, identifiable field sample collection positions and the expected mapping result based on those samples and 2) the geological map of the northern face of Apliki based on 66 samples taken in 2015 by (Antivachis, 2015).

5.5.1.1 Validation based on sample points

Figure 108 shows the hyperspectral scan with marked sample position (color-coded circles). Twenty-two sample positions could be identified within the HSI and were color-coded according to the cluster color-coding scheme utilized for the laboratory sample mapping. Eleven representative spectra of the laboratory based spectral library are shown and color-coded based on their cluster identity in Figure 108.

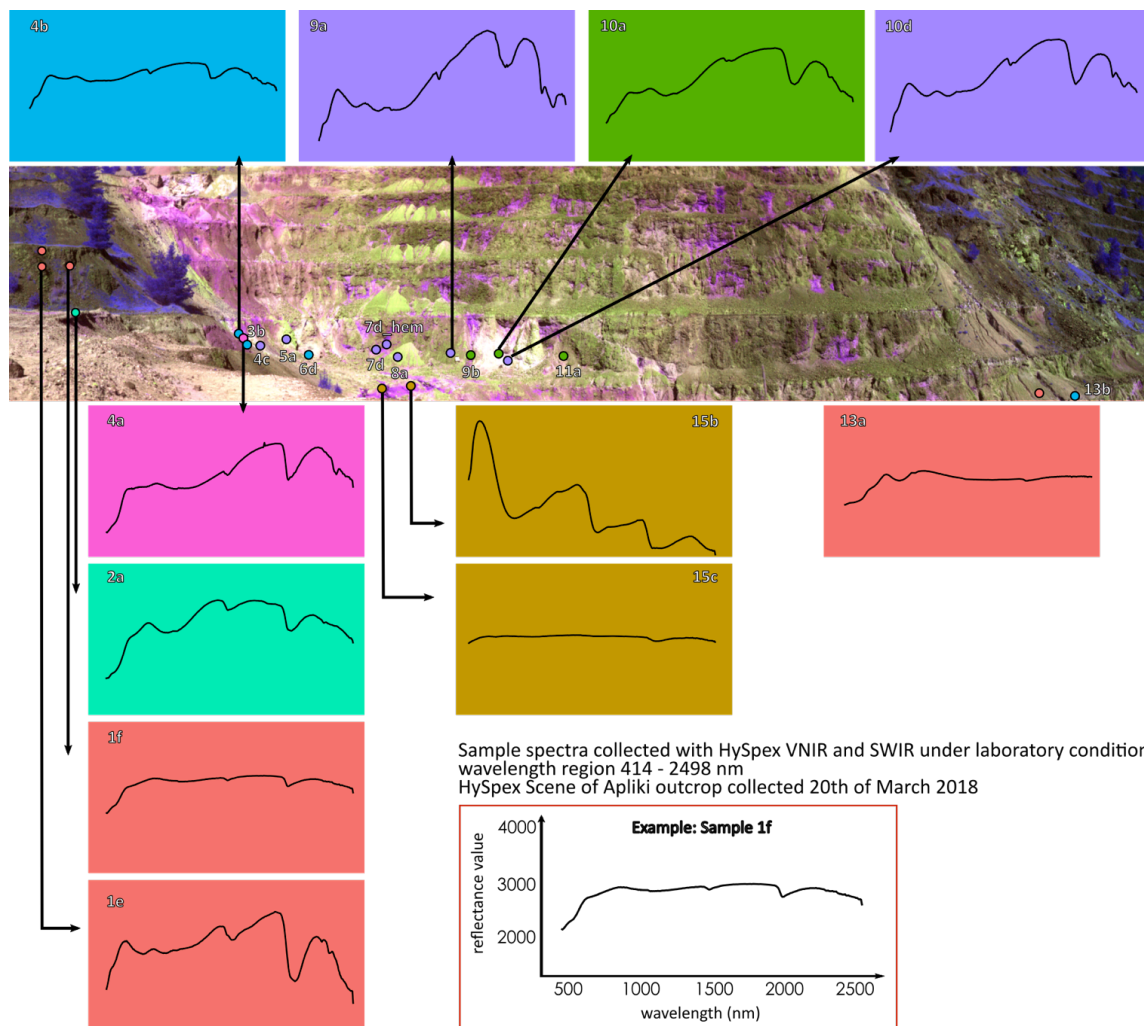


Figure 108 Field sampling positions marked in imagery. Color-coding of circles (sample points) and spectra of spectral library (laboratory based) is according to the 7 identified geochemical and spectral clusters for the Apliki samples.

5.5.1.2 *Validation based on 66 outcrop samples from (Antivachis, 2015)*

Antivachis (2015) mapped the northern open cut of Apliki based on 66 samples that were subsequently investigated by ICP-MS, AAS, petrography and X-ray diffraction. Primary and secondary mineralogy and backscattered imaging was performed with a Scanning Electron Microscope (SEM) and silicate minerals were analyzed by microprobe analyses. The result of his work is a map of the geological features of the outcrop as well as an alteration zone map. Figure 109 shows the zonation mapping of the HySpex mine face scan based on Antivachis (2015) geological mapping and is color-coded based on the 7 geochemical-spectral clusters. Figure 110 shows the combination of both the geological feature and the alteration map by Antivachis (2015).

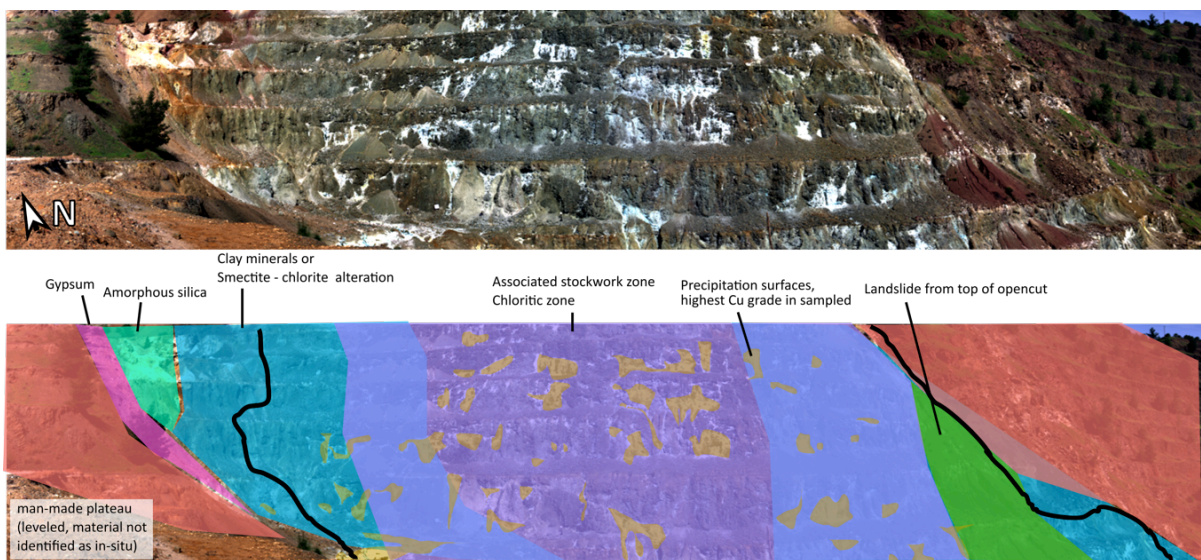


Figure 109 Apliki HySpex mine face scan RGB (top) and geological interpretation based on Antivachis (2015) (bottom).

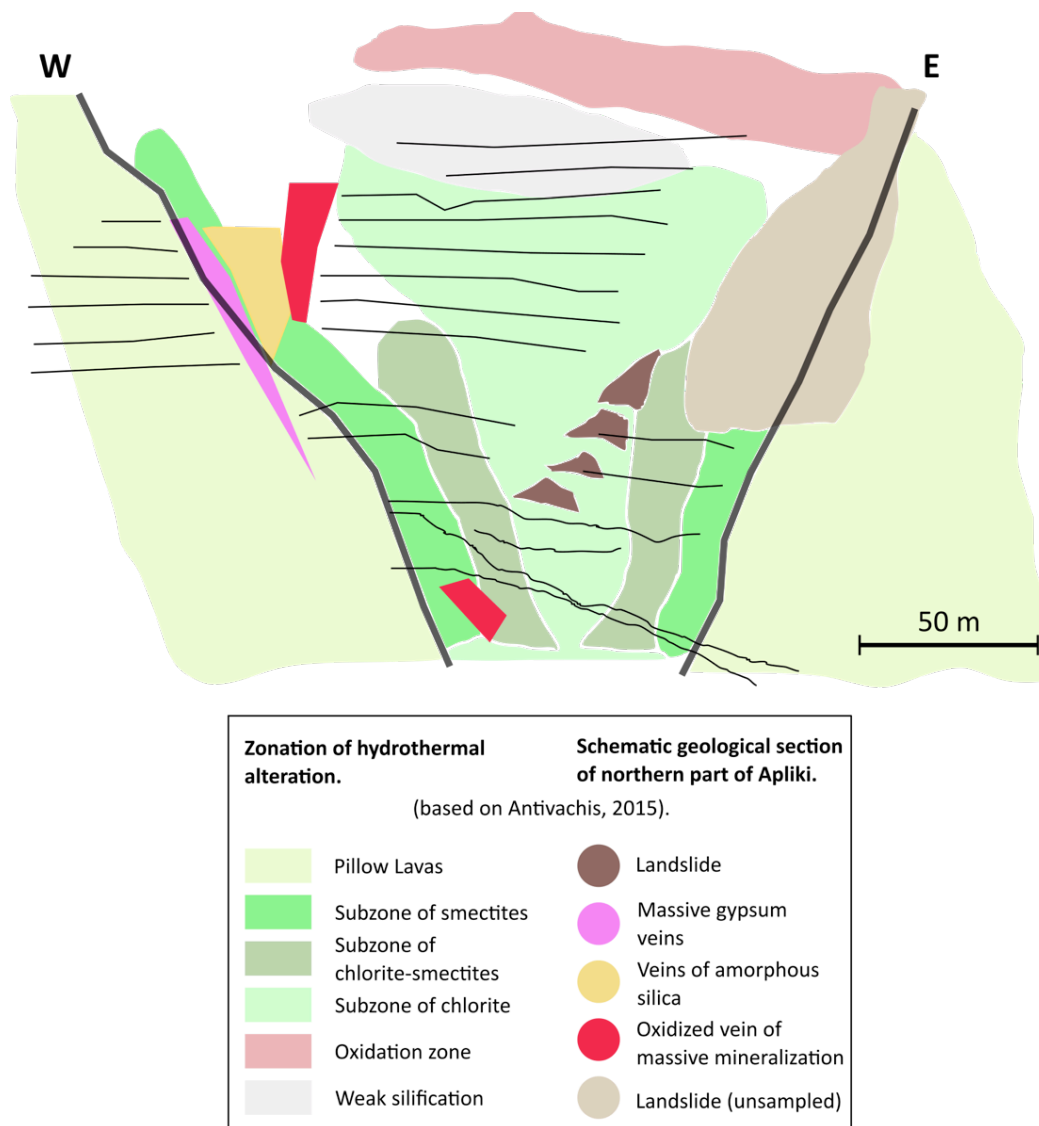


Figure 110 Combination of hydrothermal alteration zones and schematic geological section for the northern open cut in Apliki mine, Republic of Cyprus. Information derived from maps created by Antivachis (2015).

The identified geochemical-spectral clusters, the cluster-coherent dominant geochemistry and mineralogy and the associated zonation as describe in Antivachis (2015) is shown in Table 35. The cluster-coherent geochemistry and mineralogy can be linked to the geological units described by Antivachis (2015). Mapping with the cluster-color-coded spectral library should therefore be comparable to the cluster-color-coded validation map from Figure 109 (bottom). This enables a validation of the mapping by the map based on Antivachis (2015).

Table 35 Apliki mine sample clusters, dominant geochemistry and mineralogy and linked geological units.

Cluster	Generalized cluster geochemistry relative to other clusters and dominant mineralogy (XRD)	Associated zones and geological units based on Antivachis (2015)
1	Highest TiO ₂ , Al ₂ O ₃ , Na ₂ O and K ₂ O content, high TOT/C content Dominated by: Plagioclase and Montmorillonite.	Apliki pillow lavas (main magmatic minerals: iron- and titanium oxides, plagioclase, pyroxenes) and rarely olivine.
2	Highest Cu and TOT/S content Dominated by: Quartz, Sulfates and Sulfides, Fe-Hydrate (7e)	Disseminated sulfide ore, Cu-Fe sulfides and sulfates
3	Highest SiO ₂ content Dominated by: Quartz (+ chlorite-group (sample 11a and 11b))	Quartz veining, areas of silicification
4	Highest Fe ₂ O ₃ and P ₂ O ₅ content Dominated by: Sulfates	Jasper veining/ amorphous silica, veins of massive mineralization (goethite, jarosite and natrojarosite as predominant minerals, Fe-Ti, Pb, Cu, and Zn oxides as accessories).
5	Medium content of all oxides and elements compared to other clusters, relatively high K ₂ O, Fe ₂ O ₃ , Al ₂ O ₃ and MgO contents. Dominated by: Clays and smectite-chlorite group	Clay minerals identified in Pillow Lavas and smectitic alteration zone dominated by montmorillonite and illite (both can not easily be distinguished as per (Antivachis, 2015))
6	Highest MgO content, relatively high Fe ₂ O ₃ content, low K ₂ O Dominated by: Chlorite-group	Chloritic stockwork zone.
7	Highest CaO, MnO and Zn content, relatively high MgO and TOT/S, medium MgO and Fe ₂ O ₃ , lowest SiO ₂ Dominated by: Gypsum	Gypsum mineralization indicated by high CaO and TOT/S and weathering products from overlying oxidized zone

5.5.2 Superspectral analysis of downsampled Apliki mine face data

For the superspectral data analysis, the BFF and SAM algorithm were chosen and performed for all three downsampled datasets. Mapping took part with the 36 spectra spectral library created in the laboratory in Sub-Section 5.4.1. (p. 136). Additionally for the “40nm VNIR- 15nm SWIR” 51 band-dataset, MWL mapping was performed for the Al-OH feature, defined between 2160 – 2220nm (Kirsch *et al.*, 2018). The results were compared to the known and identifiable sample points in the HSI imagery. For validation purposes, the sample points were color-coded in the geochemical cluster color-scheme provided for the laboratory based analysis (Table 28, p. 139). Figure 111 repeatedly shows the sample points with their according color-coding.

IV) Proposed field workflow related to Apliki mine
 Superspectral analysis of downsampled Apliki mine face data

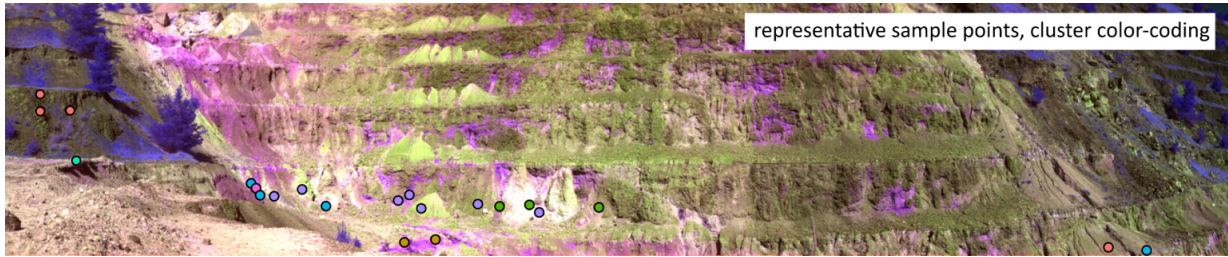


Figure 111 Field sampling position, color-coded according to geochemical and spectral cluster identity characterized in Section 5.4, p. 136 .

Figure 112 & Figure 113 present the mapping results for the BFF and SAM algorithms. Disagreement between mapping and sample validation points is indicated with yellow arrows.

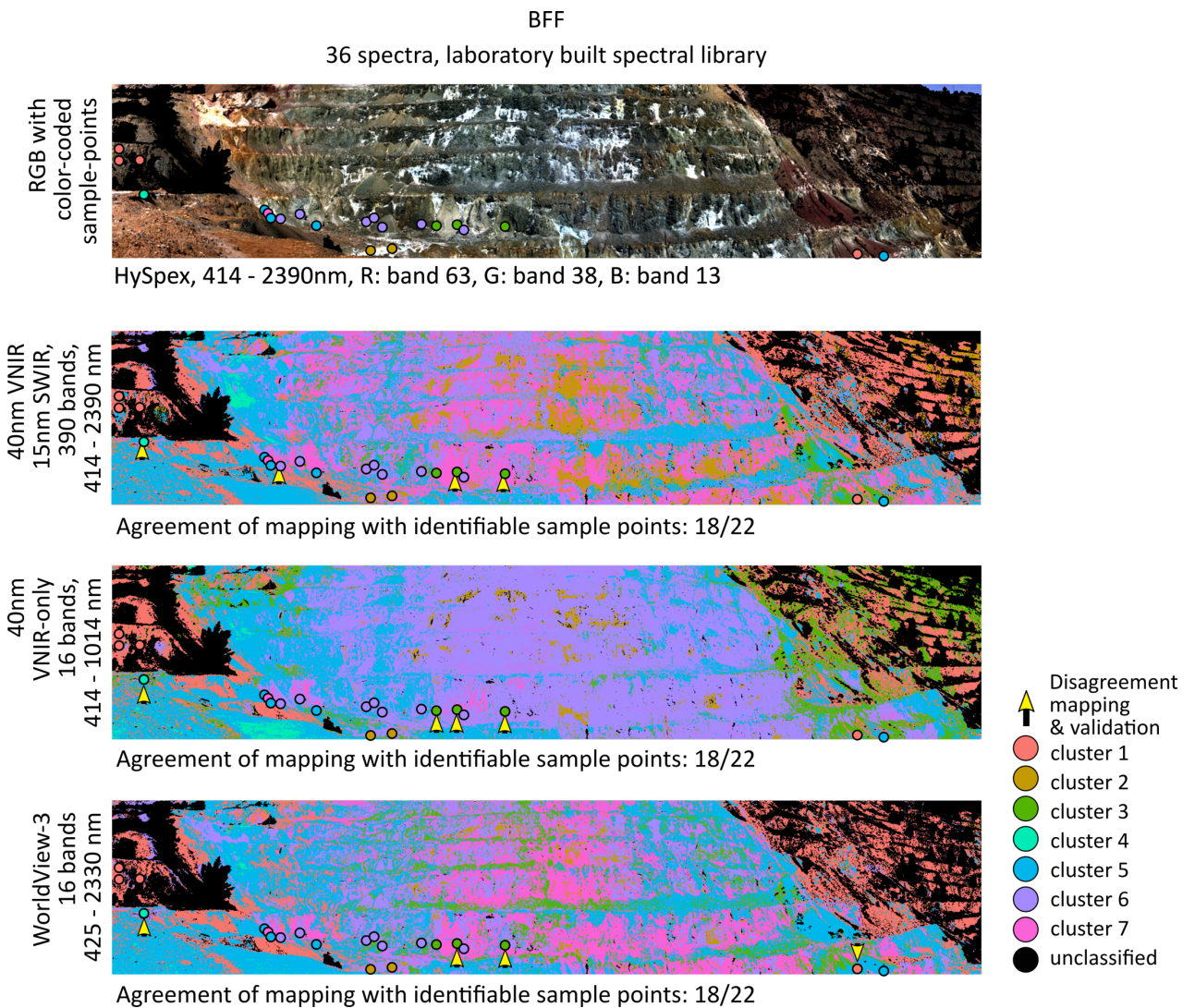


Figure 112 BFF analysis results for three different sensors. From top down: RGB representation of the mine face, analysis result for 40nm VNIR - 15nm SWIR sensor, 40nm VNIR-only sensor and WorldView-3 sensor. Color-coding based on the geochemical clusters and spectral library identified in the laboratory for the Apliki samples. Yellow arrows indicate disagreement of the mapping results with the color-coded validation sample points.

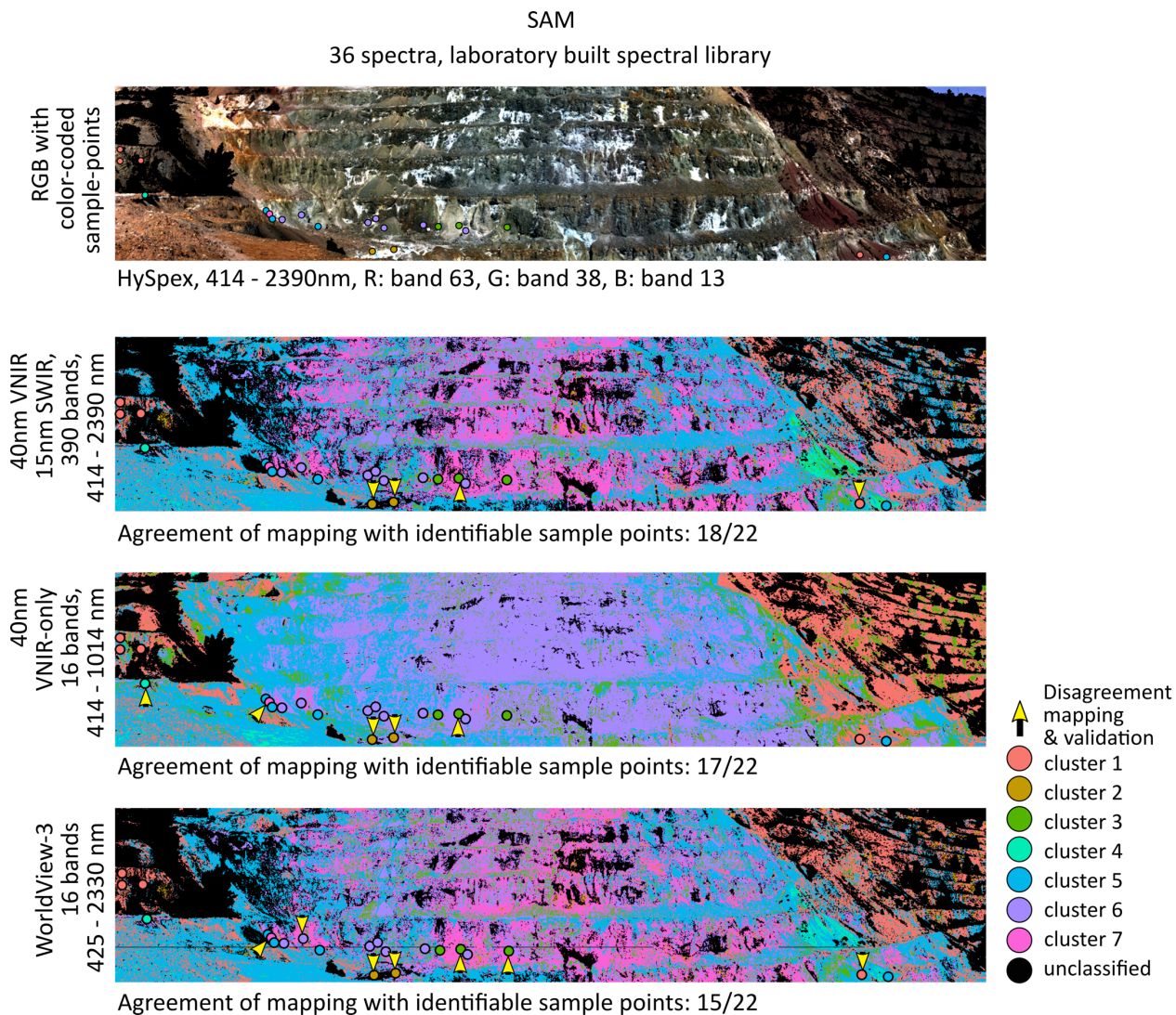


Figure 113 SAM analysis result for three different sensors. From top down: RGB representation of the mine face, analysis result for 40nm VNIR - 15nm SWIR sensor, 40nm VNIR-only sensor and WorldView-3 sensor. Color-coding based on the geochemical clusters and spectral library identified in the laboratory for the Apliki samples. Yellow arrows indicate disagreement of the mapping results with the color-coded validation sample points.

The analyses for the 40nm VNIR – 15nm SWIR, 51 bands dataset show the highest agreement between sample points and mapping results. Only this dataset could be used to map the wavelength position and feature depth of the AIOH feature between 2160 – 2220nm due to its higher spectral resolution of 15nm in the SWIR. The results of the BFF, SAM and MWL mapping for this dataset are presented in Figure 114.

IV) Proposed field workflow related to Apliki mine
 Superspectral analysis of downsampled Apliki mine face data

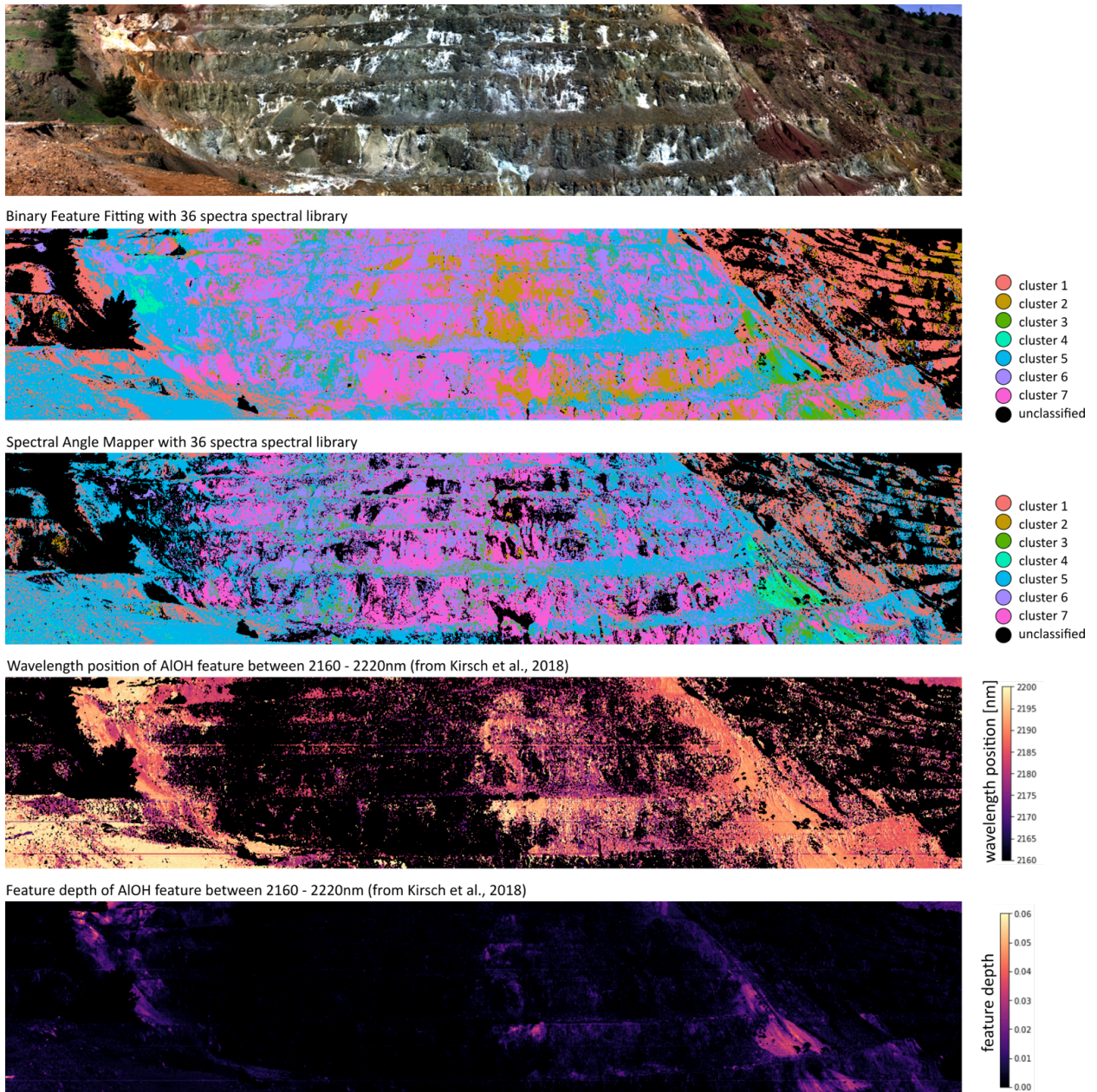


Figure 114 Analysis results for 40nm VNIR - 15nm SWIR data with atmospheric bands removed. From Top to Bottom: BFF analysis result, SAM analysis result, MWL mapping: wavelength position map for AIOH, feature depth map for AIOH.

The analysis results of the BFF and the MWL mapping for the 40nm VNIR-15nm SWIR, 51 bands-dataset is visualized on top of both DOMs in Figure 115 and Figure 116.

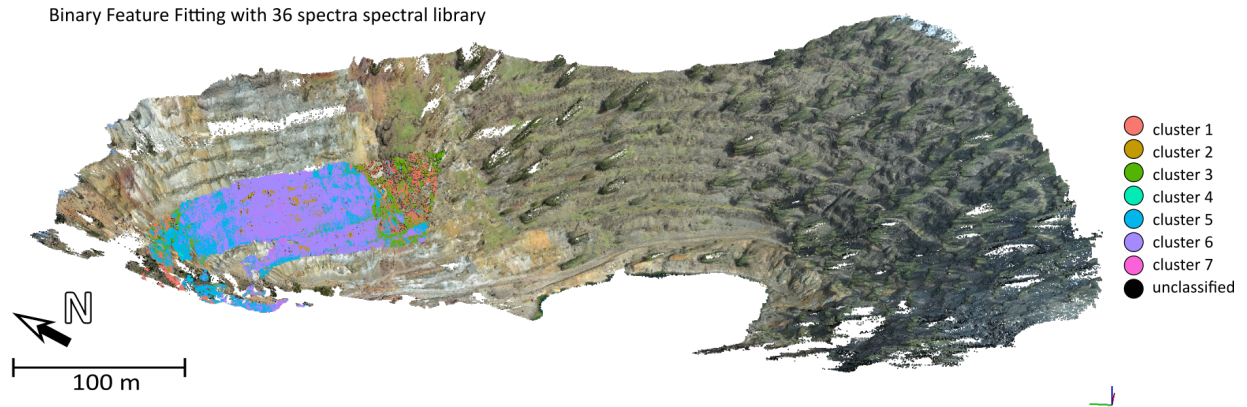


Figure 115 Binary Feature Fitting analysis of 51 bands-dataset visualized on DOM of the full Apliki open pit.

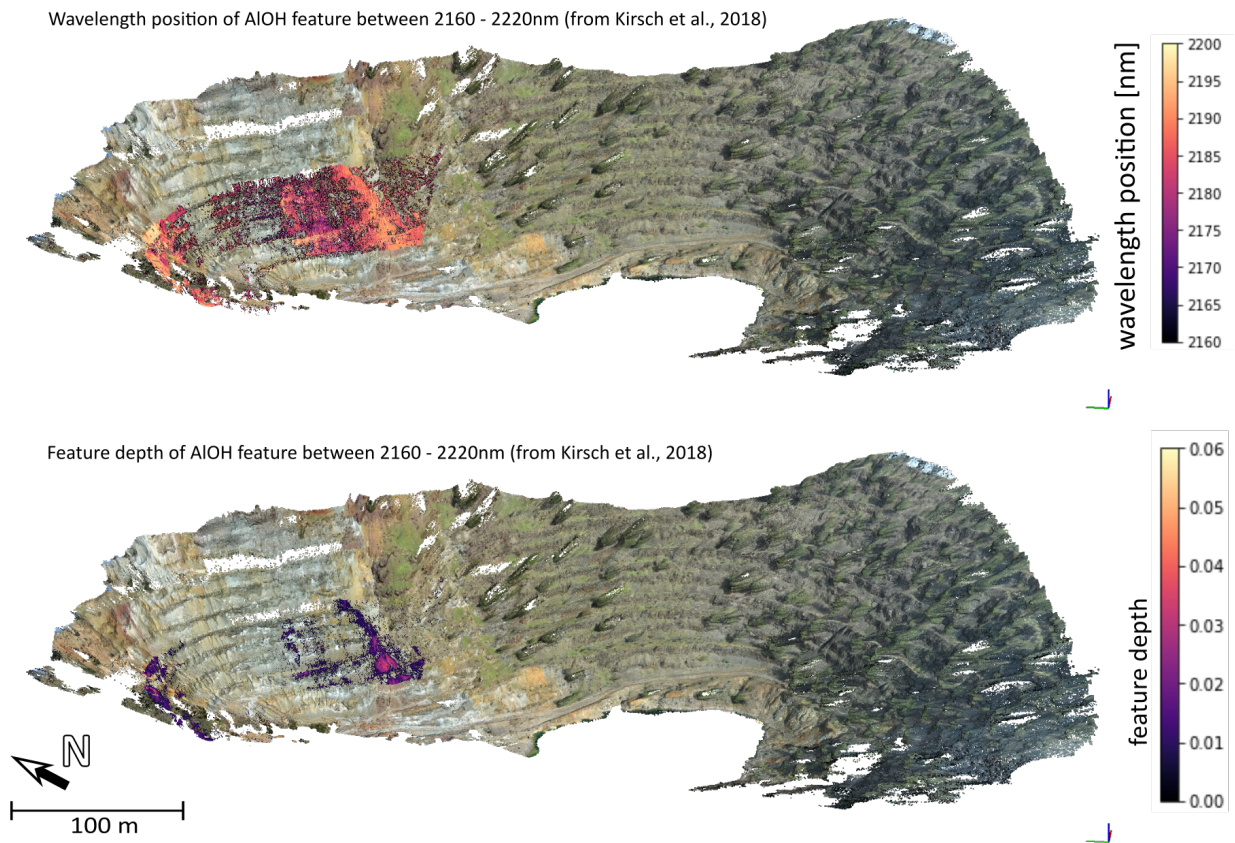


Figure 116 MWL analysis for the AIOH feature wavelength position between 2160 - 2220 nm (Top) and the AIOH feature depth (Bottom) visualized on the DOM of the full Apliki open pit.

The result can also be visualized on the close-up DOM of the NNE mine face, exemplary showing the SAM results in Figure 117.

Spectral Angle Mapper with 36 spectra spectral library

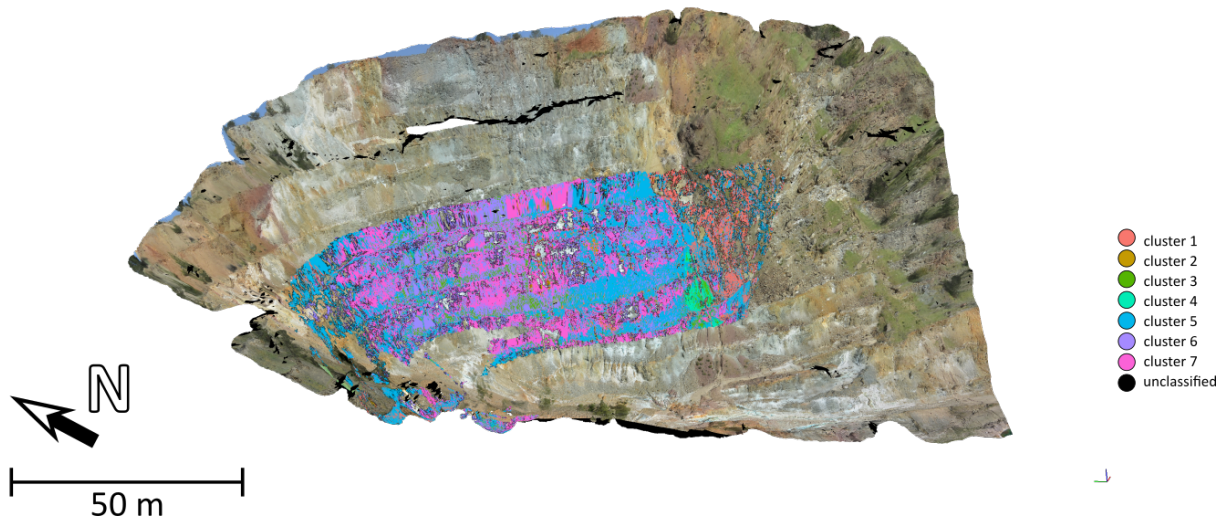


Figure 117 SAM results visualized on DOM.

The results for both mine face scans from Apliki mine will be interpreted and discussed together with the results of the Three Hills mine in the Skouriotissa deposit. This discussion can be found following Section 6.4 in Chapter 6 (starting p.178).

5.6 V) Three Hills mine – application for proposed workflow for laboratory & field data

In this chapter the methodology utilized through Section I) – IV) is applied to laboratory and field hyperspectral data from the Three Hills open pit, Republic of Cyprus.

5.6.1 Three Hills sample laboratory data

5.6.1.1 Laboratory data preparation

The laboratory-based data acquisition for the Three Hills open cut field samples was presented in Chapter 3. As previously mentioned, the reflectance data was derived by the routines by (Rogass *et al.*, 2017). The reflectance dataset was pre-processed as described in Section 3.2 before being downsampled to the sensor identified as being well suited for open pit mining applications: the “40nm VNIR – 15nm SWIR, without atmospheric bands” sensor (clipped and interpolated between the atmospherically influenced bands between 1300 – 2010 nm). The resulting superspectral dataset comprises 54 bands in the wavelength range of 414 – 2450 nm.

5.6.1.2 *Spectral Library EM*

A spectral library was built from the laboratory sample dataset. A 5x5 pixel average spectrum was collected from the prepared laboratory scan data from the “40nm VNIR-15nm SWIR, without atmospheric bands” 54 bands-sensor data. The laboratory scan of the samples is shown in Figure 118, including an outline representing the color-coding of the spectral library (pink, red, yellow) and a red rectangle showing the position of spectra collection for the EM spectral library. Where apparent, spectra have been collected from the original native surface angled towards the sensor in the field scan. The samples have been positioned with both of these factors in mind for the laboratory scan.

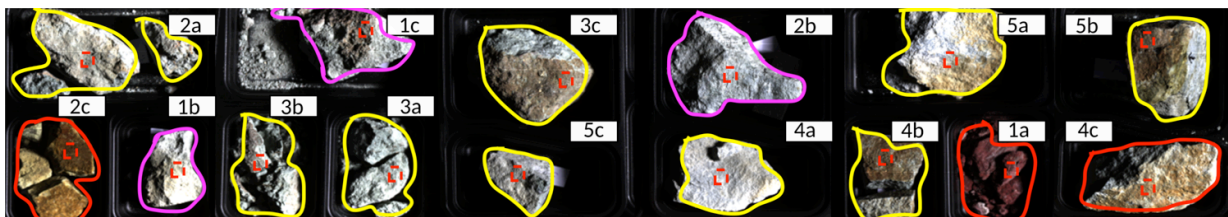


Figure 118 Three Hills sample laboratory scan. Color-coded outline of the samples is based on the mapping colors for the image-retrieved spectral library. Red, dashed rectangles mark the position of 5x5 pixel average spectra retrieval. Color-coding is based on Cu mass fraction: pink: > 0.27 % Cu; red: 0.27% < Cu < 0.1%; yellow: < 0.1% Cu

The color-coding of the spectral library is based on the categorization of the samples above 0.27wt% of Cu as “high grade ore” (pink), between 0.27wt% - 0.1wt% Cu as “ore” (red) and below 0.1wt% Cu as “waste” (yellow). This categorization was communicated by GSD during the fieldwork in March 2018. Table 36 shows the samples’ Cu mass fraction and the color-coding of the sample spectra for the subsequent analysis.

Table 36 Three Hills mine samples with associated copper content. Color-coding is based on Cu mass fraction: pink: > 0.27 % Cu; red: 0.27% < Cu < 0.1%; yellow: < 0.1% Cu

Sample	1a	1b	1c	2a	2b	2c	3a	3b
Cu [wt%]	0.22	0.43	>1.00	0.08	>1.00	0.16	0.02	0.04
Sample	3c	4a	4b	4c	5a	5b	5c	
Cu [wt%]	0.01	0.03	0.05	0.12	0.01	0.09	0.01	

Figure 119 shows the resulting spectral library that was applied for the field mine face dataset.

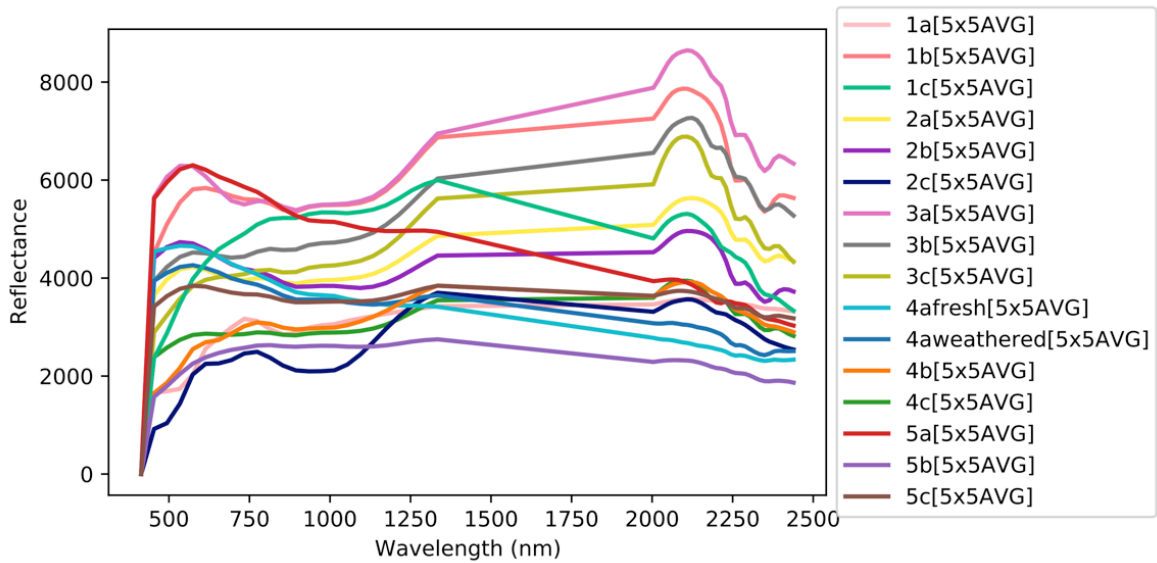


Figure 119 Spectral library plot of the Three Hills mine samples. Spectra were taken from a 5x5 pixel average window, the position of the spectral sampling is shown in Figure 118, p.162 .

5.6.2 Analysis of Three Hills mine face

After the laboratory and the field data preparation, the pre-processed and downsampled superspectral 54 band data was analyzed using the BFF algorithm. The analysis is based on the laboratory-sample-scan spectral library. The result of the mapping is shown in Figure 120 and visualized on top of the RGB DOM in Figure 121.

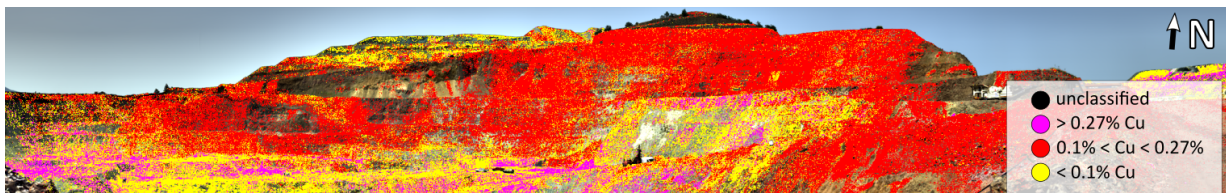


Figure 120 The analysis result of the BFF algorithm for Skouriotissa Three Hills, overlaid on the HySpex RGB representation.

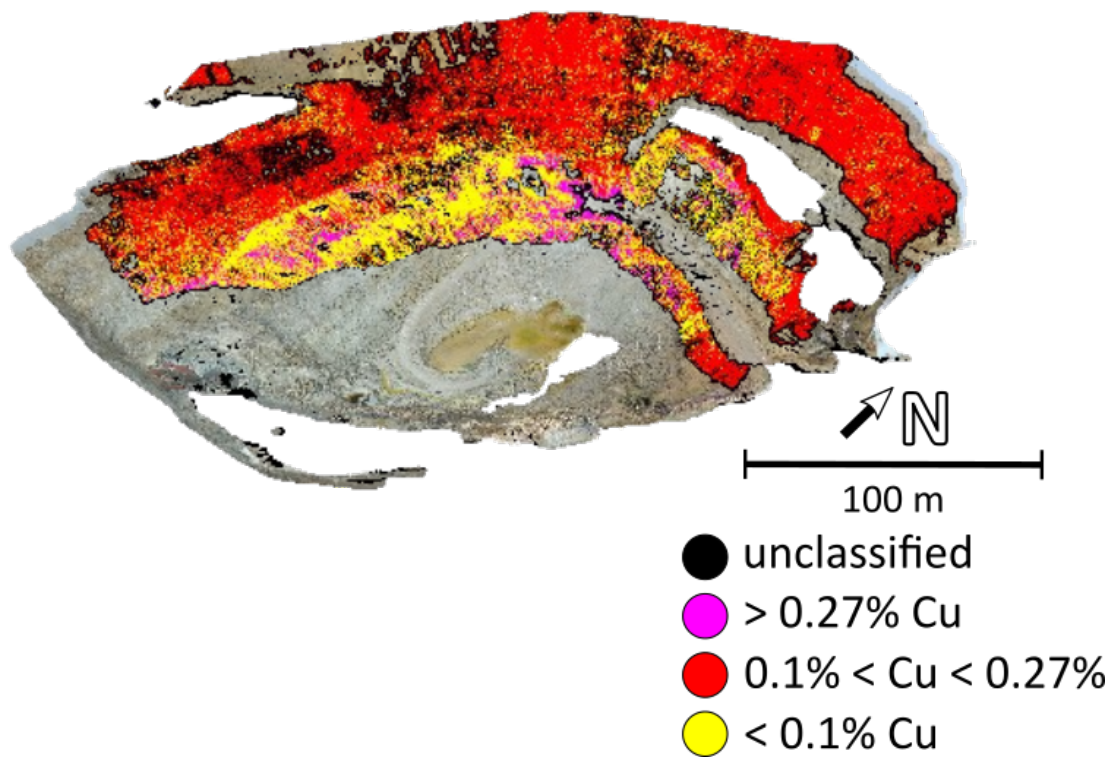


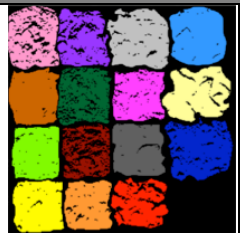
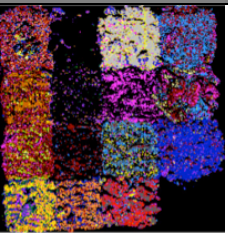
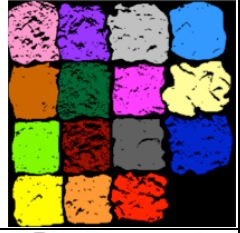
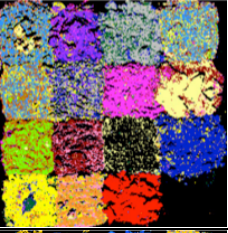
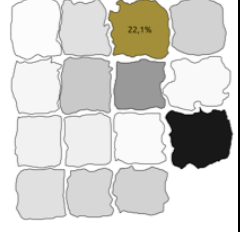
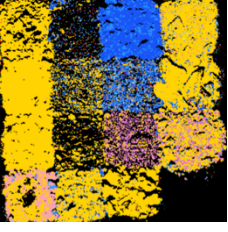
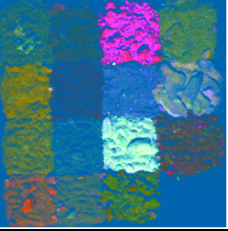

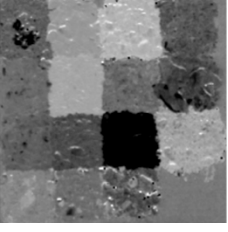
Figure 121 Textured 3D model with the BFF analysis result as an overlay over the RGB 3D model.


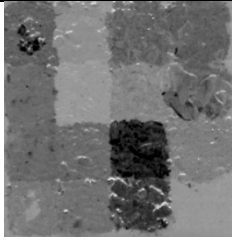

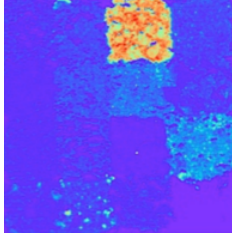
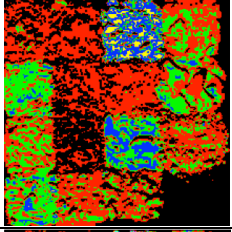
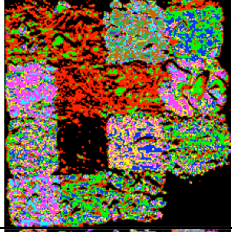
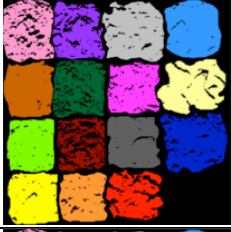
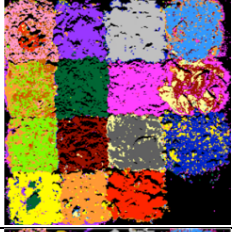
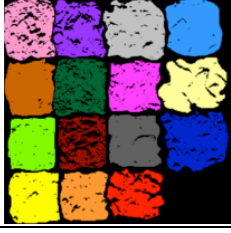
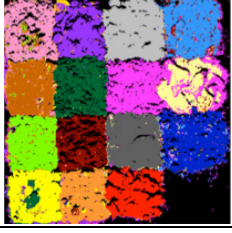
6 Discussion

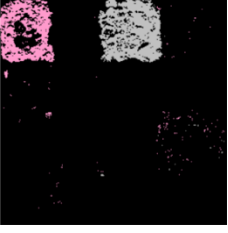

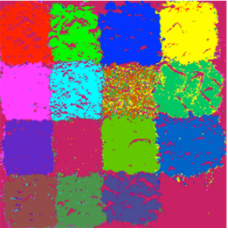

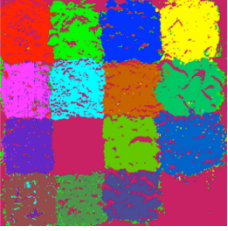
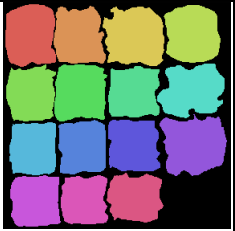
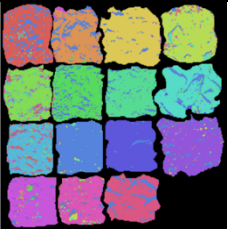
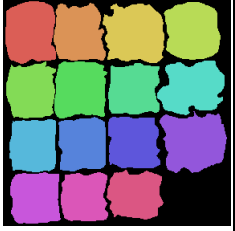
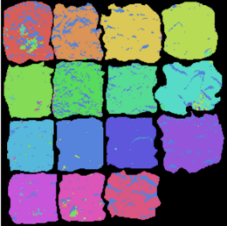
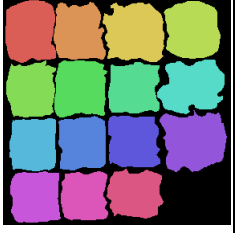
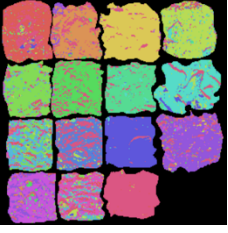
6.1 Iron ore sample mapping results


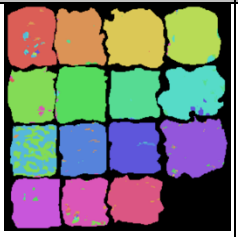

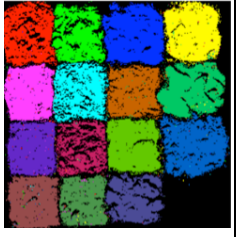
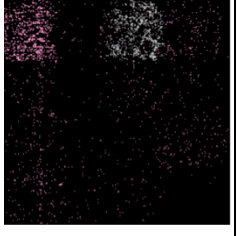
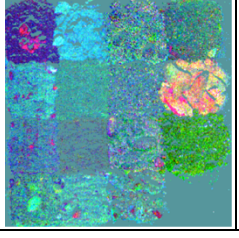
Table 37 compares the mapping results for dataset 1 with a validation image (if possible) and comments on the achieved quality of mapping and repeatability of the approach.

Table 37 Comparison of the mapping results with a validation image (expected mapping, if available).

Method	Validation image	Result image	Evaluation	Repeatable?
HYBRID				
EnGeoMap 2.0			Based on user-specific library, 408 band data, classification result not satisfactory	Yes
EnGeoMap 2.1			Based on user-specific library, 408 band data, classification result improved	Yes
PRISM MICA	 Al ₂ O ₃ content		Based on USGS command group 2 library for AIOH-rich minerals, does not identify the diversity of AIOH-poor samples	Yes
KNOWLEDGE-DRIVEN				
Absorption modeling				
PCA (RGB, 1-2-4)	None		Identifies spectrally homogeneous areas, no information about material label, user input about RGB band combination needed	No
Band ratio for ferrous iron for WorldView-3 data, based on published index (indexdatabase.de /, 2020)	 Fe Content		Mapping does not match suggested Fe content from XRF	Yes

Method	Validation image	Result image	Evaluation	Repeatable?
Band ratio for ferric oxide for WorldView-3 data, based on published index (indexdatabase.de /, 2020)	 <p>Fe Content</p>		Mapping does not match suggested Fe content from XRF	Yes
Feature modeling				
Minimum Wavelength Mapping for AlOH feature 2160 - 2220	 <p>Al₂O₃ content</p>		Matches well with the overall Al ₂ O ₃ content suggested by XRF	Yes
DATA-DRIVEN				
Hard classifier				
k-means: 7 clusters	None		Clustering not in correlation with either sample position or geochemical clusters	No
k-means: 15 clusters	None		Clustering not in correlation with either sample position or geochemical clusters	No
SAM (ENVI)			Overall satisfactory result, shadowed areas and sample-intern, inhomogeneous areas are not mapped correctly	Yes
BFF			Based on user-specific library, 42 band data, classification result is satisfactory	Yes

Method	Validation image	Result image	Evaluation	Repeatable?
SFF	Light pink: sample 1, grey: sample 2		Area of single material maps coincide well with position of samples, but user input is required for low RMS and high scale value class definition	No, user input needed to define classes
Training based				
Gaussian maximum likelihood classification			Overall satisfactory result, background (pixels with value 0) mapped	Yes, but model for inference has to be trained on representative data
Mahalanobis Distance classification			Overall satisfactory result, background (pixels with value 0) mapped	Yes, but model for inference has to be trained on representative data
Learning based				
SVM:				
SVM			Overall satisfactory result, shadowed areas and sample-intern inhomogeneous areas are not mapped correctly	Yes, but model for inference has to be trained on representative data
ANN:				
1D Baseline NN			Overall satisfactory result, shadowed areas and sample-intern inhomogeneous areas are not mapped correctly	Yes, but model for inference has to be trained on representative data
1D CNN			Overall satisfactory result, shadowed areas and sample-intern inhomogeneous areas are not mapped correctly	Yes, but model for inference has to be trained on representative data

Method	Validation image	Result image	Evaluation	Repeatable?
3D CNN			Overall satisfactory result, shadowed areas and sample-intern inhomogeneous areas are not mapped correctly	Yes, but model for inference has to be trained on representative data
Random Forest: scikit-learn RandomForestClassifier (Pedregosa et al., 2011)			Overall satisfactory result, shadowed areas are mapped as "unclassified"	Yes, but model for inference has to be trained on representative data
Soft-classifier				
MTMF	None		Area of single material maps coincide with position of samples, but user input is required for high MF and low infeasibility score class definition	No, user input needed to define classes
ICA (RGB, 4-7-6)	None		Identifies spectrally homogeneous areas, no information about material label, user input about RGB band combination needed	No

In the knowledge-driven area, the feature modeling MWL map of AIOH coincides well with the known Al_2O_3 content of the samples. As for the absorption modeling, the band ratio iron index maps based on WorldView-3 do not correlate well with the iron content – neither the ferric nor the ferrous index, similar results are shown for the chosen RGB band combination of the PCA. The random PC band generation and needed user input for the PCA RGB is another problem that does not allow for repeatability of results – at best it can be considered as a first guess of differing material portions in an unknown area. In the data-driven portion of the hard classifier analysis methods, the classic SAM analysis gives reliable results when choosing the correct spectral library as input. The SAM results based on different possible spectral libraries in Section 5.2 (p. 97) shows clearly how dependent each of these methods is for the correct choice of EM spectra. The BFF algorithm is mapping the samples with a sufficient accuracy ($\approx 75\%$) and reduced data to superspectral (42 band) resolutions. GML and MHD perform well, but are unable to classify the pixels set to zero as unclassified or to exclude them.

SVM, 1D NN, 1D CNN and 3D CNN map equally well but the computation time for training and testing significantly differs. The 3D CNN accuracy of 93% is assumingly caused by overfitting of the NN. The RF classifier gives equally well results. Evaluating the soft classifiers, the MTMF performs well for each component but needs a user input to define the classes based on best MF and lowest infeasibility score. This is not yet reproducible and requires expert knowledge. The same challenge is present for the SFF analysis in the data driven analyses section. ICA as well as PCA need user input for RGB band composition and rather high computation times without labeling or matching. The k-means clustering only requires the user to set the number of clusters expected in the imagery but the results do not coincide well with the actual material clusters.

In the hybrid model comparison, MICA is clearly able to map the clay dominant mineralogy and the mapping results are superior to those of EnGeoMap 2.0 and 2.1. Without expert knowledge, MICA can only be used with one of the two default spectral libraries from the USGS (clay vs. iron rich material). For new material spectral libraries, specific user input of the expected spectral is required as well as material dependent thresholds and weighting factors. This expert knowledge and individual level of implementation is not to be expected of the average mining workforce as of today.

Figure 122 shows the hard pixel classifier accuracies [%] relative to the computation time [s] needed. Please note the logarithmic scale of the computation time. The two EnGeoMap algorithm versions show to yield results with low overall accuracies but requiring high computation times. Random Forest, 1D CNN, BFF and SVM are present in the range below 1000s of computation time for the Brazilian iron ore samples but around or above 75% accuracy. SAM, MHD and GML plot with lower accuracies but very fast computation times (below 10s) and the two 1D NNs, 3D CNN plot with accuracies beyond 85% but computation times higher than 1000s. The exact values can be found in Table 38.

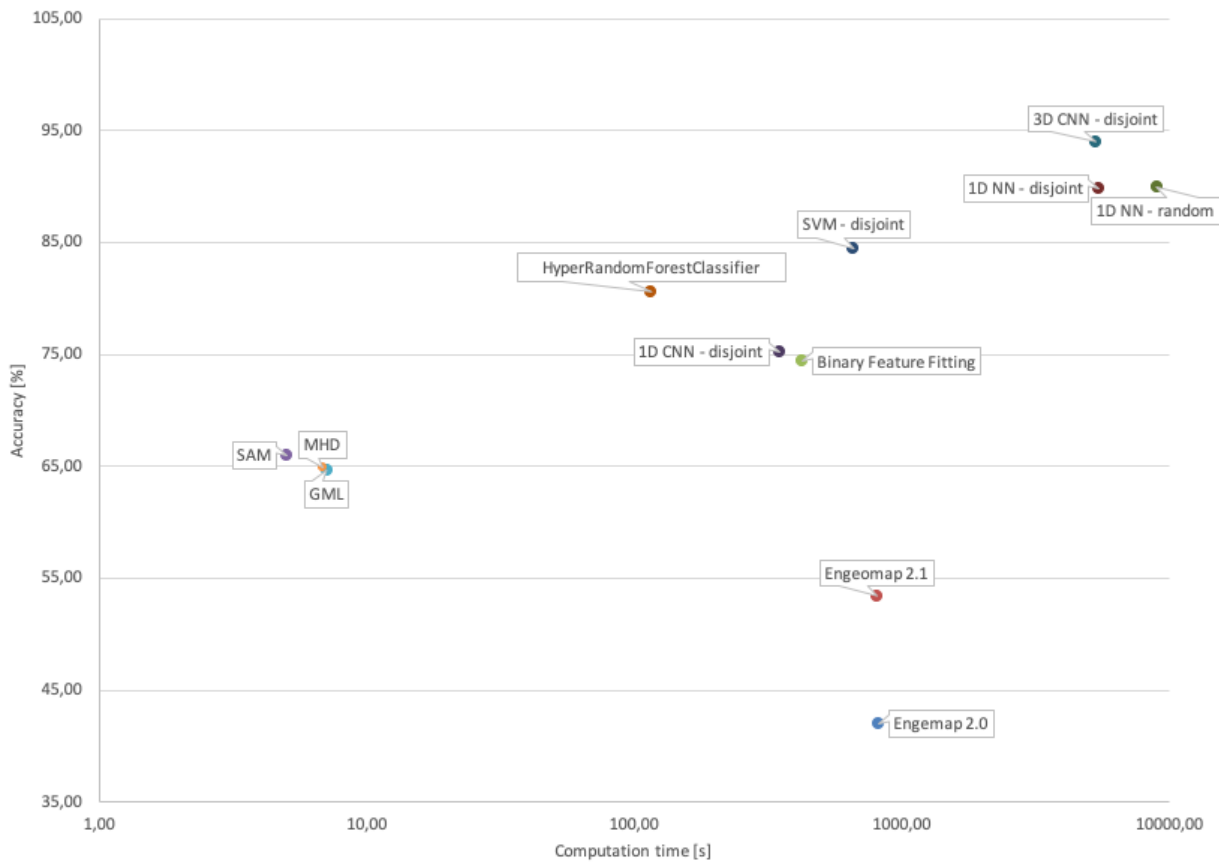


Figure 122 Hard classifier analysis results (accuracy) and computation times.

Table 38 Hard classifier analysis computation time and accuracy.

Method	Computation time [s]	Accuracy [%]
EnGeoMap 2.0	816.52	41.96
EnGeoMap 2.1	808.23	53.32
Binary Feature Fitting	422.59	74.36
SAM	5.00	65.95
Gaussian maximum likelihood classification	7.07	64.61
Mahalanobis Distance Classification	6.84	64.88
SVM - disjoint	659.47	84.50
1D Baseline NN - disjoint	5432.47	89.80
1D Baseline NN - random	8923.74	89.98
1D CNN - disjoint	347.58	75.20
3D CNN - disjoint	5318.44	93.90
HyperRandomForestClassifier	115.75	80.54

The analysis methods used to test the different theoretical sensors in Section 5.3 "II) Robust Sensor Modeling, p.119 were:

- SAM as the algorithm with the lowest computation time, as time is a key factor in the active extraction process in the mining sector.
- SVM, as the best performing learning-based classifier below 1000s computation time. Keeping in mind that once trained on a specific deposit, the computation time will decrease rapidly.
- BFF, as the best performing, comparison-based, data-driven method below 1000s.
- EnGeoMap 2.1 despite its lower accuracy, as it is another GFZ in-house hybrid data- and knowledge-driven analysis algorithm.
- The MWL method as a representative for a knowledge-based approach. It was tested for the systematic downsampling and the preservation of the AIOH absorption feature in the SWIR.

These analysis methods represent the different mapping approaches – “data-driven learning based”, “data-driven comparison-based”, a “knowledge-based approach” and a “hybrid”. The methods using the comparison-based methods were preferred, as they rely on an endmember set of spectral libraries that can be compiled from thoroughly defined sample sets. The training-based approach relies on training set and a well-defined dataset of regions of interest. These regions of interest have to be defined manually within the hyperspectral image. This can pose a challenge as the geological material is hardly homogeneous - neither in the sample scale (laboratory scale) and less so in the mine face scale where spectrally homogeneous regions of interest cannot be defined clearly enough for training. The testing showed that the trained algorithms based on laboratory data could not be inferred well to the mine face data (see example for Apliki mine on p. 183, fig. 132). This complicates the utilization of the training-based approach in the context of mine face mapping.

6.2 Robust sensor modeling

6.2.1 Spectral downsampling of VNIR & SWIR

Downsampling both in the VNIR and in the SWIR suppresses small, distinct spectral features that are indicative of minerals or elements. This is the case for example for distinct, small features of Rare Earth Elements (REE) in the VNIR (Herrmann, 2019) but also narrow features in the SWIR indicative of Al-bearing phyllosilicates (e.g. kaolinite) or Fe-, Mg- bearing minerals (e.g. chlorite, epidote and tourmaline) (Lypaczewski *et al.*, 2020). These smaller features can be utilized for absorption feature modeling e.g., MWL or EnGeoMap 2.1. The identification of the kaolinite double feature is possible up

to a downsampling to bandwidth of 15nm (see Table 24). This only proves the distinction based on spectral form (in this case the distinct doublet feature) and not exact location of feature wavelength position that is usually aimed for with MWL mapping. Interestingly, by increasing the FWHM up to 40nm and decreasing the number of bands for the theoretical sensor, the mapping accuracy of EnGeoMap 2.1 constantly improves, showing that the overall shape and location of all features can be mapped even for downsampled systems.

To repeat some of the findings for SVM, SAM, BFF and EnGeoMap that were stated in *table 23* (p. 124, showing the mapping accuracy plotted against the computation time), *figure 85* (p. 125, showing the mapping accuracies plotted against the band number of the sensors) and *figure 86* (p. 126, showing the mapping accuracy and computation time plotted against the band number): The mapping accuracies of SVM and SAM are at an approximately constant level with increasing band numbers they plot around 83% and 65% respectively. SVM training time decreases from 3361.8s (1nm bandwidth, 2084 bands) to 52.5s of training time for the WorldView-3 setting (16 bands) and the mapping accuracy (kappa) increases slightly from 82.4% to 83.2% respectively.

The BFF mapping results shows an increase in accuracies with decreasing band numbers. The computation time for BFF decreases from 2722.5s and 60.5% of accuracy to 450.7s and 71.7% of accuracy for 5nm and 50nm bandwidths respectively. EnGeoMap 2.1 peaks around 53 bands with an accuracy of 49% and stays consistent with increasing band numbers at around 48%.

Figure 86 shows the correlation of computation time and increasing band number. The accuracy of the resulting map does not increase with band number and computation time for SAM, SVM and EnGeoMap 2.1. The BFF mapping accuracy decreases with increasing band number and computation time (see pp. 124-126). The increase in mapping accuracy for the BFF with decreasing band number can be explained by the underlying calculations of the method. The comparison of the unknown pixel spectrum with the endmember set spectrum is based on the triangle parameters. With decreasing bandnumbers the triangles that are created between three consecutive datapoints become more distinct and represent larger triangles. The created triangles get larger with decreasing bandnumbers and reflect better upon the absorption features themselves instead of small incremental changes within larger absorption features. This is shown in Mielke et al., 2020 and this is also why the BFF was originally created for multispectral data. The constant mapping accuracies of SAM and SVM might reflect on two different factors: First, for a distinction between material spectra the exact position of narrow features does not play as important a role. The position of wide features, the overall trend of the curve and the albedo of the spectrum might be enough to characterize a material sufficiently. A second factor for the iron ore samples – the dataset used for this test – is that the different sample spectra are already very similar to each other and a distinction of them is based on the trend of the

curve and the albedo rather than on narrow absorption features. The iron ore samples themselves do not exhibit a large variety of narrow features in the SWIR region. This also means that the downsampling process and the optimum sensor design has to be thoroughly reviewed for any new deposit (with a different level of spectral variety) and the optimal sensors will differ for different deposits and the needed level of spectral resolution for a material distinction.

Based on these findings and the aim to simplify the theoretical sensor and lower the overall costs related to the system, the 15nm and 40nm bandwidth sensors were considered for further sensor improvements regarding the application in active mining. The MWL mapping of distinct, sharp features that only change their wavelength position by a few nanometers cannot be based on these sensors. The mapping of white mica for example (feature around 2200nm (Lypaczewski *et al.*, 2020)) and the change of wavelength position around the 2200nm feature can be an indicator for white mica (2195nm) or green, phengitic mica (2210nm) (Lypaczewski *et al.*, 2020). These distinctions cannot be achieved by downsampled spectral data but only by upsampled, 1nm FWHM data.

6.2.2 Reduction of atmospheric impact

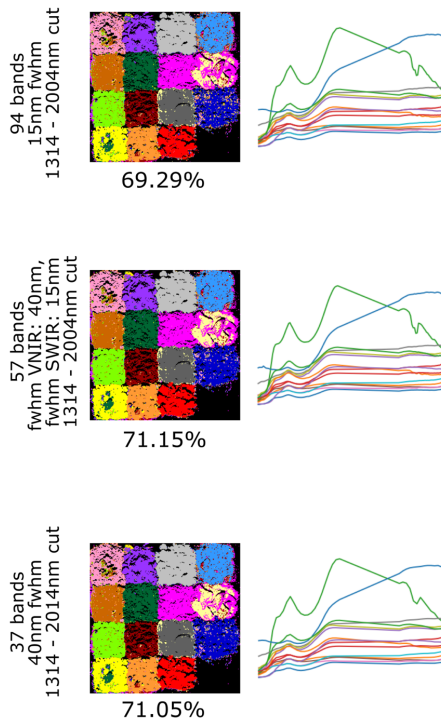
By excluding the atmospherically affected wavelength regions ($\approx 1300\text{-}2010\text{nm}$) the material classification results were not affected considerably, but it reduced the effects of atmospheric changes on the data and reduced the dimensionality of the data further, resulting in three sensors with 37, 57 and 94 bands and 40nm, 40nm and 15nm, and 15nm bandwidth respectively. By reducing the data again to two theoretical VNIR-only datasets, two sensors of 57 bands (15nm bandwidth) and 16 bands (40nm bandwidth) were created and yielded acceptable classification results.

6.2.3 VNIR-only downsampling

The analysis that is based on VNIR-only data can only take into account broad absorption features in the VNIR (usually caused by the presence of iron) for knowledge-based approaches e.g. iron feature depth modeling. Here, SWIR-active mineral features cannot be included for a knowledge-based approach. The distinction of different materials can be achieved by using data-driven analysis approaches. The results for SAM and BFF are promising and show a possible distinction of the spectrally very similar Brazilian iron ore samples. This is shown for the BFF analysis for the sensors with excluded atmospheric bands and the VNIR-only sensors in Figure 123. Both SAM and BFF are insensitive to variable illumination as they consider spectral shape parameters for classification instead of absolute spectra positions.

VNIR-SWIR

atmospherical range (1300 - 2010nm) clipped



VNIR

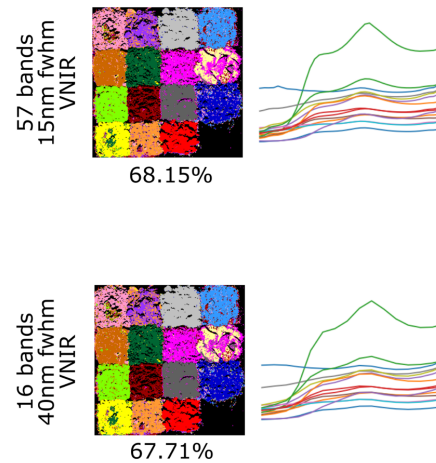


Figure 123 BFF results and spectral library of the 3 datasets with excluded atmospheric wavelength ranges (left) (414–2498nm) and of the two VNIR-only datasets (414 – 1000nm). The spectra of the spectral library are shown stylized to highlight the changes in the overall spectrum.

In short, the VNIR-only setup allows for a lighter and smaller sensor with a lower power-consumption, higher tolerance towards temperature changes and a higher spatial resolution. Additionally, the price point ratio of VNIR to SWIR is around 1:2. Utilizing spectrally lower resolved sensors and going from hyper- to hyperspectral can significantly reduce data size, storage cost and computation time.

The reduction of data size with reduced spectral band numbers is another factor to consider as routine monitoring will not only add up a lot of data for storage, but as shown, the reduction of data size enormously reduces the computation time for subsequent analyses. Figure 124 plots the data size against the band number for all systematically downsampled sensors (18 sensors with band numbers from 2084 to 16), note the logarithmic scale of the x-axis.

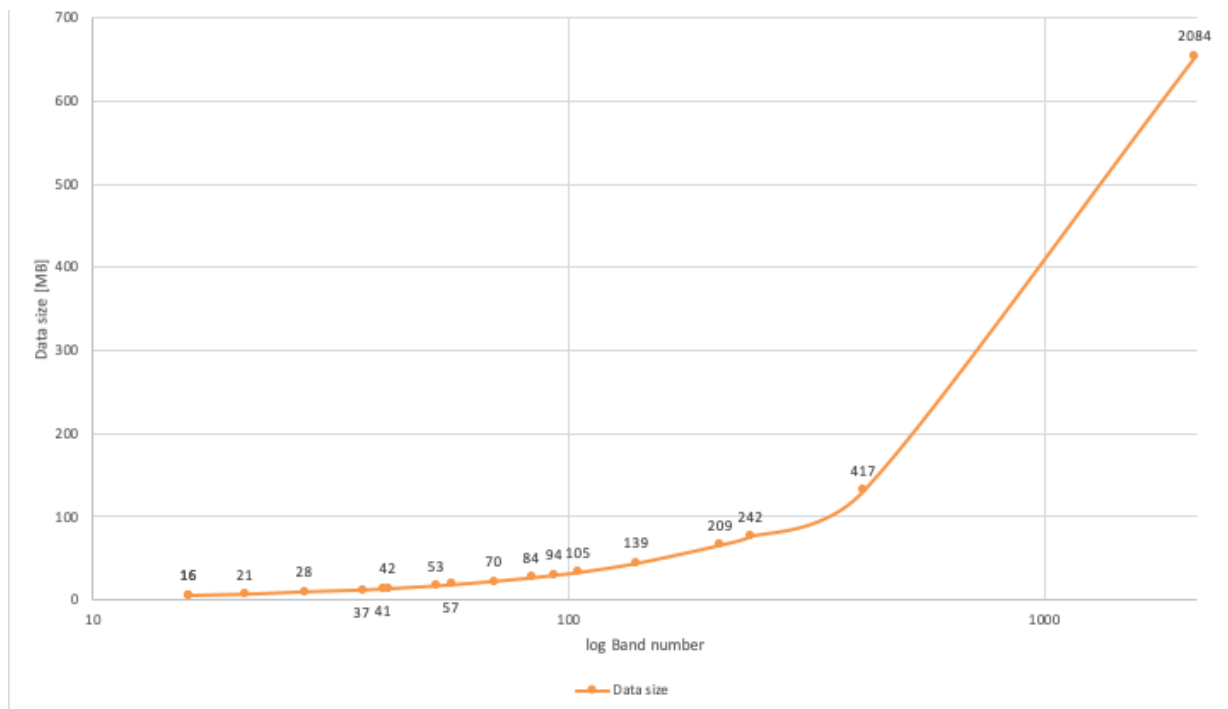


Figure 124 Plot of the data size of the successively downsampled data of the Brazilian iron ore hyperspectral scan.

The advantages and disadvantages in the context of mine face mapping in active open pit environments have to be considered in a case-specific context. Based on this laboratory-derived data of iron ore samples from Brazil, two main analysis requirements appear:

- If the detection of diagnostic SWIR-active minerals is important to map e.g. the clay content in a mine face, then VNIR and SWIR data of a high enough spectral resolution have to be utilized. This results in component maps that enable a distinction between ore bearing and waste rock by analysis distinct spectral mineral features e.g. by MWL or EnGeoMap 2.1.
- If a deposit can be characterized by a number of distinguishable, distinct rocks or mineral assemblages that can be summarized by site-specific sampling and in spectral libraries (e.g. iron rich rock, clay-iron-mix, silica-clay-mix) then a VNIR-only approach can save time and money and provides a system that is robust in handling. This results in material maps based on a site-specific library. SAM and BFF deliver acceptable results (around 70% of accuracy) and are relatively insensitive to variable illumination, another key factor for data acquisition in an open pit mining environment (Schneider *et al.*, 2011).

6.3 Apliki laboratory scan analysis

The resulting mapping accuracies for the different sensors utilized to analyze the Apliki mine sample laboratory data are again shown plotted in Figure 125.

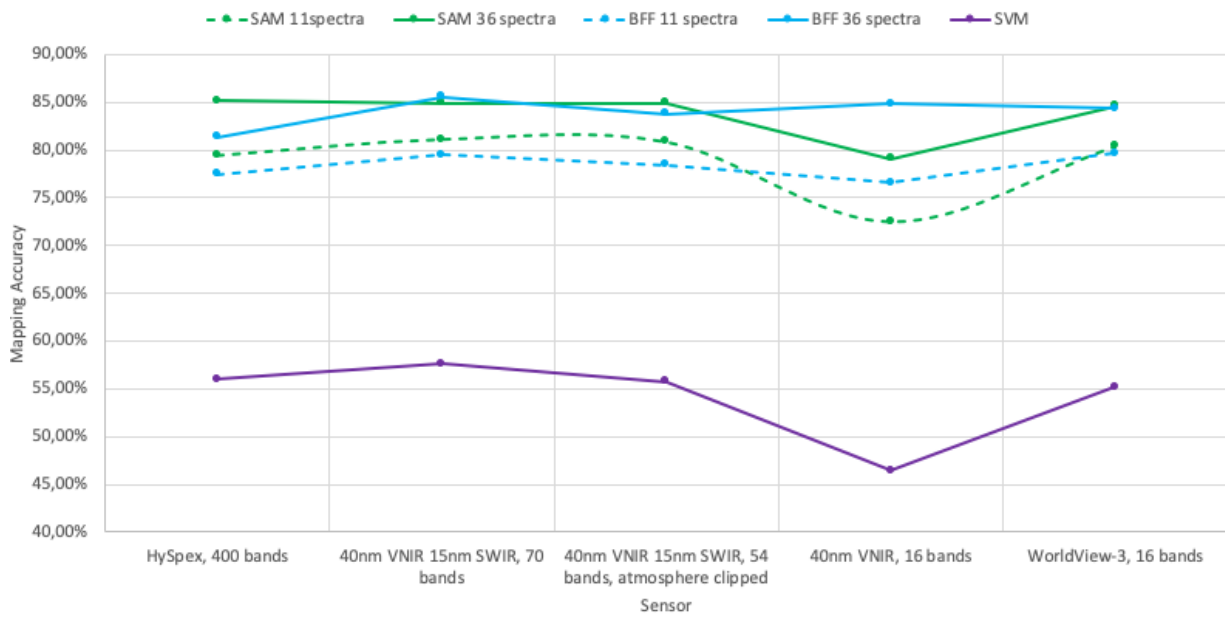


Figure 125 Apliki sample scan classification accuracies for five different sensors and three different classification algorithms (SAM, BFF and SVM).

Figure 126 present the computation times for each sensor, note the logarithmic scale of the y-axis.

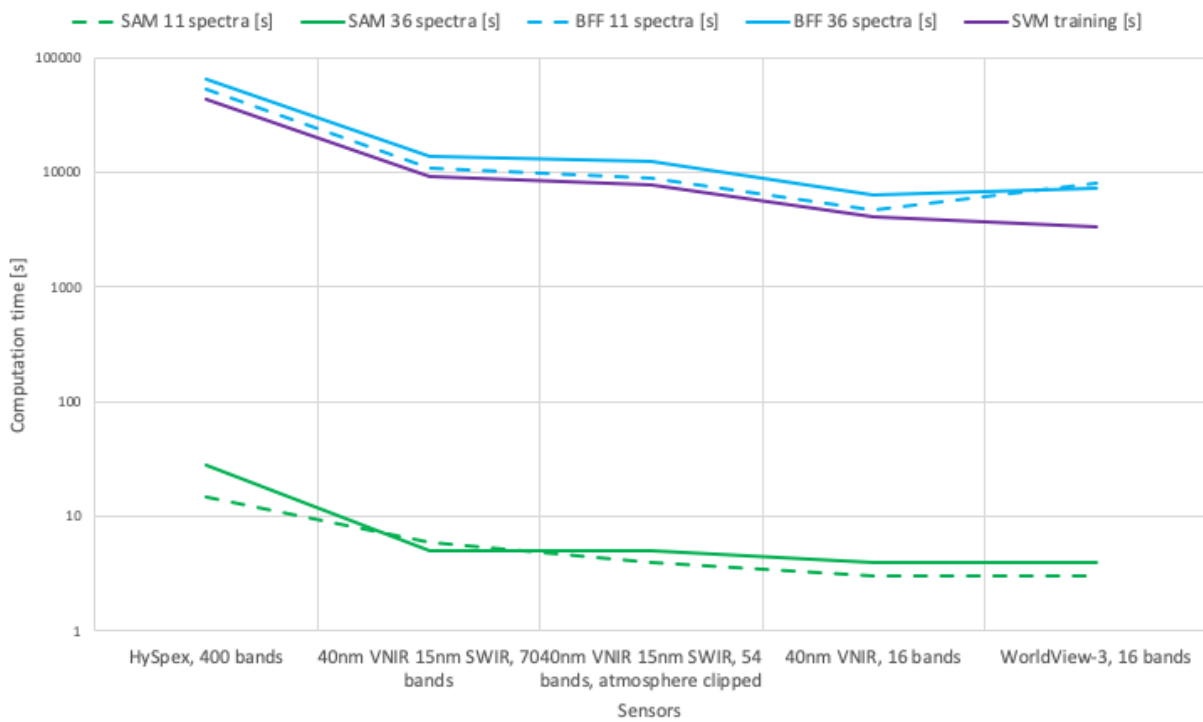


Figure 126 Computations times plotted for each sensor for the Apliki sample dataset.

Figure 126 shows significantly decreasing computation times with decreasing complexity of the sensor from hyper- (400 bands) to super- (74-54 bands) to multispectral (16 bands). The overall accuracy for the classification does not decline significantly with lower band numbers and only shows a lower accuracy for four of the five analysis methods – namely when excluding a significant portion of the wavelength range for the “VNIR-only” data. Comparing the mean classification accuracies for the two different libraries used (Table 49), it is apparent that the reduced spectral library based on the geochemical clustering underperforms.

Table 39 Classification accuracy mean compared for SAM and BFF and the two different spectral libraries utilized.

Classification	11 sample spectral library	36 sample spectral library
SAM mean result %	78.84	78.32
BFF mean result %	83.72	83.99

This leads to the conclusion, that the choice of library and of material to characterize a deposit or outcrop is one of the key factors to gain meaningful insight and accurate mapping results.

The overall accuracy of mapping is roughly similar for the BFF algorithm and SAM, but the computation time of the former is up to the factor of 3400 times higher than for the latter (see Figure 126 above).

The analysis of the radiance data set showed promising results but needs further research both in testing VNIR-based analyses and material distinctions for different deposit types and mineral samples and for developing a workflow in the field to include a physical rock/ mineral library within the outcrop scans to compile a radiance spectral library from areas of the scan. This is necessary as laboratory radiance data is not comparable with field radiance data. As the radiance data is highly influenced by the source of illumination, laboratory radiance spectra can only be applied to data derived in the same environment and not be applied to field radiance data. When deriving spectra directly from the scan (field or laboratory), either from the mine face itself or a panel positioned in front of the camera that is coated by the deposit relevant materials, even the VNIR radiance data seem promising for preliminary distinctions between different materials of interest.

6.4 Mine face mapping results

6.4.1 Apliki mine

The hyperspectral mapping results are compared to two validation sources. The first source for validation are the field samples, geochemical analyses and a set of color-coded sample points located in the accessible, 2nd level of the open cut. The second source to validate the mapping is the subzone mapping of the open cut based on the interpretation of 66 samples of the open cut (Antivachis, 2015). The Apliki open cut was analyzed with BFF and SAM. The SVM method was tested for the Apliki laboratory data but did not show sufficient results and the NN methods were not considered due to suspected overfitting or computation time concerns related to the test with the Brazilian iron ore dataset. Figure 127 shows the results of mapping for BFF and SAM compared to the 22 sample points for the 40nm VNIR- 15nm SWIR data. Both mapping approaches map the areas of sample points with the same accuracy for the optimum 40nm VNIR - 15nm SWIR data (approximately 82% in 18/22 points), but the correctly mapped points differ between the BFF and the SAM analysis.

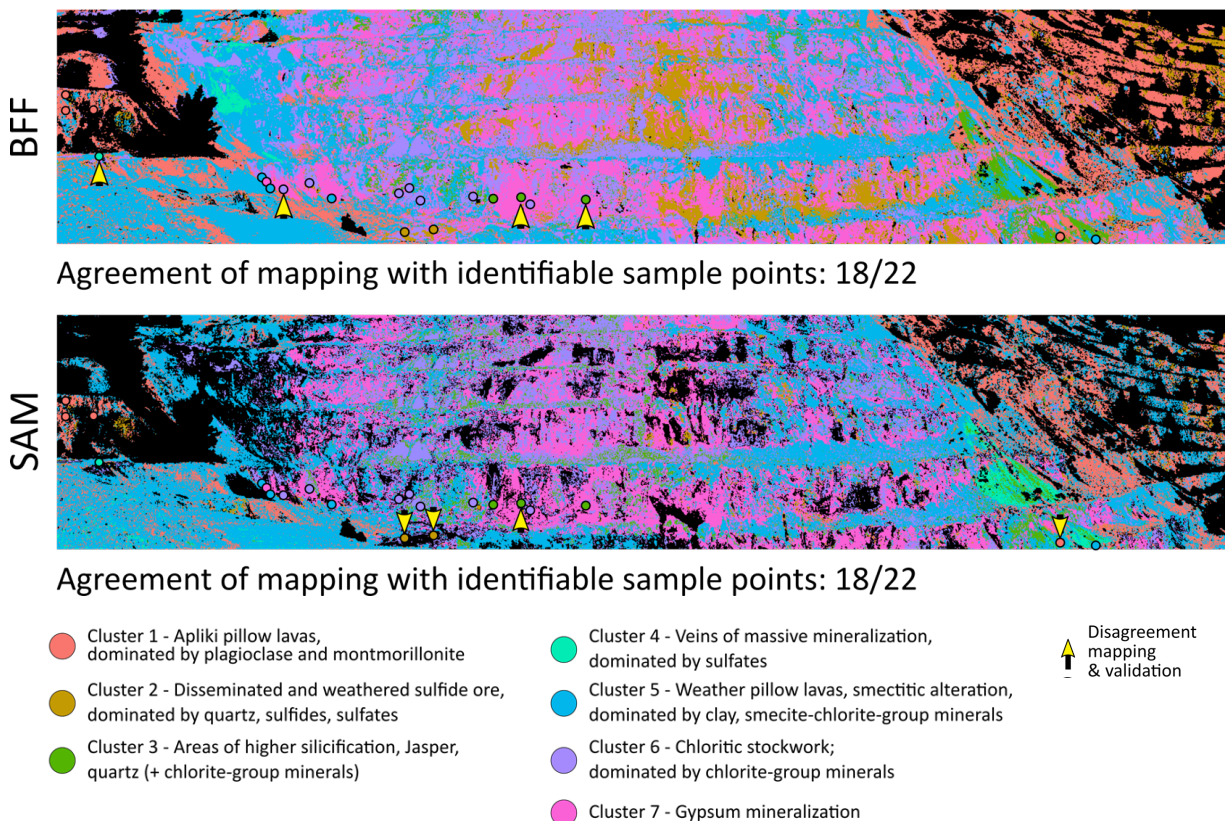


Figure 127 BFF and SAM mapping for 40nm VNIR - 15nm SWIR data of 390 spectral bands, compared to the validation field sampling points.

The BFF analysis maps an area in the west of the open cut (left side of the image) as “cluster 4” (turquoise) which correlates well with the mapped amorphous silica by Antivachis (2015). The western and eastern parts of the image scan are correctly mapped as “cluster 1” (red), related to the pillow lava occurrence. The Cu-rich precipitates in the areas of visible water runoff are mapped as “cluster 2” (yellow) in the BFF map but not the SAM map. The area of the stockwork zone is predominantly mapped as “cluster 6” (chloritic stockwork, purple) and “cluster 7” (gypsum, weathering products, pink) as well as “cluster 5” (clay alteration, smectitic-chloritic alteration, blue) for both the BFF and SAM map. The small landslide in the east of the image is either mapped as “cluster 3” (high SiO₂, green BFF) or as “cluster 4” (high Fe₂O₃, turquoise, SAM). The sampling validation in the area was classified as either “cluster 1” or “cluster 5”, red or blue respectively, and does not confirm either mapping of the BFF and SAM. SAM is unable to map the Cu-rich precipitates (color-coded in yellow, cluster 2) and seems to react stronger to albedo differences in the imagery, especially visible in the pit walls east of the open cut. Figure 128 shows a comparison of both the BFF and the SAM mapping results compared to the validation map of the open cut based on Antivachis (2015). BFF and SAM show a similar distribution of areal main components, especially in the open cut stockwork related zone. Compared to the SAM results, BFF finds more diverse material covers in the western part of the outcrop. SAM on the other hand distinguished different materials in the eastern part, where the BFF mainly maps “cluster 1”. SAM does have a higher number of “unclassified” pixels, especially in areas of higher albedo, e.g. the light precipitates in runoff, conical areas and in the western, upper levels of the open cut. The BFF analysis is able to map the light precipitates and hereby outperforms the SAM analysis for the Apliki outcrop.

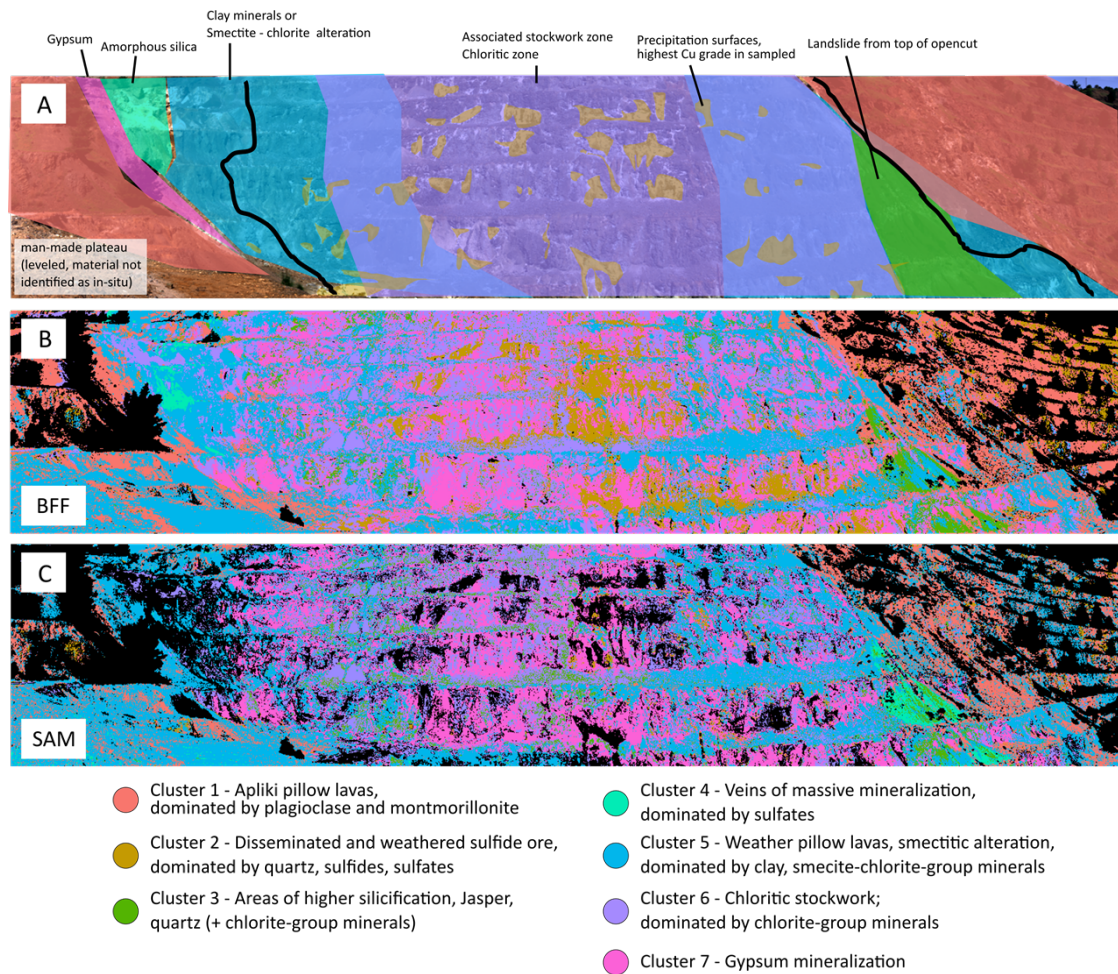


Figure 128 BFF (B) and SAM (C) analysis results for 40nm VNIR - 15nm SWIR data compared to the geological mapping of the open cut (A), based on Antivachis (2015).

Both BFF and SAM overestimate the occurrence of cluster 7 (gypsum dominated, dispersed weathering products, pink) especially in the central part of the outcrop compared to the expected geological map. When looking at the downsampled spectra used for the classification and comparing them with their full hyperspectral impression (Figure 129 & Figure 130) two apparent changes can be noticed: 1) the interpolation between 1300-2010nm excludes absorption features that are valuable in differentiating between the spectra and 2) due to downsampling from 400 to 54 bands, narrow small absorption features are smoothed out (e.g. the Fe feature around 450nm) this might additionally influence the mapping results.

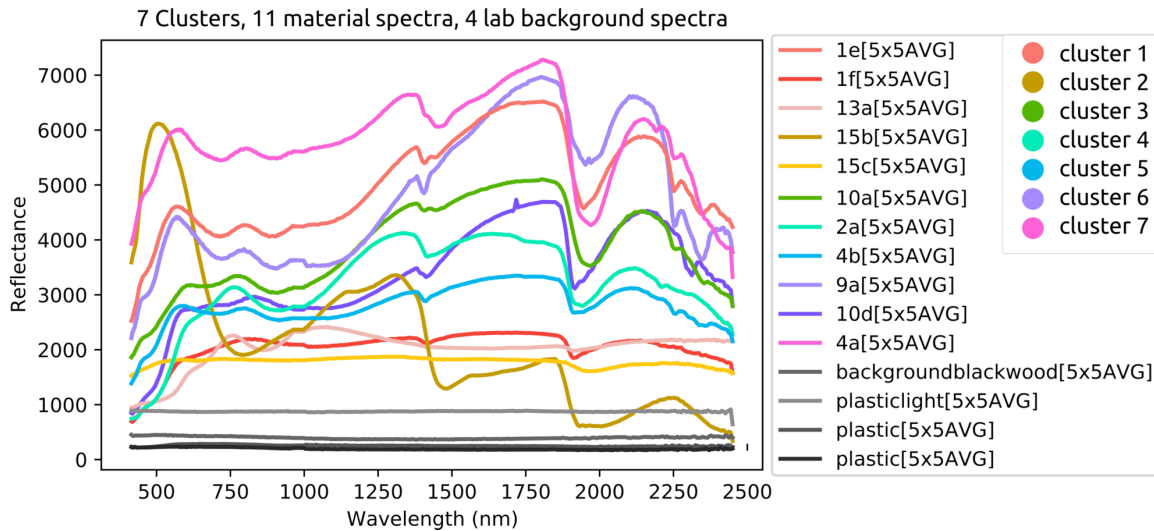


Figure 129 Spectral Library from 11 Apliki mine samples - full 400 bands, HySpex spectra. Color-coded is based on 7 clusters. Reflectance value scaled between 0-10000 (0-100%).

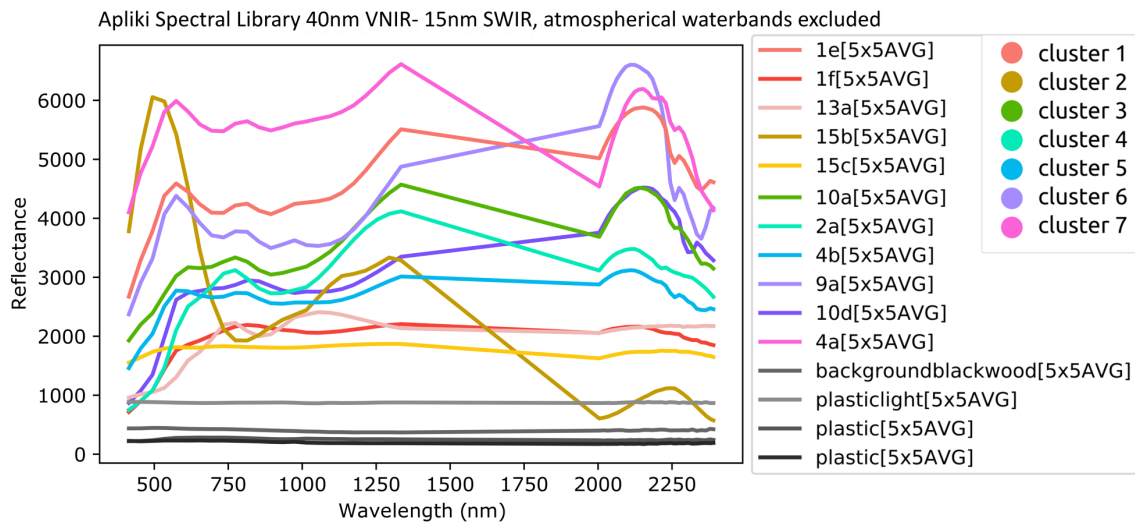


Figure 130 Spectral Library from 11 Apliki mine samples - downsampled, 40nm VNIR - 15nm SWIR spectra with interpolated spectral range between 1300 - 2010nm. Color-coding is based on 7 clusters. Reflectance value scaled between 0 – 10000 (0-100%).

Excluding the spectral range between 1300-2010nm enables the classification of field-derived data that is highly impacted by atmospheric absorption features. It also excludes valuable spectral features that can be crucial to differentiate between the different spectra. For example, gypsum (cluster 7, sample 4a, pink) shows a distinct feature around 1450nm as described in Moreira et al. (2014). This feature however is removed due to the interpolation in this range. The resulting spectrum 4a is now not representing the gypsum fingerprint anymore but resembles a spectral shape that is similar to the cluster spectrum represented by sample 1e (cluster 1, red) and 9a (cluster 6, purple). It is thereby not possible to map cluster 7 based on spectrum of 4a in its downsampled state. The color-coding “pink” now instead represents other spectra (1e, 9a) not typical for gypsum. In order to show an un-biased

analysis that is not influenced by the over-representation of the pink color-coding, the BFF analysis was repeated with a spectral library excluding cluster 7 (spectrum 4a). The analysis result is shown in Figure 131 below.

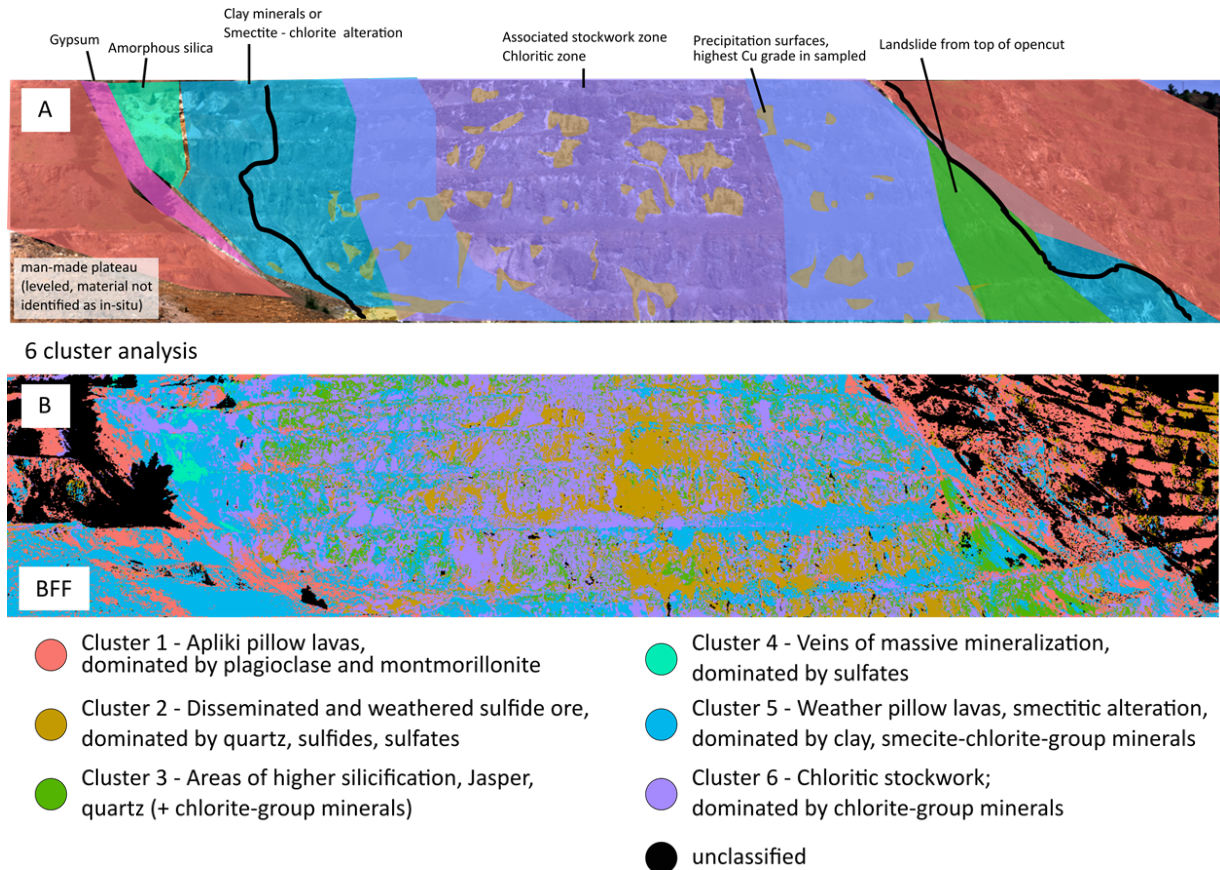


Figure 131 BFF analysis of Apliki based on 6 clusters, excluding cluster 7 (gypsum).

The new analysis based on 6 clusters represents the zones well that are mapped by Antivachis (2015). By excluding cluster 7 from the classification, the central part of the mine face becomes dominated by cluster 6 (chloritic stockwork zone) and cluster 2 (disseminated sulfide ore). From the central part outwards, the classification is dominated a mixture of cluster 6 and cluster 5 (smectitic alteration zone). Cluster 3 is now dominant in the landslide to the East but is also classified within the Western part of the mine face. As cluster 3 represents areas of silicification, a more pronounced mapping in the West correlates with the area identified as amorphous silica by Antivachis (2015). Reducing the clusters by excluding the downsampled and now spectrally inactive cluster 7 from the analysis results in a more coherent concise mapping of the mine face. This highlights how important both the geological and spectral validation is. Geologically, the ground truth needed is the comprehension of the expected zonation and the ability to realize when a material is overrepresented in the spectral map. The needed spectral validation comprises the evaluation of the spectral reference library and the

continuous re-evaluation of the data and the spectral library during the downsampling process. This holds especially true when the mapping is not based on spectral libraries (that can easily be checked and evaluated for their spectral interpretative value) but results from training-based classifiers and small training areas. An SVM was trained on the 54 bands laboratory dataset of the Apliki samples (downsampled to “40nm VNIR – 15nm SWIR atmospheric impact excluded”). The trained SVM model for the laboratory data showed results of below 60% accuracy for the mapping. When inferring the SVM model to the 54 bands field data, the resulting map does not show with the expected geological situation of the mine face (Figure 132). Please note the different color-coding of the clusters for the SVM, which is according to the validation for the SVM in the laboratory tests. Not only is the vegetation mapped as cluster 6, even though it was masked out from the data but the majority of the area is mapped as cluster 5 (“weathered pillow lava”) allowing nearly no differentiation of the zonation in the mine face. This result again underlines the importance of geological and spectral experts that understand the nature of the open pit and recognize an incorrect biased mapping result when they see one. Training based algorithms can have a huge advantage and they showed the highest accuracies in the laboratory testing for the iron samples. But when inferring the SVM model to the outcrop scale and to data impacted by different acquisition conditions the mapping results have to be scrutinized. Even when excluding the obvious atmospheric impact from both the training dataset (laboratory) and the dataset for mapping (mine face) the resulting map has to be considered carefully and in the case of the map shown in Figure 132 does not pass the examination.

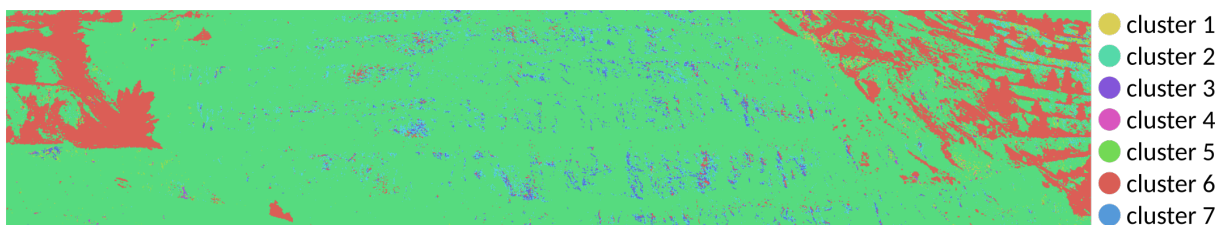


Figure 132 Apliki mine face map based on SVM trained on laboratory data. Note the different color-coding compared to the BFF and SAM maps.

6.4.2 Three Hills mine

The analysis of Three Hills was based on a rudimentary color-coding scheme and is supposed to map areas of high, medium and low Cu-content. The color-coding that was chosen in Section 5.6 (p. 161) is deliberately only supposed to depict trends in the Cu-content and did not focus on mineralogy, mineral assemblages or contaminants. From communications with HCM and the position of the stockwork indicated by geological maps of Adamides (2010b), the Cu-grade distribution in the open pit shows an increase of Cu-content towards the S of the fault line (indicated in white in Figure 133) and a decrease towards the north. An increased brecciation within the stockwork zone is accompanied by clayish alteration zones (low in Cu), whereas the upper contact to the former surface is accompanied with a higher oxidation of pyrite and brown horizons (Naden *et al.*, 2006).

Figure 133 shows the Three Hills deposit fault position and Cu-grade trends and Figure 134 depicts a sketch of visible zones from the field work performed in 2018.

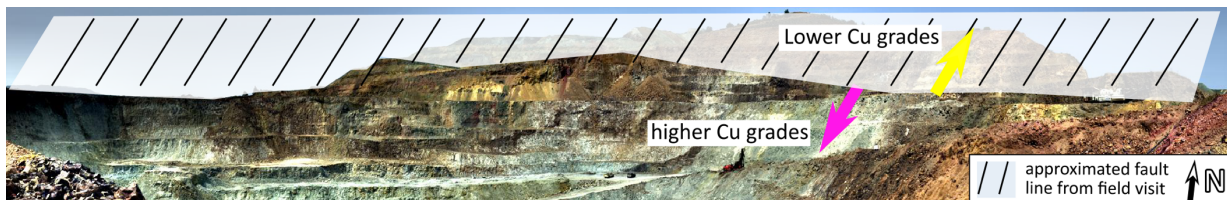


Figure 133 Three Hills deposit, fault position and Cu-grade trend.

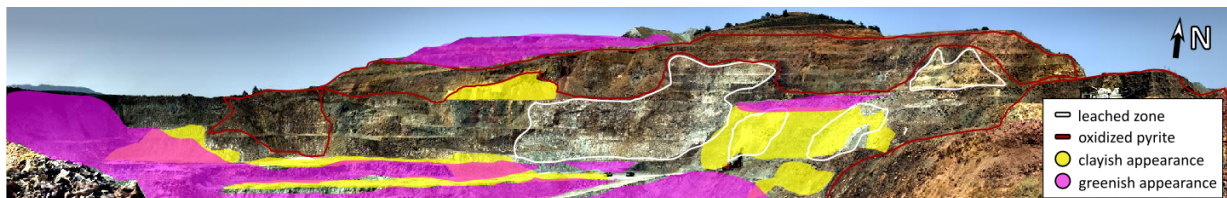


Figure 134 RGB vision based sketch of areas of clayish and chloritic appearance (yellow and pink respectively) and of areas of oxidized pyrite (red outline) and leached zones (white outline).

The applied spectral library depicts the copper trends, color-coded for high, medium and low contents. The samples color-coded as medium (red) indicate an overall average sample composition, whereas the low-Cu samples (yellow) show an increase in Na₂O and Al₂O₃, indicating the presence of feldspar and associated clay alterations in the area. Figure 135 presents the mapping results of the BFF for Three Hills.

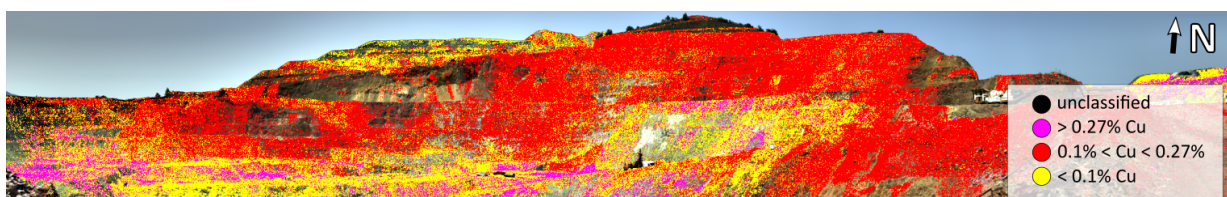


Figure 135 Mapping result of BFF with color-coding based on high, medium and low copper grade.

The open pit shows a trend along the indicated (Figure 133 above) fault line, mapping dominantly average/ medium Cu-contents in the northern part of the fault and the high- and low-Cu grades south of the fault line, lower in the open pit. The mapping of high-grade (>0.27% Cu) is constricted to the lower open pit as communicated by HCM in March 2018. The area mapped as low-Cu-grade is also associated with the lower parts of the open pit and areas mapped as “leached” in the RGB imagery (Figure 134 above). Qualitatively, the hyperspectral mapping of the pit follows the geological reasoning and along the fault line and can be seen as valid.

7 Conclusion

The material distribution within a mine face can differ substantially in the small scale and within daily assigned extraction segments. These changes are not always visually identifiable but prove to be relevant for the processing steps that follow extraction. These steps are influenced by mineralogical changes within the extracted material depending on the ore grade and contaminant content. Misclassifications result in sending ore to waste dumps and waste to the stockpiles. This must be minimized in order to reduce energy-intensive material re-handling.

The evaluated and compared approaches in this area have concentrated on mapping the mineral composition (Kurz, 2011; Schneider *et al.*, 2011; Murphy, Monteiro and Schneider, 2012), using specific mineral horizons as markers (Murphy *et al.*, 2015) and mapping units based on image-derived spectra limiting the number of geological units to those visible by the naked eye (Kirsch *et al.*, 2018). The main approach is to map minerals based on the position and depth of distinct, narrow mineral features (Dalm, Buxton and van Ruitenbeek, 2017; Kirsch *et al.*, 2018; Lypaczewski *et al.*, 2020). Mapping based on mineral-specific features is a useful tool in identifying areas dominated by different contaminants (e.g. clay, carbonates) but does not account for the natural variability and complexity of mineral compositions in the rock surfaces. Additionally, relying on hyperspectral systems for narrow absorption features implies using expensive, heavy, complex, delicate sensors that are not easy to handle for the average workforce in a mining project, neither for data acquisition nor the subsequent data processing and analysis. Additionally, the hyperspectral data cubes from the acquisition and the analyses result in the necessity of providing high volume data storage. There is a need for virtual outcrop models to accurately depict the geological units of the mine face; some proposed workflows and methods have started to find solutions for this need.

In this work, I propose an application-based sensor adaptation and analysis. This is achieved by reducing the sensor complexity, effectively by downsampling the spectral resolution of the system. The downsampling is performed by systematically decreasing the number of spectral bands whilst increasing each band's bandwidth. The successful preservation of the material-specific spectral characteristics is evaluated throughout the downsampling process and the best-fitting sensor model to represent the materials' spectral properties is selected. This spectral dimensionality reduction reduces the complexity of the data and enables reduced data sizes and computation times. The mapping results are presented as per-pixel, hard classifier maps. They were evaluated geologically and spectrally and represented the expected regional geological situation.

The main outcomes of this work are:

The theoretical reduction of sensor complexity

The hyperspectral laboratory data cubes were downsampled to superspectral resolutions and reduced in their spectral range. The results of the spectrally downsampled datasets were compared and showed good results. In order to apply this to outcrop conditions, particularly data impacted by the atmosphere, the atmospherically impacted bands were removed and interpolated between the shoulders of 1300–2010nm. The analysis of this further downsampled data again showed promising results. Successfully applying the analysis to VNIR-only data in the end presented the possibility for a lighter, less cost-intensive, robust and easy to handle system for superspectral rock differentiation. This questioned the need for a full spectral range VNIR-SWIR hyperspectral system and focused on the idea of simplifying the spectral range and spectral resolution without compromising the quality of the results achieved for the mining industry. Spectral sensors should instead be customized 1) to geological use cases and 2) to the deposit of interest. This concludes the need for further testing to develop sensors for geological applications and create sensors with deposit-specific sensor characteristics.

The correct choice of spectral libraries

The right choice of spectral library is imperative to get acceptable results for hard and soft classifier maps. The three test cases showed that automated PPI + n-D visualization or SMACC spectral EM determination is not sufficient to spectrally characterize a geological sample set or deposit. Image-derived EM spectra were not describing the complexity of the sample range sufficiently. Instead, image-derived spectra were shown to bias towards spectral peacocks at the outer ranges of the spectral variability and did not account for the more average and abundant rocks or minerals assemblages. The acquisition of spectral EMs at the mine face with handheld spectral equipment and the sampling for geochemical validation captures the variety of materials and mixtures; it does not, however, comply with the security regulations and the potentially instable cliff sections.

The on-site geologists are experts in the mineralization of the deposit and best suited to sample and provide all geologically relevant samples of the deposit. The sampling can take place from the extracted, characterized material instead of taking place at the risky mine front. Rock (mixture) samples are superior to one-phase mineral samples. The spatial resolution of the sensors almost never allows for a spectral sampling of single-phase minerals on-site, therefore providing the analysis algorithms with single-phase mineral EMs is not sufficient. This leads to the conclusion that the spectral library has to be defined around the needs of the geologist on site, sampling spectra from rocks with known ore and contaminant levels. Whilst the analysis and algorithms themselves do not have to be

expert-based, the compilation of the spectral library should be. The establishment of a suitable spectral library therefore remains an expert job both for the on-site geologist by providing the relevant samples and the spectral expert to collect and cluster the relevant spectral fingerprints for each geological unit.

Geological and spectral expert knowledge input is inevitable

The comparison of the ground truth field mapping with the BFF and SAM mapping showed a bias towards the classification of cluster 7 (gypsum-dominated). Only with the geological knowledge that gypsum occurrence is not that widespread in the mine face could the site-specific spectral library be re-evaluated. It turned out that excluding wavelengths ranges impacted by the atmosphere from the spectrum of class 7 also excluded the distinct gypsum feature. Class 7 therefore was not classifying areas of gypsum occurrence but classified a random, lab-made synthetic spectrum not indicative of any real material. This example shows that even when compiling a site-specific spectral library based on geological expert knowledge, the data and inputs for the classification have to be checked for their spectral soundness. As for many computing applications, “garbage in, garbage out” can only be avoided by a sound screening of the input files in this case the HSI and the spectral library.

Indications from measurement conditions at the mine face scale

Measurements at the mine face level have to be further improved to allow for safe labor with regard to the spectral measurements. Ground-based tripod measurements can theoretically be taken from any distance but are dependent on the desired spatial resolution of the mine face (area captured by each pixel). With distance the impact of the atmosphere is also increasing. For the SWIR-320m-e sensor (28° FOV), this means in order to capture an average mine face of 10m height, the minimum distance of the sensor to the mine face is 20m. This results in ca. 2cm of lateral pixel size. Positioning the sensor at longer distances is dependent on the size of geological structures that have to be resolved and the size of the white reflectance targets that need to be captured for the reflectance retrieval. A distance of >200m and resulting pixel size of ca. 15cm is an approximate maximum for the 28° FOV SWIR system to resolve geological structures, while still allowing for a large white reflectance target of >80 x 80cm to be resolved. The position of the tripod within the mine is reliant on safe areas to setup the cameras and to take measurements for 30min without interruptions. This leads to another challenge regarding the safety concerns. The setup of the white reflectance targets for reflectance retrieval is a major safety issue and requires the operators to access the mine face and place the targets in front of the rock outcrop. This is not always possible due to inaccessibility and instability of the outcrops nor should this be an advised procedure. Additionally, the placement of the targets is time

consuming and not easily integrated in the busy schedule regarding mine face related planning. Two possible solutions come to mind: 1) measurement of the mine face by UAVs calibrated before takeoff, flying in proximity to the mine face thereby negating the necessity to approach the outcrop to place a tripod and target. 2) Built-in irradiance sensors measuring the changes of illumination during the tripod- or UAV-based spectral measurement and allowing for a reflectance retrieval that is accurate to the split second and does not rely on physical white reflectance targets.

Within this work a non-conclusive list of challenges for the application of HSI in the context of mining was presented (Table 2, p. 6). These challenges have been addressed and discussed theoretically and some were approached in more detail. Table 40 includes the results of this work in regard to some of these challenges.

Table 40 Challenges for superspectral measurement equipment in the context of mine face scanning and possible solutions as a result of this work.

#	Challenges	Development of Solution	Results of this work
1	Ruggedness	Protective casing, dust-proof ventilation, GUI adjusted to outdoor conditions & handling with Personal Protective Equipment	A decrease of band numbers and spectral range can aid in developing smaller, lighter, less complex sensors, ruggedness could be improved simultaneously. A hardware solution for this challenge e.g. protective casing is yet to be found.
2	Measurement and analysis speed	Definition of optimal balance between spectral bands and spatial resolution in order to keep pace with the dynamics of mining operations	Downsampling to superspectral 40nm FWHM VNIR and 15nm FWHM SWIR and excluding wavelengths areas impacted by the atmosphere is a reasonable option to increase scanning speed and decrease data size, data acquisition time and analysis computation time.
3	Fast analysis	Allowing for quick decision making in the mine-pit (near-real time); Ideally onboard processing	Downsampling the data to superspectral is a valid option to increase the analysis speed. Built-in irradiance sensors can speed up the reflectance retrieval and increase the safety of the measurement.
4	Increased demand for application in mining still limited by pricing of sensors	Lower hardware prices will enable decision makers to purchase systems for each mine and advance the understanding and applications for the tool "HSI" whilst simultaneously increasing their efficiency	Smaller band numbers and smaller spectral ranges (site- or deposit-specific) enable lower hardware prices. Future research will develop "deposit-specific" sensors that have improved spectral characteristics for a geological use case and additionally for specific deposits. If the demand for the technology increases it will evolve around that demand.

#	Challenges	Development of Solution	Results of this work
5	Determination between ore, main contaminants and waste	Broad material categorization to distinguish ore grade and contaminant variability	The site-specific spectral libraries (1 spectrum per relevant sample) were superior to the automated, spectral EM retrieval from the sample suites (e.g. PPI, SMACC). Field imagery derived EMs are nearly impossible to validate sufficiently and sampling at the mine front poses too many safety risks both for physical sampling and spectral sampling with handheld systems.
6	Size & weight	Size and weight need to be reasonable for drones that do not require special pilot licenses and can be safely handled	Downsampling the sensors can improve the size and weight of the sensor by decreasing the overall complexity of the system.
7	Power consumption	Optimization of battery utilization with respect to commonly needed measurement and flight time	Again, downsampling can be part of a solution to decrease power consumption. A VNIR-only setup can negate the need for power-consuming liquid nitrogen cooling needed for the SWIR detector. The VNIR-only analyzes in this work showed promising results, but this is highly dependent on the spectral characteristics of the material of interest.
8	Cooling of sensor	Efficient and dust-proof cooling system to withstand high temperatures in mine pits	A VNIR-only setup negates the need for the SWIR detector liquid nitrogen cooling and showed sufficient results in this work.
9	Albedo correction and feature retrieval of data	Automated pre-processing of data, at-sensor reflectance retrieval and feature retrieval/enhancement enabling faster, more flexible and easier to analyze datasets	Common sense determines a solution for reflectance retrieval based on built-in irradiance measurements instead of targets that have to be placed along the mine front and do not comply with safety requirements. This is yet to be achieved. The reflectance retrieval utilized in this work produces sufficient results but is too slow to consider for big amounts of data.
10	Impact of variable incident light conditions	Flexible schedules in mining require variable acquisition times for HSI data this leads to different illumination conditions	Classification algorithms must yield consistent results under varying illumination conditions. The BFF algorithm shows consistent results even in areas of shadows and is in theory relatively insensitive to changing illumination. It performed slightly better than the SAM algorithm for the here presented data.

8 Outlook

8.1 Application to World-View 2 satellite data

WorldView-2 (WV2) VNIR archive data was provided by European Space Imaging® after it was granted within the third-party mission (TPM) Project ID 61058 by the European Space Agency (ESA) on 24th July 2020. A subset of the data was created that includes the open pit and surrounding area of Apliki. The data was delivered orthorectified in 8 VNIR bands and collected on the 15th of August 2018 at 08:58am local time with a mean sun azimuth angle of 146.1°, a mean sun elevation angle of 65.69°, a mean satellite azimuth of 244.6° and a mean satellite elevation of 62.5°. The mean off nadir angle is 24.2°. The delivered pixel size is 2mx2m. The data is projected in EPSG: 32636 - WGS 84 / UTM zone 36N and was corrected with ATCOR version 9.3.0 © DLR/ ReSe 2019, IDL 8.5 (Richter, 2007; Richter and Schläpfer, 2011). The RGB imagery of a subset of the WV2 data is shown in Figure 136. Please note, that the waste piles in the North of the open pit are located within the UN Buffer Zone and are therefore not shown.

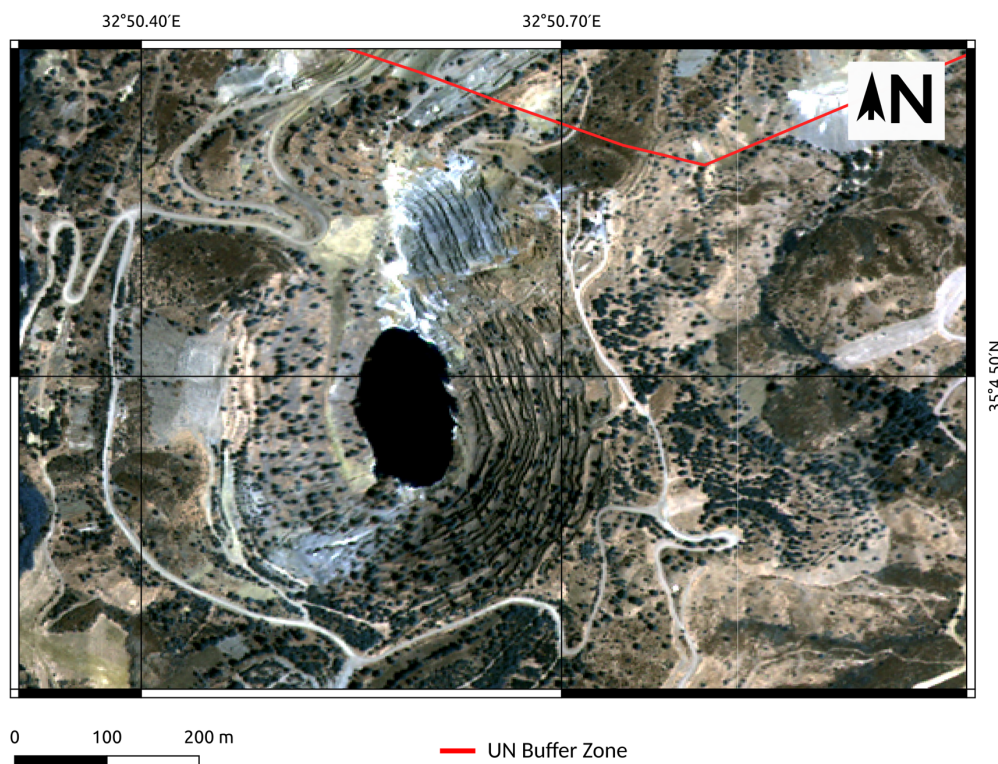


Figure 136 RGB imagery of the WV2 scene from 15th of August 2018. European Space Imaging WorldView-2 data has been provided the European Space Agency ESA within TPM Project ID 61058.

The data was analyzed using the BFF algorithm and the spectral library of Apliki with 35 samples. The spectral library without cluster 7 was applied as it showed to bias towards mapping the gypsum

occurrence. Figure 137 shows a grey-scale image of the data showing the size of the summarized triangle areas of each pixel spectrum. Pixels without significant features will not yield a high sum of their triangle areas and are represented in dark colors. Pixels with significant spectral contrast (e.g. vegetation) are represented in light colors. Areas with low spectral contrast can be identified and represent the areas with higher possible material identification errors.

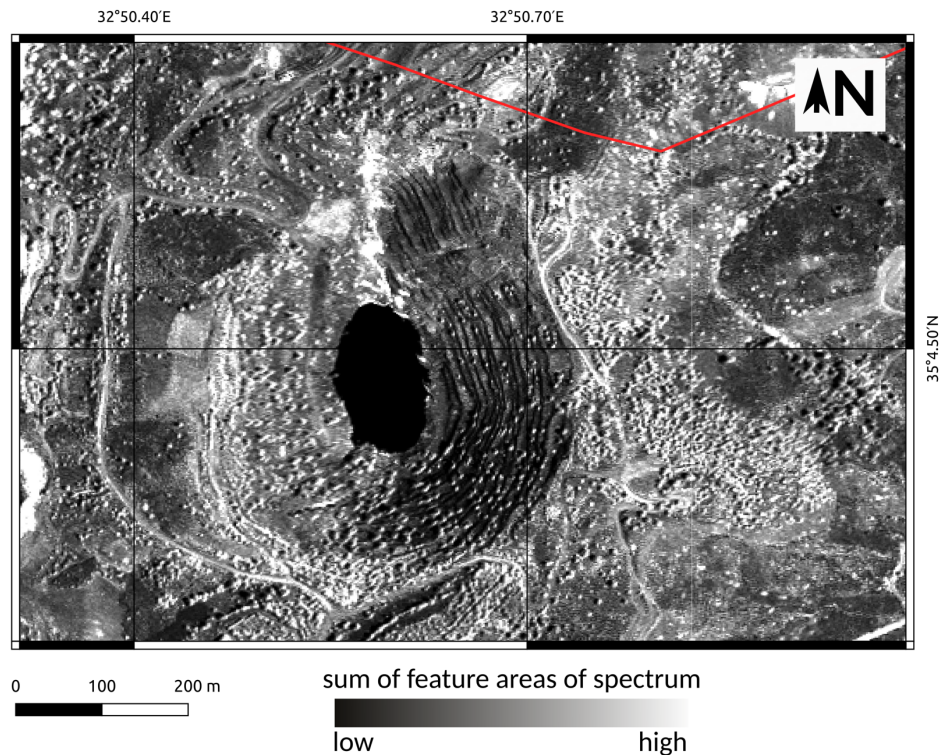
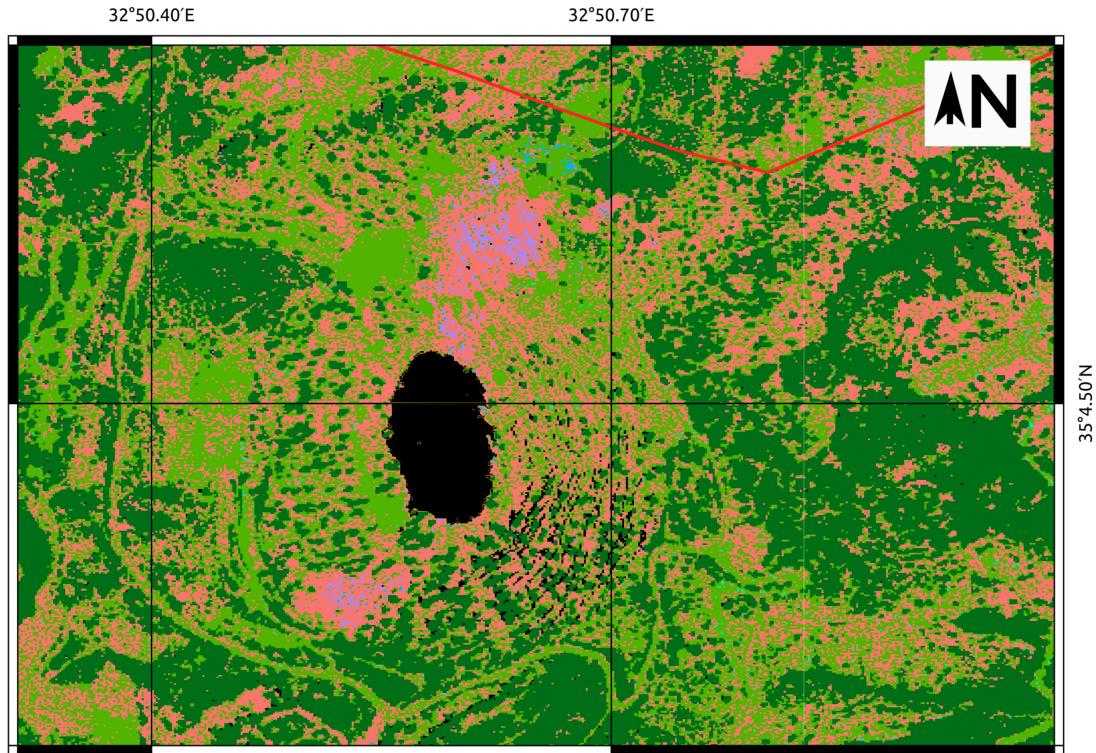


Figure 137 Quality map, pixels with high spectral contrast and therefore low possible classification error are represented in light colors. European Space Imaging WorldView-2 data has been provided the European Space Agency ESA within TPM Project ID 61058.

Figure 138 shows the result of the surface material mapping. The area is dominated by vegetation cover as already visible in Figure 138. The main surface materials is mineralized Apliki pillow lavas (red, cluster 1) and areas of higher silicification + chlorite group minerals (light green, cluster 3). The mine faces in the NNE of the open pit are mapped as chloritic stockwork (purple, cluster 6). A smaller area SSW of the open pit lake is also mapped as chloritic stockwork. This correlates well with the zone of brecciated lavas that is enclosed by two major parallel faults west and east of the pit lake, as identified by Antivachis (2015).



- Cluster 1 - Apliki pillow lavas, dominated by plagioclase and montmorillonite
 - Cluster 2 - Disseminated and weathered sulfide ore, dominated by quartz, sulfides, sulfates
 - Cluster 3 - Areas of higher silicification, Jasper, quartz (+ chlorite-group minerals)
 - Cluster 4 - Veins of massive mineralization, dominated by sulfates
- Cluster 5 - Weather pillow lavas, smectitic alteration, dominated by clay, smectite-chlorite-group minerals
 - Cluster 6 - Chloritic stockwork; dominated by chlorite-group minerals
 - Vegetation
 - Unclassified
 - UN Buffer Zone

S

Figure 138 BFF analysis of the Apliki WV2 data with site-specific spectral library with 35 samples, color-coded within 6 geochemical clusters. European Space Imaging WorldView-2 data has been provided the European Space Agency ESA within TPM Project ID 61058.

The application of the site-specific spectral library for high-resolution satellite imagery shows the possibility of acquiring consistent geological information of larger areas and understanding the spatial relationships of materials covers in a deposit. It also shows the high level of vegetation cover occurrence and that 2m x 2m pixels will be spectrally dominated by vegetation even when the RGB representation of the image does not indicate such a high level of vegetation cover.

8.2 Topics of future research

This work showed a few approaches to solve persisting challenges in applying HSI for near-field geological maps within a mining context. Other challenges are mentioned below but have not been part of this work. They will need to be considered within future research projects.

Sensor improvements

Rugged and portable instrumentation is needed that can be handled easily by the on-site workforce. Its size and weight have to be handled by one person and need to be below the requirements for special UAV license certifications. This could be achieved by detector and sensor chip developments for HSI sensors or as proposed in this work by downsampling and simplifying the spectral resolution and by creating superspectral, deposit-specific sensors. The theoretically downsampled sensors are in fact theoretical. The practical realization has to be achieved in collaboration with sensor manufacturers willing to develop and offer superspectral instead of hyperspectral systems. Higher spatial resolutions and built-in irradiance sensors for accurate reflectance retrieval are additional steps that need to be solved to achieve a successful implementation in the mining sector. In order to characterize geological materials sufficiently, the sensors have to be adapted for the environment of application. This means developing sensors with wavelength ranges and sensitivities suited to geological materials or to deposit-specific purposes. This could mean e.g. a reduced wavelength-range sensor operating in the SWIR wavelength range to map different clays and monitoring contaminant levels in a copper mine.

Image Geometry and data integration

Close-range panoramic imagery shows an angular component in the along-track direction of the sensor rotation. This results in a significant amount of non-uniformities or intensity gradients as stated by Kurz (2011). A varying amount of diffuse irradiance is received at the sensor due to the sensor's rotational movement and different mine face surfaces in the FOV as well as different exposures to the open sky. Image non-uniformity correction has been part of the outlook of Kurz (2011)'s PhD thesis. The change in the area size depicted by each pixel for ground-based measurements is another topic that has not been heavily researched. Murphy et al. (2015) showed that improper or no geometric correction of the rotational HSI resulted in over- and underestimation of surface area up to a factor of two. The change of area depicted by each pixel in the x and y direction of the imagery has to be accounted for to make volume predictions of the extractable material.

The integration of the hyper- or hyperspectral data has to be achieved seamlessly, not only with geometric data (e.g. LiDAR) but also within the modeling programs used on-site. To this end, the sensors need to be equipped with GPS systems to accurately provide geo-referenced data to be integrated with geometric models and mine planning and management software. A potential solution to reduce geometric inaccuracy offer high-spatial-resolution full frame sensors as state-of-the-art geometry approaches like SfM can be utilized straightforward on the data.

Data processing improvement

The illumination conditions and scattering effects do not only change due to differing mine face geometries or the representation of different amounts of mine face vs. sky in the recorded line but also by the changing illumination conditions during the measurements (Kurz, 2011). An ideal cloud-free sky is the optimum but far from the reality, this has to be accounted for to acquire useful data under sub-optimal conditions. Reflectance retrieval by calibrating to white reflectance targets placed in front of the outcrop do not only insufficiently model the changing illumination conditions but pose a safety hazard to the on-site workforce. It is time-consuming and inadequately fits into the busy schedules of parallel tasks taking place at the mine front. Reflectance retrieval needs to be achieved by built-in irradiance sensors. In the case of ground-based rotational measurements this implies measuring the changing irradiance for each line of the HSI.

Spectral resolution

Downsampling the spectral resolution to sensors with 50+ bands showed to be sufficient to map geological characteristics in the sample sets and mine face scans. Excluding the spectral bands impacted by interactions with the atmosphere improves the results on average. As the library based SAM and BFF analyses showed the best results but are methods that take the full spectral range and shape into consideration, a few broad spectral bands should be present in the range of atmospheric bands (1300–2010nm) in order to depict the overall shape of the spectrum better than done by be excluding these wavelength ranges completely and interpolating between them. The impact of preserving the overall spectral shape whilst excluding the impact of the atmosphere was not tested in this work and should be included in future tests.

Data products

Implementation in mine management and planning cycles requires a consistent data product that is used for planning purposes. The best-suited data product has yet to be defined by the mining sector and geologists working with this data in their day-to-day activities. Open questions need to be

addressed. Are hard classifier maps needed in order to characterize the deposit? Is it sufficient to base the classification on site- or deposit-specific spectral libraries of samples with known ore grades and contaminant content? Or is it better to map clay, mica and epidote/chlorite content (SWIR active mineralogy) separately by creating feature position and -depth maps for single mineral phases with high resolution, hyperspectral systems? The implementation to active mine planning will need some trial and error to find a way that best serves the industry and the workforce to benefit from the data. Additionally to these questions (hard- or soft pixel classifier maps) even the right visualization of the results has yet to be found (Kurz, 2011).

This research does not only illustrate the existing challenges in the field of proximal, geological remote sensing in context of the open-pit mining sector, but also highlights the possible solutions and already existing approaches. The need for fast, reproducible imaging approaches to map quickly changing deposits, open pits and mine faces will increase in the future and calls for simple, cost-efficient solutions either by ground-based or UAV-based measurements. The need for routine monitoring can only be met with robust, reliable, lightweight, safe systems. The main requirements for this future sensor and methodology have been discussed in this work and a number of building blocks towards a future solution have been presented. The hope of Tobias Kurz is as valid today as it has been 10 years ago, that “close-range imaging spectrometry will become a sub-discipline in remote sensing, and a standard tool in field-based geoscience studies” (Kurz, 2011). Adding to this, it is anticipated for superspectral imaging to become a regular tool in the mining sector to assess and characterize deposits in the mine-face scale based on ground- or UAV-based measurements in the upcoming years.

9 References

- Adamides, N. G. (2010a) "Mafic-dominated volcanogenic sulphide deposits in the troodos ophiolite, Cyprus part 1 - the deposits of the Solea graben," *Transactions of the Institutions of Mining and Metallurgy, Section B: Applied Earth Science*. doi: 10.1179/1743275811Y.0000000001.
- Adamides, N. G. (2010b) "Mafic-dominated volcanogenic sulphide deposits in the troodos ophiolite, Cyprus Part 2 - A review of genetic models and guides for exploration," *Transactions of the Institutions of Mining and Metallurgy, Section B: Applied Earth Science*. doi: 10.1179/1743275811Y.0000000011.
- Antivachis, N. D. (2015) "The geology of the northern part of the apliki Cyprus-type ore deposit," *Bulletin of the Geological Society of Greece*, 49, pp. 4–28. doi: 10.12681/bgsg.11047.
- Asadzadeh, S. and de Souza Filho, C. R. (2016) "A review on spectral processing methods for geological remote sensing," *International Journal of Applied Earth Observation and Geoinformation*. Elsevier B.V., 47, pp. 69–90. doi: 10.1016/j.jag.2015.12.004.
- Asmus, B. (2013) *Gossan or the Iron cap*. Available at: <http://en.archaeometallurgie.de/gossan-iron-cap/>.
- Audebert, N. (2020) "DeepHyperX." Available at: <https://gitlab.inria.fr/naudeber/DeepHyperX>.
- Audebert, N., Le Saux, B. and Lefevre, S. (2019) "Deep Learning for Classification of Hyperspectral Data: A Comparative Review," *IEEE Geoscience and Remote Sensing Magazine*, 7(2), pp. 159–173. doi: 10.1109/MGRS.2019.2912563.
- Aveva (2020) *Digital Mining Transformation*. Available at: <https://sw.aveva.com/mining?hsLang=en> (Accessed: April 27, 2020).
- Bakker, W. (2018) "HypPy User Manual - graphical user-interface (GUI)." Wim Bakker, p. 76.
- Bakker, W. and Oosthoek, J. (2020) "HypPy Hyperspectral Python Toolbox." © copyright 2020 - Wim Bakker, part of the University of Twente. Available at: <https://blog.utwente.nl/bakker/hyppy/> (Accessed: April 22, 2020).
- Baldrige, A. M. et al. (2009) "The ASTER spectral library version 2.0," *Remote Sensing of Environment*. Elsevier Inc., 113(4), pp. 711–715. doi: 10.1016/j.rse.2008.11.007.
- Bedini, E. (2011) "Mineral mapping in the Kap Simpson complex, central East Greenland, using HyMap and ASTER remote sensing data," *Advances in Space Research*. doi: 10.1016/j.asr.2010.08.021.
- Bellian, J. A., Beck, R. and Kerans, C. (2007) "Analysis of hyperspectral and lidar data: Remote optical mineralogy and fracture identification," *Geosphere*. doi: 10.1130/GES00097.1.
- Blom, M., Pearce, A. R. and Stuckey, P. J. (2019) "Short-term planning for open pit mines: a review," *International Journal of Mining, Reclamation and Environment*. doi: 10.1080/17480930.2018.1448248.
- Boesche, N. et al. (2015) "Hyperspectral REE (Rare Earth Element) Mapping of Outcrops—Applications for Neodymium Detection," *Remote Sensing*, 7(5), pp. 5160–5186. doi: 10.3390/rs70505160.
- Boesche, N. K. (2015) "Hyperspectral Rare Earth Element Mapping of Three Outcrops at the Fen Complex, Norway: Calcitic, Dolomitic, and Ankeritic Carbonatites," in De Lima, I. B. and Filho, W. L. (eds.) *Rare Earths Industry - Technological, Economic, and Environmental Implications*. 1st ed. Elsevier Inc., p. 434. Available at: <https://www.elsevier.com/books/rare-earths-industry/borges-de-lima/978-0-12-802328-0>.
- Boesche, N., Mielke, C. and Rogass, C. (2016) "EnGeoMAP Manual for Application : EnGeoMAP (1 . 0)," pp. 1–16.
- [boselec.com/wp-content/uploads/Linear/Vigo/VigoLiterature/BEC-Vigo-IR-Detector-Catalog-03-08-19.pdf](https://www.boselec.com/wp-content/uploads/Linear/Vigo/VigoLiterature/BEC-Vigo-IR-Detector-Catalog-03-08-19.pdf) (2020) *VIGO System product catalog - Infrared Detectors, Room Temperature and TE-Cooled*, Boston Electronics. doi: 10.1021/ac50159a772.

- Bowell, R. (2017) "What is Sustainability in the Context of Mineral Deposits?," *Elements*, 13(5), pp. 297–298. doi: 10.2138/gselements.13.5.297.
- Breiman, L. (2001) "Random forests," *Machine Learning*. doi: 10.1023/A:1010933404324.
- Brightmore, D. and Deane, R. (2020) *Changing the game for energy and resources*, IBM Industry Academy. Available at: www.ibm.com/industries/metals-mining.
- Buckley, S. J. *et al.* (2019) "LIME: Software for 3-D visualization, interpretation, and communication of virtual geoscience models," *Geosphere*. doi: 10.1130/GES02002.1.
- Buckley, S. J., Kurz, T. H. and Schneider, D. (2012) "THE BENEFITS OF TERRESTRIAL LASER SCANNING AND HYPERSPECTRAL DATA FUSION PRODUCTS," *ISPRS - International Archives of the Photogrammetry, Remote Sensing and Spatial Information Sciences*. doi: 10.5194/isprsarchives-xxxix-b7-541-2012.
- Callahan, A. and Long, G. (2017) *Digital mining: Progress... and opportunity*, Accenture. Available at: https://www.accenture.com/us-en/_acnmedia/PDF-51/Accenture-Digital-in-Mining-Progress-and-Opportunity.pdf.
- Campbell, J. B. and Randolph, H. W. (2011) *Introduction to Remote Sensing*. 5th ed. New York, London: The Guilford Press.
- Caravaca, G. *et al.* (2019) "3D Digital Reconstruction of the Kimberley Outcrop (Gale Crater , Mars) from Photogrammetry using Multi-Scale Imagery from Mars Science Laboratory," in *50th Lunar and Planetary Science Conference 2019 Proceedings*. At the Woodlands, Texas, USA, pp. 3–5. Available at: https://www.researchgate.net/publication/332037332_3D_Digital_Reconstruction_of_the_Kimberley_Outcrop_Gale_Crater_Mars_from_Photogrammetry_using_Multi-Scale_Imagery_from_Mars_Science_Laboratory.
- Clark, R. N. (1995) "Mapping minerals, amorphous materials, environmental materials, vegetation, water, ice and snow, and other materials: The USGS tricorder algorithm," in *Clark, Roger N. SwaySummaries of the Fifth Annual JPL Airborne Earth Science Workshop. Volume 1: AVIRIS Workshop*, Gregg A. Denver, CO, United States, pp. 39–40. Available at: <https://ntrs.nasa.gov/search.jsp?R=19950027321>.
- Clark, R. N. (1999) "Spectroscopy of rocks and minerals, and principles of spectroscopy," *Remote sensing for the earth sciences: Manual of remote sensing*, 3, pp. 3–58. doi: 10.1111/j.1945-5100.2004.tb00079.x.
- Clark, R. N. (2003a) "Imaging spectroscopy: Earth and planetary remote sensing with the USGS Tetracorder and expert systems," *Journal of Geophysical Research*, 108(E12), p. 5131. doi: 10.1029/2002JE001847.
- Clark, R. N. (2003b) "Imaging spectroscopy: Earth and planetary remote sensing with the USGS Tetracorder and expert systems," *Journal of Geophysical Research*, 108(E12), pp. 1–2. doi: 10.1029/2002JE001847.
- Clark, R. N. *et al.* (2007) "USGS Spectral Library splib06a: U.S. Geological Survey, Digital Data Series 231, <http://speclab.cr.usgs.gov/spectral.lib06>." Available at: <http://speclab.cr.usgs.gov/spectral.lib06>. Dataset downloaded and used locally, dated to being created the 23rd of June 2009
- Clark, R. N. and Roush, T. L. (1984) "Reflectance spectroscopy: quantitative analysis techniques for remote sensing applications.," *Journal of Geophysical Research*. doi: 10.1029/JB089iB07p06329.
- Clark, R. N., Swayze, G. A. and Gallagher, A. (1992) "Mapping the mineralogy and lithology of Canyonlands, Utah with imaging spectrometer data and the multiple spectral feature mapping algorithm," in *Summaries of the Third Annual JPL Airborne Geoscience Workshop. Volume 1: AVIRIS Workshop*. Denver, CO, United States, pp. 11–13. Available at: <https://ntrs.nasa.gov/search.jsp?R=19940012197>.
- Corescan (2016) *Corescan Logging in Copper Porphyry*. Available at: <http://www.corescan.com.au/applications/corescan-logging-in-copper-porphyry> (Accessed: April 22, 2020).

- Cracknell, M. J. and Reading, A. M. (2014) "Geological mapping using remote sensing data: A comparison of five machine learning algorithms, their response to variations in the spatial distribution of training data and the use of explicit spatial information," *Computers and Geosciences*. Elsevier, 63(February), pp. 22–33. doi: 10.1016/j.cageo.2013.10.008.
- Dalm, M. *et al.* (2014) "Application of near-infrared spectroscopy to sensor based sorting of a porphyry copper ore," *Minerals Engineering*. Elsevier Ltd, 58, pp. 7–16. doi: 10.1016/j.mineng.2013.12.016.
- Dalm, M., Buxton, M. W. N. and van Ruitenbeek, F. J. A. (2017) "Discriminating ore and waste in a porphyry copper deposit using short-wavelength infrared (SWIR) hyperspectral imagery," *Minerals Engineering*. Elsevier Ltd, 105, pp. 10–18. doi: 10.1016/j.mineng.2016.12.013.
- Dorr, J. van N. (1964) "Supergene iron ores of Minas Gerais, Brazil," *Economic Geology*, 59(7), pp. 1203–1240. doi: 10.2113/gsecongeo.59.7.1203.
- Eisele, A. (2014) *Möglichkeitender Nutzung thermal-infraroter Wellenlängen zur fernerkundlichen Erfassung/Quantifizierung von Bodenparametern in semiariden Agrarregionen –eine vergleichende Studie der spektralen Bereiche des LWIR und des VNIR-SWIR auf der Basis von Laborm.* Humboldt-Universität zu Berlin.
- Entezari, I. *et al.* (2017) "Predicting the abundance of clays and quartz in oil sands using hyperspectral measurements," *International Journal of Applied Earth Observation and Geoinformation*. Elsevier B.V., 59, pp. 1–8. doi: 10.1016/j.jag.2017.02.018.
- euspaceimaging.com/about/satellites/worldview-3/ (2018)
 euspaceimaging.com/about/satellites/worldview-3/, © 2018 European Space Imaging. Available at: <https://www.euspaceimaging.com/about/satellites/worldview-3/> (Accessed: July 27, 2020).
- EY (2018) *EY top 10 business risks facing mining and metals in 2019 - 20*, Ernst & Young Global Limited, © 2018 EYGM Limited., EYG no. 012357-18Gbl. Available at: ey.com/miningmetals.
- Feng, J., Rogge, D. and Rivard, B. (2018) "Comparison of lithological mapping results from airborne hyperspectral VNIR-SWIR, LWIR and combined data," *International Journal of Applied Earth Observation and Geoinformation*. Elsevier B.V., 64, pp. 340–353. doi: 10.1016/j.jag.2017.03.003.
- Galley, A. G., Hannington, M. D. and Jonasson, I. R. (2007) "Volcanogenic massive sulphide deposits," *Mineral Deposits of Canada: A Synthesis of Major Deposit-Types, District Metallogeny, the Evolution of Geological Provinces, and Exploration Methods: Geological Association of Canada, Mineral Deposits Division, Special Publication*, (5), pp. 141–161.
- Goodbody, A. (2018) "Earth AI - Down to earth," *Mining Magazine*, April, pp. 76–77. Available at: http://www.earth-ai.com/assets/doc/Down_to_earth_MM_April_2018.pdf.
- Google (2018) "Skouriotissa Three Hills Deposit," *Google Earth*. Available at: 35°05'50.72"N, 32°53'48.81"E, GOOGLE EARTH, data acquisition 3rd of April 2018, retrieved 21st of July 2020. (Accessed: July 21, 2020).
- Guanter, L. *et al.* (2015) "The EnMAP spaceborne imaging spectroscopy mission for earth observation," *Remote Sensing*. doi: 10.3390/rs70708830.
- Hapke, B. (1981) "Bidirectional reflectance spectroscopy: 1. Theory," *Journal of Geophysical Research: Solid Earth*. doi: 10.1029/jb086ib04p03039.
- Hapke, B. (2008) "Bidirectional reflectance spectroscopy. 6. Effects of porosity," *Icarus*. doi: 10.1016/j.icarus.2008.01.003.
- Hapke, B. (2012) *Theory of reflectance and emittance spectroscopy, second edition, Theory of Reflectance and Emittance Spectroscopy, Second Edition*. doi: 10.1017/CBO9781139025683.
- Hapke, B. and Wells, E. (1981) "Bidirectional reflectance spectroscopy: 2. Experiments and observations," *Journal of Geophysical Research: Solid Earth*. doi: 10.1029/jb086ib04p03055.
- [harrisgeospatial.com/docs/using_envi_Home.html](https://www.harrisgeospatial.com/docs/using_envi_Home.html) (2020) "L3 Harris Geospatial Solutions - ENVI - Environment for Visualizing Images." Available at: https://www.harrisgeospatial.com/docs/using_envi_Home.html (Accessed: May 1, 2020).

- Hecker, C. *et al.* (2019) "Spectral Absorption Feature Analysis for Finding Ore: A Tutorial on Using the Method in Geological Remote Sensing," *IEEE Geoscience and Remote Sensing Magazine*. IEEE, 7(2), pp. 51–71. doi: 10.1109/MGRS.2019.2899193.
- Henrich, V. *et al.* (2012) *Entwicklung einer Datenbank für Fernerkundungsindizes Einleitung und Methode Arbeiten mit der IDB*. Available at: <https://www.indexdatabase.de/info/credits.php>.
- Herrmann, S. (2019) *Capacity of Imaging Spectroscopy for the characterisation of REO, REE bearing minerals & primary REE-deposits*. doi: <http://doi.org/10.2312/GFZ.b103-19089>.
- Hierold, J. (2016) *Analysis of Element Behavior in Mylonites of the Seve Nappe of the Scandinavian Caledonides Using Different Core Scanning Methods*.
<http://www.corescan.com.au/> (2013) *Spectral imaging of drill core Applications In Mineral Exploration*. Available at: <http://www.corescan.com.au/> (Accessed: February 10, 2016).
- Hu, W. *et al.* (2015) "Deep convolutional neural networks for hyperspectral image classification," *Journal of Sensors*. doi: 10.1155/2015/258619.
- Hummel, P. and Krupa, J. (2020) "Three more spin-offs from GFZ in 2019," *GFZ Potsdam Web News*, 27 March. Available at: <https://www.gfz-potsdam.de/en/media-and-communication/news/details/article/three-more-spin-offs-from-gfz-in-2019/>.
- Hunt, G. R. (1989) "Spectroscopic Properties of Rocks and Minerals," in Carmichael, R. S. (ed.) *Practical Handbook of Physical Properties of Rocks and Minerals*. 2nd ed. CRC Press, pp. 599–669.
- Hunt, G. R. and Ashley, R. P. (1979) "Spectra of altered rocks in the visible and near infrared," *Economic Geology*. doi: 10.2113/gsecongeo.74.7.1613.
- [hypspec.no/products/disc.php](https://www.hypspec.no/products/disc.php) (2019) *Norsk Elektro Optikk AS HySpex VNIR1600 and SWIR320 m-e*: Available at: <https://www.hypspec.no/products/disc/vnir-1600.php> (Accessed: June 18, 2019).
- IBM (2020) *Instant Expertise - How an energy company retains the knowledge of its senior experts and passes it to new employees*. Available at: <https://www.ibm.com/watson/stories/woodside/> (Accessed: April 27, 2020).
- ICMM (2013) *Sustainable Development Framework: ICMM Principles*. Available at: http://www.icmm.com/website/publications/pdfs/commitments/revised-2015_icmm-principles.pdf (Accessed: January 9, 2020).
- IGF (2013) *IGF Mining Policy Framework – Mining an Sustainable development, Intergovernmental Forum on Mining, Minerals, Metals and Sustainable development*. Available at: <https://www.igfmining.org/mining-policy-framework/> (Accessed: January 10, 2020).
- im-mining.com/2020/04/30/plotlogic-raises-profile-funds-bhp-iron-ore-contract/ and Gleeson, D. (2020) *Plotlogic raises profile and funds with BHP Iron Ore contract, im-mining.com*. Available at: <https://im-mining.com/2020/04/30/plotlogic-raises-profile-funds-bhp-iron-ore-contract/> (Accessed: July 25, 2020).
- [indexdatabase.de/](https://www.indexdatabase.de/) (2020) *index data base*. Available at: <https://www.indexdatabase.de/> (Accessed: May 1, 2020).
- Jakob, S., Zimmermann, R. and Gloaguen, R. (2017) "The Need for Accurate Geometric and Radiometric Corrections of Drone-Borne Hyperspectral Data for Mineral Exploration: MEPHySTo-A Toolbox for Pre-Processing Drone-Borne Hyperspectral Data," *Remote Sensing*. doi: 10.3390/rs9010088.
- Jébrak, M. and Montel, J. M. (2017) "Educating the resource geologist of the future: Between observation and imagination," *Elements*, 13(5), pp. 331–336. doi: 10.2138/gselements.13.5.331.
- Jensen, J. R. (2010) *Remote Sensing of the Environment An Earth Resource Perspective*. 2nd ed. Pearson Education.
- Kassianidou, V. (2013) "Mining Landscapes of Prehistoric Cyprus," *Metalla*, pp. 36–45. Available at: https://www.academia.edu/6599570/Mining_Landscapes_of_Prehistoric_Cyprus.

- Kavzoglu, T. and Mather, P. M. (2003) "The use of backpropagating artificial neural networks in land cover classification," *International Journal of Remote Sensing*. doi: 10.1080/0143116031000114851.
- King, T. V. V. *et al.* (2012) "Hyperspectral remote sensing data maps minerals in Afghanistan," *Eos*. doi: 10.1029/2012EO340002.
- Kirsch, M. *et al.* (2018) "Integration of terrestrial and drone-borne hyperspectral and photogrammetric sensing methods for exploration mapping and mining monitoring," *Remote Sensing*. doi: 10.3390/rs10091366.
- Koellner, N. *et al.* (2019) *Mineral spectra and chemistry of 20 copper-bearing minerals*. doi: <http://doi.org/10.5880/GFZ.1.4.2019.003>.
- Koellner, N. (2020) *ReMon - Remote Monitoring of Tailings Using Satellites and Drones*. Available at: <https://www.gfz-potsdam.de/en/section/remote-sensing-and-geoinformatics/projects/remon/> (Accessed: April 27, 2020).
- Koerting, F. *et al.* (2015) "Drill Core Mineral Analysis by means of the Hyperspectral Imaging Spectrometer HySpex, XRD and ASD in the proximity of the Mytina Maar, Czech Republic," *ISPRS - International Archives of the Photogrammetry, Remote Sensing and Spatial Information Sciences*, XL-1-W5(Kokaly 2011), pp. 417–424. doi: 10.5194/isprsarchives-XL-1-W5-417-2015.
- Koerting, F., Herrmann, S., *et al.* (2019) *Mineral spectra and chemistry of 32 rare-earth minerals and rare-earth oxide powders including niobium- and tantalum-oxid powder*. doi: <http://doi.org/10.5880/GFZ.1.4.2019.004>.
- Koerting, F., Rogass, C., *et al.* (2019) *Mineral spectra and chemistry of 37 copper-bearing surface samples from Apliki copper-gold-pyrite mine in the Republic of Cyprus*. doi: <http://doi.org/10.5880/GFZ.1.4.2019.005>.
- Koerting, F. *et al.* (in preparation) *A solar optical hyperspectral library of rare earth-bearing minerals, rare earth oxide powders, copper-bearing minerals and Apliki mine surface samples*. doi: <https://doi.org/10.5194/essd-2019-228>.
- Köhler, C. H. (2016) "Airborne Imaging Spectrometer HySpex," *Journal of large-scale research facilities JLSRF*. doi: 10.17815/jlsrf-2-151.
- Kokaly, R. F. (2011) *PRISM: Processing Routines in IDL for Spectroscopic Measurements (Installation Manual and User's Guide, Version 1.0=, U.S. Geological Survey Open-File Report 2011-1155*.
- Kokaly, R. F., Graham, G. E., *et al.* (2016) "Hyperspectral Surveying for Mineral Resources in Alaska," (U.S. Geological Survey Fact Sheet 2016-3029), p. 2. doi: 10.3133/fs20163029.
- Kokaly, R. F., Hoefen, T. M., *et al.* (2016) "Mineral information at micron to kilometer scales: Laboratory, field, and remote sensing imaging spectrometer data from the orange hill porphyry copper deposit, Alaska, USA," in *International Geoscience and Remote Sensing Symposium (IGARSS)*. doi: 10.1109/IGARSS.2016.7730411.
- Kokaly, R. F. *et al.* (2017) *USGS Spectral Library Version 7*. Available at: <https://pubs.er.usgs.gov/publication/ds1035>.
- Kokaly, R. F., King, T. V. V. and Hoefen, T. M. (2011) "Mapping the distribution of materials in hyperspectral data using the USGS Material Identification and Characterization Algorithm (MICA)," in *International Geoscience and Remote Sensing Symposium (IGARSS)*. doi: 10.1109/IGARSS.2011.6049370.
- Köllner, N. *et al.* (2020) "Abbildende Spektroskopie im Nahbereich - innovative Methoden im Bereich der Denkmalpflege am Beispiel des barocken Erbbegräbnisses in der St.-Marienkirche, Frankfurt/Oder, Brandenburg," *Arbeitshefte des Brandenburgischen Landesamtes für Denkmalpflege und Archäologischen Landesmuseums*.
- Köllner, N. (Universität P. *et al.* (2019) *Hyperspectral Mapping of Rare Earth Elements - Abschlussbericht zur BMBF Fördermaßnahme*. doi: <https://doi.org/10.2314/KXP:1692232584>.
- Kopackova, V. *et al.* (2012) "Mapping hazardous low-pH material in mining environment: Multispectral and hyperspectral approaches," *International Geoscience and Remote Sensing Symposium (IGARSS)*, pp. 2695–2698. doi: 10.1109/IGARSS.2012.6350372.

- Körting, F. (2019) *Development of a 360 ° hyperspectral drill core scanner Test of technical conditions and validation of high-resolution near- field analysis of crystalline basement rocks using COSC-1 core samples.* doi: <http://doi.org/10.2312/GFZ.b103-19071>.
- Kraal, K. O. and Ayling, B. (2019) "Hyperspectral Characterization of Fallon FORGE Well 21-31: New Data and Technology Applications," in *Workshop on Geothermal Reservoir Engineering*.
- Krupnik, D. and Khan, S. (2019) "Close-range, ground-based hyperspectral imaging for mining applications at various scales: Review and case studies," *Earth-Science Reviews*. Elsevier, 198(September), p. 102952. doi: 10.1016/j.earscirev.2019.102952.
- Kruse, F. A. et al. (1992) "The Spectral Image Processing System (SIPS): Software for integrated analysis of AVIRIS data," in *JPL, Summaries of the Third Annual JPL Airborne Geoscience Workshop. Volume 1: AVIRIS Workshop*. Boulder, CO, United States, pp. 23–25. Available at: <https://ntrs.nasa.gov/search.jsp?R=19940012201>.
- Kruse, F. A. et al. (1993) "The spectral image processing system (SIPS)-interactive visualization and analysis of imaging spectrometer data," *Remote Sensing of Environment*. doi: 10.1016/0034-4257(93)90013-N.
- Kruse, F. A. (2003) "Mineral mapping with AVIRIS and EO-1 Hyperion," *Summaries of the 12th Annual Jet Propulsion Laboratory Airborne Geoscience Workshop, Pasadena, California, Pasadena, JPL Publication*.
- Kruse, F. A. et al. (2008) "The spectral image processing system (SIPS)-interactive visualization and analysis of imaging spectrometer data," in. doi: 10.1063/1.44433.
- Kruse, F. A. et al. (2011) "Mapping alteration minerals at prospect, outcrop and drill core scales using imaging spectrometry," *International Journal of Remote Sensing*, 33(6), pp. 1780–1798. doi: 10.1080/01431161.2011.600350.
- Kruse, F. A. (2012) "Mapping surface mineralogy using imaging spectrometry," *Geomorphology*. doi: 10.1016/j.geomorph.2010.09.032.
- Kuras, A. (2017) *Hyperspektrale 3D Labormessung an Probematerialien von Erzlagerstätten*. Technischen Universität Berlin.
- Kurz, T. H. et al. (2008) "Geological outcrop modelling and interpretation using ground based hyperspectral and laser scanning data fusion," *International Archives of the Photogrammetry, Remote Sensing and Spatial Information Sciences*, (37).
- Kurz, T. H. (2011) *Integration of ground-based hyperspectral and lidar scanning in virtual outcrop geology, PhD Dissertation*,. University of Bergen.
- Kurz, T. H. et al. (2012) "Hyperspectral image analysis of different carbonate lithologies (limestone, karst and hydrothermal dolomites): The Pozalagua Quarry case study (Cantabria, North-west Spain)," *Sedimentology*. doi: 10.1111/j.1365-3091.2011.01269.x.
- Kurz, T. H., Buckley, S. J. and Howell, J. A. (2013) "Close-range hyperspectral imaging for geological field studies: Workflow and methods," *International Journal of Remote Sensing*. doi: 10.1080/01431161.2012.727039.
- L3Harris-Geospatial-Solutions (2018) "ENVI Classic - Environment for Visualizing Images (IDL 8.7.0 + ENVI Classic 5.5)." Harris Geospatial Solutions. Available at: http://www.harrisgeospatial.com/docs/using_envi_Home.html.
- LePan, N. (2019) "Visualizing the Life Cycle of a Mine," *Visual Capitalist*, 12 September. Available at: https://www.visualcapitalist.com/visualizing-the-life-cycle-of-a-mineral-discovery/?_lsrc=34da7c96-9626-4e82-9cd7-86ae1b644b38&utm_source=elevate&utm_medium=social&utm_campaign=linkedin.
- Lessard, J., De Bakker, J. and McHugh, L. (2014) "Development of ore sorting and its impact on mineral processing economics," *Minerals Engineering*. Elsevier Ltd, 65, pp. 88–97. doi: 10.1016/j.mineng.2014.05.019.
- Li, Y., Zhang, H. and Shen, Q. (2017) "Spectral-spatial classification of hyperspectral imagery with 3D convolutional neural network," *Remote Sensing*. doi: 10.3390/rs9010067.
- lights.univ-lorraine.fr/ (2020) *LIGHTS (Lightweight Integrated Ground and Airborne Hyperspectral*

- Topological Solution*). Available at: <http://lights.univ-lorraine.fr/> (Accessed: April 27, 2020).
- Lin, M. *et al.* (2009) "Infrared (IR) Spectroscopy-Near-Infrared Spectroscopy and Mid-Infrared Spectroscopy," in Sun, D.-W. (ed.) *Infrared Spectroscopy for Food Quality Analysis and Control*. 1st ed. 30 Corporate Drive, Suite 400, Burlington, MA 01803, USA: Academic Press, Elsevier, pp. 119–141. doi: 10.1016/B978-0-12-374136-3.00006-7.
- van der Linden, S. *et al.* (2015) "The EnMAP-box-A toolbox and application programming interface for EnMAP data processing," *Remote Sensing*, 7(9), pp. 11249–11266. doi: 10.3390/rs70911249.
- Lorenz, S. *et al.* (2018) "Radiometric correction and 3D integration of long-range ground-based hyperspectral imagery for mineral exploration of vertical outcrops," *Remote Sensing*. doi: 10.3390/rs10020176.
- Lowell, J. D. and Guilbert, J. M. (1970) "Lateral and vertical alteration-mineralization zoning in porphyry ore deposits," *Economic Geology*. doi: 10.2113/gsecongeo.65.4.373.
- Lydon, J. W. (1984) "Ore Deposit Models - 8. Volcanogenic Massive Sulphide Deposits, Parti I: A descriptive Model," *Geoscience Canada*, 11(4), pp. 195–202.
- Lypaczewski, P. *et al.* (2019) "Using hyperspectral imaging to vector towards mineralization at the Canadian Malartic gold deposit, Québec, Canada," *Ore Geology Reviews*. doi: 10.1016/j.oregeorev.2019.102945.
- Lypaczewski, P. *et al.* (2020) "Characterization of mineralogy in the highland valley porphyry Cu district using hyperspectral imaging, and potential applications," *Minerals*, 10(5), pp. 1–30. doi: 10.3390/min10050473.
- Martin, A. J. *et al.* (2018) "Extreme enrichment of selenium in the Apliki Cyprus-type VMS deposit, Troodos, Cyprus," *Mineralogical Magazine*. doi: 10.1180/mgm.2018.81.
- van der Meer, F. D. *et al.* (2012) "Multi- and hyperspectral geologic remote sensing: A review," *International Journal of Applied Earth Observation and Geoinformation*. doi: 10.1016/j.jag.2011.08.002.
- van der Meer, F. *et al.* (2002) "Remote sensing and petroleum seepage: A review and case study," *Terra Nova*. doi: 10.1046/j.1365-3121.2002.00390.x.
- van der Meer, F. *et al.* (2018) "Wavelength feature mapping as a proxy to mineral chemistry for investigating geologic systems: An example from the Rodalquilar epithermal system," *International Journal of Applied Earth Observation and Geoinformation*, 64(September), pp. 237–248. doi: 10.1016/j.jag.2017.09.008.
- Meerdink, S. K. *et al.* (2019) "The ECOSTRESS spectral library version 1.0," *Remote Sensing of Environment*. doi: 10.1016/j.rse.2019.05.015.
- Mielke, C. *et al.* (2014) "Spaceborne Mine Waste Mineralogy Monitoring in South Africa, Applications for Modern Push-Broom Missions: Hyperion/OLI and EnMAP/Sentinel-2," *Remote Sensing*, pp. 6790–6816. doi: 10.3390/rs6086790.
- Mielke, C. *et al.* (2015) "New geometric hull continuum removal algorithm for automatic absorption band detection from spectroscopic data," *Remote Sensing Letters*, 6(2), pp. 97–105. doi: 10.1080/2150704X.2015.1007246.
- Mielke, C. *et al.* (2016) "EnGeoMAP 2.0—Automated Hyperspectral Mineral Identification for the German EnMAP Space Mission," *Remote Sensing*, 8(2), p. 127. doi: 10.3390/rs8020127.
- Mielke, C. *et al.* (2018) "Engeomap and Ensomap: Software interfaces for mineral and soil mapping under development in the frame of the ENMAP mission," in *International Geoscience and Remote Sensing Symposium (IGARSS)*. doi: 10.1109/IGARSS.2018.8517902.
- Mielke, C. *et al.* (2019) *EnGeoMAP Tutorial*. Available at: https://enmap-box.readthedocs.io/en/latest/usr_section/application_tutorials/engeomap/tutorial_engeomap.html.
- Mielke, C. *et al.* (2020) "Multi- und hyperspektrale Verfahren zur weltweiten Überwachung von Weltkulturerbestätten," *Arbeitshefte des Brandenburgischen Landesamtes für Denkmalpflege und Archäologischen Landesmuseums*.
- Monteiro, S. T. *et al.* (2013) "Combining strong features for registration of hyperspectral and lidar

- data from field-based platforms,” in *International Geoscience and Remote Sensing Symposium (IGARSS)*. doi: 10.1109/IGARSS.2013.6722997.
- Moreira, L. C. J., Teixeira, A. dos S. and Galvão, L. S. (2014) “Laboratory salinization of Brazilian alluvial soils and the spectral effects of gypsum,” *Remote Sensing*, 6(4), pp. 2647–2663. doi: 10.3390/rs6042647.
- Murphy, R. J. *et al.* (2015) “Mapping clay minerals in an open-pit mine using hyperspectral and LiDAR data,” *European Journal of Remote Sensing*, 48(1), pp. 511–526. doi: 10.5721/EuJRS20154829.
- Murphy, R. J., Monteiro, S. T. and Schneider, S. (2012) “Evaluating Classification Techniques for Mapping Vertical Geology Using Field-Based Hyperspectral Sensors,” *IEEE Transactions on Geoscience and Remote Sensing*, 50(8), pp. 3066–3080. doi: 10.1109/TGRS.2011.2178419.
- Murtagh, F. and Legendre, P. (2011) “Ward’s Hierarchical Clustering Method: Clustering Criterion and Agglomerative Algorithm,” (June), pp. 1–20. doi: 10.1007/s00357-014-9161-z.
- Mustard, J. F. and Sunshine, J. M. (1999) *Spectral Analysis for Earth Science: Investigations Using Remote Sensing Data, Remote Sensing for the Earth Sciences*.
- Naden, J. *et al.* (2006) *New methodologies for volcanic-hosted copper sulphide mineralization on Cyprus: A GIS-prospectivity analysis-based approach, Economic Minerals Programme Internal Report CR/06/129*. Keyworth, UK. Available at: <https://research.monash.edu/en/publications/new-methodologies-for-volcanic-hosted-copper-sulphide-mineralizat>.
- Ngcofe, L. *et al.* (2013) “Multispectral and hyperspectral remote sensing: Target area generation for porphyry copper exploration in the namaqua metamorphic province, South Africa,” *South African Journal of Geology*. doi: 10.2113/gssajg.116.2259.
- Nieto, J. I., Monteiro, S. T. and Viejo, D. (2010) “3D geological modelling using laser and hyperspectral data,” *International Geoscience and Remote Sensing Symposium (IGARSS)*, (May 2014), pp. 4568–4571. doi: 10.1109/IGARSS.2010.5651553.
- Notesco, G. *et al.* (2014) “Mineral classification of land surface using multispectral LWIR and hyperspectral SWIR remote-sensing data. A case study over the sokolov lignite open-pit mines, the Czech Republic,” *Remote Sensing*. doi: 10.3390/rs6087005.
- Okrusch, M. and Matthes, S. (2014) “Hydrothermale Erz- und Minerallagerstätten,” in, pp. 343–369. doi: 10.1007/978-3-642-34660-6_23.
- Pedregosa, F. *et al.* (2011) “Scikit-learn: Machine learning in Python,” *Journal of Machine Learning Research*. pubs.usgs.gov/of/2011/1155/ and Kokaly, R. F. (2014) *USGS PRISM* pubs.usgs.gov/of/2011/1155/. Available at: <https://pubs.usgs.gov/of/2011/1155/> (Accessed: April 20, 2009).
- Raczko, E. and Zagajewski, B. (2017) “Comparison of support vector machine, random forest and neural network classifiers for tree species classification on airborne hyperspectral APEX images,” *European Journal of Remote Sensing*, 50(1), pp. 144–154. doi: 10.1080/22797254.2017.1299557.
- Rajan Girija, R. and Mayappan, S. (2019) “Mapping of mineral resources and lithological units: a review of remote sensing techniques,” *International Journal of Image and Data Fusion*, 10(2), pp. 79–106. doi: 10.1080/19479832.2019.1589585.
- Richter, R. (2007) “Atmospheric / Topographic Correction for Satellite Imagery (ATCOR - 2/3 User Guide),” *ATCOR-2/3 User Guide, Version 6.3*. doi: 10.1017/CBO9781107415324.004.
- Richter, R. and Schläpfer, D. (2011) “Atmospheric / Topographic Correction for Satellite Imagery,” *Aerospace*.
- Rivard, B. *et al.* (2009) “Remote predictive lithologic mapping in the Abitibi Greenstone Belt, Canada, using airborne hyperspectral imagery,” *Canadian Journal of Remote Sensing*. doi: 10.5589/m10-002.
- Rodarmel, C. and Shan, J. (2002) “Principal component analysis for hyperspectral image classification,” *Surveying and Land Information Science*.
- Rogass, C. *et al.* (2013) “EnGeoMap—A geological mapping tool applied to the EnMAP mission,” in *EARSeL eProceedings*, pp. 12–17. doi: <https://doi.org/10.12760/01-2013-2-02>.

- Rogass, C. *et al.* (2017) "Translational imaging spectroscopy for proximal sensing," *Sensors (Switzerland)*. doi: 10.3390/s17081857.
- Rogge, D. *et al.* (2014) "Mapping of NiCu-PGE ore hosting ultramafic rocks using airborne and simulated EnMAP hyperspectral imagery, Nunavik, Canada," *Remote Sensing of Environment*. Elsevier Inc., 152, pp. 302–317. doi: 10.1016/j.rse.2014.06.024.
- Rosa, D. *et al.* (2016) *Architecture and mineral potential of the Paleoproterozoic Karrat Group, West Greenland Results of the 2016 season*. Available at: https://www.researchgate.net/profile/Sara_Salehi6/publication/325038466_Architecture_and_mineral_potential_of_the_Paleoproterozoic_Karrat_Group_West_Greenland_Results_of_the_2016_Season/links/5af2d8a5a6fdcc0c0304fd56/Architecture-and-mineral-potential-of-
- Rowan, L. C., Schmidt, R. G. and Mars, J. C. (2006) "Distribution of hydrothermally altered rocks in the Reko Diq, Pakistan mineralized area based on spectral analysis of ASTER data," *Remote Sensing of Environment*. doi: 10.1016/j.rse.2006.05.014.
- Van Ruitenbeek, F. J. A. *et al.* (2014) "Mapping the wavelength position of deepest absorption features to explore mineral diversity in hyperspectral images," *Planetary and Space Science*. Elsevier, 101, pp. 108–117. doi: 10.1016/j.pss.2014.06.009.
- Salehi, S. *et al.* (2018) "Integration of vessel-based hyperspectral scanning and 3D-photogrammetry for mobile mapping of steep coastal cliffs in the Arctic," *Remote Sensing*. doi: 10.3390/rs10020175.
- Salehi, S. (2018) "Potentials and challenges for hyperspectral mineral mapping in the Arctic Developing innovative strategies for data acquisition and integration," *PhD Dissertation*, p. 163.
- Savage, S. H., Levy, T. E. and Jones, I. W. (2012) "Prospects and problems in the use of hyperspectral imagery for archaeological remote sensing: A case study from the Faynan copper mining district, Jordan," *Journal of Archaeological Science*. doi: 10.1016/j.jas.2011.09.028.
- Scafutto, R. D. P. M., de Souza Filho, C. R. and Rivard, B. (2016) "Characterization of mineral substrates impregnated with crude oils using proximal infrared hyperspectral imaging," *Remote Sensing of Environment*. Elsevier Inc., 179, pp. 116–130. doi: 10.1016/j.rse.2016.03.033.
- Schneider, S. *et al.* (2011) "Autonomous mapping of mine face geology using hyperspectral data," *35th APCOM Symposium - Application of Computers and Operations Research in the Minerals Industry, Proceedings*, (May 2014), pp. 865–876.
- Shippert, P. (2003) "Introduction to hyperspectral image analysis," *Online Journal of Space Communication*, 3. Available at: <https://spacejournal.ohio.edu/pdf/shippert.pdf>, 17.02.2020, 10:23am.
- Sillitoe, R. H. (2010) "Porphyry copper systems," *Economic Geology*, 105(1), pp. 3–41. doi: 10.2113/gsecongeo.105.1.3.
- [spectralpython.net/](http://www.spectralpython.net/) (2020) "Spectral Python SPy." © Copyright 2014, Thomas Boggs. Available at: <http://www.spectralpython.net/algorithms.html?highlight=cluster>.
- Spragg, R. A. (2017) "IR Spectrometers," in *Encyclopedia of Spectroscopy and Spectrometry*. Elsevier, pp. 419–427. doi: 10.1016/B978-0-12-803224-4.00088-1.
- sustainabledevelopment.un.org/ (2020) *UN Sustainable development goals, UN Sustainable Development Goals*. Available at: <https://sustainabledevelopment.un.org/> (Accessed: May 20, 2020).
- Swayze, G. A. *et al.* (2003) "Effects of spectrometer band pass, sampling, and signal-to-noise ratio on spectral identification using the Tetracorder algorithm," *Journal of Geophysical Research*, 108(E9), p. 5105. doi: 10.1029/2002JE001975.
- Swayze, G. A. *et al.* (2014) "Mapping advanced argillic alteration at Cuprite, Nevada, using imaging spectroscopy," *Economic Geology*, 109(5), pp. 1179–1221. doi: 10.2113/econgeo.109.5.1179.
- Sykas, D. (2020) *Learn Hyperspectral Remote Sensing from Scratch*, *geo.university*. Available at: <https://www.geo.university/courses/learn-hyperspectral-remote-sensing-from-the-scratch> (Accessed: May 13, 2020).
- Therien, C. (2020) "PySptools Python Toolbox." Available at: <https://pysptools.sourceforge.io/>.

- Turner, D., Rivard, B. and Groat, L. (2014) "Rare earth element ore grade estimation of mineralized drill core from hyperspectral imaging spectroscopy," in *2014 IEEE Geoscience and Remote Sensing Symposium*. IEEE, pp. 4612–4615. doi: 10.1109/IGARSS.2014.6947520.
- virtualoutcrop.com (2020) *virtualoutcrop.com*, *Webpage*. Accessed: March 20, 2020).
- www.raddata.io (2020) *www.raddata.io*, *Webpage*. Available at: www.raddata.io (Accessed: May 20, 2020).
- Yokoya, N., Chan, J. C. W. and Segl, K. (2016) "Potential of resolution-enhanced hyperspectral data for mineral mapping using simulated EnMAP and Sentinel-2 images," *Remote Sensing*. doi: 10.3390/rs8030172.
- Yuhas, R. H., Goetz, A. F. H. and Boardman, J. W. (1992) "Discrimination among semi-arid landscape endmembers using the spectral angle mapper (SAM) algorithm," in *In JPL, Summaries of the Third Annual JPL Airborne Geoscience Workshop. Volume 1: AVIRIS Workshop p 147-149 (SEE N94-16666 03-42)*, pp. 147–149. Available at: <https://ntrs.nasa.gov/search.jsp?R=19940012238>.
- Zaini, N., van der Meer, F. and van der Werff, H. (2014) "Determination of carbonate rock chemistry using laboratory-based hyperspectral imagery," *Remote Sensing*. doi: 10.3390/rs6054149.

10 Appendix

10.1 HySpex laboratory data acquisition settings

Table 41 HySpex settings for laboratory measurements of the Brazilian samples.

HySpex settings		
<i>Lamp arrangement</i>	45°	
<i>Distance, sample to sensor</i>	1m	
<i>Wavelength range</i>	414 to 2498nm	
<i>SNR mode (frames to average)</i>	4	
	VNIR	SWIR
<i>Objective</i>	1m lens, CCD equalizer	1m lens
<i>Field of View (FOV) of objective</i>	17°	14°
<i>Sampling interval [nm]</i>	3.7	6.25
<i>Radiometric resolution</i>	12 bit	14 bit
<i>Light source</i>	Halogen GX6.35, 2 x 1000W	
	VNIR (1600 px)	SWIR (320 px)
<i>Integration time [μs]</i>	130000	5500
<i>Frame period [μs]</i>	130993	521884

Table 42 HySpex setting for the laboratory measurements of the unprepared Apliki samples.

HySpex settings		
<i>Lamp arrangement</i>	45°	
<i>Distance, sample to sensor</i>	1m	
<i>Wavelength range</i>	414 to 2498nm	
	VNIR	SWIR
<i>Objective</i>	1m lens, CCD equalizer	1m lens
<i>Field of View (FOV) of objective</i>	17°	14°
<i>Sampling interval [nm]</i>	3.7	6.25
<i>Radiometric resolution</i>	12 bit	14 bit
<i>Light source</i>	Halogen GX6.35, 2 x 1000W	
	VNIR (1600 px)	SWIR (320 px)
<i>Integration time [μs]</i>	70000 - 90000	15000 – 20000
<i>Frame period [μs]</i>	70998 - 91000	282860 - 362549

Table 43 HySpex setting for the laboratory measurements of the unprepared Skouriotissa samples.

HySpex settings		
Lamp arrangement	45°	
Distance. sample to sensor	1m	
Wavelength range	414 to 2498nm	
	VNIR	SWIR
Objective	1m lens. CCD equalizer	1m lens
Field of View (FOV) of objective	17°	14°
Sampling interval [nm]	3.7	6.25
Radiometric resolution	12 bit	14 bit
Light source	Halogen GX6.35. 2 x 1000W	
	VNIR (1600 px)	SWIR (320 px)
Integration time [μ s]	40000 - 80000	8000
Frame period [μ s]	41000 - 80998	163346 - 322701

10.2 Brazilian iron ore samples detection limits and descriptions

Table 44 Detection limit for the geochemical results from mine site 1 (sample 3, 4, 7, 8, 11, 12 and 15).

	SiO ₂	Al ₂ O ₃	P	Mn	CaO	MgO	TiO ₂	Na ₂ O	K ₂ O
	[%]	[%]	[%]	[%]	[%]	[%]	[%]	[%]	[%]
Detection limit	<0,05	<0,05	<0,005	<0,015	<0,005	<0,05	<0,010	<0,10	<0,100

Table 45 Detection limit for the geochemical results from mine site 2 (sample 1, 2, 5, 6, 9, 10, 13 and 14).







	SiO ₂	Al ₂ O ₃	P	Mn	CaO	MgO	TiO ₂	Fe
	[%]	[%]	[%]	[%]	[%]	[%]	%[%]	[%]
Detection limit	<0,10	<0,10	<0,005	<0,008	<0,01	<0,10	<0,01	<0,007
Method	XRF79C	XRF79C	XRF79C	XRF79C	XRF79C	XRF79C	XRF79C	XRF79C







Table 46 Sample descriptions for samples from mine site 1, for sample 3, 4, 7, 8, 11, 12, 15.



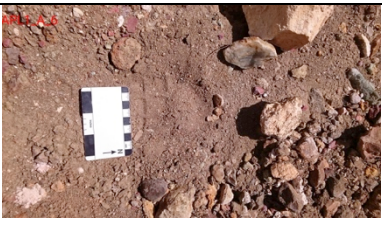


ID	Company provided sample description
3	Crispy rock, decomposed yellow to ocher with presence of clay minerals and phyllosilicates
4	Crumbly, dark gray, decomposed on contact with intrusive rock rich in lamellar hematite crystals, quartz and possible presence of phyllosilicates and clay minerals
7	Crumbly, structured, friable rock rich in hematite crystals and banding marked by alternation of clay minerals and hematite + phyllosilicate levels
8	Semi-compact, gray, structured itabirite containing banding marked by dissymmetric quartz and hematite levels. Presence of hematite and quartz crystals and possible presence of phyllosilicates
11	Compact, structured, gray color with central quartz and hematite banding.
12	Crispy itabirite contaminated with decomposed intrusive rock, presence of clay minerals and lamellar hematite crystals
15	Mineralized canga, formed from latering over the itabirite, red to ocher in color, with presence of goethite and hematite minerals and contamination of clay minerals, manganese and phyllosilicates

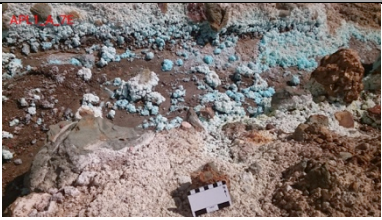






10.3 Apliki mine sample description and location of sampling



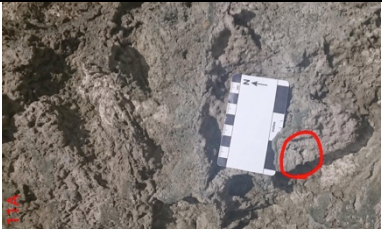



Table 47 Apliki mine samples, including description, coordinates of sampling in March 2018 and a field photo of the sample (Koerting, Rogass, et al., 2019)

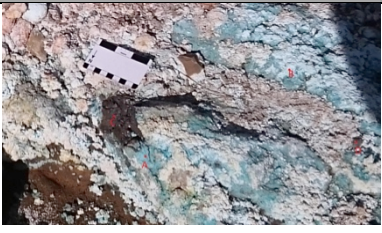
Sample	Description	Decimal latitude	Decimal longitude	Photo
<i>Apl1_A_1a</i>	<i>"fresh" surface</i>	35,077033	32,842833	
<i>Apl1_A_1b</i>	<i>hematite coloured</i>	35,077017	32,842833	
<i>Apl1_A_1d</i>	<i>"fresh" dark green</i>	35,077017	32,842833	
<i>Apl1_A_1e</i>	<i>yellow-ish orange weathered</i>	35,077033	32,8428	
<i>Apl1_A_1f</i>	<i>"soil formation", gravel</i>	35,07700	32,84275	
<i>Apl1_A_2a</i>	<i>waste, soil</i>	35,076867	32,84275	

Sample	Description	Decimal latitude	Decimal longitude	Photo
Apl1_A_3a	yellow-ish weathered, soil	35,076983	32,843083	
Apl1_A_3b	brownish weathered, soil	35,077	32,84305	
Apl1_A_4a	white, soil-ish	35,076967	32,843067	
Apl1_A_4b	grey, soil-ish	35,077	32,843033	
Apl1_A_4c	grey-green	35,077	32,842633	
Apl1_A_5a	grey-medium	35,076983	32,843167	

Sample	Description	Decimal latitude	Decimal longitude	Photo
Apl1_A_5b	<i>grey-dark</i>	35,07705	32,843167	
Apl1_A_5c	<i>grey-light</i>	35,077083	32,843183	
Apl1_A_6a	<i>soil, gravel</i>	35,076967	32,8431	
Apl1_A_6b	<i>soil, gravel</i>	35,07695	32,8432	All samples from same spot, see 6a
Apl1_A_6c	<i>soil, gravel</i>	not available	not available	All samples from same spot, see 6a
Apl1_A_6d	<i>soil, gravel</i>	not available	not available	All samples from same spot, see 6a
Apl1_A_7d	<i>Grey, crust unstable</i>	35,076967	32,84325	
Apl1_A_7d _Hem	<i>Red, hematite</i>	35,076967	32,84325	

Sample	Description	Decimal latitude	Decimal longitude	Photo
Apl1_A_7e	<i>blue crystal</i>	35,076833	32,843217	
Apl1_A_8a	<i>grey, soil-ish,</i>	35,076917	32,8433	
Apl1_A_8b	<i>grey, soil-ish,</i>	35,076933	32,84335	
Apl1_A_8c	<i>grey, soil-ish,</i>	35,076917	32,8433	
Apl1_A_9a	<i>light green</i>	35,076883	32,843333	
Apl1_A_9b	<i>hematite vein</i>	35,076833	32,843317	
Apl1_A_10a	<i>white with pink</i>	35,076733	32,843383	

Sample	Description	Decimal latitude	Decimal longitude	Photo
Apl1_A_10 b	<i>white with purple</i>	35,076833	32,843383	
Apl1_A_10 c	<i>green-ish veins</i>	35,07685	32,843333	
Apl1_A_10 d	<i>white</i>	35,076833	32,84335	See overview photo from 10c, no detail photo available
Apl1_A_11 a	<i>weathering crust</i>	35,076783	32,843533	
Apl1_A_11 b	<i>green</i>	35,076767	32,843517	
Apl1_A_13 a	<i>red, rock</i>	35,076133	32,843333	
Apl1_A_13 b	<i>red, gravel, weathered hillside rock</i>	35,076117	32,8434	

Sample	Description	Decimal latitude	Decimal longitude	Photo
Apl1_A_15 a	<i>dark blue</i>	35,076133	32,843217	
Apl1_A_15 b	<i>light blue rock+ blue crust</i>	35,076133	32,843217	See sample Apl1_A_15a
Apl1_A_15 c	<i>black pyrite</i>	35,076133	32,843217	See sample Apl1_A_15a

10.4 Geochemical analysis of Apliki mine samples

Table 48 Sample preparation and description of BVM codes, from Koerting et al. (2019b).

BVM Code	Description
SHP01	Per sample shipping charges for branch shipments
CRU80	Crush to 80% passing 10 mesh (1.70 mm)
PULHP	Hand Pulverize samples mortar and pestle
AQ250	Ultra Trace Geochemical Aqua Regia digestion, 1:1:1 Aqua Regia digestion (HNO ₃ -HCl acid digestion), Ultratrace ICP-MS analysis
PRP70-250	Crush, split and pulverize 250 g rock to 200 mesh (0.075 mm)
LF302-EXT	Lithochemical Whole Rock Fusion, LiBO ₂ /LiB ₄ O ₇ fusion ICP-ES analysis. Comment: Major oxides do not sum to 100% due to possible incomplete fusion of some minerals or other element oxides may be present.
DISP2	Heat treatment of soils and sediments.
TC000	Carbon and Sulfur Analysis

Table 49 Main geochemical components for 36 Apliki field samples in [wt.%] with sample location in decimal latitude and longitude.

The four samples with Cu grades higher than 0.4wt%Cu are marked in yellow and indicate samples valued as "ore".

Sample	Sample position	SiO ₂ [wt%]	Al ₂ O ₃ [wt%]	Fe ₂ O ₃ [wt%]	MgO [wt%]	CaO [wt%]	Na ₂ O [wt%]	K ₂ O [wt%]	TiO ₂ [wt%]	P ₂ O ₅ [wt%]	MnO [wt%]	Cr ₂ O ₃ [wt%]	Cu wt[%]
	Detection limit	0.01	0.01	0.04	0.01	0.01	0.01	0.01	0.01	0.01	0.01	0.002	0.0005
1b	N 35°4.621', E 32°50.570'	48.61	17.39	12.46	4.39	6.11	3.55	0.96	1.22	0.15	0.19	<0.002	0.0132
1d	N 35°4.621', E 32°50.570'	46.76	16.90	12.80	5.59	6.73	2.85	0.76	1.07	0.09	0.11	<0.002	0.0128
1e	N 35°4.622', E 32°50.568'	46.13	17.15	12.76	5.84	6.61	2.69	0.61	1.11	0.08	0.11	<0.002	0.0347
1f	N 35°4.620', E 32°50.565'	45.44	15.86	12.79	5.11	7.65	2.37	1.01	1.00	0.07	0.15	0.003	0.0673
2a	N 35°4.612', E 32°50.565'	40.72	8.00	31.22	2.67	0.75	0.31	0.67	0.38	0.20	0.24	0.024	0.1734
3a	N 35°4.619', E 32°50.585'	44.66	14.20	15.25	4.87	3.74	1.15	0.86	0.74	0.05	0.12	0.009	0.2070
3b	N 35°4.620', E 32°50.583'	49.15	11.83	13.91	5.40	3.59	0.85	0.51	0.58	0.05	0.10	0.035	0.1561
4a	N 35°4.618', E 32°50.584'	33.97	10.29	10.62	9.96	8.00	0.22	0.02	0.24	0.01	0.35	0.010	0.0372
4b	N 35°4.620', E 32°50.582'	42.68	16.01	13.35	8.08	2.80	0.83	0.42	0.50	0.02	0.09	0.010	0.0951
4c	N 35°4.620', E 32°50.585'	47.95	16.14	14.16	11.63	0.42	0.06	0.04	0.38	<0.01	0.12	0.010	0.0181
5a	N 35°4.619', E 32°50.590'	40.00	16.12	16.16	13.46	2.02	0.09	<0.01	0.38	0.02	0.10	0.009	0.0120
5b	N 35°4.623', E 32°50.590'	44.03	16.33	13.73	12.74	1.06	0.18	0.02	0.37	<0.01	0.12	0.011	0.0041
5c	N 35°4.625', E 32°50.591'	39.93	14.74	13.12	14.58	2.08	0.16	<0.01	0.33	0.02	0.17	0.010	0.0042
6a	N 35°4.618', E 32°50.586'	44.32	12.76	19.85	4.44	0.99	0.65	1.77	0.42	0.03	0.17	0.032	0.2511
6b	N 35°4.617', E 32°50.592'	45.93	14.81	14.24	5.49	5.43	1.63	0.85	0.79	0.07	0.17	0.009	0.1894
6c	N/A	43.27	8.94	25.45	4.54	0.79	0.31	0.48	0.27	0.02	0.10	0.019	0.3136
6d	N/A	39.93	12.47	24.96	4.30	1.19	0.53	1.24	0.41	0.06	0.26	0.025	0.1675
7d	N 35°4.618', E 32°50.595'	45.32	9.88	9.87	9.86	0.48	0.03	<0.01	0.21	<0.01	0.18	0.030	0.3290
7d-Hem	N 35°4.618', E 32°50.595'	89.91	1.28	4.70	0.88	0.40	0.02	0.02	0.03	0.09	0.02	<0.002	0.0129
7e	N 33°4.610', E 32°50.593'	2.70	6.74	0.37	11.02	0.06	0.08	<0.01	<0.01	<0.01	0.34	0.002	>1.000

Sample	Sample position	SiO ₂ [wt%]	Al ₂ O ₃ [wt%]	Fe ₂ O ₃ [wt%]	MgO [wt%]	CaO [wt%]	Na ₂ O [wt%]	K ₂ O [wt%]	TiO ₂ [wt%]	P ₂ O ₅ [wt%]	MnO [wt%]	Cr ₂ O ₃ [wt%]	Cu wt[%]
8a	N 35°4.615', E 32°50.598'	49.04	14.15	14.92	11.40	0.18	0.08	0.02	0.33	<0.01	0.12	0.013	0.1334
8b	N 35°4.616', E 32°50.601'	49.00	14.59	14.73	11.89	0.17	0.06	0.01	0.34	<0.01	0.12	0.011	0.1073
8c	N 35°4.615', E 32°50.598'	56.96	12.92	11.27	10.39	0.21	0.08	0.01	0.30	<0.01	0.11	0.011	0.0372
9a	N 35°4.613', E 32°50.600'	56.29	12.07	12.18	11.21	0.09	<0.01	<0.01	0.29	<0.01	0.14	0.040	0.0574
9b	N 35°4.610', E 32°50.599'	88.97	2.15	4.47	1.72	0.10	0.02	<0.01	0.03	0.05	0.02	0.003	0.0717
10a	N 35°4.604', E 32°50.603'	80.97	2.73	9.36	2.38	0.17	0.06	<0.01	0.03	0.02	0.08	0.003	0.1509
10b	N 35°4.610', E 32°50.603'	47.88	12.97	15.88	12.94	0.53	0.03	<0.01	0.31	<0.01	0.10	0.046	0.1569
10c	N 35°4.611', E 32°50.600'	52.69	12.88	13.47	12.90	0.12	<0.01	<0.01	0.31	<0.01	0.08	0.044	0.0813
10d	N 35°4.610', E 32°50.601'	46.17	15.02	14.57	14.31	0.06	0.02	<0.01	0.36	<0.01	0.08	0.052	0.0686
11a	N 35°4.607', E 32°50.612'	69.59	6.55	7.25	6.05	1.68	0.10	<0.01	0.16	<0.01	0.03	0.027	0.1083
11b	N 35°4.606', E 32°50.611'	76.04	6.73	7.25	5.11	0.10	0.07	<0.01	0.15	0.02	0.02	0.024	0.1313
13a	N 35°4.568', E 32°50.600'	58.77	14.42	9.56	3.29	4.71	3.23	0.30	0.90	0.10	0.14	0.016	0.2064
13b	N 35°4.567', E 32°50.604'	57.20	13.23	14.08	3.77	0.71	0.35	0.08	0.82	0.03	0.07	0.006	0.3698
15a	N 35°4.568', E 32°50.593'	67.22	0.73	14.13	0.96	0.12	0.05	0.02	0.20	<0.01	0.03	0.004	>1.000
15b	N 35°4.568', E 32°50.593'	77.48	0.66	8.12	0.87	0.09	0.05	<0.01	0.20	<0.01	0.03	0.005	>1.000
15c	N 35°4.568', E 32°50.593'	31.72	1.09	29.38	0.27	0.03	0.12	0.01	0.08	<0.01	0.01	0.009	>1.000

10.5 XRD diffractograms of Apliki mine samples

In the following section the diffractograms for the 36 Apliki mine samples are presented in ascending sample order.

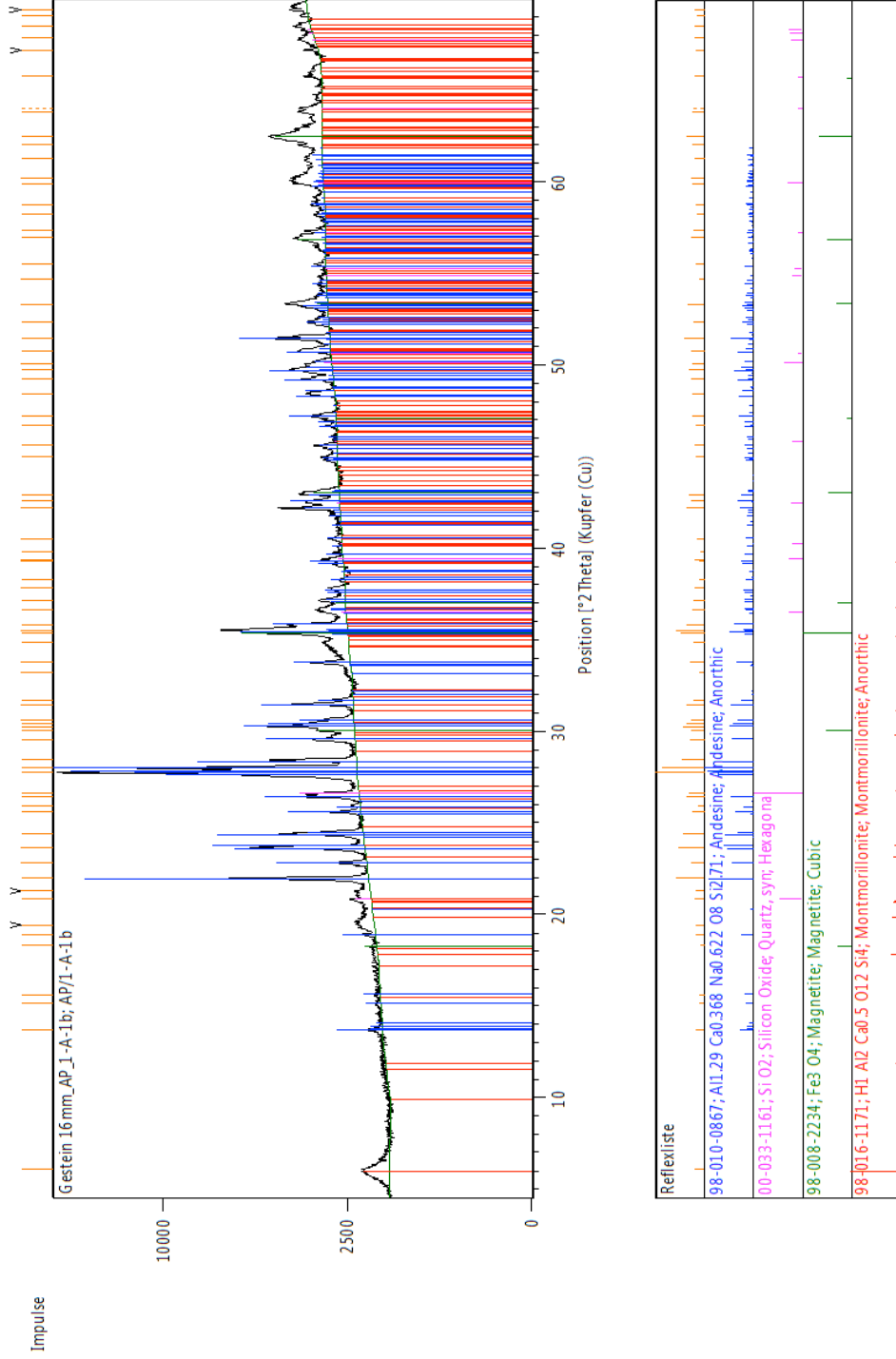


Figure 139 X-Ray diffractogram for sample 1b

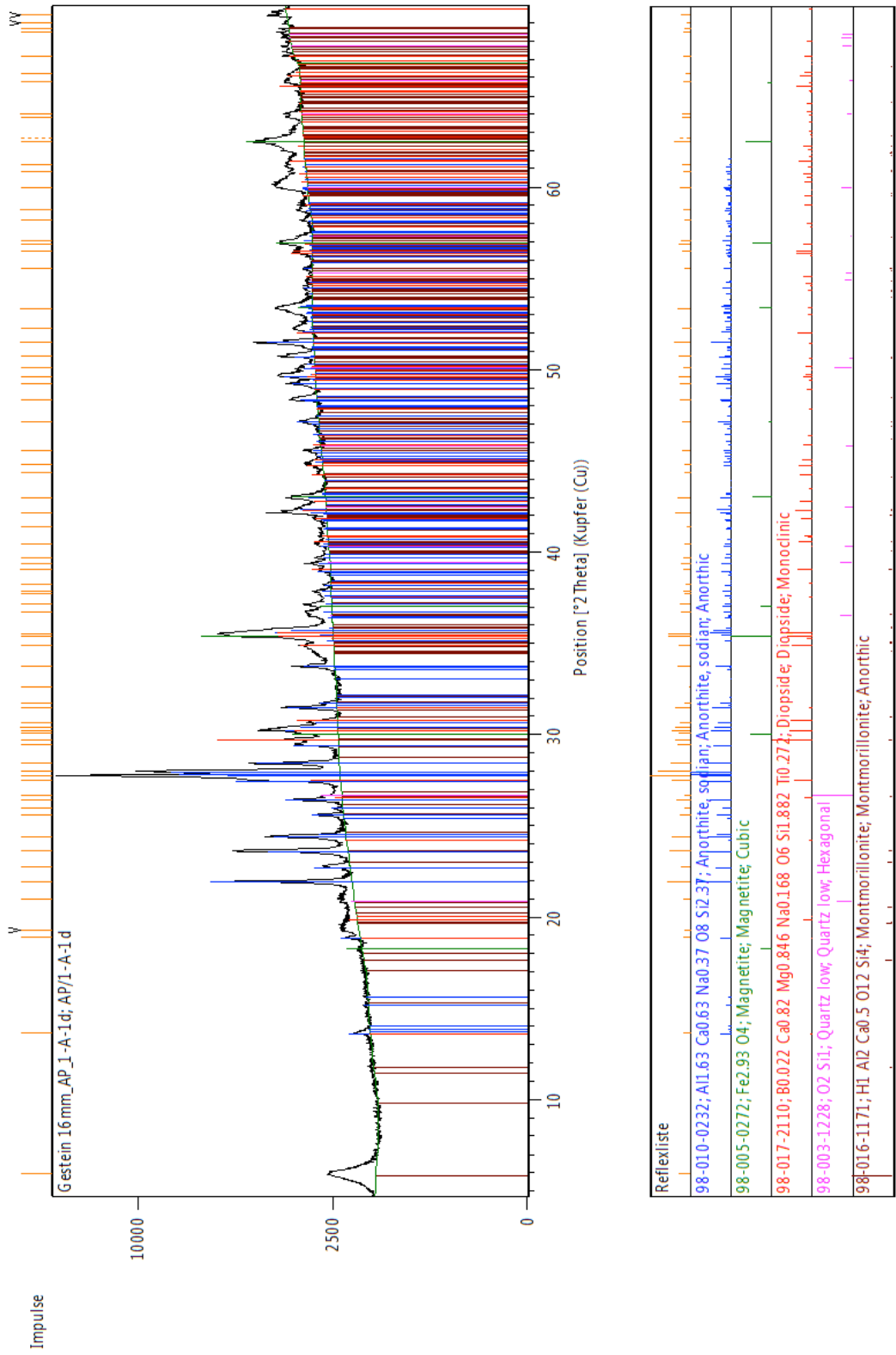


Figure 140 X-Ray diffractogram for sample 1d

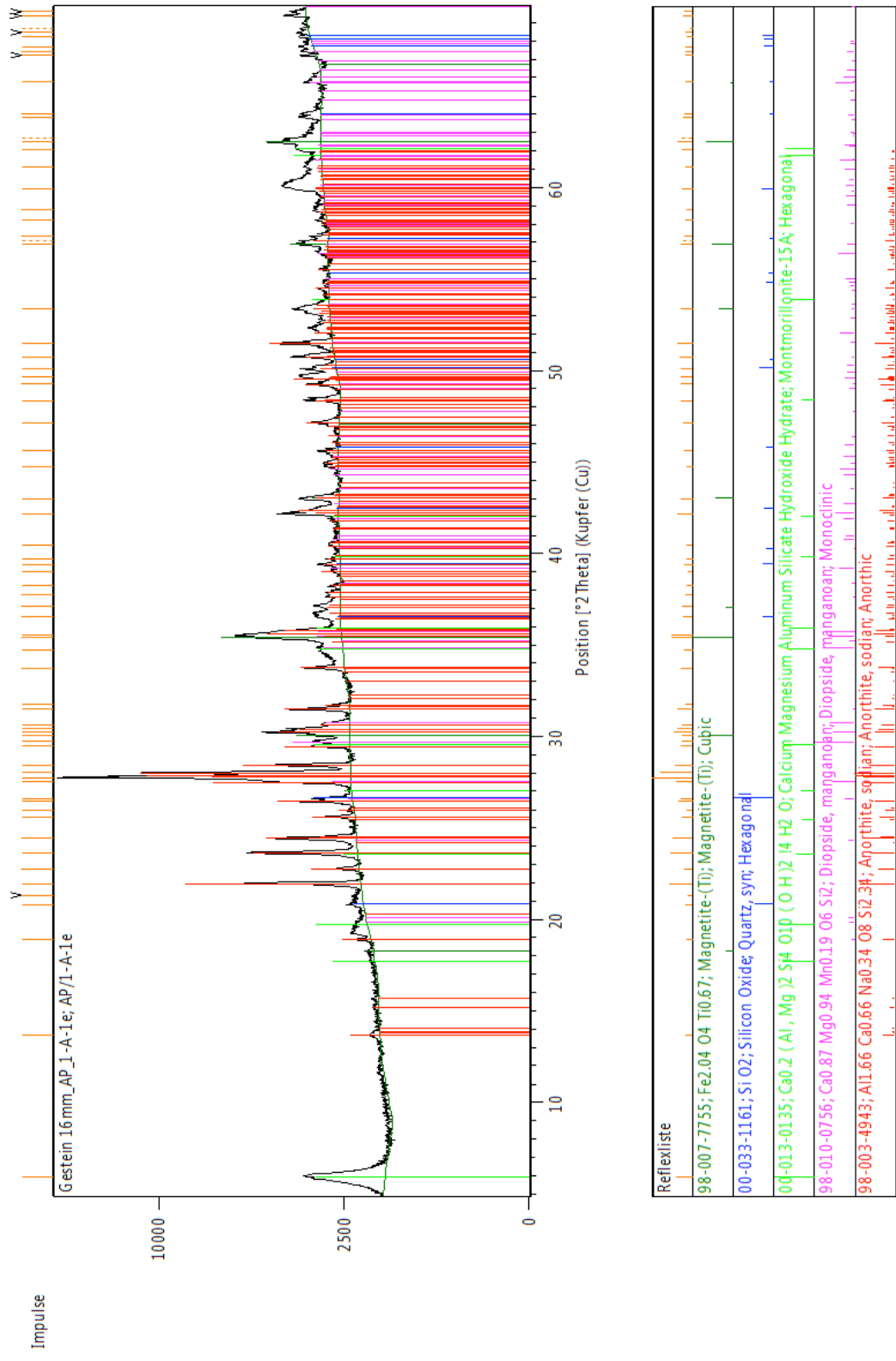


Figure 141 X-Ray diffractogram for sample 1e

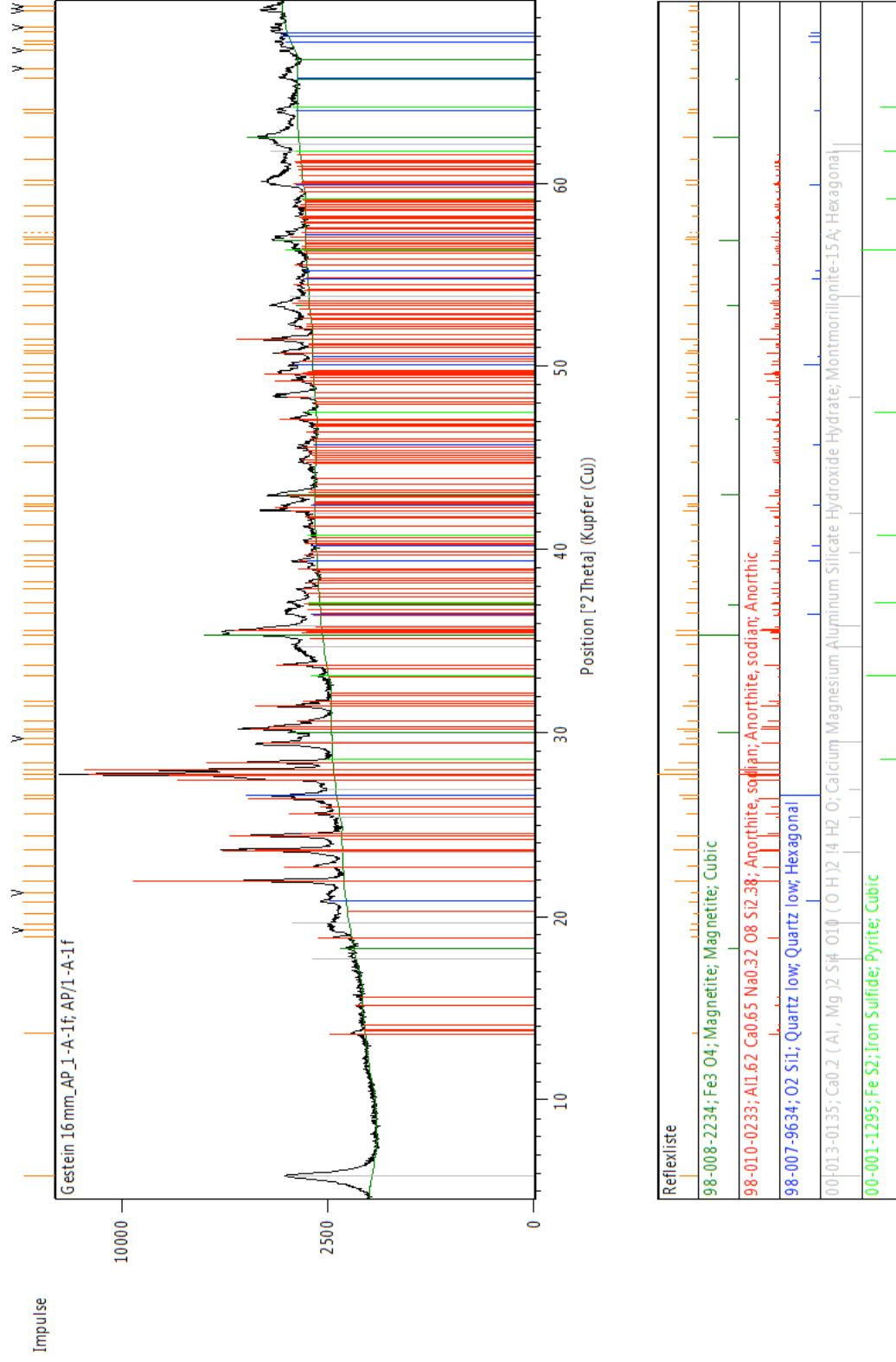


Figure 142 X-Ray diffractogram for sample 1f

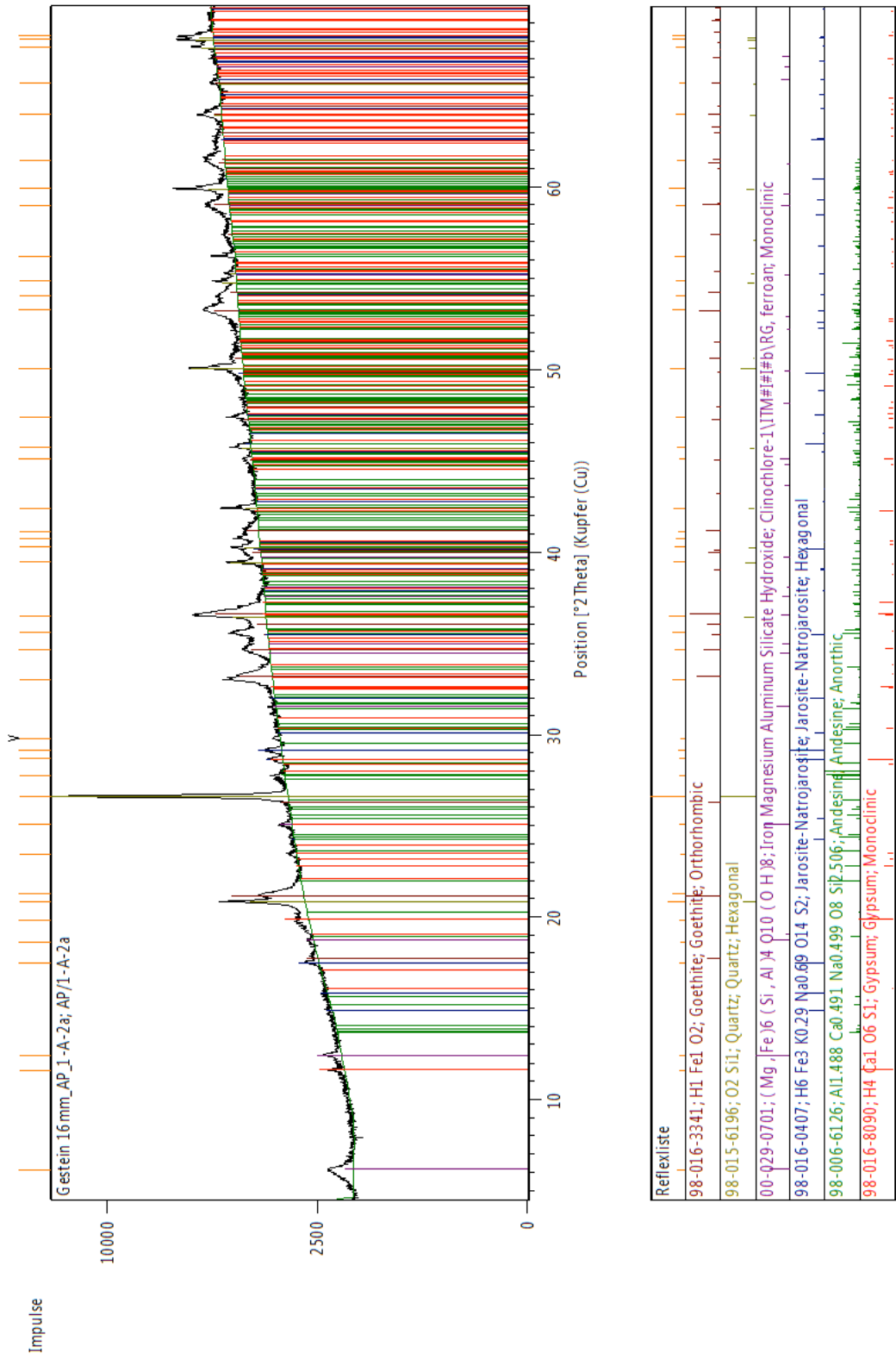


Figure 143 X-Ray diffractogram for sample 2a

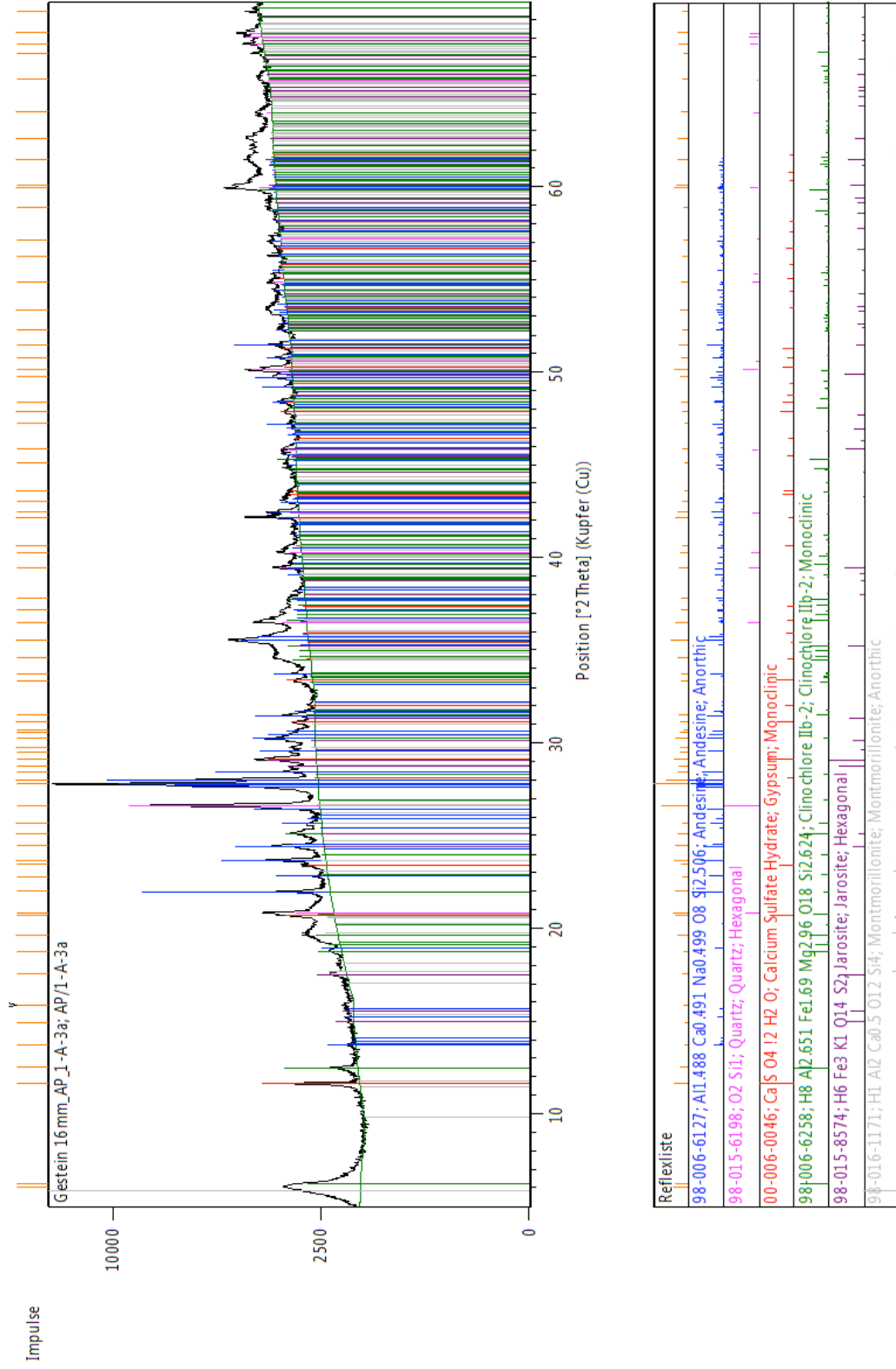


Figure 144 X-Ray diffractogram for sample 3a

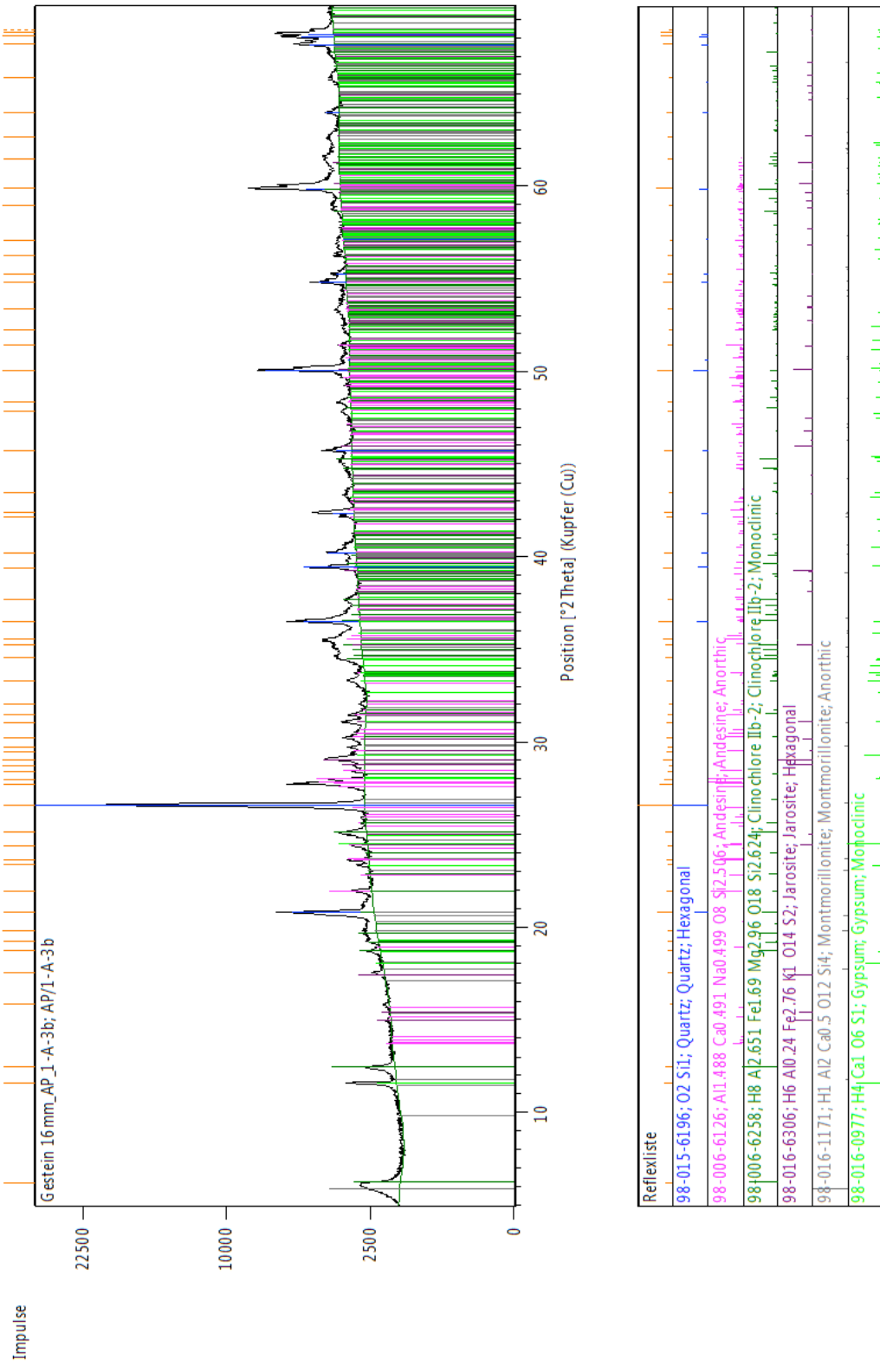


Figure 145 X-Ray diffractogram for sample 3b

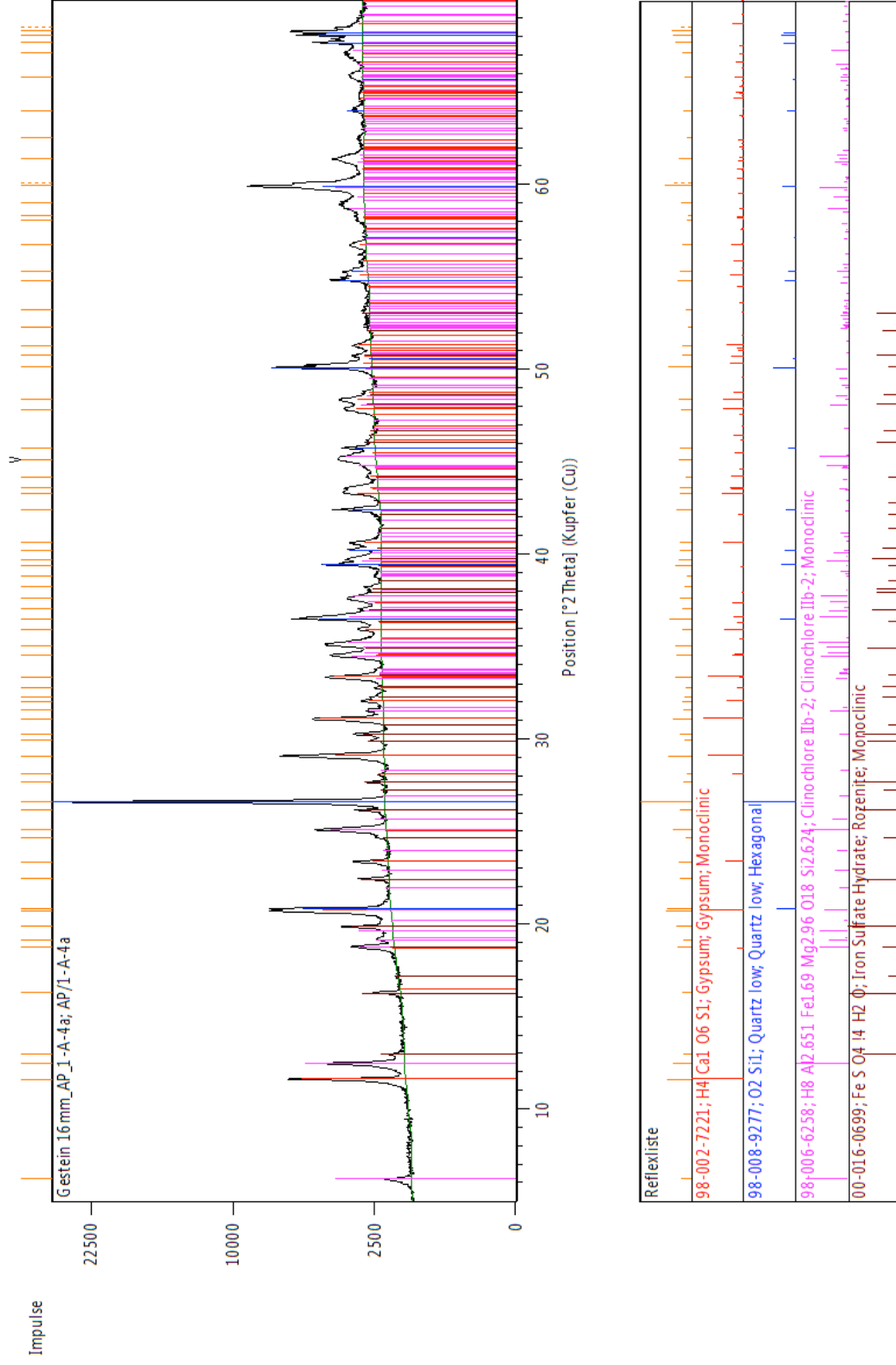


Figure 146 X-Ray diffractogram for sample 4a

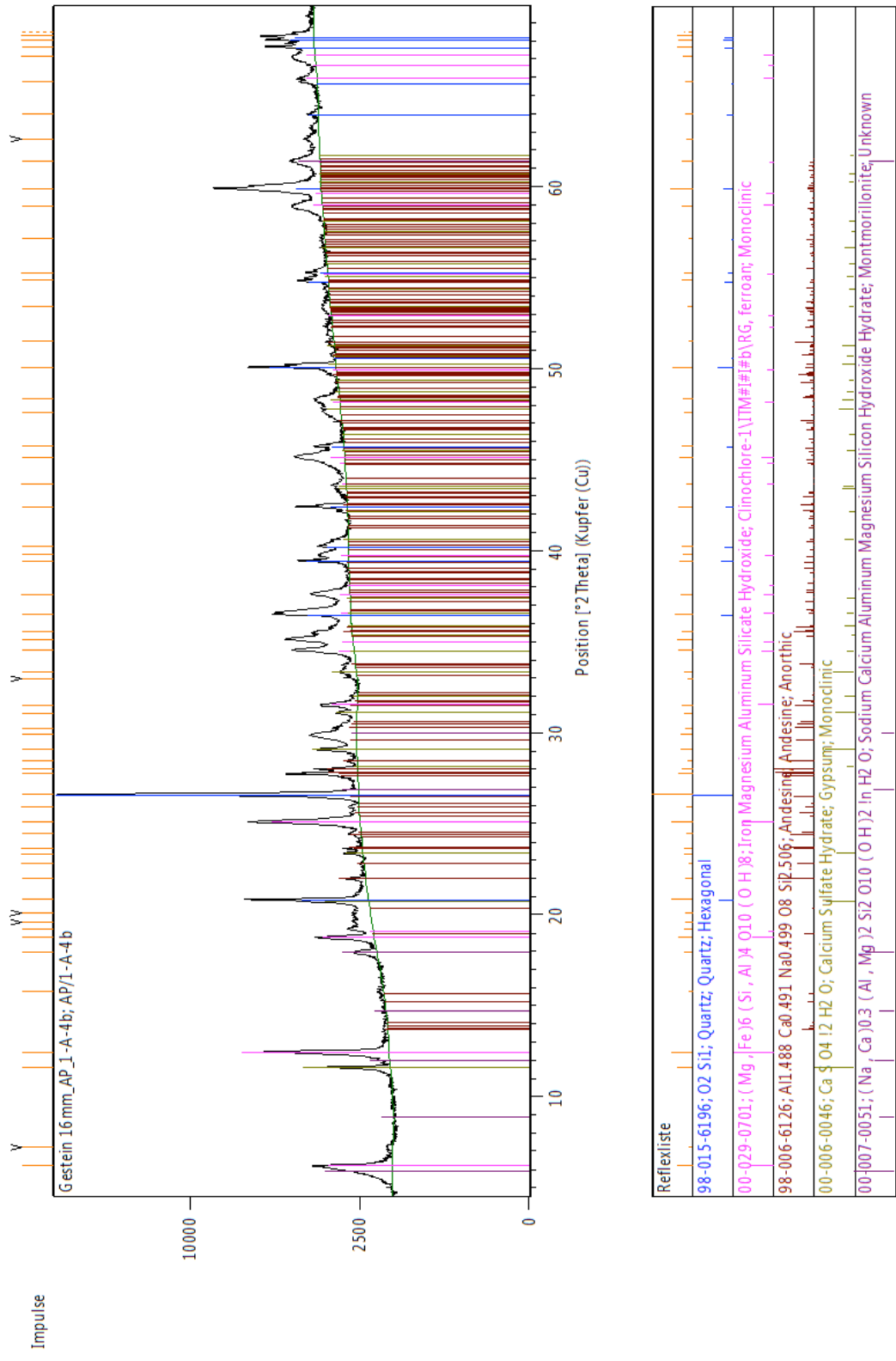


Figure 147 X-Ray diffractogram for sample 4b

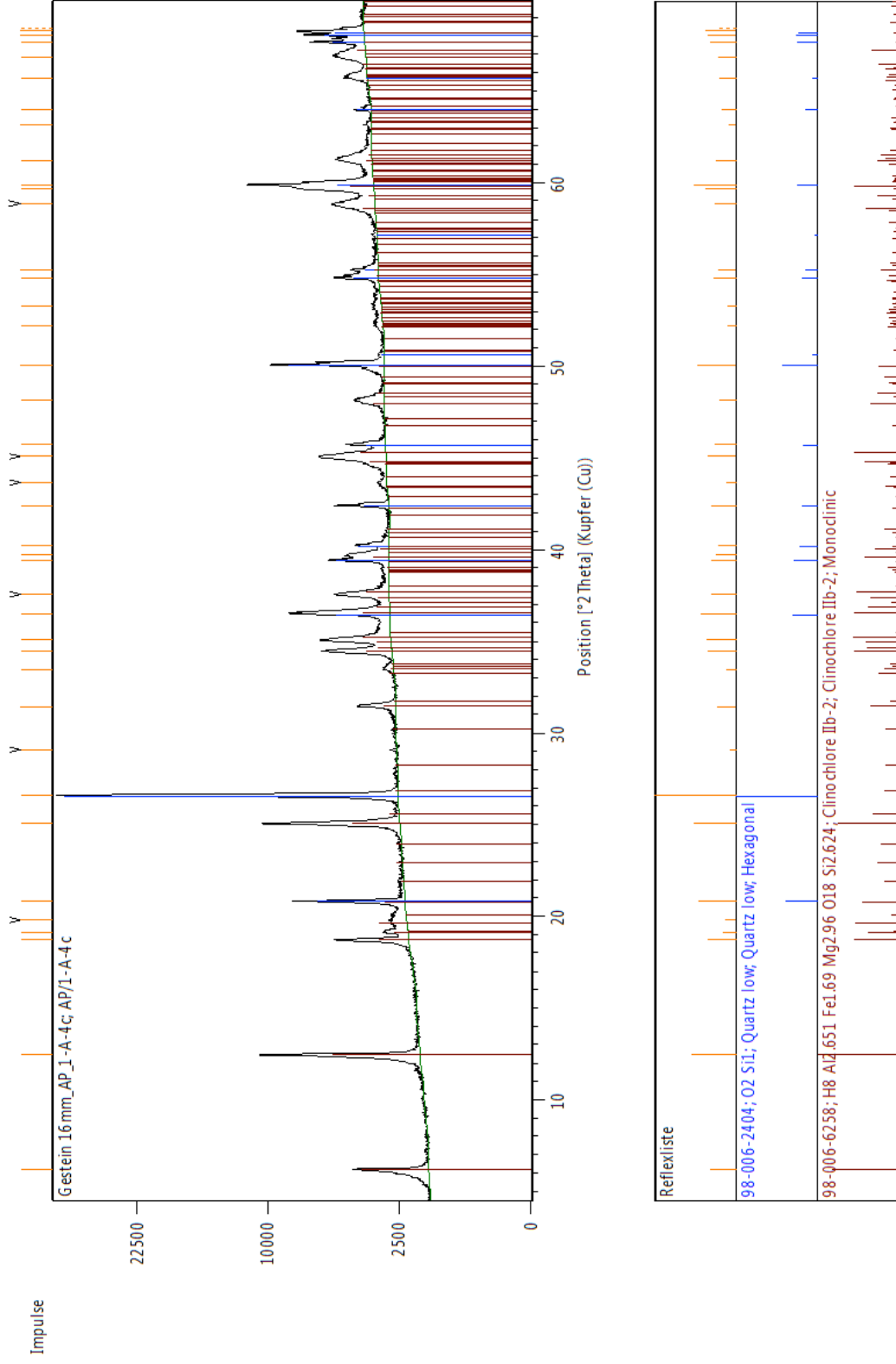


Figure 148 X-Ray diffractogram for sample 4c

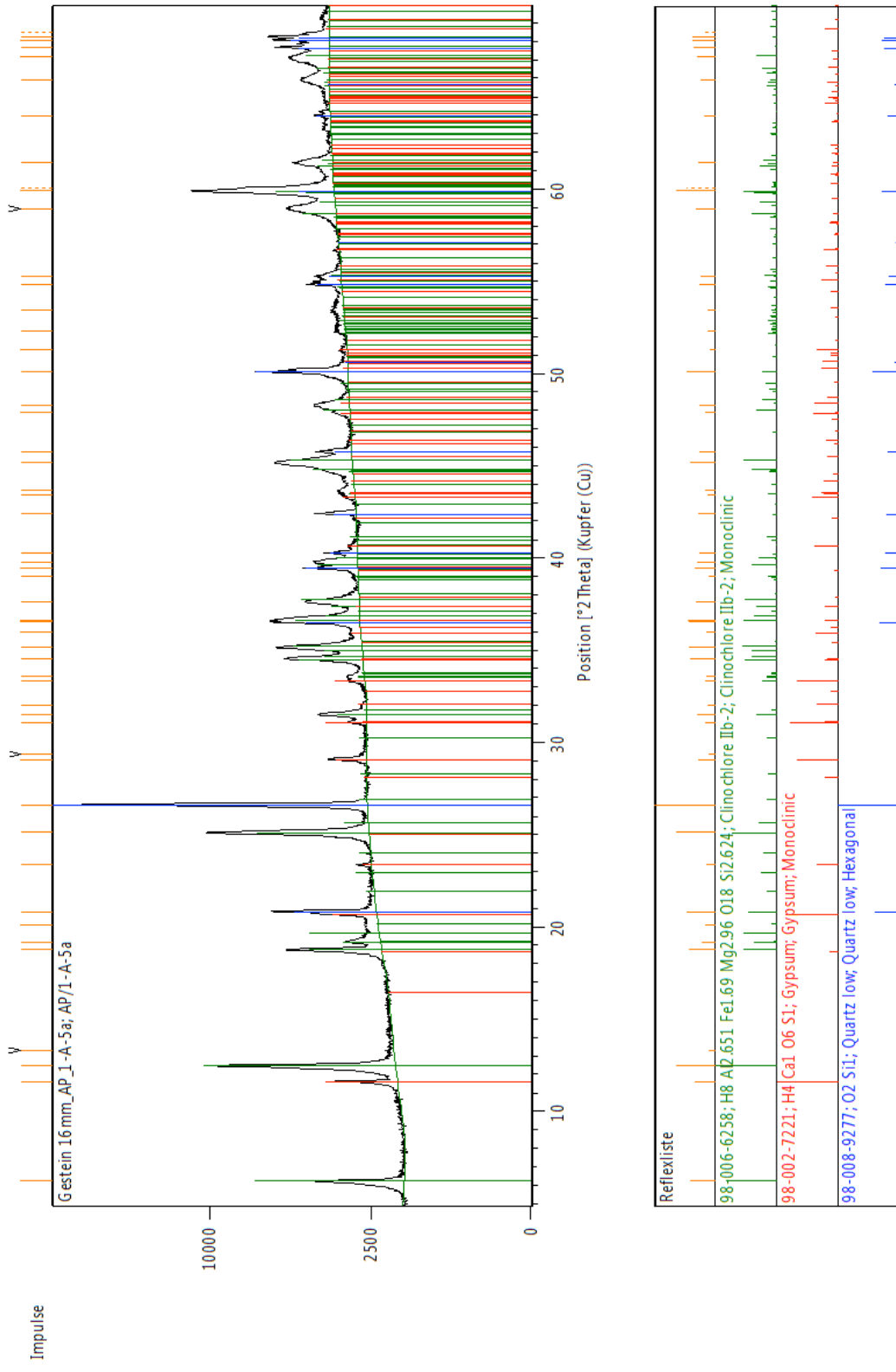


Figure 149 X-Ray diffractogram for sample 5a

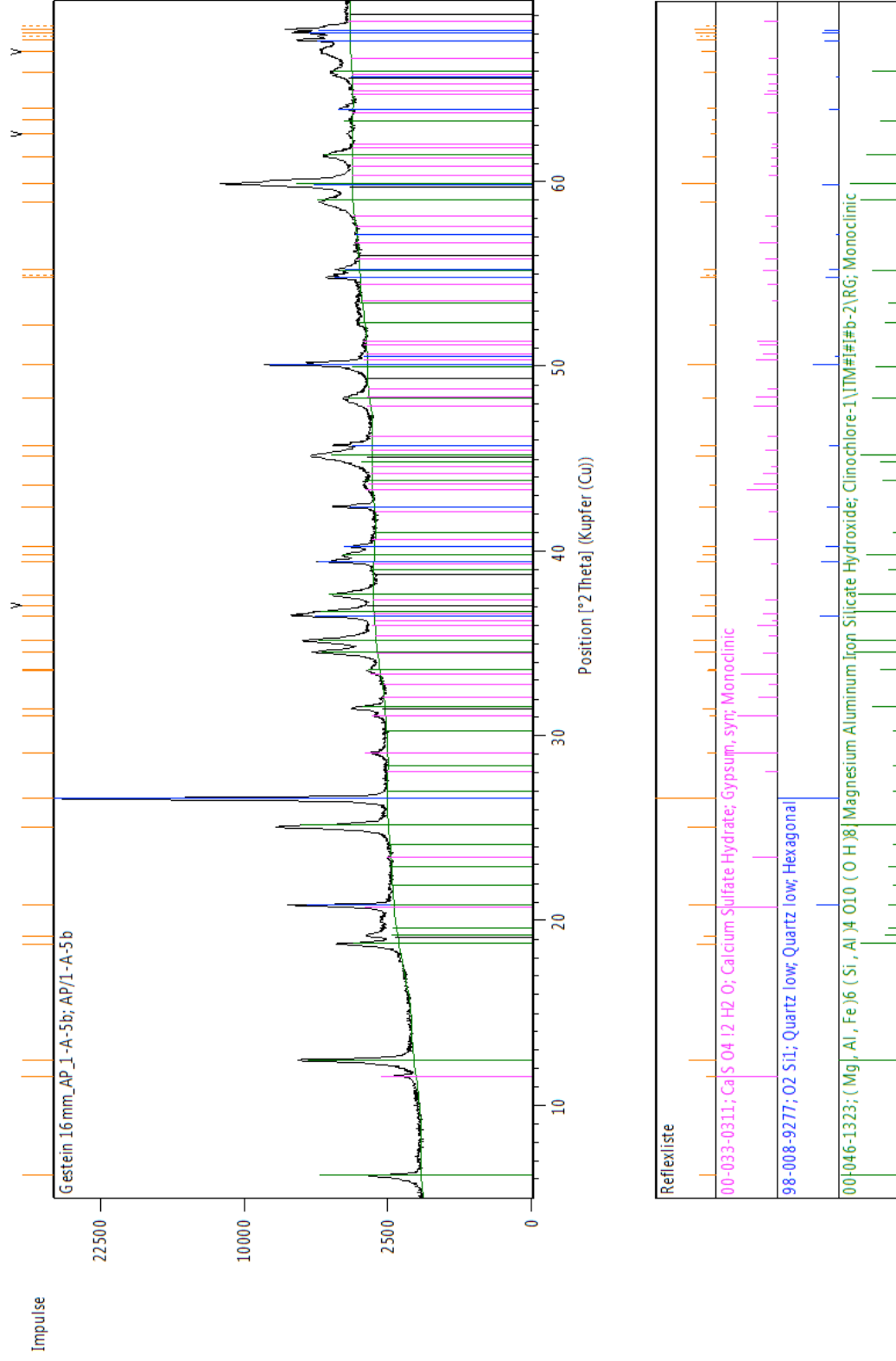


Figure 150 X-Ray diffractogram for sample 5b

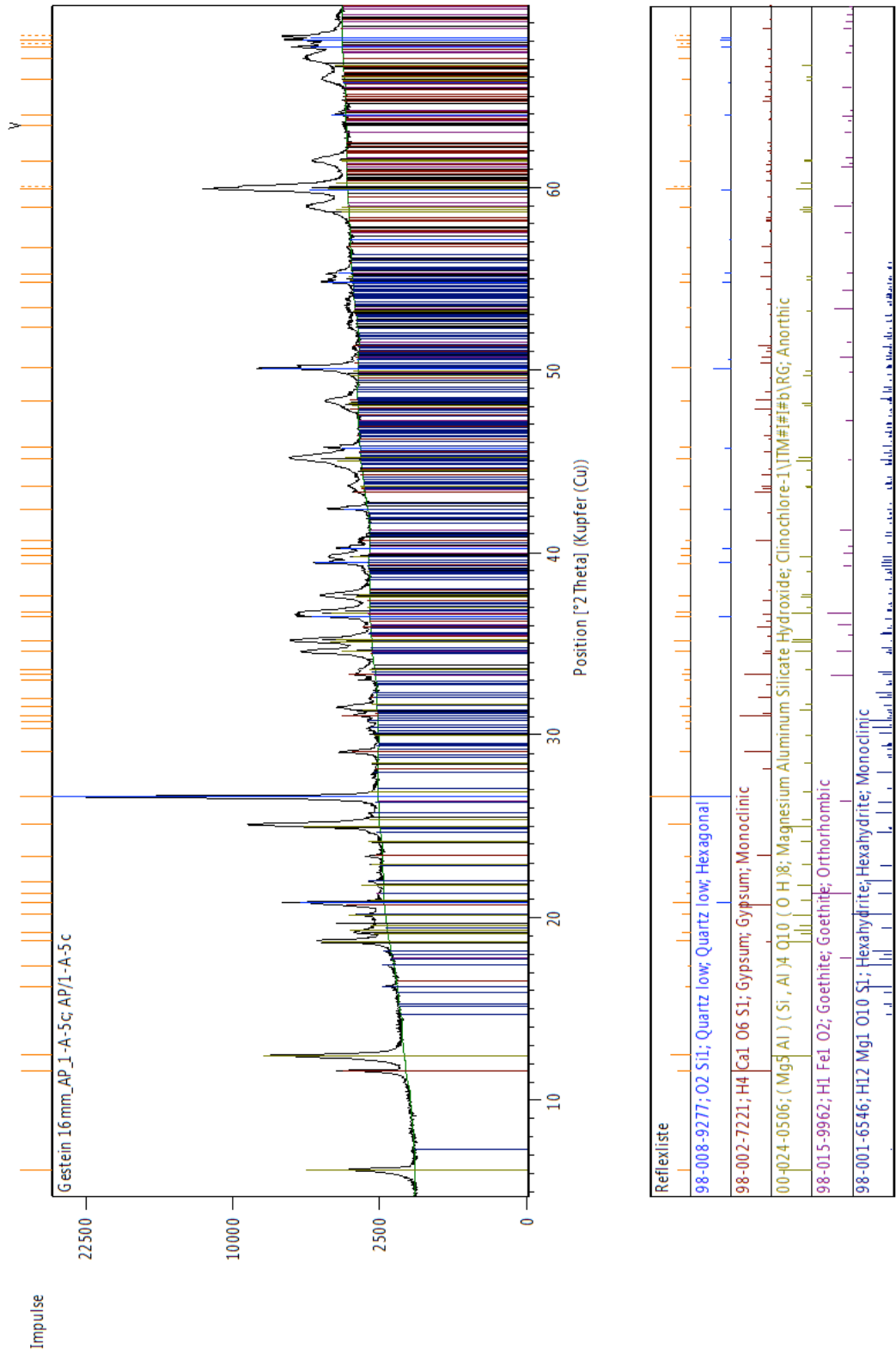


Figure 151 X-Ray diffractogram for sample 5c

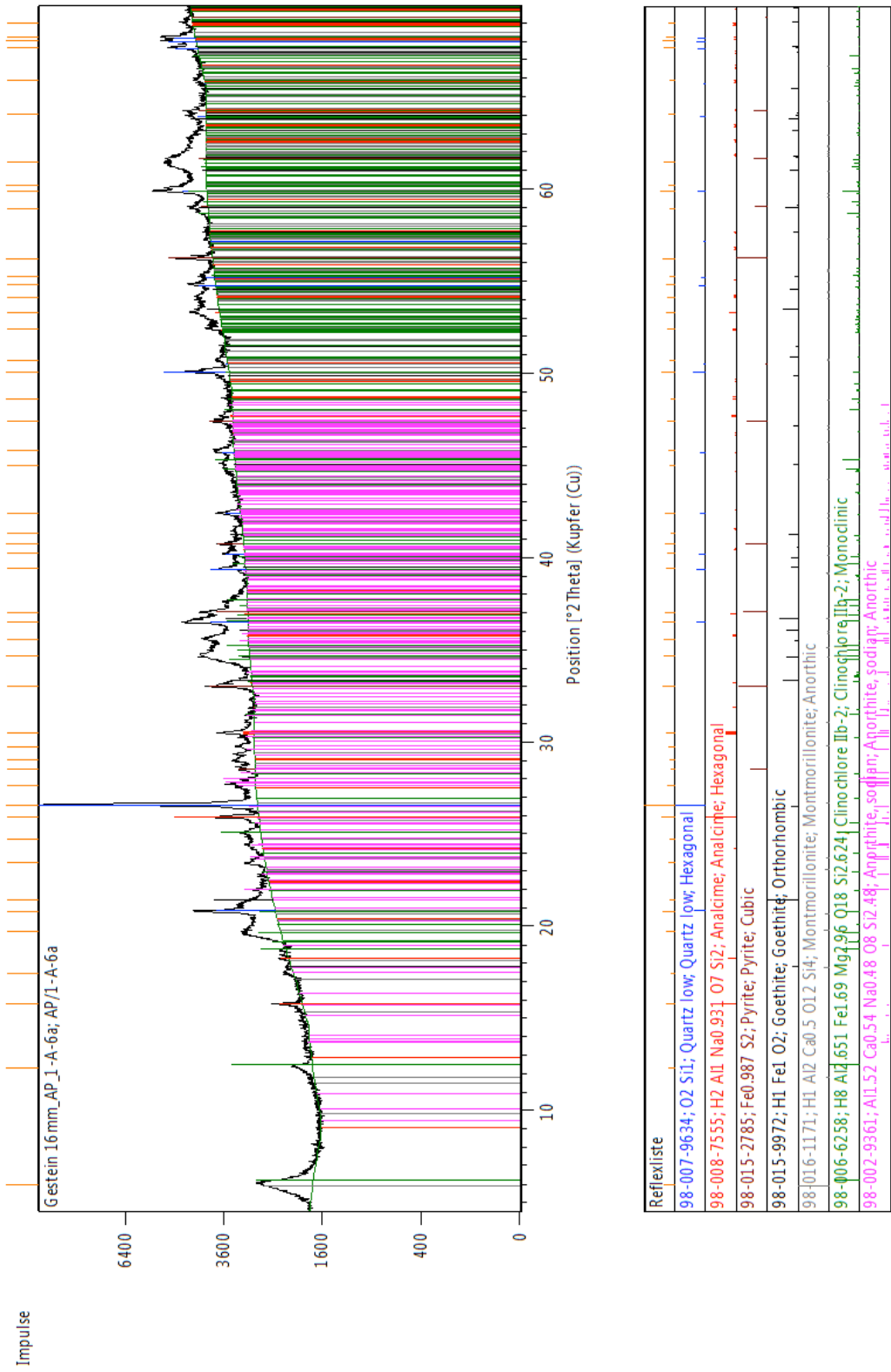


Figure 152 X-Ray diffractogram for sample 6a

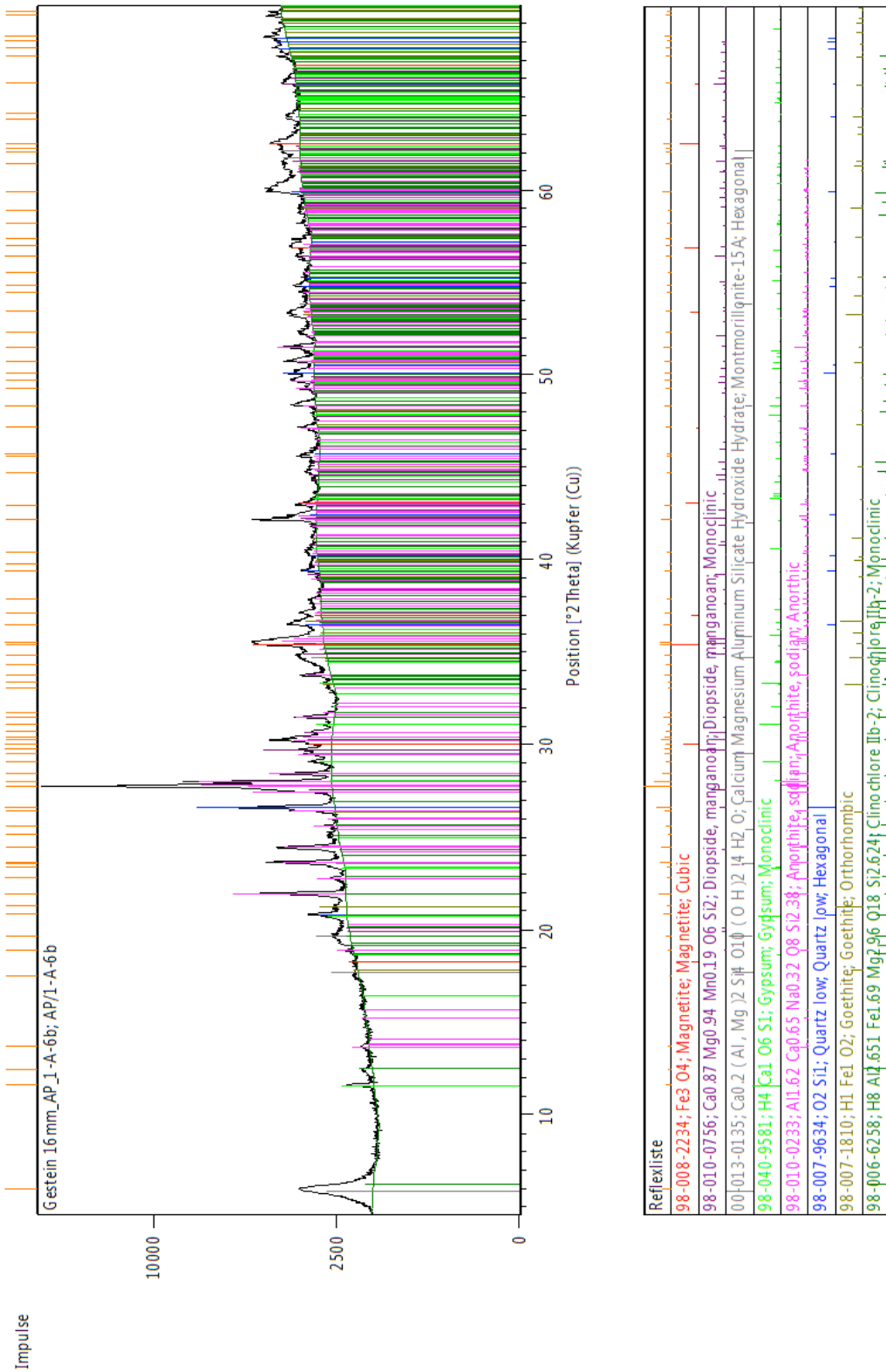


Figure 153 X-Ray diffractogram for sample 6b

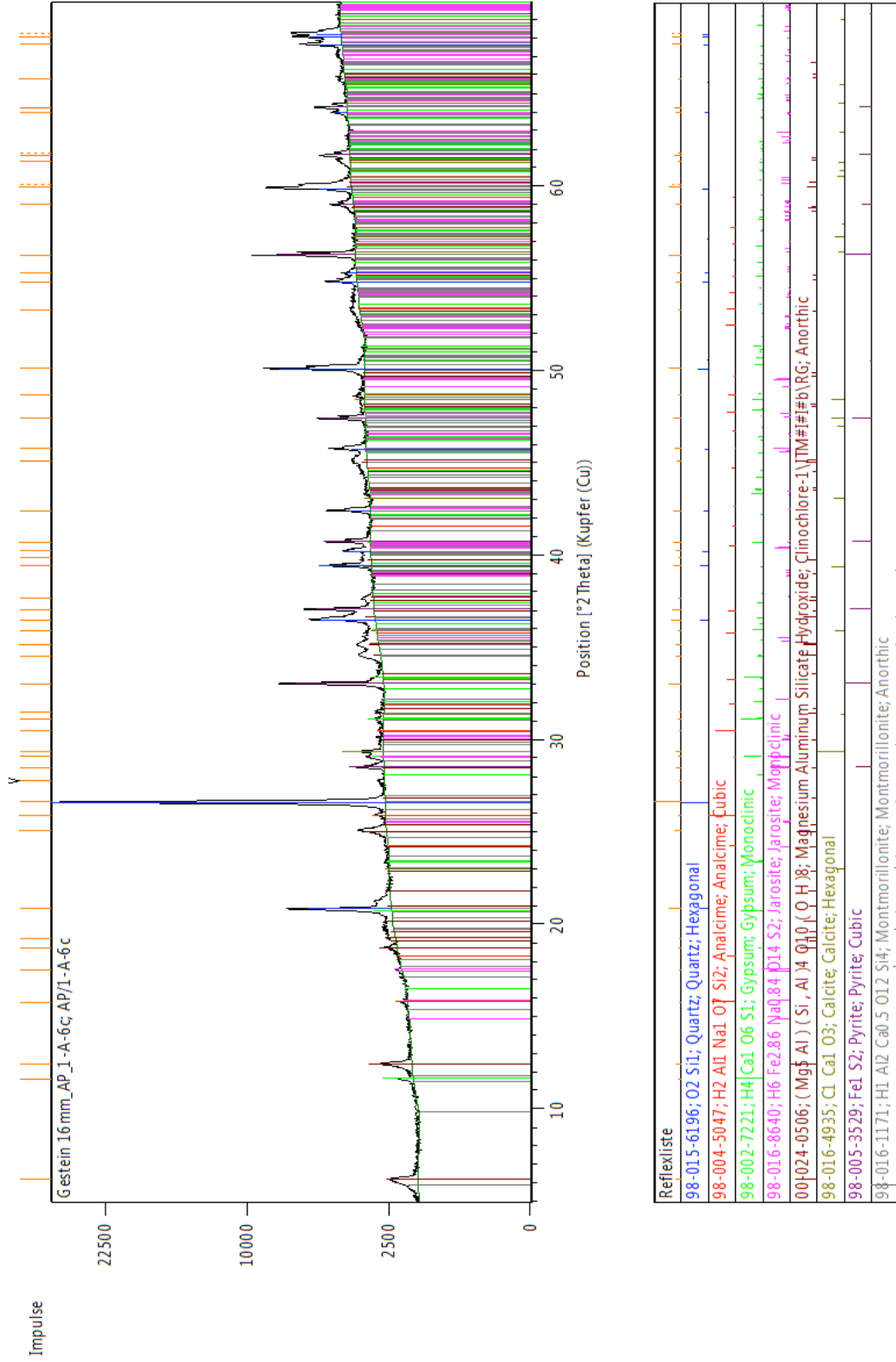


Figure 154 X-Ray diffractogram for sample 6c

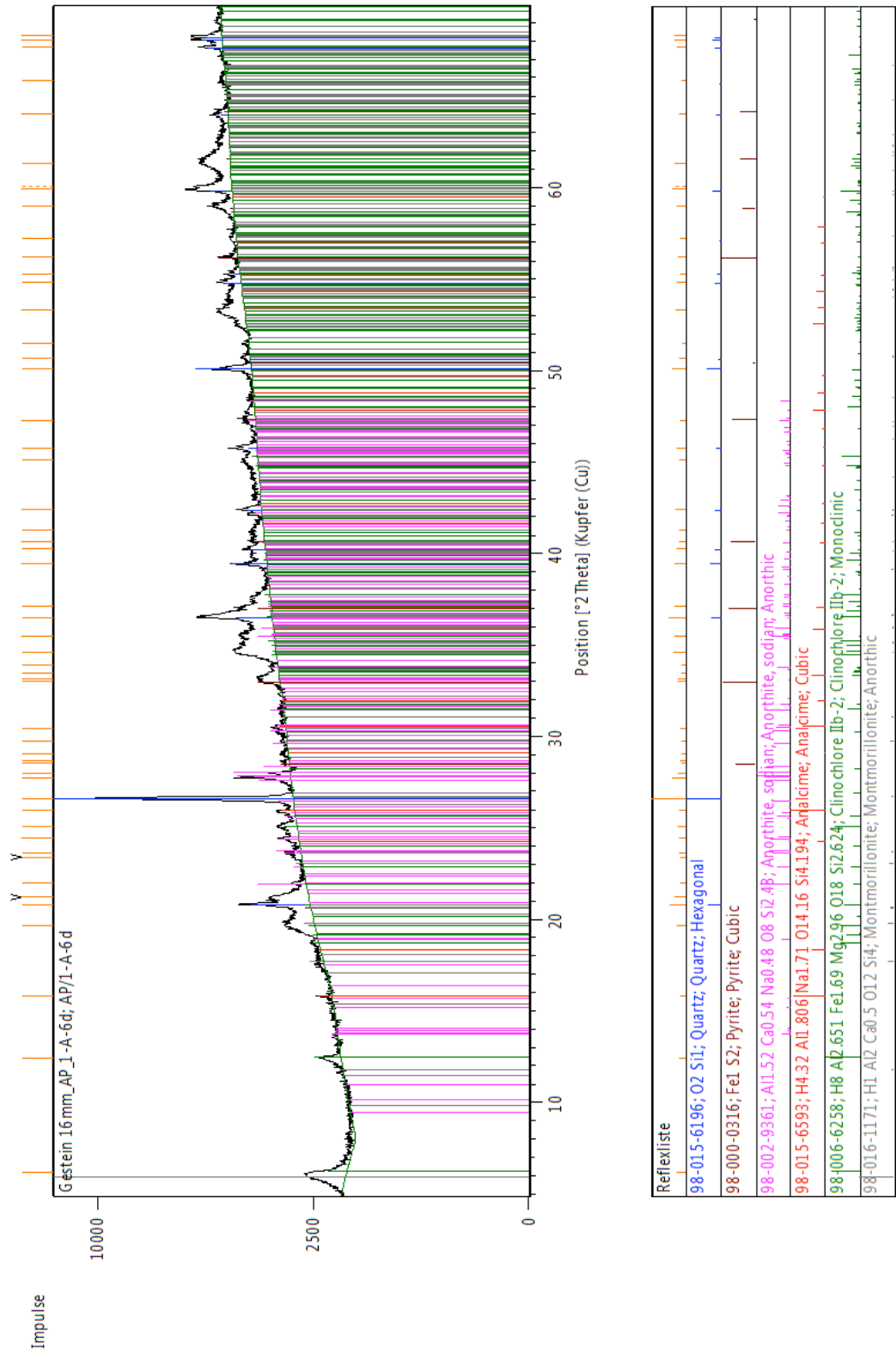


Figure 155 X-Ray diffractogram for sample 6d

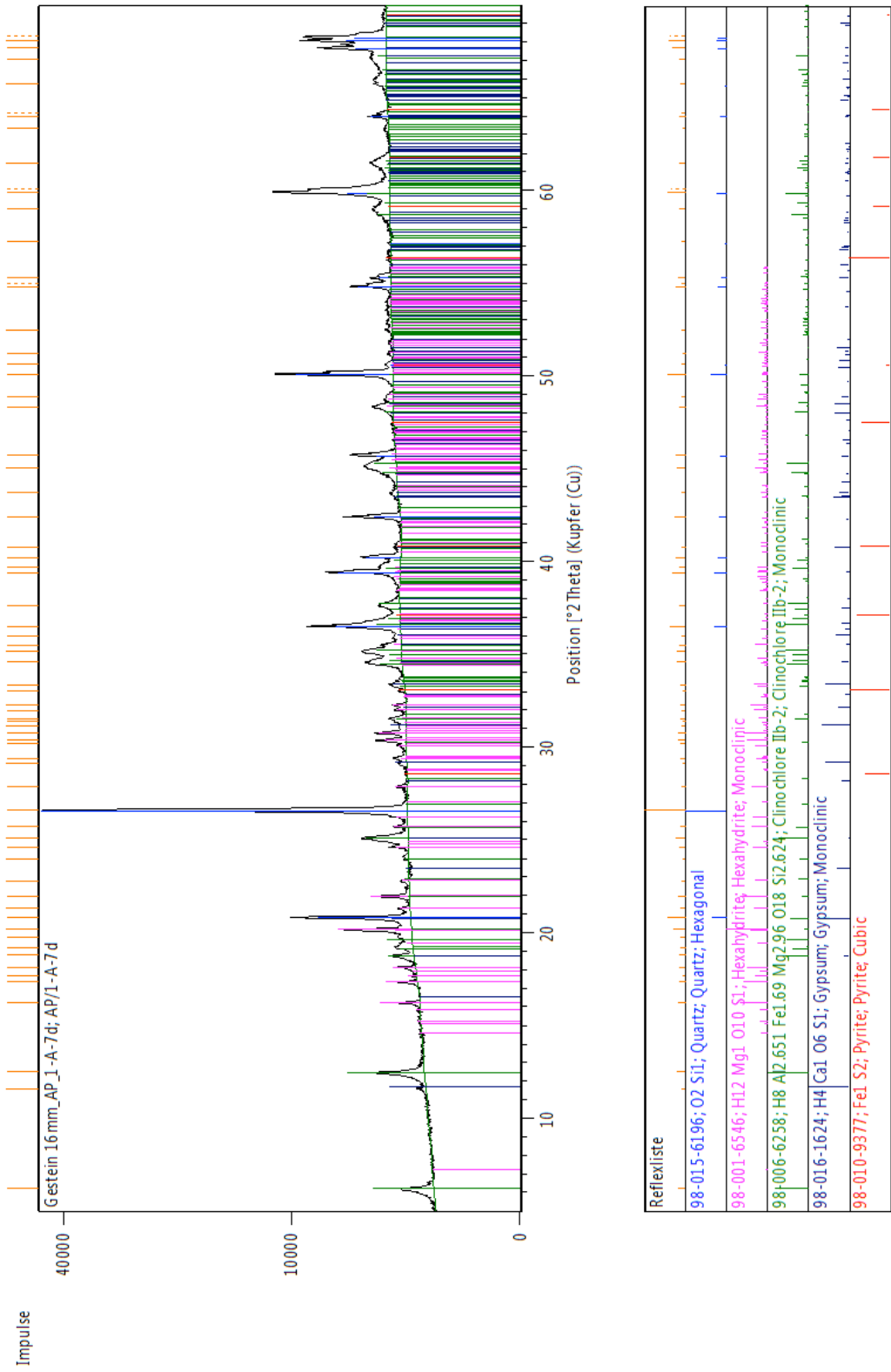


Figure 156 X-Ray diffractogram for sample 7d

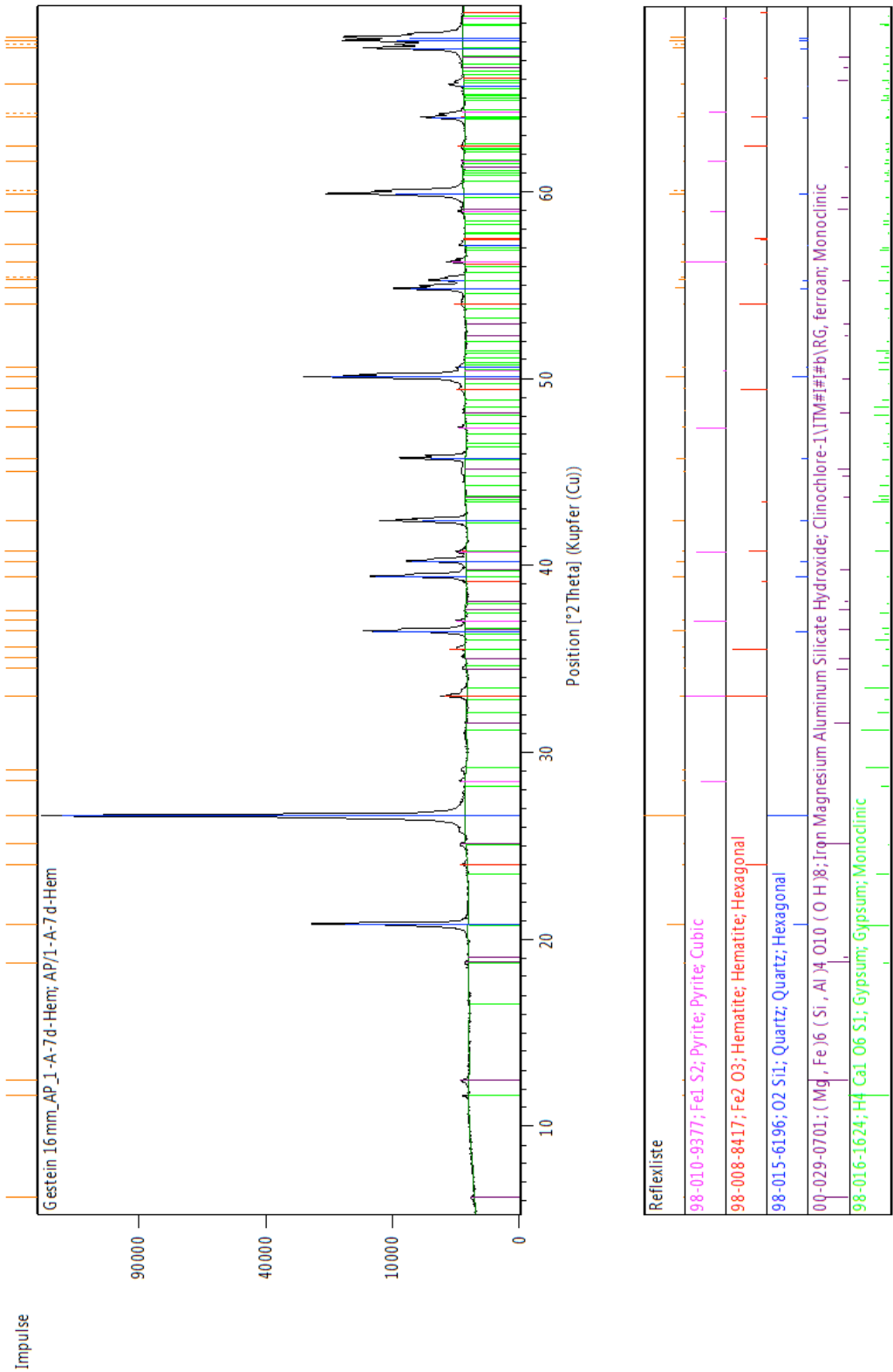


Figure 157 X-Ray diffractogram for sample 7d_Hem

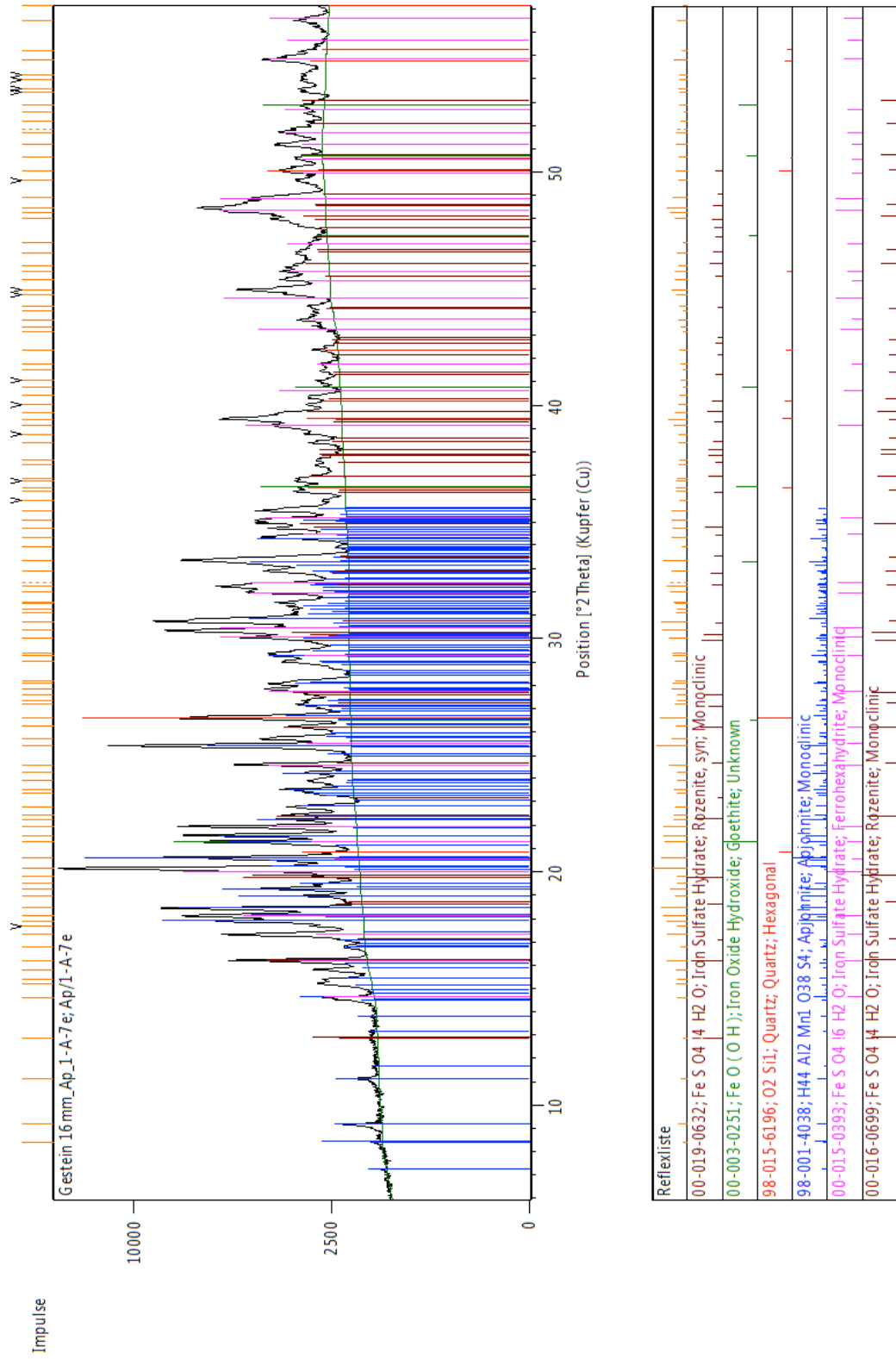


Figure 158 X-Ray diffractogram for sample 7e

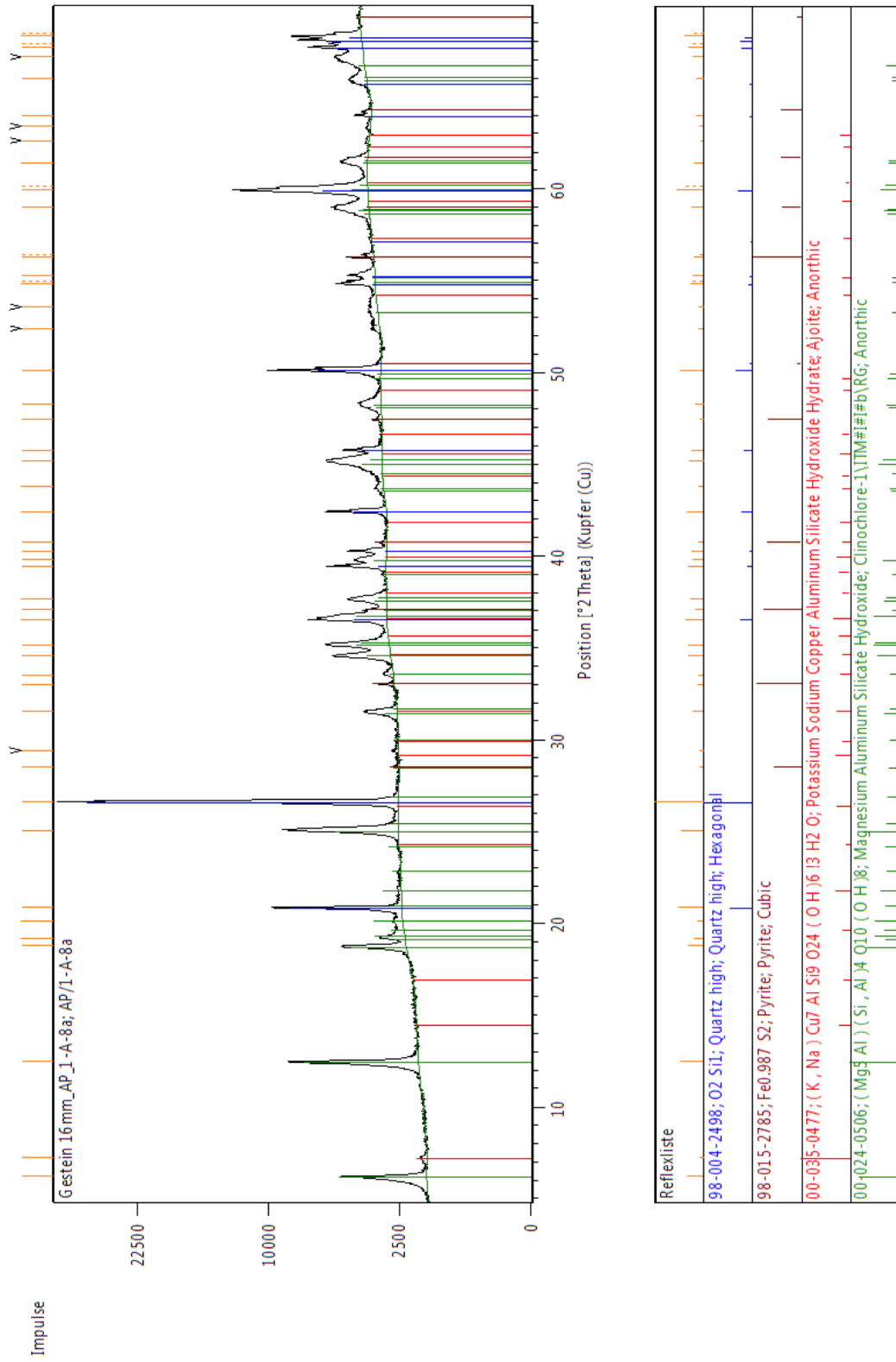


Figure 159 X-Ray diffractogram for sample 8a

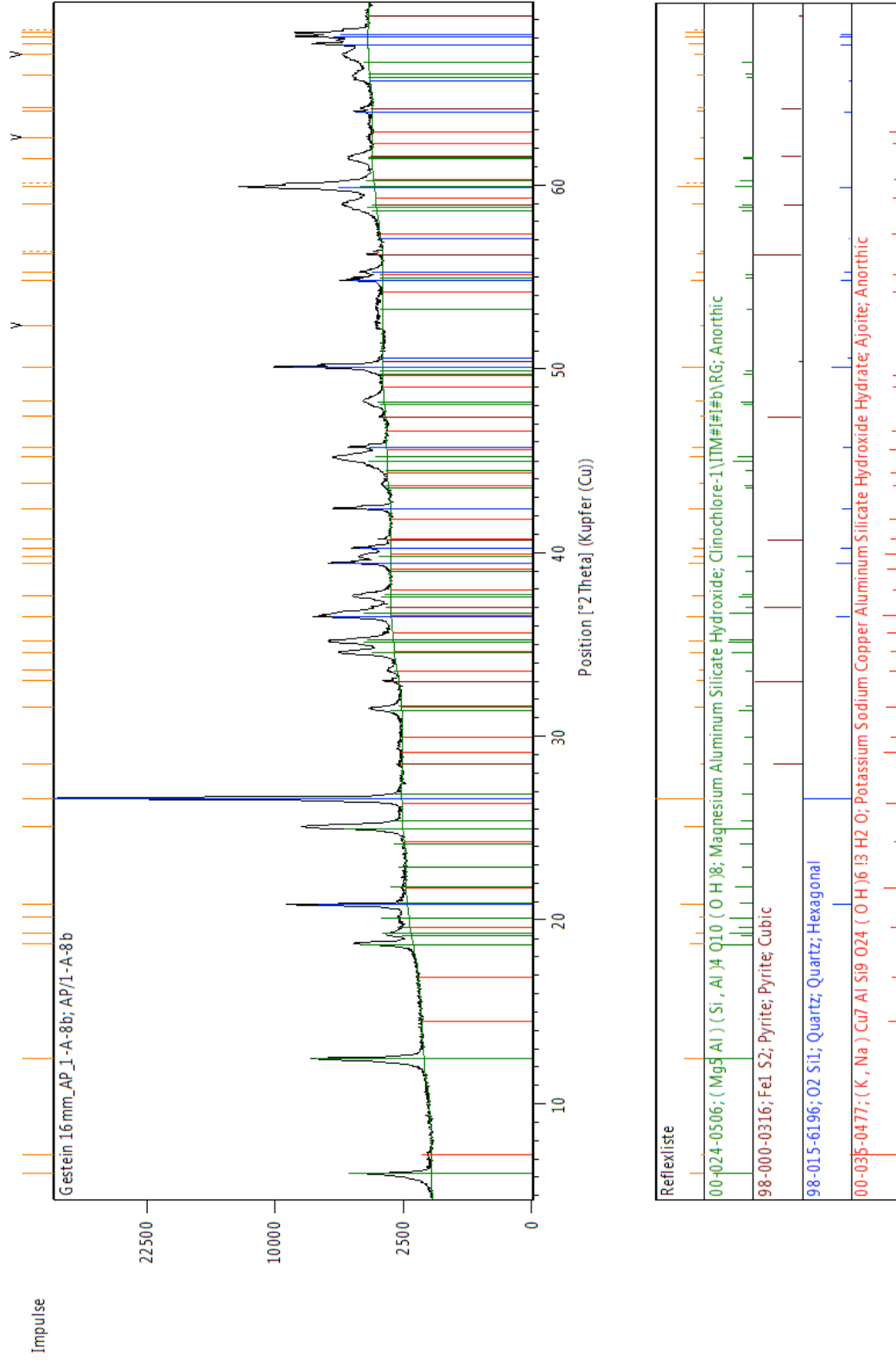
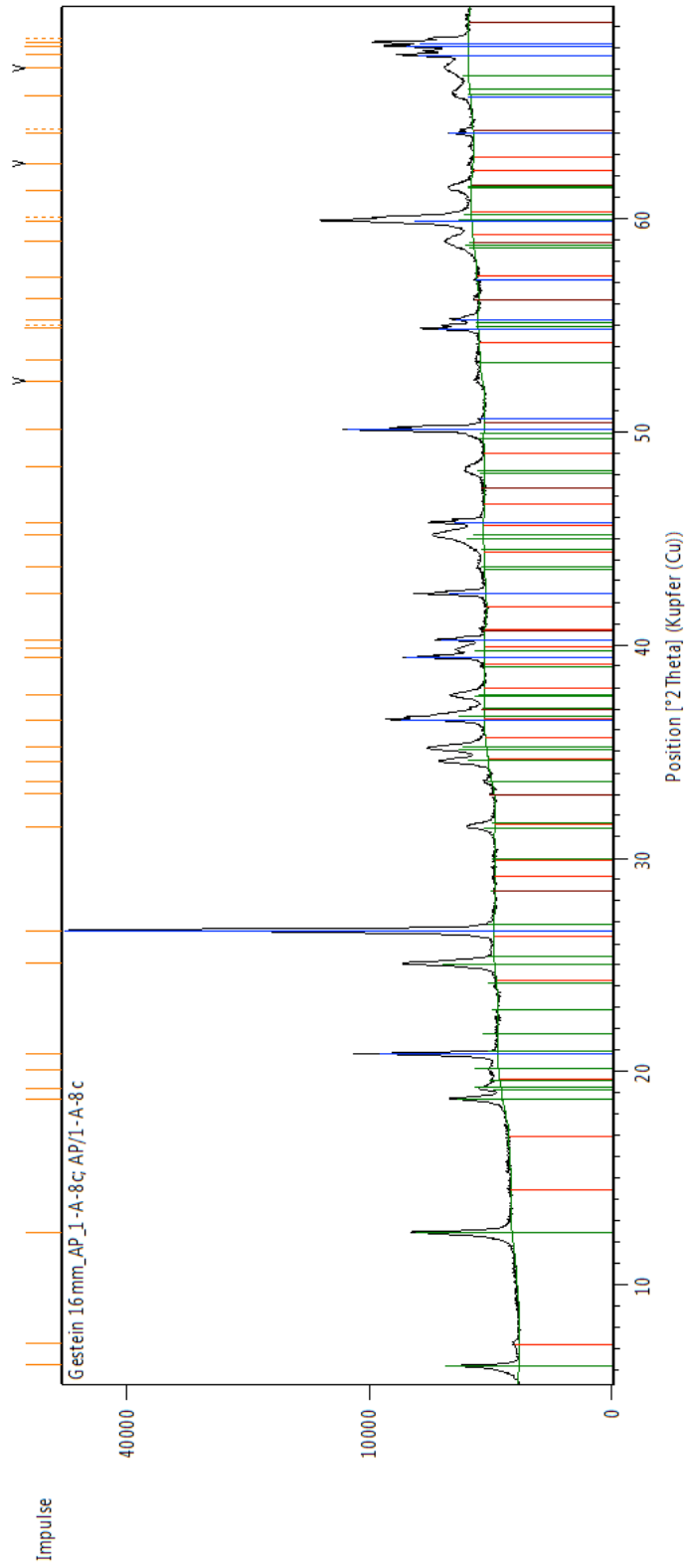


Figure 160 X-Ray diffractogram for sample 8b



Reflexliste
98-008-9277; O2 Si1; Quartz low; Quartz low; Hexagonal
00-035-0477; (K, Na) Cu7 Al Si9 O24 (OH)6 H2 O; Potassium Sodium Copper Aluminum Silicate Hydroxide Hydrate; Ajoite; Anorthic
00-024-0506; (Mg5 Al) (Si, Al)4 O10 (OH)8; Magnesium Aluminum Silicate Hydroxide; Clinochlore-1\1TM#i#b'RG; Anorthic
98-000-0316; Fe1 S2; Pyrite; Cubic

Figure 161 X-Ray diffractogram for sample 8c

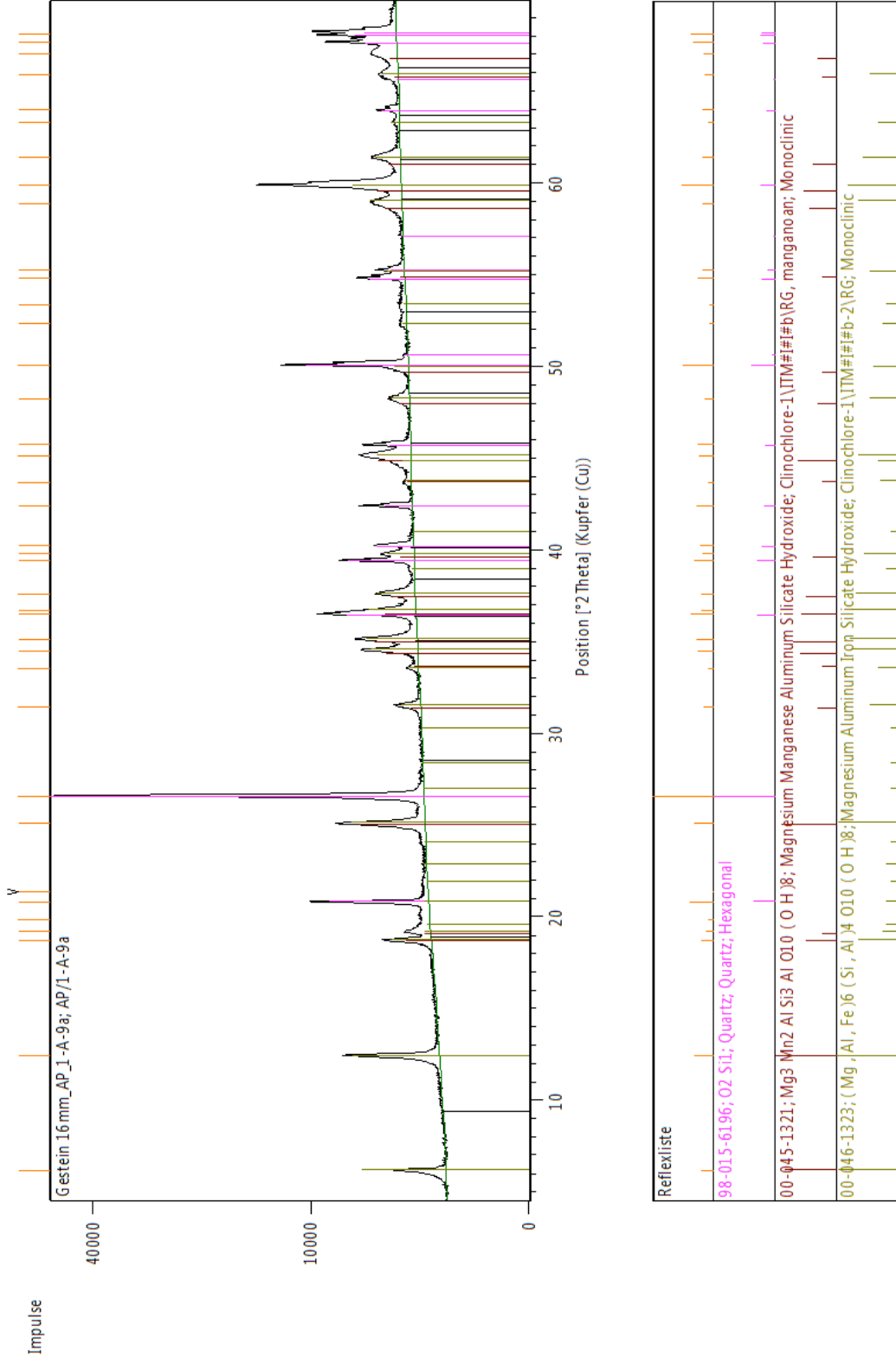


Figure 162 X-Ray diffractogram for sample 9a

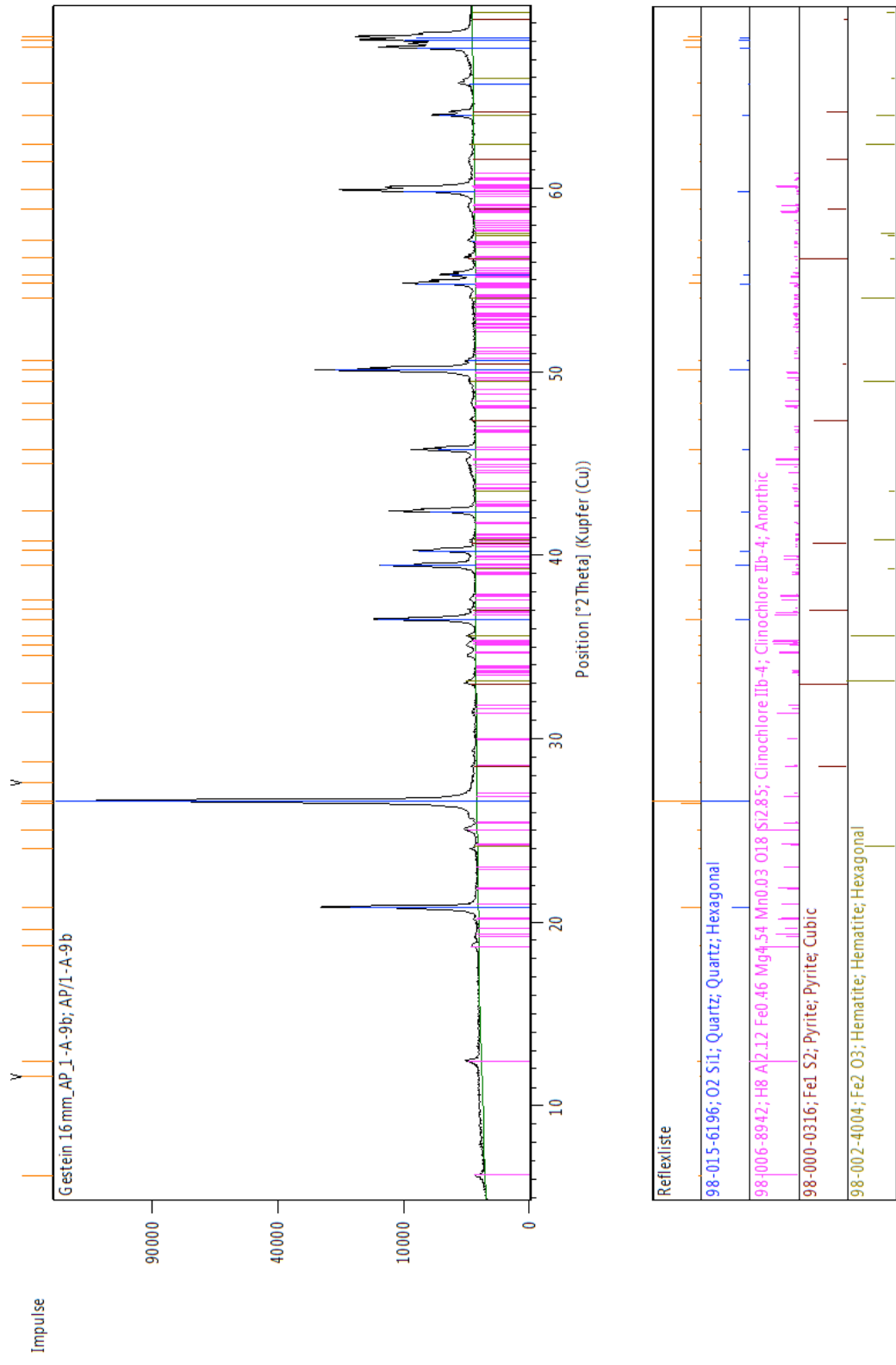


Figure 163 X-Ray diffractogram for sample 9b

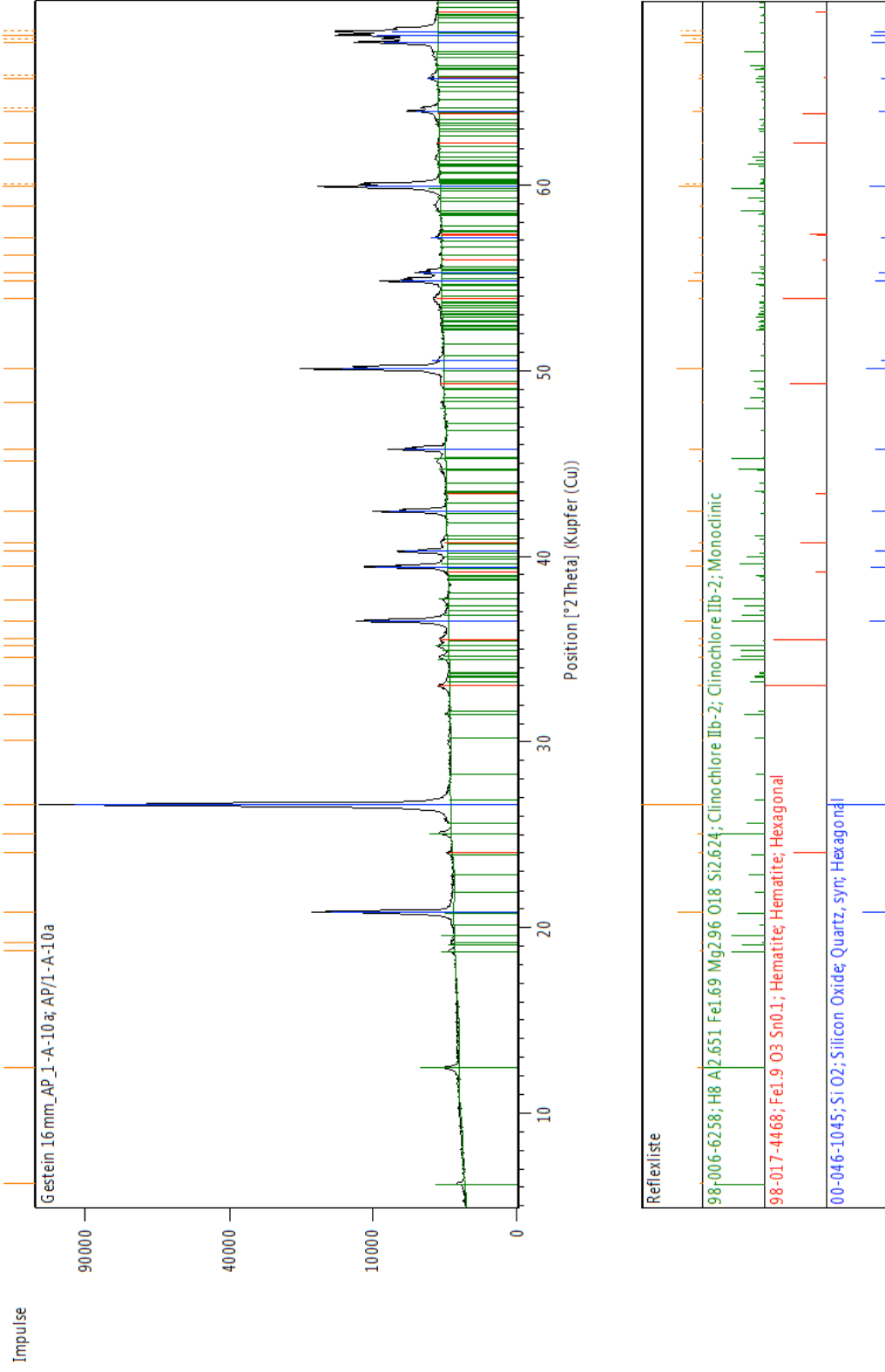


Figure 164 X-Ray diffractogram for sample 10a

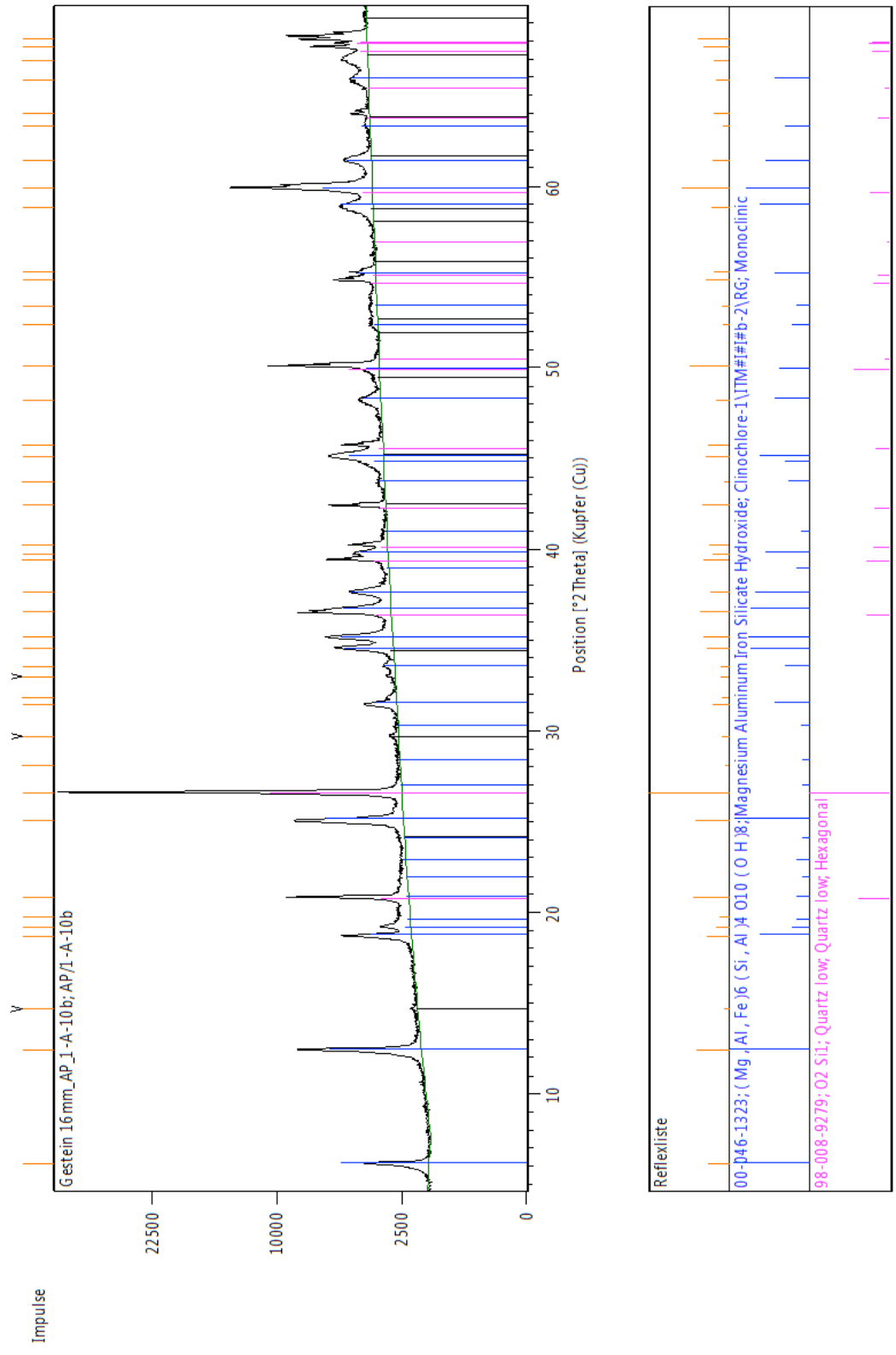


Figure 165 X-Ray diffractogram for sample 10b

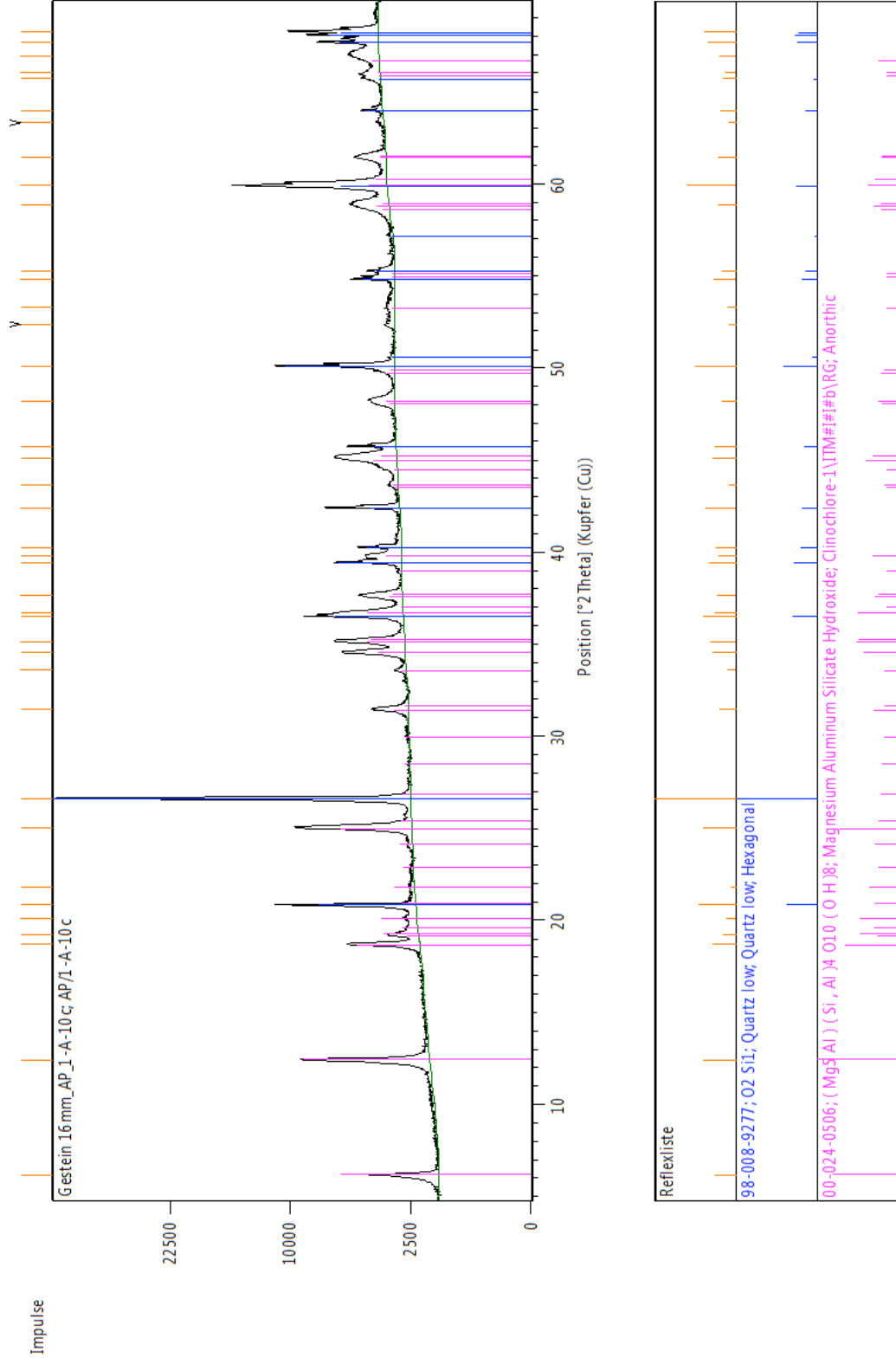


Figure 166 X-Ray diffractogram for sample 10c

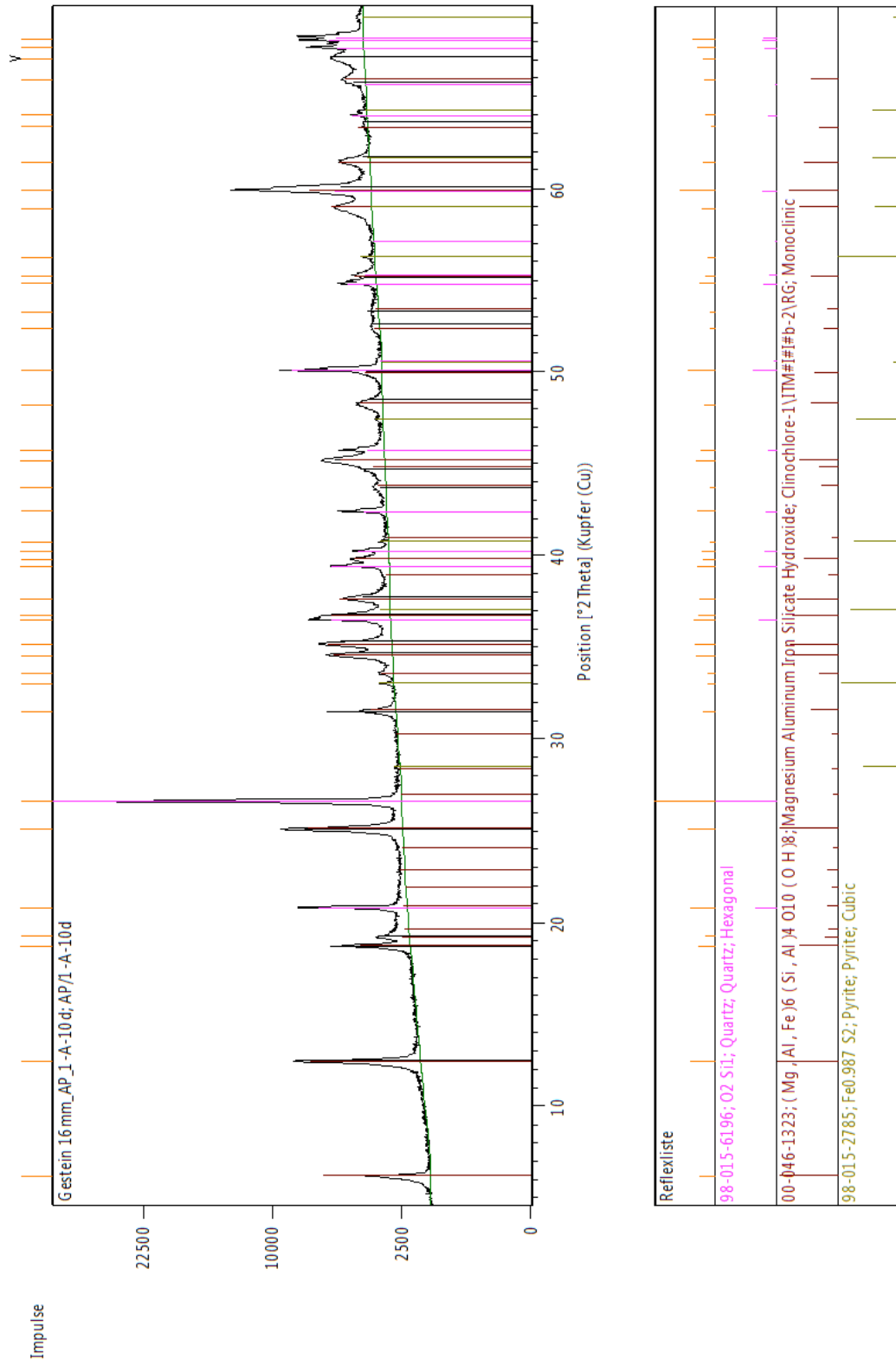


Figure 167 X-Ray diffractogram for sample 10d

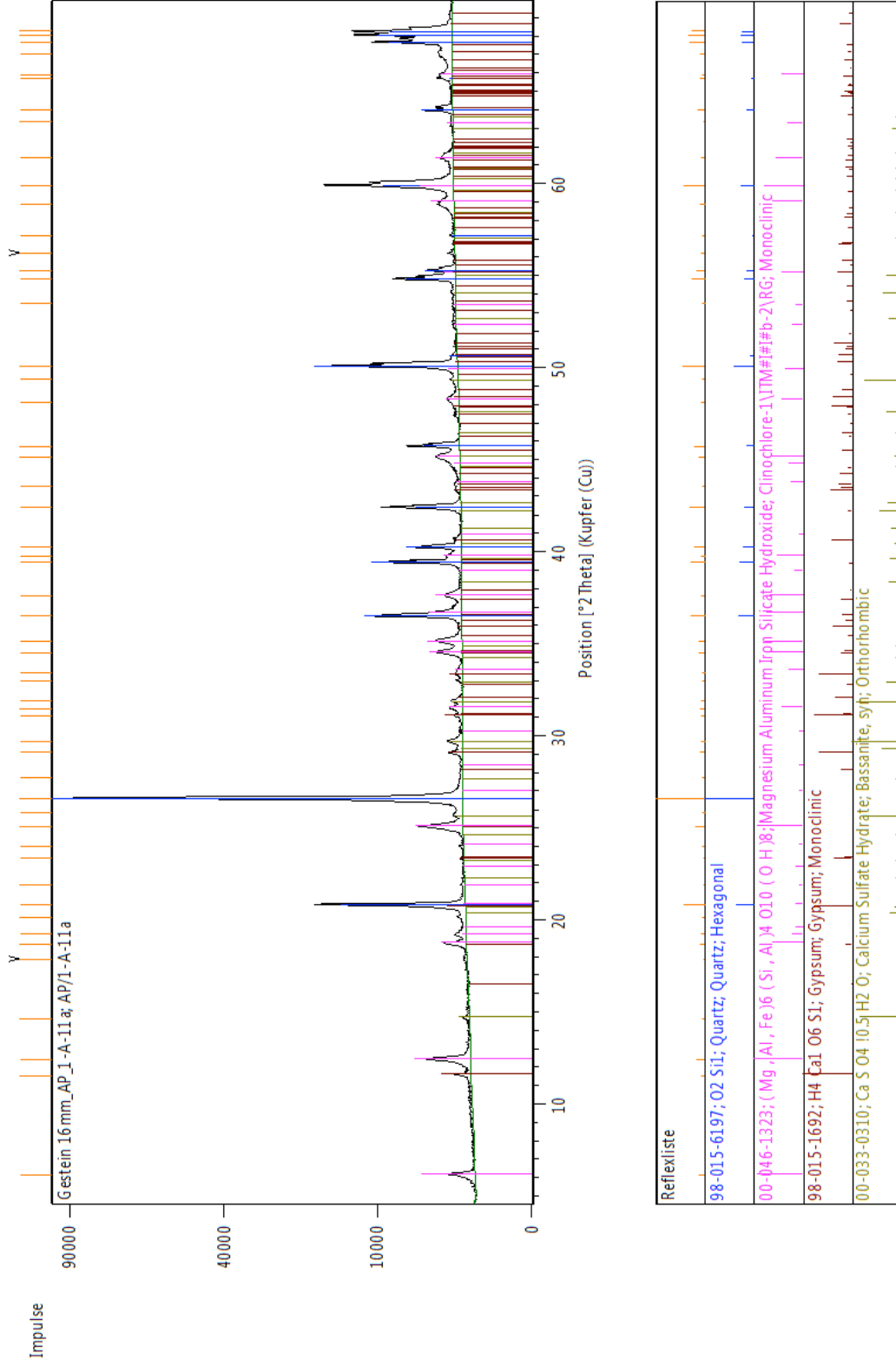
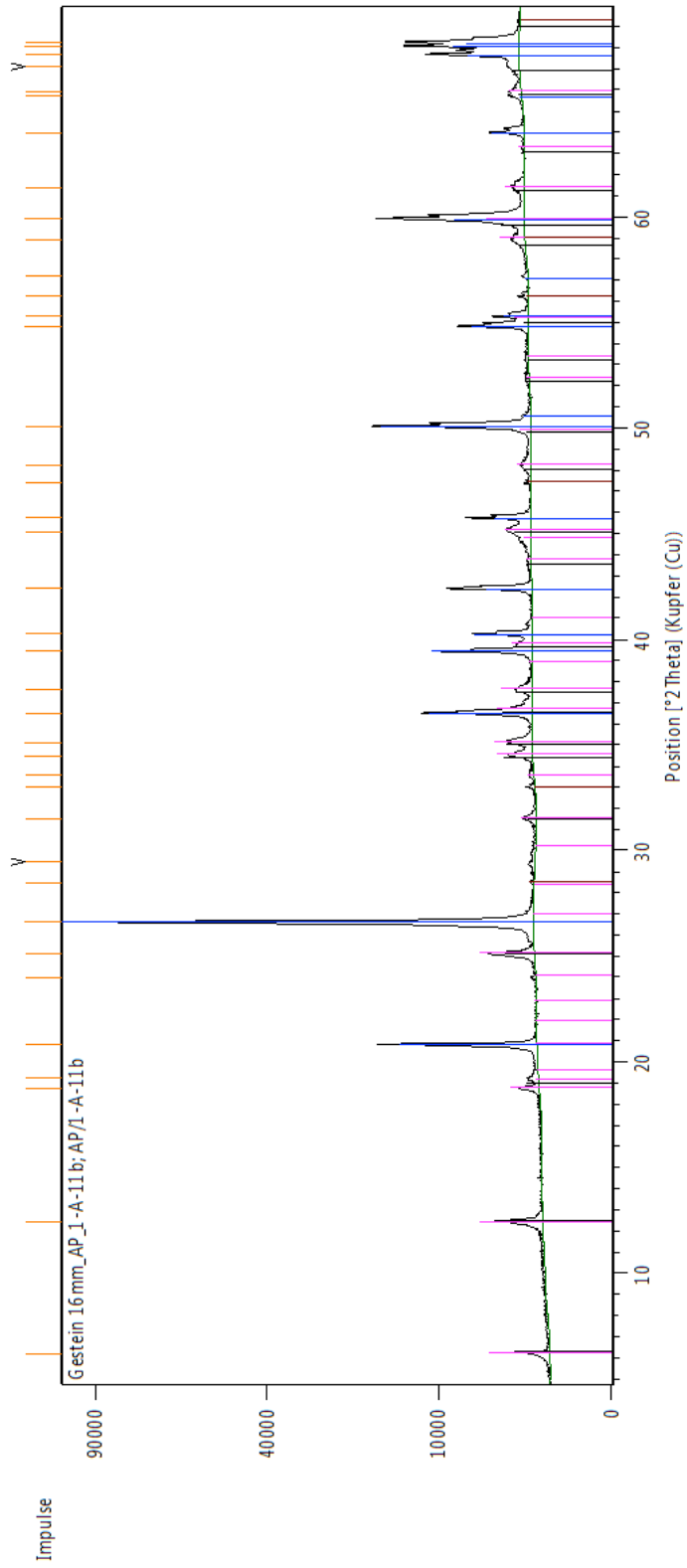


Figure 168 X-Ray diffractogram for sample 11a



Reflexliste
98-015-6196; O2 Si1; Quartz; Quartz; Hexagonal
00-046-1323; (Mg, Al, Fe)6 (Si, Al)4 O10 (OH)8; Magnesium Aluminum Iron Silicate Hydroxide; Clinoclhire-1\ITM#\#b-2\RG; Monoclinic
98-007-6189; Fe0.224 Si Zn0.776; Sphalerite, ferroan; Sphalerite, ferroan; Cubic

Figure 169 X-Ray diffractogram for sample 11b

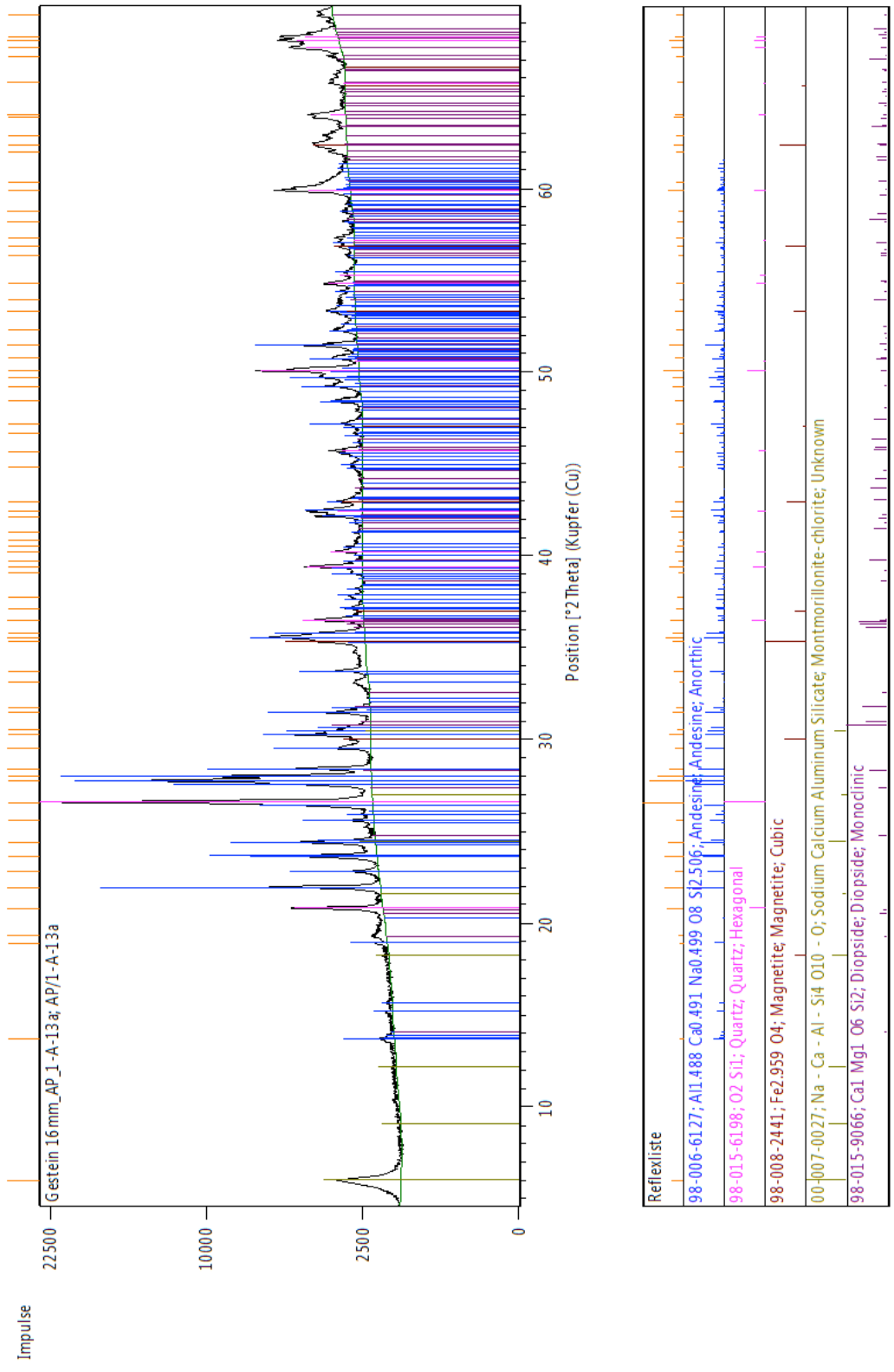


Figure 170 X-Ray diffractogram for sample 13a

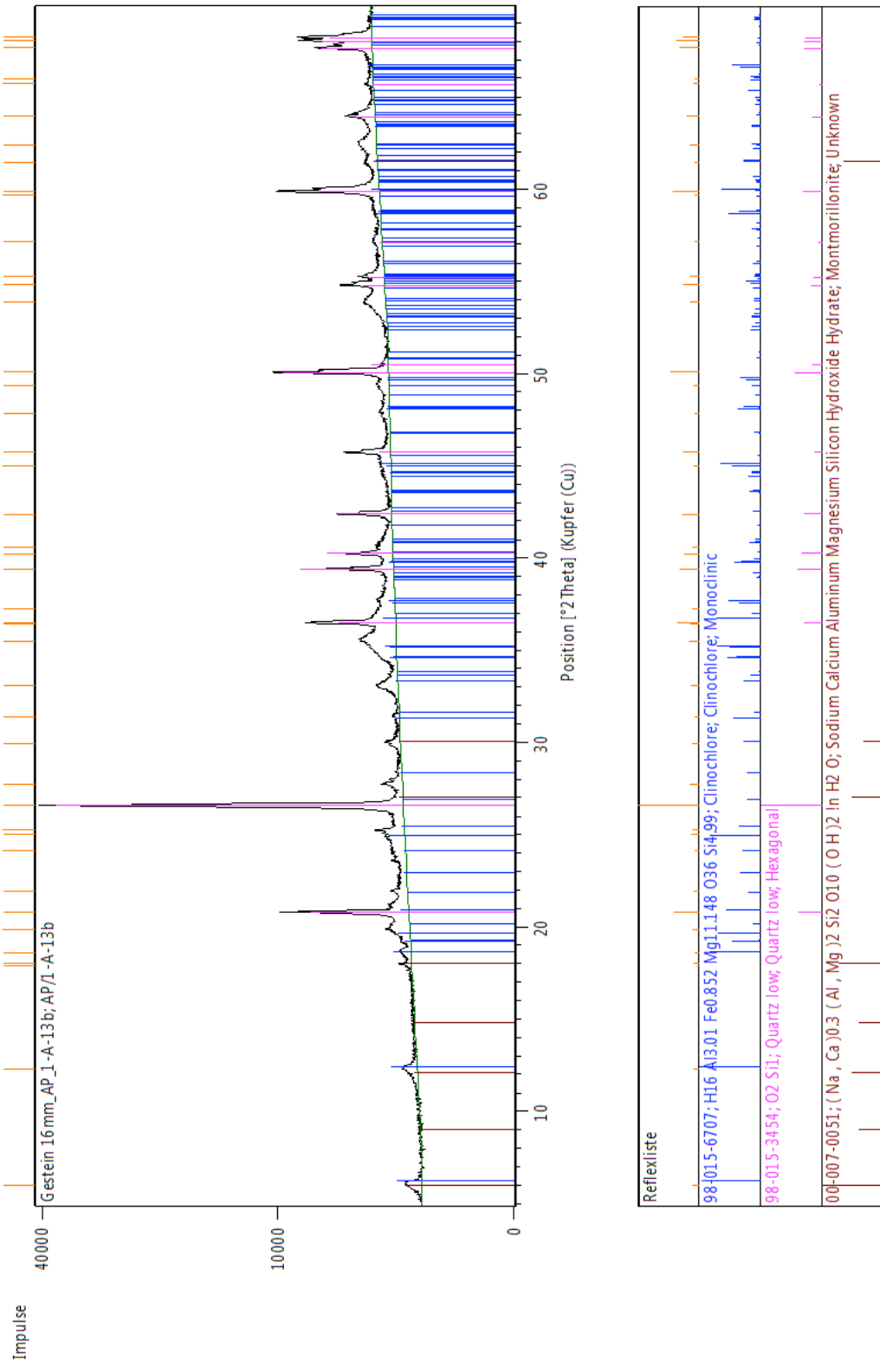


Figure 171 X-Ray diffractogram for sample 13b

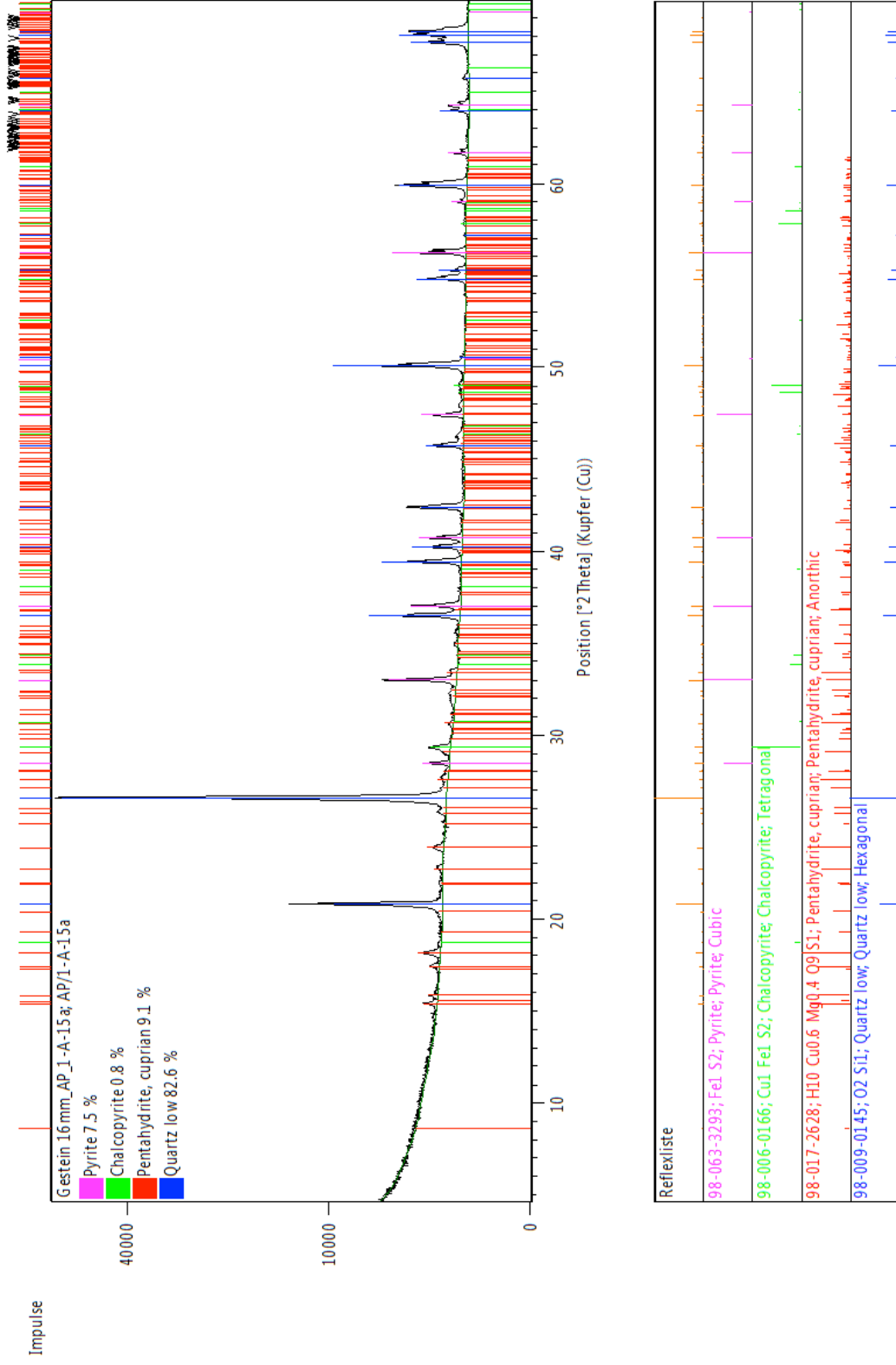


Figure 172 X-Ray diffractogram for sample 15a

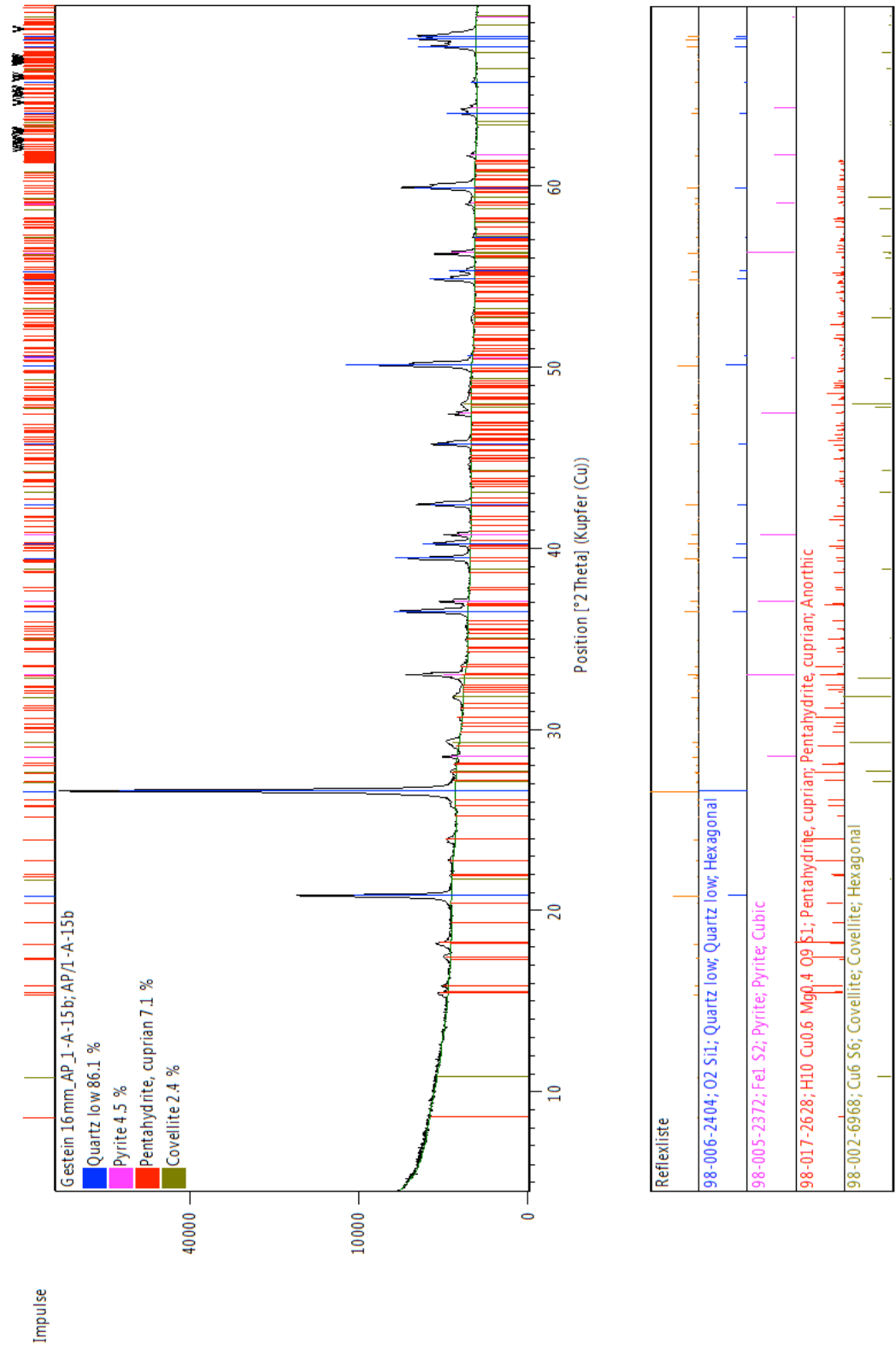


Figure 173 X-Ray diffractogram for sample 15b

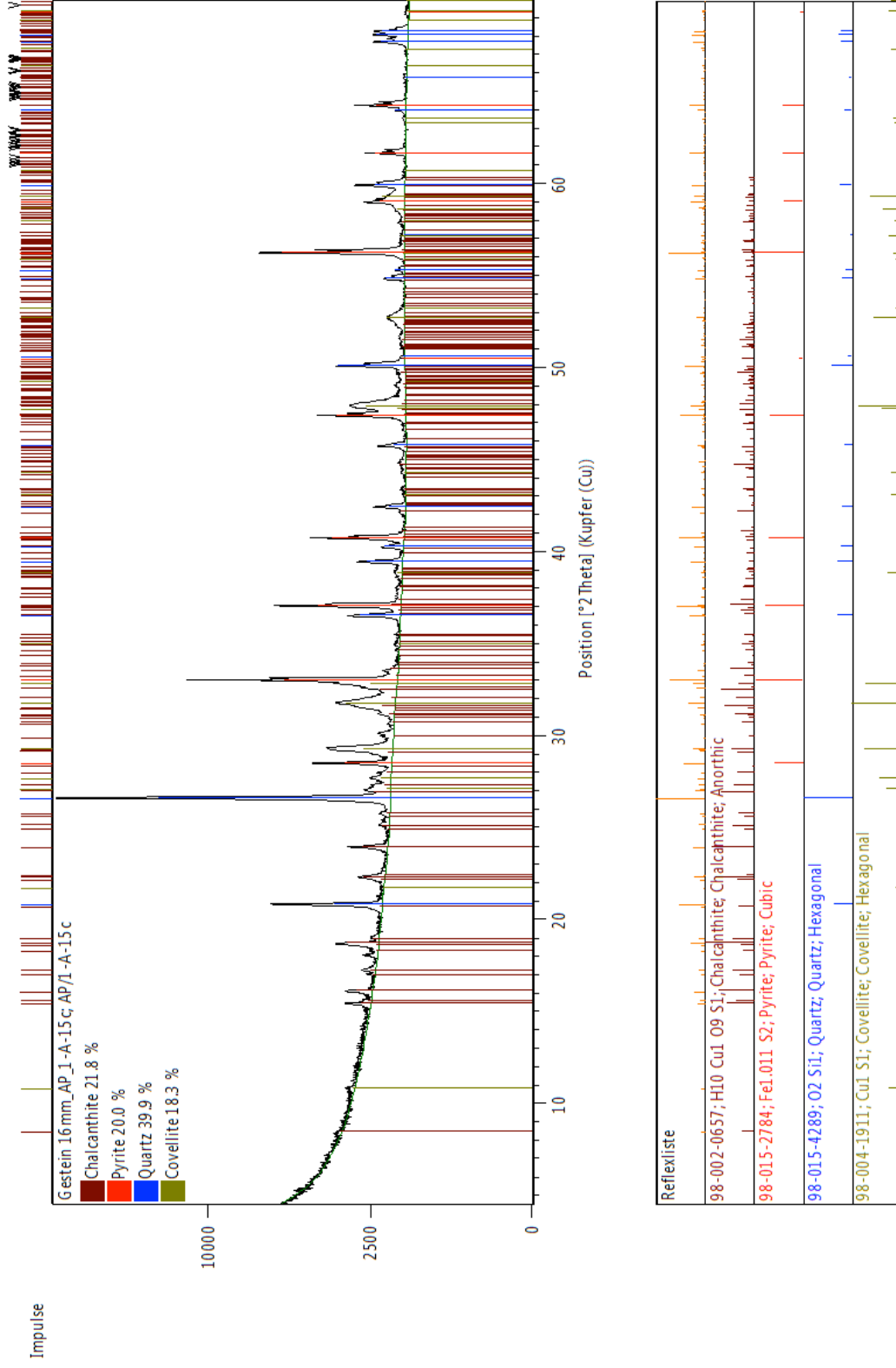









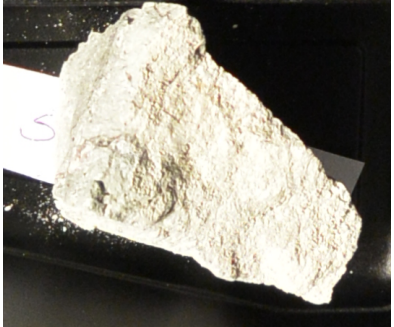







Figure 174 X-Ray diffractogram for sample 15c

10.6 Three Hills mine sample description and location of sampling

Table 50 Skouriotissa - Three Hills mine samples, including a description, the coordinates of sampling in March 2018 and a lab photo of the sample.

Sample	Description	Sampling Coordinate	Photo
<i>Sko1_B_1a</i>	<i>Hematite</i>	N 35° 5.359, E 32° 53.945'	
<i>Sko1_B_1b</i>	<i>Light grey, weathered</i>	N 35° 5.362, E 32° 53.942'	
<i>Sko1_B_1c</i>	<i>Brownish</i>	N 35° 5.364, E 32° 53.944'	
<i>Sko1_B_2a</i>	<i>Brownish</i>	N 35° 5.368, E 32° 53.944'	
<i>Sko1_B_2b</i>	<i>Yellow brownish</i>	N 35° 5.367, E 32° 53.943'	

Sample	Description	Sampling Coordinate	Photo
<i>Sko1_B_2c</i>	<i>Dark brown</i>	N 35° 5.365, E 32° 53.946'	
<i>Sko1_B_3a</i>	<i>Sand colored</i>	N 35° 5.371, E 32° 53.928'	
<i>Sko1_B_3b</i>	<i>Brownish</i>	N 35° 5.369, E 32° 53.931'	
<i>Sko1_B_3c</i>	<i>Dark grey</i>	N 35° 5.367, E 32° 53.929'	
<i>Sko1_B_4a</i>	<i>Very light grey</i>	N 35° 5.381, E 32° 53.926'	
<i>Sko1_B_4b</i>	<i>Dark brown</i>	N 35° 5.381 E 32° 53.927'	

Sample	Description	Sampling Coordinate	Photo
<i>Sko1_B_4c</i>	<i>Yellow brownish</i>	N 35° 5.381, E 32° 53.928'	
<i>Sko1_B_5a</i>	<i>White</i>	N 35° 5.388, E 32° 53.923'	
<i>Sko1_B_5b</i>	<i>Dark brown</i>	N 35° 5.390, E 32° 53.925'	
<i>Sko1_B_5c</i>	<i>Grey</i>	N 35° 5.388, E 32° 53.925'	

10.7 Geochemical analysis of Three Hills mine samples

Table 51 Main geological components for the Three Hills mine field samples in [wt.%] with sampling location.

Sample	Sample position	SiO ₂ [wt%]	Al ₂ O ₃ [wt%]	Fe ₂ O ₃ [wt%]	MgO [wt%]	CaO [wt%]	Na ₂ O [wt%]	K ₂ O [wt%]	TiO ₂ [wt%]	P ₂ O ₅ [wt%]	MnO [wt%]	Cr ₂ O ₃ [wt%]	Cu [wt%]
	Detection limit	0.01	0.01	0.04	0.01	0.01	0.01	0.01	0.01	0.01	0.01	0.002	0.0005
1a	N 35° 5.359, E 32° 53.945'	67.60	1.66	21.28	0.64	0.55	0.02	<0.01	0.03	0.01	0.09	0.005	0.2147
1b	N 35° 5.362, E 32° 53.942'	51.38	12.91	18.26	7.09	1.26	0.18	0.06	0.41	0.03	0.42	0.056	0.4334
1c	N 35° 5.364, E 32° 53.944'	34.13	17.66	23.77	5.40	5.30	0.12	0.14	0.52	0.04	0.37	0.067	>1.00
2a	N 35° 5.368, E 32° 53.944'	59.03	13.95	13.11	4.11	0.47	0.64	0.07	0.43	0.01	0.34	0.052	0.0838
2b	N 35° 5.367, E 32° 53.943'	63.71	11.87	11.96	3.60	0.51	0.49	0.05	0.38	0.02	0.33	0.052	>1.00
2c	N 35° 5.365, E 32° 53.946'	52.59	12.78	17.69	5.28	0.64	0.29	0.08	0.39	0.01	0.41	0.052	0.1587
3a	N 35° 5.371, E 32° 53.928'	59.87	13.35	12.10	4.78	0.27	3.08	0.07	0.40	<0.01	0.99	0.058	0.0183
3b	N 35° 5.369, E 32° 53.931'	70.30	10.35	8.46	3.79	0.30	2.25	0.07	0.32	0.02	0.76	0.041	0.0388
3c	N 35° 5.367, E 32° 53.929'	63.08	12.51	10.87	3.89	0.26	3.53	0.01	0.39	<0.01	0.92	0.052	0.0129
4a	N 35° 5.381, E 32° 53.926'	62.37	12.24	8.86	7.20	0.25	2.24	0.02	0.38	0.01	1.46	0.049	0.0301
4b	N 35° 5.381 E 32° 53.927'	56.39	12.04	16.46	6.13	0.22	0.27	0.10	0.37	0.02	0.74	0.053	0.0495
4c	N 35° 5.381, E 32° 53.928'	59.51	12.34	13.34	6.54	0.22	1.38	0.06	0.38	<0.01	0.61	0.056	0.1229
5a	N 35° 5.388, E 32° 53.923'	61.34	14.56	8.78	5.26	0.30	3.92	0.06	0.44	0.03	0.47	0.048	0.0111
5b	N 35° 5.390, E 32° 53.925'	56.39	12.69	14.00	7.28	0.16	0.78	0.19	0.41	0.06	0.59	0.044	0.0874
5c	N 35° 5.388, E 32° 53.925'	62.27	12.61	9.24	6.61	0.27	2.68	0.02	0.36	0.02	0.69	0.036	0.0106

10.8 HySpex field data acquisition settings for Apliki and Three Hills

Table 52 HySpex data acquisition parameters for Apliki mine.

HySpex settings		
<i>Sensor position</i>	Latitude	Longitude
	35° 4' 35,49" N	32° 50' 33,666" E
<i>Atmospheric conditions</i>	Sahara dust in atmosphere, occasionally cirrus clouds (max. 20% coverage)	
<i>Start time of measurement</i>	13:46 UTC+3	
<i>No. of measurements averaged</i>	11	
<i>Approximated solar azimuth angle</i>	200°	
<i>Approximated sun elevation angle</i>	52°	
<i>Distance, sample to sensor</i>	1 m	
<i>Lense objective</i>	FOV expander	
<i>Wavelength range</i>	414 to 2498 nm	
<i>SNR mode (frames to average)</i>	1	
	VNIR (1600 px)	SWIR (320 px)
<i>FOV</i>	34°	28°
<i>Sampling interval</i>	3.7	6.25
<i>Radiometric resolution</i>	12 bit	14 bit
<i>Frames</i>	12000	3013
<i>Integration time [μs]</i>	4000	6000
<i>Frame period [μs]</i>	10000	47808
<i>Data size radiance BSQ file / Header file</i>	6.1 GB/ 2.6 kB	495.6 MB/ 4.0 kB
<i>Data size: BSQ file/ Header file</i>	1.6 GB / 22.3 kB	

Table 53 HySpex data acquisition parameters for Three Hills mine.

HySpex settings		
<i>Sensor position</i>	Latitude	Longitude
	35° 05' 23.58" N	32° 54' 01.34"E
<i>Atmospheric conditions</i>	Sahara dust in atmosphere, occasional cirrus clouds (max. 10% coverage)	
<i>Start time of measurement</i>	13:46 UTC+3	
<i>Approximated solar azimuth angle</i>	143°	
<i>Approximated sun elevation angle</i>	47°	
<i>Distance, sample to sensor, approximately</i>	100 - 200m	
<i>Lens objective</i>	FOV expander	
<i>Wavelength range</i>	414 to 2498nm	
<i>SNR mode (frames to average)</i>	4	
	VNIR (1600px)	SWIR (320px)
<i>FOV</i>	34°	28°
<i>Sampling interval</i>	3.7	6.25
<i>Radiometric resolution</i>	12 bit	14 bit
<i>Frames</i>	10000	2511
<i>Integration time [μs]</i>	3000	6000
<i>Frame period [μs]</i>	9000	35856
<i>Data size radiance BSQ file</i>	5.1GB	413MB
<i>Data size: reflectance BSQ file/ Header file</i>	1.3 GB / 29.4kB	

10.9 3D reconstruction parameters for Apliki and Three Hills

Table 54 3D reconstruction parameters for the Apliki DOMs with Agisoft Professional PhotoScan Software

	Full Open Pit	Mine Face Close-Up
	Nikon 1AW1 + HySpex RGB	Nikon 1AW1 + HySpex RGB
<i>General</i>		
<i>Aligned Cameras/ Total Cameras</i>	118	98/98
<i>Nikon 1 AW1 Cameras</i>	117	97
<i>HySpex RGB</i>	1	1
<i>Point Cloud</i>		
<i>Points</i>	4,007 of 9,159	3,072 of 6,833
<i>RMS projection error</i>	0.122611 (0.745662 pix)	0.119667 (0.760139 pix)
<i>Max projection error</i>	0.524674 (16.0471 pix)	0.650378 (13.1985 pix)
<i>Mean key point size</i>	5.72367 pix	5.56145 pix
<i>Effective overlap</i>	16.9367	19.2295
<i>Accuracy/ Pair pre-selection</i>	Medium/ Disabled	Medium/ Disabled
<i>Key point limit/ tie point limit</i>	4,000 / 1,000	4,000 / 1,000
<i>Adaptive camera fitting</i>	Yes	Yes
<i>Matching time</i>	5 min 32 sec	3 min 38 sec
<i>Alignment time</i>	1 min 9 sec	52 sec
<i>Dense Point Cloud</i>		
<i>Points</i>	7,566,533	5,779,009
<i>Quality</i>	Medium	Medium
<i>Depth filtering</i>	Mild	Mild
<i>Depth map generation time</i>	30 min 51 sec	36 min 7 sec
<i>Dense cloud generation time</i>	30 min 51 sec	12 min 53 sec
<i>Model</i>		
<i>Faces</i>	168,145	128,421
<i>Vertices</i>	86,275	65,514
<i>Surface Type</i>	Arbitrary	Arbitrary
<i>Source Data</i>	Dense	Dense
<i>Interpolation</i>	Enabled	Enabled
<i>Quality</i>	Medium	Medium
<i>Depth filtering</i>	Mild	Mild
<i>Face count</i>	168,145	128,421
<i>Processing time</i>	9 min 54 sec	7 min 10 sec
<i>Mapping mode</i>	Orthophoto	Orthophoto
<i>Blending mode</i>	Mosaic	Mosaic
<i>Texture size/ count</i>	4,096 x 4,096	4,096 x 4096
<i>Enable color correction</i>	Yes	Yes
<i>Enable hole filling</i>	Yes	Yes
<i>Blending time</i>		14 min 59 sec
<i>Tiled Model</i>		
<i>Source data</i>	Dense cloud	Dense cloud
<i>Tile size</i>	256	256
<i>Processing time</i>	32 min 21 sec	20 min 44 sec
<i>Pixel size</i>	0.0258 m	0.0258 m

Table 55 3D reconstruction parameters for the Three Hills DOM with Agisoft Professional PhotoScan Software

Skouriotissa Three Hills - Open Pit			
	Nikon 1AW1 + HySpex RGB		
<i>General</i>		Model	
<i>Aligned Cameras</i>	185	Faces	133,117
<i>Nikon 1 AW1 Cameras</i>	184	Vertices	68,695
<i>HySpex RGB</i>	1	Surface Type	Arbitrary
<i>Markers</i>	28	Source Data	Dense
		Interpolation	Enabled
<i>Point Cloud</i>		Quality	Medium
<i>Points</i>	10,839 of 19,447	Depth filtering	Mild
<i>RMS projection error</i>	0.643958 (4.7003 pix)	Face count	133,118
<i>Max projection error</i>	83.2283 (556.025 pix)	Processing time	7 min 41 sec
<i>Mean key point size</i>	5.16612 pix	Mapping mode	Orthophoto
<i>Effective overlap</i>	10.6046	Blending mode	Mosaic
<i>Accuracy/ Pair pre-selection</i>	Medium/ Disabled	Texture size/ count	4,096 x 4,096
<i>Key point limit/ tie point limit</i>	4,000 / 1,000	Enable color correction	Yes
<i>Adaptive camera fitting</i>	Yes	Enable hole filling	Yes
<i>Matching time</i>	10 min 0 sec	Blending time	14min 7 sec
<i>Alignment time</i>	2 min 55 sec		
		Tiled Model	
<i>Dense Point Cloud</i>		Source data	Dense cloud
<i>Points</i>	5,990,609	Tile size	256
<i>Quality</i>	Medium	Processing time	46 min 39 sec
<i>Depth filtering</i>	Mild	Pixel size	0.0231 m
<i>Depth map generation time</i>	1 h 29 min		
<i>Dense cloud generation time</i>	47 min 32 sec		

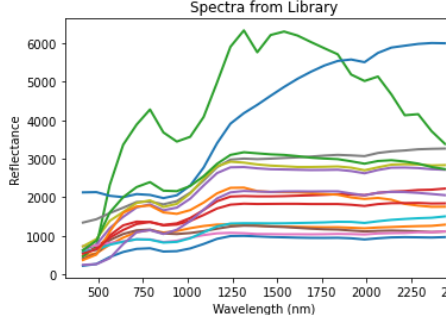
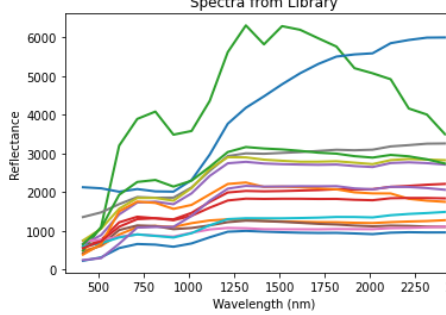
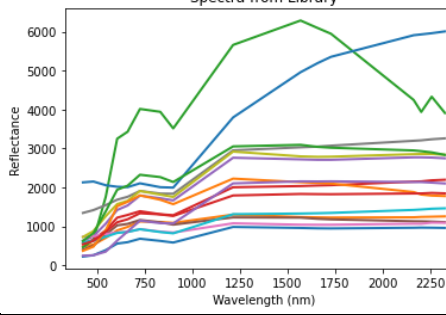
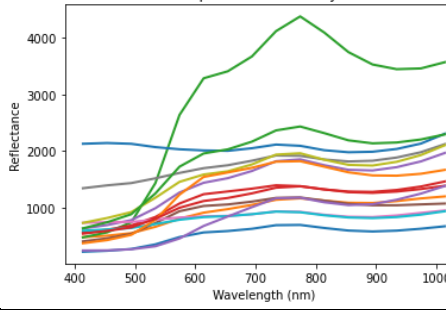
10.10 Downsampling of data from hyperspectral to superspectral dimensions

Table 56 Downsampling approaches of the Brazilian iron ore samples.

Sensor / band width [nm]	Wavelength range [nm]	Number of bands	Spectral Library of Brazilian Ore samples	Analysis method for testing
1	414-2497	2084		SAM, SVM, MWL
5	414-2494	417		SAM, SVM, MWL, EngeoMap 2.1, BFF
EnMAP	423-2493	242		SAM, SVM, MWL
10	414-2494	209		SAM, SVM, MWL, EngeoMap 2.1, BFF

Sensor / band width [nm]	Wavelength range [nm]	Number of bands	Spectral Library of Brazilian Ore samples	Analysis method for testing
15	414-2484	139	<p>The graph displays multiple spectral curves for 139 different ore samples. The x-axis represents Wavelength (nm) from 500 to 2500, and the y-axis represents Reflectance from 0 to 6000. The curves show various absorption features, with a prominent peak around 1300-1400 nm and another around 2100 nm.</p>	SAM, SVM, MWL, EngeoMap 2.1, BFF
20	414-2494	105	<p>The graph displays multiple spectral curves for 105 different ore samples. The x-axis represents Wavelength (nm) from 500 to 2500, and the y-axis represents Reflectance from 0 to 6000. The curves show various absorption features, with a prominent peak around 1300-1400 nm and another around 2100 nm.</p>	SAM, SVM, MWL, EngeoMap 2.1, BFF
15, 1314 – 2004nm clipped	414 - 2484	94	<p>The graph displays multiple spectral curves for 94 different ore samples. The x-axis represents Wavelength (nm) from 500 to 2500, and the y-axis represents Reflectance from 0 to 6000. The curves show various absorption features, with a prominent peak around 1300-1400 nm and another around 2100 nm. The region between 1314 nm and 2004 nm is clipped.</p>	SAM, EngeoMap 2.1, BFF
25	414-2489	84	<p>The graph displays multiple spectral curves for 84 different ore samples. The x-axis represents Wavelength (nm) from 500 to 2500, and the y-axis represents Reflectance from 0 to 6000. The curves show various absorption features, with a prominent peak around 1300-1400 nm and another around 2100 nm.</p>	SAM, SVM, MWL, EngeoMap 2.1, BFF
30	414-2484	70	<p>The graph displays multiple spectral curves for 70 different ore samples. The x-axis represents Wavelength (nm) from 500 to 2500, and the y-axis represents Reflectance from 0 to 6000. The curves show various absorption features, with a prominent peak around 1300-1400 nm and another around 2100 nm.</p>	SAM, EngeoMap 2.1, BFF

Sensor / band width [nm]	Wavelength range [nm]	Number of bands	Spectral Library of Brazilian Ore samples	Analysis method for testing
40nm VNIR, 15nm SWIR, 1314 – 2004 nm clipped	414 – 2484	57		SAM, EngeoMap 2.1, BFF
40	414-2494	53		SAM, SVM, MWL, EngeoMap 2.1, BFF
50	414-2464	42		SAM, SVM, MWL, EngeoMap 2.1, BFF
15nm VNIR only	414 – 1014	41		SAM, BFF, (EnGeoMap 2.1 was tested but was unable to give results)
40nm, 1334 – 2004nm clipped	414 – 2494	37		SAM, EngeoMap 2.1, BFF

Sensor / band width [nm]	Wavelength range [nm]	Number of bands	Spectral Library of Brazilian Ore samples	Analysis method for testing
75	414-2439	28	 <p>The graph displays multiple spectral curves for various Brazilian ore samples. The x-axis represents Wavelength (nm) from 500 to 2500, and the y-axis represents Reflectance from 0 to 6000. The curves show varying reflectance levels across the spectrum, with a notable peak around 1500 nm.</p>	SAM, SVM, MWL, EngeoMap 2.1, BFF
100	414-2414	21	 <p>The graph displays multiple spectral curves for various Brazilian ore samples. The x-axis represents Wavelength (nm) from 500 to 2500, and the y-axis represents Reflectance from 0 to 6000. The curves show varying reflectance levels across the spectrum, with a notable peak around 1500 nm.</p>	SAM, SVM, MWL, EngeoMap 2.1, BFF
WorldView -3	425-2330	16	 <p>The graph displays multiple spectral curves for various Brazilian ore samples. The x-axis represents Wavelength (nm) from 500 to 2500, and the y-axis represents Reflectance from 0 to 6000. The curves show varying reflectance levels across the spectrum, with a notable peak around 1500 nm.</p>	SAM, SVM, MWL, EngeoMap 2.1, BFF
40nm VNIR only	414 – 1014	16	 <p>The graph displays multiple spectral curves for various Brazilian ore samples. The x-axis represents Wavelength (nm) from 400 to 1000, and the y-axis represents Reflectance from 0 to 4000. The curves show varying reflectance levels across the visible and near-infrared spectrum, with a notable peak around 800 nm.</p>	SAM, BFF, (EnGeoMap 2.1 was tested but was unable to give results)

10.11 Spectral Features in the VNIR and SWIR

Table 58 and Table 59 lists the most common silicate and non-silicate minerals relevant to hydrothermal deposits with their VNIR and SWIR response (Krupnik and Khan, 2019).

Table 58 VNIR and SWIR response of common silicate minerals after Krupnik and Khan (2019). Absorption bands within the range of atmospheric absorptions (1300–1500nm and 1750–2000nm) are not included. Absorption features from additional literature centered on open pit mining where added and are explicitly referenced in the table.

Mineral structure/type	Mineral group	Example	VNIR response	VNIR feature location(s) [nm]	SWIR response	SWIR feature location(s) [nm]
Iono-silicates	Amphibole	Actinolithe	Non-diagnostic	N/A	Good	2315, 2390; 2330, 2390 (Lypaczewski <i>et al.</i> , 2020)
	Pyroxene	Diopside	Good	655	Moderate	1055, 2310
Cyclo-silicates	Tourmaline	Elbaitte	Non-diagnostic	N/A	Good	2175, 2205, 2255, 2305
	Tourmaline (Lypaczewski <i>et al.</i> , 2020)		Non-diagnostic	N/A		2205, 2245, Slope 100/1180
Neso-silicates	Garnet	Grossular	Moderate	Weak ≈440	Moderate	2200 and 2400
	Olivine	Fosterite	Non-diagnostic	N/A	Good	1000-1010
Soro-silicates	Epidote	Epidote	Non-diagnostic	N/A	Good	2255, 2335; 1540, 2250 (Lypaczewski <i>et al.</i> , 2020)
		Muscovite	Non-Diagnostic	N/A	Good	2200, 2350
Phyllo-silicates	Mica	Muscovite, coarse grained (Lypaczewski <i>et al.</i> , 2020)	Non-Diagnostic	N/A	Good	2125, 2200
		Phengite	Non-Diagnostic	N/A	Good	2220, 2350; ≈2225 (Dalm, Buxton and van Ruitenbeek, 2017)
	Chlorite	Fe-chlorite	Non-Diagnostic	N/A	Good	2260, 2360
		Mg-chlorite	Non-Diagnostic	N/A	Good	2245, 2325
	Chlorite (Lypaczewski <i>et al.</i> , 2020)		Non-Diagnostic	N/A	Good	2000, 2250

Mineral structure/type	Mineral group	Example	VNIR response	VNIR feature location(s) [nm]	SWIR response	SWIR feature location(s) [nm]
		Chlorite (Murphy et al., 2015)	Non-Diagnostic	N/A	Good	Broad 2319
	Clay minerals	Illite	Non-Diagnostic	N/A	Good	2200–2220, 2350
		Illite-smectites (Murphy et al., 2015)	Non-Diagnostic	N/A	Good	Main: 2208, weak ≈2235
		Kaolinite	Non-Diagnostic	N/A	Good	2160, 2205
		Kaolinite (Murphy et al., 2015)	Non-Diagnostic	N/A	Good	doublet around 2196 or 2202
		Kaolinite (Lypaczewski et al., 2020)	Non-Diagnostic	N/A	Good	2160
		Montmorillonite	Non-Diagnostic	N/A	Good	1467nm (Lypaczewski et al., 2020)
	"Ferruginous smectite" (Murphy et al., 2015)	-	Non-Diagnostic	N/A	Good	2288, 2233 (Murphy et al., 2015)
		Nontronite (Murphy et al., 2015)	Non-Diagnostic	N/A	Good	Single feature, 2282–2288
Tecto-silicates	Feldspar	Albite, Orthoclase	Non-Diagnostic	N/A	Non-Diagnostic	N/A
	Silica	Quartz	Non-Diagnostic	N/A	Non-Diagnostic	N/A

Table 59 VNIR and SWIR response of common non-silicate minerals after Krupnik and Khan (2019). Absorption bands in within the range of atmospheric absorptions (1300–1500nm and 1750–2000nm) are not included. Absorption features from additional literature centered on open pit mining where added and are explicitly referenced in the table.

Mineral Group	Example	VNIR response	VNIR feature location(s) [nm]	SWIR response	SWIR feature location(s) [nm]
Carbonates	Calcite	Non-Diagnostic	N/A	Good	2282, 2340; ≈2340 (Lorenz <i>et al.</i> , 2018)
	Dolomite	Non-Diagnostic	N/A	Good	2315–2320; 2320 (Lorenz <i>et al.</i> , 2018)
	Dolomite + Tremolite	Non-Diagnostic	N/A	Good	≈2315 (Lorenz <i>et al.</i> , 2018)
Hydroxide	Gibbsite	Non-Diagnostic	N/A	Good	2270
	Goethite	Good	≈500, 650, & 1000 (Clark, 2003a)	Non-Diagnostic	N/A
Sulfates	Alunite	Moderate	Weak ≈500	Good	2165, 2316
	Jarosite	Moderate	Weak ≈440	Good	2268
	Gypsum	Non-Diagnostic	N/A	Good	1450, 1750, 1950, 2220 (Moreira, Teixeira and Galvão, 2014); 2170, 2210, 2260
Phosphates	Apatite	Moderate	≈754	Non-Diagnostic	N/A
Oxides	Hematite	Good	650, 860; ≈500 & 900 (Clark, 2003a)	Non-Diagnostic	N/A
	Pyrite	Non-Diagnostic	N/A	Non-Diagnostic	N/A
Sulfides	Chalcopyrite	Non-Diagnostic	N/A	Non-Diagnostic	N/A
	Bornite	Moderate	Weak ≈600	Non-Diagnostic	N/A

Non - Silicates

10.12 Geochemical clustering of Apliki sample data

To compare the data, some geochemical results had to be adjusted to be comparable. This only applies to element or oxide mass fractions yielding below or above the detection limit and therefore being denoted with “<” or “>” values. The geochemical values were adapted as seen in Table 60.

Table 60 Adaptation of the element and oxide geochemical values that could not clearly be denoted as they were below or above the detection limit.

Element or Oxide	Detection Limit	Notation	Adaptation for geochemical clustering
Na ₂ O	0.01 %	< 0.01	0
K ₂ O	0.01 %	< 0.01	0
TiO ₂	0.01 %	< 0.01	0
P ₂ O ₅	0.01 %	< 0.01	0
Cr ₂ O ₃	0.002 %	< 0.002	0
Cu	5 - 10000 ppm	> 10000	10000
Ba	5 ppm	< 5	0
Ni	20 ppm	< 20	0
Co	20 ppm	< 20	0
Sr	2 ppm	< 2	0
Zr	5 ppm	< 5	0
Y	3 ppm	< 3	0
Nb	5 ppm	< 5	0
Ce	30 ppm	<30	0